AD-A246 343

AGARD-AG-319

AGARD-AG-319

AGARD

ADVISORY GROUP FOR AEROSPACE RESEARCH & DEVELOPMENT
7 RUE ANCELLE 92200 NEUILLY SUR SEINE FRANCE

AGARDograph 319

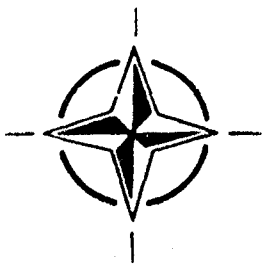
Design and Testing of High-Performance Parachutes

(La Conception et les Essais des Parachutes à Hautes Performances)

DTIC
ELECTE
FEB 13 1992
S B D

DISTRIBUTION STATEMENT A
Approved for public release;
Distribution Unlimited

This AGARDograph has been produced at the request of the Fluid Dynamics Panel of AGARD.



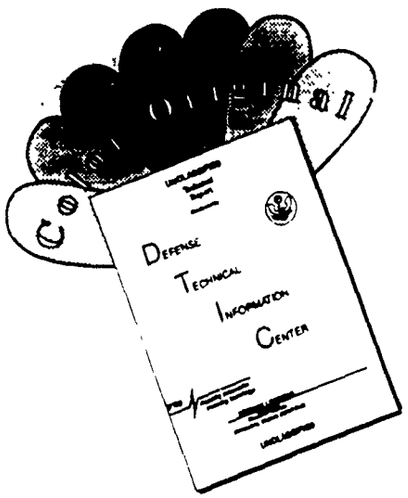
NORTH ATLANTIC TREATY ORGANIZATION

Best Available Copy

Published November 1991

Distribution and Availability on Back Cover

DISCLAIMER NOTICE



THIS DOCUMENT IS BEST QUALITY AVAILABLE. THE COPY FURNISHED TO DTIC CONTAINED A SIGNIFICANT NUMBER OF COLOR PAGES WHICH DO NOT REPRODUCE LEGIBLY ON BLACK AND WHITE MICROFICHE.

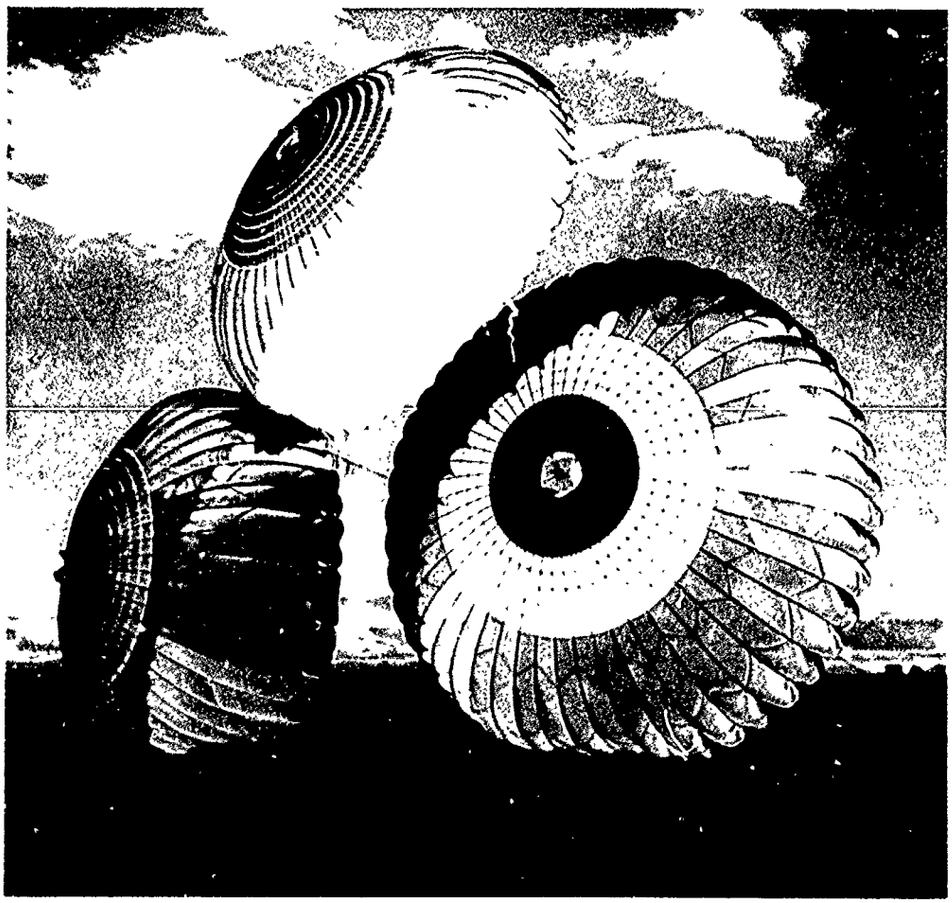
AGARDograph 319

Design and Testing of High-Performance Parachutes

(La Conception et les Essais des Parachutes à Hautes Performances)

92-03510

92 2 11 132



Prototype of F-111 Crew Escape Module parachute system

AGARD
ADVISORY GROUP FOR AEROSPACE RESEARCH & DEVELOPMENT
7 RUE ANCELLE 92200 NEUILLY SUR SEINE FRANCE

AGARDograph 319

Design and Testing of High-Performance Parachutes

(La Conception et les Essais des
Parachutes à Hautes Performances)

by

R.C. Maydew and **C.W. Peterson**
Sandia National Laboratories
Albuquerque, New Mexico 87185, United States

Edited by

K.J. Orlik-Rückemann
Applied Aerodynamics Laboratory
Institute for Aerospace Research, Government of Canada
Ottawa K1A 0R6, Canada

This AGARDograph has been produced at the request of the
Fluid Dynamics Panel of AGARD



North Atlantic Treaty Organization
Organisation du Traité de l'Atlantique Nord

The Mission of AGARD

According to its Charter, the mission of AGARD is to bring together the leading personalities of the NATO nations in the fields of science and technology relating to aerospace for the following purposes

- Recommending effective ways for the member nations to use their research and development capabilities for the common benefit of the NATO community,
- Providing scientific and technical advice and assistance to the Military Committee in the field of aerospace research and development (with particular regard to its military application),
- Continuously stimulating advances in the aerospace sciences relevant to strengthening the common defence posture,
- Improving the co-operation among member nations in aerospace research and development,
- Exchange of scientific and technical information;
- Providing assistance to member nations for the purpose of increasing their scientific and technical potential,
- Rendering scientific and technical assistance, as requested, to other NATO bodies and to member nations in connection with research and development problems in the aerospace field

The highest authority within AGARD is the National Delegates Board consisting of officially appointed senior representatives from each member nation The mission of AGARD is carried out through the Panels which are composed of experts appointed by the National Delegates, the Consultant and Exchange Programme and the Aerospace Applications Studies Programme The results of AGARD work are reported to the member nations and the NATO Authorities through the AGARD series of publications of which this is one

Participation in AGARD activities is by invitation only and is normally limited to citizens of the NATO nations

The content of this publication has been reproduced
directly from material supplied by AGARD or the authors

Published November 1991

Copyright © AGARD 1991
All Rights Reserved

ISBN 92 835 0649-9

Printed by Specialised Printing Services Limited
40 Chigwell Lane, Loughton, Essex IG10 3TZ

Recent Publications of the Fluid Dynamics Panel

AGARDOGRAPHS (AG)

Experimental Techniques in the Field of Low Density Aerodynamics
AGARD AG-318 (E), April 1991

Techniques Expérimentales Liées à l'Aérodynamique à Basse Densite
AGARD AG-318 (FR), April 1990

A Survey of Measurements and Measuring Techniques in Rapidly Distorted Compressible Turbulent Boundary Layers
AGARD AG-315, May 1989

Reynolds Number Effects in Transonic Flows
AGARD AG-303, December 1988

Three Dimensional Grid Generation for Complex Configurations – Recent Progress
AGARD AG-309, March 1988

REPORTS (R)

Aircraft Dynamics at High Angles of Attack: Experiments and Modelling
AGARD R-776, Special Course Notes, March 1991

Inverse Methods in Airfoil Design for Aeronautical and Turbomachinery Applications
AGARD R 780, Special Course Notes, November 1990

Aerodynamics of Rotorcraft
AGARD R-781, Special Course Notes, November 1990

Three-Dimensional Supersonic/Hypersonic Flows Including Separation
AGARD R-764, Special Course Notes, January 1990

Advances in Cryogenic Wind Tunnel Technology
AGARD R-774, Special Course Notes, November 1989

ADVISORY REPORTS (AR)

Effects of Adverse Weather on Aerodynamics
AGARD AR-306, Technical Evaluation Report, November 1991

Aerodynamics of Combat Aircraft Controls and of Ground Effects
AGARD AR-271, Technical Evaluation Report, July 1991

Appraisal of the Suitability of Turbulence Models in Flow Calculations
AGARD AR-291, Technical Status Review July 1991

Rotary-Balance Testing for Aircraft Dynamics
AGARD AR-265, Report of WG 11, December 1990

CONFERENCE PROCEEDINGS (CP)

Manoeuvring Aerodynamics
AGARD CP-497, November 1991

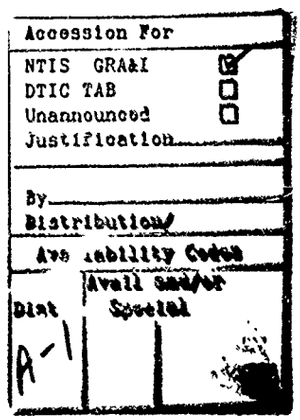
Effects of Adverse Weather on Aerodynamics
AGARD CP-496, November 1991

Vortex Flow Aerodynamics
AGARD CP-494, July 1991

Missile Aerodynamics
AGARD CP-493 October 1990

Aerodynamics of Combat Aircraft Controls and of Ground Effects
AGARD CP-465 April 1990





Computational Methods for Aerodynamic Design (Inverse) and Optimization
AGARD CP-463, March 1990

Applications of Mesh Generation to Complex 3-D Configurations
AGARD CP-464, March 1990

Fluid Dynamics of Three-Dimensional Turbulent Shear Flows and Transition
AGARD CP-438, April 1989

Validation of Computational Fluid Dynamics
AGARD CP-437, December 1988

Aerodynamic Data Accuracy and Quality: Requirements and Capabilities in Wind Tunnel Testing
AGARD CP-429, July 1988

Aerodynamics of Hypersonic Lifting Vehicles
AGARD CP-428, November 1987

Aerodynamic and Related Hydrodynamic Studies Using Water Facilities
AGARD CP-413, June 1987

Applications of Computational Fluid Dynamics in Aeronautics
AGARD CP-412, November 1986

Store Airframe Aerodynamics
AGARD CP-389, August 1986

Unsteady Aerodynamics - Fundamentals and Applications to Aircraft Dynamics
AGARD CP-386, November 1985

Aerodynamics and Acoustics of Propellers
AGARD CP-366, February 1985

Improvement of Aerodynamic Performance through Boundary Layer Control and High Lift Systems
AGARD CP-365, August 1984

Wind Tunnels and Testing Techniques
AGARD CP-348, February 1984

Aerodynamics of Vortical Type Flows in Three Dimensions
AGARD CP-342, July 1983

Missile Aerodynamics
AGARD CP-336, February 1983

Prediction of Aerodynamic Loads on Rotorcraft
AGARD CP-334, September 1982

Wall Interference in Wind Tunnels
AGARD CP-335, September 1982

Fluid Dynamics of Jets with Applications to V/STOL
AGARD CP-308, January 1982

Aerodynamics of Power Plant Installation
AGARD CP-301, September 1981

Computation of Viscous-Inviscid Interactions
AGARD CP-291, February 1981

Subsonic/Transonic Configuration Aerodynamics
AGARD CP-285, September 1980

Turbulent Boundary Layers Experiments, Theory and Modelling
AGARD CP-271, January 1980

Aerodynamic Characteristics of Controls
AGARD CP-262, September 1979

High Angle of Attack Aerodynamics
AGARD CP-247, January 1979

Dynamic Stability Parameters
AGARD CP-235, November 1978

Foreword

ABOUT THE AUTHORS

In Chapter 2 of this AGARDograph, the authors have included brief biographical notes on a few outstanding individuals who have led the development of high-performance parachute technology and its applications. Characteristically enough, they did not include themselves among these major contributors. It is this omission that the Editor feels should be corrected and rectified in this brief foreword.

Both authors are Members of Technical Staff at Sandia National Laboratories, which is one of the lead parachute design laboratories in the United States. Both have been eminently involved in parachute design and testing, the senior author since 1956 and the junior author since 1977.

Randall C. Maydew

After a distinguished service as B-29 Navigator/Bombardier in the Pacific in 1944—45, Randy Maydew received his B.S. and M.S. degrees in Aeronautical Engineering from the University of Colorado, in Boulder. He then spent three years at NACA (NASA) Ames Research Center, performing studies of laminar and turbulent boundary layers at supersonic speeds, before joining Sandia Corporation (now Sandia National Laboratories) in 1952.

As a staff member of the Aerodynamics Department and later as Supervisor of the Experimental Aerodynamics Division, Randy was involved in designing bombs and missiles, conducting wind tunnel tests, and designing and putting into operation new transonic and hypersonic wind tunnels at Sandia.

In 1956, Randy originated research and development on parachutes at Sandia, an activity in which he was to be involved, to various degrees, for the next 30 years and which has resulted in the design of some 200 parachute systems, many having unique, heavy-duty and high-performance characteristics. His staff pioneered the use of Kevlar and the development of computer codes for parachute design; they were also involved in the organization of several courses in the United States and Europe on parachute design. Randy was co-recipient of the Department of Energy 1987 *Weapon Recognition of Excellence Award* for "Development of High-Performance Parachutes for Nuclear Weapons."

From 1965 to 1988, Randy served as Manager of Sandia's Aerodynamics Department, with a staff of 60 to 100 and with the responsibility for aerodynamics research and aerodynamic design of bombs, shells, rockets, ballistic and maneuvering reentry vehicles, guided missiles, parachute systems, and wind turbines. During this time, in addition to his work on parachutes, Randy was personally involved in leading an analysis team that located a missing thermonuclear device off the coast of Spain in 1966, in sophisticated boundary layer transition research, in the first United States studies of vertical-axis wind turbines, and in a number of computational and experimental studies of the aerodynamics and aerothermodynamics of ballistic reentry, and winged vehicles as well as parachute flotation systems.

Randy is an Associate Fellow of the American Institute of Aeronautics and Astronautics (AIAA) and was General Chairman of the 1971 AIAA Aerodynamics Testing Conference. He served as Secretary (1963—64) and President (1969—70) of the Supersonic Tunnel Association, an international organization of some 45 universities, aerospace companies, and government laboratories, which meets semiannually to exchange information on wind-tunnel simulation of flight. He has authored some 75 papers and reports.

Carl W. Peterson

Carl Peterson earned B.S., M.A., and Ph.D. degrees in Aeronautical Engineering from Princeton University, graduating Summa Cum Laude and Phi Beta Kappa. He conducted research in hypersonic viscous wakes, boundary layer flows, and shock wave gas dynamics. He taught gas dynamics for three years before joining Sandia Laboratories in 1969.

As a Member of Technical Staff at Sandia, Carl developed advanced flow-field diagnostic techniques for Sandia's wind tunnels. He designed nozzles and developed electric heaters for Sandia's Hypersonic Wind Tunnels. Carl was promoted to Supervisor of the Experimental Aerodynamics Division at Sandia in 1971. He conducted research in hypersonics, gas dynamic lasers, turbulent boundary layers, and jet/fin interactions. Carl served as Secretary (1974—75) and President (1978) of the Supersonic Tunnel Association (described above).

Beginning in 1977, Carl supervised Sandia's Parachute Systems Division. He initiated and conducted research in parachute aerodynamics. He and his staff are responsible for developing parachute systems for the Department of Defense and NASA as well as for Sandia programs. Carl has authored numerous papers in parachute technology. He served as Chairman of the AIAA Aerodynamic Decelerator and Balloon Technology Technical Committee in 1986 and 1987. Carl was co-recipient of the 1987 United States Department of Energy *Weapon Recognition of Excellence Award* for "Development of High-Performance Parachutes for Nuclear Weapons." He is an Associate Fellow of the AIAA.

Since May 1988, Carl has served as Manager of Sandia's Aerodynamics Department. In addition to parachutes, Carl manages projects and research programs in aerodynamic and thermal analyses of reentry systems, missiles, bombs, shells, and rockets. He oversees the technical aspects of design development, and stockpile maintenance of all United States nuclear weapon parachute systems. Carl is responsible for research and technology development programs in computational aerodynamics and hydrodynamics, as well as for trisonic and hypersonic wind tunnels, range safety at the Tonopah and Kauai test ranges, and organization distributed computers. He has authored some 75 publications in aerodynamics.

The AGARD Fluid Dynamics Panel is fortunate indeed to have two of the world's foremost experts on high-performance parachutes as authors of this much needed AGARDograph.

K.J. Orlick-Ruckemann
AGARD Fluid Dynamics Panel

Avant-Propos

LES AUTEURS

Les auteurs de cette AGARDographie ont pensé inclure au chapitre 2 de l'ouvrage, des résumés bibliographiques concernant certaines personalités exceptionnelles qui ont conduit le développement des technologies des parachutes à hautes performances et leurs applications. Il est a noter que ces auteurs ont volontairement omis de mettre leurs noms a cote de ceux de leurs distingués collaborateurs Par consequent, en tant que Directeur de la publication, j'ai voulu remédier a cette omission par cet avant-propos

Les deux auteurs font partie du personnel technique du Sandia National Laboratories, l'un des premiers laboratoires specialisés dans la conception des parachutes aux Etats-Unis Tous les deux travaillent dans le domaine de l'étude et des essais des parachutes, où leurs contributions sont universellement reconnues, depuis 1956 dans le cas de Randall Maydew, et depuis 1977 dans le cas de Carl Peterson

Randall C. Maydew

Apres une periode de service exemplaire comme navigateur/bombardier au Pacifique de 1944 a 1945, Randy Maydew s'est vu decerne les diplomes de B.S et M S en geme aeronautique de l'Universite de Colorado à Boulder Il a ensuite passe trois ans au NACA (NASA) Ames Research Center, ou il a realise des etudes sur les couches limites turbulentes et laminaires aux vitesses supersoniques, avant d'entre chez la Sandia Corporation (actuellement Sandia National Laboratories) en 1952

En tant que cadre dans la section aérodynamique et par la suite de superviseur de la division de l'aérodynamique experimentale, Randy Maydew a travaille sur la conception de bombes et de missiles, la realisation d'essais en soufflerie, ainsi que sur la conception et la mise en oeuvre des nouvelles soufflleries transsoniques et hypersoniques à Sandia.

En 1956, Randy a lance des travaux de recherche et developpement sur les parachutes, à Sandia, activite qui devait l'occuper, a divers degres pendant les trentes prochaines années, et qui a permis la conception de quelques 200 systemes à parachutes, dont plusieurs sont dotes de caracteristiques uniques de resistance et de hautes performances Sont equipe a ete l'une des premieres à utiliser le Kevlar et l'elaboration de codes machine pour l'etude des parachutes Cette même equipe a egalement organise divers cours sur la conception des parachutes aux Etats-Unis et en Europe. En 1987, Randy a ete nomme co-recipiendaire de la distinction d'excellence dans le domaine de l'armement du United States Department of Energy pour "le developpement de parachutes à hautes performances pour les armes nucléaires"

De 1965 à 1988, il a assure les fonctions de directeur de la section aerodynamique de Sandia, avec un personnel de 60 a 100 effectifs et la responsabilite de la recherche en aérodynamique et de la conception aerodynamique de bombes, d'obus, de roquettes, de vehicules balistiques, de vehicules de rentree manoeuvrants, de missiles guidés, de systemes a parachutes et d'eoliennes Pendant cette periode, en plus des travaux qu'il menait sur les parachutes, il a ete implique personnellement en tant que chef d'une equipe d'experts, qui a reussi a localiser un engin thermonucleaire perdu au large des cotes de l'Espagne en 1966

Il a egalement participe a des travaux de recherche avancees sur la transition de la couche limite et il a fait partie de la premiere equipe americaine a etudier les eoliennes a axe vertical Pendant cette même periode il a participé à bon nombre d'etudes informatiques et experimentales de l'aerodynamique et de l'aerothermodynamique de vehicules balistiques, de vehicules de rentree et de vehicules alaires ainsi que de système de parachute/de flottaison

Randy est membre associe de l'American Institute of Aeronautics and Astronautics (AIAA) et il a preside la "Aerodynamics Testing Conference" organise par l'AIAA en 1971 Il a egalement servi comme secretaire (1963—64) et President (1969—70) de la Supersonic Tunnel Association, que est une organisation internationale regroupant quelques 45 universites, compagnies aerospatiales et laboratoires nationaux et qui siege tous les six mois pour echanger des informations sur la simulation du vol en soufflerie Il est l'auteur de plus de 75 rapports et communications divers

Carl W. Peterson

Carl Peterson a obtenu les diplomes B S E , M A et Ph D de l Universite de Princeton, avec mention Summa Dum Laude et Phi Betta Kappa Il a conduit des travaux de recherche sur les sillages visqueux hypersoniques, les ecoulements des couches limites, la dynamique des ondes de choc et la dynamique des gaz Il a enseigne ces matieres pendant trois ans avant d'entrer chez la Sandia Laboratories

En tant que membre du personnel technique, Carl a participe au developpement des techniques avancees de diagnostic des champs d ecoulement pour les soufflleries de Sandia Il a etudie des tuyeres et a developpe des rechauffeurs pour les soufflleries hypersoniques Carl fut promu superviseur de la division d'aerodynamique experimentale de Sandia en 1971 Il a conduit des travaux de recherche dans le domaine de l hypersonique, des lasers a dynamique gazeuse, de couches limites turbulentes et des interactions jet empennage Carl a assure les fonctions de secretaire (1974—1975) et de president (1978) de la Supersonic Tunnel Association (voir ci-dessus)

A partir de 1977, Carl a supervisé les travaux de la division des systèmes à parachutes de Sandia. Il a initié et réalisé de la recherche dans le domaine de l'aérodynamique des parachutes. Avec son équipe, il est responsable du développement des systèmes à parachutes pour le ministère de la défense et la NASA, ainsi que pour les programmes de la Sandia. Carl est l'auteur de nombreuses communications sur les technologies des parachutes Il a été nommé président du comité technique pour les technologies des ralentisseurs aérodynamiques et des ballons de l'AIAA en 1986 et en 1987. Carl a été co-récipiendaire de la distinction d'excellence du United States Department of Energy pour "le developpement de parachutes a hautes performances pour les armes nucléaires". Il est membre associé de l'AIAA

Depuis le mois de mai 1988, Carl a assuré les fonctions de directeur de la division aérodynamique de Sandia En plus de son travail dans ce domaine, Carl gere des projects et des programmes de recherche en aérodynamique et sur l'analyse thermique des systèmes de rentrée, les missiles, les bombes, les obus et les roquettes Il supervise les aspects techniques de l'etude, du développement et de l'entretien de la réserve de tous les systèmes à parachutes des armes nucleaires US Carl est responsable de différents programmes de recherche et de développement des technologies en aérodynamique numérique et en hydrodynamique, ainsi que des souffleries hypersoniques et trisoniques, de la sécurité sur les champs de tir de Tonopah et Kauai et de l'informatique répartie Il est l'auteur de quelques 75 publications traitant de l'aérodynamique

Les Panel AGARD de la dynamique des fluides peut s'enorgueillir d'avoir choisi comme auteurs de cette AGARDographie tant attendue les deux premiers experts mondiaux sur les parachutes à hautes performances

K J Orlik-Ruckemann

Contents

	Page
Recent Publications of the Fluid Dynamics Panel	v
Foreword	vii
Avant-Propos	ix
Dedication and Acknowledgements	xv
Chapter 1 — Introduction	1
1.1 The origins of high-performance parachute technology	1
1.2 Scope of this work	1
1.3 Purpose of this AGARDograph	2
References	3
Chapter 2 — Historical Review	5
2.1 Evolution of high-performance parachutes	5
2.2 Major contributors to high-performance parachute technology	6
2.2.1 Professor Helmut G Heinrich	7
2.2.2 Donald W Johnson	7
2.2.3 Theodore W. Knacke	8
2.2.4 William B Pepper Jr	9
References	10
Chapter 3 — Description of High-Performance, Deployable Aerodynamic Decelerators	11
3.1 Retardation system basics	11
3.2 High-performance decelerator configurations	15
3.2.1 Parachutes	16
3.2.1.1 Flat circular ribbon parachutes	16
3.2.1.2 Conical ribbon parachutes	16
3.2.1.3 Lifting conical ribbon parachutes	20
3.2.1.4 Hemisflo ribbon parachutes	26
3.2.1.5 Ringslot parachutes	28
3.2.1.6 Ringslot solid-canopy parachutes	29
3.2.1.7 Ringsail parachutes	30
3.2.1.8 Disk-gap-band parachutes	31
3.2.1.9 Ribbed guide surface parachutes	31
3.2.1.10 Ribless guide surface parachutes	34
3.2.1.11 Rotating parachutes	35
3.2.2 Ballutes	37
References	39
Chapter 4 — Steady-State Aerodynamics	43
4.1 Characterization of parachute aerodynamics	43
4.2 Steady-state parachute drag	44
4.2.1 Flat circular ribbon parachute drag	45
4.2.2 Conical ribbon parachute drag	45
4.2.3 Hemisflo parachute drag	50
4.2.4 Drag of other parachute configurations	50
4.2.5 Parachute drag at supersonic speeds	51
4.2.6 Effects of forebody wake on parachute drag	56
4.2.6.1 Effects of forebody wake at low speeds	56
4.2.6.2 Effects of forebody wake at supersonic speeds	59
4.2.7 Reefed parachute drag	63
4.2.8 Parachute cluster drag	67

Page

4.3 Canopy pressure distribution 69
4.3.1 Analytical methods for predicting canopy pressure distributions 69
4.3.2 Canopy pressure distribution data 72
4.4 Stability 76
4.4.1 Static stability 76
4.4.2 Dynamic stability 78
4.4.3 Inflation instabilities 80
4.5 Aerodynamic heating 81
References 82

Chapter 5 — Nonsteady Aerodynamics 87
5.1 Introduction 87
5.2 Parachute deployment 88
5.2.1 Line sail 88
5.2.2 Snatch loads 96
5.3 Canopy inflation 98
5.3.1 Added mass approximation in nonsteady flows 99
5.3.2 Canopy drag and filling time 105
5.3.2.1 Maximum inflation force predictions 106
5.3.2.2 Empirical methods for predicting filling time 107
5.3.2.3 Semiempirical methods for predicting inflation loads and filling time 109
5.3.2.4 Computational fluid dynamics inflation models 110
5.3.2.5 Wind tunnel test data on inflation and canopy aerodynamics 113
5.3.2.6 Flight test data 114
5.3.3 Wake-induced canopy distortion or collapse 116
5.4 Trajectory dynamics 121
References 124

Chapter 6 — Structural Analysis 129
6.1 Background 129
6.2 Analytical methods and design applications 129
6.3 Stress measurement 135
References 137

Chapter 7 — Wind Tunnel Testing 139
7.1 Motivation 139
7.2 Types of tests 142
7.2.1 Drag 142
7.2.2 Pressure distribution 146
7.2.3 Stability 149
7.2.4 Lifting parachute aerodynamic characteristics 151
7.2.5 Aerodynamic heating 152
7.2.6 Stress measurements 152
7.2.7 Other parachute-related wind tunnel tests 152
7.3 Wind tunnel blockage 155
7.4 Special parachute instrumentation and testing methods 157
7.5 Model parachute design and fabrication 162
7.6 Conceptual design of a parachute wind tunnel for nonsteady testing 162
References 166

Chapter 8 — Parachute Materials 169
8.1 Background 169
8.2 Kevlar development and application 170
8.3 New materials 175
8.4 Material degradation 175
References 179

Page

Chapter 9 — Deployment Systems 181
9.1 Purpose and operation of deployment systems 181
9.2 Deployment methods 181
9.2.1 Background 181
9.2.2 Pilot and drogue parachutes 182
9.2.3 Mortars and drogue guns 188
9.2.4 Thrusted base plate 189
9.2.5 Tractor rockets 191

9.3 Deployment bags 196
9.3.1 Background 196
9.3.2 Theory 197
9.3.3 Bag Design 197
References 201

Chapter 10 — Ancillary Devices, Parachute Fabrication, and Packing 203
10.1 Ancillary devices 203
10.1.1 Reefing line cutters 203
10.1.2 Cut knives 207
10.1.3 Flotation bags and location aids 207
10.2 Fabrication and packing 213
10.2.1 Parachute drawings and fabrication 213
10.2.2 Packing 214
10.2.3 Reliability 219
References 222

Chapter 11 — Full-Scale Testing 223
11.1 Background 223
11.2 Instrumented ballistic ranges 225
11.2.1 Aircraft drops 225
11.2.2 Rocket boosting 229
11.2.3 Ballistic range instrumentation 231
11.2.3.1 Radars 233
11.2.3.2 Optical trackers 233
11.2.3.3 Telemetry 237
11.3 Sled track testing 237
11.3.1 Holloman High-Speed Test Track 237
11.3.2 Naval Weapons Center's supersonic test tracks 238
11.3.3 Sandia Rocket Sled Track 238
11.3.4 Captive-sled parachute testing 239
11.3.5 Sled-ejector parachute testing at the Sandia Rocket Sled Track 240
11.4 Other full-scale test methods 242
11.5 Test vehicles 242
11.5.1 Examples of test vehicle designs 243
11.5.2 Onboard instrumentation 244
References 247

Chapter 12 — Parachute Design Examples 249
12.1 Background 249
12.2 Cost trade-offs in parachute system design 249
12.3 Design of a staged parachute system for low-altitude payload delivery 250
12.4 Design of a 24-ft-diameter Kevlar/nylon ribbon parachute 252
12.4.1 The deployment system 252
12.4.2 Main parachute and deployment bag design 252
12.4.3 Flight test verification 254
12.5 Design of a high-performance 46.3-ft-diameter Kevlar/nylon parachute 259
12.5.1 The deployment system 259
12.5.2 Design and flight testing of first prototype (40-ft-dia) main parachute 260
12.5.3 Design and flight testing of second prototype (46.3-ft-dia) main parachute 263

Page

12.6 Design notes on other high-performance parachute systems 272
12 6 1 Design of a 5-ft diameter Mach 2 parachute for missile payload deceleration 272
12.6.2 Design of Space Shuttle SRB parachute recovery system 272
12 6 3 Design of parachute recovery systems for artillery shells 276
References 280

Chapter 13 — Summary and Conclusions 281

Author Index 283

Subject Index 287

Dedication

We dedicate this AGARDograph to our wives, Jean Maydew and Linna Peterson.

Acknowledgements

Compiling and documenting a lifetime of accomplishments in the development of high-performance parachutes would be difficult if not impossible without the cooperation and support of countless individuals. To all of you, our sincere thanks and appreciation.

We are very indebted to Dr. Venkatesh Narayanamurti, Vice President, Research and Exploratory Technology, Dr. Gerold Yonas, Vice President, Systems Applications; and Mr. Arlyn Blackwell, Director, Design Engineering at Sandia National Laboratories, who provided the resources and support to write this AGARDograph. We are indebted also to the staff of the Aerodynamics Department for their many technical contributions, and specifically to Don Johnson, who provided technical guidance during the writing and carefully reviewed the final manuscript; to Jacqueline McWilliams for the meticulous editing of this document and for overseeing its overall preparation; to Lynn Bonner for her excellent compositing and layout support, and to Glorianne Martinez for coordinating and cleaning up of our numerous drafts on the word processor. We thank the artists at Subia Corporation for their fine work on our illustrations.

Lastly, our thanks and everlasting gratitude to our colleague and technical editor, Dr. Kazik Orlik-Rückemann, Head of the Applied Aerodynamics Laboratory, Institute for Aerospace Research, Ottawa, Canada. It was Dr. Orlik-Rückemann who first proposed this AGARDograph. His guidance in the many months that followed has been invaluable, his encouragement steadfast.

CHAPTER 1

INTRODUCTION

1.1 The origins of high-performance parachute technology

For many years, parachute technology developed in an evolutionary fashion. It was sufficient to rely on additional test data to build the experience base needed to meet the performance requirements of the next high-performance parachute system. An evolutionary approach to parachute technology development was appropriate then because parachute performance requirements were increasing in small steps rather than by quantum jumps. Flight tests were both affordable and plentiful. Companion technologies were evolving. This approach to parachute technology development worked very well; many parachutes developed during that era are still in use today.

Several factors forced parachute technology to advance much more rapidly during the past two decades. Of primary significance was the specification of more stringent parachute performance requirements, imposed to keep up with the rapid expansion of the flight envelopes of aircraft, missiles, rockets, reentry vehicles, and spacecraft. Companion aerospace technologies such as electronics, computers, and material sciences had also accelerated rapidly, making these new flight environments possible.

Concurrently, payloads became much more expensive and, as a result, recovery became much less of an "option" than in the past. Aerospace system managers required greater assurance of success for new parachute systems, even at these more severe recovery environments. Not only did they have little tolerance for parachute failures, they also had little sympathy for the traditional parachute designer excuse that the physical phenomena associated with parachute inflation are extremely complex and underappreciated. Having observed the successful advancements in the companion technologies leading to quantum jumps in flight environments, they expected parachute technology to keep pace.

At this juncture, the approach for developing parachute technology was at a crossroads. Flight testing costs had increased by more than an order of magnitude, making unaffordable the "design-by-test" method of parachute design. Minimizing development costs of a project now required shortening the time scales for development. As a result, parachute designers could no longer afford the *time* required by an evolutionary parachute design process, even if they could afford the costs. These constraints forced consideration of an alternate approach for developing parachute technology, one that could support the development of parachute systems with substantially higher performance. The alternate approach was to understand enough about the time-dependent aerodynamics and structural dynamics of the inflating parachute to allow constructing *approximate models* of the inflation process that, in turn, could be used as parachute design tools.

A phenomenological approach to parachute design is not new. It is an old concept that was rejected repeatedly in the past because modeling the aerodynamics of the inflating parachute was considered to be impossibly complex. But, faced with the fact that the evolutionary approach was no longer viable, the organizations responsible for designing high-performance parachute systems reluctantly redirected their parachute technology programs toward achieving a better understanding of how those systems work. Initially, they validated the reasons for having abandoned this approach before: the inflating parachute *really is* one of the most complex aerodynamic systems to model, as this AGARDograph will demonstrate. But progress was made. New design tools were developed as we learned more about how parachutes interacted with the air around them. Although we have much more to learn, we have at least acknowledged our ignorance and have redirected ourselves to learn how to design today's high-performance parachutes.

1.2 Scope of this work

The term "high-performance parachute" is unavoidably subjective, yet it is necessary to bound the types of parachutes considered in this AGARDograph. We have chosen to define several categories of parachutes as "high performance." The first category includes parachutes that are deployed at Mach numbers above 0.7 or at dynamic pressures above 500 lb/ft^2. An example is the 24-ft-diameter Kevlar/nylon ribbon parachute developed for a 760-lb payload to provide impact velocities of 75 ft/s after release from an aircraft at altitudes of only 100 ft above the ground at release Mach numbers up to 1.2. Pepper[11] reported that this 90-lb parachute developed a maximum opening deceleration of 240 g at a deployment dynamic pressure of 2650 lb/ft^2. Another illustration of a high-speed parachute is the 5.2-ft-diameter Kevlar/nylon ribbon parachute[12] developed to decelerate an 800-lb payload from a deployment velocity of 2300 ft/s (M = 2.2) at an altitude of 3000 ft.

Parachutes that recover very heavy payloads at any deployment velocity are also considered to have high performance. An example of a very heavy payload for parachute recovery is the 174,000-lb expended case of the Solid Rocket Booster (SRB) for the Space Shuttle. The original SRB recovery system consisted of a 54-ft-diameter drogue ribbon parachute deployed at Mach 0.5 at 16,000 ft above sea level followed by the deployment of three 115-ft-diameter ribbon parachutes at an altitude of 6500 ft to decelerate the booster to an ocean impact velocity of 90 ft/s. Runkle and Woodis[13] report that the design drag load limit of the SRB drogue parachute is 270,000 lb. It was tested to failure at a drag load of 548,000 lb that, to the authors' knowledge, is the highest drag load ever developed by a parachute.

We have also designated as high-performance parachutes those with high pack densities, with long pack life, or with unusual or severe test environments and/or deployment conditions. The 24-ft-diameter parachute mentioned earlier is packed to a density of 43 lb/ft^3 and has an intended pack shelf life of 25 years. An example of a parachute system designed to operate under severe test and deployment conditions is a 4-ft-diameter guide surface parachute to recover a 100-lb, 155-mm artillery shell.[14] The parachute is packed in the nose cone ogive of the shell, the projectile is fired from an artillery gun at an elevation angle of 87 degrees, and the parachute is deployed at apogee altitudes as high as 70,000 ft by explosively separating the ogive from the shell. The spin rate of the shell is 250 revolutions per second (rps) at parachute deployment. In the gun barrel at launch, the shell recovery system is subjected to an axial acceleration of 20,000 g, a muzzle velocity of 3000 ft/s, and a spin rate of 300 rps.

Parachutes whose weight is small compared to their size and the drag they produce are considered to be high-performance parachutes. Most modern parachute applications allocate minimal weight and volume for the recovery system while requiring high drag efficiency. Designers are forced to build parachutes whose strength-to-weight ratios have been maximized and whose aerodynamic drag surpasses that of existing configurations. An example of a high-performance parachute in this category is a new 52.5-ft-diameter parachute proposed for the F-111 aircraft Crew Escape Module.[15] It weighs only 30 lb, yet its design load is 8000 lb and it has a drag coefficient of 1.1, based on the constructed diameter of the canopy.

Gliding parachutes are legitimate examples of high-performance parachutes; they incorporate modern materials and are capable of exceptional lift-to-drag ratios. Development of these systems has been focused on man-rated applications, especially in the sport parachuting field. Gliding parachutes for sport jumping have been designed in the more traditional manner of cut-and-try because the cost of this approach is affordable and because designers are eager to fly their new configurations. The aerodynamics of gliding parachutes is complex, especially in transient maneuvers such as flaring before landing. Developing computer simulations of these phenomena would cost more than evolutionary development using test results.

Gliding parachutes with guidance and control systems can potentially impact payload recovery beyond the special field of sport jumping because they provide an opportunity to land the payload on a specified target, not just where the winds carry it. As the need increases for controlled parachute recovery to a specific landing zone, development of both gliding parachute technology and flight control technology is expected to increase. This AGARDograph does not include gliding parachute design, however, because the authors expect future advances in this technology to exceed by far the current knowledge base. When this occurs, a summary of that technology should be prepared.

1.3 Purpose of this AGARDograph

The purpose of this AGARDograph is to provide general state-of-the-art procedures for the design and testing of high-performance parachutes. This includes the use of aerodynamic and structural analysis and application of numerical codes to predict parachute inflation, deceleration forces, payload and parachute trajectories, and canopy/suspension line stresses. Design problems such as parachute collapse, parachute line sail, parachute stability, and body-wake interaction are discussed. The use of nylon, Nomex, Kevlar, Teflon, and other materials is covered. Techniques for the design and fabrication of prototype parachutes and deployment bags are presented, and parachute packing methods are discussed. A section is included on testing of model parachutes in wind tunnels. Full-scale testing, using a sled track or aircraft drop or rocket boost to deploy the parachute at the desired Mach number and altitude, and descriptions of onboard and ground-based instrumentation are outlined. Example parachute designs are given for differing system requirements of payload weight, deployment Mach number and dynamic pressure, parachute weight/volume, etc.

Other references should be used with this one to design high-performance parachutes. Cockrell's AGARDograph[16] on the aerodynamics of parachutes is recommended as a reference in the fundamentals of parachute aerodynamics. This work extends his contributions to the aerodynamic

concepts, analyses, and numerical codes unique to the design of high-performance parachutes. Useful experience, analytical techniques, and semiempirical design methods are contained in the *Recovery Systems Design Guide*.[1.7] Knacke[1.8] has recently published a comprehensive parachute design manual that the authors used as a primary reference resource. Design problems unique to high-performance parachutes are treated in greater detail in this work. Eleven AIAA Aerodynamic Decelerator Conferences[1.9-1.19] have been held in the United States since 1966. Four workshops in parachute technology[1.20-1.23] have been conducted since 1982. The USAF[1.24] and The Royal Aeronautical Society[1.25] sponsored parachute symposiums in 1964 and 1971, respectively. Peterson[1.26] gives an overview of high-performance parachutes. The parachute R&D reported in these conferences, the extensive parachute material in the open literature, and the parachute design material furnished by the NATO scientific community form the background material for this AGARDograph.

References

1.1 W. B. Pepper Jr., "Design and Development of the 24-ft-diam Hybrid Kevlar-29/Nylon Ribbon Parachute," *J Aircraft*, Vol. 17, No 1, January 1980.

1.2 C. W. Peterson, D E. Waye, L. R. Rollstin, and I. T. Holt, "Design and Performance of a Parachute for Supersonic and Subsonic Recovery of an 800-lb Payload," AIAA 86-2435, October 1986.

1.3 R. E. Runkle and W. R. Woodis, "Space Shuttle Solid Rocket Booster Deceleration Subsystem—Drop Test 3: Anatomy of a Failure," AIAA 79-0431, March 1979.

1.4 D E. Waye, C. W. Peterson, and W. T. Botner, "Design and Performance of a Parachute Recovery System to Recover 155-mm and 8-Inch-Diameter Artillery Shells," AIAA 86-2445, October 1986.

1.5 D. W. Johnson, "Status Report of a New Recovery Parachute System for the F111 Aircraft Crew Escape Module," AIAA 86-2437, October 1986.

1.6 D J Cockrell, "The Aerodynamics of Parachutes," AGARDograph No. 295, July 1987.

1.7 E. G. Ewing, H. W. Bixby, and T. W. Knacke, *Recovery Systems Design Guide*, USAF AFFDL-TR-78-151, December 1978.

1.8 T. W. Knacke, *Parachute Recovery Systems Design Manual*, NWC TP 6575, Naval Weapons Center, China Lake, California, June 1987.

1.9 AIAA 1st Aerodynamic Deceleration Systems Conference, Houston, Texas, September 1966.

1.10 AIAA/DoD 2nd Aerodynamic Deceleration Systems Conference, El Centro, California, September 1968, Technical Report FTC-TR-69-11, Air Force Flight Test Center, Edwards Air Force Base, California, April 1969.

1.11 AIAA 3rd Aerodynamic Deceleration Systems Conference, Dayton, Ohio, September 1970.

1.12 AIAA 4th Aerodynamic Deceleration Systems Conference, Palm Springs, California, May 1973.

1.13 AIAA 5th Aerodynamic Deceleration Systems Conference, Albuquerque, New Mexico, September 1975.

1.14 AIAA 6th Aerodynamic Deceleration Systems Conference, Houston, Texas, March 1979.

1.15 AIAA 7th Aerodynamic Decelerator and Balloon Technology Conference, San Diego, California, October 1981.

1.16 AIAA 8th Aerodynamic Decelerator and Balloon Technology Conference, Hyannis, Massachusetts, April 1984.

1.17 AIAA 9th Aerodynamic Decelerator and Balloon Technology Conference, Albuquerque, New Mexico, October 1986.

1.18 AIAA 10th Aerodynamic Decelerator Systems Technology Conference, Cocoa Beach, Florida, April 1989.

1.19 AIAA 11th Aerodynamic Decelerator Systems Technology Conference, San Diego California, April 1991.

1.20 Helmut G. Heinrich Short Course on Parachute Systems Technology, University of Minnesota, July 1982.

1.21 Helmut G. Heinrich Short Course on Decelerator Systems Engineering, University of Minnesota/Sandia National Laboratories, Albuquerque, New Mexico, July 1985.

1.22 University of Minnesota/Carl-Cranz-Gesellschaft Parachute Systems Technology Course, Wessling, West Germany, June 1987.

1.23 University of Minnesota Parachute Systems Technology Short Course, Framingham, Massachusetts, June 1990.

1.24 E C. Myers, Editor, *Symposium on Parachute Technology and Evaluation—Proceedings* (2 vols.), El Centro. California, USAF FTC-TDR-64-12, September 1964.

1.25 *Two-Day Symposium on Parachutes and Related Technologies—Proceedings*, The Royal Aeronautical Society, London, September 1971.

1 26 C. W. Peterson, "High-Performance Parachutes," *Scientific American*, Vol. 262, No 5, May 1990.

CHAPTER 2

HISTORICAL REVIEW

2.1 Evolution of high-performance parachutes

Parachutes have been known in China for two thousand years. Leonardo da Vinci made sketches of parachutes in the fifteenth century, and people began to use them in flight three centuries later. Brief reviews of those early days of parachute development are given by Cockrell,[16] Knacke,[18] and in the USAF 1978[17] and 1963[21] Parachute Design Guides. Not until the middle of the twentieth century did the progenitors of what we would call "high-performance" parachutes begin to appear.

A major milestone in the development of high-performance parachutes was the invention of the FIST ribbon parachute* by Messrs. Madelung, Isermann, Knacke, and Keller in 1938.[22,23] Knacke[24] indicated that in 1933 the Flugtechnisches Institut der Technischen Hochschule Stuttgart (FIST) began theoretical and experimental investigations to determine the most suitable method of decelerating aircraft in flight (and in landing) with parachutes. Conventional solid flat parachutes were tested initially; but these parachutes oscillated so violently as to render the aircraft uncontrollable. These test results stimulated the FIST to begin development of nonoscillating parachutes with the following characteristics:

- Reliable and controllable inflation
- High drag
- Low opening shock
- Stability
- Simple design and construction
- Simple maintenance

According to Knacke, initial tests showed that a higher porosity canopy resulted in increased stability and decreased drag. FIST tested vented canopies, ringslot canopies, highly porous fabric canopies, and lattice-fabric canopies before finally arriving at the FIST ribbon design that satisfied their criteria. Knacke[24] provided detailed ribbon parachute design guidance in 1948, including the use of pocket bands as inflation aids and selvage ribbons to increase ribbon drag and strength. The pocket bands and selvage ribbons were developed in Germany in the early 1940s.

Much of the pioneering work in ribbon parachute development and application took place in Germany in the 1940s. In 1943, Knacke developed a quick-opening (0.45 s) unreefed 18-ft-diameter ribbon parachute[25] to decelerate an 1100-lb bomb after an aircraft release at an altitude of 340 ft and a Mach number of 0.67. No failures of this parachute occurred during 50 ballistic development drop tests at aircraft release Mach numbers up to 0.77. A total of 900 of these bombs were used in this project "Liesele," with no reports of parachute failures. Ribbon parachutes were also used in 1944 to recover V-1 and V-2 guided missiles and their components.

Knacke[26] designed an 8.3-ft-diameter flat ribbon parachute to stabilize the 980-lb XS-2 Crew Escape Module in the late 1940s. After reaching terminal velocity and an altitude of less than 10,000 ft above the ground, the pilot was to bail out manually from the nose section using a standard 28-ft-diameter personnel parachute. Knacke conducted 3/8-scale wind tunnel and aircraft drop tests of the XS-2 parachute behind the aircraft to verify the design. The full-scale parachute was successfully tested up to a deployment Mach number of 1.3 at the Edwards AFB High-Speed Track. An uncontrollable flight condition developed during an XS-2 high-speed, high-altitude flight in 1953; a violent pitch-up occurred to the Crew Escape Module as it separated from the aircraft, but the Crew Module stabilized after parachute deployment near Mach 3.

A second milestone in the development of high-performance parachutes was the invention in 1941 of the guide surface parachute by Dr. Helmut Heinrich.[27] The guide surface parachute was first used in Germany in 1943 for trajectory control of finless bombs and torpedoes because of its excellent stability characteristics. Sandia National Laboratories has used the guide surface parachute since 1954 as a pilot parachute to deploy the main ribbon canopy and for recovery of rocket payloads, artillery shells, and reentry vehicles.

The U.S. Air Force at Wright-Patterson AFB initiated a program in 1950 with Cook Research Laboratories (CRL) to develop supersonic parachutes for the recovery of missiles and drones.[28] They

* The various types of parachutes are discussed in Chapter 3.

conducted 115 sled tests at Edwards AFB of small (28 ft^2) guide surface, flat ribbon, and rotafoil parachutes at deployment Mach numbers up to Mach 0.66. Engstrom[2 9] subsequently flight-tested several small ribbon and guide surface parachutes at altitudes between 15,000 ft and 96,000 ft and deployment Mach numbers from 0.38 to 2.38. Parachute operation at high Mach numbers was unreliable; the canopies did not inflate fully, violent canopy dynamics were noted, and considerable parachute damage occurred.

CRL combined theoretical studies with wind tunnel, high-speed sled, and free-flight, rocket-boosted tests to develop the hemisflo and hyperflo parachutes. Pederson[2 10] conducted sled tests at Holloman AFB, New Mexico, at Mach numbers of 1.0 to 1 5 of small (2.0- to 8.44-ft-diameter) guide surface, conical ribbon, hemisflo, and hyperflo parachutes. These sled tests, conducted at infinite mass test conditions, demonstrated successful operation of the parachutes at dynamic pressures up to 3000 lb/ft^2, a major advance in high-performance parachutes. Pepper[1 10,2 11] successfully tested a 2-ft-diameter hyperflo parachute with a composite structure (nylon coated with a silicon-glass-fiber cloth heat shield and RTV silicone rubber for ablative protection) at a Mach number of 4 and an altitude of 114,000 ft. Despite these successes, hyperflo parachutes have not been widely used in system applications.

In 1952, Lockheed Aircraft Corporation[2 5] designed a parachute system to recover a 2700-lb ramjet test vehicle from an altitude of 22,000 ft at Mach 2.5 The system consisted of a 67-in.-diameter first-stage ribbon parachute and a 29-ft-diameter second-stage reefed ribbon parachute. The first-stage parachute was successfully deployed at a dynamic pressure of 2960 lb/ft^2 (M = 2.4 at an altitude of 22,500 ft).

Sandia and the Retardation and Recovery Branch at Wright-Patterson AFB initiated a joint "Low-Level Delivery" flight test program in 1954 to demonstrate the feasibility of reliably and repeatedly deploying a parachute from gravity bombs released from an aircraft flying at very low altitudes at transonic speeds.[2 5] Thirty-three aircraft (B-47 and F-7U) drop tests were made to deploy reefed 16-, 20-, 24-, 28-, and 40-ft-diameter, heavy-duty ribbon parachutes at Mach numbers of 0.6 to 1.0 at low altitudes using an instrumented recoverable parachute test vehicle. The test vehicle weight was varied from 1750 to 2600 lb. By 1956, these tests had demonstrated that ribbon parachutes could provide the necessary deceleration to prove the feasibility of low-altitude delivery of gravity bombs (including laydown on the ground).[2 12]

Flight-testing techniques and instrumentation technology were improved to provide the data needed to develop these ribbon parachutes. Parachute tests were conducted at the DOE/Sandia ballistic ranges at Salton Sea Test Range in California and Tonopah Test Range, Nevada. The test vehicles were tracked with radar and cinetheodolites to obtain metric (space position) data for deriving velocity and acceleration data. Range tracking telescopes provided documentary film coverage of parachute opening and performance. Range receiving stations recorded telemetry signals from the vehicle onboard accelerometers and other instrumentation. Onboard cameras (operating at 96 and 200 frames per second) provided photo coverage of the parachute deployment and inflation. These measurements provided a quantitative assessment of the parachute performance for each test.

Sandia conducted supersonic deployments in early 1959 of a 20-ft-diameter reefed conical ribbon parachute[2 13,2 14] using a rocket-boosted parachute test vehicle to demonstrate repeatable and reliable parachute operation at high dynamic pressures. Three tests were conducted at parachute deployment Mach numbers of 1.45 to 1.57 and dynamic pressures up to 2840 lb/ft^2. Onboard cameras showed an orderly deployment and parachute opening, and the parachutes were not damaged. The maximum measured deceleration of the 1130-lb test vehicle during the reefed first-stage parachute opening was 119 g.

The U.S. Air Force and Sandia have designed many heavy-duty, high-performance parachutes for weapon systems during the last 30 years. Sandia has designed over 200 parachute systems up to 130 ft in diameter for payloads up to 50,000 lb since 1954. Over 4000 development and reliability verification flight tests (using sled tracks, rocket boosters, or aircraft) of full-scale parachute systems have been conducted to date by Sandia[1 9 1 23,2 15] at deployment speeds up to Mach 2.8.

2.2 Major contributors to high-performance parachute technology

Many engineers, scientists, and technicians have contributed to the literature on the design and testing of high-performance parachutes. A few have made exceptional, lifelong contributions to parachute technology development, as evidenced by their inventions, their technical papers and reports, their successful designs and applications of high-performance parachute systems, the impact of their teaching on other parachute designers, and their service to the parachute technical community

in organizing conferences and serving on committees. The following individuals have led their colleagues in both parachute technology advancement and its application.

2.2.1 Professor Helmut G. Heinrich

Helmut G. Heinrich was born in Berlin, on August 5, 1910. He received a Dr. Ing. in Aeronautical Engineering from the Technische Hochschule, Stuttgart, Germany, in 1943. From 1935 to 1946 he was employed first as a project engineer and later as Head of the Department of Aerodynamics at the Research Institute Graf Zeppelin, in Stuttgart; he was also on the faculty of the Technische Hochschule. He developed and patented the guide surface parachute in 1941. In 1946 he came to the United States as a Technical Advisor to the Parachute Branch Equipment Laboratory of the Wright Air Development Center at Wright-Patterson AFB in Dayton, Ohio. From 1951 until his death, he was Professor of Aerospace Engineering and Mechanics at the University of Minnesota.

"Doc" Heinrich was best known for his research on the theory and experiment of the aerodynamics of decelerators. This research led to new decelerator designs, including the ribbed guide surface parachute, the supersonic guide surface parachute, and a guide surface rotor. He also designed the "omega sensor," a device used to measure stress in flexible parachutes. For the Gemini space program, he developed the Parasail parachute system; and his patented guide surface parachutes were used on two unmanned Viking Mars space probes and the Venus probe. He was awarded 10 U.S. patents and numerous patents in foreign countries. He published dozens of archival journal papers and many more Air Force and University of Minnesota reports on parachutes. At the University of Minnesota and elsewhere, he organized and helped teach several parachute short courses.

Doc was elected a Fellow of the American Institute of Aeronautics and Astronautics (AIAA) and Fellow of the Royal Aeronautical Society of Great Britain. He received the Thurman H. Bane Award from the Institute of Aeronautical Sciences, the Aeronaut Leo Stevens Memorial Medal from the Wings of America Club, a citation for a Special Act of Service from the U.S. Air Force in 1956, and the Outstanding Teaching Award in 1972. He was continuously engaged in research at the University of Minnesota, where he trained hundreds of undergraduate and graduate students in analytical methods and experimental techniques.



Doc died on March 7, 1979, in Houston, Texas, one day after receiving the AIAA's first "Aerodynamic Decelerator and Balloon Technology Award." His citation reads:

For forty years of continuous involvement with, and significant contributions to, the science and technology of aerodynamic deceleration systems, and for teaching by doing and doing by teaching.

2.2.2 Donald W. Johnson



Don was recently awarded the 1991 AIAA "Aerodynamic Decelerator Systems Award." The citation reads:

For comprehensive and sustained contributions to parachute technology in the areas of ribbon parachute development, rocket recovery, and the applications of Kevlar to high-performance parachute design.

Don was born in Bloomington, Illinois. After serving in the U.S. Air Force, he graduated from Purdue University in 1957 with a B.S. in Aeronautical Engineering. He was elected to Sigma Gamma Tau and Tau Beta Pi honorary engineering fraternities. In 1957 he joined Sandia Corporation (now Sandia National Laboratories) as a Member of Technical Staff and was promoted to Distinguished Member of Technical Staff in 1985.

In the late 1950s, Don designed and successfully flight-tested a 130-ft-diameter ribbon parachute, the largest ribbon parachute ever fabricated until the recovery parachutes for the Space Shuttle Solid Rocket Boosters (SRBs) were developed in the 1970s. In the 1960s, he developed a 76-ft-diameter ribbon parachute for an 8500-lb store and a 69-ft-diameter ribbon parachute for the B-58 aircraft pod store, both parachutes capable of deployment at transonic velocities. Don worked with the USAF to develop a 22.2-ft-diameter (temporarily reefed) ribbon parachute capable of deployment at Mach 1.2 at low altitude for the laydown delivery of a 2100-lb store. He developed a family of parachute recovery systems (including flotation gear for overwater recovery) for sounding rocket payloads. These systems used payload center-of-gravity control to force the payload into a flat spin from reentry speeds as high as Mach 10; the resulting high drag allowed subsonic deployment of the parachute. These 6- to 24-ft-diameter parachutes have been used to recover over 200 rocket payloads since 1963. This same flat spin technique was adopted by NASA to decelerate the SRBs after reentry to subsonic speeds before parachute deployment.

In the 1970s, Don developed a 13-ft-diameter lifting ribbon parachute for deployment at 300 to 800 knots at low altitude for a 2400-lb store. In the 1980s he developed a 46.3-ft-diameter ribbon parachute for a 2465-lb store (for transonic, low-altitude deployment), and he developed drawings and specifications for the production fabrication and packing of heavy-duty parachutes for four stores He also developed a new recovery system for the F-111 aircraft Crew Escape Module.

Don has presented 10 papers, published 5 journal articles, and published 20 Sandia reports. He has been awarded patents for "an all-radial construction ribbon parachute" and for "a method of simultaneously disreefing a parachute cluster." He is an Associate Fellow and 35-year member of AIAA. He is serving his second appointment on the AIAA Aerodynamic Decelerator Systems Technical Committee and was Technical Committee chairman for 1990 and 1991. Don was Technical Co-chairman of the 1989 Aerodynamic Decelerator Systems Technology Conference. He taught courses in parachute technology in Albuquerque, New Mexico, in 1985 and Munich, Germany, in 1987.

Don was a co-recipient of the U.S. Department of Energy, Division of Military Application "Award of Excellence" in 1987. The citation reads:

> *For significant contribution to the nuclear weapons program development of high-performance parachutes for nuclear weapons.*

2.2.3 Theodore W. Knacke



The citation for Theo's 1981 AIAA "Aerodynamic Decelerator and Balloon Technology Award" reads:

For the introduction of modern technology and sound engineering principles to the former art of parachute design, thereby enabling aircraft, ordnance, spacecraft, and other advanced system designers to successfully use parachutes to satisfy system requirements

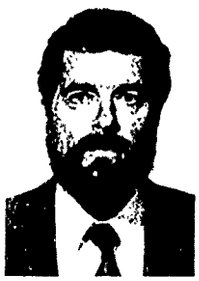
Theodore W. Knacke was born in Zirtow, Germany, on December 20, 1910. He received B.S. degrees in both Civil and Aeronautical Engineering in 1934, and his M.S. in Aeronautical Engineering in 1940 from the Engineering College, Strelitz, Germany. From 1934 to 1946, he conducted parachute recovery system R&D at the Aeronautical Institute Graf Zeppelin, Stuttgart-Ruit (FGZ) and its predecessor (FIST), first as a group engineer and later as Chief of the Aeromechanical Department. In 1938 he co-invented the ribbon parachute. He worked for the Parachute Branch Equipment Laboratory at the Wright Air Development Center, Wright-Patterson AFB, from 1946 to 1952, and he designed the landing deceleration parachute systems for the B-47, B-51, and B-52 aircraft. Co-author of the first USAF Parachute Handbook, he developed the ringslot parachute and started an extensive supersonic parachute research program.

Theo was Technical Director of the U.S. Air Force 6511th Test Group (Parachutes), El Centro, California, from 1952 to 1957. From 1957 to 1962, he was Vice President of Engineering at Space Recovery Systems, Inc., El Segundo, California, where he guided the development of recovery systems for the U.S. Army SD-5 Drone, the B-70 encapsulated seat, and the U.S. Air Force HETS reentry vehicle. From 1962 to 1975, he was with the Northrop Corporation, Ventura Division, Newberry Park,

California, first as Chief, Technical Staff, Recovery Systems and later as engineering representative in Dayton, Ohio. The Apollo and Gemini manned landing recovery systems were developed under his direction. Since retiring from Northrop, he has been a consultant for the U.S. Army, Navy, Air Force, and private industry.

Theo was awarded 10 parachute patents in Germany and the U.S. between 1937 and 1961; his patents on ribbon parachutes, reefing, and pocket bands were major contributions to the successful design of high-performance parachutes. He lectured extensively from 1955 to 1987 at special parachute short courses conducted at universities and research agencies. He has made many presentations and has published 33 reports and papers on parachutes. In 1967-68 he was Chairman of the AIAA Aerodynamic Decelerator Committee, and he was elected an AIAA Fellow in 1982.

2.2.4 William B. Pepper Jr.



Bill received the 1986 AIAA "Decelerator and Balloon Technology Award." The citation for this award reads:

In recognition of twenty-seven years of major contributions to parachute technology and design in the areas of weapon parachute systems, reentry vehicle and scientific payload recovery, and Kevlar parachute technology.

Born in Montrose, Colorado, William B. Pepper received a B.S. in Aeronautical Engineering from the University of Minnesota in 1946 and an M.S. in Aeronautical Engineering from the University of Colorado in 1947. He conducted aeronautical research and development at the NACA/NASA-Langley Station, Pilotless Aircraft Division, from 1947 to 1953. This work consisted of parametric studies of aircraft wing and engine nacelle configurations. He used rocket-launched vehicles for aerodynamics flight research.

Bill joined Sandia Corporation (now Sandia National Laboratories) in 1953 and worked until 1958 on bomb and missile aeroballistics. He conducted parachute R&D studies and designed parachutes from 1958 until his retirement from Sandia in 1985, and since then he has been a consultant to industry.

In the 1960s, Bill worked with the U.S. Air Force in the design and testing of heavy-duty parachutes for five stores. He developed parachutes for test vehicles used in the atmospheric test readiness program and developed a reefed 20-ft-diameter ribbon parachute that was flight-tested successfully at Mach 2.42 (at a dynamic pressure of 5700 lb/ft^2). Bill also developed a parachute recovery system for a spinning (200 rps) 155-mm artillery shell. In the 1970s, he developed parachute recovery systems for high-beta reentry vehicles, pioneered the use of Kevlar ribbons and suspension lines in ribbon parachutes, and developed a Kevlar/nylon 24-ft-diameter ribbon parachute for transonic deployment of a store. In the 1980s, Bill studied parachute/store ballistic dispersion, conducted supersonic parachute research, and developed an underwater parachute system for an ocean-bottom piston corer.

Bill has presented 19 papers, published 18 AIAA articles, and published 91 NACA and Sandia reports. He was issued one patent on parachutes. An Associate Fellow of AIAA, he was a charter member of the first AIAA Aerodynamic Decelerator Technical Committee. He was General Chairman of the 2nd AIAA Aerodynamic Decelerator Conference.

References

2.1 *Performance of and Design Criteria for Deployable Aerodynamic Decelerators*, USAF ASD-TR-61-579, December 1963.

2.2 T. W. Knacke, "Technical-Historical Development of Parachutes and Their Applications Since World War I," AIAA 86-2423, October 1986.

2.3 T. W. Knacke, *Report on the Works of the Parachute Department (Forschungsanstalt Graf Zeppelin)*, USAF F-SU-1107-ND, May 1946.

2.4 T. W. Knacke, *Design, Use, and Construction of FIST Type Parachute*, USAF MCREXE-672-19LL, June 1948.

2.5 R. C. Maydew, *Feasibility of Parachutes for Low-Level Delivery*, Sandia Corporation Technical Memorandum 6-54-51, January 1954.

2.6 T. W. Knacke, *Wind Tunnel Tests for Defining the Parachute Retardation System for the Ejectable Nose Section of the XS-2 Research Aircraft*, USAF AFWAL-TM-81-130, June 1980.

2.7 H. G. Heinrich, *Parachutes, Guide Surface*, USAF MCREXE-672-25F, February 1948.

2.8 J. R. Downing, D. L. Arenson, and J. H. McClow Jr., *Recovery Systems for Missiles and Target Aircraft*, USAF TR-5853, Part I, March 1954.

2.9 B. A. Engstrom, *Performance of Trailing Aerodynamic Decelerators at High Dynamic Pressures*, USAF WADC TR-58-284, Part II, Phase 2 Test Results, January 1960.

2.10 P. E. Pederson, *Study of Parachute Performance and Design Parameters for High Dynamic Pressure Operation*, USAF FDL-TDR-64-66, May 1964.

2.11 W. B. Pepper Jr., "Development of a Composite Structure Hypersonic Parachute," *J Spacecraft and Rockets*, Vol. 6, No. 4, April 1969.

2.12 R. C. Maydew and T. Blanchard Jr., *Status of Parachute Research for Tactical Laydown Weapon Application*, Sandia Corporation, SC-3931(TR), November 1956.

2.13 M. T. Kane, *Test Results of the First Two Supersonic Parachute Test Vehicle Firings*, Sandia Corporation, SCTM 329-59(51), October 1959.

2.14 M. T. Kane, *Test Results of the Third and Fourth Supersonic Parachute Test Vehicle Firings*, Sandia Corporation, SCTM 399-59(51), February 1960.

2.15 W. B. Pepper and R. C. Maydew, "Aerodynamic Decelerators—An Engineering Review," *J Aircraft*, Vol. 8, No. 1, January 1971.

CHAPTER 3

DESCRIPTION OF HIGH-PERFORMANCE, DEPLOYABLE AERODYNAMIC DECELERATORS

3.1 Retardation system basics

This chapter describes configurations of various high-performance decelerators, subject to the definition of "high performance" as used in this AGARDograph. It draws heavily on Chapter 2 of Reference 1.7 for the basics of retardation systems, and it extends these precepts to modern developments in high-performance parachutes. The descriptions of configurations are accompanied by limited aerodynamic performance data to permit comparisons of decelerator types so that the designer's initial choice of decelerator type may be closest to meeting system performance requirements. The designs discussed in the following sections represent those that have been extensively used in operational recovery systems or that have shown potential for future application for high-performance systems.

A retardation system consists of components that function together to control deceleration and to stabilize the payload in flight. The system also provides controlled descent and flight termination functions for the payload. The basic component of a retardation system is the deployable aerodynamic decelerator, which transfers the momentum of the moving payload (or forebody) to the atmosphere by acceleration of the ambient air. Other components of the system may provide the method of deploying the decelerator, control of forces, support for the suspended body, landing impact attenuation, and, in some cases, automatic detachment of the decelerator when its function is completed.

The decelerator's aerodynamic lift, drag, and stability determine its operational characteristics. Lift, the aerodynamic force perpendicular to the flight path, may be incorporated into a decelerator to provide divergence from a ballistic path, a longer downtime, a decreased impact velocity, or glide to a target. Drag, the aerodynamic force aligned with the flight path, is usually the decelerator's primary reason for being. Aerodynamic stability is important in determining dispersion and impact conditions. Each of these aerodynamic characteristics may be adjusted by careful design of the parachute geometry.

A modern decelerator must be efficient in terms of weight and packed volume. It must be flexible so that it can be stored in a relatively dense package before use. Also important is the decelerator's capability of being deployed from this stowed position and of rapidly inflating to develop the required transient aerodynamic force/time impulse. The design and fabrication of the deployment bag (with the appropriate breakable line and canopy ties, bag liner, and cut knives) are just as important as the design and fabrication of the decelerator in achieving reliable, repeatable performance. Deployment and opening force characteristics of a decelerator significantly affect not only the weight and packed volume of the decelerator, but also the integrity of the structure and contents of the object being recovered.

Before discussing specific high-performance decelerator configurations in detail, we must identify their principal parts and define the parameters and nomenclature used to measure their performance. Figure 3.1 illustrates the basic features of a high-performance decelerator. Most decelerators are symmetric about the system axis, which passes through the center of the canopy and the confluence point of the suspension lines. Lifting parachutes are symmetric about a plane through the system axis. Rotating parachutes have consistent asymmetries in each gore to generate spin about the system axis.

The canopy is the cloth surface that inflates to a developed aerodynamic shape to provide the lift, drag, and stability needed to meet performance requirements. The canopy's inflated shape (and therefore its aerodynamic characteristics) can be varied by modifying canopy design parameters. Specific parachute types were developed to optimize specific aerodynamic performance characteristics. It is the geometry of the canopy that distinguishes one parachute type from another.

Suspension lines transmit the retarding force from the canopy to the payload, either directly or through risers attached below the convergence point of the suspension lines to the body. The point of convergence of all suspension lines of a parachute is called the confluence point. The distance from the canopy skirt to the confluence point is the effective suspension line length ℓ_e.

The portion extending below the major diameter of the inflated canopy shape to the leading edge of the canopy is the skirt. The crown is the region of the canopy above the major diameter of the

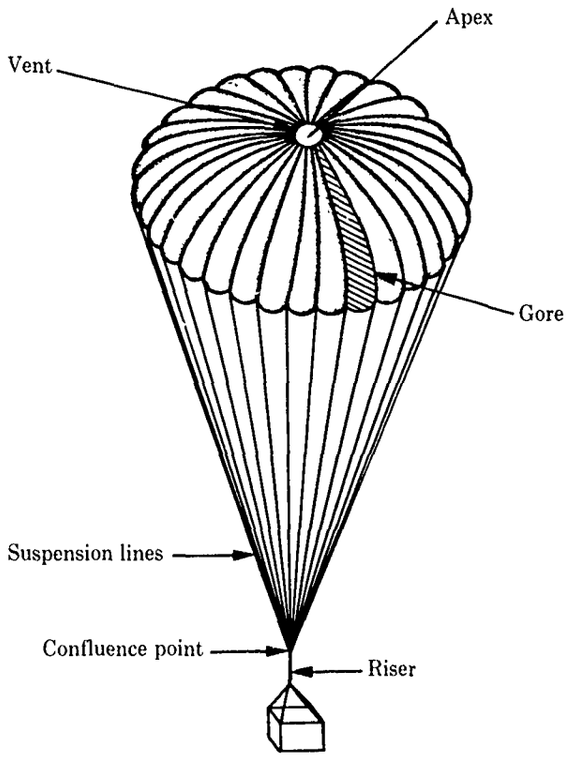


Figure 3.1. Principal components of a parachute (taken from Ref. 1.7)

inflated shape. Other parts of a parachute are also identified in Figure 3.1. The small circular opening at the center of the crown is called the vent, which serves to simplify fabrication and provides flowthrough relief for the initial surge of air when it impacts the canopy at the start of inflation. The choice of the local porosity distribution in the vent and the upper crown is critical in the design of ribbon parachutes for deployment at high dynamic pressures and supersonic speeds because vent porosity can play a major role in determining both inflation time and structural loads.

The apex is the center of the canopy. Vent lines (Figure 3.2) are canopy elements that are fixed to opposed points on the vent hem (also called the vent band or vent reinforcement) and that cross the vent through the apex, providing structural continuity across the canopy to each suspension line. Many modern high-performance ribbon parachutes are designed using continuous radials across the vent. In a continuous radial parachute, one continuous webbing is used to form the suspension lines and radials on one side of the canopy, the vent line, and the radial and suspension line on the other side of the canopy.

All of the high-performance decelerator canopies discussed herein are formed from an even number of gores bounded on each side by a radial seam, on the top edge by the vent band, and on the bottom edge by the skirt hem (also called the skirt band or skirt reinforcement). The gore length is measured along the center of the gore from the vent band to the skirt band. The simplest gore shape is triangular with a linear variation of gore width between the vent band and the skirt band. Some parachutes use shaped gores to optimize aerodynamic characteristics and minimize material stresses.

For flat circular canopies with N_g gores, each gore has a vertex angle β of $360/N_g$ degrees. A conical parachute has the uninflated canopy shape of either an N_g-sided pyramid or a cone, depending on construction details; its base cone angle is μ (Figure 3.3). Other parachute types use variations of the basic triangular gore to gain improved stability. A biconical canopy has a cone angle μ_1 beginning at the apex of the parachute, but the cone angle is changed to μ_2 beginning at an arbitrary location between the vent and skirt reinforcements. The biconical construction (and the triconical canopy construction, which uses three cone angles in each gore) reduces the stresses at midcrown of the canopy.

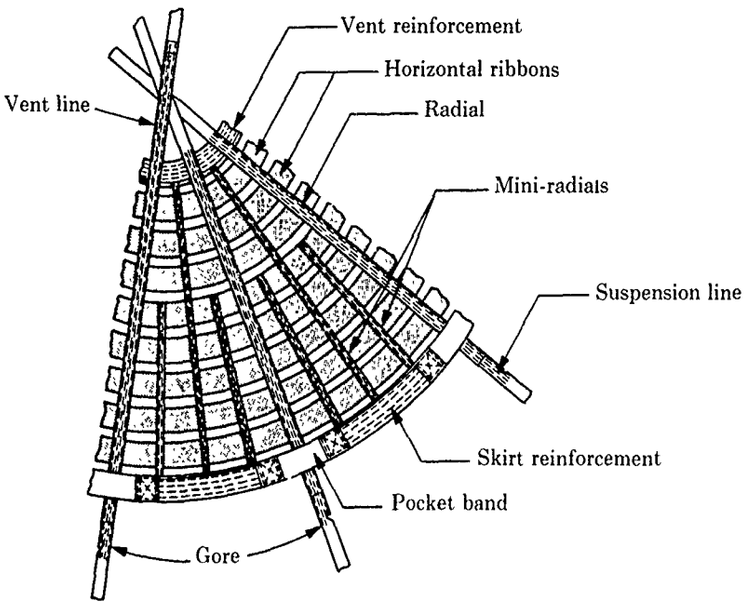


Figure 3.2. All-radial construction of a continuous ribbon parachute

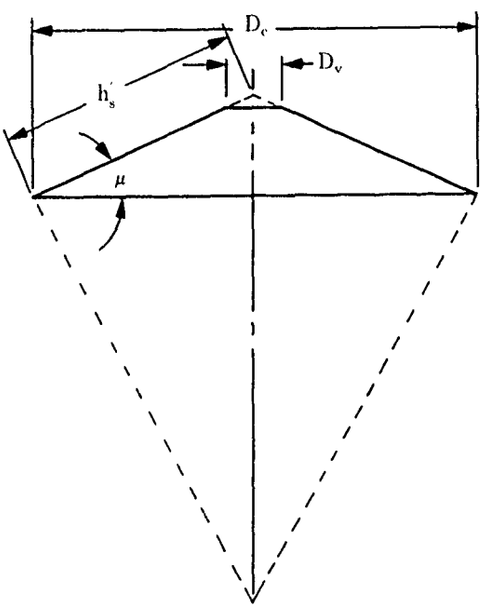


Figure 3.3. Constructed profile of a conical canopy (taken from Ref. 1.7)

Parachute engineers use two different methods for defining the size of a parachute. One approach defines a nominal area and nominal diameter of the parachute. Nominal area S_o is the actual three-dimensional canopy constructed surface area. For most canopy designs, S_o is computed as the sum of the gore areas inclusive of vent area, slots, and other openings within the gore outline. Areas of surfaces such as ribs, flares, panels, or additional fullness to the cloth are also included. Nominal diameter D_o is the diameter of a circle whose area is S_o.

A second reference dimension of parachutes is the constructed diameter D_c. D_c is the diameter of the parachute (measured along the radial seam) when projected on a planar surface. For all flat circular and conical parachutes, D_c is the actual "as-built" diameter of the canopy; whereas nominal diameter is a hypothetical effective diameter, D_c is an actual dimension of the parachute. Except for flat circular parachutes, D_c differs from D_o. The constructed area S_c is the area of a circle whose diameter is D_c.

Aerodynamic forces change the shape of the canopy from its constructed configuration to a concave scalloped contour when it fills to its inflated shape. To characterize the dimensions of the inflated decelerator in constant-velocity flight requires projecting the area of the inflated canopy onto the plane of the skirt reinforcement. This measured projected area is S_p. Projected diameter D_p is defined as the diameter of a circle whose area is S_p. Figure 3.4 defines other characteristic dimensions of the inflated canopy. Other parachute and gore layout dimensions from Reference 1.7 are given for completeness in several figures even though the dimensions are not discussed in the text.

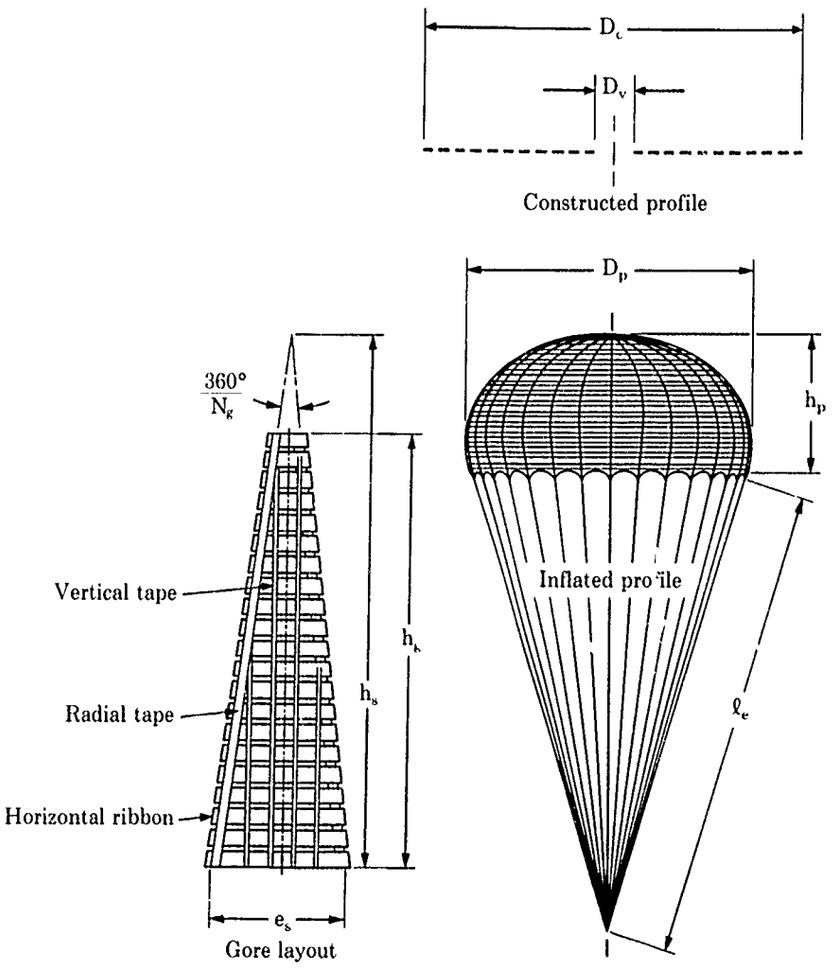


Figure 3.4. Flat circular ribbon parachute (taken from Ref. 1.7)

3.2 High-performance decelerator configurations

Most of the shape factors, general aerodynamic characteristics, and applications of high-performance decelerators listed in Table 3.1 are taken from Reference 1.7. Numerical values for inflated shape factor D_p/D_o and the unreefed aerodynamic drag coefficient C_{D_o}* represent a range of values influenced by geometric factors and fluid dynamic parameters such as:

- Canopy size
- Canopy porosity
- Suspension line length
- Mach number
- Forebody shape and size
- Number of gores
- Material type, strength, and porosity
- Air density
- Dynamic pressure, q
- dq/dt

Applications of specific high-performance decelerators are noted in Table 3.1. The term "drogue parachute" refers to an initial-stage decelerator whose purpose is to decelerate the payload from its initial flight speed and orientation with respect to the oncoming air. A pilot parachute, typically a guide surface or a ribbon canopy, is commonly used to extract the deployment bag containing the main canopy from the payload. Other high-performance decelerators provide cargo extraction, payload stabilization, payload trajectory modification, and terminal descent functions such as providing a specified impact velocity and impact angle.

Table 3.1. High-Performance Decelerator Characteristics

Type	Constructed Shape D_c/D_o	Inflated Shape D_p/D_o	C_{D_o}	Average Angle of Oscillation	General Application
Parachutes					
1. Flat circular ribbon	1.0	0.67	0.45 to 0.50	0 to ±3°	Pilot, drogue, deceleration, descent
2. Conical ribbon	0.95 to 0.97	0.70	0.50 to 0.55	0 to ±3°	Pilot, drogue, deceleration, descent
3. Lifting conical ribbon	~0.95	~0.70	0.55 to 0.65	Lateral instability	Lifting stores (L/D~0.7)
4. Hemisflo ribbon	0.62	0.62	0.30 to 0.46	±2°	Supersonic drogue
5. Ringslot	1.0	0.67 to 0.70	0.56 to 0.65	0 to ±5°	Extraction, deceleration, descent
6. Ringslot/solid canopy	0.97	0.65 to 0.68	0.85 to 0.95	±18° to±22°	Deceleration, descent
7. Ringsail	1.16	0.69	0.75 to 0.90	±5° to ±10°	Descent
8. Disk-gap-band	0.73	0.65	0.52 to 0.58	±10° to ±15°	Supersonic drogue, descent
9. Guide surface (ribbed)	0.63	0.62	0.28 to 0.42	0 to ±2°	Stabilization, pilot, drogue, descent
10. Guide surface (ribless)	0.66	0.63	0.30 to 0.34	0 to ±3°	Pilot, drogue, descent
11. Rotafoil	1.05	0.90	0.85 to 0.99	0 to ±2°	Drogue
12. Vortex ring	1.90	N/A	1.5 to 1.8	0 to ±2°	Descent
Other					
1. Ballute	0.51	0.51	0.51 to 1.20	⩽±1°	Stabilization, supersonic drogue

* Based on nominal canopy area, S_o

3.2.1 Parachutes

All high-performance decelerators are parachutes except for the inflatable ballute. Type designations of parachutes relate generally to the profile of the canopy, its planform, or other characteristic features. While many parachutes are constructed with solid textile canopies, most high-performance parachutes incorporate slotted textile configurations to relieve stresses at high deployment velocities. These configurations are based on the flat circular ribbon parachute but include design features to extend their performance to meet more stringent system requirements. The sections that follow describe successful high-performance parachute configurations in greater detail and provide recent examples. More detailed aerodynamic information on these parachutes is contained in Chapters 4 and 5.

3.2.1.1 Flat circular ribbon parachutes

Figure 3.4, taken from Reference 1.7, shows the constructed geometry and inflated profile of the flat circular ribbon parachute. The canopy lies in a flat plane and consists of ribbons (also called horizontals) separated by open spaces. Most of the drag is generated by the pressure differential across the ribbons; these forces are transmitted to the radials and down the suspension lines to the payload.

The gore layout in Figure 3.4 is for a cut-gore canopy construction in which each gore is built separately from other gores. Gores are then sewn together along the radial tapes. The resulting canopy geometry is a regular polygon of N_g sides. Horizontal ribbons are straight segments that are parallel to each other and that intersect the radials at an angle of $90 - (360/2N_g)$ degrees. Horizontal ribbons are supported by small tapes called verticals, which are oriented perpendicular to the horizontals. The primary purposes of the verticals are to control the spacing (gap size) between horizontals and to minimize ribbon camber and twist during inflation and descent. Without verticals, gap sizes and ribbon twist may increase until the local canopy porosity becomes high enough to prevent complete inflation of the parachute. The spacing between horizontal ribbons and verticals is selected to provide the porosity (the ratio of open space in the canopy to total canopy area) needed to obtain repeatable inflation times and manageable loads.

The higher porosity of the flat circular ribbon parachute causes it to have lower drag, better stability, longer inflation times, and lower inflation loads than the flat solid cloth circular parachute. Reference 1.7 gives detailed comparisons of aerodynamic characteristics. An example is the 44-ft-diameter flat circular ribbon landing/braking parachute for the B-52.[17] Another successful application is the 8.3-ft-diameter deceleration and stabilization parachute for the XS-2 aircraft ejectable nose section for crew escape.[26]

3.2.1.2 Conical ribbon parachutes

Because the conical ribbon parachute exhibits ~10% higher drag than the flat circular ribbon parachute without sacrificing stability, conical ribbon parachutes have superseded flat ribbon parachutes for most high-performance applications. Figure 3.5 shows the construction of a cut-gore conical ribbon parachute.[17] The canopy is constructed as the surface of a regular pyramid of N_g sides and base angle μ by joining gores having a vertex angle β less than $360/N_g$ degrees. Other design features are the same as for a flat circular ribbon canopy.

Several design modifications have been made to the conical ribbon canopy over the past 30 years to improve its reliability and performance. One such modification was the introduction of a new method for constructing conical ribbon parachutes to obtain higher ratios of parachute strength to weight than could be achieved from cut-gore constructions. This new method is called continuous ribbon construction. Instead of constructing gores separately and sewing them together, a single piece of material is used to form each ribbon in the canopy. Each ribbon passes from one gore to the next, continuing around the entire canopy with only one splice per ribbon instead of $2N_g$ splices. Since cutting and sewing the ribbon material makes it weaker than the original uncut ribbons, the continuous ribbon parachute is inherently stronger than the cut-gore parachute. Because the canopy is constructed as a whole rather than on a gore-by-gore basis, construction complexity, fabrication time, and costs are greater for a continuous ribbon parachute.

Another modification to the conical ribbon parachute involved the use of a single length of webbing to form four suspension lines. When laid on the table, the webbing assumes a "figure-eight" shape as it forms the radials and suspension lines of one gore, then passes continuously across the vent to form the radials and suspension lines of the opposing gore. Only one suspension line splice is used for every four suspension lines, instead of one splice for each suspension line. Like the continuous

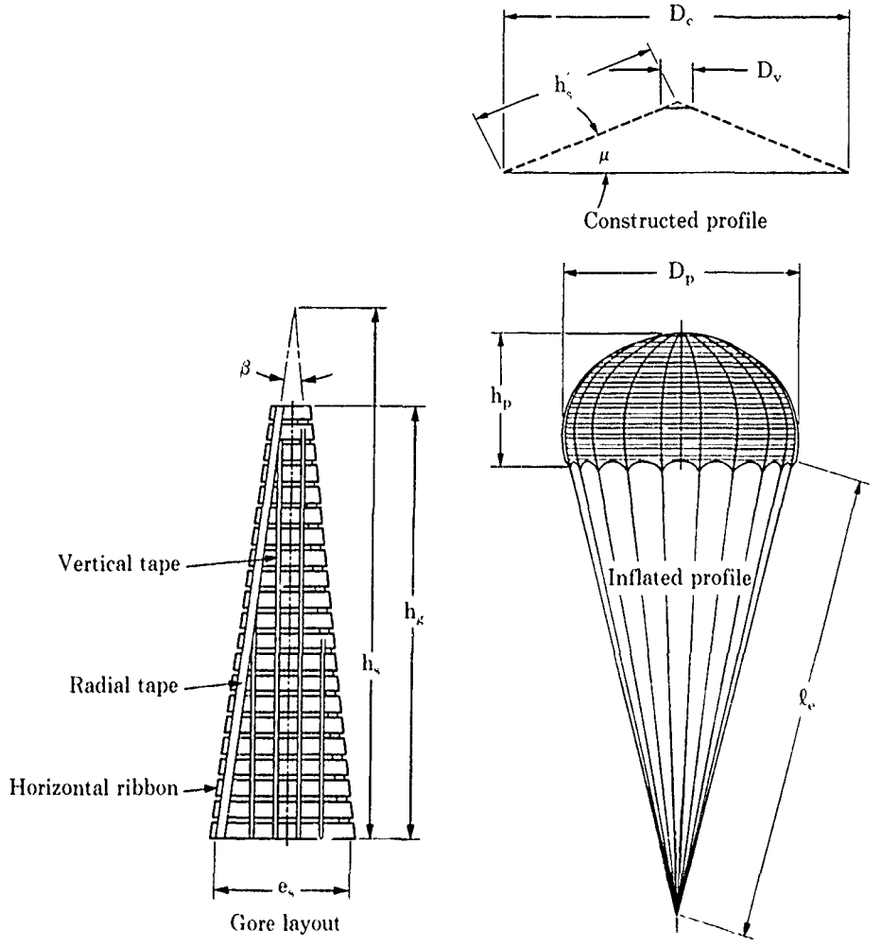


Figure 3.5. Conical ribbon parachute (taken from Ref. 1.7)

ribbon construction, the figure-eight suspension line design increases parachute strength while decreasing parachute weight and volume.

An example of a conical ribbon parachute that uses these design features is described by Maydew and Johnson.[3.1] The parachute is a 22.2-ft-diameter conical ribbon configuration for decelerating a 2100-lb store. The typical gore construction is shown in Figure 3.6. The parachute is composed of 32 gores and 32 suspension lines with a 20-degree conical shape. The calculated geometric porosity of the canopy is 23%. The entire parachute, including suspension lines, is fabricated of nylon materials except for the fiberglass cutter pocket lining.

The gores are composed of 46 equally spaced, continuous horizontal ribbons. Ribbon 1, which is closest to the apex and is called the vent band, consists of two plies of 1.75-in.-wide, 10,000-lb nylon webbing. Horizontal ribbons 2 through 13 are constructed of 2-in.-wide, 3000-lb breaking-strength nylon webbing. Horizontal ribbons 14 through 26 are constructed of 2-in.-wide, 2200-lb nylon webbing, and horizontal ribbons 27 through 45 are constructed of 2-in.-wide, 1000-lb nylon webbing. Horizontal ribbons 14 and 27 are reinforced with one ply of 0.75-in.-wide, 3000-lb nylon webbing. The skirt band (ribbon 46) is made of one ply of 1.75-in.-wide, 10,000-lb nylon webbing. The ends of the continuous horizontal ribbons are joined at the radials using 3-cord nylon thread in a 4-point cross-stitch pattern. The radial on which the joint (called a "lap") is placed varies with ribbon number; on this canopy, the laps form spirals around the canopy. All horizontal ribbons are held in place by 0.56-in.-wide, 500-lb vertical tapes. One tape lies over the horizontal ribbons and one tape lies underneath.

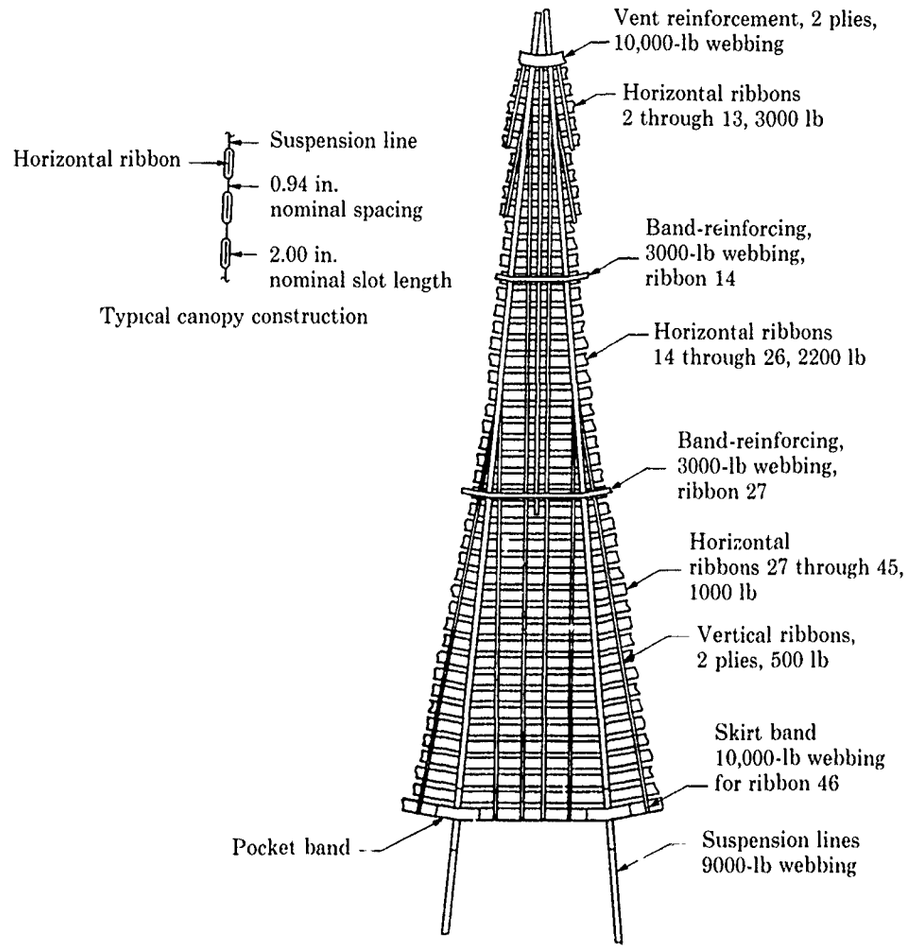


Figure 3.6. Typical gore construction for 22.2-ft-diameter, 20-degree conical ribbon parachute

Pocket bands are used on the canopy to provide a more rapid, symmetrical, and repeatable inflation by generating radial outward forces at the skirt. On this parachute, a pocket band constructed of 3600-lb nylon webbing, 1.72 in. wide, is positioned on the skirt band at each suspension line, except at lines 1 and 17. At these two positions is a reefing line cutter pocket fabricated of nylon cloth lined with fiberglass material.

Suspension lines are fabricated of slotted nylon webbing 1.13 in. wide with 9000-lb breaking strength. Each suspension line begins with an attachment loop ~24 ft from the skirt and continues over the canopy, terminating in a loop ~24 ft from the opposite skirt. One length of webbing forms four suspension lines, and all suspension lines are spliced in the vent area. Two attachment loops (four suspension lines) are brought together to form a line group. Each line group is covered with a protective sleeve of nylon cloth.

Reefing is used in this parachute to decrease the initial opening-shock load on the canopy to allow incorporating lighter materials into the parachute design. A canopy skirt reefing line, 19.25 ft long and fabricated from 1-in.-wide, 9000-lb nylon webbing, is used to restrict temporarily the opening of the canopy to an effective diameter of ~14 ft. The reefing line's cutter powder train is initiated with a lanyard at parachute line stretch; the reefing line is severed 0.5 s later. A chrome-plated steel reefing line ring is incorporated underneath the canopy skirt at each suspension line, except at positions where a reefing line cutter is present. These rings are held in place with a 6.75-in. length of 1.75-in.-wide, 6500-lb nylon webbing stitched to the skirt.

Maydew and Johnson[3 1] conducted 29 aircraft and rocket-boosted tests to deploy this 22.2-ft-diameter reefed parachute at dynamic pressures from 390 to 2720 lb/ft^2, corresponding to low release altitudes at Mach numbers up to 1.7. The reefed and full-open peak loads measured with accelerometers in the 2100-lb test vehicle varied from 12 to 66 g and from 15 to 49 g, respectively, over the range of dynamic pressures of reefed stage deployment. A typical vehicle deceleration record for a supersonic deployment of this reefed parachute is shown in Figure 3.7. Note that most of the deceleration occurs within 1.5 s. These data confirm that parachute deployment and inflation are very time-dependent aerodynamic and structural interactive processes.

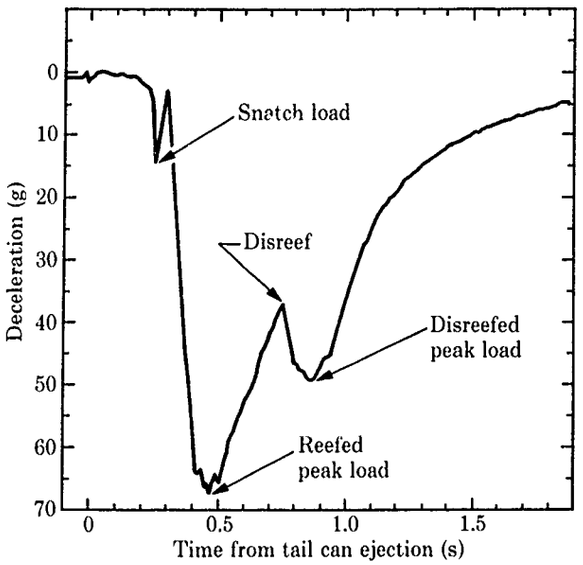


Figure 3.7. Typical vehicle deceleration record

Other examples of high-performance conical ribbon parachutes include those developed by the USAF and Sandia National Laboratories for ordnance deployed at very high dynamic pressures. Pepper[3 2] and Pepper and Maydew[2 15] describe the design of 12.5-, 17-, 20-, 48- and 76-ft-diameter heavy-duty conical ribbon parachutes. Pepper[3 3,3 4] discusses a 20-ft-diameter reefed ribbon parachute designed for deployment dynamic pressures up to 5700 lb/ft^2. At these extreme dynamic pressures, the failure of a single ribbon can cause the progressive failure of the entire gore. Consequently, new horizontal nylon ribbons of up to 4000-lb tensile strength, with special reinforced selvage, were developed for this heavy-duty parachute. The selvage ribbon has three times the edge-tearing strength of a flat ribbon. To achieve tear resistance, some of the fill yarn is moved to the edges of the selvage ribbon by a special weaving process. Selvage ribbons were used in all of the parachutes discussed above.

An extension of the continuous conical ribbon parachute, called an "all-radial" construction, has been developed by Johnson.[3 5] The new design feature involves the substitution of "mini-radials" for the verticals (shown in Figure 3.4). Figure 3.2 shows that the ribbons in a continuous ribbon parachute are actually constructed as concentric circles centered at the apex rather than as parallel straight lines. Each ribbon is perpendicular to the radial tape. Mini-radials are used instead of verticals in all-radial continuous ribbon parachutes because they are also perpendicular to the continuous ribbons. The magnitude of stress concentrations at ribbon/radial and ribbon/mini-radial crossings is reduced by making these crossings perpendicular, even when low elongation materials such as Kevlar are used. Since the mini-radials do not intersect the radials, bulky sewn joints and undesirable stress concentrations are eliminated. The term "all-radial" comes from the observation that both radials and mini-radials are segments of lines that pass through the apex.

The first application of all-radial construction for a high-performance system is discussed by Johnson and Peterson.[3 6] Both the 3.8-ft-diameter, 20-degree conical ribbon pilot parachute (a cluster of three is used) and the 46.3-ft-diameter, 20-degree conical ribbon main parachute were designed using this all-radial construction. Since this type of parachute cannot be placed on a flat pattern,

fixtures[3 5] are used during the layout and basting of the parachute to control the alignment of the ribbons and the radial members.

Waye[3 7] recently developed an interactive computer code to define the layout of conical (either single or multiconic) ribbon parachutes. The code determines the pattern length, vent diameter, radial length, top and bottom lengths of the ribbon, and geometric local and average porosity for the designer with inputs of constructed diameter, ribbon widths, ribbon spacings, radial width, and number of gores. The gores are designed with one mini-radial in the center and an option for the addition of two outer mini-radials. The code output provides all of the dimensions necessary for the design and construction of the parachute. The output can also be used as input into other computer codes used to predict parachute loads.

3.2.1.3 Lifting conical ribbon parachutes

In 1973, Rychnovsky[3 8,3 9] initiated the development of a two-stage lifting parachute system to provide a method for delivering a 2400-lb payload only 100 ft above the ground from an aircraft traveling at Mach numbers up to 1.2. A lifting parachute has intentional canopy asymmetries that cause it to trim at an angle of attack with respect to the direction of flight. It is designed to slow the payload down while simultaneously increasing its altitude above the ground. At this point, sufficient altitude is available for the deployment and inflation of a large, lightweight, second-stage parachute that provides a vertical ground impact at very low speeds. This lifting parachute development program included analyses,[3 10 3 14] extensive wind tunnel tests,[3 15 3 19] and over 40 full-scale flight tests using B-52, A-7, F-4, and F-111 carrier aircraft.[3 19] It is summarized here because it represents the first major attempt to use a lifting parachute for a high-performance application.

A sketch of the 13-ft-diameter slanted ribbon lifting parachute is shown in Figure 3.8. Its canopy configuration is based on a 20-degree conical all-radial ribbon design. There are 24 gores with thirty-one 2-in.-wide continuous ribbons. The vent band (ribbon 1) is made of 3000-lb nylon reinforced with 10,000-lb nylon webbing. Ribbons 2 through 10 are made of 3000-lb nylon and ribbons 11 through 31 are made of 1500-lb nylon. These ribbon strengths were based on structural analysis of the canopy,[3 10] on wind tunnel tests, and on full-scale flight tests. The skirt band reinforcement of ribbon 1 is 10,000-lb, 1-in.-wide Kevlar webbing. Figure-eight suspension lines are used on this parachute; they are 18 ft long and made of 13,500-lb Kevlar webbing. The radials are reinforced with 1000-lb nylon ribbon, with one ply over the horizontal ribbons and one ply under the suspension line at the radial juncture.

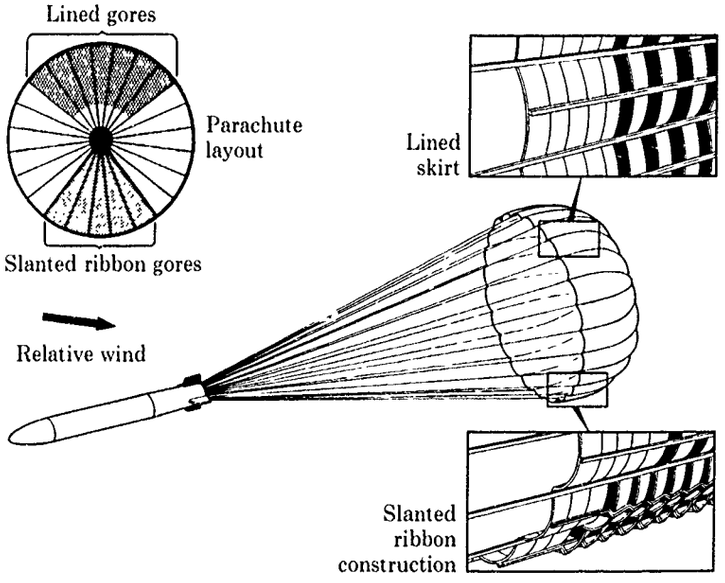


Figure 3.8. Slanted ribbon lifting parachute

The basic ribbon parachute was made to trim at a nonzero angle of attack by creating a porosity asymmetry across the canopy. On early configurations, the seven gores on the top of the canopy, where lift is required, were lined with 7 oz/yd^2 nylon cloth from ribbons 6 through 30 to create a local region of low porosity. In the five lower gores diametrically opposite the low-porosity region, a high-porosity region is created by inclining the horizontal ribbons relative to the basic canopy-inflated contour. The slanted ribbons were intended to act as a cascade, allowing increased flow through that portion of the parachute and deflecting the flow downward through a larger angle than would be possible without the slanted ribbons. Extensive wind tunnel and flight test data indicated that the trim angle of this 13.5-ft lifting parachute was ~35 degrees and the lift-to-drag ratio (L/D) was 0.7. Similar performance was obtained when the slanted ribbons were replaced by standard ribbon construction and when other liner configurations were used at the top of the canopy.

Rychnovsky and Everett[3.15] and Bolton[3.16] presented the first wind tunnel aerodynamic data on this lifting parachute. Bolton, Holt, and Peterson[3.19] conducted wind tunnel, whirl tower, and full-scale aircraft drop tests to increase the trim angle and L/D of this basic lifting parachute. Modifications investigated included increased liner area, increased slanted ribbon area, flow-directing side vents, and ram-air-inflated leading-edge chambers. Trim angles as high as 46 degrees (Figure 3.9a) were obtained with small-scale (40-in.-diameter) wind tunnel models (Figure 3.9b), whereas maximum trim angles of 40 degrees were obtained subsequently with flight tests of full-scale parachutes.

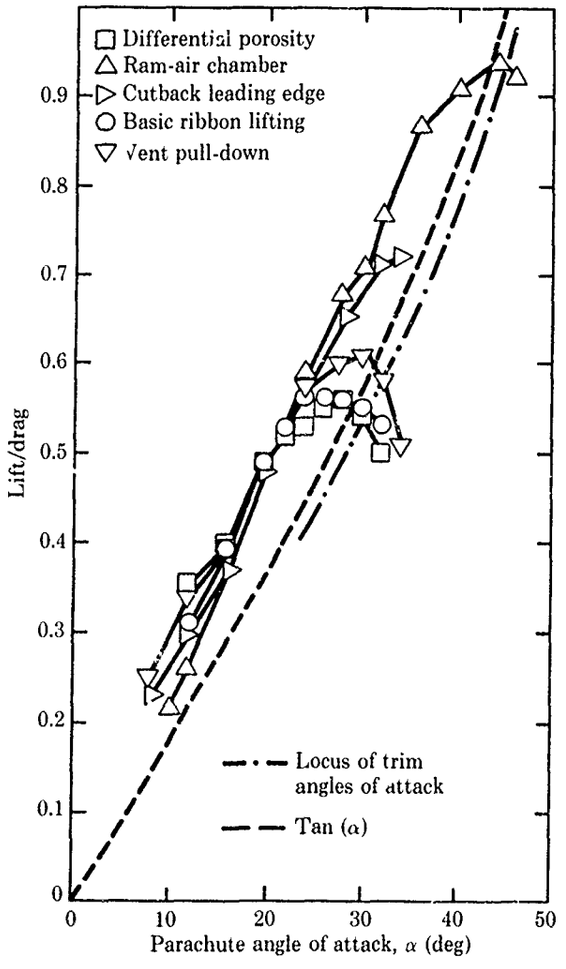


Figure 3.9a. Lifting parachute lift/drag wind tunnel data

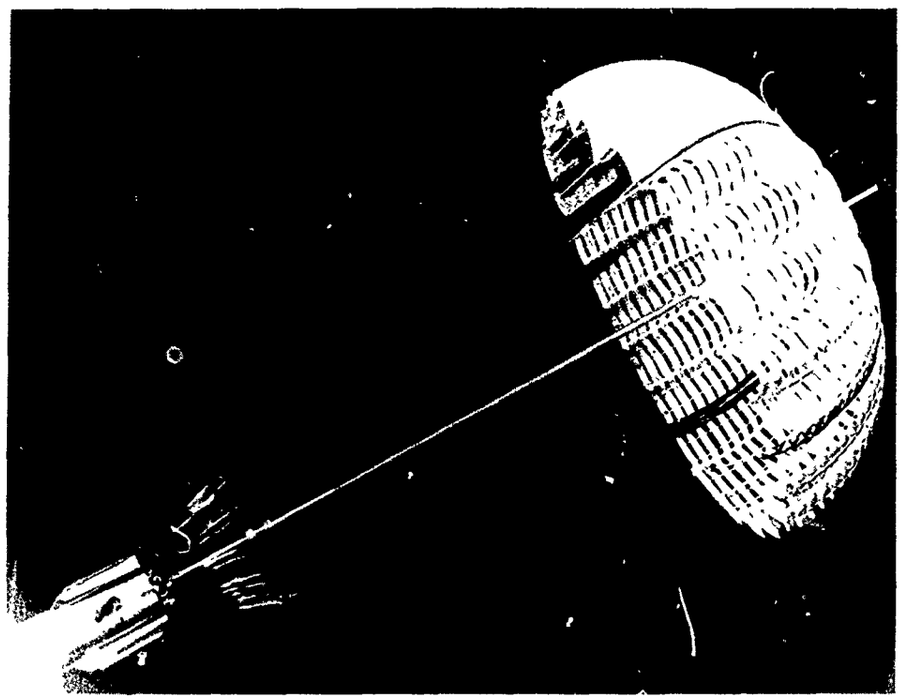


Figure 3.9b. Small-scale wind tunnel lifting parachute canopy

Full-scale tests of different configurations of the 13-ft lifting parachute were conducted in the NASA-Ames 40-ft by 80-ft wind tunnel.[3.18,3.19] Figure 3.10 is a photograph of a lifting parachute in this facility. The full-scale payload shape was mounted on the wind tunnel strut for this test. Potentiometers measured the model pitch and yaw angles, and parachute axial force and roll moment were measured by strain gauges located within the forebody. Parachute pitch, yaw, and roll relative to the forebody were measured using a small computer-controlled video camera mounted on the model base. Table 2 of Reference 3.19 summarizes the aerodynamic performance of these full-scale, lifting parachute parametric wind tunnel tests. Trim angles as high as 40 degrees were obtained in these full-scale wind tunnel tests.

Analysis of the flight mechanics of lifting parachutes proved to be essential in developing their design. Flight dynamics test data were analyzed on an analog computer using a two-body model with 7 degrees of freedom. Computer simulations indicated that the major source of roll torque was the parachute normal force, coupled with the yaw angle of the lifting parachute relative to the forebody. The pure roll torque is small compared to this yaw-induced rolling torque. NASA wind tunnel data confirmed that yaw-roll interaction was a prime source of aerodynamic roll moment of the lifting parachute.

A roll attitude control system was used for all of the flight tests of the 13-ft lifting parachute. It orients the payload after aircraft separation and before and during parachute deployment so that, when the parachute inflates, the lift vector is directed upward. The roll-control system eliminated roll rates induced by the store ejectors and turbulence beneath the aircraft. The system consisted of a solid-propellant gas generator and valved nozzle assemblies. The valved nozzle assemblies are constant-flow, three-position devices (clockwise thrust, null thrust, and counterclockwise thrust) with 40-Hz minimum response. The generator contains ~8.3 lb of fuel that will generate a total angular impulse of 675 ft-lb-s with a nominal 2-s burn time. The roll attitude of the store is obtained by electronically integrating the roll rate sensor output.

Bolton[3.11,3.13] developed an analog/digital (hybrid) computer simulation of the equations of motion for a forebody/parachute system. The system was modeled as a composite body in the translational and rotational equations of motion, and the parachute was treated as a flexible extension of the body, free to rotate in pitch, yaw, and roll relative to the body. The hybrid simulation was used extensively to analyze the forebody/lifting parachute flight mechanics. This included an evaluation

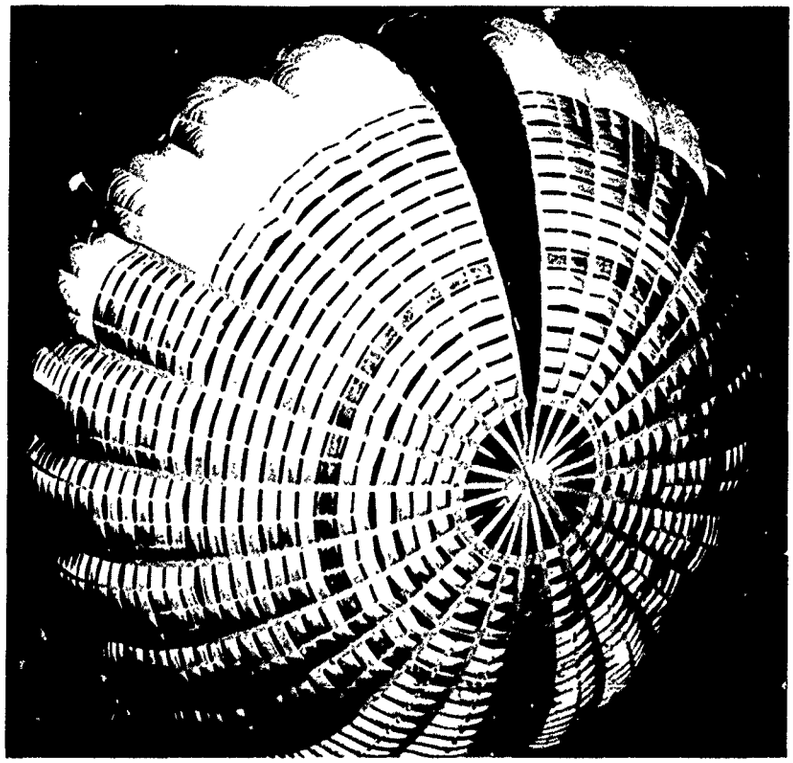


Figure 3.10. Full-scale lifting parachute in NASA-Ames 40-ft by 80-ft wind tunnel

of the effect of parachute aerodynamic modifications on the system motion, an evaluation of the effectiveness of the body-mounted, roll-control system in maintaining the correct parachute roll orientation (i.e., lift vector nearly vertical), and an evaluation of the effect of the lifting parachute aerodynamic/flight mechanic characteristics on the ground dispersion and impact velocity and angle of the store.

Schatzle and Curry[3.11] also developed a hybrid 9-degree-of-freedom (9-DOF) code to simulate the flight characteristics of an aircraft-delivered vehicle with a lifting parachute system. They compared their predicted flight dynamics and trajectory of a forebody with a lifting first-stage parachute and a ringsail second-stage parachute with output from a 6-DOF digital code and with flight test data. The agreement was very good, indicating that both digital and hybrid computers provide valid simulations.

Analyses of the wind tunnel data, flight test data, and computer simulation of the store/lifting parachute indicated that the hot-gas roll-control system used for full-scale flight tests performed satisfactorily. It oriented the lift vector of the 13-ft parachute nearly vertical during the 2-s operational time of the lifting parachute. In addition to the roll-control system, accurate fabrication and quality assurance techniques[3.20] were developed to ensure a very symmetrical lifting parachute and thereby minimize the pure roll torque coefficient developed by the lifting parachute, especially during the opening process, when the dynamic pressures are very high.

The lifting parachute canopy is reefed for 0.5 s to decrease the opening-shock loads. After investigating 16.5-ft and 18-ft lengths, a 20.6-ft, 13,500-lb Kevlar reefing line was used for reefing the lifting parachute at the middle of each gore. A special pyrotechnic-actuated reefing line cutter was developed[3.21] for cutting the Kevlar line. A programmable time delay firing signal is provided by means of an interconnecting cable that is attached to one of the suspension lines and terminates in a plastic connector attached to the cutter assembly on the parachute.

The maximum inflation axial forces generated by the 13-ft lifting parachute were measured with accelerometers on the payload in 13 flight tests and are presented in Figure 3.11 for the three reefing line lengths. The predicted decelerations for the 18-ft-long reefing line are also shown in Figure 3.11. The measured decelerations are, in general, less than the predicted decelerations, probably due to the asymmetric opening process of this lifting parachute, which is not taken into account by the predictive

model. Note that the maximum opening-shock load was ~185,000 lb at a dynamic pressure of 2750 lb/ft^2. Rocket-boosted parachute structural overtests were conducted at these high dynamic pressures (25% above the maximum design dynamic pressure) to verify the parachute structural design margin.

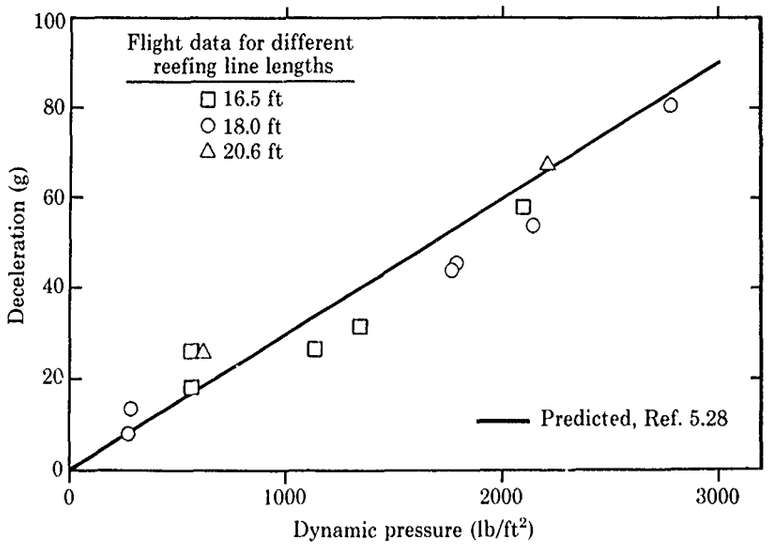


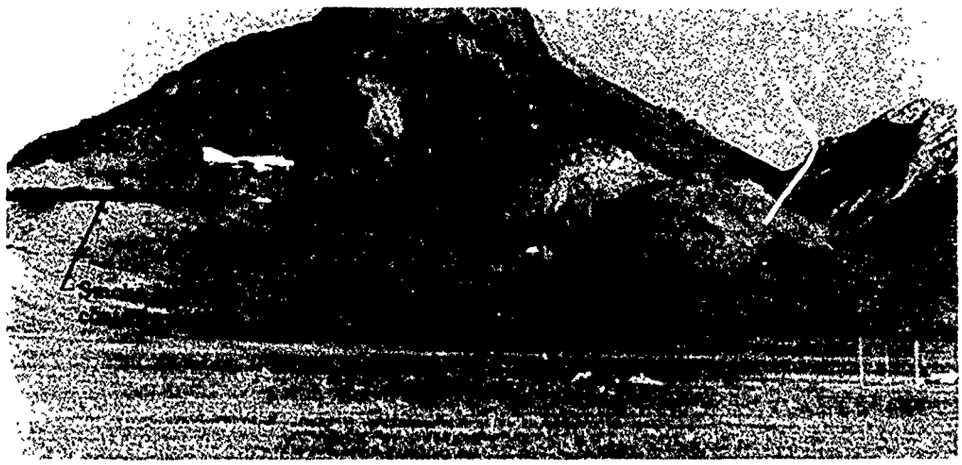
Figure 3.11. Measured and predicted reefed lifting parachute opening-shock loads

The lifting parachute's performance was demonstrated in a 1978 flight test wherein the 2400-lb payload was lifted 460 ft above the aircraft release altitude. The F-4 aircraft was flying at Mach 0.97 and at an altitude of 180 ft above ground level at release. The time sequence of events and the resulting store altitude, range, and velocity are given in Table 3.2. The aircraft was climbing at 15 ft/s at the time of payload release. A series of photographs (Figure 3.12) shows the payload lifting from 0.68 s to 2.3 s after release from the aircraft.

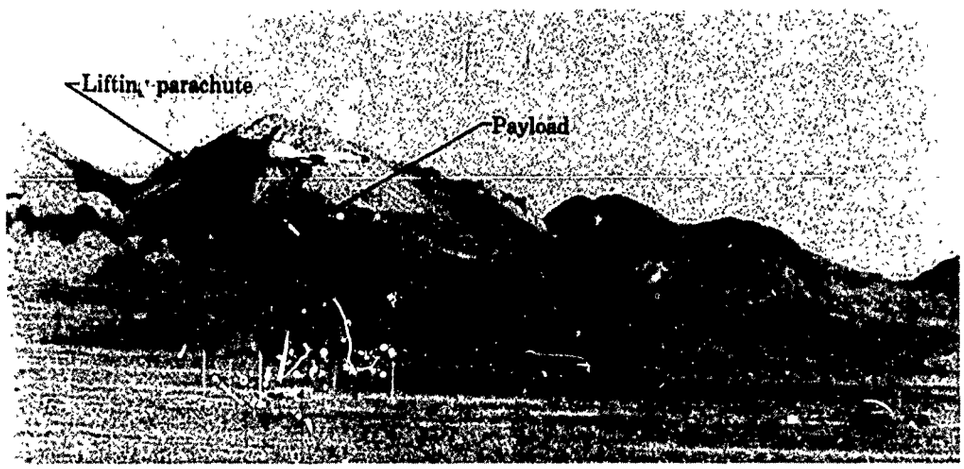
Table 3.2. Sequence of Events on Lifting Parachute Flight Test

Event	Time of Event (s)	Altitude (ft above MSL)	Velocity (ft/s)	Range (ft)
Release	0	5548	1073	0
Roll control initiated	0.47	5547	1064	502
Tail can off	0.60	5546	1062	639
Lifting chute inflated	1.00	5536	951	1055
Lifting chute acting	3.00	5748	297	2044
Ringsail chute deployed	5.35	5959	155	2431
Store apogee	6.80	6005	133	2624
Ringsail chute inflated	7.75	5994	80	2719
Impact	19.45	5367	58	2729

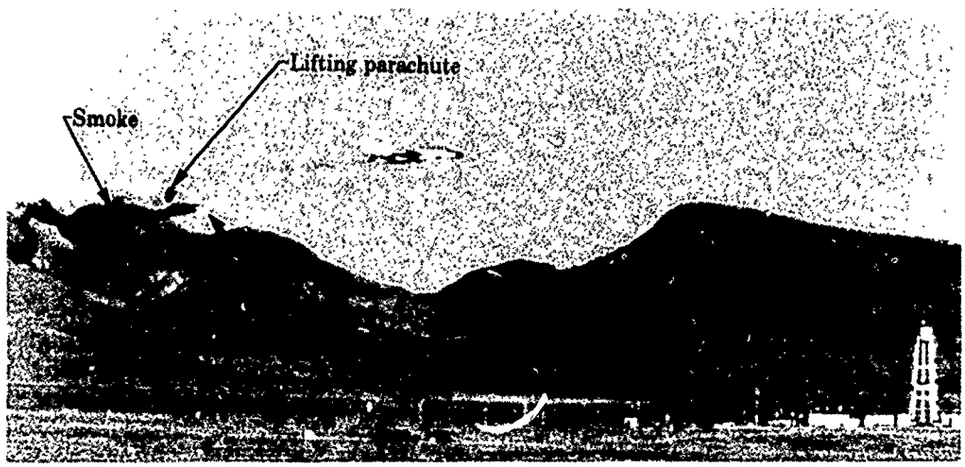
MSL = mean sea level



Frame 1: t = 0.68 s, −3 ft

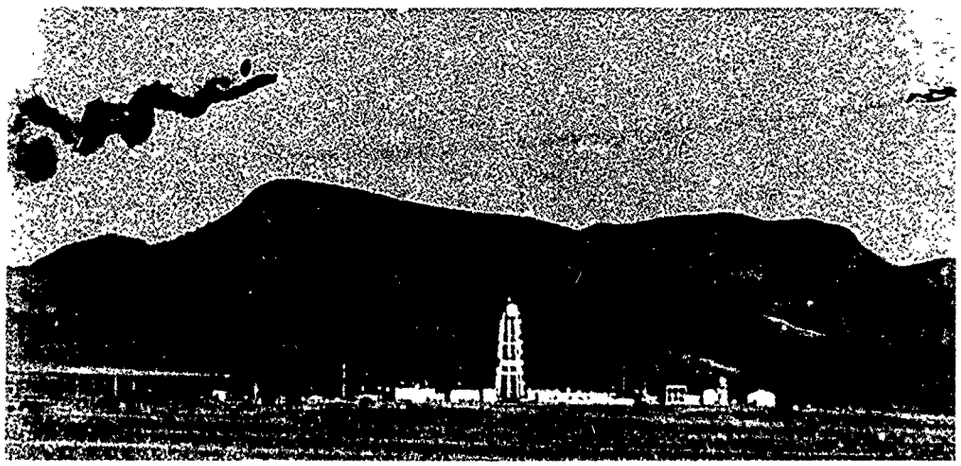


Frame 2: t = 1.08 s, −15 ft

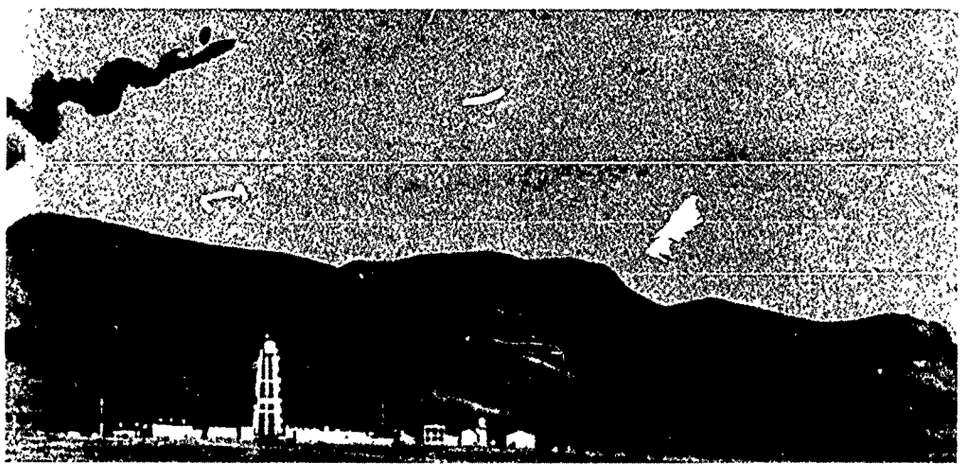


Frame 3: t = 1.41 s, +43 ft

Figure 3.12. Photos of test PTU-101, F-4 release of lifting parachute/store (continued on next page)



Frame 4: t = 1.99 s, +68 ft



Frame 5: t = 2.3 s, +109 ft

Figure 3.12. Photos of test PTU-101, F-4 release of lifting parachute/store (concluded)

3.2.1.4 Hemisflo ribbon parachutes

The constructed shape of the hemisflo canopy is a portion of a spherical surface that usually continues past a hemisphere at the skirt. Figure 3.13[17] is a sketch of a 15-degree hemisflo parachute. This configuration has adequate drag and good stability over the range of Mach numbers from 1.5 to 2.5, although conical ribbon parachutes are as good or better at speeds below Mach 1.5 (Table 3.1). Hemisflo parachutes are used almost exclusively for drogue applications at supersonic speeds.

Considerable design information, including the results of wind tunnel and flight tests, has been developed for hemisflo parachutes.[29,3 22-3 31] Bloetscher[3 28] successfully conducted rocket-boosted tests of a reefed 16-ft-diameter hemisflo parachute (with 10% extended skirt and 14% porosity) at Mach numbers from 1.5 to 1.84 at altitudes to 15,500 ft. The tests confirmed that this parachute had excellent aerodynamic characteristics and adequate strength to withstand opening-shock loads of up to 200,000 lb. An application of the hemisflo parachute is the stabilization brake parachute for the 3130-lb aircraft crew module for the F-111.[17,3 32] This 6-ft-diameter parachute has a geometric porosity of 15% and sixteen 2400-lb suspension lines. The F-111 drogue is designed to operate up to a Mach number of 2.2.

Peterson et al.[12] investigated using a hemisflo parachute for decelerating an 800-lb payload from Mach 2.15 to subsonic Mach numbers at low altitudes. The maximum dynamic pressure at parachute deployment was 4400 lb/ft^2. Wind tunnel tests at NASA-Lewis Research Center indicated that the

conical ribbon parachute models had higher drag than the hemisflo parachute, but the drag of the hemisflo was more constant over the Mach number range of 0.1 to 2.6. Additional wind tunnel tests[3 22] showed that only the hemisflo was stable in the wake of the actual payload to be recovered; most conical ribbon parachutes were unstable and exhibited periodic inflation and deflation motions (squidding). However, 19 rocket-boosted flight tests of these 3.7-ft- to 5.3-ft-diameter conical ribbon and hemisflo parachutes showed that the conical ribbon parachutes stayed inflated during the deceleration to subsonic speeds, whereas the hemisflo collapsed when the payload slowed to Mach 1. Although a conical ribbon parachute was subsequently chosen for this systems application, the flight tests[1 2] and wind tunnel tests[3 22] suggest that this hemisflo parachute might have performed satisfactorily if its suspension lines had been made longer to allow placing the canopy farther behind the base of the forebody.

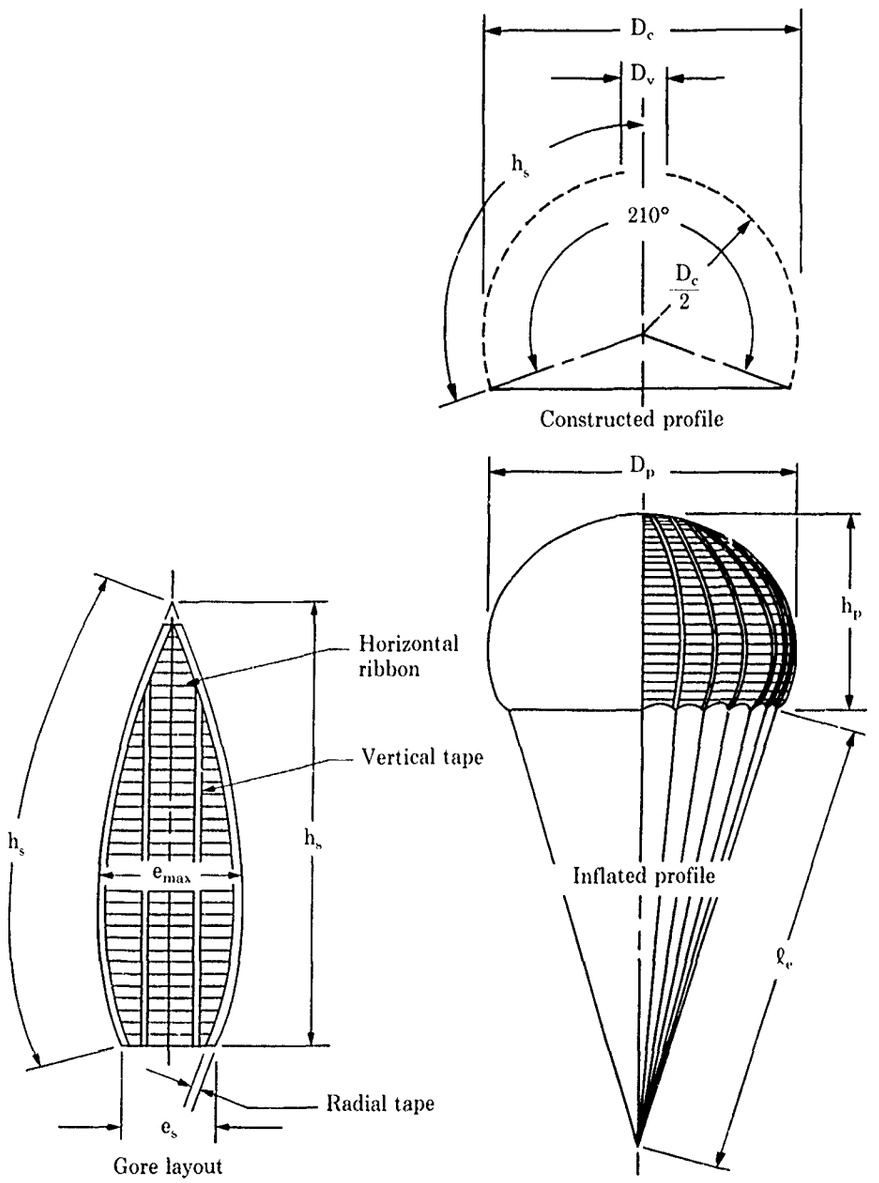


Figure 3.13. Hemisflo parachute (taken from Ref. 1.7)

3.2.1.5 Ringslot parachutes

The ringslot parachute was invented by Knacke and co-workers at the FIST[2.4] in Germany in the 1930s during the evolutionary process of their invention of the ribbon parachute. It was developed by Knacke and Hegele in 1949 at Wright-Patterson AFB as a low-cost substitute for ribbon parachutes.[2.9] This parachute is constructed with either flat or conical designs. The canopy is constructed of concentric cloth strips, generally 1 ft wide, separated by slots in a manner similar to the assembly of ribbon designs. Fewer operations are required, simplifying manufacture and reducing cost, compared to ribbon parachutes. A gore layout and the inflated profile are illustrated in Figure 3.14.[1.7]

The performance characteristics lie between those of the ribbon and solid cloth canopies (Table 3.1). The ringslot is more stable than a solid canopy and is suitable for deployment at moderate subsonic speeds, higher than a solid canopy could withstand. Ringslot parachutes are used for aircraft landing deceleration, extraction of air drop equipment,[3.33] tandem engagement midair recovery systems,[3.34] and final recovery parachutes. The opening reliability is comparable to that of ribbon parachutes. Purvis[3.35] systematically varied the canopy reefing ratio in his wind tunnel studies of the effect of pocket bands on the drag of 5-ft-diameter ringslot parachutes at subsonic speeds.

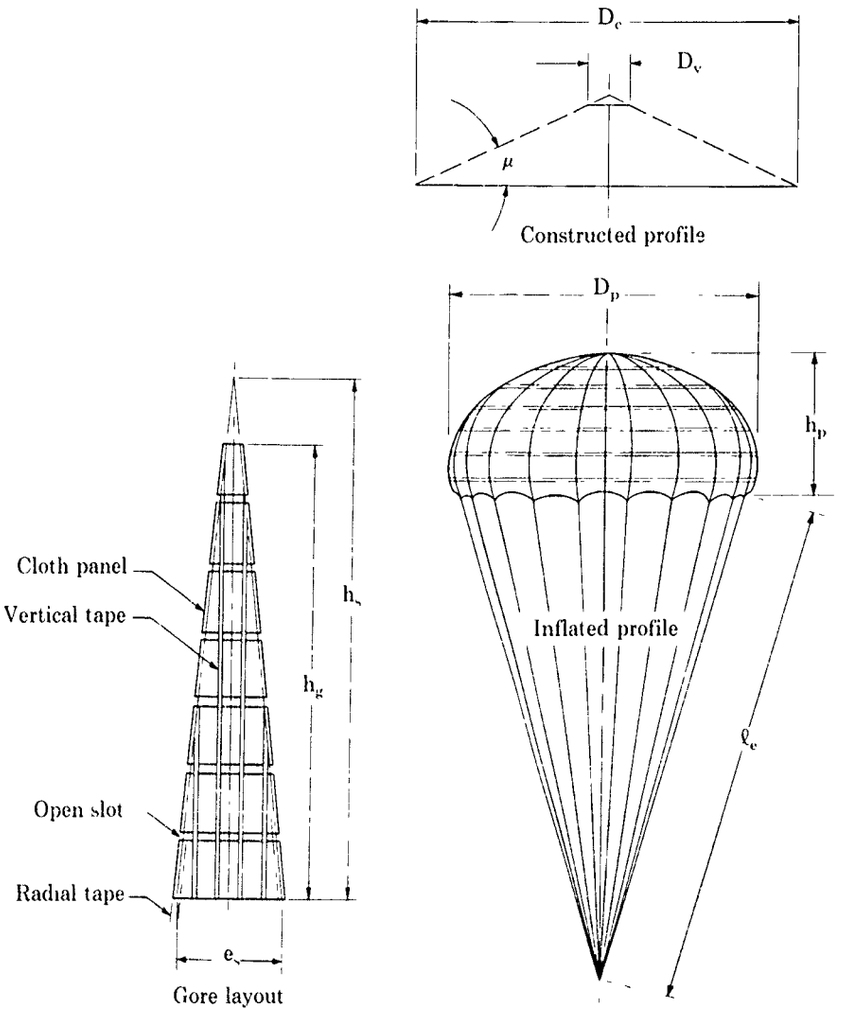


Figure 3.14. Ringslot parachute (taken from Ref. 1.7)

3.2.1.6 Ringslot/solid-canopy parachutes

Johnson[1,5,37] (also see Peterson and Johnson[3,36]) invented the ringslot/solid-canopy parachute to satisfy the system requirements of a prototype parachute cluster to decelerate the F-111 aircraft Crew Escape Module to an impact velocity of 25 ft/s. Since the parachute system must be deployed at dynamic pressures as high as 300 lb/ft^2, the parachute was designed with geometric porosity in the center of the canopy to control inflation loads. The low impact velocity, coupled with the restrictions in parachute system weight and volume, required this parachute to have the highest possible drag coefficient. This requirement suggested designing the outer portions of the canopy to have no geometric porosity.

The resulting ringslot/solid-canopy parachute is shown in Figure 3.15. It is a 20-degree conical solid canopy with eight 12-in.-wide rings spaced 1 in. apart in the vent area. The constructed diameter of this 48-gore parachute was originally 52.5 ft, but higher-than-expected drag coefficients measured in flight tests have permitted a reduction in canopy diameter to 49 ft. Nylon was used for the vent rings and the solid canopy, and Kevlar was used wherever possible for the rest of the parachute structure to save weight. The suspension lines are 60 ft long and made of 400-lb Kevlar tape. Two stages of reefing are used to control aerodynamic loads. The three parachutes are connected at the skirts to provide position control during inflation. Each parachute weighs only 30 lb. Several aircraft drop tests with a 3200-lb test vehicle demonstrated the feasibility of this new hybrid parachute design.

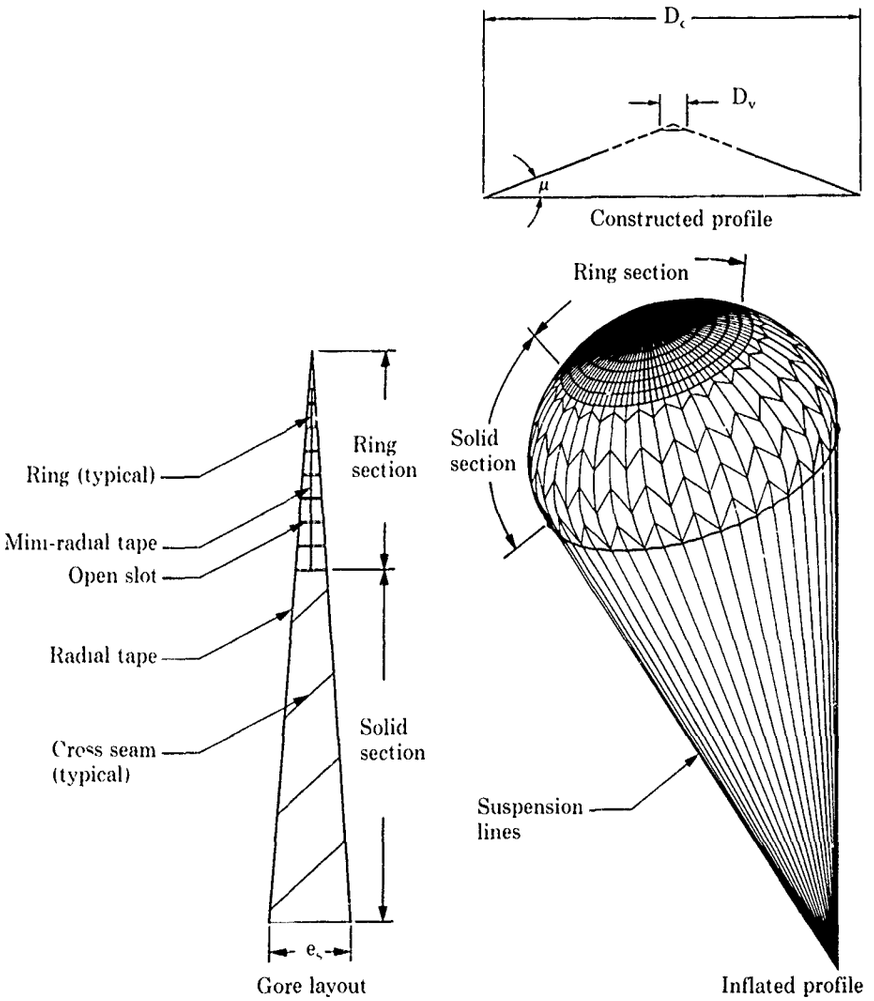


Figure 3.15. Ringslot/solid-canopy parachute

3.2.1.7 Ringsail parachutes

The ringsail is another derivative of the ringslot design. It was invented by E. G. Ewing[3.38] in 1953. This parachute design[1 7.2.1] is complex and develops a unique shape from the combination of a curved basic profile and fullness at the leading edge of annular cloth rings. Geometric features, including leading- and trailing-edge fullness, are illustrated in Figure 3.16. The constructed profile is a circular arc, tangent to a 15-degree cone at the apex and tangent to a 55-degree cone at the skirt. The ringsail canopy is constructed of wide concentric cloth strips separated by gaps in the upper crown; this portion is like the ringslot parachute. Over the remainder of the canopy, the gap spacing is zero and geometric porosity is obtained from the crescent-shaped slots, which result from the fact that the cloth dimension between radials is longer for the leading edge of each sail than for the trailing edge of the sail below it. Geometric porosity is determined by the three-dimensional inflated shape of the sails as well as by gap spacing.

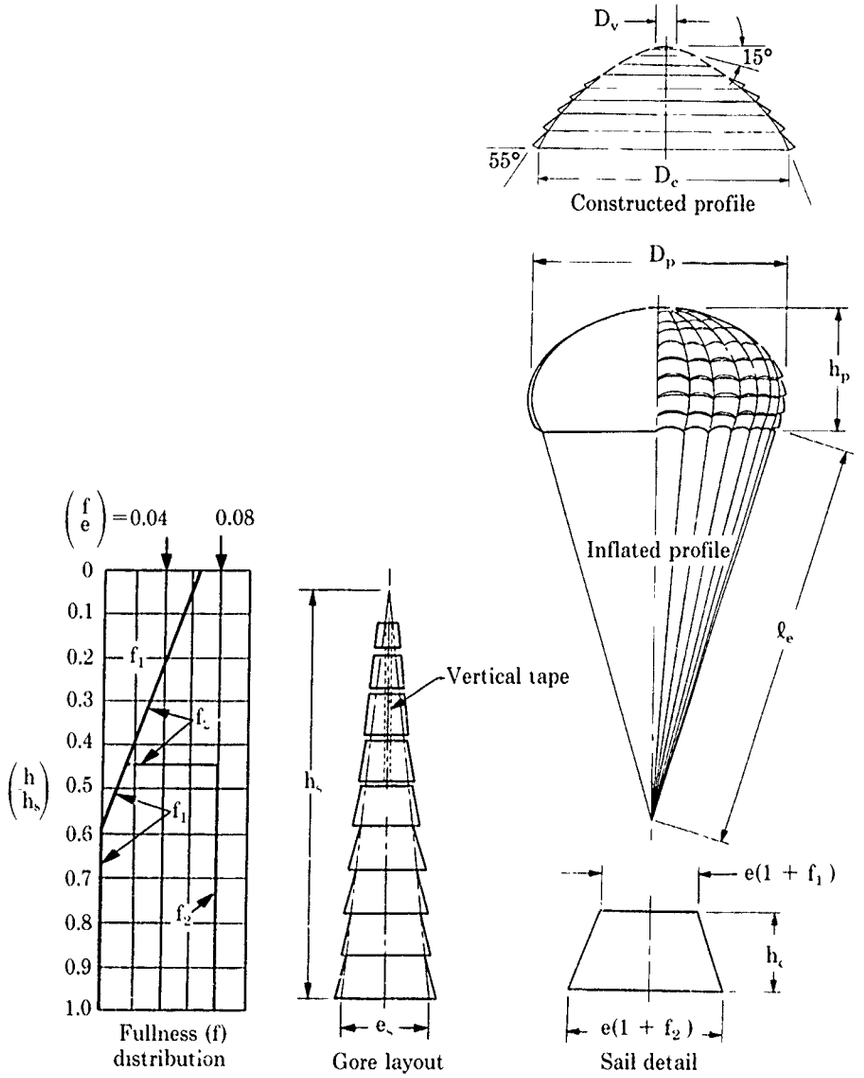


Figure 3.16. Ringsail parachute (taken from Ref. 1.7)

Major applications of the ringsail parachute include a 63.1-ft-diameter parachute for the 2340-lb Mercury capsule,[1,7] a cluster of three 85.6-ft-diameter parachutes for the 13,000-lb Apollo capsule,[1,7,3,38,3,39] and the 70-ft-diameter parachute for the 3130-lb F-111 Crew Module.[3,32] The ringsail parachute was selected as the final recovery parachute for the U.S manned orbital and space flights because of its lighter weight, slower inflation rate (thus lower opening-shock load), and improved stability, compared to a solid canopy. Pepper[3,40] designed and tested a 32-ft-diameter ringsail parachute as the second stage for a transonic, low-altitude, store application; 16 rocket-boosted tests demonstrated the feasibility of this parachute system at deployment dynamic pressures up to 2600 lb/ft^2.

A 38-ft ringsail parachute was used as the second-stage decelerator with the lifting parachute described in Section 3.2.1.3. This ringsail canopy had 36 gores and seven rings of 2.25-oz/yd^2 nylon cloth with 90 lb/in. tensile strength. The top three rings were the ringslot pattern (no fullness) for the higher loading in the vent area during opening. The bottom four rings were the ringsail pattern. The suspension lines, made of 2000-lb Kevlar, were 44 ft long. Analysis of phototheodolite data of several full-scale tests indicated that the drag area (C_DS) of this parachute in terminal descent was 736 ft^2, with a standard deviation of 25 ft^2. The maximum oscillation of this parachute in terminal descent with the 2400-lb payload was ± 6 degrees.

3.2.1.8 Disk-gap-band parachutes

The disk-gap-band parachute was developed and patented by C. V. Eckstrom in the mid-1960s, under contract to NASA-Langley Research Center. Intended to operate at very low dynamic pressures at high altitudes (above 200,000 ft) and supersonic speeds,[3,41,3,43] this parachute is designed to have better stability than a solid flat canopy without loss of the desirable features of drag efficiency and ease of construction. The canopy is constructed as a flat circular disk and a cylindrical band separated vertically by an open space (Figure 3.17). The right-angle change in constructed shape from the band to the disk portion of the canopy provides a discontinuity in the surface shape and causes the airflow to become separated around the edge at all times. By adjusting the width of the gap, the flow of air exiting from the interior of the canopy can be controlled sufficiently to maximize the drag of the parachute while maintaining the required degree of stability. The air flowing through the gap provides an additional disturbance to the air flowing over the outer surface of the canopy.

A gore consists of a triangular top and rectangular bottom (Figure 3.17). The disk, gap, and band areas are 53%, 12%, and 35% of the nominal area S_o, respectively. Dacron materials were used for the Viking 53-ft-diameter disk-gap-band parachute to withstand the effects of heat sterilization and densely packed storage until deployed in the Martian atmosphere. The Viking parachute was developed by NASA-Langley Research Center; Martin Marietta Corporation, Denver, Colorado; and Goodyear Aerospace Corporation, Akron, Ohio.[3,44,3,46]

3.2.1.9 Ribbed guide surface parachutes

Heinrich[2,7,3,47,3,48] invented the ribbed guide surface parachute in Germany (FGZ, Stuttgart-Ruit) in 1941 for braking and stabilizing finless bombs, torpedoes, containers, and mines. The shape of the guide surface parachute was designed to provide exceptional stability. To understand how this is accomplished requires comparing how the airflow separates from conventional flat circular parachutes with how the airflow separates from the guide surface parachute.

Because flat circular cloth parachutes have continuous, smoothly-varying elliptical inflated shapes, the location of flow separation is determined by the local flow conditions along the curved canopy skirt, such as Reynolds number and streamwise pressure gradients. As the flat circular parachute oscillates, the location of separation moves around the canopy and creates a time-dependent pressure distribution that sustains the oscillatory motion. By changing the inflated canopy shape from a smoothly-varying ellipse to the discontinuous canopy configuration shown in Figure 3.18, the guide surface parachute fixes the location of flow separation at the discontinuity in canopy slope (at the position of maximum diameter), even when this canopy is displaced to large angles of attack. Therefore, the pressure distribution on the guide surface canopy is nearly independent of parachute oscillation angle. Without time-dependent pressures to sustain the motion of the canopy, the guide surface parachute remains at its equilibrium angle of attack of zero degrees with respect to the oncoming flow. Additional stability is provided by the conical guide surface at the canopy skirt.

The design of a typical ribbed guide surface parachute is illustrated in Figure 3.18.[1,7] The canopy shape is intricate. It is constructed from roof panels, guide surface panels, and internal ribs joined together to form the main seams. The canopy has a slightly rounded crown (roof) and an inverted

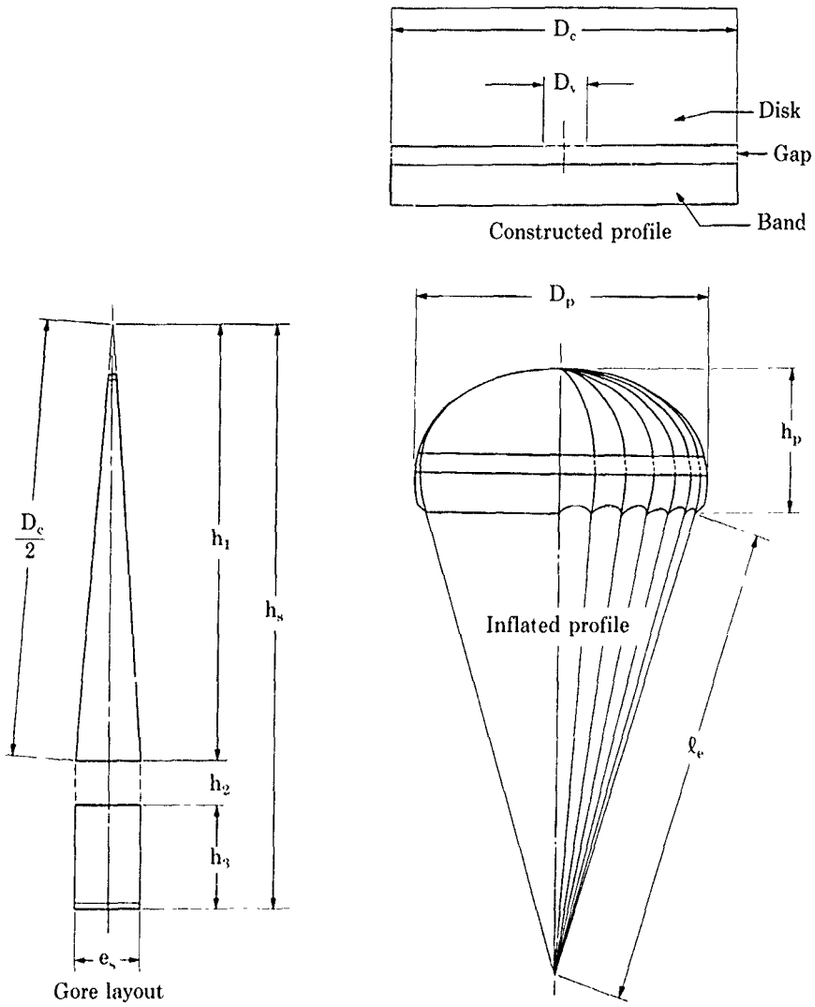


Figure 3.17. Disk-gap-band parachute (taken from Ref. 1.7)

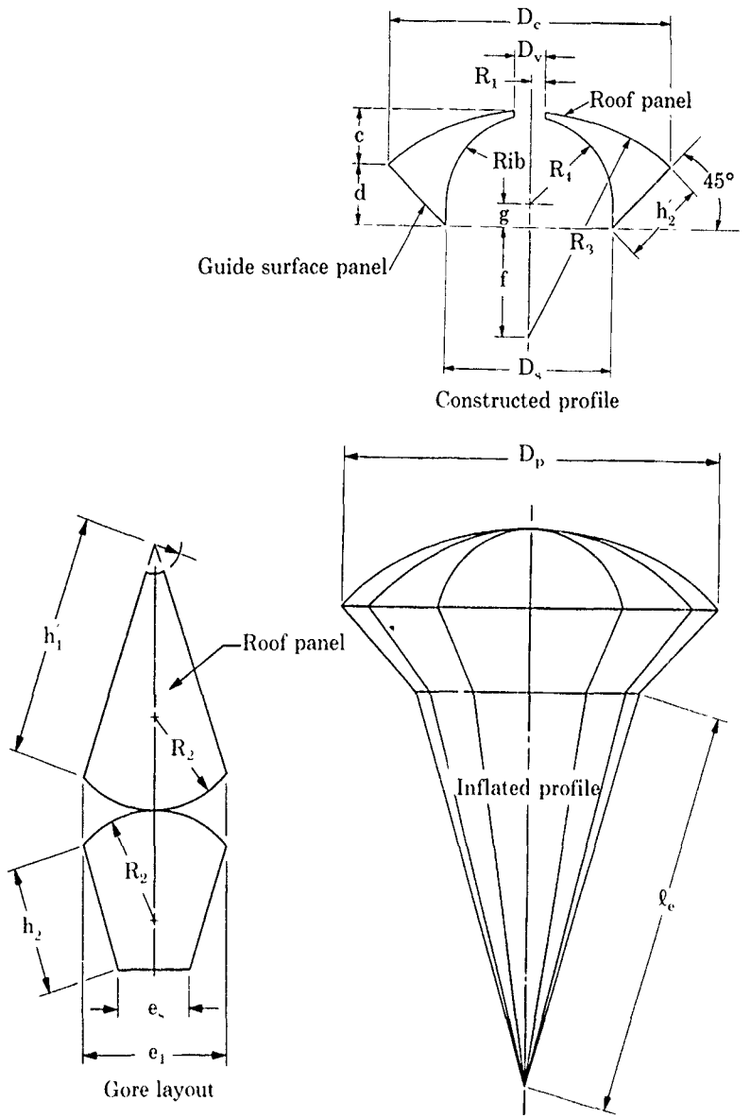


Figure 3.18. Ribbed guide surface parachute (taken from Ref. 1.7)

conical front (guide surface) extending from roof edge to skirt reinforcement. Ribs are placed between gores in a plane with suspension lines to maintain the constructed profile during operation. As discussed above, stability comes from the abrupt flow separation edge formed at the juncture of the guide surface and roof panels. Maximum coning angles are 2 degrees. Low-porosity cloth is used in the roof and guide surfaces to promote fast inflation and to maintain its inflated shape.

The ribbed guide surface parachute is reliable and very stable, but it has a lower drag coefficient than other parachute configurations and is difficult to manufacture. Heinrich describes both stabilization and brake guide surface parachutes in Reference 2.7. On a stabilization guide surface parachute, the size of the guide surface is increased to improve the stability. This decreases the drag and the parachute opening-shock load. The drag coefficient of a typical brake guide surface parachute is ~20% higher than the drag coefficient of a typical stabilization guide surface parachute.

In 1943, Heinrich et al.[3.47] successfully tested a 7.2-ft-diameter guide surface parachute with a geodesic suspension system to stabilize a finless torpedo after an aircraft release at 456 ft/s. Heinrich[3.48] discusses the extensive use of guide surface parachutes in Germany in the early 1940s to stabilize 1100-lb to 8810-lb bombs, 1100-lb to 2200-lb mines, and torpedoes. The U.S. Navy[3.49] used an 87-in.-diameter guide surface parachute to stabilize the Mark 44 and 46 torpedoes after release from a helicopter. Another systems application of the ribbed guide surface parachute is the 5-ft-diameter pilot parachute used to deploy the main ringsail canopy to recover the F-111 Crew Escape Module.[3.32]

3.2.1.10 Ribless guide surface parachutes

The ribless guide surface parachute was developed by H. G. Heinrich and R. S. Gross at Wright Air Development Center, Ohio, in 1948 as a low-cost substitute for the ribbed guide surface parachute. This type is constructed of bell-shaped roof panels and guide surface panels, joined together to form the main seams. The desired shape[1.7] is obtained by widening the roof panel to extend around the edge of the guide surface panel to the skirt edge. The rib is eliminated, thereby simplifying construction. The resulting flow separation edge is less abrupt, accounting for a slightly higher oscillation angle than the ribbed guide surface parachute. A vent at the outer edge of each guide surface panel also promotes flow separation. Dimensions for roof and guide surface panels depend on canopy diameter and the number of gores in the canopy. A sketch of the ribless guide surface parachute is shown in Figure 3.19.

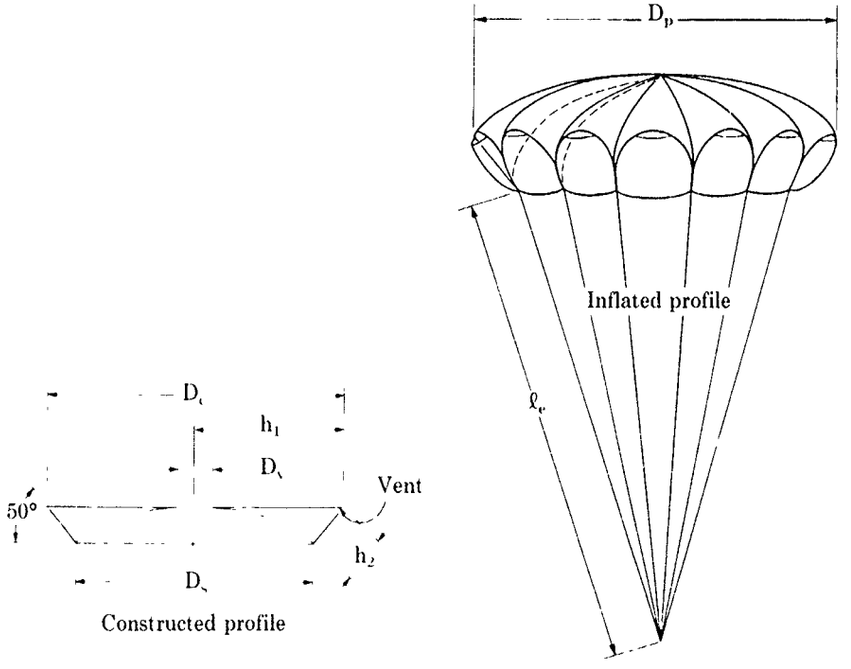


Figure 3.19. Ribless guide surface parachute (taken from Ref. 1.7)

The ribless guide surface canopy may be used for stabilization, deceleration, or extraction applications, and for other applications requiring extreme stability, quick opening, and high reliability. Cook Research Laboratories,[2.28] under contract to the USAF, conducted extensive wind tunnel, sled, and flight tests of the ribless guide surface parachute. They conducted a successful sled test of a 6.5-ft-diameter parachute at a velocity of 1214 ft/s.[2.9] Sandia National Laboratories has used ribless guide surface parachutes for many system applications over the last 30 years. Typical examples are the pilot parachute to extract the main canopy for low-altitude delivery of payloads,[3.1] recovery of rocket payloads,[3.50–3.52] and recovery of spinning shells.[1.4,3.53]

The "modified" ribless guide surface canopy[2.1] is also used by Sandia. This canopy is constructed by joining gore panels that were formed by a single gore pattern rather than the two patterns required in constructing the conventional ribless guide surface canopy. This canopy may also be used for stabilization, deceleration, extraction, and for other applications requiring a high degree of stability and reliability. This parachute is not as stable as the conventional ribless guide surface canopy; nonetheless, canopy oscillation is less than ±5 degrees. The manufacturing cost of this canopy is somewhat lower than that of the conventional ribless guide surface parachute and can replace it for most extraction applications.

3.2.1.11 Rotating parachutes

We describe three types of rotating parachutes in this section for completeness, even though the systems applications have been very limited. Rotation is achieved by providing openings (both asymmetrical and symmetrical) in gores to create a cascade of rotationally identical pitched sails. An alternate approach is to assemble a number of identical fabric sails rigged to provide the desired pitch and twist. Improved parachute performance and weight efficiency are obtained in exchange for the added complication of canopy rotation and the need for a swivel. The rotating parachutes have low opening loads, good stability, and high drag. These parachutes work well if limited to diameters of less than 10 ft. Problems with inflation and rotation have occurred with larger rotating parachutes.

3.2.1.11.1 Rotafoil

The rotafoil was invented by E. G. Ewing[3.54] of the Radioplane Company in the early 1950s. The construction is similar to that of a flat circular parachute. Each gore is a flat polygon with an open slot on one side of the gore (Figure 3.20).[1.7] The openings in each gore transform each roof panel into a sail during operation, which causes canopy rotation. The parachute is relatively low in bulk and weight. Slot areas should vary from ~20% to 32% of the total parachute area, S_o, as parachute diameter is decreased from 10 ft. A swivel has to be used to permit parachute rotation, relative to the suspended payload, while transmitting minimum torque to the payload.

The stability of the rotafoil is very much a function of the design. Models range from stable to unstable, with a decrease in drag coefficient in the stable models. The parachute canopy is relatively low in weight and bulk but, because of the swivel, this parachute system becomes bulkier and weighs more than do comparable ribbon, ringslot, or guide surface parachute systems. This parachute canopy may be used for general deceleration applications, and most designs are reliable in opening. A 7-ft-diameter rotafoil has been deployed at a velocity of 590 ft/s.[2.1]

3.2.1.11.2 Vortex ring

The vortex ring canopy was developed by Barish Associates of New York. It consists of four sail-like panels that rotate about its apex like helicopter blades in autorotation.[1.7] The panels, unlike the gores of conventional parachutes, are rigged to produce the panel shape and pitch needed to achieve the desired rotation rate. Pitch is determined by employing shorter leading-edge lines than trailing-edge lines from the junction of each suspension line (Figure 3.21). A swivel minimizes the torque transmitted to the payload. This canopy has excellent stability characteristics. Gross and Riffle[3.55] present wind tunnel and aircraft drop test data for this vortex ring parachute. Reefed vortex ring parachutes of 9.5 and 105 ft in diameter have been deployed at velocities of 676 ft/s and 220 ft/s, respectively.[1.7] Care must be taken in rigging to avoid inflation problems, and large vortex ring parachutes take a very long time to inflate.

3.2.1.11.3 Rotating flexible decelerator

Pepper[3.56] designed the rotating flexible decelerator (RFD) in 1979. A sketch of a 2-ft-diameter RFD is shown in Figure 3.22. The RFD "blades," as well as the circular vent cap required for positive inflation, are made of Kevlar cloth. Since the blades cover only about two-thirds of the gore width, they assume an angle of attack relative to the rotational velocity vector as a result of the interradial bulge from air loads. This results in a force vector that is tilted relative to the plane of rotation and therefore generates a rotational moment

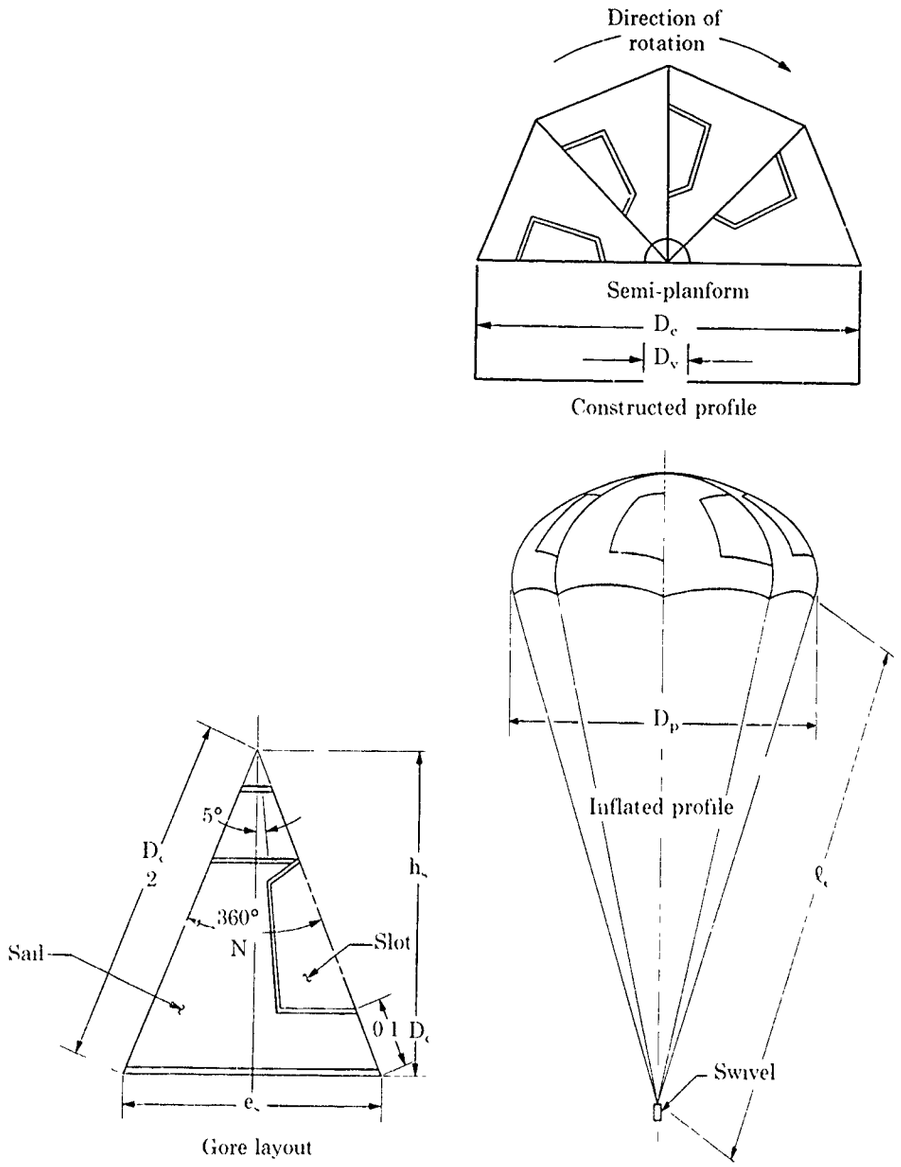


Figure 3.20. Rotafoil parachute (taken from Ref. 1.7)

Pepper conducted wind tunnel tests of the 2-ft-diameter RFD at speeds to Mach 2. He also conducted flight tests at transonic speeds of both a 2-ft-diameter and a 6-ft-diameter RFD. These test results indicated a drag coefficient of 1.0 to 1.25 (based on disk area) and excellent stability (negligible coning angle). The high spin rate of the canopy creates gyroscopic stability and large centrifugal forces that extend the rotor blades radially, producing additional drag. The flying shape of the RFD is much more like a flat spinning disk than the semielliptical shape of nonrotating cross parachutes.

Doherr and Synofzik[3.57] have used rotating parachutes to decelerate submunitions. They measured the drag coefficient and the propeller advance ratio inverse using scale-model rotating parachutes (circular flat, extended skirt, cross, and guide surface) in wind tunnel tests at DLR, FRG. They also defined (and measured) a rotor quality coefficient for comparison of different rotating parachutes. The altitude loss per revolution of a rotating parachute decreases as the rotor quality number increases.

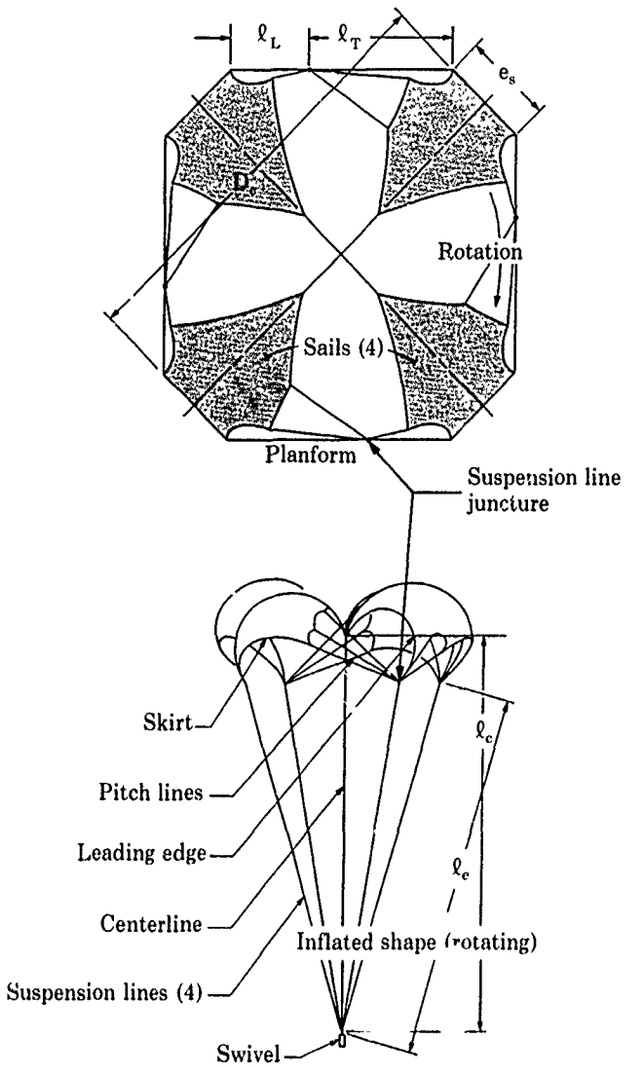


Figure 3.21. Vortex ring parachute (taken from Ref. 1.7)

3.2.2 Ballutes

Goodyear Aircraft Corporation, Akron, Ohio, developed the ram-air-inflated conical balloon "ballute" in the early 1960s for the USAF to stabilize and decelerate payloads at high altitudes and high speeds. Inflatable closed-envelope decelerators evolved from early experiments with towed spherical balloons.[17] The sphere provided a high-drag blunt body and was fabricated from material of very low porosity so as to stay inflated from a stored gas source.

Alexander[3 58] investigated the feasibility of deploying inflatable decelerators at altitudes to 200,000 ft and speeds to Mach 10. A "burble fence," made from a tubular ring affixed to the balloon just aft of the sphere's maximum diameter, is incorporated to provide flow separation for subsonic stability (Figure 3.23). Suspension lines are extended over the top of the sphere and around the radials, leaving the balloon surface from the point of tangency to the line confluence point. The trailing spherical balloon decelerator became known as a "ballute" and has evolved into a more uniformly stressed shape (Figure 3.24), which incorporates the cone of suspension lines into radial members of the balloon's forward surface. The compressed gas supply was replaced by ram-air inflation to minimize installed weight. Air scoops forward of the ballute's maximum diameter provide air inlets for inflation and ram pressure to fill and maintain its final shape.

McGirr, Aebischer, and Weinberg[3 59] conducted aircraft flight tests of 29-in.- and 41-in.-diameter ram-air-inflated ballutes and successfully demonstrated deceleration of 500-lb stores at ballute deployment speeds up to 1000 ft/s.

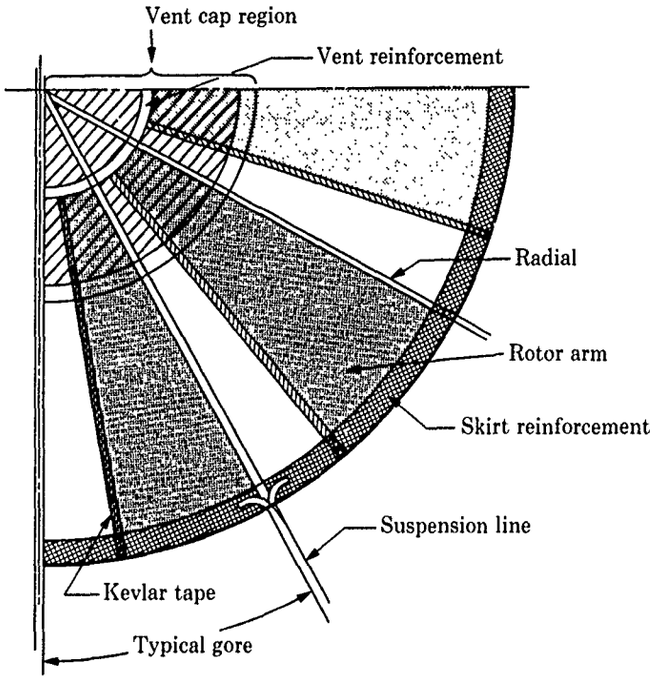


Figure 3.22. Rotating flexible decelerator

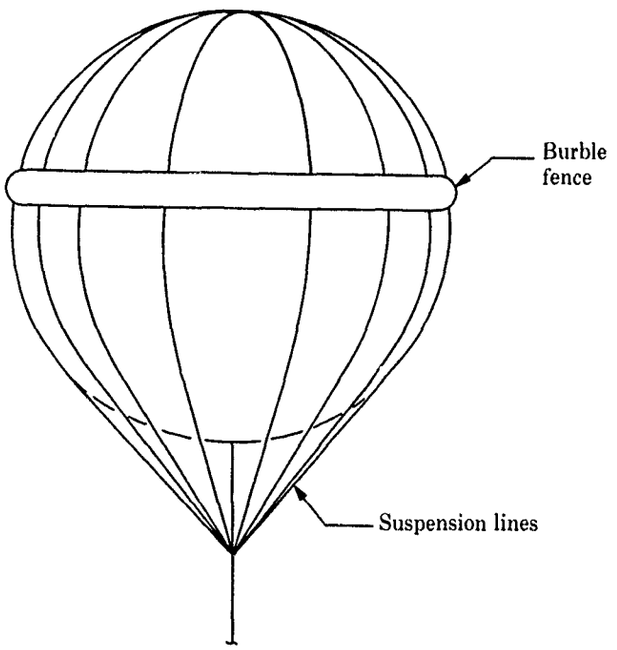


Figure 3.23. Balloon decelerator (taken from Ref. 1.7)

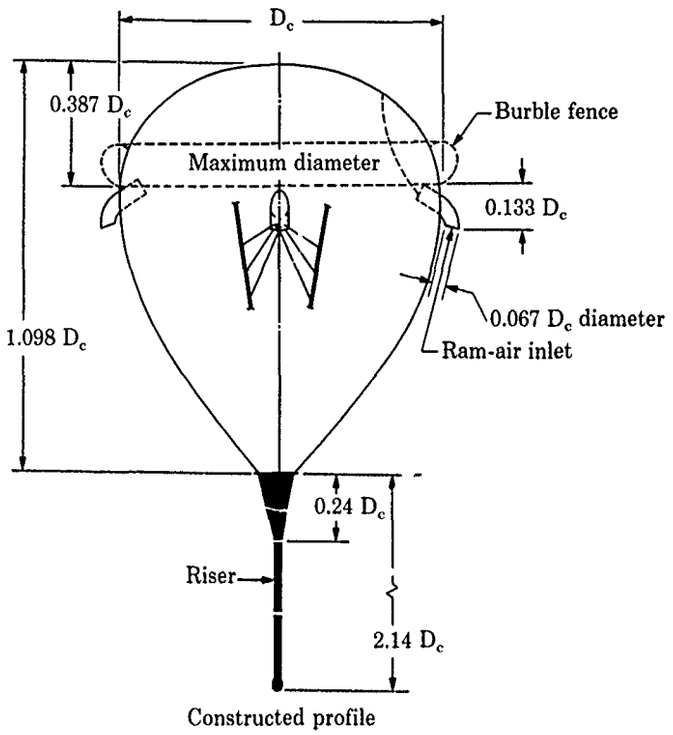


Figure 3.24. Ballute geometry (taken from Ref. 1.7)

References

3.1 R. C. Maydew and D. W. Johnson, "Supersonic and Transonic Deployment of Ribbon Parachutes at Low Altitudes," *J Aircraft*, Vol. 9, No. 7, July 1972.

3.2 W. B. Pepper Jr., *Parachute Design and Performance for Supersonic Deployment and for the Recovery of Heavy Loads*, SC-DC-69-1883, Sandia Laboratories, September 1969.

3.3 W. B. Pepper, "A 20-ft-diam Ribbon Parachute for Deployment at Dynamic Pressures Above 4000 psf," *J Aircraft*, Vol. 4, No. 3, May-June 1967.

3.4 W. B. Pepper, "Recent Flight-Test Results in Deploying a 20-ft-diam Ribbon Parachute," *J Aircraft*, Vol. 6, No. 1, January-February 1969.

3.5 D. W. Johnson, *All-Radial Construction for Continuous Ribbon Parachutes*, United States Patent 4,343,448, August 10, 1982.

3.6 D. W. Johnson and C. W. Peterson, "High-Speed, Low-Altitude Delivery Using a Single Large Parachute," AIAA 84-0803, April 1984.

3.7 D. E. Waye, "Computer Design Code for Conical Ribbon Parachutes," AIAA 86-2487, October 1986.

3.8 R. E. Rychnovsky, *Lifting Parachute*, United States Patent 3,927,850, December 23, 1975.

3.9 R. E. Rychnovsky, "A Lifting Parachute for Very-Low-Altitude, Very-High-Speed Deliveries," *J Aircraft*, Vol. 14, No. 2, February 1977.

3.10 S. D. Meyer, P. C. Klimas, and D. F. Wolf, "Structural Analysis and Design of a High-Performance Lifting Ribbon Parachute," AIAA 79-0428, March 1979.

3.11 W. R. Bolton, "Trajectory Simulation of a Parachute System," AIAA 79-0470, March 1979.

3.12 W. R. Bolton, *Hybrid Trajectory Simulation of the B77 System*, SAND77-8040, Sandia Laboratories, November 1977.

3.13 W. R. Bolton, *Hybrid Trajectory Simulation of a Parachute System*, SAND78-8668, Sandia Laboratories, April 1978.

3.14 P. R. Schatzle and W. H. Curry, "Flight Simulation of a Vehicle with a Two-Stage Parachute System," AIAA 79-0448, March 1979.

3.15 R. E. Rychnovsky and R. N. Everett, "Wind Tunnel Tests to Evaluate a Lifting Transonic Parachute," AIAA 75-1365, November 1975.

3.16 W. R. Bolton, *Aerodynamic Description of the B77 Parachute System*, SAND76-8045, Sandia Laboratories, November 1976.

3.17 R. H. Croll and C. W. Peterson, "A Computer-Controlled Video Instrument for Wind-Tunnel Testing of Lifting Parachutes," *J Aircraft*, Vol. 16, No. 4, April 1979.

3.18 R. H. Croll, P. C. Klimas, R. E. Tate, and D. F. Wolf, "Summary of Pa.achute Wind Tunnel Testing Methods at Sandia National Laboratories," AIAA 81-1931, October 1981.

3.19 W. R. Bolton, I. T. Holt, and C. W. Peterson, "Development of New Lifting-Parachute Designs With Increased Trim Angle," *J Aircraft*, Vol. 19, No. 11, November 1982.

3.20 R. E. Rychnovsky, "Fabrication and Quality Assurance Procedure to Assure a Symmetrical Lifting Parachute," AIAA 79-0427, March 1979.

3.21 J. R. Craig, *Development of the MC3133 Reefing Line Cutter*, SAND77-0955, Sandia Laboratories, September 1977.

3.22 W. B. Pepper, R. J. Buffington, and C. W. Peterson, "Exploratory Testing of Supersonic Ribbon Parachutes in the NASA 9-ft by 7-ft Wind Tunnel," AIAA 86-2446, October 1986.

3.23 A. B. Riffle, *Determination of the Aerodynamic Drag and Static Stability of Reefed Parachute Canopies*, USAF AFFDL-TR-64-166, January 1965.

3.24 L. L. Galigher, *Investigation of F-111 Crew Module Stabilization Parachute Models at Mach Numbers 0.5, 2.0, 2.2, and 2.5, Phase I*, USAF AEDC-TR-65-83, April 1965.

3.25 J. S. Deitering and E. E. Hilliard, *Wind Tunnel Investigation of Flexible Aerodynamic Decelerator Characteristics at Mach Numbers 1.5 to 6*, USAF AEDC-TR-65-110, June 1965.

3.26 W. C. Alexander and J. T. Foughner, "Drag and Stability Characteristics of High-Speed Parachutes in the Transonic Range," AIAA 73-473, May 1973.

3.27 J. K. Buckner, "Application of Axisymmetric Flow Analysis to Inflation Stability of Supersonic Flexible Parachutes," *Proceedings of Retardation and Recovery Symposium*, USAF ASD-TDR-63-329, May 1963.

3.28 F. Bloetscher, *Aerodynamic Deployable Decelerator Performance Evaluation Program, Phase II*, USAF AFFDL-TR-67-25, June 1967.

3.29 M. L. Homan, *Aerodynamic Characteristics of Several Flexible Decelerators at Mach Numbers From 1.8 to 2.5*, USAF AEDC-TR-71-6, January 1971.

3.30 C. A. Babish III, *Performance Characteristics of 5 ft Diameter Nylon and Kevlar Hemisflo Ribbon Parachutes at Dynamic Pressures up to 6000 psf*, USAF AFFDL-TR-78-75, June 1978.

3.31 C. A. Babish III, "A Continuous Surface of Revolution Parachute for Supersonic/Hypersonic Speeds," AIAA 70-1173, September 1970.

3.32 *The F-111 Crew Module*, Document FZM-12-4094E, General Dynamics, Fort Worth Division, April 1974.

3.33 F. B. Morris, *Performance Evaluation of Heavy Duty 28-ft D_o Ring Slot Extraction Parachutes*, USAF FTC-TR-69-43, December 1969.

3.34 M. W. Higgins and R. J. Speelman III, "A Stability Analysis of Tandem Parachute Mid-Air Recovery Systems," AIAA 73-461, May 1973.

3.35 J. W. Purvis, "Pocket Band Effects on Ringslot Parachutes," University of Minnesota/Carl-Cranz-Gesellschaft Parachute Systems Technology Course, Wessling, West Germany, June 1987.

3.36 C. W. Peterson and D. W. Johnson, "Advanced Parachute Design," University of Minnesota/Carl-Cranz-Gesellschaft Parachute Systems Technology Course, Wessling, West Germany, June 1987.

3.37 D. W. Johnson, "Testing of a New Recovery System for the F-111 Aircraft Crew Escape Module—An Update," AIAA 89-0891, April 1989.

3.38 E. G. Ewing, *Ringsail Parachute Design*, USAF AFFDL-TR-72-3, January 1972.

3.39 W. M. Mullins, D. T. Reynolds, K. G. Lindh, and M. R. Bottorff, *Investigation of Prediction Methods for the Loads and Stresses of Apollo Type Spacecraft Parachutes, Volume II—Stresses*, NVR-6432, Northrop Corporation, Ventura Division, California, June 1970.

3.40 W. B. Pepper, *Design and Development of a Three-Stage Parachute System for Low-Level Deployment up to Mach 1.2*, SC-DR-66-2707, Sandia Corporation, May 1967.

3.41 C. V. Eckstrom, *Development and Testing of the Disk-Gap-Band Parachute Used for Low Dynamic Pressure Applications at Ejection Altitudes at or Above 200,000 ft*, NASA CR-502, June 1966.

3.42 R. Lemke, *40-ft DGB Parachute*, NASA CR-66587, October 1967.

3.43 C. V. Eckstrom and J. S. Preisser, *Flight Test of a 40-foot Nominal Diameter Disk-Gap-Band Parachute Deployed at a Mach Number of 2.72 and a Dynamic Pressure of 9.7 psf*, NASA TM-X-1623, August 1968.

3.44 C. L. Gillis, "The Viking Decelerator System—An Overview," AIAA 73-442, May 1973.

3.45 S. Steinberg, P. M. Siemers III, and R. G. Slayman, "Development of the Viking Parachute Configuration by Wind Tunnel Investigation," AIAA 73-454, May 1973.

3.46 R. D. Moog, R. J. Bendura, J. D. Timmons, and R. A. Lau, "Qualification Flight Tests of the Viking Decelerator System," AIAA 73-457, May 1973.

3.47 Fl. Haupt-Ing. Wernitz Forschungsführung, Dr. Ing. Lange, Dr. A. Weible, Dr. Ing. Heinrich, and Ing. Heesemann, *Protokoll über Abswurfversuche mit Schirmstabilisiertem Torpedo F 5 a*, Forschungsanstalt Graf Zeppelin, Stuttgart-Ruit, July 1943, USAF Air Materiel Command, Wright Field, Ohio, Air Documents Division T-2, R8281-868.

3.48 H. G. Heinrich, *Bericht über die Arbeiten der Aerodynamischen Abteilung der Forschungsanstalt Graf Zeppelin*, FGZ, Stuttgart-Ruit, Spring 1945.

3.49 A. R. Ferrier, *Torpedo Stabilizer Mark 31, Mod 0, Development Phase*, Naval Air Test Unit, Quonset Point, Rhode Island, NAVAIRTORPU-TM-189, January 1966.

3.50 D. W. Johnson, "Development of Recovery Systems for High-Altitude Sounding Rockets," *J Spacecraft and Rockets*, Vol. 6, No. 4, April 1969.

3.51 D. W. Johnson, "Sounding Rocket Recovery Systems for Payload Weights From 50 to 1000 Pounds (23 to 454 kilograms)," AIAA 73-305, March 1973.

3.52 G. A. Fowler, R. C. Maydew, and W. R. Barton, "Sandia Laboratories Rocket Program—A Review," *Proceedings of the AIAA Fourth Sounding Rocket Technology Conference*, Boston, Massachusetts, June 1976 (also SAND76-0184, Sandia Laboratories, April 1976).

3.53 W. B. Pepper and R. D. Fellerhoff, "Parachute System to Recover Spinning Shell Subjected to 20,000 g's," *J Spacecraft and Rockets*, Vol. 6, No. 3, March 1969.

3.54 E. G. Ewing, *Rotafoil Performance Evaluation*, Radioplane Company, Van Nuys, California, Report No. 705, January 1953.

3.55 R. S. Gross and A. B. Riffle, *Performance Evaluation of the Vortex Ring Parachute Canopy*, USAF ASD-TR-61-410, October 1961.

3.56 W. B. Pepper Jr., "A New Rotating Parachute Design Having High Performance," *J Spacecraft and Rockets*, Vol. 23, No. 2, March-April 1986.

3.57 K.-F. Doherr and R. Synofzik, "Investigations of Rotating Parachutes for Submunitions," AIAA 86-2438, October 1986.

3.58 W. C. Alexander, *Investigation to Determine the Feasibility of Using Inflatable Balloon Type Drag Devices for Recovery Applications in the Transonic, Supersonic, and Hypersonic Flight Regime, Part II, Mach 4 to Mach 10 Feasibility Investigation*, USAF ASD-TDR-62-702, December 1962.

3.59 P. A. McGirr, A. C. Aebischer, and S. A. Weinberg, "Development and Testing of Ballute Stabilizer Decelerators for Aircraft Delivery of a 500-lb Munition," AIAA 73-485, May 1973.

CHAPTER 4

STEADY-STATE AERODYNAMICS

4.1 Characterization of parachute aerodynamics

The complexity of parachute aerodynamics is a direct consequence of the mission that parachutes are designed to accomplish. They are required to decelerate payloads that will not slow to a sufficiently low speed quickly enough on their own. Hence, parachutes must have much more drag than the object that they decelerate. Whereas most of the aerodynamics community is concerned with optimization of the aerodynamic efficiency of streamlined, low-drag shapes, parachute designers seek to create the *maximum* amount of disturbance to the oncoming airflow that can be achieved within the constraints of parachute weight and volume. As a result, parachute aerodynamics is irrevocably associated with the airflow around bluff bodies, which includes some of the most difficult problems in fluid mechanics. For example, the air flowing around the parachute separates from an unknown (a priori) location on the canopy and consists of air that flowed around the canopy and air that flowed through the canopy. The shedding of vorticity from the bluff canopy shape may affect canopy stability and cause a periodic motion of the parachute and payload.

These bluff-body aerodynamic phenomena are further complicated by the presence of the payload just ahead of the parachute. The turbulent wake generated by the payload flows into the parachute, causing a reduction in parachute drag and stability. At supersonic and transonic speeds, the location of shock waves is determined by the combined payload/parachute configuration, rather than by the parachute configuration alone. Since shock wave location affects canopy pressure distributions, the performance of the parachute depends on the payload's physical characteristics as well as the parachute's characteristics.

If the parachute is successful in decelerating the payload, the oncoming airflow velocity (relative to the parachute) decreases during the initial phase of parachute function. For many high-performance parachutes, the oncoming airflow velocity can change significantly during the time required for the parachute to inflate. The process of parachute inflation is intrinsically time-dependent when this occurs. The adjectives "nonsteady" or "transient" will be used instead of "unsteady" to distinguish between these irreversible time-dependent aerodynamic events and periodic fluid motion having ordered frequencies. In addition to the dependence of inflation parameters on nonsteady flow parameters, other time-dependent aerodynamic events are observed during the operation of high-performance parachutes. An example is the phenomenon of wake recontact, sometimes called "canopy collapse." This phenomenon occurs when the parachute decelerates the payload so rapidly that the air behind the parachute catches up to the canopy, causing it to deform ("collapse") and lose drag.

The final complexity comes from the requirement that the parachute provide drag only after the payload is allowed to fly by itself while it accomplishes its own mission. Before the parachute is needed, the payload must retain its own aerodynamic characteristics, not the aerodynamic characteristics of the parachute. This requirement means that the parachute must be stored out of the airstream until it is needed. Space limitations on the payload invariably dictate that the parachute's stored shape be much different from its inflated shape. When it is time for the parachute to be used, it must be deployed in its stored shape and then transformed into its high-drag shape as quickly as possible after it is ejected from the payload into the airstream. No other aerodynamic structure undergoes such an enormous change in shape during the course of performing its aerodynamic mission. From a fluid mechanics perspective, the changing parachute shape during inflation creates a "chicken and egg" dilemma: the shape of the parachute depends on the aerodynamic forces acting on the canopy, but the airflow that generates the aerodynamic forces depends on the shape of the parachute canopy. From a structural perspective, the maximum structural loads that must be withstood by the parachute occur while the parachute is changing shape, and the magnitude of these forces is influenced by that shape.

To summarize, calculation of parachute deployment, inflation, and payload deceleration requires a solution to the nonlinear, time-dependent equations of motion for turbulent, separated airflow around and through bluff bodies traveling at supersonic, transonic, and subsonic speeds. The upstream boundary condition for the calculation is the nonuniform flow generated by the payload. The boundary condition representing the parachute surface is a porous body whose shape must be calculated at each time step. The equations of motion for the parachute are coupled to the equations of motion for the airflow. In view of the extreme complexity of this problem, it is not surprising that

parachute designers have for many years traditionally relied on empirical methods rather than analysis. As recently as 1971, parachute design and development was viewed as "largely empirical."[2 15] Even today, the full three-dimensional inflation problem described above is much too large to be solved on the largest, fastest computers.

Advances in computer technology and numerical modeling make it both feasible and desirable to begin development of numerical models of parachute inflation. These numerical models will be the parachute design tools of the future. In the meantime, analysts have attacked smaller parts of parachute aerodynamics separately, a piece at a time. Simplifying assumptions are made to include only some aerodynamic phenomena in approximate simulations of the complete parachute problem. Predictions are compared with data from flight and wind tunnel tests of parachutes to determine which phenomena are important in describing each aspect of the parachute inflation process for a given flight regime and parachute configuration. One important result of this approach, which has been pursued for less than two decades, has been a better understanding of how parachutes work. A second result has been the creation of approximate-design tools which, when used in conjunction with experimental data and design experience, have reduced the time and cost of producing successful parachute designs.

The approximation that allows the greatest simplification in modeling parachute dynamics is the assumption of steady-state aerodynamics. Expressed in physical terms, the steady-state approximation views parachute inflation as a series of events, each of which is in static equilibrium and related to the instantaneous velocity. At any instant in time, the parachute's aerodynamic and structural characteristics are assumed to be a function of the oncoming airflow velocity and parachute shape at that time, as if the velocity and shape had always had those values. The steady-state approximation implies that the aerodynamic phenomena related to the changes in velocity of the parachute/payload are not as important as the phenomena related to the magnitude of the velocity itself.

It may seem contradictory to express the inflation of high-performance parachutes in terms of steady-state aerodynamics, when the very definition of "high performance" implies rapid decelerations. Yet, for many high-performance parachute systems, such as small parachutes deployed at supersonic speeds, the steady-state approximation is an appropriate model of the fluid dynamics. Even in cases where nonsteady aerodynamics is important in characterizing parachute motion, an understanding of steady-state parachute aerodynamics is essential for appreciating the effects of the transient fluid dynamics. This chapter examines the steady-state aerodynamics of high-performance parachutes, including analytical methods, numerical approaches, and wind tunnel and flight test data. The reader is referred to Cockrell's AGARDograph[1 6] for a first-principles derivation of steady-state aerodynamic equations of motion.

4.2 Steady-state parachute drag

The single most significant aerodynamic characteristic of a parachute is its drag, defined as the component of the aerodynamic force in the direction of the relative airflow (Figure 4.1). The aerodynamic drag produced by the parachute decelerates the payload and accelerates the air in the vicinity of the parachute. The momentum of the payload is transferred to the air through which it passes. The primary source of parachute drag is the pressure differential across the canopy, but inertial and viscous forces also contribute to parachute drag. The parachute drag, D, is related to parachute drag area, C_DS, and dynamic pressure, q, by this definition:

$$D = q \cdot C_DS \quad . \tag{4.1}$$

The drag area of a parachute depends on its type, inflated shape, size, Reynolds number, Mach number, Froude number, material elasticity, and porosity. Depending on the relative size and positions of the parachute and its payload, the payload wake may also affect parachute drag. The parachute designer has control over some of these parameters and can therefore perform trade-off studies among them to obtain the desired drag performance. Among the adjustable decelerator design parameters are the parachute type, shape of the gore pattern, suspension line length, material type and strength, and porosity of the fabric and geometry. Clustering and reefing greatly influence the measured drag coefficient by causing major changes in the parachute's inflated shape; they are also treated in this chapter.

In parachute canopies, the generation of drag differs from that produced by solid bodies in two respects. First, the drag-producing surface of a parachute is porous; air may pass between ribbons and through the material itself. Second, the airflow pattern around the canopy is usually not steady, even when the parachute is moving at a constant speed. The motion of the canopy during descent may be

oscillatory, gliding, spiraling, or any combination of these. Because of these complexities, accurate theoretical methods to calculate the drag of textile canopies have not been developed. Drag coefficients are usually determined experimentally, either from captive tests (wind tunnel, whirling arm, or rocket sled) or from free-flight tests (aircraft drop, rocket boost, tower drop, or ejection from rocket sled).

Wind tunnel and flight test drag data at subsonic, transonic, and supersonic velocities from selected references are presented by type of parachute in this section on parachute drag. Approximate subsonic drag coefficient values for the different kinds of high-performance parachutes are listed in Table 3.1. In addition, drag coefficients are given in the 1963[2.1] and the 1978[1.7] USAF Parachute Design Guides. These drag coefficient values are sufficiently accurate for preliminary parachute design.

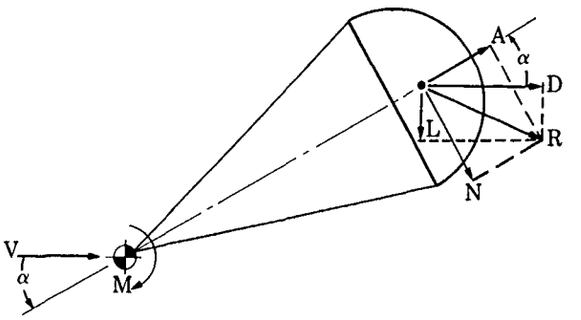


Figure 4.1. Forces acting on a parachute

4.2.1 Flat circular ribbon parachute drag

In 1971, Heinrich and Haak[4.1] made careful measurements of drag coefficients of 16-in.-diameter rigid and flexible parachute models (without a forebody) of flat circular ribbon parachutes at angle of attack in a subsonic wind tunnel. Maynard[4.2] measured the drag of 1.5- to 1.25-ft-diameter rigid and flexible parachute models (with cone-cylinder or Mercury capsule forebodies) in a wind tunnel at Mach numbers 1.6 to 3.0. Downing, Arenson, and McClow[2.8] measured the drag area of four ribbon parachutes with porosities between 8.6% and 23.3% at deployment speeds up to 500 mph, using a rocket-boosted test vehicle on the USAF sled track at Edwards AFB. In 1958, Rosenlof[4.3] conducted 37 flight tests of a general-purpose bomb casing released from a C-119 aircraft to measure the drag coefficients in terminal descent of seven ribbon parachutes 12 to 40 ft in diameter. Engstrom[2.9] measured the drag coefficients of flat ribbon parachutes between 2 and 6 ft in diameter in free-flight tests at Mach numbers 0.38 to 2.38 at altitudes of 15,000 ft to 96,000 ft. These tests were conducted with a special parachute test vehicle released to free-fall from a balloon or an aircraft, or rocket-boosted from an aircraft.

4.2.2 Conical ribbon parachute drag

McVey, Pepper, and Reed[4.4] tested 3-ft-diameter, 20-degree conical ribbon parachutes with geometric porosities from 15% to 30% and suspension line lengths one to two times the parachute's constructed diameter. These wind tunnel tests were conducted at dynamic pressures of 75 to 500 lb/ft^2. Utreja[4.5] developed an empirical formula for the subsonic drag coefficient of a 20-degree conical ribbon parachute which accounts for the effects of geometric porosity and suspension length. Bacchus, Vickers, and Foughner[4.6] measured the effect of porosity, suspension line length, and reefing line length on the drag of a 1/8-scale model of the 54-ft-diameter, 20-degree ribbon drogue parachute for the Space Shuttle Solid Rocket Booster in the NASA-Langley 16-ft wind tunnel. Pepper and Reed[4.7] show the effect of subsonic Mach numbers and geometric porosity on the drag coefficient of a 20-degree, 3-ft-diameter conical ribbon parachute; they also show reasonable agreement between the drag measured with a force balance and the drag calculated from canopy pressure measurements.

Purvis[4.8] presented a combination of old and new wind tunnel data to illustrate the effects of inflated diameter, geometric porosity, reefing line length, suspension line length, number of gores, and number of ribbons on parachute drag. He used the Sandia National Laboratories data published by Heinrich and Uotila[4.9,4.10] and the data from five 1985-86 Sandia wind tunnel tests conducted in the LTV Low-Speed Wind Tunnel. Figure 4.2 illustrates the effects of diameter ratio (inflated diameter divided by constructed diameter) on subsonic drag coefficient. Data lie along a single curve, even

though results for both ribbon and solid canopies are plotted. Figure 4.3a shows the effects of suspension line length (L_{SL}) on the drag coefficient for ribbon parachutes with geometric porosities between 10% and 40%. Figure 4.3b shows the effects of suspension line length and number of ribbons on drag for a 10% geometric-porosity ribbon parachute with 8, 16, and 32 gores. Figures 4.4a and 4.4b present the drag data for 5-ft-diameter, 10% porosity, 5-, 10-, 20-, and 40-ribbon parachutes as a function of suspension line length ratio. Purvis' measurements represent state-of-the-art information on parachute drag in wind tunnel subsonic flow and provide insight into the physical mechanisms by which these ribbon, solid, and ringslot parachutes generate drag.

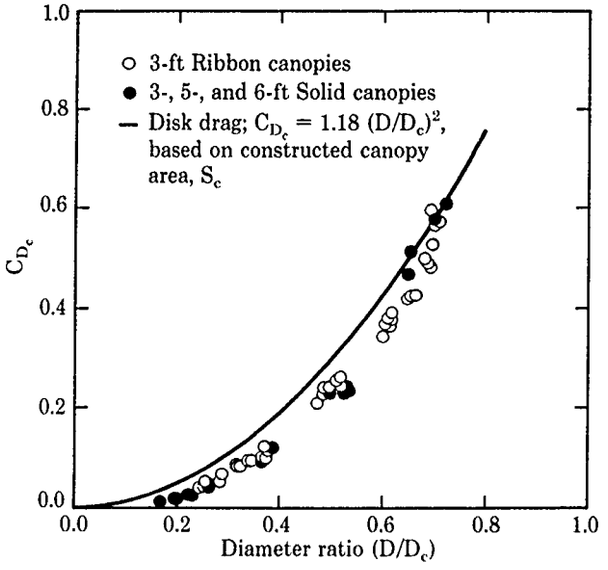


Figure 4.2. Effect of inflated diameter on drag coefficient

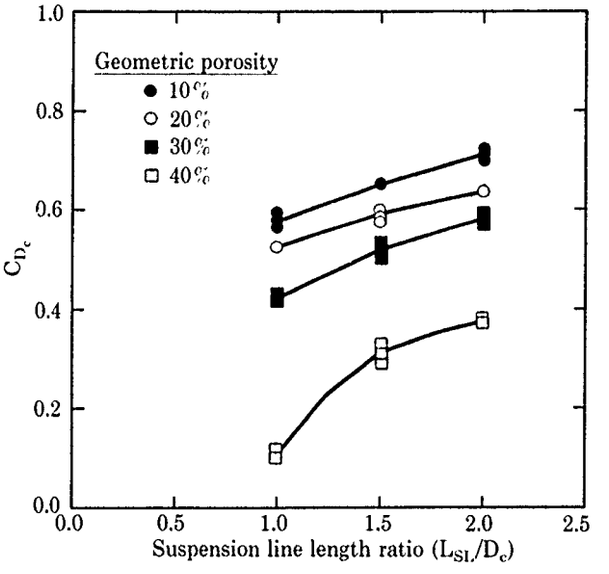


Figure 4.3a. Effects of suspension line length and geometric porosity on the drag coefficient of 3-ft-diameter ribbon parachutes

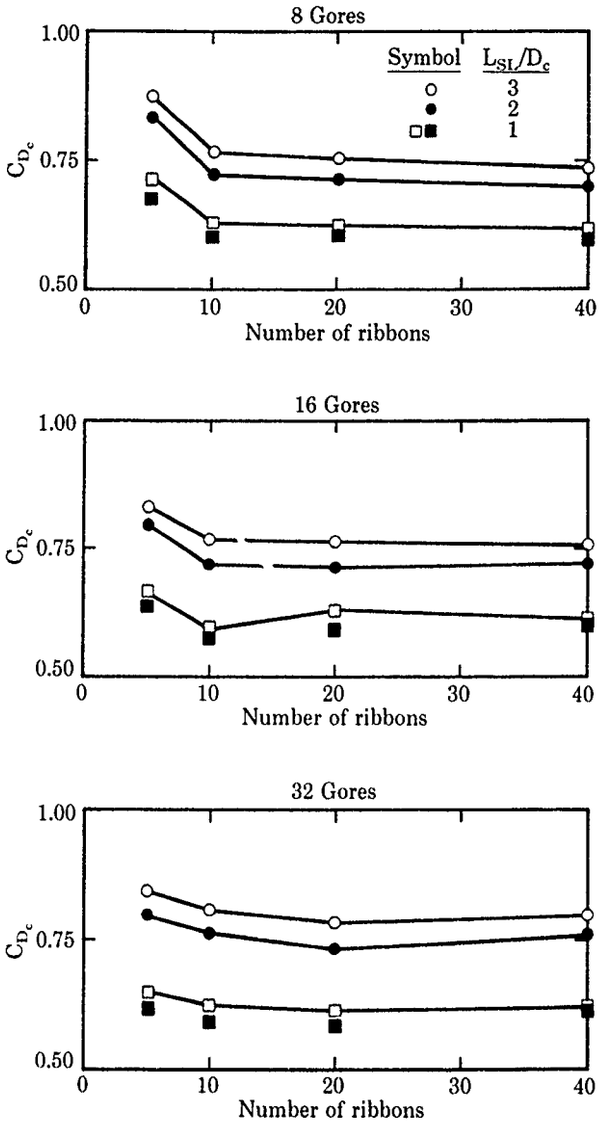


Figure 4.3b. Effects of suspension line length and number of ribbons on the drag coefficient of 10% geometric-porosity ribbon parachutes with 8, 16, and 32 gores

Measurements of conical ribbon parachute drag by Peterson and Johnson[4 11] also show the effect of suspension line length on parachute drag coefficient (Figure 4.5). As the suspension line length is decreased, the suspension line angle increases and the inward radial component of suspension line load becomes larger, causing the canopy to assume a smaller diameter and a more streamlined shape. These changes cause corresponding decreases in the parachute drag.

Subsonic and supersonic flight test drag data for conical ribbon parachutes are presented by Pepper,[3 4] who conducted three rocket-boosted tests of a reefed, 20-ft-diameter conical ribbon parachute. These parachutes were deployed at dynamic pressures of 4700 to 5700 lb/ft^2, corresponding to Mach numbers of 2.34 to 2.43. Pepper measured reefed (using a 12-ft-long reefing line) and full-open drag areas (C_DS) of 35 ft^2 and 130 ft^2, respectively. Moog, Sheppard, and Kross[4 12] conducted flight tests to measure the drag area of the reefed and full-open stages of the 54-ft-diameter drogue and the cluster of three 115-ft-diameter, 20-degree conical ribbon parachutes for the Space Shuttle Solid Rocket Booster.

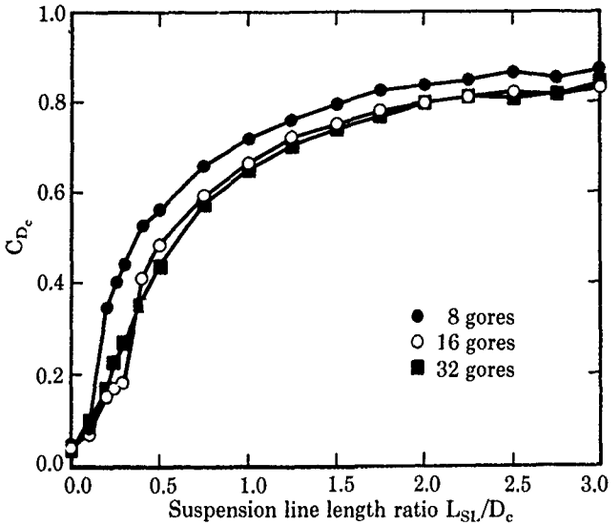


Figure 4.4a. Effects of number of gores and suspension line length on the drag coefficient of 5-ft-diameter, 10% porosity, 5-ribbon parachutes

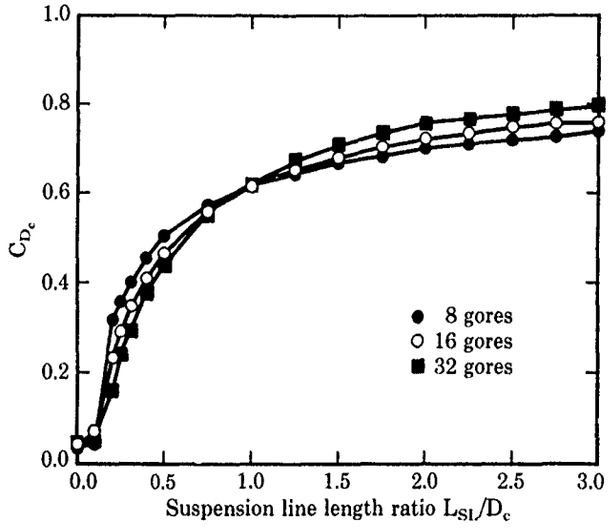


Figure 4.4b. Effects of number of gores and suspension line length on the drag coefficient of 5-ft-diameter, 10% porosity, 40-ribbon parachutes

Maydew and Johnson[3.1] analyzed the results of 29 flight tests of a reefed, 22.2-ft-diameter conical ribbon parachute at deployment dynamic pressures up to 2700 lb/ft^2 (Mach 1.7) to calculate transient and terminal parachute drag areas. A typical deceleration record for the 2100-lb payload is shown in Figure 3.7 and the measured drag area during inflation is shown in Figure 4.6. No discernible effect of Mach number on the drag area of the reefed parachute was observed over the Mach number range of 0.7 to 1.0. The parachute's terminal drag area of 189 ft^2 was determined by using theodolite trajectory data with Eq. 4.1.

Pepper[1 1,4 13] developed a 24-ft-diameter hybrid Kevlar/nylon parachute for the recovery of a 760-lb payload released from an aircraft at low altitude at subsonic and supersonic release speeds. He analyzed the results of 70 flight tests (31 aircraft drop tests, 28 rocket-boosted sled-launched free-flight tests, and 11 rocket-boosted tests) and calculated drag areas. The parachutes were deployed at dynamic pressures from about 300 to 2700 lb/ft^2 and at Mach numbers up to 1.58. The

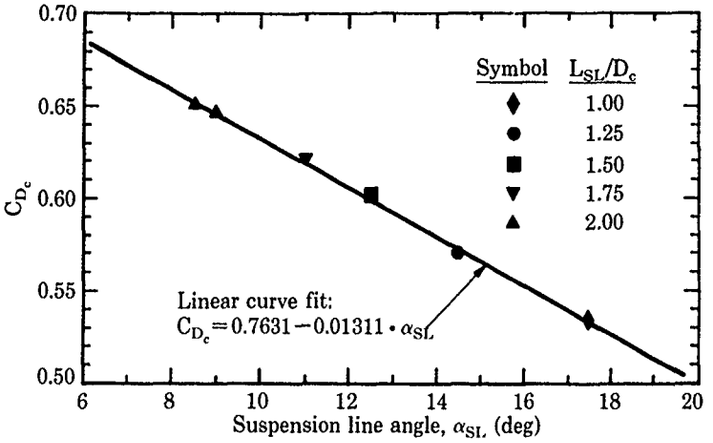


Figure 4.5. Wake-free parachute drag measurements

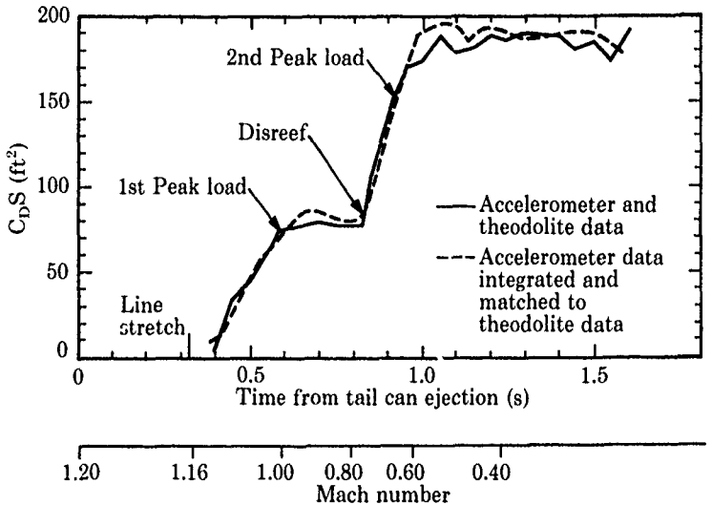


Figure 4.6. Comparison of two methods of determining steady-state drag area

measured full-open drag area of 265 ft^2 agreed well with the drag area measured in subsonic tests of the same parachute in the NASA-Ames 40-ft by 80-ft wind tunnel. This results in a drag coefficient of 0.59 (based on the constructed area of 452 ft^2) for this low-geometric-porosity (20%) ribbon parachute. The drag area of this parachute when permanently reefed with a 28-ft reefing line was 122 ft^2. In flight tests, this parachute produced a peak deceleration load of 240 g when deployed at M=1.58. It generated these peak loads very early in the inflation of the canopy; as a result, measured peak g forces were approximately the same for both reefed and full-open parachutes. The 24-ft-diameter parachute decelerated the 760-lb payload from 1753 ft/s to 100 ft/s in less than 1 s.

Peterson et al.[12] conducted 18 rocket-boosted tests of 4.3- to 5.3-ft-diameter conical ribbon parachutes designed to recover an 800-lb payload flying at subsonic and supersonic speeds. The maximum design condition was a deployment dynamic pressure of 4400 lb/ft^2, corresponding to a Mach number of 2.15 at an altitude of 11,000 ft. Typical drag area of the ribbon parachute as a function of flight Mach number (as calculated from onboard accelerometer and theodolite ground track data) is presented in Figure 4.7 and compared with a fairing of flight and wind tunnel data from the 1963 USAF Parachute Design Guide.[21] They observed that the drag area at both subsonic and supersonic speeds is a strong function of the length of suspension lines; however, the length affects inflation, squidding, and stability of the parachute in the forebody wake. Additional information on

the drag of these conical ribbon parachutes at supersonic speeds is contained in the discussion of forebody wake effects of parachute drag (Section 4.2.6). The reason for discussing conical ribbon parachute drag in that section is because of the major influence of the forebody on the drag of supersonic conical ribbon parachutes.

Additional information on the drag of conical ribbon parachutes at subsonic, transonic, and supersonic speeds can be found in References 4.13 through 4.15 and in the examples used in other chapters of this AGARDograph. References 1.1, 1.3, 1.7, 1.8, 2.10, 2.13, 2.14, 3.2, and 3.28 are a few of the references from the previous chapters that contain data on conical ribbon parachute drag for various applications and configurations. The conical ribbon parachute is probably the most common design for high-performance applications in the transonic and low supersonic speed range.

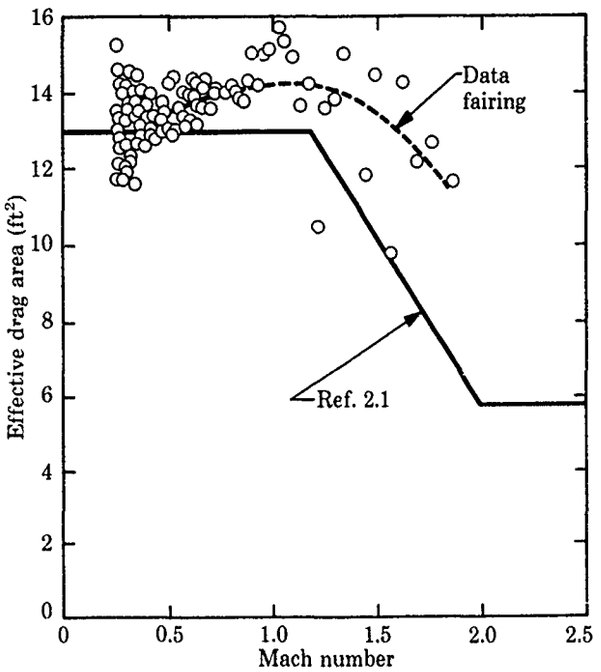


Figure 4.7. Drag area for l-open 5.27-ft-diameter conical ribbon parachute with 9-ft-long suspension lines

4.2.3 Hemisflo parachute drag

Transonic and supersonic wind tunnel tests were conducted by Galigher,[3.24] Deitering and Hilliard,[3.25] Homan,[3.29] Bloetscher and Arnold,[4.16] and Alexander and Foughner[3.26] to measure hemisflo parachute drag coefficients. Of particular note were Galigher's tests of the 6-ft-diameter and 1.5-ft-diameter F-111 crew capsule stabilization hemisflo parachutes in the AEDC Propulsion Wind Tunnel 16S at Mach numbers of 0.5 to 2.5. Pederson[2.10] measured the drag area of 4.1- to 6.8-ft-diameter hemisflo parachutes at transonic speeds using the USAF sled track at Holloman AFB, New Mexico. Bloetscher[3.28] and Bloetscher and Arnold[4.16] measured the drag area of 16-ft-diameter hemisflo parachutes in rocket-boosted flight tests at deployment Mach numbers 1.5 to 2.7 (dynamic pressures up to 5155 lb/ft^2). Babish[3.30] measured the drag of 5-ft-diameter nylon and Kevlar hemisflo parachutes in sled tests at dynamic pressures up to 6000 lb/ft^2 and Mach numbers up to 2.2. Peterson et al.[1.2] and Pepper, Buffington, and Peterson[3.22] also investigated hemisflo parachutes at supersonic speeds; their results are presented in the section on forebody wake effects.

4.2.4 Drag of other parachute configurations

Heinrich and Haak[4.1] made careful drag measurements of 16.6-in.-diameter ringslot parachutes of varying porosity in a subsonic wind tunnel. Wind tunnel and flight test drag data for ringsail parachutes are presented by Ewing[3.38] in his comprehensive design manual. Eckstrom,[3.41] Bobbitt and Mayhue,[4.17] Mayhue and Bobbitt,[4.18] and Alexander and Foughner[3.26] measured the drag coefficients of disk-gap-band parachutes in wind tunnels at speeds up to Mach 3. Eckstrom[3.41] and Eckstrom and

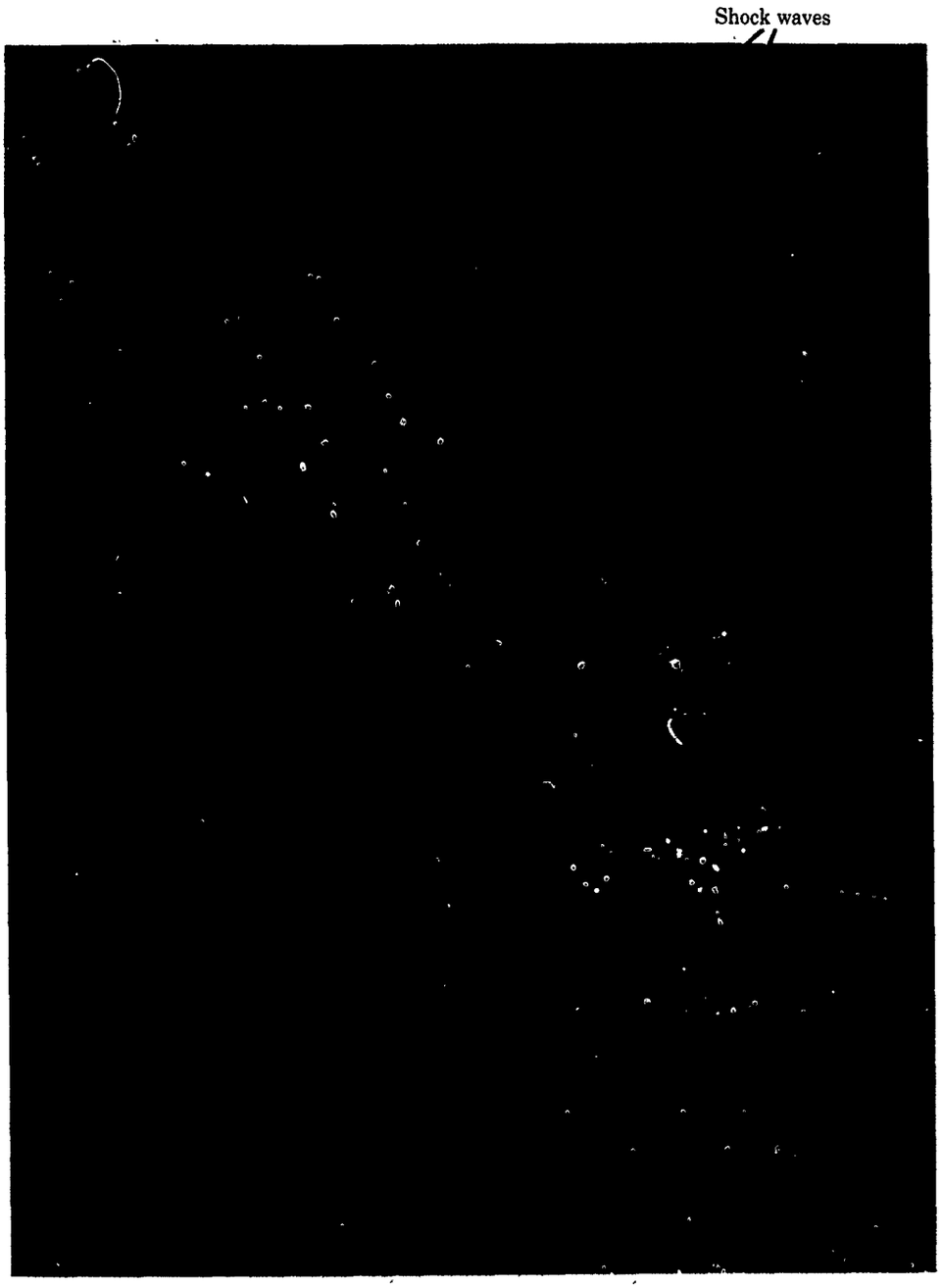


Figure 4.11. Schlieren photograph of hemisflo parachute at M = 1.9

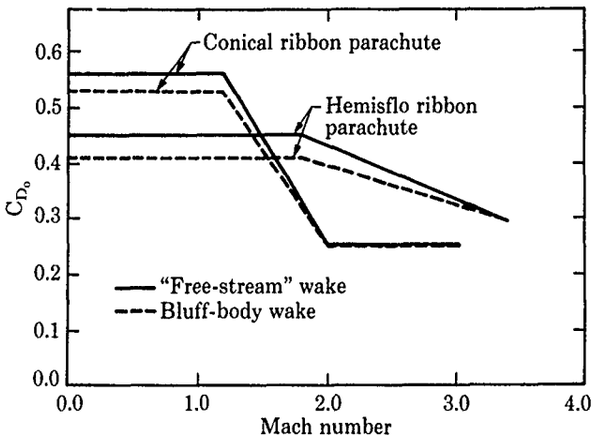


Figure 4.9. Comparison of drag coefficient vs. Mach number for conical ribbon and hemisflo parachutes (taken from Knacke, Ref. 1.20)

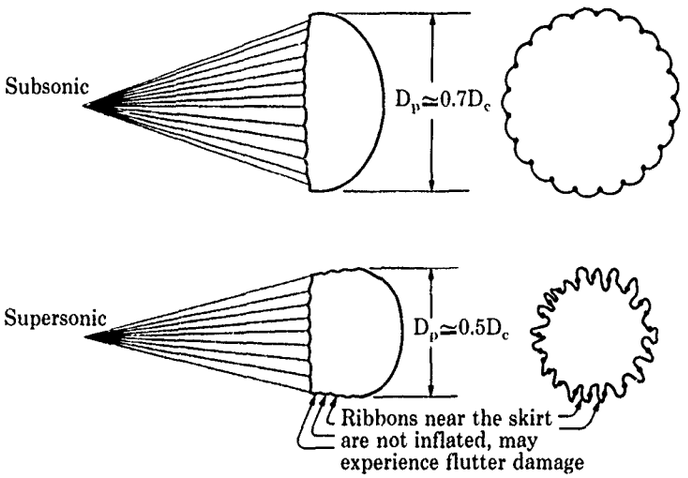


Figure 4.10. Shape of conical ribbon parachutes at subsonic and supersonic speeds

The behavior of an inflating parachute is governed by the nonlinear interaction between the flow field (which includes the forebody wake) and the deformable textile structure. Even though the detailed fluid dynamic phenomena are not completely understood or accurately modeled, there is little doubt that these phenomena control parachute performance and behavior. If a supersonic parachute behaves differently from the same parachute flying at subsonic speeds (as is indicated in Figures 4.8 through 4.10), then it is reasonable to assume that the differences in parachute behavior are linked to the differences in the fluid dynamic interactions.

If this premise is valid, then any investigation of supersonic parachute aerodynamics should focus on developing an understanding of how the supersonic flow field around (and through) the parachute/forebody combination differs from the subsonic flow field around the same parachute/forebody combination. Figure 4.11 provides insight into the changes in fluid dynamics of the parachute flow field when the oncoming velocity is increased above the speed of sound. It is a schlieren photograph of a hemisflo parachute taken in the NASA-Ames Research Center's 9-ft by 7-ft Supersonic Wind Tunnel at Mach 1.9. The complex shock wave structure and the supersonic jets of air flowing from between the ribbons of the parachute are evidence of both the complexity of supersonic parachute aerodynamics and the differences between subsonic and supersonic speeds.

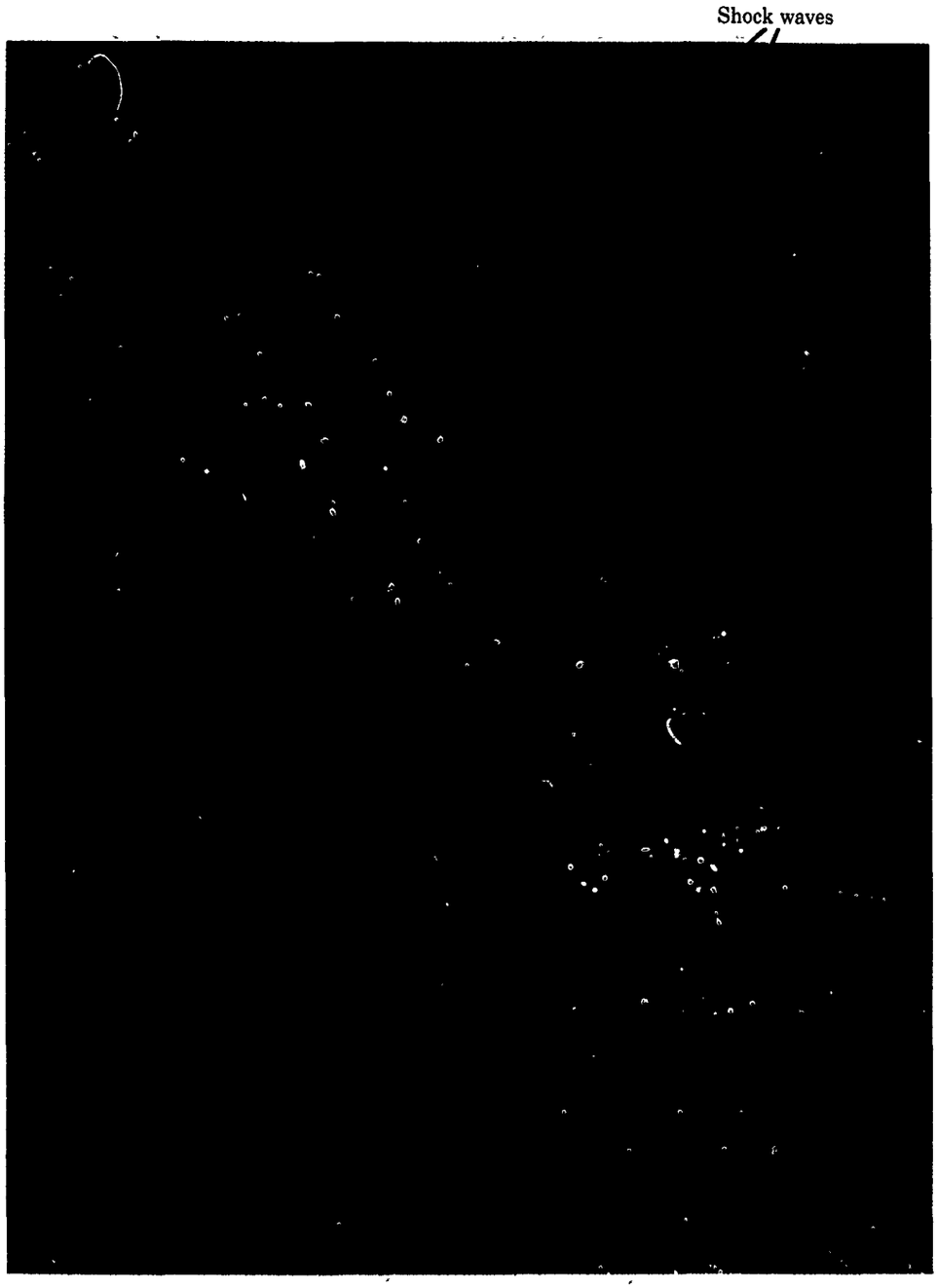


Figure 4.11. Schlieren photograph of hemisflo parachute at M = 1.9

Perhaps the greatest aerodynamic changes occur at the skirt of the parachute. At subsonic speeds, there is a large pressure differential at the skirt (positive outward) that causes full inflation of the parachute. At supersonic speeds, the shock wave extends from in front of the canopy across the skirt plane and beyond the canopy, as shown in Figure 4.11. The pressure differential across the skirt is determined primarily by the pressure behind the shock wave; since the shock wave angle changes very little in the vicinity of the skirt, it is expected that the pressure differential across the skirt is much smaller at supersonic speeds (when the normal shock wave is present) than at subsonic speeds. This model would explain why conical ribbon parachutes assume the "partially inflated" shape observed in wind tunnel and flight tests, and sketched in Figure 4.10.

If the normal shock wave across the skirt of a conical ribbon parachute is indeed responsible for causing weak pressure differentials across the skirt (with canopy shape change and flutter as the consequence), then it would seem prudent to attempt to swallow the normal shock wave and contain it in the mouth of the parachute. If this can be accomplished, a large pressure differential is created across the skirt: the pressure level inside the canopy is approximately the normal shock recovery pressure, and the pressure outside the canopy is approximately free-stream static pressure. By restoring this large (positive outward) pressure differential, the shape of the parachute canopy can be restored to its normal subsonic shape, the drag coefficient will increase, and flutter damage to the skirt ribbons will be minimized.

Many of the parachutes designed specifically for supersonic flight attempt to swallow the shock waves, for the reasons cited above. Figure 4.12 compares the shock wave in front of the conical ribbon parachute with the swallowed shock wave in the mouth of the supersonic-X parachute (see Babish[3.31]). Because the shock wave is contained inside the supersonic-X parachute, its inflated shape is stable and the structure does not suffer flutter damage. The supersonic guide surface parachute (see Heinrich[4.21-4.23]) also attempts to contain the shock wave inside the canopy mouth, but it does so by using a conical centerbody as a shock generator (Figure 4.13). In order to swallow the shock wave, all of the mass entering the parachute must pass through the parachute. Consequently, these special supersonic parachutes are constructed with higher canopy porosity than is used for subsonic configurations. They also are designed to allow less air to pass out of the canopy at the skirt, so that the positive pressure differential at the skirt will cause the skirt to remain fully inflated. In essence, these specialized supersonic parachutes are based upon the same principles used to design the diffuser section of a supersonic wind tunnel.

Unfortunately, the ratio of inlet (skirt) area to outlet area (vent area plus canopy porosity) needed to swallow the shock wave is a function of Mach number. Therefore, these supersonic parachutes perform well over a limited range of Mach numbers, but at lower Mach numbers their performance is reduced because the shock is disgorged. Drag efficiency is usually lower than that of the conical ribbon parachute at subsonic speeds, because of the high porosity designed into the canopy (see Figure 4.8). If good drag efficiency is required at both supersonic and subsonic speeds, conical ribbon or hemisflo parachutes may be preferable to special supersonic parachutes.

Lingard, Barnard, and Kearney[4.24] conducted a detailed study of 20-degree conical ribbon, equiflo, hyperflo, supersonic-X, and ballute decelerators at Mach numbers between 0.5 and 4.35 to provide comparative performance data for design purposes. From their results and the work of others,[1.2,3.22,4.20] it can be concluded that none of these parachute configurations is to be preferred over the other configurations at *all* Mach numbers between 0.5 and 4.35. Each canopy type performs well at some Mach numbers but not at others. Variations in drag coefficient, inflation performance, stability, and flutter among these parachutes were significant. All data indicate that the designer must select a parachute configuration based on its performance across the full Mach number range that the parachute will experience in flight, not just the Mach number at deployment. Special configurations developed specifically for supersonic flight should be chosen if operational emphasis is focused on that speed regime. If both supersonic and subsonic performance is important, the parachute designer should consider more traditional configurations, such as conical ribbon and hemisflo parachutes.

Parachute designers must be careful how they apply supersonic parachute drag data from the literature to specific systems, even when they use quality data from the references cited in this section. The reason for caution is that the drag of the parachute is not solely determined by parachute parameters, but also by forebody parameters such as forebody shape, diameter, and proximity to the parachute canopy. If published test data were obtained using different forebody diameters and shapes than is planned for the new application, the designer should not expect these data to apply directly to the new system. Consideration of forebody wake effects on parachute drag, especially at supersonic speeds, is a prerequisite in designing a supersonic parachute system.

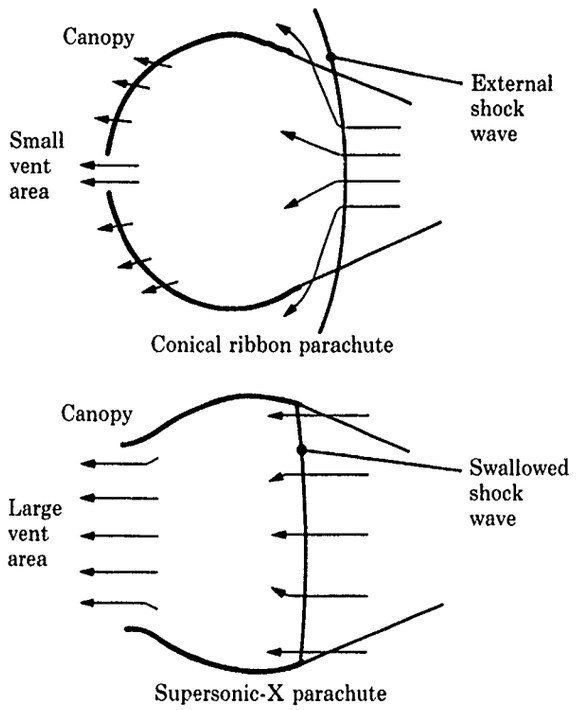


Figure 4.12. Comparison of shock wave location between a conical ribbon parachute and a supersonic-X parachute

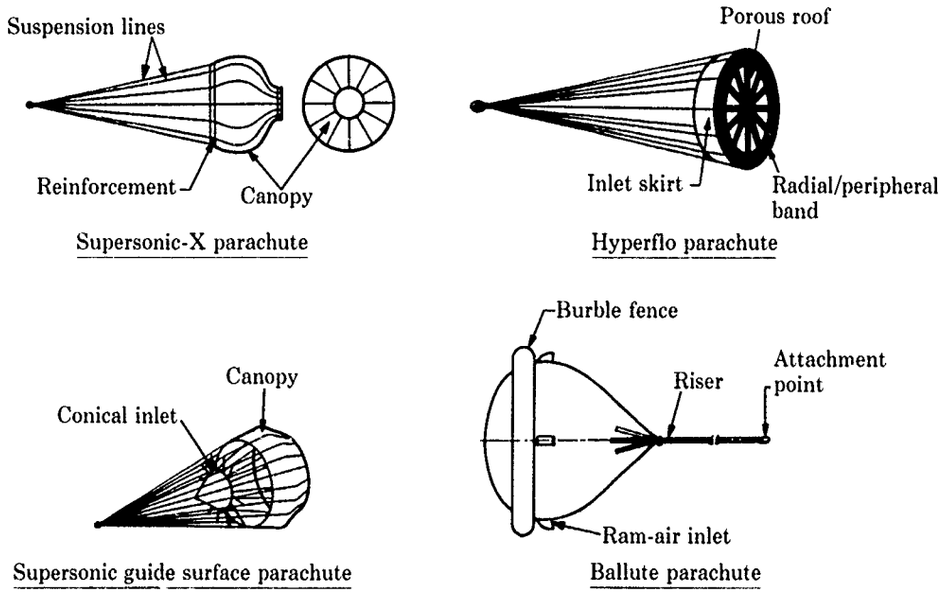


Figure 4.13. Examples of specialized supersonic parachute configurations

4.2.6 Effects of forebody wake on parachute drag

The drag and stability of high-performance parachutes may be strongly influenced by the character of the wake from the forebody that flows into the parachute canopy (Figure 4.14). The aerodynamic drag of the forebody causes the forebody wake to have reduced streamwise velocity and dynamic pressure relative to the free-stream (undisturbed) airflow. The low-momentum air in the forebody wake flows into the parachute canopy and, depending on the drag of the forebody and the diameter of the canopy relative to the wake diameter, the resulting loss in parachute drag due to the oncoming wake may be significant. This is particularly true for parachutes whose inflated diameter is comparable to the diameter of the forebody wake. Most forebody wakes are turbulent at the operational flight conditions when high-performance parachutes are deployed.

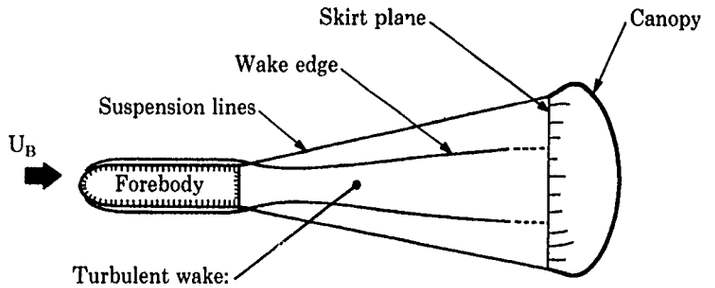


Figure 4.14. Description of the interaction between the parachute and the forebody wake

Any analysis for predicting the wake-induced parachute drag loss must contain a model of the turbulent wake velocity distribution and a method of predicting how that velocity distribution affects the performance of the parachute. Both of these tasks involve complex and, in the case of turbulence, unsolved problems in fluid mechanics. There are no completely analytical descriptions of the turbulent wake for which simplifying assumptions have not been made. Yet, parachute designers need a method for calculating the reduction in parachute drag caused by the forebody turbulent wake, in order to obtain an efficient parachute system. Current analytical (albeit approximate, empirical, or both) wake-effect design methods, along with samples of experimental wind tunnel data, are presented here for both subsonic and supersonic flows. Comprehensive discussions of the effects of forebody wakes on the drag of parachutes are also given in the 1963[2.1] (pp. 205–211) and the 1978[1.7] (pp. 278–283 and 373–375) USAF Parachute Design Guides.

4.2.6.1 Effects of forebody wake at low speeds

Several approximate, semiempirical formulations[4.25–4.31] have been developed for the incompressible, turbulent, axisymmetric forebody wake with no axial or radial static pressure gradients. In order to obtain a closed-form solution for the velocity defect u(Z,R) in a turbulent wake, it is assumed that the velocity defect on the wake centerline, u(Z,0), is small compared to the free-stream velocity. This assumption is valid only at distances many forebody diameters downstream of the forebody base. Similarity solutions are postulated for the wake width b(Z), the radial coordinate R, and u(Z,0). Assumptions about turbulent mixing lengths are also made. A complete derivation of the governing equations is given by Peterson and Johnson.[4.32] The resulting linearized equation for the streamwise velocity defect distribution in the turbulent wake is presented below in the form used by Heinrich and Eckstrom:[4.29]

$$\frac{u}{U_B} = \frac{a}{(Z/D_B)^m} \cdot \exp\left[\frac{-r^2}{0.435 \cdot k^2 \cdot (Z/D_B)^{2n}}\right], \tag{4.2}$$

where

$$u = U_B - U(Z,R) \tag{4.3a}$$

$$m = 0.85 \tag{4.3b}$$

$$n = 0.47 \tag{4.3c}$$

$$a = 0.42 \cdot \exp(0.99 \cdot C_{DB}) \tag{4.3d}$$

$$k = 0.54 \cdot \exp(0.84 \cdot C_{DB}) \tag{4.3e}$$

and

$$r = \frac{R}{R_B} \quad . \tag{4.4}$$

In these equations, U_B is the free-stream velocity, U(Z,R) is the axial velocity anywhere in the wake, Z is the physical dimension in the axial direction, and R is the physical dimension from the wake centerline in the radial direction. D_B is the forebody diameter, R_B is the forebody radius, and C_{DB} is the forebody drag coefficient. The parameter H is an empirical constant that is defined using experimentally determined values of velocity defect on the wake centerline. Heinrich and Eckstrom[4 29] have used the following empirical expression for H:

$$H = \frac{nk(Z/D_B)^{m+n-1}}{9.20a} \quad . \tag{4.5}$$

Heinrich and Riabokin[4 27] recognized that the reduction in parachute drag is directly related to the reduction of dynamic pressure in the turbulent forebody wake. Etherton, Burns, and Norman[4 33] integrated the equation for the dynamic pressure distribution over the area of the inflated canopy to obtain the effective average value of dynamic pressure acting on the parachute. They assumed that the ratio of actual parachute drag C_{D_c} (with the forebody wake flowing into it) to the ideal parachute drag $C_{D_{c\infty}}$ (with no forebody wake effects) was equal to the effective dynamic pressure q_{eff} acting on the canopy divided by the free-stream (undisturbed) dynamic pressure q_∞. The effective dynamic pressure is found by integrating q from the wake centerline (R = 0) to the skirt of the inflated canopy ($R = R_p$).

$$\frac{C_{D_c}}{C_{D_{c\infty}}} = \frac{q_{eff}}{q_\infty} = \frac{1}{\pi R_p^2} \int_0^{R_p} \left(1 - \frac{u}{U}\right)^2 2\pi R dR \quad . \tag{4.6}$$

Substituting Eqs. 4.2 through 4.5 into Eq. 4.6 provides an approximate equation for estimating the drag loss caused by forebody wake effects:

$$\frac{C_{D_c}}{C_{D_{c\infty}}} = 1 + \frac{2}{r_p^2} \cdot \frac{f}{g}\left[1 - \exp(g \cdot r_p^2) + \frac{f}{4}\exp(2g \cdot r_p^2) - \frac{f}{4}\right] \quad , \tag{4.7}$$

where

$$f = \frac{a}{(Z/D_B)^m} \tag{4.8a}$$

and

$$g = \frac{-1.0}{0.435\, k^2 \cdot (Z/D_B)^{2n}} \quad . \tag{4.8b}$$

Peterson and Johnson[4 32] conducted an experiment in a low-speed wind tunnel to evaluate existing approximate analytical methods for predicting the reduction in drag caused by forebody wake effects. The drag of a 15-in.-diameter, 20-degree conical ribbon parachute was measured at several axial stations behind a 4.5-in.-diameter ogive-cylinder forebody with and without fins. The parachute was tested at five different axial distances behind the forebody. The tests were made at forebody angles of attack of 0, 10, and 20 degrees.

Parachute drag was measured with an axial force balance located in the aft section of the forebody model. Photographs of the parachute were taken to measure the inflated canopy position, the angle of the suspension lines, and the *X* and *Y* dimensions across the canopy skirt. These data were used to

determine the amount of forebody wake that flowed into the parachute. The same parachute was tested in "undisturbed flow" (where wake effects were negligible) so that the effects of suspension line length on parachute drag could be separated from the drag losses caused by the turbulent wake. Surveys of total head pressure were made across the forebody wake at these same axial stations and integrated across the canopy skirt area to determine the effective dynamic pressure acting on the parachute.

The measured velocity distributions in the forebody wake were compared with the predictions of Heinrich and Riabokin[4.27] and Heinrich and Eckstrom[4.29] for all zero angle-of-attack data. A typical comparison is given in Figure 4.15. The poor agreement between the experimental velocity data and both predictions (using their empirical constants) points out a major weakness in the parachute drag loss analysis. The simplified equations for the velocity distribution in the turbulent wake, upon which the drag loss analysis is based, do not provide good predictions of velocity across the wake for an arbitrary forebody shape. However, if wake measurements are available, better agreement can be obtained by adjusting the empirical constants. The empirical constants in the expressions for m, n, a, and k (Eqs. 4.3b through 4.3e) were modified to provide optimal agreement with velocity defect measurements in this experiment:

$$m = 0.64 \tag{4.9a}$$

$$n = 0.33 \tag{4.9b}$$

$$a = 0.51 \cdot \exp(2.02 \cdot C_{DB}) \tag{4.9c}$$

$$k = 0.85 \cdot \exp(0.65 \cdot C_{DB}) \tag{4.9d}$$

With these modified constants, Heinrich and Eckstrom's[4.29] analytical wake velocity defect profiles showed acceptable agreement with measured profiles (Figure 4.15).

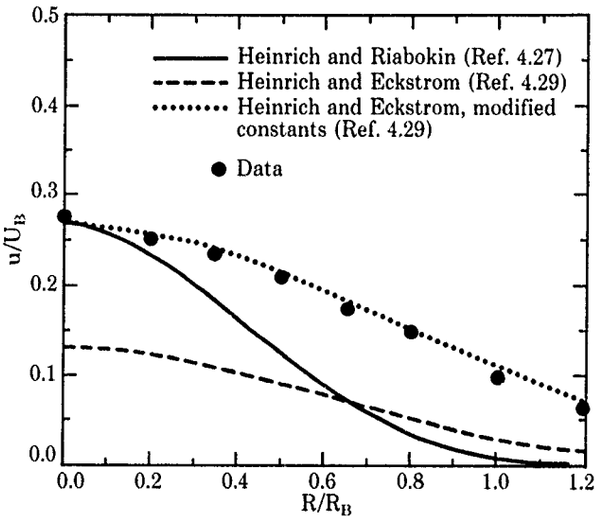
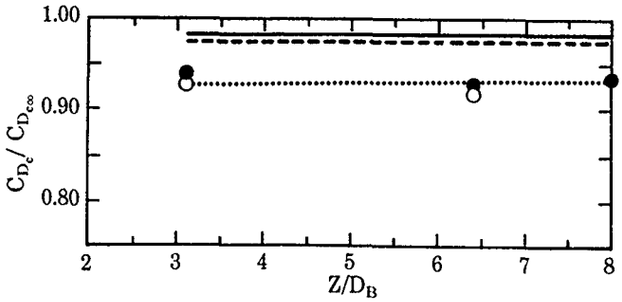


Figure 4.15. Velocity distribution across the turbulent wake at 4.83 body diameters downstream

Typical measured values of parachute drag loss due to the forebody wake are compared with effective dynamic pressure ratios from wake surveys in Figure 4.16. The excellent agreement confirms that parachute drag loss is proportional to the reduction in effective dynamic pressure acting across the canopy. Using empirical constants determined from wake surveys, the modified Heinrich and Eckstrom[4.29] method produced good agreement with drag loss measurements. One can conclude that accurate estimates of wake-induced parachute drag can be obtained from existing theory if wake velocity profiles are known and the empirical constants used in theoretical models of turbulent wake are adjusted accordingly.



Drag loss data sources

- ○ Measured $C_{D_c}/C_{D_{c\infty}}$ using parachute with and without forebody
- ● Derived by integrating wake dynamic pressures across canopy skirt and assuming

$$\frac{C_{D_c}}{C_{D_{c\infty}}} = \frac{q_{eff}}{q_\infty}$$

Drag loss theories

- — Heinrich and Riabokin (Ref. 4.27)
- -- Heinrich and Eckstrom (Ref. 4.29)
- ··· Heinrich and Eckstrom using modified constants (Ref. 4.29)

Figure 4.16. Comparison of measured parachute drag loss due to forebody with theory

4.2.6.2 Effects of forebody wake at supersonic speeds

Figure 4.17 is a sketch of the interaction between the forebody wake and the parachute system at supersonic speeds. As discussed in the last section, experiments and analyses conducted at subsonic speeds have shown that the momentum defect in the forebody wake can cause reductions in parachute drag. Parachute drag loss due to forebody wake is usually greater at supersonic speeds than at subsonic speeds, because the momentum defect of the supersonic wake is usually significantly larger than the momentum defect of the subsonic wake. A second reason is related to the higher dynamic pressures associated with supersonic flight. These high dynamic pressures usually restrict the size of the parachute so that the parachute can survive. As a result, many supersonic parachutes are constrained to approximately the same size as the diameter of the forebody wake. When $D_c/D_B \approx 1$, drag loss due to effects of forebody wake is larger than for $D_c/D_B \gg 1$.

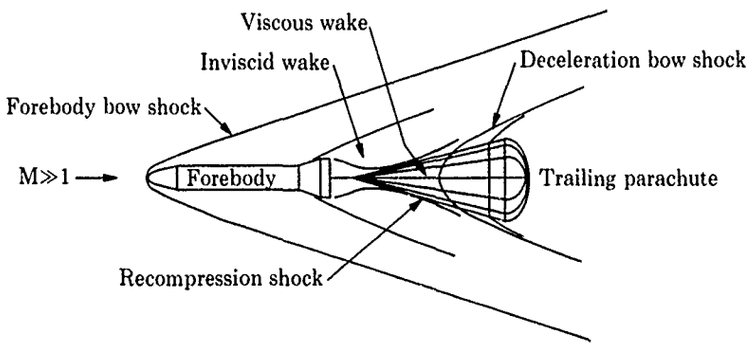


Figure 4.17. Forebody and trailing decelerator flow field

A comprehensive discussion of the effect of forebody-induced wakes on parachute drag at transonic and supersonic speeds is given in the 1963[2.1] (pp. 211–224) and the 1978[1.7] (pp. 283–286 and 375–378) USAF Parachute Design Guides. Reference 1.7 cites 41 wind tunnel test programs in which the decelerator performance was measured in a body wake. Typical parameters that were varied during these tests included Mach number, decelerator trailing distance, body-decelerator diameter ratio, and decelerator porosity.

The supersonic wake behind slender forebodies is shown in Figures 4.17 and 4.18. The near wake (with an internal free-shear layer) is the region of recirculation between the base of the forebody and the downstream location where the wake core necks down to its minimum thickness. The far wake is the region aft of the core neck that spreads in a rather uniform manner downstream. The 1963 USAF Parachute Design Guide[2.1] develops approximate equations (again based on similarity assumptions) that describe the far wake behind the forebody. These equations can be used to compute the approximate average dynamic pressure in the wake that a parachute would experience. This approach is the same as that used to estimate drag reductions in subsonic wakes.

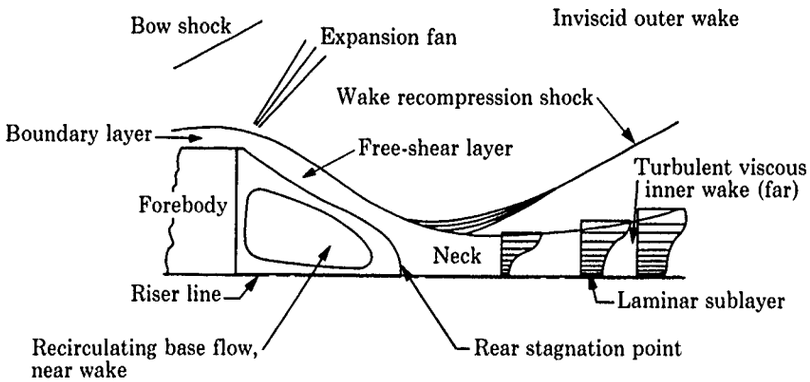


Figure 4.18. Turbulent wake in presence of riser line

In 1968, Nerem and Henke[4.31] developed a momentum-integral theory for the turbulent axisymmetric far wake; the viscous wake profiles compared favorably with wind tunnel wake data. They also made supersonic wind tunnel drag measurements of parachutes in turbulent wakes. They concluded that, from a fluid mechanics viewpoint, the general features of the wake behind a high-speed body in the absence of any trailing decelerator are well understood. However, the presence of a decelerator in such a wake may alter the characteristics of the forebody wake because of the presence of the decelerator, the suspension lines, and the risers. Intuitively, the interaction can be expected to depend on both forebody wake characteristics and parachute characteristics. Nerem and Henke sought to define the extent of the alteration of the upstream wake by the decelerator. They showed that the supersonic turbulent wake behind the forebody is not significantly disturbed when the trailing decelerator is placed in the far wake. They obtained reasonable agreement between their numerical far-wake solutions using the momentum-integral method and Mach 5 wind tunnel data behind a wire-supported, 9-degree half-angle cone model.

Henke[4.35] conducted wind tunnel tests at Mach numbers between 2 and 5 of a parachute located 4.5 to 8 forebody base diameters (X/D) aft of a cone-cylinder-flare forebody, shown schematically in Figure 4.17. The forebody was a 0.182-scale model of the Arapaho C free-flight test vehicle. Tests were made at ratios of canopy area to forebody base areas (A_c/A_B) of 3.4 and 5.9. The Parasonic parachutes (members of the hyperflo family of supersonic parachutes) used in this test were constructed with an uninflated shape that approximates the fully inflated shape of the standard hyperflo parachute (see Figure 4.13).

The Parasonic parachute data (Figure 4.19) show the typical decrease in drag coefficient with increasing Mach number. Note that the drag data also depend on the distance from the parachute to the forebody base. The minimum axial distance between the canopy and the base of the forebody (4.5 body base diameters) was found to be a critical location; when the canopy was located closer to the forebody base than this distance, severe wake deformation resulted. In some cases, the modification to forebody wake characteristics was so severe that the wake was considered to be "blown." In this "blown" wake condition, the flow separates from the forebody before it reaches the forebody base. The entire flow field between the forebody and the parachute is subsonic, enabling

most of the oncoming airflow to pass around (rather than through) the canopy. An extremely low parachute drag coefficient results from this situation.

At canopy inlet locations greater than 7 body base diameters aft of the forebody base, the oscillation stability of the parachute was found to be very time-dependent; at times, the motion became divergent. It was concluded that, from a combined wake and stability standpoint, the optimum location of the canopy inlet was approximately 6 body base diameters downstream. Parachute designers should note that this result applies to the specific experiments conducted in Reference 4.34. The optimum location of a supersonic parachute behind the forebody is a function of forebody shape and size, parachute type and size, Mach number, and Reynolds number. Data from specific experiments are useful guidelines but not assurances of success when applied to other systems, forebodies, and flight regimes.

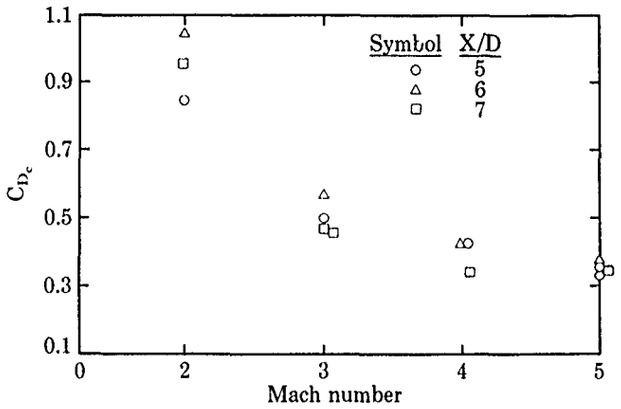


Figure 4.19. Drag coefficient vs. Mach number, Arapaho C with nose cone forebody, $A_c/A_B=3.4$ (taken from Ref. 4.35)

Babish[4.36] defines a critical trailing distance beyond which there is no modification of the body base flow region by the decelerator. His empirical evidence shows that, for any practical body-drogue combination, the critical trailing distance is not likely to exceed 7 body base diameters. This distance is frequently used for the design of subsonic and supersonic systems. Another "rule of thumb" design criteria successfully used at Sandia for many parachute systems is to place the canopy 11 body diameters downstream of the forebody. McShera[4.37] measured the total and static pressures in the wake of a 2.38-in.-diameter cone cylinder at 0.21 to 7.6 forebody diameters downstream at wind tunnel test Mach numbers of 2.30 and 4.65. He concluded that a decelerator should be located at least 7.5 body diameters downstream to minimize the unsteady flow effects, especially in the near wake.

A complete discussion of wake flow at subsonic, supersonic, and hypersonic speeds of laminar and turbulent near and far wakes, including the mathematical modeling, is presented by Chang.[4.38] Noreen, Rust, and Rao[4.39] developed a method for calculating the flow-field characteristics of a body-decelerator system in supersonic flow. The flow around the forebody, the forebody wake, and the flow around the decelerator are considered separately. Numerical solutions were generated for the flow field about a cone-cylinder body at a Mach number of 3. The analysis used for the decelerator extends axially from the upstream tip of the decelerator downstream to its apex. The wake of the decelerator is not included in the analysis; hence, the base pressure coefficient of the parachute must be obtained from another source to obtain a complete pressure distribution for a drag coefficient calculation. Results of the decelerator analysis were compared with experimental surface pressure and shock shape data obtained in a wind tunnel test of a 30-degree, half-angle cone decelerator model. Differences between calculated and measured values of ~10% were observed. Lau[4.40] developed a theory for analyzing a supersonic wake for decelerator applications. He correlated this theory with wind tunnel data (including McShera's) and, qualitatively, with shallow-water tow channel test results.

Babish[4.41] proposed the idea of supersonic drag-level staging by deploying the decelerator in the near wake. In this approach, the parachute would modify the base flow by producing a divergent or blown wake, thereby lowering the drag. Drag-level staging was intended as a concept to replace mechanical reefing. He conducted subsonic and supersonic scale-model wind tunnel tests and made trajectory calculations to demonstrate the feasibilty of the concept. While the principles underlying this concept are valid, the loss in drag can be accompanied by unsteadiness of the wake flow, which

could cause flutter damage and reduce the reliability and repeatability of such a parachute system; these problems were observed in M=2 tests of ribbon parachutes located 4.6 diameters behind the forebody.[1,2] The authors are not aware of any full-scale system applications of Babish's concept.

Pepper, Buffington, and Peterson[3,22] conducted comprehensive tests of hemisflo and 20-degree ribbon parachutes with several forebody shapes in the NASA-Ames 9-ft by 7-ft Supersonic Wind Tunnel in 1986. The purpose of this test series was to evaluate the effects of forebody shape and diameter, parachute porosity and reefing, and Mach number on parachute drag and stability. In addition, these experiments sought to define the influence of test technique, forebody mounting system, and parachute attachment method on supersonic wind tunnel parachute drag, in order that the validity of these and previous wind tunnel measurements of supersonic parachute drag could be assessed.

Hemisflo and 20-degree conical ribbon parachutes were initially tested in the Ling-Temco-Vought (LTV) Low-Speed Wind Tunnel prior to the NASA-Ames test in order to measure subsonic drag coefficients. The measured drag coefficient of both the 10% and 20% porosity ribbon parachutes was 0.45. At NASA Ames, they were tested at nominal Mach numbers of 1.55, 1.71, 1.86, 2.06, and 2.53. The diameter of these model parachutes was 15 in. The two ribbon parachutes (of 10% and 20% porosity) and the hemisflo parachute were tested with suspension lines (L_{SL}) 15 in. and 30 in. long, respectively. The parachutes were tested both reefed and full-open; the length of the reefing line was 53% of the constructed canopy circumference.

Several forebody shapes (with diameters ranging from 3.2 to 5.9 in.) were tested to generate different forebody wake structures that flow into the parachute canopy. Both boattail and ogive-cylinder forebody models of varying diameters were used to assess the effects of forebody wake on supersonic drag; the "boattail forebody" model consisted of fore and aft boattails and either a flat or an aero-streamlined nose. Detailed photographic data (using still photography, motion pictures, high-speed video, and schlieren photographs) were taken at each Mach number and for each forebody/parachute configuration. Without photographic data it would not have been possible to identify test runs where reflected shock waves (see Figure 4.20) or suspension line rollup invalidated the data.

Pepper, Buffington, and Peterson[3,22] indicate that the drag of both hemisflo and conical ribbon parachutes was lower at supersonic speeds than at low subsonic speeds behind all forebodies. Hemisflo parachutes provided higher drag and better canopy stability than the conical ribbon shapes. It was not possible to determine whether the difference in canopy shape or in suspension line length was responsible for the better performance of the hemisflo parachutes. Porosity changes (10% to 20%) did not significantly change the drag of the conical ribbon parachute (Figure 4.21). Reefing the conical ribbon parachutes did not cause significant changes in drag because the inflated diameter of the full-open parachute was nearly the same as the reefed diameter. Reefing the hemisflo parachutes caused substantial reductions in drag.

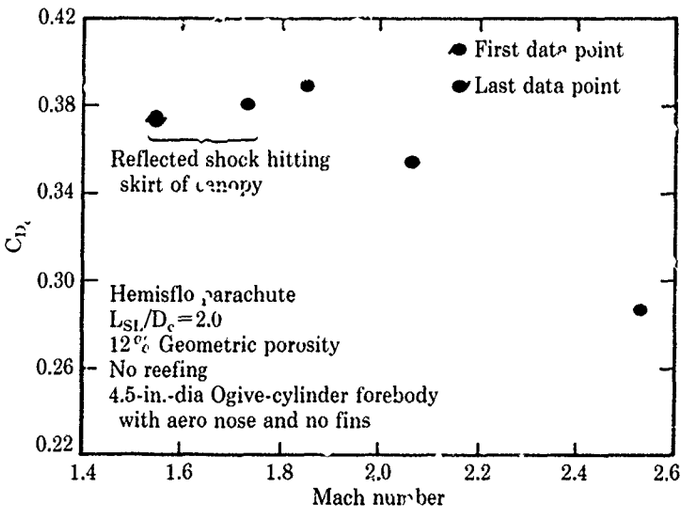


Figure 4.20. Effects of forebody's reflected shock wave impingement on the model parachute drag measurements

Figure 4.22 shows that changes in the forebody diameter caused major changes in drag of the ribbon parachute. For example, the parachutes inflated to a smaller diameter and exhibited more dynamic motion (squidding*, shape changes, and angular motion) behind a larger-diameter forebody, thereby resulting in lower drag. These tests confirmed that the influence of the forebody wake on parachute drag is greater at supersonic speeds than at subsonic speeds. They also proved that it is very difficult to obtain valid wind tunnel parachute drag measurements at supersonic speeds.

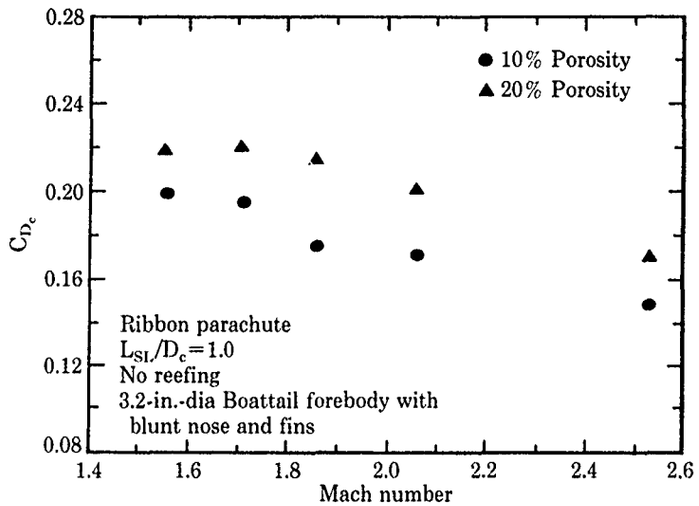


Figure 4.21. Effects of canopy porosity on drag coefficient

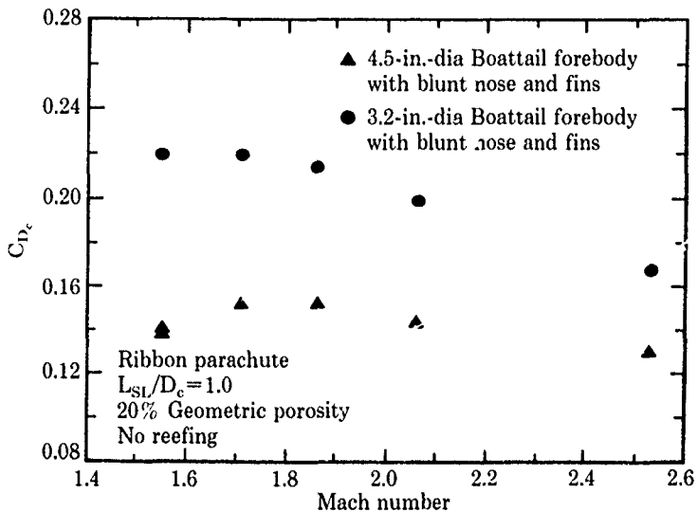


Figure 4.22. Effects of forebody diameter on conical ribbon parachute drag

4.2.7 Reefed parachute drag

Temporary reefing, using one or more stages, is a method of sequentially controlling the drag area of a parachute canopy to limit the maximum structural loading of the parachute. Skirt reefing, with one or more reefing lines passing through reefing rings attached to the skirt band of each gore at a suspension line juncture, is most commonly used for high-performance systems. The reefing lines are

* Squidding is defined on page 80.

passed through reefing line cutters, which consist of a pyrotechnic or an electronic timer along with an explosively driven cutter knife to sever the reefing line. After a preselected time, the cutter fires and the knife severs the reefing line, allowing the parachute canopy to open fully or to the next reefed stage. By limiting the inflation loads, temporary reefing allows the parachute to be constructed from lighter materials, thereby minimizing the packed parachute weight and volume.

Permanent reefing is similar to temporary reefing in implementation, except that the permanent reefing line is not cut; it remains as an integral structure of the parachute. Permanent reefing serves several purposes. A small amount of permanent reefing will usually increase the stability of a parachute. Permanent reefing may be used as an overinflation control line, which allows the parachute to open fully but prevents overinflation with the accompanying higher aerodynamic loading. A third use of permanent reefing is to minimize canopy collapse due to the overtaking wake (see Johnson and Peterson[3.6]).

Parachute skirt reefing was developed at the Forschungsanstalt Graf Zeppelin in Germany in 1941 (see Knacke[2.2-2.4,4.42]) for better control in limiting aircraft diving and landing/approach speeds. References that describe reefing of high-performance parachutes (especially ribbon canopies) are Knacke,[1.8,4.42,4.43] the 1963 Parachute Design Guide,[2.1] and Ewing, Bixby, and Knacke.[1.7] These references also provide data on reefed parachute drag coefficients. Riffle[3.23] conducted an extensive wind tunnel test of 18-in.-diameter models of reefed parachute canopies to measure drag and static stability. His data (see Table 4.1) for flat circular ribbon, 20-degree conical ribbon, ringslot, hemisflo, and ringsail canopies are directly applicable to high-performance parachute systems.

Table 4.1. Drag Coefficient and Comparative Static Stability of Reefed Parachute Canopy Model (taken from Ref. 3.23)

Canopy Type	D_r/D_c	Geometric Porosity (%)	C_{D_c} at $\alpha=0$	$\left(\frac{dC_m}{d\alpha}\right)_{\alpha=0}$
Flat circular ribbon	··	21.60	0.500	−0.0016
	0.466		0.365	−0.0018
	0.366		0.272	−0.0044
	0.282		0.197	−0.0070
	0.172		0.094	−0.0098
20° Conical ribbon	··	21.48	0.533	−0.0012
	0.466		0.365	−0.0014
	0.366		0.280	−0.0052
	0.282		0.205	−0.0109
	0.172		0.115	−0.0063
Ringslot	··	17.48	0.521	−0.0030
	0.466		0.355	−0.0040
	0.366		0.272	−0.0111
	0.282		0.186	−0.0077
	0.172		0.115	−0.0092
Hemisflo	··	19.70	0.466	−0.0103
	0.466		0.406	−0.0133
	0.366		0.300	−0.0126
	0.282		0.168	−0.0330
	0.172		0.090	−0.0100
Ringsail	··	8.85	0.540	−0.0034
	0.417		0.350	−0.0034
	0.328		0.260	−0.0034
	0.252		0.200	−0.0035
	0.154		0.100	−0.0040

where
D_c = 18-in. constructed diameter of parachute
D_r = diameter of circle formed by reefing line — fully inflated

Sandia National Laboratories has conducted several subsonic wind tunnel tests of reefed, conical ribbon parachutes. McVey, Pepper, and Reed[4.4] measured the effects of porosity, reefing line length, and suspension line length on the drag and inflated shape of a 3-ft-diameter, 20-degree conical ribbon canopy. Figure 4.23 illustrates the effects of reefing line length (L_r/D_c) and porosity on the drag coefficient. They noted that the suspension line length had only a minor effect on the drag coefficient of the reefed canopy. Purvis[4.8] measured the effect of number of gores and reefing line length on the drag coefficients of 5-ft-diameter, 10% porosity ringslot and conical ribbon canopies. Figure 4.24 illustrates these effects for the ribbon canopy. Baca[4.44] measured the effect of riser length and number of parachutes in a cluster (up to eight) on the cluster drag efficiency of 15-in.-diameter conical ribbon canopies reefed with a 15-in.-long line. His results (Figure 4.25) show that reefed cluster drag was greater than the drag of a single reefed parachute for certain riser lengths.

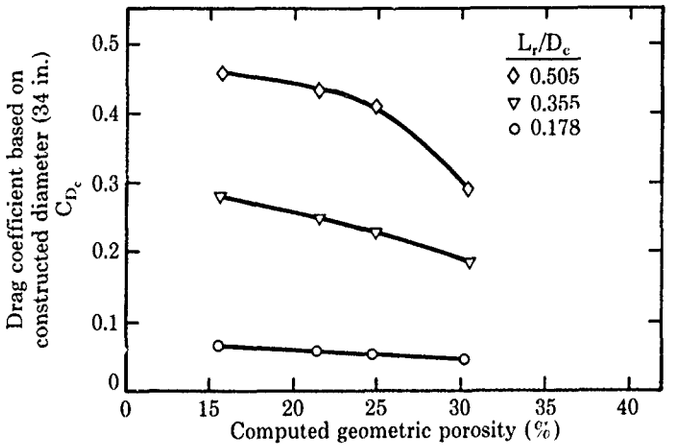


Figure 4.23. Drag coefficient based on constructed diameter vs. geometric porosity

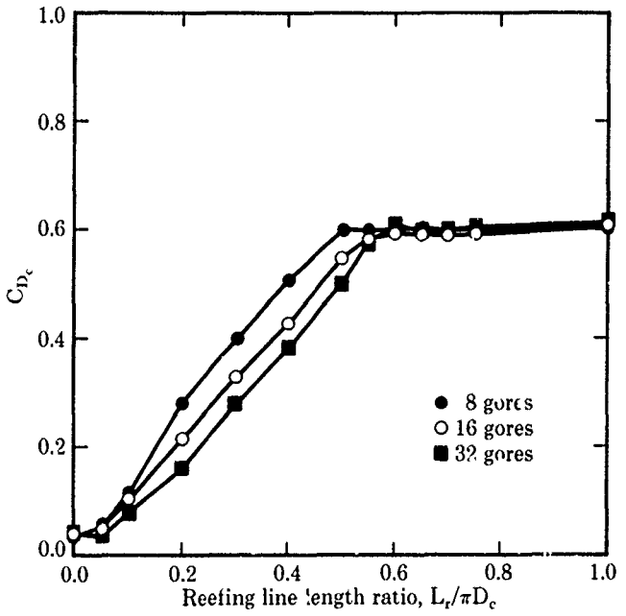


Figure 4.24. Gore effects on a 5-ft-diameter, 10% porosity, 40-ribbon reefed canopy

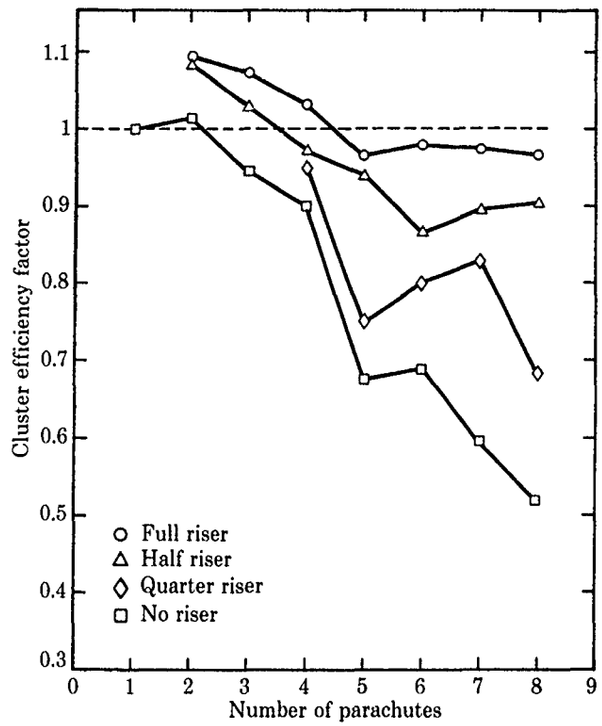


Figure 4.25. Cluster efficiency factor for reefed ribbon parachutes

Reefed parachute flight test drag data for high-performance ribbon parachutes were measured by Rosenlof[4.3] in 1958. He conducted 37 aircraft drop tests of 12-, 16-, 20-, 24-, 32-, and 40-ft-diameter flat ribbon parachutes (full-open and reefed to approximately 10%, 30%, and 60% of the full-open drag area). He measured the terminal rate of descent and the resulting drag area. Rosenlof obtained a good correlation of reefed drag coefficient with reefing ratio for all six parachutes.

Holt[4.45] conducted 21 high-altitude aircraft drop tests of a 76-ft-diameter conical ribbon parachute (with two stages of skirt reefing) attached to 20,000- to 45,000-lb test vehicles. The reefing line lengths and reefing line cutter time delays were 35 to 45 ft and 75 to 90 ft and 4 s and 10 s for the first and second stages, respectively. He measured the drag area of both reefed stages, as well as for the full-open parachute in terminal descent.

Pepper[3.4] conducted three rocket-boosted tests of a 20-ft-diameter conical ribbon parachute (skirt-reefed for 2 s with a 12-ft-long line) deployed from an 1100-lb test vehicle at dynamic pressures of 4700 to 5700 lb/ft^2 (Mach 2.29 to 2.43). He measured a reefed drag area of ~35 ft^2 and noted that this value was essentially constant over the Mach range of 0.44 to 1.92. He also presents a correlation plot of drag area reefing ratio versus reefing line length ratio for wind tunnel and flight data. Maydew and Johnson[3.1] conducted 29 rocket-boosted and aircraft drop tests of a 22.2-ft-diameter conical ribbon parachute (skirt-reefed for 0.5 s with a 15.5- or 19.25-ft-long line) deployed from a 2100-lb test vehicle at dynamic pressures up to 2723 lb/ft^2 (Mach 1.7). The reefed drag area is shown in Figure 4.26 as a function of Mach number. L_r is the reefing line length. These data also indicate that the reefed drag area is invariant from Mach 0.5 to 1.5. During the design of the 54-ft-diameter conical ribbon drogue parachute for the Space Shuttle Solid Rocket Booster recovery system, Utreja[4.5] correlated the reefed, drag area data from Riffle's[3.23] wind tunnel tests and the flight tests by Holt[4.45] and Maydew and Johnson.[3.1] This correlation of drag area ratio as a function of reefing ratio is shown in Figure 4.27. The subscript r indicates reefed, and λ_g is the geometric porosity.

Buhler and Wailes[4.46] designed a cluster of three 69.8-ft-diameter ringsail parachutes with one stage of mid-gore reefing for the B-1 Crew Module. They measured drag area ratio as a function of reefing line ratio from several full-scale drop tests. These useful design data are presented in their paper.

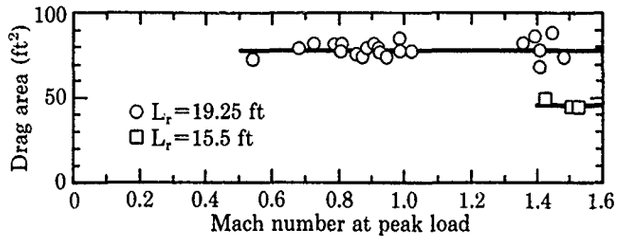


Figure 4.26. Steady-state drag areas for reefed parachutes

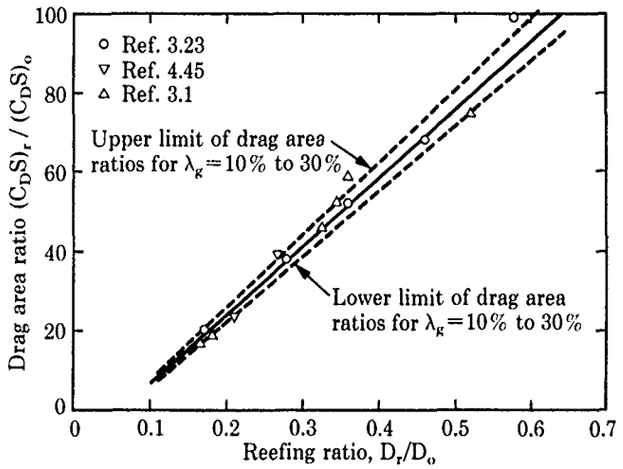


Figure 4.27. Effect of reefing ratio on drag coefficient (taken from Ref. 4.5)

4.2.8 Parachute cluster drag

Multiple parachutes may be deployed together in clusters to meet special system requirements. Clustered parachutes inflate more rapidly than a single parachute of comparable drag area. Clustering allows the use of the same type of parachute for a wide range of loads. Clusters may be used to provide redundancy or backup parachutes, in case other parachutes in the cluster fail. Knacke[1.8] and Peterson and Johnson[1.21] discuss advantages and some of the disadvantages of clusters.

Cluster interference effects are discussed in the 1963 USAF Parachute Design Guide[2.1] and by Braun and Walcott,[4.47] Heinrich and Noreen,[4.48] Pepper,[4.49] Ewing, Bixby, and Knacke,[1.7] Moog, Sheppard, and Kross,[4.12] Moog, Bacchus, and Utreja,[4.50] Heinrich and Schmitt,[4.51] Baca,[4.44] and Knacke.[1.8] Braun and Walcott[4.47] measured the drag of ringslot and ribbon parachutes of different porosities in clusters of two to seven canopies in a subsonic wind tunnel. Their data showed that the number of canopies, the riser line length, and the angle of attack (up to 25 degrees) had only a small effect on the drag coefficient of clustered canopies. On the other hand, Heinrich and Noreen[4.48] measured a 22% decrease in drag for a four-canopy cluster compared to a single canopy in subsonic wind tunnel tests of a 16-in.-diameter ringslot parachute.

Moog, Sheppard, and Kross[4.12] and Moog, Bacchus, and Utreja[4.50] present scale-model wind tunnel and flight drag data for the cluster of three 115-ft-diameter ribbon parachutes for the Space Shuttle Solid Rocket Booster recovery system. Figure 4.28 shows that the drag efficiency for the full-open cluster is ~0.95, whereas the drag efficiency at various reefing ratios (L_r/D_o) is >1. The wind tunnel data for the reefed canopies show a higher drag efficiency than the flight data. L_{SL} is the length of the suspension lines.

Baca[4.41] conducted a comprehensive subsonic wind tunnel test to measure the effect of riser line length and number of canopies in the cluster (two to eight) using a 15-in.-diameter conical ribbon parachute, both reefed and full-open. Figure 4.29 illustrates typical data, showing the decrease in drag efficiency as a function of number of canopies and length of risers for full-open canopies. Baca's data

for reefed parachutes (Figure 4.25) show the same trends as Moog's results. Knacke[18] compared Baca's wind tunnel data on 1.25-ft-diameter ribbon parachutes with Apollo flight data for 88- and 129-ft-diameter ringsail parachutes. He found a good correlation of drag loss as a function of number of canopies. Moog, Bacchus, and Utreja[4.50] reported that the Apollo ringsail parachutes, which have a geometric porosity of 12%, experienced a drag loss of about 6%.

In summary, most drag data for cluster parachutes show a decrease in drag efficiency for full-open porous canopies and either an increase or a decrease in drag efficiency for reefed porous canopies, depending on the number of canopies and length of the risers. The cited references may be used to estimate the drag of a cluster from single-canopy drag data.

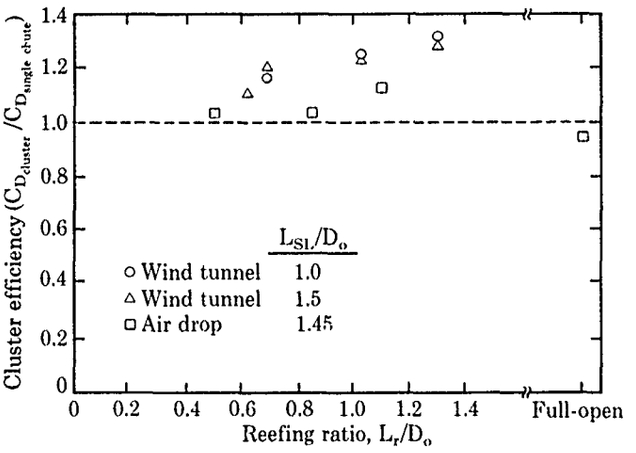


Figure 4.28. SRB main parachute (115-ft-dia) reefed and full-open cluster efficiency (taken from Ref. 4.50)

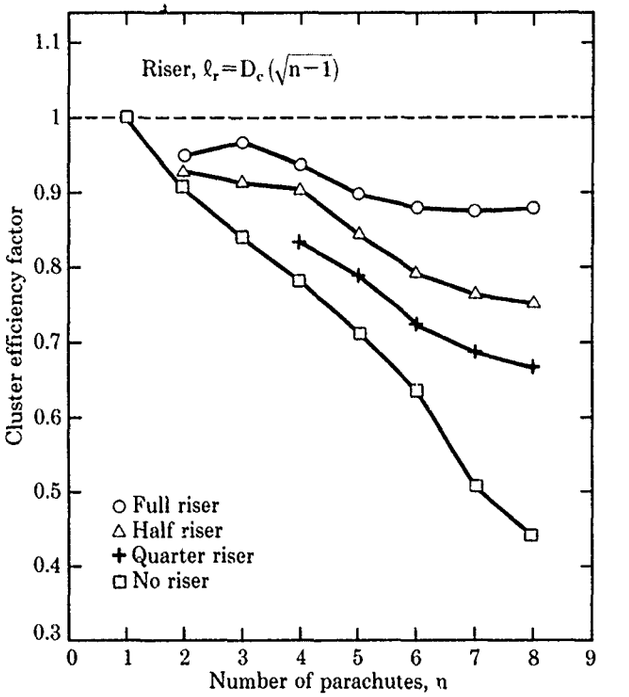


Figure 4.29. Cluster efficiency factor for unreefed ribbon parachutes

4.3 Canopy pressure distribution

Most of the drag generated by a parachute is created by the pressure differential between the upstream (concave) and downstream (convex) sides of the canopy. The magnitude of the drag (and therefore the performance of the parachute) is largely determined by the magnitude and distribution of pressure differential across the canopy. Brown[4 52] derived the relationship for the component of parachute drag resulting from the differential pressure distribution p, which is assumed to be known everywhere on the canopy:

$$D_{pressure} = \iint p \cdot \cos\theta \cdot dS \quad . \tag{4.10}$$

In Eq. 4.10, θ is the angle between a line tangent to the canopy at any location on the surface and a line perpendicular to the parachute axis. dS is the elemental surface area of the canopy at the same location.

In addition to being the dominant force in establishing parachute drag, the canopy pressure distribution also determines the stability of the canopy, and it must be known in order to predict stresses throughout the canopy material during the inflation process. Unfortunately, canopy pressure distributions are difficult to predict or measure because they depend strongly on the rapidly changing shape of the inflating canopy, canopy type and porosity distribution, velocity of flight, and deceleration history. Parachute designers must rely on both analysis and experimental data to predict the canopy pressures expected for each new parachute configuration and application. Analytical and experimental methods for determining the steady-state pressure distribution over a canopy are discussed in this section. Numerical methods for predicting canopy pressures are discussed in Chapter 5.

4.3.1 Analytical methods for predicting canopy pressure distributions

Since most of the parachute drag is caused by the differential pressure distribution across the canopy, rather than by the friction of the air flowing over the parachute, analytical methods for predicting canopy pressure distributions have neglected viscous effects. The flow is considered to be an ideal inviscid fluid, which was started from rest and is therefore irrotational at all times. With these assumptions, a velocity potential ϕ is defined to satisfy the linear Laplace equation within the domain of the flow:

$$\nabla^2\phi = 0 \quad . \tag{4.11}$$

The flow velocity $\bar{U}$ is

$$\bar{U} = \nabla\phi \tag{4.12}$$

and the boundary condition on the canopy surface equates the known velocity through the canopy to the derivative of ϕ normal to the surface:

$$\partial\phi/\partial n_s = \bar{U} \cdot \bar{n}_s \quad . \tag{4.13}$$

Cockrell[1 6] gives a concise summary of potential flow analytical methods for calculating the steady-state canopy pressure distribution.

Ibrahim[1 9] analyzed the steady potential flow about an idealized parachute using conformal transformation techniques. Thin-walled, rigid cup shapes are used instead of an actual parachute shape to permit derivation of an exact analytical expression for the velocity potential. Ibrahim compares the velocity distributions of a shallow spherical cup, a hemispherical cup, and a deep spherical cup (on both convex and concave sides) with that of a sphere. His analytical solution for the nondimensional velocity distribution V/V_B on the cup is

$$\frac{V}{V_B} = \frac{\cos\theta}{\pi}\left\{3\tan^{-1}\left[\left(\frac{B^{1/4}+B^{-1/4}\mp 2\cos\left(\frac{\beta}{2}\right)}{B^{1/4}+B^{-1/4}\pm 2\cos\left(\frac{\beta}{2}\right)}\right)^{1/2}\right] \pm \frac{\sin\left(\frac{\beta}{2}\right)}{\sqrt{2(\cos\beta+\sin\theta)}}\left(\frac{2+3\sin\theta+\cos\beta}{1+\sin\theta}\right)\right\} \tag{4.14}$$

where the upper and lower signs in Eq. 4.14 correspond to the convex and concave sides of the cup, respectively. The angles β and θ are shown in Figure 4.30. The parameter B in Eq. 4.14 is

$$B = \frac{1-\sin(\beta-\theta)}{1+\sin(\beta+\theta)} \quad . \tag{4.15}$$

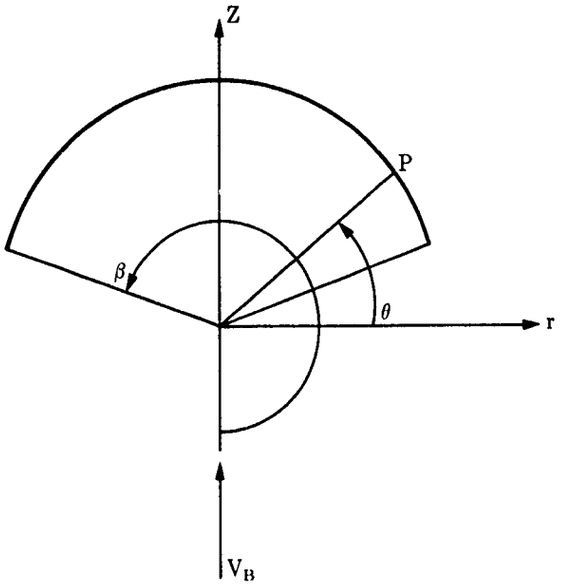


Figure 4.30. Velocity distribution on a spherical cup

Klimas[4.53] modeled the parachute canopy as a series of vortex rings, enabling him to include the effects of geometric porosity on canopy pressure distribution. Calculated internal surface canopy pressures agreed fairly well with measured wind tunnel values. His method cannot predict pressures on the convex side of the canopy because the flow there is separated and rotational. Klimas[4.54] used this same vortex method to calculate the convex and concave side velocity distributions over a hemispherical cup, which agreed exactly with Ibrahim's[1.9] calculations (Figure 4.31). He also calculated the pressure distributions over 10% and 25% geometric-porosity ribbon parachutes (for incompressible, inviscid flow) and compared these with wind tunnel-measured pressure distributions of scale-model ribbon parachutes. A comparison for the 25% porosity parachute is shown in Figure 4.32. The pressures agree fairly well from the skirt region around the canopy until the probable flow separation region is reached (about 30% of the distance from the skirt to the vent); as expected, the inviscid model breaks down in the separated flow region.

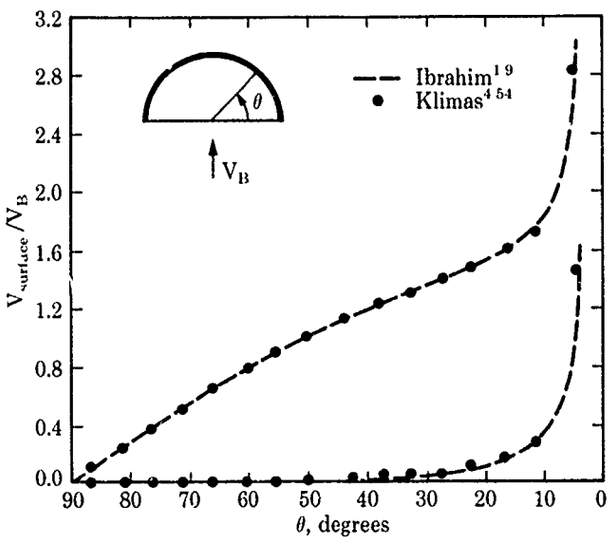


Figure 4.31. Velocity distribution on hemispherical cup

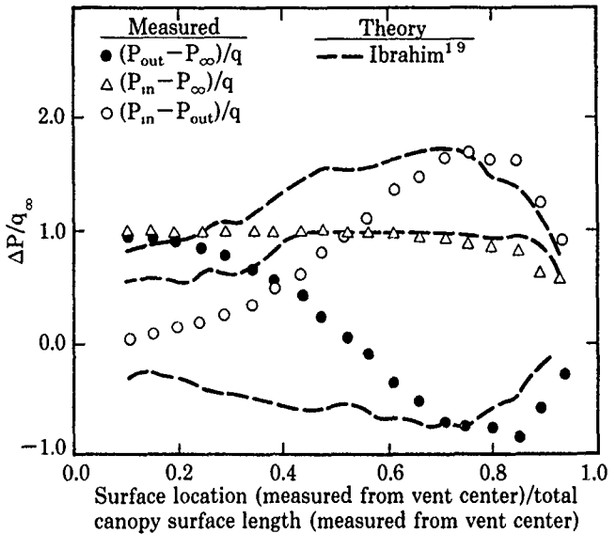


Figure 4.32. Comparison of measured and calculated canopy pressure distribution (∞ is free-stream)

Roberts[4.55] developed an approximate theory for predicting the pressure distribution over porous disks. He also made systematic measurements of pressure distribution over a series of slotted 9-in.-diameter disks in a low-speed wind tunnel which he compared with his and other theories. Muramoto and Garrard[4.56] mathematically modeled the pressure field about a ribbon parachute in steady descent by replacing the canopy with a continuous distribution of axisymmetric ring sources. The numerical solution for differential pressure across the canopy is compared with wind tunnel pressure data in Figures 4.33a and 4.33b for 20% and 30% geometric-porosity parachutes. Again, the agreement is good near the skirt region but breaks down near the vent region where the increase in geometric porosity causes flow separation.

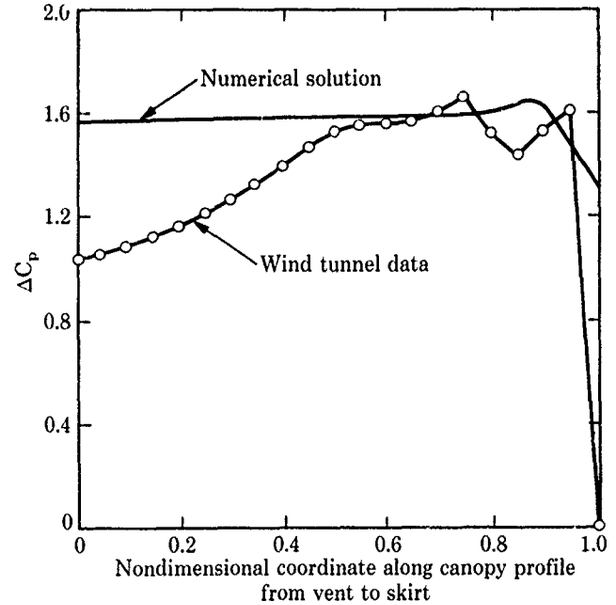


Figure 4.33a. Calculated and measured differential pressures on a fully inflated, 20% geometric-porosity ribbon parachute (taken from Ref. 4.56)

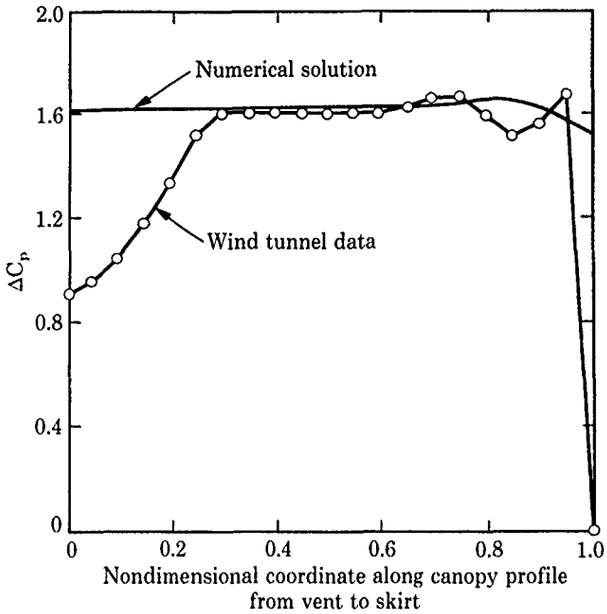


Figure 4.33b. Calculated and measured differential pressures on a fully inflated, 30% geometric-porosity ribbon parachute (taken from Ref. 4.56)

4.3.2 Canopy pressure distribution data

The value of the inviscid methods described in the previous section is limited to calculating steady-state pressure distribution on the inside of the parachute canopy. None of them are intended to predict pressures on the outside of the canopy, where separation and other viscous effects are important. Numerical methods are being developed that take into account viscous effects; these are discussed in Chapter 5. In the meantime, it is necessary to use experimental canopy pressure distributions to design parachutes for steady-state conditions.

Heinrich, Ballinger, and Ryan[4.57] measured the pressure distribution over rigid, 2.5-in.-diameter models of a flat circular ribbon canopy with 20% geometric porosity and a guide surface canopy in a transonic wind tunnel at Mach numbers between 0.6 and 1.2. These stainless-steel models were sting-mounted with no suspension lines and were tested over the Reynolds range of 0.7 to 1.0×10^6, based on the model diameter. Both internal and external canopy surface pressures were measured. These pioneering wind tunnel studies are of particular interest because these two canopy designs have been used extensively for high-performance applications. These pressure data provide physical insight into the flow field around the canopy and the effect of Mach number on that flow field.

Typical pressure coefficient data[2.1] over the external surface from these carefully executed experiments are presented in Figures 4.34 and 4.35 for the ribbon and guide surface canopies, respectively. Data for the ribbon canopy show a decrease in external pressure coefficient (i.e., the external pressure minus free-stream pressure, nondimensionalized by dynamic pressure q) and an increase in internal pressure coefficient with increasing Mach number. The combined effect is a decreasing differential pressure coefficient across the canopy as Mach number increases. Shadowgraph pictures taken during these tests (one of these photos is Figure 4-92 of Ref. 2.1) were able to characterize the air jet passing through the slots between the individual ribbons. This air jet is subsonic below a free-stream Mach number of ~0.8. Beginning at Mach 0.8, the airstream between the ribbons begins to show the diamond pattern that is characteristic of sonic flow between the ribbons expanding to supersonic flow farther behind the canopy. Supersonic flow is generated by the combination of low pressure on the outside of the simulated canopy and (approximately) isentropic stagnation pressure inside the simulated canopy.

The pressure distribution across the roof of the guide surface canopy[4.57] does not change appreciably with Mach number. The internal pressure distribution is also nearly constant and nearly equal to the isentropic stagnation pressure. However, a significant change of the external pressure coefficient with Mach number was observed along the guide surfaces. The net force that keeps the

canopy inflated decreases rather rapidly with Mach number. Figure 4.35 shows that for the taps located on the guide surfaces the external pressure coefficient changes from negative to positive values at transonic free-stream velocities.

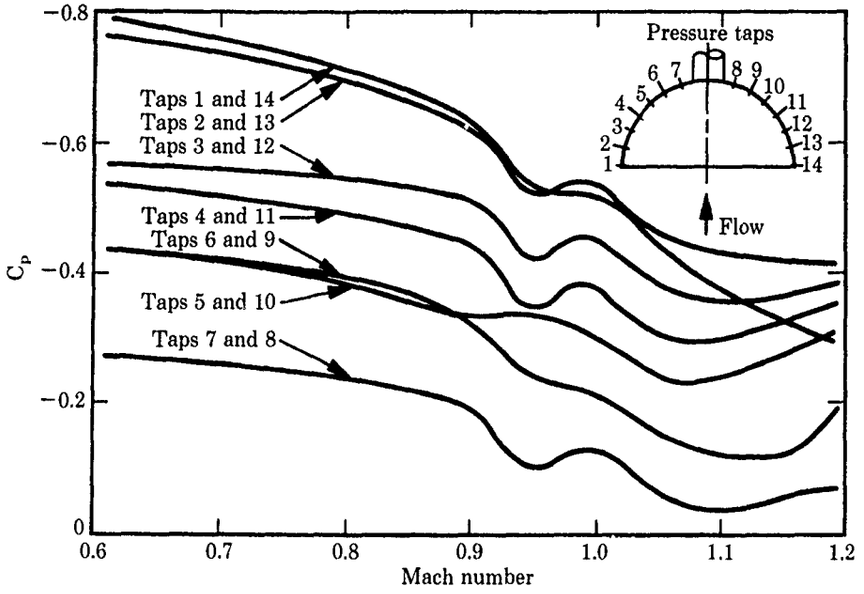


Figure 4.34. External pressure coefficients vs. Mach number for flat circular ribbon canopies (taken from Ref. 2.1)

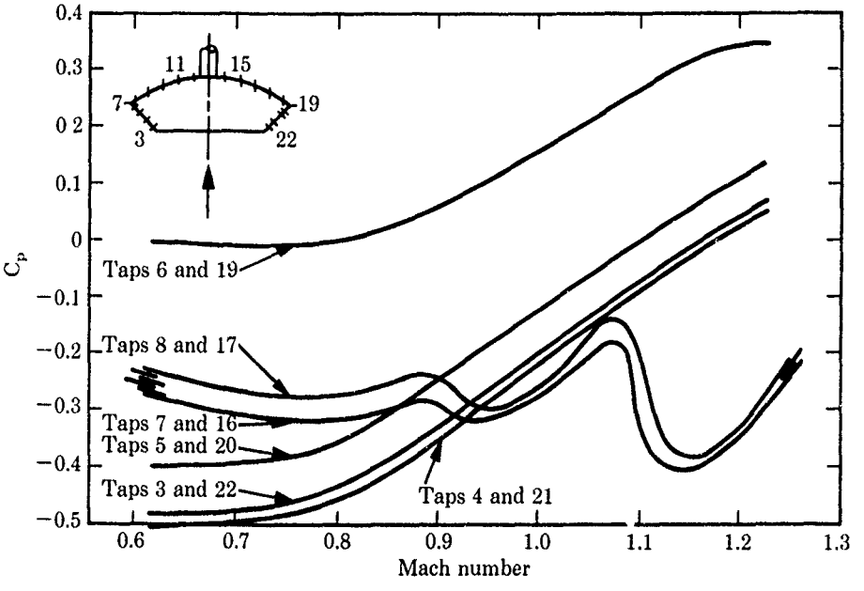


Figure 4.35. External pressure coefficients vs. Mach number for guide surface canopies (taken from Ref. 2.1)

Sandia National Laboratories measured pressures on a 34.4-in.-diameter, 25% geometric-porosity, nylon ribbon parachute in a subsonic wind tunnel over dynamic pressures ranging from 100 lb/ft^2 to 400 lb/ft^2.[4.58] Heinrich et al.[4.59] conducted wind tunnel tests at Mach 1.08, 1.2, and 3.0 to measure the pressure distribution over a rigid model of a 26% porosity circular flat ribbon canopy with and without suspension lines and an ogive-cylinder forebody. Representative data from these tests are presented in Reference 2.1. Haak and Niccum[4.60] measured the pressure distribution over a 26% porosity rigid model of a flat ribbon parachute in wind tunnels at Mach numbers of 0.8, 1.2, and 3.0.

Other experimental measurements of canopy pressure distributions include the work of Melzig and Schmidt,[4.61] who measured canopy pressures at four points on a flexible, flat ribbon parachute in a subsonic wind tunnel. Niccum, Goar, and Lenius[4.62] measured the steady-state pressure distribution over a rigid, 1.94-in.-diameter model of a 20% porosity, flat ribbon parachute at wind tunnel test Mach numbers of 0.8, 1.2, and 3.0. Heinrich and Saari[4.63] found large discrepancies between the drag force measured by Melzig and Schmidt[4.61] and the drag force calculated by integrating the pressure distribution over the surface area of the parachute. Heinrich, Noreen, and Dale[4.64] measured aerodynamic coefficients and pressure distributions of solid flat and ringslot model canopies in a subsonic wind tunnel with a streamwise velocity gradient.

In the early 1970s, Sandia concluded that the experimental data base of pressure distribution over ribbon canopies (both for steady state and during inflation) was inadequate for computing parachute stresses. Hence, a comprehensive wind tunnel test program was initiated to test several ribbon parachutes over a range of dynamic pressures from 35 to 500 lb/ft^2 in the LTV Low-Speed Wind Tunnel[4.65,4.66] and the Naval Ship Research and Development Center (NSRDC) Transonic Wind Tunnel.[4.67] These nylon model parachutes had a nominal diameter of 3 ft and were constructed with a 20-degree conical angle and 24 gores. The vent diameter was 10% of the base diameter D_c. Suspension line lengths of $1.0 \cdot D_c$, $1.5 \cdot D_c$, and $2.0 \cdot D_c$; geometric porosities of 0%, 10%, 15%, 20%, 25%, 30%, and 40%; and skirt reefing line lengths of $0.53 \cdot D_c$, $1.06 \cdot D_c$, and $1.58 \cdot D_c$ were tested.

The first LTV test[4.65] and the NSRDC test observed the disreefing characteristics and measured the drag (using a strain gauge balance) before, during, and after disreefing the parachute in the wind tunnel. The pressure distribution around the parachute was measured simultaneously with the strain gauge balance drag. Pressure instrumentation consisted of two flexible, clear plastic tubes glued and tied to each radial, alternating inside and outside of the canopy and extending out of the canopy through the vent. Notches were cut in the tubes at 23 radial stations both on the inside and outside of the canopy to provide 46 pressure orifices; the flexible pressure tubing terminated in a Scanivalve. A pressure transducer scanned the 46 pressure ports. Side view photographs were taken of each configuration to determine the inflated shape of the canopy profile. Typical side view sketches (Figures 4.36 and 4.37, reproduced from the photographs) illustrate the effect of geometric porosity and suspension line length on the shape of the fully inflated canopy.

Pepper and Reed discuss some of the canopy pressure distribution results from the two LTV and the NSRDC wind tunnel tests in Reference 4.7. The effect of suspension line length on the pressure distribution inside and outside a 25% porosity canopy is shown in Figure 4.38. Test results established general relationships concerning the effect of porosity, line length, and reefing on steady-state canopy pressure distribution. They observed that the parachute drag force obtained by integrating the

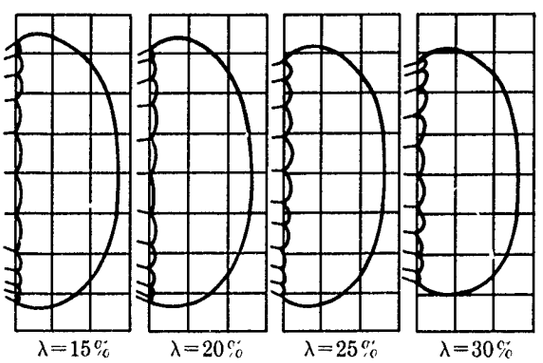


Figure 4.36. Side view sketches of fully inflated parachutes ($L_{SL}/D_c = 1.0$) with geometric porosities of 15%, 20%, 25%, and 30% (LTV test)

measured pressure distribution over the photographically obtained canopy side profiles agreed within 10% of the drag measured by a force balance in the test body.

Heinrich and Uotila[4.9,4.10] carefully analyzed all of the data from the first LTV test.[4.65] These results are presented as pressure distributions, measured and calculated drag coefficients, and projected diameters and drag areas of reefed and unreefed parachutes as a function of geometric porosity and suspension line length. In addition, radial force coefficients were calculated from the pressure data. These differential pressure distribution data have been used at Sandia as generic inputs for the stress analysis (using the CANO and CALA codes) of conical ribbon parachutes.

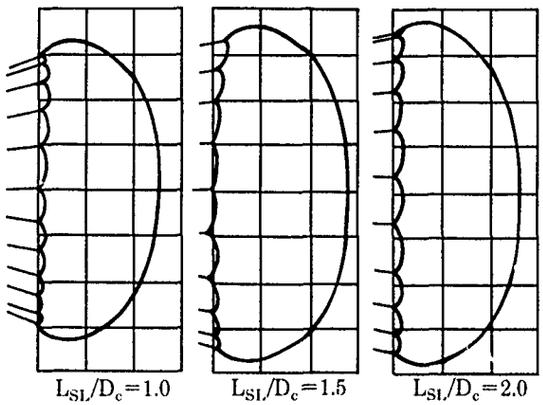


Figure 4.37. Side view sketches of fully inflated parachutes with line lengths of 1.0, 1.5, and 2.0 D_c ($\lambda=25\%$) (LTV test)

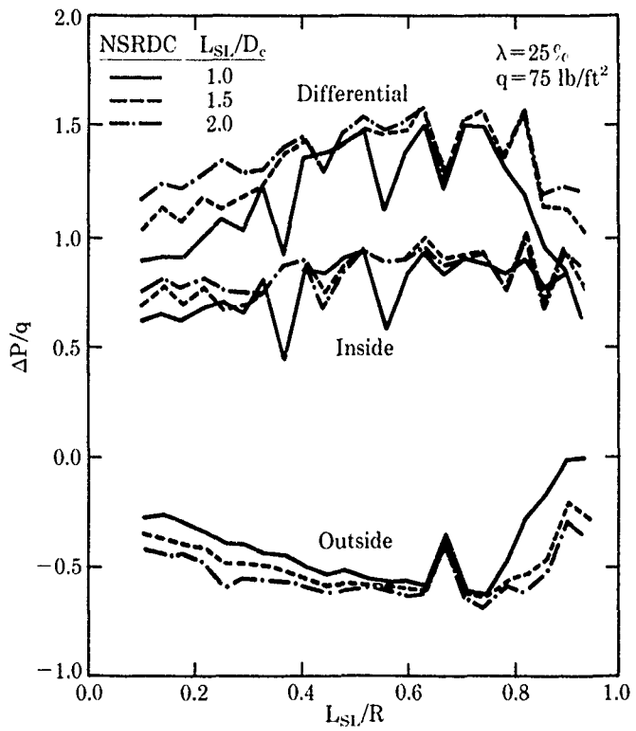


Figure 4.38. Effect of suspension line length on pressure distribution (NSRDC test)

Long after these tests were conducted, the wind tunnel models used in these experiments were found to be too flexible. They stretched enough at the dynamic pressures of the test to cause significant changes in effective porosity between their inflated shapes and the constructed (no-load) shape. Hence, the use of the correlations presented in References 4.7, 4.9, 4.10, and 4.64 through 4.66 should be limited to indicate trends only. Operational parachutes (especially those with Kevlar radials and suspension lines) will undoubtedly stretch much less than these model parachutes, and will therefore have different inflated shapes, effective porosities, and pressure distributions.

Garrard and Piper[4.68] measured the pressure distribution at thirteen points inside and outside the canopy of a 4.5-ft-diameter flat ribbon parachute of 20% geometric porosity at low dynamic pressures and strain levels. Their pressure data compare favorably with the pressure data of Niccum, Goar, and Lenius.[4.62] Garrard, Wu, and Muramoto[4.69] also measured the pressure distribution at six points inside and outside the canopy of a 1.5-ft-diameter cut-gore ribbon parachute of 25% geometric porosity in a low-speed, subsonic wind tunnel. They used these two sets of pressure data to calculate steady-state stresses in ribbon canopies; these stress calculations will be discussed in a later section.

Henfling and Purvis[4.70] measured the pressure distribution across the surface of parachute ribbons at five chordwise points and several spanwise stations in a low-speed wind tunnel. Kevlar was used in the parachute models to prevent them from stretching under load. Because of its high modulus, the Kevlar material can eliminate stretching without adding stiffness, which can also affect parachute shape (and therefore the measured pressures). Henfling and Purvis observed significant variations of the differential pressure distribution, both in the chordwise direction (at a fixed spanwise location) and along the span of the ribbons. These data show that both ribbon angle of attack and ribbon curvature have significant effects on the ribbon pressure distribution. Since chordwise and spanwise pressure measurements were not made in any previous tests, the specific values of pressures measured in earlier ribbon parachute experiments are called into question.

We conclude that the existing body of experimental pressure data must be used with care, to avoid the consequences of assuming more accuracy and applicability than actually exists. This caveat is no different from the care that should be exercised when using analytical/numerical approaches to estimate canopy pressure distributions. Despite the honorable intentions of both experimenters and analysts, the parachute technical community has fallen short of its goals to provide adequate quantitative steady-state pressure distributions for use in designing high-performance parachutes.

4.4 Stability

The stability of the parachute may affect the motion of payload and the trajectory of the payload/parachute. Parachute instabilities may cause problems for the payload when it impacts the ground or for sensors located on the payload. The stability of a parachute depends on its canopy configuration, its location behind its payload, and the interaction of the payload wake with the parachute.

Parachute aerodynamics considers two classes of stability. The parachute is considered to be statically stable if it returns to its equilibrium position when it is displaced from its equilibrium position. The parachute is considered to be dynamically stable if its aerodynamic moments and forces damp out unsteady motion. A third type of parachute "stability" involves the constancy of the canopy's inflated shape rather than the motion of the parachute with respect to its payload. Although this is not stability in the classical sense, the stability of the inflated shape of the canopy is important for achieving adequate drag efficiency; it is also considered in this section.

4.4.1 Static stability

Cockrell,[1.6] Ewing, Bixby, and Knacke,[1.7] and Knacke[1.8] present detailed discussions of the concepts of parachute static stability. Figure 4.39 provides a qualitative illustration of parachute stability. A parachute is statically stable at angles of attack where the pitching moment coefficient C_m decreases with increasing angle of attack. Its equilibrium angle of attack α_{eq} is where

$$\frac{\partial C_m(\alpha_{eq})}{\partial \alpha} < 0 \tag{4.16a}$$

and

$$C_m(\alpha_{eq}) = 0 \quad . \tag{4.16b}$$

It should be noted that the formal mathematical definition of static stability contradicts the common vocabulary used by parachute designers. Flat circular and conical solid-canopy parachutes meet the formal mathematical stability criteria for equilibrium at large angles of attack; they exhibit limit cycles or pendular motions with an amplitude of 25 degrees from the flow direction (see Table 3.1). However, many parachute designers consider these parachutes to be "unstable" because of the large amplitude of motion exhibited by these parachutes and because they will not "fly quietly" at small angles of attack. The same is often said about the ringsail and disk-gap-band canopies, whose limit cycle angles are between 10 and 15 degrees. With due respect for the mathematical definition of stability, the parachute design engineer's definition has more practical significance. Although these solid canopies are "stable" because they satisfy Eqs. 4.16a and 4.16b, many applications cannot tolerate the dynamic motion associated with such large angles of attack.

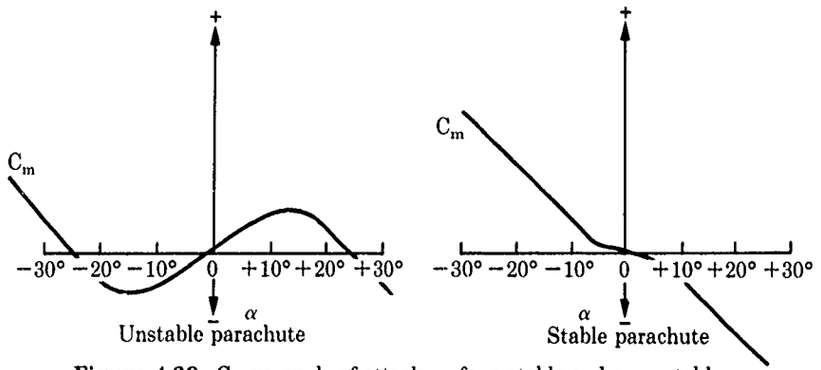


Figure 4.39. C_m vs. angle of attack, α, for a stable and an unstable parachute (taken from Ref. 1.8)

The cycle limit of ringslot canopies is ~5 degrees. Conical ribbon and guide surface parachutes have equilibrium angles of attack of <3 degrees. The stability of the geometrically porous canopies is a weak function of the porosity; increasing the porosity of ringslot and ribbon parachutes will reduce the equilibrium angle of attack, but only slightly.

Knacke[1.8] provides an excellent physical explanation of the stability characteristics of various parachutes using sketches of the parachute wake flow. Smoke flow visualization in a subsonic wind tunnel of a hemispherical cup shows that the airflow separates from the leading edge of the hemisphere in alternating vortices. This alternating flow separation causes large differences in the skirt's pressure differential on opposite sides of the canopy, which in turn produce large destabilizing normal forces and large amplitudes of oscillation. The solid flat circular canopy exhibits this kind of motion.

For parachutes with geometric porosity, part of the air flows through the canopy and pushes vortices in the near wake farther downstream behind the canopy. Since more air passes through the canopy, less air flows around the canopy skirt; hence, the vortices shed at the skirt are weaker for porous-canopy parachutes than for solid-canopy parachutes. Separation can occur at each slot in the canopy, rather than only at the skirt. As a result, the airflow separates more uniformly around the canopy, thereby minimizing the destabilizing alternate flow separation of the vortex trail. This is the aerodynamic design principle for the stable ribbon and slotted parachute canopies.

The guide surface parachute is designed with a sharp edge around the canopy, which causes separation uniformly around the canopy over a wide range of angles of attack. In addition, the inverted leading edge (guide surface) creates a large stabilizing normal force. Both the normal force and the drag force create a stabilizing moment if the parachute is displaced from its zero angle-of-attack position. The guide surface parachute has the largest stabilizing moment and the best damping characteristics of any parachute.

Static stability data for high-performance parachutes in wind tunnels are presented in the 1963 Parachute Design Guide[2.1] and by Ewing, Bixby, and Knacke.[1.7] Braun and Walcott[4.47] measured the effect of reefing ratios, riser lengths, and number (up to 7) and type (ribbon and ringslot) of parachutes in a cluster upon the static stability in a subsonic vertical wind tunnel. Measurements were made at angles of attack up to 25 degrees. They concluded from this systematic study that the static stability increased with increasing riser length. The stability of reefed parachutes peaked at a reefing ratio of ~0.5. They also observed that single-canopy test results cannot be used to predict the aerodynamics of clustered configurations because of interference effects.

Riffle[3.23] measured the effect of reefing ratio on the static stability of 18-in.-diameter flat and conical ribbon, ringslot, hemisflo, and ringsail parachute models in a subsonic wind tunnel. The slope of the pitching moment is tabulated as a function of reefing ratio for these five canopies in Table 4.1. Heinrich and Haak[4.1] measured the effect of porosity on the stability of ten 16-in.-diameter ringslot, ribbon, and guide surface parachute models in a subsonic wind tunnel. Their normal force and moment wind tunnel data for the ribbon and ringslot parachutes were considerably different for a rigid metal canopy than for a cloth canopy.

When the forebody diameter is small relative to the parachute diameter, the destabilizing effect of the wake on the parachute's static stability is negligible. Problems can be avoided when small parachutes are used as drogues or payload stabilizers by placing the parachute far behind the payload. If this is not possible, the strong body wake interaction with a small-diameter parachute (at both subsonic and supersonic deployment conditions) requires very careful design trade-offs on type of parachute, suspension line length, permanent reefing, porosity, and gore shaping. Using a porous canopy and placing it as far behind the payload as practical (10 body diameters aft of the base is desirable) are perhaps the most effective design strategies for minimizing wake effects on static stability.

These scale-model wind tunnel data adequately demonstrate the effects of various parachute design parameters for the preliminary design of subsonic high-performance parachute systems. In most cases, static stability has not been a major problem for high-performance parachutes since they consist primarily of the stable guide surface, conical ribbon, and ringslot configurations. If parachute stability is a primary design objective, it can be enhanced by designing the canopy to provide uniform airflow separation around the leading edge of the canopy skirt, increasing the airflow through the canopy, shaping the skirt through reefing and gore shaping, and providing a large restoring moment as created by a guide surface or extended skirt.

4.4.2 Dynamic stability

A system is dynamically stable when the parachute's aerodynamic forces and moments decrease the amplitude of each succeeding oscillation toward zero or to a small steady-state amplitude. Selected references on the dynamic stability of parachutes are Lester[4.71] White and Wolf,[4.72] Wolf,[4.73] Tory and Ayres,[4.74] Doherr and Saliaris,[4.75] Eaton,[4.76] Cockrell et al.,[4.77] and Cockrell.[1.6] Cockrell[1.6] and Cockrell et al.[4.77] discuss the work of the other references with regard to the significance of added mass coefficients on the parachute's unsteady motion. Ludwig and Heins[4.78] modeled the dynamic stability of personnel guide surface parachutes. Heinrich and Rust[4.79,4.80] modeled the dynamic stability of a stable parachute decelerating an unstable payload.

Neustadt et al.[4.81] developed a 3-DOF model of the motion of a spacecraft stabilized and decelerated with two parachutes deployed serially. Two high-altitude aircraft drop tests were conducted to measure the motion of a parachute-retarded "boilerplate vehicle." A stabilization parachute was deployed after the vehicle was released from an aircraft at an altitude of ~30,000 ft. The stabilization parachute oriented the vehicle to an angle of attack of ~30 degrees. The stabilization parachute was then released and a drogue parachute was deployed at an altitude of ~25,000 ft. Figure 4.40 shows the approximate orientation of the vehicle at line stretch of the drogue parachute. Figure 4.41 shows the damping of the vehicle attitude for about 10 s after drogue parachute deployment, and illustrates the excellent agreement between theory and experiment.

White and Wolf[4.72] studied the three-dimensional motion of a freely descending parachute system with a 5-DOF analysis (the roll motion was neglected). The system consisted of a symmetrical parachute rigidly connected to a payload. They developed the first criteria for longitudinal and lateral dynamic stability of a steady gliding motion, and they were the first to analyze coning motion. Their theoretical coning rate calculations agreed well with Sandia's coning rate measurements of a 50.5-ft-diameter parachute attached to a 700-lb test shape descending through the altitude range of 180,600 to 121,800 ft. Wolf[4.73] continued this work by studying the stability and the three-dimensional motion of a nonrigid parachute and payload system. From a small-disturbance stability analysis of the equations, he showed that a relatively small parachute could be used to stabilize a statically unstable payload.

Wolf and Spahr[4.82] modeled the three-dimensional motion of multiple parachutes attached to a forebody; the motion of each parachute in the cluster was individually modeled. Computer-generated motion pictures of a cluster of three 48-ft-diameter parachutes showed qualitative agreement of the motion with pictures of the full-scale flight.

Perhaps the greatest aerodynamic changes occur at the skirt of the parachute. At subsonic speeds, there is a large pressure differential at the skirt (positive outward) that causes full inflation of the parachute. At supersonic speeds, the shock wave extends from in front of the canopy across the skirt plane and beyond the canopy, as shown in Figure 4.11. The pressure differential across the skirt is determined primarily by the pressure behind the shock wave; since the shock wave angle changes very little in the vicinity of the skirt, it is expected that the pressure differential across the skirt is much smaller at supersonic speeds (when the normal shock wave is present) than at subsonic speeds. This model would explain why conical ribbon parachutes assume the "partially inflated" shape observed in wind tunnel and flight tests, and sketched in Figure 4.10.

If the normal shock wave across the skirt of a conical ribbon parachute is indeed responsible for causing weak pressure differentials across the skirt (with canopy shape change and flutter as the consequence), then it would seem prudent to attempt to swallow the normal shock wave and contain it in the mouth of the parachute. If this can be accomplished, a large pressure differential is created across the skirt; the pressure level inside the canopy is approximately the normal shock recovery pressure, and the pressure outside the canopy is approximately free-stream static pressure. By restoring this large (positive outward) pressure differential, the shape of the parachute canopy can be restored to its normal subsonic shape, the drag coefficient will increase, and flutter damage to the skirt ribbons will be minimized.

Many of the parachutes designed specifically for supersonic flight attempt to swallow the shock waves, for the reasons cited above. Figure 4.12 compares the shock wave in front of the conical ribbon parachute with the swallowed shock wave in the mouth of the supersonic-X parachute (see Babish[3.31]). Because the shock wave is contained inside the supersonic-X parachute, its inflated shape is stable and the structure does not suffer flutter damage. The supersonic guide surface parachute (see Heinrich[4.21-4.23]) also attempts to contain the shock wave inside the canopy mouth, but it does so by using a conical centerbody as a shock generator (Figure 4.13). In order to swallow the shock wave, all of the mass entering the parachute must pass through the parachute. Consequently, these special supersonic parachutes are constructed with higher canopy porosity than is used for subsonic configurations. They also are designed to allow less air to pass out of the canopy at the skirt, so that the positive pressure differential at the skirt will cause the skirt to remain fully inflated. In essence, these specialized supersonic parachutes are based upon the same principles used to design the diffuser section of a supersonic wind tunnel.

Unfortunately, the ratio of inlet (skirt) area to outlet area (vent area plus canopy porosity) needed to swallow the shock wave is a function of Mach number. Therefore, these supersonic parachutes perform well over a limited range of Mach numbers, but at lower Mach numbers their performance is reduced because the shock is disgorged. Drag efficiency is usually lower than that of the conical ribbon parachute at subsonic speeds, because of the high porosity designed into the canopy (see Figure 4.8). If good drag efficiency is required at both supersonic and subsonic speeds, conical ribbon or hemisflo parachutes may be preferable to special supersonic parachutes.

Lingard, Barnard, and Kearney[4.24] conducted a detailed study of 20-degree conical ribbon, equiflo, hyperflo, supersonic-X, and ballute decelerators at Mach numbers between 0.5 and 4.35 to provide comparative performance data for design purposes. From their results and the work of others,[1.2,3.22,4.20] it can be concluded that none of these parachute configurations is to be preferred over the other configurations at *all* Mach numbers between 0.5 and 4.35. Each canopy type performs well at some Mach numbers but not at others. Variations in drag coefficient, inflation performance, stability, and flutter among these parachutes were significant. All data indicate that the designer must select a parachute configuration based on its performance across the full Mach number range that the parachute will experience in flight, not just the Mach number at deployment. Special configurations developed specifically for supersonic flight should be chosen if operational emphasis is focused on that speed regime. If both supersonic and subsonic performance is important, the parachute designer should consider more traditional configurations, such as conical ribbon and hemisflo parachutes.

Parachute designers must be careful how they apply supersonic parachute drag data from the literature to specific systems, even when they use quality data from the references cited in this section. The reason for caution is that the drag of the parachute is not solely determined by parachute parameters, but also by forebody parameters such as forebody shape, diameter, and proximity to the parachute canopy. If published test data were obtained using different forebody diameters and shapes than is planned for the new application, the designer should not expect these data to apply directly to the new system. Consideration of forebody wake effects on parachute drag, especially at supersonic speeds, is a prerequisite in designing a supersonic parachute system.

Doherr[4.83] conducted subsonic wind tunnel tests at the Deutsche Forschungs- und Versuchsanstalt für Luft- und Raumfahrt in West Germany to measure the dynamic stability characteristics of parachutes and parachute/payload systems. The payload had 2 rotational degrees of freedom (no roll) and the parachute had 3 rotational degrees of freedom relative to the load. The experimental data were compared with dynamic stability results from a numerical investigation of the nonlinear 5-DOF motion of the wind tunnel models. Wind tunnel three-component (axial, normal force, and pitching moment) data for the parachute were used in the numerical analysis. These comparisons suggested that the numerical method was satisfactory only for highly statically stable parachutes.

Saari[4.84] developed a dynamic model of the three-dimensional motion of a lifting or gliding nonsymmetrical parachute.

In general, achieving acceptable dynamic stability has not been a major problem in parachute design. Cockrell[1.23] points out that this conclusion is largely due to the fact that high-performance parachutes usually have high porosity, which gives them excellent static stability in pitch. Good static stability characteristics are the largest contributors to satisfactory dynamic stability criteria.

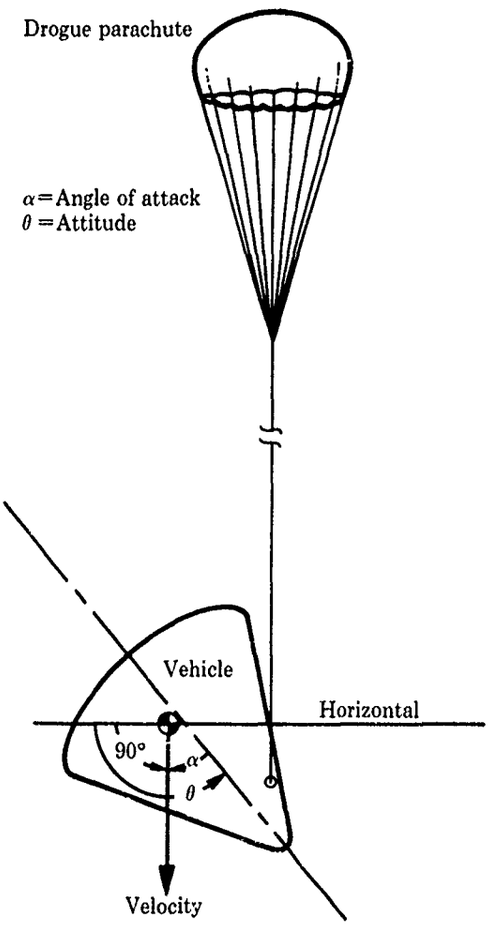


Figure 4.40. Vehicle orientation at drogue parachute line stretch (taken from Ref. 4.81)

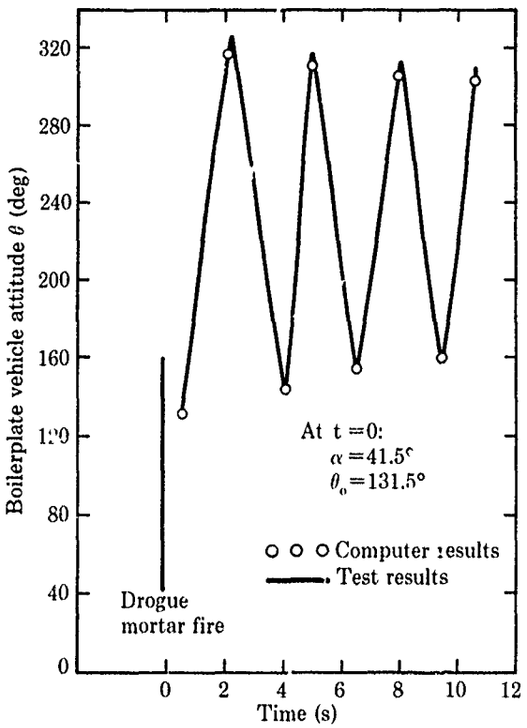


Figure 4.41. Vehicle attitude vs. time—computer and drop test results (single drogue) (taken from Ref. 4.81)

4.4.3 Inflation instabilities

Inflation instabilities can cause a parachute to lose drag and to develop motions that may fatigue canopy materials and result in the failure of the parachute. These instabilities are not related to the slope of the pitching moment curve. They are caused by the periodic coupling between the canopy shape and the unsteady airflow in and around the canopy. At low speeds, inflation instabilities are often called "squidding" and are usually observed in parachutes whose porosity is so high that inflation becomes marginal. Severely reefed parachutes exhibit this problem when the reefed diameter is approximately equal to the vent diameter, allowing the air flowing into the mouth of the parachute to flow out of the vent without generating the positive canopy pressure differential needed to keep the parachute inflated. Reducing the porosity in the vent region or changing the reefing ratio has solved squidding problems in the past.

At supersonic speeds, inflation instabilities can result from forebody wake interactions as well as from excessive porosity. Wake-induced inflation instabilities were reported by Pepper, Buffington, and Peterson,[3.22] who tested 15-in.-diameter hemisflo and conical ribbon parachutes behind several forebody shapes in the NASA-Ames 9-ft by 7-ft wind tunnel at Mach 1.5 to 2.5. The schlieren photograph in Figure 4.11 shows the complicated interaction of the forebody wake with a hemisflo parachute at Mach 1.9. They made qualitative observations of canopy inflation stability (determined from video images and defined as the squidding), shape changes, and dynamic motion of the canopy. These authors concluded that changes in the inflated shape of the canopy caused changes in the flow approaching the canopy which, in turn, further changed the shape of the canopy. The hemisflo parachute was observed to have better canopy stability than the conical ribbon parachutes. However, the hemisflo parachute had longer suspension lines than the conical ribbon parachutes used in this test. It was not possible to determine whether the difference in canopy inflation instabilities was due to the longer suspension line lengths of the hemisflo parachutes or to the different canopy configurations.

Peterson et al.[1 2] and Peterson[4.20] used these wind tunnel data to design a parachute system to operate at low altitudes at deployment velocities of 690 to 2300 ft/s to decelerate an 800-lb payload. Nineteen rocket-boosted flight tests were conducted to validate this subsonic/supersonic parachute

design. The forebody diameter was 13 in. and the diameter of the conical and biconical ribbon and hemisflo parachutes varied from 3.7 to 5.3 ft. All three parachute configurations with 5-ft-long suspension lines experienced squidding, inflation problems, and drag areas that were very dependent on Mach number. These parachutes oscillated behind the payload at subsonic speeds. The conical ribbon parachutes with 9-ft-long suspension lines experienced no inflation problems and produced drag areas that were not strong functions of Mach number; their stability was excellent at supersonic velocities, but oscillations persisted at subsonic velocities. The parachute oscillation frequency coupled with the pitch frequency of the test vehicle, which resulted in a coning motion of the test vehicle. The driving force that sustains the oscillations appears to be the interaction of the payload wake with the parachute canopy. Permanent reefing of the ribbon canopy eliminated the subsonic oscillations; this became the baseline design. It was concluded that permanent reefing, extended skirts, and gore shaping improve supersonic parachute drag, enhance stability, and reduce the maximum opening-shock loads of ribbon parachutes.

4.5 Aerodynamic heating

The two most recent USAF recovery system design guides both discuss high-temperature parachute materials and aerodynamic heating of parachutes. The 1963 Parachute Design Guide[2.1] (p. 340) tabulates the thermal characteristics of nylon, Dacron, glass fiber, etc. Ewing, Bixby, and Knacke[1.7] describe the use of high-melting-point organic polymers (from Freeston et al.[4.85]) and the use of protective coatings to create textile materials that retain structural integrity at temperatures above 300°F. Freeston et al.[4.85] propose fabrics woven of fine metallic wires, high-melting-temperature glasses, coated refractory fibers, metal and metal oxide whiskers, and ceramic fibers. Nylon has limited supersonic decelerator application because it melts at about 482°F. Ewing, Bixby, and Knacke[1.7] point out that the aramids Nomex and Kevlar, synthetic organic fibers that do not melt, are more suitable than nylon for parachutes operating at high speeds. Nomex and Kevlar lose all their tensile strength at about 700°F and 930°F, respectively. Aramids do not melt, drip, or fuse together when exposed to flame, and they have good resistance to commonly used chemicals and solvents. Bisbenzimidazobenzophenanthroline (BBB) polymers have been produced as fibers with demonstrated heat-resistant properties in yarn and textiles in environments up to 1100°F (Jones et al.[4.86]). More information on high-temperature materials is presented in Chapter 8 and by Hartnett, Eckert, and Birkebak[4.87] and Olevitch.[4.88]

The 1963 Parachute Design Guide[2.1] (p. 262), Nerem,[1.9] Scott,[4.89] and Ewing, Bixby, and Knacke[1.7] provide excellent background material on the theoretical methods for estimating the aerodynamic heating of parachutes. Wind tunnel measurements of aerodynamic heating of parachute ribbons, cloth, and mesh have been conducted by Block,[4.90] Schoeck, Hool, and Eckert,[4.91] Scott and Eckert,[4.92] Eckert et al.,[4.93] and Scott, Eckert, and Ruiz-Urbieta.[4.91] Corce[4.19] tested 5- and 8-in.-diameter supersonic-X model parachutes, constructed of BBB and Kevlar, in low-density wind tunnel wake flow tests at Mach 8 at temperatures up to 760°F.

The effects of aerodynamic heating on parachute system design and performance are presented by Bloetscher and Arnold,[4.16] Alexander,[1.9] Pepper,[2.11,4.95] Gillis,[3.44] Peterson et al.,[4.96] and Peterson and Johnson.[1.22] Bloetscher and Arnold[4.16] reported that a 40-ft-diameter disk-gap-band parachute made of 2-oz Dacron cloth suffered "extensive" aerodynamic heating damage after deployment at Mach 3.31. Pepper[2.11] designed a 2-ft-diameter hyperflo nylon ribbon parachute using a silicone-coated, glass-fiber cloth as an upstream-facing heat shield on the canopy and four coats of RTV flexible silastic as an ablative coating on the ribbons and suspension lines. This parachute was deployed from a 140-lb test vehicle at Mach 4.1 at an altitude of 104,000 ft during atmospheric exit. The recovered parachute showed severe aerodynamic heating damage from the approximately 20 s of flight above Mach 3 both during atmospheric exit and reentry. Pepper redesigned the parachute by reinforcing the skirt band and stitching glass-fiber cloth ribbons on both edges of the nylon-roof grid structure. This parachute was deployed at Mach 4 at 114,000 ft altitude during reentry and spent only 9 s above Mach 3. The recovered parachute suffered only moderate heating damage.

Pepper[4.95] designed a 19-in.-diameter Kevlar conical ribbon parachute as the first stage of a parachute system to recover a 57-lb reentry vehicle nosetip. He conducted four sled-launched free-flight tests at deployment Mach numbers of 1.93 to 2.74 (dynamic pressures of 4500 to 9000 lb/ft^2). There was evidence of aerodynamic heating on the recovered Kevlar parachutes at deployment Mach numbers >2.5, where stagnation temperatures were above 665°F. The Kevlar retained adequate structural strength, but the high temperature levels, combined with the high dynamic pressure, caused the canopy to remain "set" in its inflated shape after the flight was completed. Peterson et al.[4.96] and Peterson and Johnson[1.22] discuss the use of Kevlar for thermal protection at moderate supersonic speeds. It appears to have the best strength-to-weight ratio of all high-temperature parachute textiles.

References

4.1 H. G. Heinrich and E. L. Haak, *Stability and Drag of Parachutes With Varying Porosity*, USAF AFFDL-TR-71-58, February 1971.

4.2 J. D. Maynard, *Aerodynamic Characteristics of Parachutes at Mach Numbers From 1.6 to 3*, NASA TN D-752, May 1961.

4.3 K. D. Rosenlof, *Drag Coefficient of FIST Ribbon Parachutes—Reefed and Fully Inflated*, USAF AFFTC-TR-58-5, May 1958.

4.4 D. F. McVey, W. B. Pepper, and J. F. Reed, "A Parametric Wind Tunnel Study of Ribbon Parachutes," AIAA 75-1370, November 1975.

4.5 L. R. Utreja, "Drag Coefficient of 20-Degree Conical Ribbon Parachute," AIAA 75-1354, November 1975.

4.6 D. L. Bacchus, J. R. Vickers, and J. T. Foughner Jr., "Wind Tunnel Investigation of Space Shuttle Solid Rocket Booster Drogue Parachutes and Deployment Concepts," AIAA 75-1366, November 1975.

4.7 W. B. Pepper and J. F. Reed, "Parametric Study of Parachute Pressure Distribution by Wind Tunnel Testing," *J Aircraft*, Vol. 10, No. 11, November 1976.

4.8 J. W. Purvis, "Parachute Drag and Radial Force," AIAA 86-2461, October 1986.

4.9 H. G. Heinrich and J. I. Uotila, *Pressure and Profile Data of 20° Conical Ribbon Parachutes (Vol. I)*, SAND77-7005, Sandia Laboratories, October 1976.

4.10 H. G. Heinrich and J. I. Uotila, *Pressure and Profile Data of 20° Conical Ribbon Parachutes (Vol. II)*, SAND77-7005, Sandia Laboratories, May 1977.

4.11 C. W. Peterson and D. W. Johnson, *An Experimental and Theoretical Investigation of the Reduction in Parachute Drag Caused by Forebody Wake Effects: Data Compilation and Program Summary*, SAND81-0510, Sandia National Laboratories, November 1982.

4.12 R. D. Moog, J. D. Sheppard, and D. A. Kross, "Space Shuttle Solid Rocket Booster Decelerator Subsystem Drop Tests," AIAA 79-0463, March 1979.

4.13 W. B. Pepper, "Overtest Results for the 7.3-m (24-ft) Diameter Hybrid Kevlar-29/Nylon Ribbon Parachute," *J Aircraft*, Vol. 16, No. 1, January 1979.

4.14 W. B. Pepper, *Test Results Relevant to the Selection of the 12.5-Foot-Diameter Ribbon Parachute for the TX-57*, Sandia Laboratory, SC-DR-64-18, April 1964.

4.15 W. B. Pepper, *Results of Rocket-Boosted Overtests of the 17-Foot Ribbon Parachute for the B-61*, Sandia Laboratories, SC-DR-68-790, November 1968.

4.16 F. Bloetscher and W. V. Arnold, *Aerodynamic Deployable Decelerator Performance—Evaluation Program, Phase III*, USAF AFFDL-TR-67-60, June 1967.

4.17 P. J. Bobbitt and R. J. Mayhue, "Supersonic and Subsonic Wind-Tunnel Tests of Reefed and Unreefed Disk-Gap-Band Parachutes," AIAA 70-1172, September 1970.

4.18 R. J. Mayhue and P. J. Bobbitt, *Drag Characteristics of a Disk-Gap-Band Parachute With a Nominal Diameter of 1.65 Meters at Mach Numbers From 2.0 to 3.0*, NASA TN D-6894, October 1972.

4.19 J. D. Corce, *Aerodynamic and Thermal Performance Characteristics of Supersonic-X Type Decelerators at Mach Number 8*, USAF AEDC-TR-77-7, February 1977.

4.20 C. W. Peterson, "The Aerodynamics of Supersonic Parachutes," University of Minnesota/ Carl-Cranz-Gesellschaft Parachute Systems Technology Course, Wessling, West Germany, June 1987.

4.21 H. G. Heinrich, *Aerodynamic Principles of the Supersonic Surface Parachute*, Sonderdruck aus dem Jahrbuch 1964 der WGLR.

4.22 H. G. Heinrich, *Aerodynamic Characteristics of the Supersonic G se Surface and the Spiked Ribbon Parachutes*, USAF AFFDL-TR-65-104, December 1965.

4.23 H. G. Heinrich, "Aerodynamics of the Supersonic Guide Surface Parachute," *J Aircraft*, Vol. 3, No. 2, March-April 1966.

4.24 J. S. Lingard, S. Barnard, and P. Kearney, "Comparative Study of the Performance of Parachutes at Mach 0.5–Mach 4.35 With Reference to Suitability for Use With the HERMES Crew Escape Capsule," AIAA 89-0889, April 1989.

4.25 L. M. Swain, "Turbulent Wake Behind a Body of Revolution," *Proceedings of the Royal Society of London*, Series A, Vol. 125, 1929.

4.26 S. Goldstein, "On the Velocity and Temperature Distribution in the Turbulent Wake Behind a Heated Body of Revolution," *Proceedings of the Royal Cambridge Philosophical Society*, Vol. 34, 1938.

4.27 H. G. Heinrich and T. Riabokin, *Analytical and Experimental Considerations of the Velocity Distribution in the Wake of a Body of Revolution*, USAF WADD 60-257, December 1959.

4.28 H. Schlichting, *Boundary Layer Theory*, 4th Edition, McGraw Hill, New York, 1960.

4.29 H. G. Heinrich and D. J. Eckstrom, *Velocity Distribution in the Wake of Bodies of Revolution Based on Drag Coefficient*, USAF ASD-TDR-62-1103, December 1963.

4.30 A. A. Hall and G. S. Hislop, "Velocity and Temperature Distributions in the Turbulent Wake Behind a Heated Body of Revolution," *Proceedings of the Cambridge Philosophical Society*, Vol. 34, 1938.

4.31 H. G. Heinrich and E. L. Haak, *The Drag of Cones, Plates, and Hemispheres in the Wake of a Forebody in Subsonic Flow*, USAF ASD-TR-61-587, December 1961.

4.32 C. W. Peterson and D. W. Johnson, "Reductions in Parachute Drag Due to Forebody Wake Effects," *J Aircraft*, Vol. 20, No. 1, January 1983.

4.33 B. D. Etherton, F. T. Burns, and L. C. Norman, *B58 Escape Capsule Stabilization Parachute System Development*, General Dynamics, Report FZA-4-408, February 1962.

4.34 R. M. Nerem and D. W. Henke, *Theoretical and Experimental Studies of Supersonic Turbulent Wakes and Parachute Performance*, USAF FTC-TR-69-11, April 1969.

4.35 D. W. Henke, *Establishment of an Unsymmetrical Wake Test Capability for Aerodynamic Decelerators, Vol. II—Analysis of High-Speed Axisymmetric Wakes and Parasonic Parachute Performance*, USAF AFFDL-TR-67-192, August 1968.

4.36 C. A. Babish III, *The Influence of Aerodynamic Decelerators on Supersonic Wakes: With an Application of the Gas Hydraulic Analogy*, USAF AFFDL-TR-72-54, August 1972.

4.37 J. T. McShera Jr., *Wind-Tunnel Pressure Measurements in the Wake of a Cone-Cylinder Model at Mach Numbers of 2.30 and 4.65*, NASA TN D-2928, August 1965.

4.38 P. K. Chang, *Separation of Flow*, Pergamon Press, New York, 1970.

4.39 R. A. Noreen, L. W. Rust Jr., and P. P. Rao, *Analysis of the Supersonic Flow Field About a Forebody-Decelerator Combination, Vol. 1—Theoretical Methods and Result Comparisons*, USAF AFFDL-TR-71-35, March 1972.

4.40 R. A. Lau, *Wake Analysis for Supersonic Decelerator Applications*, Vol. I, NASA CR-1543, March 1970.

4.41 C. A. Babish III, "Drag Level Staging Through Modification of Supersonic Wake Fields by Trailing Aerodynamic Decelerators," *Proceedings of the AIAA 6th Aerodynamic Deceleration Systems Conference*, Houston, Texas, September 1966.

4.42 T. W. Knacke, *Reefing Methods, Parachute*, USAF Air Materiel Command, Equipment Laboratory Report, TSEPE-672-25D (DTIC-ADB 953436), October 1947.

4.43 T. W. Knacke, *Reefing of Parachutes—Drag Area Ratio vs Reefing Ratio*, USAF ASD-TR-76-2, July 1976.

4.44 B. K. Baca, "An Experimental Study of the Performance of Clustered Parachutes in a Low-Speed Wind Tunnel," AIAA 84-0822, April 1984.

4.45 I. T. Holt, "Design and Development of a Heavy-Duty 76-ft Ribbon Parachute," AIAA 68-930, September 1968.

4.46 W. C. Buhler and W. K. Wailes, "Development of a High-Performance Ringsail Parachute Cluster," AIAA 73-468, May 1973.

4.47 J. F. Braun and W. B. Walcott, *Wind Tunnel Study of Parachute Clustering*, USAF ASD-TDR-63-159, April 1963.

4.48 H. G. Heinrich and R. A. Noreen, *Drag and Dynamics of Single and Clustered Parachutes in Freestream and With Wake and Ground Effects*, USAF AFFDL-TR-66-104, November 1966.

4.49 W. B. Pepper, *Comparison of Retardation Efficiency of a Single-Ribbon Parachute With a Clusier of Four-Ribbon Parachutes*, SAND75-0027, Sandia Laboratories, June 1975.

4.50 R. D. Moog, D. L. Bacchus, and L. R. Utreja, "Performance Evaluation of Space Shuttle SRB Parachutes From Air Drop and Scaled Model Wind Tunnel Tests," AIAA 79-0464, March 1979.

4.51 H. G. Heinrich and J. C. Schmitt, "Aerodynamic Coefficients of a Twin Parachute Cluster," AIAA 79-0461, March 1979.

4.52 W. D. Brown, *Parachutes*, Pitman and Sons, London, 1951.

4.53 P. C. Klimas, "Internal Parachute Flows," *J Aircraft*, Vol. 9, No. 4, April 1972.

4.54 P. C. Klimas, "Fluid Mass Associated With an Axisymmetric Canopy," *J Aircraft*, Vol. 14, No. 6, June 1977.

4.55 B. W. Roberts, "Drag and Pressure Distribution on a Family of Porous, Slotted Disks," AIAA 79-0462, March 1979.

4.56 K. K. Muramoto and W. L. Garrard, "A Method for Calculating the Pressure Field About a Ribbon Parachute Canopy in Steady Descent," AIAA 84-079 , April 1984.

4.57 H. G. Heinrich, J. G. Ballinger, and P. E. Ryan, *Pressure Distribution in Transonic Flow of Ribbon and Guide Surface Parachute Models*, USAF WADC 59-32, February 1959.

4.58 G. D. Dickie Jr., *Tests of FIST Ribbon Parachutes in the UAC 8-ft Subsonic Wind Tunnel*, United Aircraft Corporation, Hartford, Connecticut, Report R-1403-1, February 1959.

4.59 H. G. Heinrich et al., *Quarterly Progress Reports*, Contract USAF 33(616)-6372, University of Minnesota, January 1960 - June 1961.

4.60 E. L. Haak and R. J. Niccum, *Pressure Distribution Measurements of Conventional Ribbon Parachutes in Supersonic Flow*, USAF ASD-TDR-63-662, September 1964.

4.61 H. D. Melzig and P. K. Schmidt, *Pressure Distribution During Parachute Opening, Phase I—Infinite Mass Operating Case*, USAF AFFDL-TR-66-10, March 1966.

4.62 R. J. Niccum, K. J. Goar, and W. W. Lenius, *Experimental Determination of Transonic and Supersonic Pressure Distribution and Mass Flow Accommodation for Ribbon Parachutes During Inflation*, USAF AFFDL-TR-65-105, Vol. 2, April 1968.

4.63 H. G. Heinrich and D. P. Saari, *Study of Parachute Forces and Canopy Pressure Distribution Measured in a Subsonic Wind Tunnel Under Infinite Mass Conditions*, USAF AFFDL-TR-71-175, March 1972.

4.64 H. G. Heinrich, R. A. Noreen, and J. N. Dale, *Aerodynamic Coefficients and Pressure Distribution of Solid Flat and Ringslot Models in One-Dimensional Velocity Gradients*, USAF AFFDL-TR-72-113, December 1973.

4.65 J. W. Holbrook, *Sandia Corporation Pressure and Disreefing Test of Model Parachutes in the Vought Systems Division Low-Speed Wind Tunnel*, SAND74-0278, Sandia Laboratories, September 1974.

4.66 J. B. Vaughn, *Sandia Corporation Pressure and Disreefing Test of Model Parachutes in the Vought Systems Division Low-Speed Wind Tunnel*, SAND74-0278A, Sandia Laboratories, September 1974.

4.67 J. Ottensoser, *Ribbon and Gliding Type Parachutes Evaluated in the 7 by 10 Foot Transonic Wind Tunnel*, SAND75-7072, Sandia Laboratories, September 1975.

4.68 W. L. Garrard and J. L. Piper, *Steady-State Canopy Pressure Distributions and Shapes for a Ribbon Parachute*, Interim Technical Report, Department of Aerospace Engineering and Mechanics, University of Minnesota, September 1982.

4.69 W. L. Garrard, K. S. Wu, and K. K. Muramoto, "Steady-State Stresses in Ribbon Parachute Canopies," AIAA 84-0816, April 1984.

4.70 J. F. Henfling and J. W. Purvis, "Pressure Distributions on Parachute Ribbon Shapes," AIAA 84-0815, April 1984.

4.71 W. G. S. Lester, *A Note on the Theory of Parachute Stability*, Royal Aircraft Establishment, Technical Note 358, July 1962.

4.72 F. M. White and D. F. Wolf, "A Theory of Three-Dimensional Parachute Dynamic Stability," *J Aircraft*, Vol. 5, No. 1, January-February 1968.

4.73 D. Wolf, "Dynamic Stability of a Nonrigid Parachute and Payload System," *J Aircraft*, Vol. 8, No. 8, August 1971.

4.74 C. Tory and R. Ayres, "Computer Model of a Fully Deployed Parachute," *J Aircraft*, Vol. 14, No. 7, July 1977.

4.75 K.-F. Doherr and C. Saliaris, "On the Influence of Stochastic and Acceleration Dependent Aerodynamic Forces on the Dynamic Stability of Parachutes," AIAA-81-1941, October 1981.

4.76 J. A. Eaton, "Added Fluid Mass and the Equations of Motion of a Parachute," *Aeronautical Quarterly*, Vol. 34, August 1983.

4.77 D. J. Cockrell, C. Q. Shen, R. J. Harwood, and A. C. Baxter, "Aerodynamic Forces Acting on Parachutes in Unsteady Motion and the Consequential Dynamic Stability Characteristics," AIAA 86-2470, October 1986.

4.78 R. Ludwig and W. Heins, *Investigations on the Dynamic Stability of Personnel Guide Surface Parachutes*, NATO/AGARD Report 444, April 1963.

4.79 H. G. Heinrich and L. W. Rust Jr., *Dynamic Stability of a System Consisting of a Stable Parachute and an Unstable Load*, USAF AFFDL-TR-64-194, May 1965.

4.80 H. G. Heinrich and L. W. Rust Jr., *Dynamic Stability of a Parachute Point-Mass Load System*, USAF AFFDL-TR-64-126, June 1965.

4.81 M. Neustadt, R. E. Ericksen, J. J. Guiteras, and J. A. Larrivee, "A Parachute Recovery System Dynamic Analysis," *J Spacecraft*, Vol. 4, No. 3, March 1967.

4.82 D. F. Wolf and H. R. Spahr, "Parachute Cluster Dynamic Analysis," *J Aircraft*, Vol. 14, No. 4, April 1977.

4.83 K.-F. Doherr, "Theoretical and Experimental Investigations of Parachute-Load-System Dynamic Stability," AIAA 75-1397, November 1975.

4.84 D. P. Saari, "Dynamics and Stability of Lifting Parachutes," Thesis for Doctor of Philosophy in Mechanics, University of Minnesota, June 1976.

4.85 W. D. Freeston Jr., S. C. Temin, J. W. Gardella, and M. M. Schoppee, *Mechanical Properties of High-Temperature Fibrous Structural Materials, Part I—Metal Textiles*, USAF AFML-TR-67-267, October 1967.

4.86 R. S. Jones, J. A. Parker, A. J. Rosenthal, and J. M. Steinberg, *Thermally Stable Polymeric Fibers, Part III*, USAF AFML-TR-67-172, October 1969.

4.87 J. P. Hartnett, E. R. G. Eckert, and R. Birkebak, *Values of the Emissivity and Adsorptivity of Parachute Fabrics*, USAF WADC Technical Note 57-433, December 1957.

4.88 A. Olevitch, *Emerging Aerospace Materials and Fabrication Techniques*, USAF AFML-TR-69-11, January 1969.

4.89 C. J. Scott, *The Prediction of Material Temperatures on Woven Retardation Devices*, USAF AFFDL-TR-67-170, March 1968.

4.90 L. C. Block, *Aerodynamic Heating of Parachute Ribbons*, USAF WADC TR-54-572, November 1955.

4.91 P. A. Schoeck, J. N. Hool, and E. R. G. Eckert, *Experimental Studies for Determining Heat Transfer on the Ribbons of FIST Type Parachutes*, USAF WADC TN 59-345, February 1960.

4.92 C. J. Scott and E. R. G. Eckert, *Experiments on the Thermal Performance of Ribbon Parachutes*, USAF AFFDL-TR-64-192, May 1965.

4.93 E. R. G. Eckert, J. E. Anderson, M. Ruiz-Urbieta, C. J. Scott, and K. M. Krall, *An Experimental Study of the Distribution of Convective Heat Transfer to a Large-Scale Model of Parachute Cloth*, USAF AFFDL-TR-66-13, May 1966.

4.94 C. J. Scott, E. R. G. Eckert, and M. Ruiz-Urbieta, "Measurements of Average Heat Transfer Coefficients for a Mesh Simulating Porous Parachute Cloth," *Int J Heat Mass Transfer*, Vol. 12, Pergamon Press, 1969.

4.95 W. B. Pepper, "Preliminary Report on Development of an Interim Parachute Recovery System for a Re-entry Vehicle," *J Aircraft*, Vol. 17, No. 3, March 1980.

4.96 C. W. Peterson, W. B. Pepper, D. W. Johnson, and I. T. Holt, "Application of Kevlar to Parachute System Design," *J Aircraft*, Vol. 23, No. 1, January 1986.

CHAPTER 5

NONSTEADY AERODYNAMICS

5.1 Introduction

This chapter treats those aspects of parachute aerodynamics whose physical processes are fundamentally time-dependent. The deployment process, which occurs when the parachute is withdrawn from its stored configuration and stretched out in the sky, is the first time-dependent event. The transient nature of parachute deployment is illustrated in Figure 5.1 (from Pepper[4.13]) for a 24-ft-diameter parachute deployed from a 760-lb test vehicle at a dynamic pressure of about 2600 lb/ft^2. A gas-generator-powered telescopic tube, installed along the centerline of the parachute pack, deployed the parachute at a velocity of about 160 ft/s relative to the test vehicle. Table 5.1 shows the sequence for deploying the 24-ft-diameter parachute from the two-leaf bag; many critical events take place during the ~0.25 s required for parachute deployment. Design of the deployment system (which includes the design of the deployment bag, bag-lacing cut knives, suspension line ties, canopy ties, and other cut or break ties) is just as important in the successful design of a high-performance parachute system as the accurate prediction of aerodynamic and structural loading of the canopy during inflation. Procedures for designing parachute deployment systems and predicting their performance are reviewed in this chapter and in Chapter 9.

The inflation of a high-performance parachute also involves time-dependent changes to the canopy and the surrounding airflow. Again, Pepper's[4.13] 24-ft-diameter parachute illustrates these nonsteady events. Note that the time from generator firing to the peak opening aerodynamic load of about 220 g is only 0.30 s; the total time from gas generator fire to the end of the parachute deceleration spike is only about 0.7 s. This chapter reviews both analytical and experimental work characterizing the body mechanics (trajectory and motion) and the fluid mechanics of the parachute/forebody combination, beginning with parachute deployment and continuing through inflation, when the parachute is rapidly decelerating the payload.

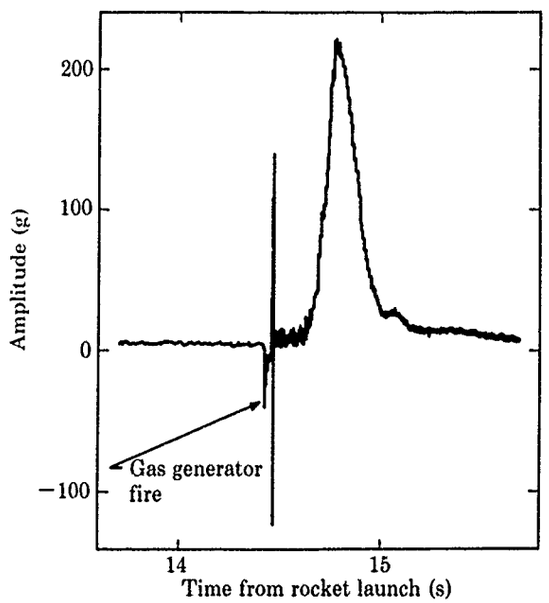


Figure 5.1. Parachute deceleration of a 760-lb test vehicle

Table 5.1. Sequence for Deploying a 24-ft Parachute From a Two-Flap Bag (deployment time is 0.15 to 0.40 s)

1. Fire the gas generator.
2. Break fourteen nylon dust cover tacks (one turn of 24-lb nylon).
3. Break twelve nylon thread-line loop tacks to bag (two turns of doubled 40-lb nylon).
4. Cut 1500-lb nylon bag lacing at forward end of bag in two places.
5. Cut cable (lanyard tacked with one turn of doubled 40-lb thread).
6. Break two doubled 90-lb nylon line ties at two stations.
7. Cut line retainer 1500-lb nylon in two places (each knife safe-tacked with one turn of doubled 24-lb nylon).
8. Break two 200-lb nylon line ties at fifteen stations.
9. Cut two 1000-lb nylon expansion loops.
10. Cut bag lacing at grommet 8.
11. Cut reefing cutter cable in two places (safe-tied with one turn of 40-lb nylon thread).
12. Cut 1500-lb nylon canopy retainer in two places (knives safe-tacked with one turn of doubled 40-lb nylon thread).
13. Cut bag lacing in canopy compartment in two places at grommet 14 (safe-tied with one turn of doubled 40-lb thread).
14. Break two 200-lb nylon canopy ties at three stations.
15. Canopy inflates. Tail can and bag are attached permanently to parachute at vent area.

5.2 Parachute deployment

The 1963 Parachute Design Guide,[2.1] the 1978 Recovery Systems Design Guide (Ewing, Bixby, and Knacke[1.7]), and Knacke[1.21] address different methods of initiating deployment. Methods commonly used for high-performance parachute systems include pilot parachutes, drogue guns, tractor rockets, and thrusted base plates; these are discussed in Chapter 9. Static lines are seldom used to deploy high-performance parachutes.

5.2.1 Line sail

Figure 5.2 shows the sequence for an orderly deployment of a high-performance 46.3-ft-diameter ribbon parachute from a 2465-lb (at release), 18-in.-diameter payload. A cluster of three 3.8-ft-diameter ribbon parachutes[3.6] was developed to deploy the main parachute in the presence of severe aircraft flow-field effects and large payload angles of attack. Orderly deployment (taut suspension lines and stretched-out/taut canopy exiting the deployment bag to provide a symmetrical canopy inlet/mouth at the start of inflation) is a difficult design task, but it is essential in order to avoid parachute damage during inflation. The sequence of events that occur during deployment of the 46.3-ft-diameter parachute from its four-leaf bag is given in Table 5.2. The bag design required careful selection of line and canopy ties, location of cut knives, selection of canopy retainer and bag lacing, and other facets of bag construction in order to achieve the orderly deployment shown in Figure 5.2. Deployment bag design is discussed in Chapter 9.

If the parachute is deployed at an angle to the relative wind (instead of with the wind), aerodynamic forces associated with the crosswind component of drag on the suspension lines may cause the suspension lines to be pulled out of the deployment bag prematurely. The resulting phenomenon is called "line bowing," "line sail," or "fish hooking," depending on the severity of the process. Line sail has been known to cause (or contribute to) increased deployment times, excessive snatch loads, asymmetrical deployment, canopy damage from bag friction, and unpredictable canopy inflation such as false venting or unsymmetrical inflation. The design parameters that may be chosen to control line sail are pilot parachute drag area, the number and strength of line ties, and deployment bag configuration.

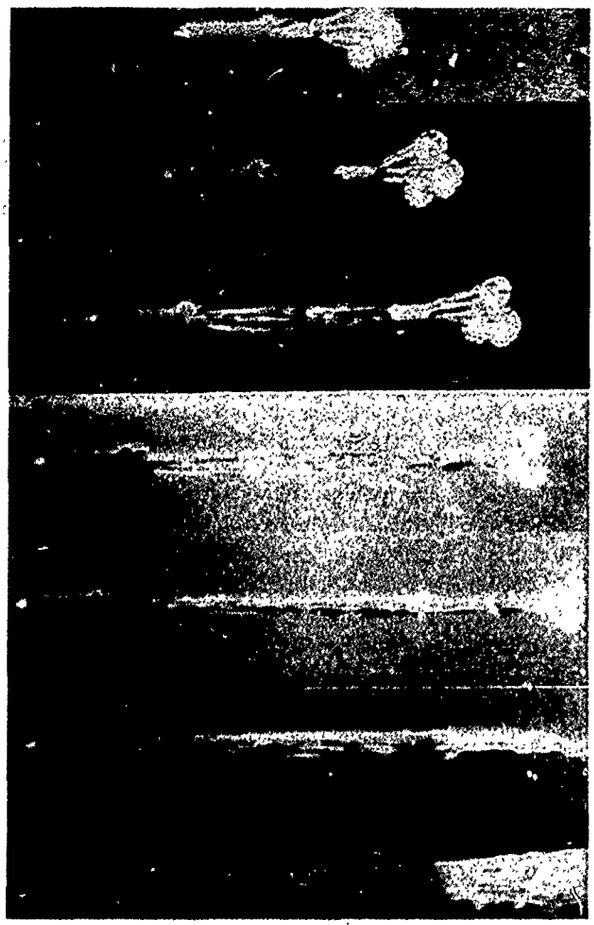


Figure 5.2. Orderly deployment of the main parachute using the cluster of three 3.8-ft-diameter pilot parachutes

Figure 5.3 shows the severe line sail observed during deployment of the same 46.3-ft-diameter parachute when the payload was at a 20-degree angle of attack and traveling at Mach 1.28. Aircraft flow-field interference caused the payload to pitch to this high angle of attack after exiting the bomb bay. The high angle of attack of the payload at supersonic speeds results in a turbulent wake with large lateral pressure and velocity gradients. The 5-ft-diameter ribbon pilot parachute was unable to remain inflated in such an asymmetric and violent wake flow field. The F-111 aircraft flow field, with the strong lateral and longitudinal pressure gradients resulting from the shock waves shown in Figure 5.3, also caused the parachute to collapse after its initial inflation. Once the pilot parachute collapses, it cannot provide enough drag to avoid the severe suspension line sail. The severity of the line sail at line stretch is evident from the lines looping over and past (downstream of) the deployment bag in Figure 5.3. The severe line sail caused poor canopy deployment and unacceptable damage to the canopy.

Moog[5.1] and Purvis[1.21,5.2,5.3] have modeled line bowing and line sail. Moog's model consists of breaking the suspension lines and canopy into several point masses, each acted upon by the aerodynamic drag of a line segment. The point masses are elastically coupled in chain-like fashion between the deployment bag and the vehicle. By tracking the line masses relative to the vehicle, the extent of the line bowing can be calculated at any time. Moog calculated the line bowing of a parachute to recover the Space Shuttle Solid-Fuel Rocket Boosters (SRBs). He showed that mortar-deployment of the SRB nose cap (which acted as a pilot parachute to deploy the main parachute) reduced line bowing over mortar-deployment of the main parachute because the nose cap increased the bag strip velocity. Moog validated his model with Viking decelerator flight test data.

Table 5.2. Sequence of Events Occurring During Deployment of the 46.3-ft Main Parachute From Its Four-Leaf Deployment Bag

1. Deploy and inflate the cluster of three 3.8-ft pilot parachutes.
2. Break fifteen doubled 24-lb nylon tacks holding the dust cover and suspension line groups.
3. Break twelve 90-lb nylon line ties (three stations on four bag panels).
4. Break loose two line-retainer cut knives (snubbed with 200-lb nylon and with doubled 50-lb safety tacks in two places).
5. Cut 6000-lb nylon retainer in two places.
6. Break fifty-two 500-lb nylon line ties (thirteen stations on four bag panels).
7. Break safe-ties (doubled 50-lb nylon tacks) on four bag-lacing cut knives.
8. Cut 2000-lb Kevlar bag lacing at four places.
9. Break twenty 500-lb nylon line ties (five stations on four bag panels).
10. Break loose two canopy retainer cut knives (snubbed with 200-lb nylon and with doubled 50-lb nylon safety tacks in two places).
11. Cut 6000-lb nylon canopy retainer in two places.
12. Break safe-ties (doubled 50-lb nylon tacks) on four bag-lacing cut knives.
13. Cut 2000-lb Kevlar bag lacing at four places.
14. Break eight 500-lb nylon line ties (two stations on four bag panels).
15. Break safe-ties (doubled 50-lb nylon tacks) on four bag-lacing cut knives.
16. Cut 2000-lb Kevlar bag lacing at four places.
17. Break sixteen 200-lb nylon canopy ties (four stations on four bag panels).
18. Break 1000-lb nylon vent break cord.
19. Bag separates from deployed 46.3-ft parachute; bag strip time (from step 2 through step 19) is 0.4 to 0.7 s.

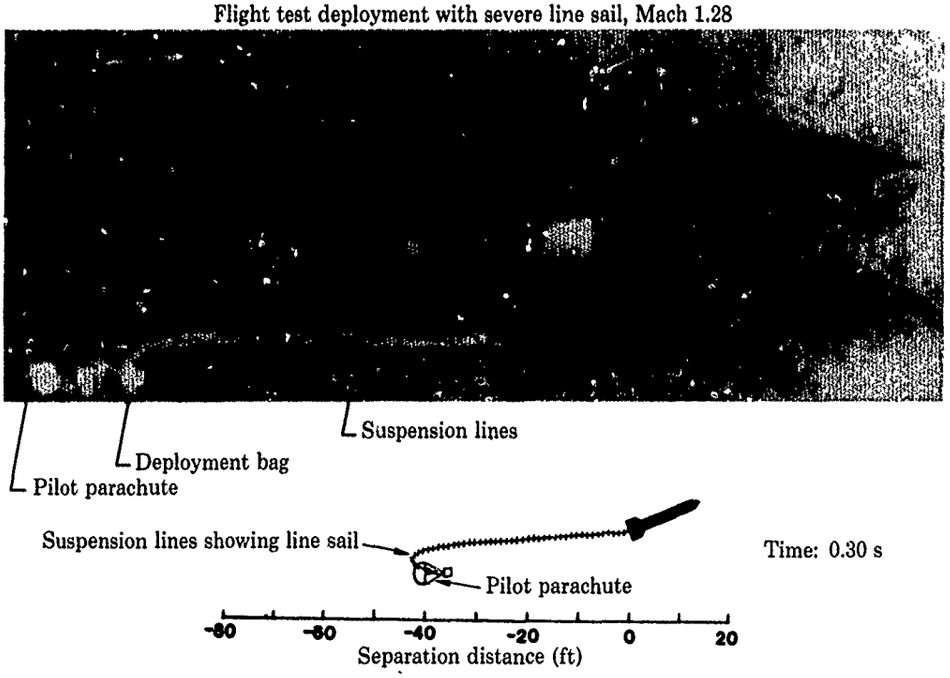


Figure 5.3. Comparison of flight test with computer simulation of line sail

Purvis[5.2,5.3] developed his numerical simulation of deployment (called LINESAIL) to provide analytical guidance for the redesign of the deployment system for the 46.3-ft-diameter parachute. His finite-element approach is similar to that of Sundberg,[5.4] in which both the suspension lines and canopy are modeled as flexible, distributed mass structures connected to a finite mass forebody. The physical system and a schematic representation of Purvis' discrete element model are shown in Figure 5.4. The forebody, suspension lines, canopy, and pilot parachute/deployment bag are modeled as a series of elastically connected mass nodes. The motion of each node is determined by the tensile and aerodynamic forces acting on the structural segment represented by the node. The forebody and pilot parachute/deployment bag are separate special nodes, with all undeployed suspension line or canopy nodes lumped in the pilot parachute/deployment bag node. The aerodynamic forces on the forebody and pilot parachute/deployment bag nodes consist of forebody drag and pilot parachute drag, respectively. Table 5.3 lists the nomenclature used in the Purvis equations that follow.

Referring to Figure 5.5, the equations of motion for the ith deployed mass node are

$$m_i\ddot{x}_i = T_i\cos\theta_i - T_{i-1}\cos\theta_{i-1} + F_{x_i} \tag{5.1}$$

$$m_i\ddot{r}_i = T_i\sin\theta_i - T_{i-1}\sin\theta_{i-1} + F_{r_i} \tag{5.2}$$

where T_i is the tension between nodes i and i+1, and F_x, F_r are the axial and radial components of the aerodynamic forces acting on the line segment represented by the ith node.

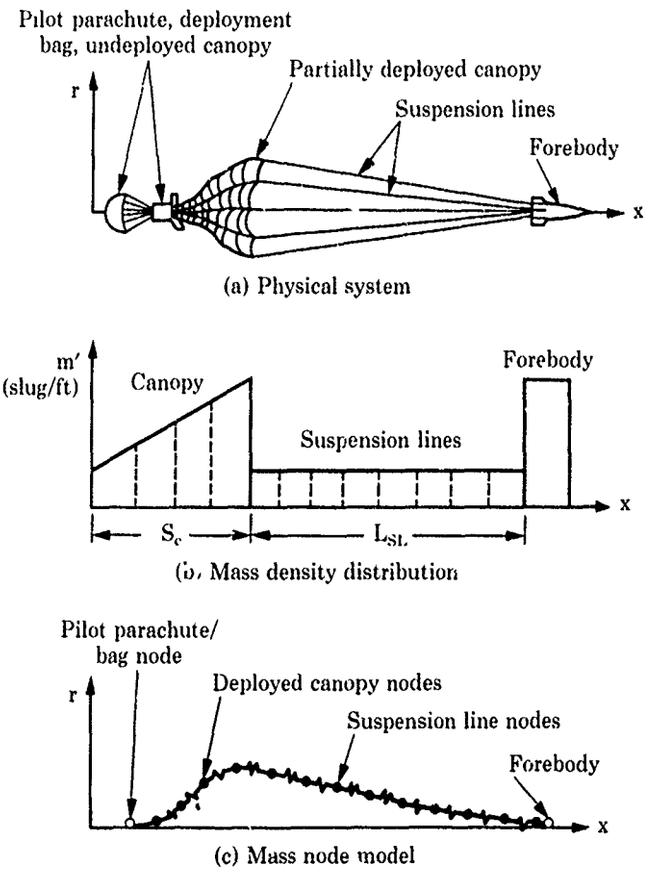


Figure 5.4. Discrete element model

Table 5.3. Nomenclature Used in the Purvis Equations

A_i	cross-sectional area of suspension line at *i*th node (ft^2)
a_∞	speed of sound (ft/s)
B_i	tensile damping coefficient at *i*th node (lb-s)
B_0	tensile damping constant (s^{-1})
C_A	tangential aerodynamics force coefficient
C_D	drag coefficient
C_{N_α}	aerodynamic normal-force coefficient derivative
E_i	elastic modulus of *i*th node (lb/ft^2)
$f(M_\infty)$	viscous cross-flow normal-force derivative
$F_{N_i}F_{A_i}$	aerodynamic forces at *i*th node (lb)
$F_{x_i}F_{r_i}$	axial and radial forces at *i*th node (lb)
K_{LG}	line group interference factor
K_T	line twist factor
m_i	mass of *i*th node, slugs
N	number of suspension lines
q	dynamic pressure (lb/ft^2)
S	aerodynamic coefficient reference area (ft^2)
s_i	distance between nodes i and i+1 (ft)
L_{SL}	suspension line length (ft)
s_{0_i}	unstretched distance between nodes i and i+1 (ft)
T_i	tension in *i*th line segment (lb)
V_i	total speed of *i*th node (ft/s)
V_{T_i}	tangential velocity component at node i (ft/s)
w	suspension line width (ft)
x,r	cylindrical coordinates
α_i	aerodynamic angle of attack of *i*th line segment
ϵ_i	strain of *i*th line segment
ρ_i	material density at node i ($slugs/ft^3$)
ρ_∞	ambient air density ($slugs/ft^3$)
μ_∞	ambient air viscosity (slugs/ft-s)
θ_i	line segment orientation angle

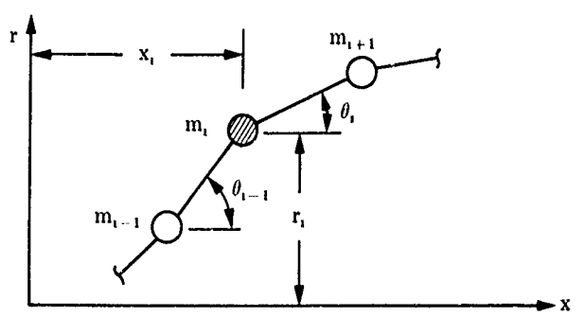


Figure 5.5. Mass node geometric parameters

Following Moog,[5.1] the tension between two mass nodes is expressed as a low strain rate stress-strain relation plus a linear damping term

$$T_i = E_i A_i N\epsilon_i + B_i \dot{\epsilon}_i \quad . \tag{5.3}$$

The strain and strain rate are computed from

$$\epsilon_i = (s_i - s_{0_i})/S_{0_i} \tag{5.4}$$

and

$$\dot{\epsilon}_i = \dot{s}_i/s_{0_i} \quad . \tag{5.5}$$

Negative values of tension are not allowed. From the geometry of Figure 5.6, the line segment length is

$$s_i = \sqrt{(x_{i+1} - x_i)^2 + (r_{i+1} - r_i)^2} \quad . \tag{5.6}$$

Differentiation gives

$$\dot{s}_i = \left[(x_{i+1} - x_i)(\dot{x}_{i+1} - \dot{x}_i) + (r_{i+1} - r_i)(\dot{r}_{i+1} - \dot{r}_i)\right]/s_i \quad . \tag{5.7}$$

The elastic modulus E_i is computed using the linear stress-strain assumption[5.1] and rated strength versus elongation-at-failure data

$$E_i = \text{rated strength}/A_i\epsilon_{max} \quad . \tag{5.8}$$

The damping parameter B_i is

$$B_i = 2B_0 m_i \sqrt{E_i/\rho_i} \tag{5.9}$$

where E_i/ρ_i is the wave speed in the line material and the constant B_0 has a value between 0 for no damping and 1 for critical damping. The form of the damping parameter was determined analytically from the longitudinal equation of motion of a single line segment fixed at one end and given an initial unit displacement at the other. The constant B_0 was determined by numerical experiment, and was found to be 85% of that required for critical damping (Moog[5.1] recommended using 5% to 10%). The large value was required in part by the one-step Euler integration scheme used in Purvis' analysis.

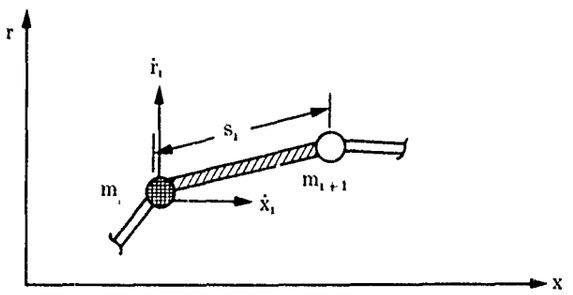


Figure 5.6. Line segment tension parameters

The axial and radial components of the line segment aerodynamic forces, shown in Figure 5.7, are

$$F_{x_i} = -F_{N_i}\sin\theta_i + F_{A_i}\cos\theta_i \tag{5.10}$$

$$F_{r_i} = F_{N_i}\cos\theta_i + F_{A_i}\sin\theta_i \quad . \tag{5.11}$$

The expression for the normal force is similar to that used by Sundberg,[54] which is based on the familiar cross-flow/drag formulations

$$F_{N_i} = (NK_TK_{LG})qSC_N\sin\alpha_i|\sin\alpha_i| \quad . \tag{5.12}$$

The dynamic pressure, q, and angle of attack, α_i, in Eq. 5.12 are based on the speed orientation of the ith node with respect to the absolute velocity vector. The dynamic pressure q has the usual form based on the square of the node velocity. The node reference area, which is an individual line segment planform area, is

$$S = ws_{0_i} \tag{5.13}$$

where w is the suspension line width and s_{0_i} is the unstretched length of the element. The normal-force coefficient derivative is

$$C_{N_\alpha} = f(M_\infty) \quad . \tag{5.14}$$

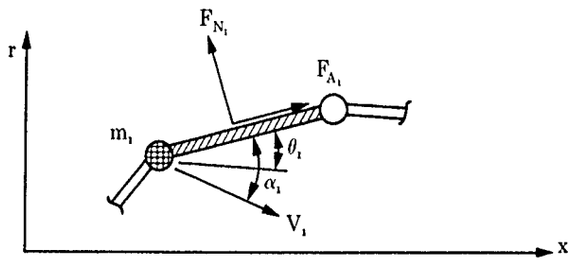


Figure 5.7. Line segment aerodynamic forces

Since the suspension lines for the systems of interest in the current work are flat ribbons, the aerodynamic normal force due to cross-flow on an isolated ribbon segment should be the same as that on a two-dimensional flat plate. However, during deployment the lines are bunched together, forming a rough cylinder with a diameter equal to the deployment bag diameter. The net aerodynamic normal force due to cross-flow on the line segment bunch should then be approximately the same as that on a two-dimensional circular cylinder. To model both behaviors, the form of the function $f(M_\infty)$ was taken from viscous cross-flow effects on a circular cylinder, with the magnitude adjusted such that the zero Mach value corresponds to the two-dimensional incompressible flat plate drag coefficient. The behavior of the function in the critical Reynolds number regime was found to be important.

The net normal force on a node is reduced by the product of a line twist factor, K_T, and a line group factor, K_{LG}. The line twist factor represents a reduction in the actual load on a line segment due to the fact that the line segment may be twisted. When the line segment is twisted, the cross-flow velocity component is no longer perpendicular to the maximum planform area of the segment. The actual cross-flow velocity component normal to the planform is the net cross-flow component reduced by the cosine of the twist angle. Assuming that each line segment has a specific twist angle, and that the distribution of twist angles is uniform between 0 and π, then the twist factor may be expressed as

$$K_T = \left(\frac{2}{N}\right)\sum_{i=1}^{N/2}\cos\left(\frac{\pi i}{N}\right) \tag{5.15}$$

where N is the total number of lines. The summation must be evaluated numerically.

Similarly, the line group factor (sometimes known as the shadow factor) accounts for the shielding of some lines in the group from the cross-flow velocity by other segments which are upwind. Assuming a uniform distribution in load between zero and the maximum, the line group factor may be expressed as

$$K_{LG} = \frac{1}{N}\sum_{i=1}^{N}\left(\frac{i}{N}\right) = \frac{N+1}{2N} \quad . \tag{5.16}$$

The axial (tangential) aerodynamic load on a line segment is assumed to consist solely of a turbulent skin-friction drag acting on the wetted area of each segment. The form of the tangential force is

$$F_{A_i} = -\tfrac{1}{2}\rho_\infty V_{T_i}|V_{T_i}|N(2S)C_A \tag{5.17}$$

where the negative sign and the absolute value are used to give the proper direction to the force. The factor of 2 in front of the area accounts for the fact that the wetted area is twice the planform area of a line segment. The axial-force coefficient, given by

$$C_A = 0.37/\left[\rho_\infty a_\infty L_{SL}/\mu_\infty\right]^{0.2} \tag{5.18}$$

is based on an approximate turbulent skin-friction drag formula derived from an experiment by Blasius (see Ref. 5.5). The formula is based on free-stream speed of sound and suspension line length rather than line segment velocity and length; however, the magnitude is still small, and experimental data show that the turbulent skin-friction coefficient for a flat plate varies less than 10% for Mach numbers up to 2.

The effects of line ties and deployment bag friction, where appropriate, are incorporated into the tension and force equations, respectively. Line tie effects are represented as a node deployment restriction. Untied nodes are allowed to deploy only when two conditions are met: (1) the previous node has been deployed, and (2) a nonzero tension exists in the line segment between the deployed and undeployed nodes. When a node is tied, the second condition is modified such that the tension in the segment must be greater than the rated strength of the ties before the node is allowed to deploy.

As noted by Moog,[5.1] the magnitude of the deployment bag friction force, also known as inelastic bag stripping force, is commonly determined in ground tests. In the present analysis, bag friction is represented as a constant force acting only on the last deployed node. The force is assumed to act on the node from the time it is deployed until the next successive node is deployed. The line of action of the force is along the segment between the last deployed node and the deployment bag node.

Figure 5.8 shows the flowchart for the deployment simulation program, which incorporates the complete analysis. Prior to any attempt at predicting line sail, various aspects of the simulation were studied and compared with experiment. In addition, values for driving parameters, such as canopy/deployment bag friction and pilot parachute drag area, were obtained from experimental data.

Purvis used the simulations described in References 5.2 and 5.3 to guide the redesign of the deployment system for the 46.3-ft-diameter parachute that experienced the severe line sail shown in Figure 5.3. The dynamics equations (5.1 to 5.7) were verified with data from a static parachute deployment test (ground tests with no airflow) and flight of other parachute systems. Using LINESAIL, he then reproduced the line sail shown in Figure 5.3. Subsequent simulation results indicated that practical changes in line tie strengths did not control the line sail, but increasing the pilot parachute drag was a very effective method of controlling it. The pilot parachute drag area was increased from about 10 ft^2 to 17 ft^2 by replacing the 5-ft-diameter parachute with a cluster of three 3.8-ft-diameter parachutes. An advantage of the cluster is that the individual canopies extend farther out of the store wake into the higher dynamic pressure and less turbulent airstream, thus reducing their tendency to collapse and maximizing their tendency to reinflate if collapse does occur. The deployment system baseline design was changed to this cluster pilot parachute system, which operated successfully (with no line sail problems) in many flight tests during the development of this currently operational store (see Figure 5.2 and Johnson and Peterson[3.6]). Purvis lectured on the use of these line sail codes at the 1985 Helmut G. Heinrich Short Course on Decelerator Systems Engineering.[1.21]

Johnson[3.37] investigated the performance of a cluster of three 49-ft-diameter parachutes for the 3130-lb F-111 Crew Escape Module (CEM). A drogue gun is used to deploy the pilot parachute. Deployment may occur with the drogue gun firing at CEM angles of attack between −30 and +120 degrees. This means that the pilot parachute and main deployment bag may be deployed into the wind. Adding to the problem of avoiding line sail was the length of the suspension lines; the main parachute deployment bag reaches line stretch about 80 ft from the CEM. LINESAIL showed that controlling the line sail caused by the crosswind deployment required larger pilot parachute drag. However, the pilot parachute had to be so large that the bag strip velocities would be high enough to cause significant damage to the parachutes, even with a Teflon-lined bag. Johnson's solution was to use a dual pilot parachute system, with a 5-ft-diameter ribless guide parachute placed inside a 10-ft-diameter circular flat parachute. The 10-ft parachute breaks away at a drag force of 2000 lb, leaving the inflated 5-ft parachute to deploy the main parachutes at high deployment velocities.

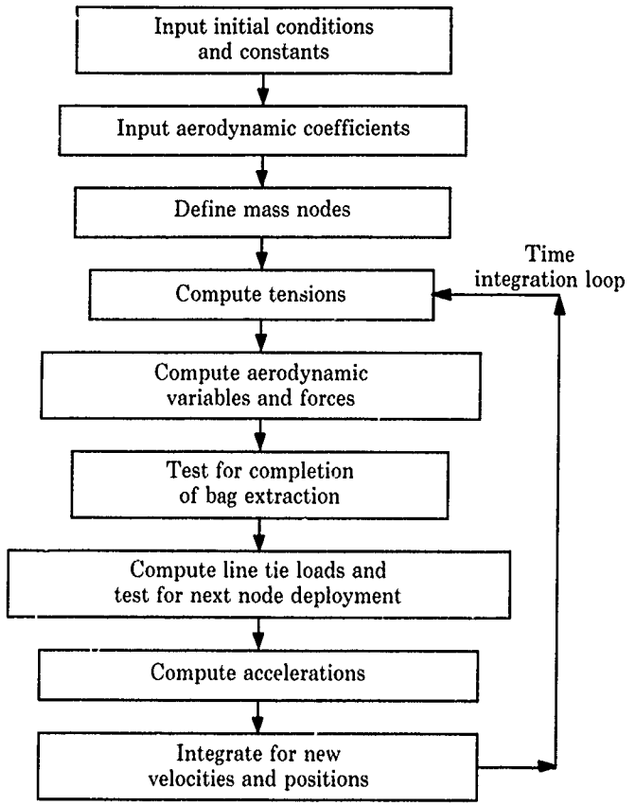


Figure 5.8. Flowchart for deployment simulation program LINESAIL

LINESAIL has proved to be accurate and easy to use for designing deployment systems. It is one of the few parachute predictive numerical codes that can be trusted and used as a design tool. LINESAIL is being modified to provide improved modeling of the energy dissipated during the breaking of line ties, and it is being written for use on small personal computers. It should be useful in the preliminary design of new high-performance parachute systems to ascertain whether line sail problems might occur and, if so, to calculate what pilot parachute drag area and line tie strengths are required to minimize line sail problems.

5.2.2 Snatch loads

The Parachute Design Guide[2] [1]and Ewing, Bixby, and Knacke[1] [7] present thorough discussions of canopy suspension line extension and the resulting impulsive loading of suspension lines when the canopy is deployed. This short-duration loading, known as "snatch load," arises from the difference in velocity between the suspended payload and the deploying decelerator. The rapid deceleration of the decelerator, in contrast to the relatively slow deceleration of the suspended load, creates a sizable differential velocity that must be reduced to zero. The snatch load is defined as that force imposed upon the suspended load by the decelerator to accelerate the mass of the decelerator from its velocity at line extension (not stretch) to the velocity of the payload. Snatch loads are imposed before inflation; hence, snatch loads and opening-shock loads are not additive. An example of a measured snatch load from a flight test is shown in Figure 3.7.

The 1963 Parachute Design Guide[2.1] derives the energy and the velocity equations to develop a method for calculating the snatch force. Snatch loads can be reduced by controlling the deployment. Controlling the deployment may be difficult if the parachute must function over a wide range of dynamic pressures, but several approaches have been used successfully. Perhaps the most effective means for reducing snatch loads and controlling deployment is to pack the parachute in a deployment bag in a manner that allows the suspension lines to be pulled out of the bag before the canopy. "Lines-first" deployments reduce snatch loads because the canopy is unable to inflate (and therefore increase the differential velocity between the deploying mass and the payload) until its velocity is the same as

the payload's. Reducing the weight of the parachute also lowers the amount of mass that must suddenly be brought up to the speed of the payload. Parachutes should not be made much heavier than is needed to accommodate inflation loads. Reducing uninflated-canopy drag area or pilot parachute drag area also reduces the inertial loads at line extension. Reducing these parameters, however, will have a large effect on proper deployment and inflation; they cannot be changed without affecting deployment and reliability.

Ewing, Bixby, and Knacke[1.7] point out that the high-onset shock generated by the snatch force can cause unacceptable inertial loads in attached devices such as reefing line cutters. The shock has been known to fail the pryotechnic fuse train or to prevent the firing pin from actuating the percussion initiator in a cutter improperly mounted on the skirt. Snatch-generated inertial loads may tear reefing line cutters loose from the canopy skirt. This has occurred in tests of the 46.3-ft-diameter parachute developed by Johnson and Peterson.[3 6] Two 2-lb reefing line cutters are attached to two of the sixty 6000-lb Kevlar suspension lines at the canopy skirt. The deployment bag was very carefully designed to minimize snatch loads. Deceleration histories from onboard accelerometers indicate that the snatch load is less than half the opening-shock load. However, extensive flight testing showed repeated failure of the two 6000-lb Kevlar suspension lines that support the reefing line cutters at deployment dynamic pressures above 1500 lb/ft^2.

Reference 1.7 (p. 240) presents a method (unpublished work by Wolf in 1976) for estimating the body-canopy separation velocity at line stretch. It has proved to be quite useful because, for many practical systems, the approximation to measured values is close.

Holt[4 45] measured snatch load and opening-shock data for 21 flight tests from 1963 to 1967 of a reefed, 76-ft-diameter ribbon parachute. The maximum measured snatch and opening-shock loads were 91,500 and 123,000 lb, respectively. The snatch load exceeded the opening shock in four of the flight tests. These high snatch loads suggested that the deployment system (primarily the deployment bag) had not been properly designed. Since 1954, Sandia has conducted many high-dynamic-pressure flight tests of high-performance parachutes. Several parachute failures have occurred because of excessive snatch loads. In 1958, a parachute laboratory was established at Sandia and, shortly after, a development program was undertaken to minimize or control snatch loads. This development program, which required many flight tests with trial-and-error deployment bag designs, resulted in the very successful four-leaf deployment bag patented in 1964 by Widdows.[5.6] These basic deployment bag design techniques (discussed in detail in Chapter 9) have been used successfully at Sandia ever since.

Pepper[3 2] tested a 20-ft-diameter reefed, conical ribbon parachute on an 890-lb payload at a dynamic pressure of 5700 lb/ft^2 (Mach 2.43). The opening-shock load was 200 g, but the snatch load was less than 50 g. The deployment bag for this system was designed by Widdows, using his patented techniques. Maydew and Johnson[3.1] conducted 29 instrumented flight tests of a 22.2-ft-diameter reefed, conical ribbon parachute at dynamic pressures of 390 to 2695 lb/ft^2. The opening-shock loads varied from 12 to 77 g (the test vehicle weighed 2100 lb), but the snatch loads were much lower, varying from 5.3 to 27 g over the range of dynamic pressures. As before, this two-panel deployment bag was designed by Widdows using the same patented techniques. These latter two flight test examples graphically demonstrate how the snatch loads can be minimized by careful design of the deployment system, especially the bag.

Toni[1.10] and Huckins[5 7] have published theoretical models for predicting snatch loads for lines-first deployment. Huckins treated the suspension lines as a one-dimensional continuum and used the solution of the wave equation to predict the snatch load. Heinrich[5 8] developed a method of calculating snatch force that included the effects of the riser and suspension disengagement impulses. He was perhaps the first to demonstrate analytically that the disengagement impulses strongly affect the magnitude of the snatch load; he concluded that snatch loads could be decreased by careful design of the deployment bag. Poole and Whitesides[5.9] used a finite difference solution to the one-dimensional-wave equation to model tension waves in the suspension lines during the complete canopy unfurling phase.

McVey and Wolf[6.10] developed a dynamic model, based on integration of axial and radial momentum equations, for predicting deployment and snatch loads. The parachute deployment sequence starts with deployment initiation through bag stripping and continues until the parachute suspension lines and canopy are fully extended. McVey and Wolf made detailed comparisons of the bag stripping and snatch loads for several full-scale flight tests of 22.2- and 76-ft-diameter ribbon parachutes. The bag stripping and time to full parachute extension were matched accurately for both systems. The internal bag force results largely from breaking loops of nylon tape that tie the suspension lines to the bag and ensure orderly deployment. They assumed a distributed mass of the

suspension lines and canopy at line stretch for calculating the snatch load. They concluded that the magnitude of the snatch load was a strong function of (1) the time required for the canopy retaining flaps and bag lacings to react (after being cut) and release the canopy so that it can act as a distributed mass rather than a concentrated mass, and (2) the canopy mass distribution (i.e., the manner in which the canopy is distributed and packed in the bag and how strongly it sticks together after the bag is cut). McVey and Wolf's study provides insight into snatch loading and bag stripping phenomena for high-performance parachutes and bag design techniques required to reduce snatch loads.

Sundberg[5.4] developed a finite-element model that provides a detailed dynamic model for all points on a parachute during its deployment and inflation. Both canopy and suspension lines are modeled as two-dimensional, flexible, distributed mass structures. Solutions obtained with the model show the tension wave motion that occurs during deployment and early inflation. His model provided predictions of the time-dependent loads in the suspension lines. As mentioned in the previous section, Sundberg's work formed the basis for Purvis' LINESAIL code, which is now used at Sandia instead of Sundberg's model.

Banerjee and Utreja[5.11] conducted a theoretical analysis and an experimental investigation of two deployment concepts of the drogue parachute deployment for the Space Shuttle SRB. Wind tunnel test data compared reasonably well with the theory. French[5.12] extended Wolf's methods (see Ref. 1.7) for the calculation of parachute/forebody separation velocity and deployment time to consider the effects of line ties on the deployment of a pilot extracted and deployed parachute.

5.3 Canopy inflation

Inflation of the canopy begins as soon as the parachute is pulled free from the deployment bag. Air flows into the canopy through the plane of the skirt. Some of the air passes through the porous canopy fabric, the vent, and the gaps between ribbons. However, the porosity of the parachute material and configuration is chosen so that some of the air is retained in the canopy. This "captured" air causes the pressure inside the canopy to increase above the pressure outside of the canopy. The radial component of force generated by the pressure differential across the canopy accelerates the canopy outward and causes it to inflate. Inflation continues as long as the integrated outward radial pressure forces remain greater than the integrated radial tension and no structural constraints such as skirt reefing are encountered.

Canopy porosity plays an important role in establishing the inflation rate. When the total porosity is excessive, the radial forces generated by the pressure inside the canopy may not exceed the inward component of the load in the suspension lines. This results in an oscillatory motion of the canopy (called "squidding"), which stops the inflation process. The amount of porosity that can be allowed without stopping the inflation process depends on the type of parachute, the shape of the gore pattern, the distribution of porosity in the canopy, and the length of the suspension lines relative to the parachute diameter. Slotted canopies of ribbon and ringslot parachutes, both flat and conical, retain a positive opening tendency at much higher porosity levels than solid canopies. This is attributed to the difference in character of the through-flow in slots relative to the fabric pores, the former functioning like sharp-edged orifices with a marked jet contraction effect, thereby offering a relatively greater through-flow resistance.

The time-dependent nature of the inflation process is evidenced by the fact that the parachute is changing shape throughout the inflation process. Even in cases when the oncoming velocity does not decrease much during the inflation, the behavior of the parachute and the surrounding airflow is inherently time-dependent. Inflations wherein negligible velocity changes occur are called *infinite mass* inflations; examples of infinite mass inflations include aircraft deceleration applications or tests of parachutes in a constant-velocity wind tunnel. The term *finite mass* inflation is used to describe cases where the change in velocity during the inflation has a direct effect on the inflation process. Finite mass inflations occur when large parachutes are used on small payloads, generating large decelerations while the parachute is still inflating. Reference 1.7 provides an excellent description of the stages of finite mass parachute inflation (Figure 5.9).

The complexity of the time-dependent inflation process has forced parachute designers to resort to a wide spectrum of solution approaches, ranging from semiempirical, approximate analyses to more complete numerical models. This section reviews the methods available for predicting canopy inflation and cites experimental data used to guide analysis.

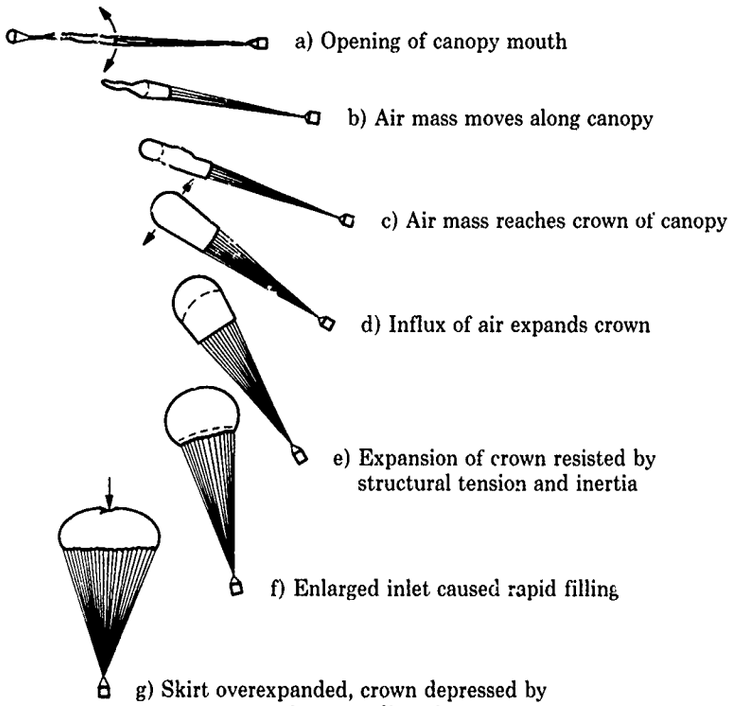


Figure 5.9. Stages in parachute inflation (taken from Ref. 1.7)

5.3.1 Added mass approximation in nonsteady flows

Not all of the drag produced by a parachute decelerates the payload. Some of the parachute's drag *accelerates the air through which it passes.* To appreciate the fluid physics of this process, observe that the parachute collects the air into the canopy and brings the air up to the velocity of the payload. The same is true of the air immediately in front of and behind the canopy. The energy required to accelerate this mass of air from rest to the velocity of the payload is taken from the kinetic energy of the payload by the drag of the parachute. Our observations of inflating parachutes may cause us to ignore the acceleration of the surrounding air because we can only "see" the parachute system and not the air moving in and around the parachute. For large parachutes, however, the portion of parachute drag that accelerates the surrounding air can be the same order of magnitude as the portion that decelerates the forebody. Ignoring the acceleration of the surrounding airflow by the parachute can lead to parachute structural failures, as will be discussed later in this section.

Fluid inertia effects can be included in the equation of motion for the inflating parachute system by making use of the *added mass* approximation. The equation of motion for the parachute/payload equates the change in momentum of the parachute/payload system to the sum of the instantaneous drag of the parachute and the gravitational force:

$$\underset{\substack{\text{Force exerted on the}\\ \text{parachute/payload}}}{\frac{d}{dt}[MV]} = \underset{\substack{\text{Drag of the}\\ \text{parachute}}}{-\frac{1}{2}\rho V^2 \cdot C_D S} + \underset{\substack{\text{Vertical component of}\\ \text{gravitational force}}}{m_b g \cdot \sin\theta} . \tag{5.19}$$

In this equation, M is the total mass of the parachute/payload system and V is the velocity of that system. Rather than solve this equation simultaneously with the equations of motion for the airflow, fluid inertia effects are included in the equation above by adding the mass of the air accelerated by the parachute to the mass of the payload decelerated by the parachute:

$$M = m_a + m_b \tag{5.20}$$

where m_a is the added mass of the air and m_b is the mass of the payload.

The mass of the payload is constant, but the added mass depends on the volume of air affected by the parachute, which changes throughout the inflation process. Combining Eq. 5.20 and Eq. 5.19 with the knowledge that $m_a = m_a(t)$ yields

$$V\frac{dM}{dt} + M\frac{dV}{dt} = -\frac{1}{2}\rho V^2 \cdot C_D S + m_b g \cdot \sin\theta \ ,$$

or

$$(m_b + m_a)\frac{dV}{dt} = -\frac{1}{2}\rho V^2 \cdot C_D S - V\frac{dm_a}{dt} + m_b g \cdot \sin\theta \ . \tag{5.21}$$

Equation 5.21 shows that the added mass appears on the left side of the equality as an additional mass that must be accelerated (in addition to the payload mass) and on the right side of the equality as a contributor to the acceleration of the payload/parachute system while the parachute is inflating (i.e., while dm_a/dt has a positive value). At best, this is a *very approximate* expression; there is disagreement within the parachute community that such nonlinear fluid dynamic phenomena should ever be expressed as simple additive terms in the equation of motion for the parachute and payload. This review calls attention to the nature of the approximations and the research available from the literature. Once they understand the limitations and risks of the added mass approximation, parachute engineers may consider using Eq. 5.21 to predict time-dependent parachute deceleration of the payload if the magnitude of the added mass terms can be determined either experimentally or analytically at all times during the inflation process.

The added mass approximation for predicting forces acting on a parachute in unsteady motion has been used for many years. The reader is referred to Cockrell's AGARDograph[1,6] and Cockrell, Huntley, and Ayres[5,13] for a thorough development of the concept of apparent mass as it applies to parachutes and the unsteady flow problem. Von Kármán[5,14] stressed the importance of the role of fluid inertia effects on parachute dynamics. He used the concepts of added mass to explain the larger-than-expected decelerations recorded when parachutes are deployed at high altitudes. Similarly, Ibrahim[19] indicated that the apparent mass and the moment of inertia of the parachute *system* are often larger than the mass and moment of inertia of the canopy alone.

We find considerable inconsistency within the fluid mechanics literature regarding the definitions and nomenclature of added mass and related terms such as included mass, apparent mass, hydrodynamic mass, induced mass, and virtual mass. This report follows the lead of Ibrahim,[19,5,15] Heinrich,[5,16] and Ewing, Bixby, and Knacke[17] in defining these terms. *Included mass* considers the air captured by the canopy; its effects on the parachute system are present during both steady and unsteady motions. Included mass is related to the capture volume of the parachute and, therefore, it increases during canopy inflation. *Apparent mass* is the part of the added mass whose effects are manifested only in unsteady flows, such as parachute inflation and deceleration.

In his 1965 lecture notes for a parachute course at the University of Minnesota, Heinrich[5,16] derived analytical expressions for the equations of motion for an inflating parachute. His approach employed the concept of added mass to approximate unsteady fluid inertia effects. He defined the apparent mass, m′, as

$$m' = k \cdot \frac{4}{3}\pi\rho r^3 \ , \tag{5.22}$$

where ρ is the density of the air, r is the radius of the parachute, and k is a coefficient whose value depends on the parachute shape and the direction, type, and history of its motion. Theoretical values for k are possible for idealized shapes in inviscid flows; for a sphere, m′ can be shown to be half of the mass of a sphere with radius r, giving $k = 0.5$. Analytical values of k are difficult to obtain for more complex shapes, so Heinrich carried out experiments to measure the coefficient k for parachute models. He found that a value of $k = 0.25$ was a good approximation. He also concluded that the apparent mass of a parachute was ~3/8 of the included air mass of the parachute. Heinrich defined the added mass, m_a, as the sum of the apparent mass, m′, and the included air mass, m_i:

$$m_a = m' + m_i \ . \tag{5.23}$$

The added mass, m_a, is combined with the mass of the body (Eq. 5.20) for calculating system deceleration.

Ibrahim[1.9,5.15] used potential flow theory to calculate the added mass for spherical cups of any concavity ranging between the limiting cases of the flat circular disk and the pinholed sphere. He proposed a form for the added mass, m_a, that followed the form of the expression for apparent mass, m′:

$$m_a = k_a \cdot \frac{4}{3}\pi\rho r^3 \quad . \tag{5.24}$$

Using his potential flow analytical solutions, Ibrahim calculated k_a for these spherical cups. For a hemispherical cup, he obtained $k_a = 1.068$. The equivalent k_a value for Heinrich's[5.16] measured and estimated apparent mass plus included air mass is approximately 0.92. Ibrahim found that the added mass was greater than the included fluid mass for every cup configuration.

Klimas[4.54] developed a numerical technique for calculating the fluid mass associated with porous parachute canopies of arbitrary cross sections operating in an inviscid, incompressible fluid. His procedure replaces the physical parachute canopy with a mathematical vortex sheet. The strength of the vortex sheet is chosen to satisfy porosity boundary conditions on the canopy surface. The vortex sheet strength is used to determine the fluid kinetic energy, from which the added mass coefficients are calculated. The velocity distributions on the inside and outside of the simulated canopy are also calculated by this method; they agree closely with Ibrahim's[5.15] analytical solutions.

Klimas calculates $k_a = 0.994$ for an "imporous" hemispherical cup, somewhat lower than Ibrahim's[5.15] value of $k_a = 1.068$. Klimas attributes the lower value to the inability of the vortex sheet method to meet the zero porosity boundary condition everywhere on the surface of the solid hemispherical cup. The boundary condition of zero velocity normal to the vortex sheet is satisfied at only one location on each of the sheets used to describe the canopy. At the sheet nearest the skirt of the canopy, fluid speeds become infinite and differential pressures across the canopy generate correspondingly high mass flows across the canopy. As a result, the calculations for "zero porosity" hemispherical cup actually have some "numerical leakage" corresponding to an effective porosity of 0.044. Sarpkaya[5.17] discusses the validity of these numerical approximations in simulating the actual porosity distributions in real parachute canopies.

Using the same vortex sheet method, Klimas calculated values of k_a for porous hemisphere ribbon parachutes with simulated "gaps" between the "ribbons." For these configurations, the effects of numerical leakage may be appreciable at the trailing edge of each of the sixteen sheets used to represent the ribbons, not just at the sheet nearest the skirt. Hence, the value of k_a for zero canopy porosity obtained from Klimas' sixteen-sheet model does not agree with the k_a obtained from Klimas' single-element cup. Nevertheless, Klimas' calculations are useful because they show a trend of decreasing associated fluid mass with increasing geometric porosity (Figure 5.10) for hemispherical ribbon parachutes. The ratio of k_a at porosity λ to the value of k_a for zero porosity ($\lambda = 0$) from Klimas' calculations is shown in Figure 5.10. This figure can be used to obtain an estimate of k_a for porous parachutes if k_a is known (using either data or analysis) for an imporous canopy; engineering estimates of added mass could then be obtained from Eq. 5.24.

Heinrich[5.18] incorporated apparent mass effects in developing a linearized theory of parachute opening dynamics. Payne[5.19] uses the analogy of an underwater explosion as a starting point to understand the inertia effects of the air that must be displaced during the parachute filling process (i.e., the apparent mass effects) in his analysis of parachute opening dynamics. DeSantis[5.20] included apparent mass effects in his computer analysis of parachute system parameters and concluded that increasing the altitude resulted in shorter filling times and higher deceleration forces on the payload. His analysis was verified by flight test data.

Cockrell and collaborators (Refs. 5.13, 5.21–5.23) defined, analyzed, and measured (in a wind tunnel) the apparent mass components and apparent moment of inertia terms associated with a descending parachute for application to predicting dynamic stability. Preliminary data for added mass coefficients for reefed and full-open flat circular ringslot parachutes with geometric porosities of 10%, 20%, and 30% are reported by Cochran, White, and Macha.[5.24]

Eaton[5.25] reviews the effect of added mass on the dynamic stability of parachutes and includes for the first time the complete form of the added mass tensor. He indicates that the added mass effects are even more significant than previously predicted. However, design and testing experience shows that dynamic stability is a second-order design problem for high-performance parachutes, compared to the first-order design problems of snatch loads, opening shocks, etc. Most high-performance parachutes, such as guide surface or conical ribbon, possess high static stability and high dynamic stability (i.e., rapid damping).

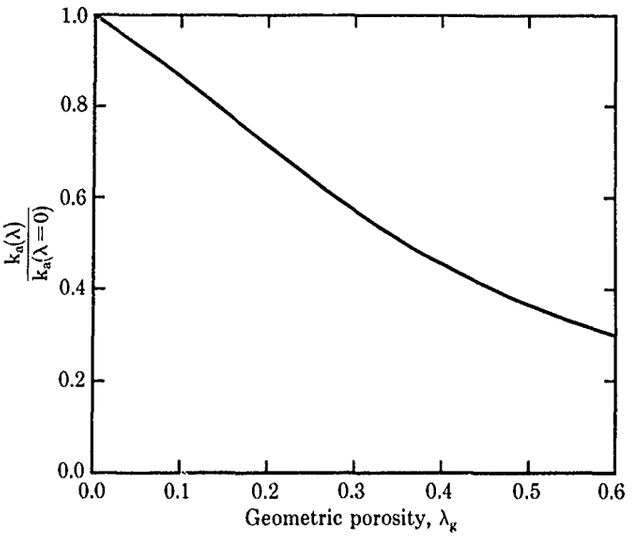


Figure 5.10. Effect of geometric porosity on added mass, k_a, where $k_a\ (\lambda=0) = 1.068$

Knacke[1.8] reported that, in 1944, the U.S. Army Air Corps conducted tests with five types of personnel parachutes dropped at indicated airspeeds of 115 mph with a 200-lb torso dummy at altitudes of 7000 to 40,000 ft. To the great surprise of the technical community, the parachute opening forces at 40,000 ft were approximately four times as great as the forces measured at 7000 ft, even though all parachutes were opened at the same dynamic pressure. To explain this force increase with altitude, note that the true velocity is twice as high at 40,000 ft altitude than it is at sea level for parachutes inflating at constant dynamic pressure; therefore, the kinetic energy of the payload/store to be removed by the parachute is four times greater at 40,000 ft than at 7000 ft. In addition, the filling time of the canopy at 40,000 ft altitude is only half as long as it is at sea level because the true velocity is double the sea-level value at 40,000 ft altitude. The third contributor to these large parachute opening forces was caused by the reduction in added mass. At the lower air density associated with high-altitude deployments, most of the parachute drag contributed to decelerating the payload; a smaller fraction of parachute drag was involved in accelerating the added mass at high altitudes than at low altitudes. This was perhaps the first definitive flight test observation of added mass effects on parachute inflation in the United States.

Contrary to his findings with large parachutes attached to light payloads, Knacke[1.8] observed no parachute opening-force increase with altitude for an "infinite mass" parachute/payload system. In 1954, the U.S. Air Force deployed a 15.6-ft-diameter ringslot parachute approach brake from a B-47 at altitudes of 2000 ft and 30,000 ft at the same indicated airspeeds; the measured parachute opening force was ~7000 lb for both tests. Knacke suggested that there is no altitude effect on the opening shock of the B-47 brake parachute because of the high canopy loading. The parachute/B-47 system does not decelerate appreciably during canopy inflation, whereas the personnel parachute/torso system with low canopy loading decelerates considerably during canopy inflation, especially at low altitudes.

Heinrich and Saari[5.26] include added mass effects in their comparison of calculated and measured (full-scale flight tests of a 28-ft-diameter C-9 personnel parachute and a 64-ft-diameter G-12D parachute) force-time histories; the calculations agreed well with the data.

Wolf[5.27] modified his INFLAT parachute inflation model[5.28] to include a coupling apparent mass effect. His original model predicted faster inflations and larger opening-shock loads than those observed in flight test data. He suggests that the deficiency in the original theory was the absence of unsteady fluid dynamic coupling between radial and axial degrees of freedom. This effect is most important when the ratio of parachute apparent mass to payload mass approaches unity. It then causes a large reduction in parachute inflation rate and a corresponding reduction in maximum parachute force. Wolf defined three apparent mass (A) terms and apparent mass coefficients (B) for the axial (xx subscript), radial (rr subscript), and coupled axial/radial (xr subscript) degrees of freedom:

$$A_{xx} = B_{xx} \cdot \frac{4}{3}\pi\rho R_c^3 \tag{5.25a}$$

$$A_{rr} = B_{rr} \cdot \frac{4}{3}\pi\rho R_c^3 \tag{5.25b}$$

$$A_{xr} = B_{xr} \cdot \frac{4}{3}\pi\rho R_c^3 \,. \tag{5.25c}$$

R_c is the constructed radius of the canopy. Wolf used $B_{xx} = 1$ (from theory), $B_{rr} = 3$ (theory for a sphere), and $B_{xr} = 1.3$ (determined as the best fit with experimental flight test data). All of the apparent mass coefficients were reduced for the effects of porosity. He demonstrated good agreement between calculations and flight test data of dynamic pressure, parachute force, parachute diameter, and drag area versus time during the inflation process of a 46.3-ft-diameter ribbon parachute. This parachute system is discussed by Johnson and Peterson.[3,6] Wolf showed a similar set of good correlations between theory and flight test data for the more heavily loaded 54-ft-diameter drogue parachute for the NASA Space Shuttle Solid Rocket Booster case. Inclusion of the coupling-mass effects to the INFLAT parachute inflation improved the accuracy prediction of filling time and aerodynamic loading over a wide range of parachute loadings.

All of these investigators provide evidence that the inertia of the surrounding air plays an important role in determining the deceleration that the parachute exerts on the payload when the parachute is large and when the payload experiences significant reduction in velocity while the parachute is inflating. Equation 5.21 can help us explain their observations. To simplify the explanation, we shall ignore the vertical gravity term because (1) high-performance parachutes often generate decelerations that are much larger than 1 g, and (2) the trajectory angle θ is often negligible because many high-performance applications are for "straight and level" releases of the payload. After eliminating the gravity term, Eq. 5 21 can be written as

$$(m_b + m_a)\frac{dV}{dt} = -\frac{1}{2}\rho V^2 \cdot C_D S - V\frac{dm_a}{dt} \,. \tag{5.26}$$

Substituting Eq. 5.24 for the added mass in Eq. 5.26 yields this approximate expression for the deceleration of the payload:

$$-\frac{dV}{dt} = \frac{\frac{1}{2}\rho V^2\left[C_D S + 8k_a\pi r^2 \cdot \frac{1}{V}\frac{dr}{dt}\right]}{m_b + k_a \cdot \frac{4}{3}\pi\rho r^3} \,. \tag{5.27}$$

Equation 5.27 shows that there are two places where added mass terms affect the deceleration provided by the parachute. The time-dependent term in the numerator is always positive during inflation and, therefore, it increases the deceleration of the payload. Because the parachute radius r is increasing and the velocity V is decreasing during inflation, the increase in effective drag area due to the time-dependent added mass term is greatest just before reaching the maximum ("fully inflated" or "full-open") parachute diameter. Offsetting this increased contribution to deceleration is the amount of added mass itself, which is added to the payload mass in the denominator of Eq. 5.27. For large parachutes at low altitudes, this term can become significant. Its effect is to reduce the deceleration experienced by the payload.

Data obtained by Johnson and Peterson[3,6] in flight tests of their 46.3-ft-diameter parachute with a 2400-lb* payload (including parachute weight) can be used to assess the accuracy of the added mass approximation in predicting inflation loads and to show the magnitude of both added mass contributions to the prediction of payload deceleration. PDU-45 was a rocket-boosted parachute test at an altitude of 9285 ft above sea level. At deployment, the Mach number was 1.43, the velocity was 1574 ft/s, and the dynamic pressure was 2182 lb/ft^2. Line stretch occurred 0.32 s after deployment and canopy stretch occurred 0.40 s after deployment. The inflation time (from canopy stretch to full-open) was 1.88 s. At the time of full inflation of the 46.3-ft-diameter parachute, the velocity had decreased to 162 ft/s and the dynamic pressure had decreased to 23 lb/ft^2. The values of r and dr/dt at full inflation were determined from ground-based motion picture photography. Note that analytical values could be used instead of experimental data for r and dr/dt in order to estimate the magnitude of added mass effects. The steady-state drag area of this 46.3-ft-diameter canopy has been determined from many flight tests to be ~845 ft^2.

* To approximately simulate the store design weight of 2465 lb for these flight tests, 2400-lb vehicles were used.

Substituting these flight test data and other quantities into Eq. 5.27 gives an estimate of the magnitude of the deceleration ($-dV/dt$) of this parachute and payload when the parachute first reached its fully inflated diameter.

$$-\frac{dV}{dt} = \frac{23.0 \cdot (845 + 250)}{(2400 + 613)} = 8.4\,g\ . \tag{5.28}$$

At this altitude and for this size parachute, the added mass term in the denominator is one-fourth of the forebody mass; hence, *approximately 20% of the total deceleration provided by the parachute goes to accelerating the surrounding air rather than decelerating the payload.* However, the time-dependent increase in added mass (the second term in the numerator of Eq. 5.27) increases the effective drag area of the parachute by 30% over the terminal descent drag area. The net result of added mass effects is small at this altitude; added mass contributes an increase in deceleration of only 0.4 g from the value of 8.1 g that is predicted if both added mass terms were ignored in Eq. 5.27. Both predictions are higher than the measured decelerations at canopy full-open. Onboard accelerometers recorded 5 g and optical tracking data give 7 g. Equation 5.27 provides a conservative estimate of deceleration, which is appropriate for an approximate method that should be used during preliminary design.

It should be noted that the maximum measured deceleration during the test was 40 g at 0.58 s after the initiation of canopy inflation; hence, this parachute has already experienced its maximum deceleration by the time it reaches full inflation. This is consistent with Knacke's[18] observation of a significant increase in deceleration with increased altitude *only for parachutes that experience a significant decrease in velocity during their inflation.*

FTU-34 was an aircraft release at parachute deployment conditions of 5533 ft above sea level at Mach 0.51 and a dynamic pressure of 316 lb/ft^2. Line and canopy stretch occurred at 0.55 s and 0.67 s after deployment initiation, respectively, with the canopy full-open at 2.11 s; this results in an inflation time from canopy stretch of 1.44 s. As the parachute reached full inflation, the velocity was 140 ft/s and the dynamic pressure was 20.5 lb/ft^2. Using these data and motion picture photographic data for r and dr/dt, Eq. 5.27 gives

$$-\frac{dV}{dt} = \frac{20.5 \cdot (845 + 370)}{(2400 + 727)} = 8.0\,g\ . \tag{5.29}$$

The measured deceleration was 7.6 g from optical tracking and 6.0 g from an onboard accelerometer. Had added mass terms been ignored, the predicted deceleration would have been 7.2 g. Notice that the 46.3-ft-diameter parachute is accelerating 727 lb of air in addition to decelerating 2400 lb of payload and parachute; the added air mass is ~30% of the payload weight. For this reason, the effects of added mass should be included in any estimates of deceleration for this parachute, even though the increase in drag area due to the nonsteady added mass term in the numerator compensated for the large added mass in the denominator for this particular parachute and deployment condition.

Now consider the same parachute when deployed at a higher altitude. The parachute deployment conditions for FTU-23, an aircraft release at 27,349 ft altitude, were Mach 0.752 and a dynamic pressure of 285 lb/ft^2. Line and canopy stretch occurred at 0.55 s and 0.66 s after deployment initiation, respectively, with the canopy full-open at 1.74 s; this results in an inflation time from canopy stretch of 1.08 s. Payload/parachute system velocity was determined from cinetheodolite ground measurements. The velocity at full inflation of the canopy was 276 ft/s and the dynamic pressure was 37.7 lb/ft^2. Substituting the data at the time of full inflation into Eq. 5.27 yields

$$-\frac{dV}{dt} = \frac{37.7 \cdot (845 + 248)}{(2400 + 340)} = 15.0\,g\ . \tag{5.30}$$

As before, the predicted value of 15.0 g is higher than the measured decelerations of 10 g (from an onboard accelerometer) and 13 g (from optical tracking).

At 27,349 ft altitude, the added mass is less than half its magnitude at 5533 ft. However, the nonsteady added mass term also decreased from 370 ft^2 to 248 ft^2. If both added mass terms are ignored, the predicted deceleration would be only 13.3 g. The added mass terms in Eq. 5.27 increased the predicted deceleration by 13%. However, the most important conclusion to be drawn from examining both the flight data and the predictions from Eq. 5.27 is that the deceleration exerted by the same parachute deployed at the same dynamic pressure was approximately 70% higher at 27,000 ft than at 5500 ft. Some of this increase in deceleration with increased altitude is due to the differences in added mass effects.

The maximum measured deceleration recorded during FTU-23 was 20 g at 0.74 s after the initiation of canopy inflation. This parachute has already experienced its maximum deceleration and has slowed down to only 30% of its deployment velocity by the time it reaches full inflation. Since the 46.3-ft-diameter parachute experiences its maximum structural loads early in the inflation process (when the canopy is reefed), we conclude that added mass effects do not drive the structural design of this parachute. Because of the flight data available from tests of this parachute, it was used to illustrate the physics of the added mass approximation and to provide some feel for the accuracy of the approximation. Different parachutes operating at different deployment conditions may develop maximum structural loads as the canopy reaches full-open; for these parachutes, added mass effects may well have a direct bearing on the structural design of the parachute.

Equation 5.27 and its application to these three test cases reveal two important parachute design issues that should be taken into account when designing large high-performance parachutes for use at both low and high altitudes. Parachutes deployed at the same dynamic pressure will generate higher decelerations of the payload at high altitudes, where the added mass can be significantly lower than at low altitudes. Remember that higher deceleration means higher loads transmitted through suspension lines. Therefore, the design point for the parachute's structure is for the high-altitude release, not the low-altitude release. Also, be careful when parachutes designed for low altitude are given a new application at high altitude. Even if the deployment dynamic pressure at the high altitude is the same as at low altitude, the parachute will experience higher loads at the higher altitude. Differences in added mass effects are one reason why the loads increase with altitude. If the parachute's structural design margin was predicated on the low-altitude loads, the parachute might fail at the same dynamic pressure at higher altitudes. This can be a problem for large imporous parachutes with human payloads operating at high altitudes; even if the parachute survives, the loads imparted to the parachutist may be more than they can endure.

Waye and Johnson[5.29] used Eq. 5.27 to conclude that a cluster of three parachutes with the same terminal drag area of a single parachute should provide higher deceleration than the single parachute during the unsteady aerodynamic inflation phase because the cluster should have smaller added mass effects. The reduction in added mass effects was expected because added mass is a function of the cube of the parachute radius. Three parachutes having the same steady-state drag area as a single canopy should have $1/\sqrt{3}$ of the apparent mass of the single canopy. Their experiments showed that higher deceleration loads could indeed be achieved by the cluster, as long as special steps were taken to ensure simultaneous disreefing and inflation of all parachutes in the cluster.

Other overviews of added mass approaches for time-dependent parachute flows are given by Sarpkaya,[5.17] Sarpkaya and Isaacson,[5.30] and Cockrell.[5.31] These and other researchers acknowledge the limitations of the added mass approximation for unsteady motion of bodies immersed in real fluids. Cockrell, Frucht, and Harwood[5.23] concluded that added mass effects need not be considered in the equations of motion for parachute dynamic stability. Sarpkaya[5.17] disputes this conclusion. Cockrell[5.31] concludes that the added mass components are complex and "largely unnecessary to the successful development of both inflation and dynamic stability studies." Others recommend investing research effort in more advanced parachute flow-field and inflation models instead of investing in more experiments to determine added mass coefficients for the full spectrum of parachute shapes and motion associated with high-performance systems.

While parachute engineers await more accurate methods for predicting parachute inflation loads, they must be pragmatic in taking full advantage of available design tools. For large parachutes, the effects of added mass on the deceleration of the payload provided by the parachute can be significant and must be taken into account. The added mass approximation, as expressed by Eq. 5.21 or Eq. 5.27 and supported by the estimates of added mass constants discussed in this section, provides the parachute designer with a conservative estimate of inflation loads. It is therefore recommended for use in preliminary design studies. It will probably be necessary to use this approximation until parachute designers have access to proven semiempirical analyses or computational fluid mechanics techniques for solving the full turbulent-flow Navier-Stokes equations for the viscous, compressible flow field about an inflating, decelerating parachute. Semiempirical methods are coming soon, as described in the next sections. Affordable computational fluid dynamics parachute design tools may still be a decade away.

5.3.2 Canopy drag and filling time

Because maximum parachute structural loads almost always occur during inflation, and because performance and load predictions frequently require accurate inflation time predictions, the parachute designer must be able to predict parachute inflation time. Although parachute inflation predictions have been pursued for 40 years, there exists no *exact* analytical model or numerical

simulation to date. The complexity of the inflation process is the reason why no exact solutions exist. Parachute inflation is an unsteady viscous and compressible flow about a porous body with large shape changes; the structural dynamics theory must model a tension structure that undergoes large transient deformations; the materials are nonlinear with complex strain, strain rate, and hysteresis properties; and all of these physical phenomena are strongly connected.

Predictions of the transient drag of the inflating parachute and the canopy filling time have long relied on semiempirical approaches because of the complexity of the problem. Modeling has progressed from empirical filling time models to continuity inflation models, and is now moving to computer models that include calculations of the aerodynamics in and around the parachute. Excellent surveys of parachute inflation theories are given by Cockrell,[1.6] Wolf,[1.20] Roberts and Reddy,[5.32] and Purvis.[5.33] They discuss the simplifying assumptions, the approaches taken, the limitations, and the complexity of selected theories in the literature. The three parachute design manuals (Refs. 1.7, 1.8, and 2.1) provide good examples of commonly used empirical methods for predicting filling times and opening-shock loads. This section summarizes these methods and reviews more recent numerical approaches not yet available as design/prediction tools but which will become available in the future if research and computational advances continue to accelerate.

5.3.2.1 Maximum inflation force predictions

Knacke[1.8] recommends an empirical method for calculating the maximum parachute opening force F_A:

$$F_A = q_s \cdot C_D S \cdot C_x \cdot X_1 \quad , \tag{5.31}$$

where q_s is the dynamic pressure at line stretch and $C_D S$ is the drag area at the time when the maximum inflation load is expected. This equation is similar to the one written for steady-state drag, Eq. 4.1. The empirical parameter C_x, called the *opening load factor*, adjusts F_A for an additional force due to the inflation dynamics ("overinflation") of the parachute. Table 2.1 of Reference 1.7 presents values of C_x for a variety of unreefed parachute types operating under infinite mass inflation conditions; these values for high-performance parachutes range from a high of 1.8 for a solid flat canopy to a low of 1.0 for a hemisflo ribbon canopy. Since there is little drag overshoot for a reefed parachute, a value of C_x of 1.0 should be used for inflation to a reefed stage. The force reduction factor X_1 reduces F_A as a function of canopy loading $W/C_D S$, where W is payload weight. For infinite mass inflations, $X_1 = 1.0$. Figure 5.11 shows how X_1 varies as a function of canopy loading. Using these values of X_1 and C_x, one can then calculate the maximum opening drag force for a given parachute drag area and deployment dynamic pressure.

Equation 5.31 makes no attempt to include unsteady aerodynamics in the calculation of maximum drag; time does not appear explicitly in this equation. The premise of this expression is that maximum inflation force can be calculated if we know the drag area at the time that the maximum inflation force occurs. The effects of unsteady aerodynamics are included in the empirical data for C_x and X_1. As simple as Eq. 5.31 is, it works well for many subsonic parachutes. Chapter 12 gives comparisons of

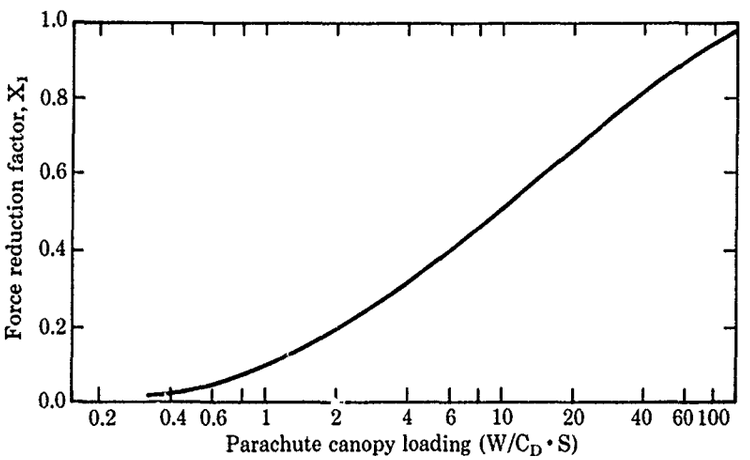


Figure 5.11. Opening-force reduction factor vs. canopy loading (taken from Ref. 1.8)

predictions using Eq. 5.31 with maximum inflation data from 24-, 40-, and 46.3-ft-diameter ribbon parachutes (Figures 12.6, 12.10, and 12.17, respectively). The good agreement encourages the use of Eq. 5.31 for preliminary design of parachutes for which empirical data are available.

5.3.2.2 Empirical methods for predicting filling time

French[5.34] extended the ideas of O'Hara[5.35] in proposing that a given parachute in incompressible flow should open in a fixed distance, regardless of the altitude or the velocity at which it was deployed. The inflation distance was expressed as n multiples of the canopy diameter D_o. The inflation time was calculated as the time needed to traverse that distance traveling at the deployment velocity V:

$$t_f = \frac{n \cdot D_o}{V} . \tag{5.32}$$

Experiments and analyses were conducted to evaluate and modify this postulated equation for parachute filling time t_f. Garrard[5.36] incorporates Knacke's filling time equation in a preliminary parachute design computer program. He tabulates values of n for a variety of parachute types. Greene[5.37] concluded, based on an approximate compressible flow analysis and NASA data, that the opening distance increased with Mach number. He presented a technique for predicting opening distance and inflation times for parachutes deployed supersonically, based on their subsonic performance. His method correlated well with flight data up to a Mach number of 3.2.

Heinrich[5.38] used the continuity equation (in conjunction with wind tunnel data on canopy size-time functions) and determined the mass captured by the canopy that causes the parachute to inflate. He developed equations for predicting filling times for solid-cloth, ribbon, and ringslot parachutes for the infinite mass case. These predicted filling times agreed well with the measured values. Further refinements on constant inflation distance models were contributed by Heinrich[5.39] and Lingard.[5.40]

After correlating data from flight tests, Knacke[1.8] modified Eq. 5.32 to provide a more accurate correlation of filling times for ribbon parachutes. His correlation is

$$t_f = \frac{8 \cdot D_o}{V_s^{0.9}} , \tag{5.33}$$

where D_o is the nominal parachute diameter and V_s is the velocity at line stretch. Note that Eq. 5.33 is dimensionally incorrect, requiring that values for D_o and V_s be in the same units used by Knacke in his correlation (ft, ft/s) for this equation to be applicable. The fact that a dimensionally incorrect equation provides better correlation with data than one that is dimensionally correct suggests that the correlation does not include a complete description of the true physics. Therefore, parachute designers should use such a correlation only if they have some data to justify its applicability to their own parachute and payload.

Inflation time flight test data from Maydew and Johnson[3.1] for a reefed, 22.2-ft-diameter parachute, Pepper[1.1] for a 24-ft-diameter parachute, Johnson and Peterson[3.6] for a 46.3-ft-diameter parachute, and Peterson et al.[1.2] for a 5-ft-diameter parachute are compared with Eq. 5.33 in Figures 5.12a, b, c, and d, respectively. The first three systems were flight-tested at low altitudes at deployment Mach numbers up to about 1.2. The maximum dynamic pressures at deployment were 2650, 2750, and 2400 lb/ft^2 for the 22.2-, 24-, and 46.3-ft-diameter parachutes, respectively. The 5-ft-diameter system was tested at low altitudes at deployment Mach numbers up to 2.22 (dynamic pressure of 5280 lb/ft^2).

Optical data indicated that the inflated diameter of the aft portion of the reefed, 22.2-ft-diameter ribbon parachute is consideral ly larger than the reefing line circle diameter; therefore, it was reasoned that an effective diameter based on drag area would be more representative for filling time calculations. The calculated effective diameter of the reefed, 22.2-ft-diameter parachute (see Ref. 3.1) was 14.3 ft. All of the measured filling times were determined from motion picture camera data; estimation of the time when the canopy is fully inflated is very subjective. Knacke's empirical method predicts the filling time fairly well for the reefed, 22.2-ft-diameter parachute (Figure 5.12a) and for the supersonic 5-ft-diameter parachute (Figure 5.12d).

There is considerable scatter in the filling time flight test data (a factor of 2 or greater) for the 24-ft-diameter parachute, Figure 5.12b. The nonrepeatable opening characteristics of this parachute may be due to the different "Venetian-blind" effects of low-stretch Kevlar ribbons (numbers 22 through 54) compared to the high-stretch nylon ribbons (numbers 1 through 21)—see Figures 12.2 and 12.4. These effects can increase the local effective canopy porosity during opening.

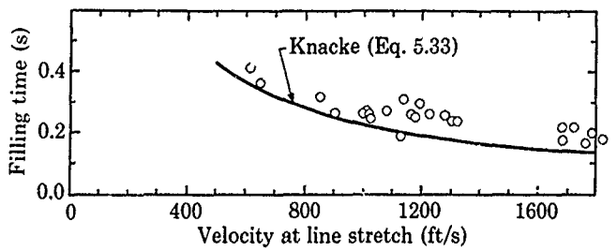


Figure 5.12a. Comparison of calculated and measured inflation times of reefed (19.5-ft line), 22.2-ft-diameter parachute

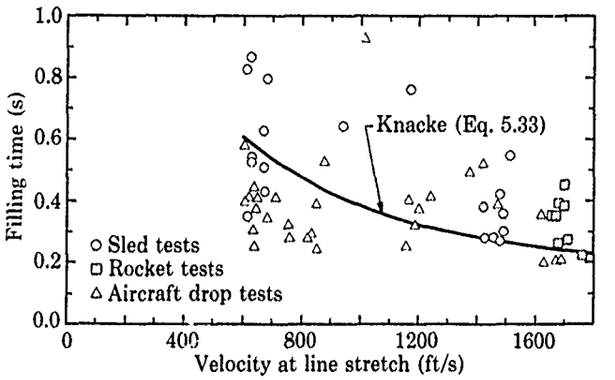


Figure 5.12b. Comparison of calculated and measured inflation times of 24-ft-diameter parachute

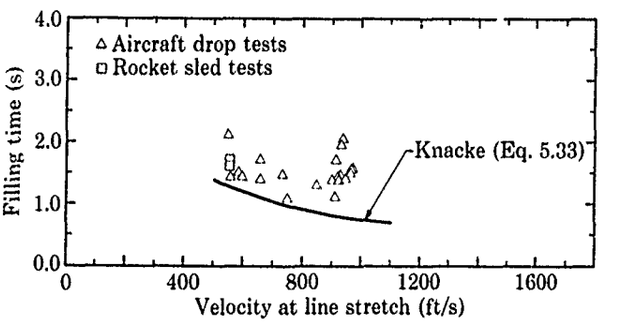


Figure 5.12c. Comparison of calculated and measured inflation times of 46.3-ft-diameter parachute

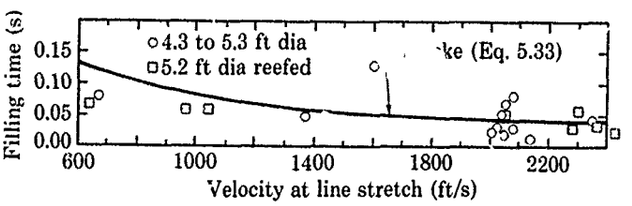


Figure 5.12d. Comparison of calculated and measured inflated times of ~5-ft-diameter ribbon parachutes

The 46.3-ft-diameter parachute was reefed for 0.85 s (from start of deployment) with a 23-ft-long reefing line to control inflation loads for high-speed deployment. An 89-ft-long permanent reefing line was used to control overinflation. The flight test data showed that the reefing line was cut before the parachute filled to the reefed condition for all parachute deployment speeds below 980 ft/s. Hence, the flight test data in Figure 5.12c represent the time for the parachute to inflate to the full-open diameter.

Knacke's empirical method predicts filling times about 50% lower than measured values for the 46.3-ft-diameter parachute. The geometric porosity is very high (21%) for a parachute of this size. The porosity was chosen to be as high as possible for a slow but repeatable opening, in order to minimize parachute collapse. Therefore, Knacke's empirical method should be expected to underestimate the filling time of the 46.3-ft-diameter parachute because the empirical data that defined the correlation of Eq. 5.33 did not account for such high porosity. We conclude that Knacke's empirical equation is an adequate approximation for calculating the filling time of parachutes whose inflation characteristics are similar to those used to derive Eq. 5.33. Designers are cautioned to use Eq. 5.33 with conservatism, however, because the consequences of overestimating inflation time are often the destruction of the parachute.

5.3.2.3 Semiempirical methods for predicting inflation loads and filling time

Semiempirical methods for predicting parachute inflation loads and filling time couple simplified equations of motion with limited empirical data with the intent to extend their range of applicability to a broader range of parachutes and deployment conditions than would be possible with purely empirical correlations. Successful semiempirical methods include those of Wilcox,[5.41] Jamison,[5.42] Ludtke,[5.43,5.44] Heinrich, Noreen, and Hedtke,[5.45] Heinrich and Saari,[5.26] Toni,[5.46] Heinrich,[5.18,5.39] Nerem and Pake,[5.47] Keck,[5.48] Sundberg,[5.4] Wolf,[5.27,5.28] and McVey and Wolf.[5.10]

Wilcox[5.41] developed his method specifically for application to heavy-duty ribbon parachutes. He used a momentum method for calculating opening time and transient drag. Solution of his equations required a priori knowledge of the initial diameter of the parachute at line stretch, K_1 (flow coefficient for sharp-edged orifices) and K_2 (ratio of velocity of air flowing into canopy relative to the canopy and the free-stream velocity). He showed good agreement of calculated filling times and transient drag with flight test data for the high subsonic speed, low-altitude deployment of 16-, 24-, and 28-ft-diameter ribbon parachutes. He also developed a fairly accurate method of calculating snatch loads for these heavy-duty ribbon canopies. However, Wilcox's method has not been used extensively because of the uncertainty in predicting the magnitude of the "K" terms.

Jamison[5.42] solved the ordinary differential equations of motion for the parachute-payload trajectory in conjunction with algebraic descriptions of the canopy behavior during inflation. He used the conservation of mass equation to determine the mouth diameter, D_m, and the volume of the truncated cone and hemisphere assumed for the parachute shape. He assumed a cubic relationship of the projected diameter of the parachute with time. Closure of his set of equations was obtained by assuming that the velocity at the end of inflation is 30% higher than terminal velocity.

Ludtke[5.43,5.44] used wind tunnel data to specify parachute diameter as a function of time in his method for calculating opening forces of solid-canopy parachutes. Heinrich, Noreen, and Hedtke[5.45] measured inflation histories of ringslot parachutes in a wind tunnel to provide input on inflation dynamics to the equations of motion. Heinrich and Saari[5.26] used data from a flat circular parachute to obtain the area-time history and inflow function needed as inputs to their calculation of inflation forces.

Toni[5.46] assumed that the canopy shape is hemispherical and used the conservation of mass in the canopy to determine the radius as a function of time during inflation. Heinrich[5.18,5.39] also based his inflation model on the mass equation in the canopy. As noted earlier, Heinrich included added mass effects in his model. Following Toni's approach, Nerem and Pake[5.47] employed the conservation of mass equation in an analysis wherein the parachute is allowed to alter its shape (in a specified manner) during inflation.

Keck[5.48] and Sundberg[5.4] modeled the parachute suspension lines and canopy as a collection of point masses connected elastically. They calculated the motion of each mass in response to the inertial, tension, gravitational, and aerodynamic forces acting on it. Aerodynamic forces were input to the computer code as either empirical data or as an analytical function for canopy differential pressure distribution. Computational results depend strongly upon the pressure distribution used to approximate the aerodynamic forces acting on the inflating parachute.

The inflation model of Wolf[5.27,5.28] and McVey and Wolf[5.10] is a significant advance beyond inflation models that rely on either prescribed parachute diameter as a function of time or on the conservation of mass in the canopy. These authors were the first to solve equations for the axial and radial momentum of the parachute in addition to the equations of motion of the system along its flight path. Wolf[5.28] used a single radial degree of freedom, which restricted the inflation model to unreefed parachutes. McVey and Wolf[5.10] included additional degrees of freedom, which allowed the modeling of reefed configurations and elastic modes. The parachute canopy is modeled as two lumped masses—one at the skirt and the other at the parachute canopy's maximum radius. The equations for the tangential and radial momentum are solved to obtain the motion of the parachute lumped masses. McVey and Wolf introduced an empirical radial force coefficient, C_R, that is proportional to the axial coefficient, C_A, and varies with canopy porosity. Wolf[5.27] included the effect of unsteady fluid dynamic coupling between the radial and axial degrees of freedom in his model; this coupling effect becomes important when the ratio of parachute apparent mass to payload mass approaches unity. The computerized implementation of this model was called INFLAT by these authors.

References 5.10, 5.27, and 5.28 show that INFLAT-predicted filling times and transient loads agree well with flight test data for ribbon and other porous high-performance parachutes. INFLAT is superior to its predecessors in terms of its physical modeling and its applicability to a variety of parachute types. It is limited in accuracy primarily by the values of C_R/C_A used in the empiricism. Experience with INFLAT at Sandia has shown that C_R/C_A plays a major role in determining canopy inflation times and drag. The reliability and accuracy of INFLAT predictions depend on the degree to which the empirical formulation of C_R/C_A in the code simulates the C_R/C_A of the parachute being designed. In an actual inflation of a real parachute, C_R/C_A depends on several design parameters that can be defined by the parachute engineer; these include such parameters as the distribution of porosity in the canopy, the reefing schedule, and the type of parachute. Unfortunately, C_R/C_A is not always known with sufficient accuracy for a specific parachute before it is designed. In addition, the code output is sensitive to several input parameters, such as initial diameter of the parachute at line stretch (at the start of inflation) and the magnitude of added mass coefficients. Hence, it can be used only by an experienced parachute designer, one who is very familiar with the code. INFLAT is currently used at Sandia only by its author.

Despite these limitations, INFLAT has set the standard for parachute inflation prediction tools. While it is evident that computational fluid dynamic models of parachute inflation will someday become the basis for predicting parachute performance and establishing parachute design, it will be years before CFD (computational fluid dynamics) simulations will be available to design a real parachute. In the meantime, parachute designers need an INFLAT-type parachute inflation model. Efforts to extend INFLAT or to develop a similar inflation model based on the equations for the momentum of the parachute should receive top priority within the parachute community. The goals of this research should be to seek the level of empiricism needed to:

- Avoid making extensive fluid dynamic calculations to describe the parachute inflation process. If calculations are too time-consuming or expensive, the resulting computational method will not be used as a design tool.
- Reduce the sensitivity of the accuracy of predictions to the particular empiricism used.
- Make the empiricism applicable to a broad range of parachute types and use scenarios.
- Make the cost of obtaining empirical data affordable (much less than the cost of performing fluid dynamic calculations). If obtaining sufficient empirical data is too expensive, the money might better be used to develop CFD simulations that contain more inflation physics and less empiricism.

What should be used for today's parachute design assignment? The parachute engineer should not waste time trying to use semiempirical methods based on conservation of mass or specific parachute-diameter-vs.-time correlations. The simpler empirical models such as Knacke's[1.8] or Garrard's[5.36] provide nearly the same physical insight and accuracy for much less effort. Their use, however, is encouraged only after the designer feels assured that the empiricism inherent in these approaches is applicable to the parachute being designed.

5.3.2.4 Computational fluid dynamics inflation models

Numerical methods and computational hardware have matured to the point where it is feasible to solve more of the fluid dynamics of parachute inflation directly on a computer and to rely less on empiricism to describe the inflation process. Such an approach was not realistic ten years ago. Even today, numerical simulations of parachute inflation should not be construed as being ready for use to design actual parachute systems. The more recent models discussed in this section are research

studies, not design tools. They are "computational experiments" to determine which numerical and fluid dynamic approximations to the full equations of motion have the potential to become the parachute design tools of the future. Parachute designers should be apprised that these CFD inflation models still contain approximations to the real physics of inflation; they are not "exact," even though no empirical data are incorporated in their models. The approximations in CFD simulations are in the choice of the equations used to describe the fluid motion, in the description of the canopy (its dimensionality and degrees of freedom), and in the numerical methods used to solve the equations. This section reviews the inflation models, the approximations in those models, and their strengths and weaknesses as future parachute design tools.

The first attempts at computing the fluid mechanics of parachute inflation focused on determining analytical expressions of the canopy pressure distributions that drive the inflation process. This is a logical extension of the approaches in the previous section, which used empirical data or presumed pressure distributions as the forcing functions for parachute inflation. Having constructed relatively sophisticated computer models of the parachute structure, researchers found that they did not have enough computational memory or power to solve the viscous, compressible equations for the airflow in and around the parachute canopy. Therefore, they sought analytical methods for calculating parachute pressure distributions in unsteady flow.

Eldred and Mikulas[5.49] suggested the use of one-dimensional piston theory as a simple means for estimating canopy pressure distributions. Others turned to inviscid vortex methods similar to those used for parachutes in steady flow (Chapter 4). Roberts[5.50] derived the stress-displacement equations for the canopy and lines and commented on the form of the unsteady pressure distribution on the inflating canopy. He then speculated on how the pressure equations might be solved with the stress-displacement equations. Roberts[5.51] next derived the unsteady pressure distribution on a decelerating, inflating parabolic shell of revolution in the presence of an unsteady starting vortex flow. The unsteady pressure distribution could then be used with the parachute structural constraints to calculate opening loads and opening times. In each of these papers, Roberts used conformal mapping techniques to determine the canopy differential pressures. This mathematical approach limited his modeling to two-dimensional flow and simple canopy shapes (a parabola was used in Refs. 5.50 and 5.51).

Reddy[5.52] considered the analogy to a two-dimensional unsteady flow past an inflating decelerating wedge; he developed an equation that related the rate of opening with the strength of a vortex sheet on the wedge. The solution gives the transient pressure distribution across the wedge surface. Reddy and Roberts[5.53] examined the time history of the inflation of a two-dimensional canopy by modeling the canopy as a series of hinged plates. They assumed a finite wake flow and a vortex sheet buried in the canopy. They solved the resulting set of differential equations to calculate the inflation history of the canopy.

Klimas[5.54] developed a method of calculating inflating parachute canopy differential pressures based on his steady flow model of a parachute.[4.54] For the unsteady problem, the time-dependent Bernoulli equation was used in conjunction with a vortex sheet mathematical representation of the canopy. This method compared favorably with differential pressures measured in a wind tunnel on inflating 3-ft-diameter ribbon and solid-canopy models.

As computational capabilities increased, concurrent solution of the equations of motion for the parachute with the equations of motion for the flow was considered. Purvis[5.33] coupled solutions of the ballistic equations of motion for the canopy, payload, and suspension line masses to the solution of unsteady fluid conservation equations for a deforming, accelerating control volume to determine the behavior of the captured fluid and its interaction with the canopy. He included only first-order effects, and the analysis was limited to inviscid, incompressible flow of only the air entering the canopy. The canopy shape was simplified to represent a cylinder whose height-to-diameter ratio decreased as more air "inflated" the cylinder. This was the first time that the dynamics equations for the parachute system and the conservation equations for the enclosed fluid had been solved simultaneously. Comparison of this method with flight data for a 46.3-ft-diameter parachute showed reasonable prediction of inflation times and inflation radius histories. The value of this work is not in its predictive capabilities, however, but in showing that this approach holds promise as a basis for developing future parachute inflation prediction tools.

Purvis[5.55] extended this theory by combining the same fluid conservation approach with the equations of motion for a discrete element representation of the canopy, suspension lines, payload, and deployment bag/pilot parachute. The discrete element model is the same as the one developed by Purvis[5.2] for predicting parachute line sail. As in his earlier work,[5.33] Purvis considered only the air flowing into the canopy; the air flowing around and behind the canopy was not considered.

Computations began at deployment initiation, continued through canopy stretch, and predicted the canopy shape and drag throughout inflation. Purvis' results showed good qualitative agreement with observations of parachute inflation. They also proved that quantitative agreement could not be achieved until calculations of the entire flow field (around and behind the canopy in addition to the flow into the canopy) were included in the inflation model.

With the realization that computations of the entire flow field in and around the parachute are needed for accurate predictions of canopy pressure distributions and inflation parameters, more recent development of vortex models has concentrated on methods for simulating the wake behind the parachute. Meyer and Purvis[5.56] developed a vortex lattice theory for predicting the unsteady, viscous, incompressible flow about bluff, parachute-like bodies. Since all vortex panel and vortex lattice methods are inviscid, some approximate method must be introduced for simulating the boundary layer on the canopy. This is necessary to model the generation of free vorticity which, in this work, is convected and diffused within the boundary layer and passes into the wake. Meyer and Purvis[5.56] applied their model to the time-dependent flow over a cylinder started impulsively from rest. They calculated the pressure distribution over a circular cylinder and described how to extend this method to parachute shapes. Purvis lectured on these methods at the 1985 Helmut G. Heinrich University of Minnesota Short Course on Decelerator Systems Engineering.[1.21]

McCoy and Werme,[5.57] Strickland,[5.58] Sarpkaya,[5.59] Sarpkaya and Lindsey,[5.60] and Frucht and Cockrell[5.61] have also constructed two-dimensional vortex models that describe the unsteady flow about various representations of a parachute canopy. Each model has its own approximations for modeling the canopy surface, satisfying the flow boundary conditions at the surface, and initiating the vorticity shed into the wake behind the canopy. Shirayama and Kuwahara[5.62] have developed a "vortex stick" method to simulate a three-dimensional wake behind circular disks and parts of a sphere impulsively started from rest. Strickland[5.63] and Sarpkaya[5.17] have reviewed these vortex methods, whose predictions have been compared with data from controlled experiments by Higuchi and Park,[5.64] Sarpkaya,[5.65] Higuchi,[5.66] and Oler, Lawrence, and Adamson.[5.67] Belotserkovskii et al.[5.68] use vortex methods to model both cup-shaped parachute canopies and gliding parachutes. Some of their calculations model the payload as well as the parachute. Note that all of these computational models presume the shape of the canopy and assume that it is constant during the time span of the unsteady fluid calculation. To date, only Purvis[5.33,5.55] has attempted to include the change of canopy shape as part of the fluid dynamic calculation.

Vortex methods show promise for predicting the unsteady pressure distribution around an inflating, decelerating parachute, as long as they include sufficiently accurate methods for determining where vortices are shed from the canopy during inflation. Viscous dissipation of the shed vortices is not taken into account in these inviscid computations, but viscous dissipation is not important in the short period of time during which the vortices are created and move well downstream of the parachute canopy. Computations of pressure distributions over the canopy using vortex panel methods should be accurate even though viscous dissipation is ignored.

To minimize errors associated by representing the canopy by a finite number of discrete vortices, many vortices must be included in the computation. However, the time and expense of the computation increase as the square of the number of vortex elements. Today's computations involve thousands of vortices in the flow field. Researchers are beginning to observe that the cost of such computations may not be substantially less than flow-field solutions of the viscous Navier-Stokes equations, which hold the promise of being able to calculate where vortices are shed from the canopy without requiring the approximations made in inviscid computational methods. Although other disciplines in aerodynamics and fluid mechanics have been using computational Navier-Stokes methods for years, the parachute community is just beginning to develop Navier-Stokes solutions for parachute-like bluff body shapes.

The nonsteady Navier-Stokes equations consist of separate nonlinear, coupled equations for the conservation of mass, momentum, and energy. They are written in many different forms, depending on the coordinate system and the particular class of flow problems to be solved. Approximations to the full Navier-Stokes equations can be made to recover only the essential fluid physics for restricted classes of problems; "Parabolized" and "Thin Layer" Navier-Stokes equations are examples of approximations to the full Navier-Stokes equations that are valid for special classes of flows. Additional approximations are made in the discrete numerical representation of the set of Navier-Stokes equations chosen for the flow problems. This is true even for the full set of Navier-Stokes equations, which contain no fluid dynamic assumptions beyond those associated with treating the airflow as a continuum of molecules and describing the nature of the viscous interaction of the molecules in a continuum sense. Further approximations are made in the representation of the body around which the flow field is to be calculated. Each of these approximations are necessary in order

to describe nature's continuum of geometric and flow changes on a computer that has finite limits on memory and operates in a discrete, digital mode. Hence, the parachute designer must realize that even Navier-Stokes solutions of an inflating parachute will be approximate and will therefore require careful evaluation before computed characteristics can be trusted to design a parachute.

Steeves[5 69,5.70] was the first to attempt Navier-Stokes calculations for the parachute problem, using the SALE code developed at Los Alamos National Laboratory. The time-dependent, two-dimensional Navier-Stokes equations are solved using a finite difference algorithm. He couples the motion of a free-falling decelerator to the fluid dynamics algorithm. He has studied a flat circular disk, a hemispherical shell, and a flat circular canopy in steady flow. Stein[5.71] has extended this work to include cylinders and an annular canopy.

Using a combination of commercially available grid generation packages and graphics postprocessors, Barnette[5.72] obtained a solution of the steady flow around a hemispherical cup using the F3D Navier-Stokes code originally developed by the NASA-Ames Research Center and further refined at Sandia National Laboratories. His work stresses that much must be learned about the effects of computational approximations and techniques used to perform Navier-Stokes calculations for parachutes, in addition to what must be learned about the fluid dynamics. However, his work also shows that computations of this kind will not be limited to those organizations with large computational fluid dynamics staffs and access to very expensive computers. With the continuing advancements in mainframe computer capabilities (more storage and faster computations), Navier-Stokes calculations of parachute inflation will undoubtedly become the parachute engineering design tools for future high-performance parachute designs. Development of Navier-Stokes methods for predicting parachute inflation must be given high priority by the parachute technical community.

As advanced computational techniques are improved and engineers are able to calculate the unsteady flow around an inflating parachute in greater detail, the parachute community will require extensive experimental data at all Reynolds numbers in order to validate and calibrate the codes. The development of a well-planned experimental program to guide modeling is lagging behind the numerical development work and must be accelerated in order to provide full benefit to code developers.

5.3.2.5 Wind tunnel test data on inflation and canopy aerodynamics

Wind tunnel measurements of canopy pressure distribution, parachute drag, and canopy shape during canopy filling are difficult to obtain and are therefore not generally available in the open literature. Some data are considered proprietary and are not reported. Other data apply to parachute geometries and/or test conditions that are not fully described, thereby limiting the value of the data. This section reviews data that are well documented with respect to the geometries and conditions under which they were obtained. Even though all wind tunnel data apply to the "infinite mass" condition, where deceleration of the payload during inflation is not taken into account, these data are nevertheless useful as design information and can be used to benchmark numerical inflation prediction codes as well.

Melzig and Schmidt[4 61] measured the external and internal pressure distributions over the canopy surface and the canopy shape during the inflation of 62-in.-diameter solid and extended skirt models and 53.5-in.-diameter ringslot and flat ribbon models in a 9-ft by 12-ft low-speed wind tunnel. The result is an excellent data base of transient flow measurements for the parachute/wind tunnel infinite mass operating case.

Heinrich and Noreen[5 73] tested a 3-ft-diameter model of a 28-ft-diameter standard, flat circular parachute at snatch velocities of 50, 70, and 85 ft/s, and measured the nonsteady drag and the canopy shape (and volume) as a function of time. They compared these measured nonsteady drag values with calculated values from their analysis of parachute opening dynamics under infinite mass conditions. The measured values agreed fairly well with the predicted values.

Sandia conducted a series of tests in the LTV 7-ft by 10-ft Low-Speed Wind Tunnel (Holbrook[4.65]) and in the Naval Ship Research and Development Center's 7-ft by 10-ft Transonic Wind Tunnel (Ottensoser[4.67]) to measure transient drag and canopy pressure distribution before and after disreefing a model 3-ft-diameter, 20-degree conical ribbon parachute in the wind tunnel. The transient drag measurements were made on parachute models with geometric porosities of 0%, 10%, 15%, 20%, 25%, 30%, and 40% with suspension line lengths of 1.0, 1.5, and 2.0 constructed diameters. Reefing line lengths of 19, 38, and 57 in. were tested. Transient drag measurements were made with a one-component strain gauge force balance while the canopy was filling after being disreefed in the wind tunnel. The strain gauge balance was located in the cable-supported ogive-cylinder model. The tests were conducted at wind tunnel dynamic pressures of 35 to 600 lb/ft^2. The model parachutes were constructed of 24 gores. The transient shape of the canopy during filling (after disreefing) was

measured with a 70mm motion picture camera. These transient drag and canopy shape measurements are documented by Ottensoser.

Transient canopy pressure distribution tests were made only with the 3-ft-diameter, 25% porosity canopy model and a suspension line length of 1.0 constructed diameter. These pressure tests were made at dynamic pressures of 35, 75, and 100 lb/ft^2 in the LTV Low-Speed Wind Tunnel. The pressures were measured with seven Kulite differential pressure transducers (ranging from −1 to +3 lb/ft^2 gauge) sewn to the inside of the canopy at seven radial stations. Transient pressures were measured during canopy inflation after disreefing from these three initial reefed conditions. The transient drag was also measured with a strain gauge balance. As before, the shape of the canopy was determined from 70mm motion picture camera photographs. Pepper and Reed[4.7] give an example of these canopy pressure distributions during filling. Heinrich[5.74] analyzed these data and calculated drag areas and radial-force coefficients from the transient pressures. The calculated drag from the pressure data agreed well with the transient drag measured with the strain gauge balance.

Klimas[5.75] extended the canopy pressure data base into the compressible regime by testing 3-ft-diameter parachutes of 0%, 12%, and 25% porosity in the Calspan 8-ft by 8-ft Transonic Wind Tunnel at Mach numbers 0.3, 0.6, 0.9, and 1.2. The three nylon parachute models had 3-ft-long suspension lines. One was a solid flat canopy and the other two were 20-degree conical ribbon canopies. Six Kulite differential pressure transducers were sewn to the inner radials at equal intervals; they were evenly distributed circumferentially. An electrically actuated cutter was used to sever the 9-in.-long reefing line, and the output of the transducers was subsequently recorded on magnetic tape. Klimas' pressure coefficient data and the calculated drag coefficients show a nearly linear decrease with Mach number.

Wind tunnel test data of parachute inflation is useful because of the control that can be exercised over the experiment and because more detailed measurements can be made in the wind tunnel than can usually be made in flight. Additional wind tunnel test data are needed to assist in developing inflation models. Macha[5.76] reviews modern methods for conducting tests of parachutes in wind tunnels.

5.3.2.6 Flight test data

Three references on personnel parachute flight test data are included because they shed some light on the phenomena of the transient filling process. These references are Melzig (Ref. 1.9, p. 100), Berndt and Deweese (Ref. 1.9, p. 17), and Heinrich and Saari.[5.26] Heinrich and Saari's work was reviewed in Section 5.3.1. Melzig[1.9] measured the pressure distribution during the opening of 28-ft-diameter circular flat and hemispherical parachutes at low altitudes at deployment speeds of 110 knots. He used four differential pressure transducers equally spaced from vent to skirt for these measurements. The side profile of the inflating parachutes during these 18 drop tests was photographed with a 35mm (100 frames per second) ground camera. Melzig provides a good description of the dynamic process of solid-cloth parachute filling based on these flight test data.

Berndt and Deweese[1.9] conducted 60 flight tests of 28-ft-diameter, Type C-9 flat circular parachutes and 35-ft-diameter, Type T-10 extended skirt parachutes at deployment velocities of 150 to 355 ft/s at altitudes of near sea level, 6000 ft, 13,000 ft, and 21,000 ft. The canopy shape during filling was photographed. Their analysis of the data showed that the developing shape of both canopies could be described by relatively simple geometric shapes. They developed a simplified filling time analysis and compared their empirical predictions with the flight test data for the two parachutes, showing good correlation. This is an excellent data base for filling time of personnel parachutes.

Holt[4.45] conducted 21 drop tests of a 76-ft-diameter, 20-degree conical ribbon parachute with test vehicles weighing from 20,000 to 45,000 lb at release altitudes of 25,000 to 45,000 ft at deployment velocities of 660 to 780 ft/s (dynamic pressures of 125 to 275 lb/ft^2). Two reefing stages limited the opening-shock design loads to 150,000 lb. Most of the tests were conducted with first-stage reefing line lengths of 35 to 45 ft (with a 4-s time delay) and second-stage reefing line lengths of 75 to 85 ft (with a 10-s time delay). A 5-ft-diameter guide surface pilot parachute and an 18-ft-diameter ribbon extraction parachute were used to deploy the main canopy. This parachute system weighed ~900 lb with a packed volume of ~25 ft^3. The test vehicles were tracked with Contraves phototheodolite ground cameras for trajectory data, and onboard accelerometer data were telemetered to ground stations to measure the drag. Onboard free gyros were used to measure the oscillation of the vehicle. Holt presents data on the opening times of all three stages as well as the times to the occurrence of maximum load for all three stages. In addition, he tabulated the snatch loads, the maximum drag loads, and the final drag area for all three stages. The maximum measured drag load was 148,000 lb.

This parachute-payload system was quite stable, with oscillations of less than ±3 degrees reefed and less than ±6 degrees full-open.

Pepper[3.4] conducted three rocket-boosted supersonic (about Mach 2.3) low-altitude tests of a 20-ft-diameter, heavy-duty, reefed, conical ribbon parachute with an 890-lb test vehicle at deployment dynamic pressures of 4700 to 5700 lb/ft^2. The reefing time delay for the 12-ft-long reefing line was 2 s. Trajectory data were obtained from ground cinetheodolites, and the parachute drag data were obtained with onboard accelerometer data telemetered to the ground station. The maximum deceleration measured (during the reefed stage) was about 200 g, or 178,000 lb. This was the maximum drag load measured for a parachute at that time, at least to the authors' knowledge. The first-stage filling times were less than 0.1 s. Pepper presents deceleration and drag area versus time for these flights.

Maydew and Johnson[3.1] conducted 29 aircraft drop and rocket-boosted flight tests of a 22.2-ft-diameter, reefed (the 15.5- or 19.3-ft long reefing line was cut after 0.5 s), conical ribbon parachute with a 2100-lb test vehicle at deployment dynamic pressures of ~400 to 2700 lb/ft^2. Trajectory data were obtained with ground cinetheodolites, and the parachute drag data were measured with onboard accelerometers and telemetered to a ground station. Motion picture cameras (200 and 1000 frames per second) onboard the test vehicle were used to photograph the parachute deployment and filling. Four ground station tracking telescopes with 35mm and 70mm cameras documented the inflations and event times. The maximum measured drag (first-stage opening shock) was about 165,000 lb. They present the time sequences from deployment to second-peak load and the drag loading on the vehicle at line stretch, at first-peak load, at disreefing, and at second-peak load for the 29 tests. They also tabulate the Mach number, velocity, and dynamic pressure for each of these transient parachute filling conditions. A typical vehicle deceleration is presented. Reefed and full-open drag areas were determined from these flight data.

Pepper[1.1,4.13] conducted 31 aircraft drop tests, 11 rocket-boosted tests, and 28 sled-launched free-flight tests of a 24-ft-diameter Kevlar/nylon conical ribbon parachute with a 760-lb test vehicle at deployment dynamic pressures of 310 to 2700 lb/ft^2 (up to Mach 1.6). The onboard and ground-based cameras and other instrumentation were similar to those used by Maydew and Johnson.[3.1] The top 21 horizontal ribbons of this 24-ft-diameter parachute were nylon, whereas the lower 33 horizontal ribbons and the suspension lines were Kevlar. An opening-shock deceleration load of ~240 g was measured on two rocket-boosted tests; this is believed to be a record for a parachute decelerator. Pepper tabulates the deployment time, filling time, deployment dynamic pressure, and opening-shock load for each test. He also presents plots of typical deceleration versus time, and parachute inflated area versus time.

Johnson and Peterson[3.6] conducted 23 aircraft drop tests, 4 rocket-boosted tests, and 8 sled-launched free-flight tests of a reefed 46.3-ft-diameter conical ribbon parachute with a 2465-lb test vehicle at deployment dynamic pressures of 300 to 2400 lb/ft^2 (up to Mach 1.48). The onboard and ground cameras and instrumentation were similar to those described by Maydew and Johnson.[3.1] They measured a maximum opening-shock drag load of about 165,000 lb. They tabulated the deployment conditions (Mach, velocity, altitude, and dynamic pressure), the maximum deceleration, and the inflation time for each test. They also plot a sample deceleration versus time, and canopy and skirt diameter versus time during and after canopy filling.

Peterson et al.[1.2] conducted 19 rocket-boosted tests of 4- to 5-ft-diameter hemisflo, biconical, and 20-degree conical ribbon parachutes with an 800-lb test vehicle at deployment dynamic pressures of ~400 to 4500 lb/ft^2 (Mach numbers up to 2.12). The onboard and ground cameras and instrumentation were similar to those described by Maydew and Johnson.[3.1] They tabulated the deployment conditions (Mach and dynamic pressure) and the maximum vehicle deceleration or parachute drag. They also present plots of effective drag area versus Mach number during the inflation and transient deceleration process for the five parachute configurations. These tests showed that the 20-degree conical parachute with 9-ft-long suspension lines best satisfied the drag and stability design criteria.

Analysis of flight test parachute drag and filling time data for high-performance parachutes should provide the designer with some insight into the design compromises required to design, fabricate, and flight-test-prove a new high-performance system successfully. Flight tests are very expensive; therefore, organizations that conduct or sponsor flight tests should emphasize the importance of analyzing and documenting *all* data from the tests. Unfortunately, potentially valuable data are not obtained from flight tests because sponsors may be unwilling or unable to pay for anything beyond the most basic understanding of how the parachute system performed. The parachute community must educate themselves and the sponsors of flight tests so that full advantage may be taken of the knowledge that can be derived from flight tests of high-performance parachutes.

5.3.3 Wake-induced canopy distortion or collapse

In late 1979, Sandia encountered wake-induced canopy collapse in flight tests of a 40-ft-diameter, 20-degree conical ribbon parachute with a 2465-lb payload. Severe canopy collapse occurred shortly after full inflation of the parachutes during transonic, low-altitude releases of the payload from an A-7C aircraft at Tonopah Test Range (TTR). A rocket-boosted parachute test was conducted in December 1979 at a deployment dynamic pressure of 1530 lb/ft^2; again, the 40-ft-diameter parachute collapsed and then reinflated. In January 1980, a low-deployment dynamic pressure (302 lb/ft^2) free-flight test was conducted at the Sandia Rocket Sled Track with similar results.

The photographs in Figure 5.13 illustrate the severity of the 40-ft-diameter parachute collapse; they were taken at TTR with ground documentary motion picture cameras during the November 1979 A-7C aircraft drop test. The test vehicle was released from the A-7C at 514 KCAS (knots calibrated airspeed) and 2051 ft above ground level. The 88-ribbon, 40-ft-diameter parachute with a 23-ft-long reefing line developed a peak load of 32 g, as predicted, and inflated from canopy stretch to full-open diameter in 0.98 s. Shortly after reaching its full-open diameter, however, the canopy experienced major collapse, as illustrated in the sequential photos shown in Figure 5.13. Opposite sides of the canopy skirt were almost touching, and there was risk that the suspension lines or cut knife lanyards could become entangled. Motion pictures revealed that the parachute recovered from the collapse and eventually reinflated.

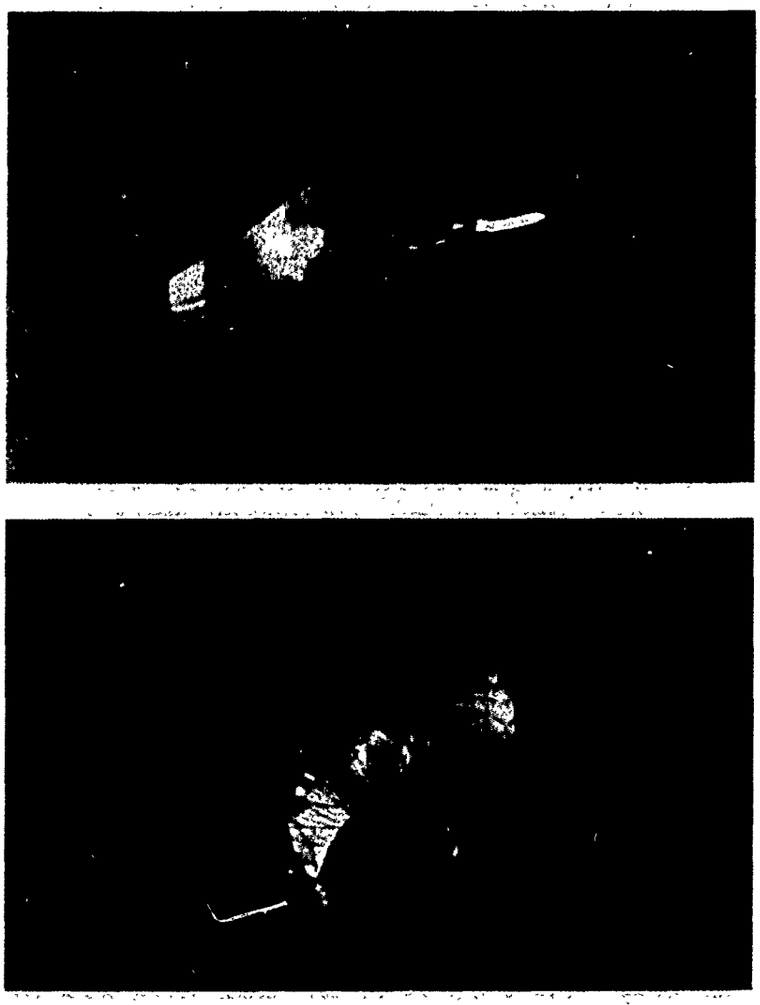


Figure 5.13. Postinflation canopy collapse of the 40-ft-diameter main parachute

Review of the documentary film of the four flight tests showed that parachute collapse occurred over the entire deployment Mach number range of interest for low-altitude delivery of payloads. The magnitude and duration of parachute collapse were severe enough to alter parachute performance dramatically. Collapse occurred while the payload was at a relatively low velocity, but still significantly above the desired impact velocity of 70 ft/s. Since collapse occurred at relatively low dynamic pressures, parachute reinflation occurred slowly; the typical duration of the collapse was several seconds. During this time, the deceleration history of the payload changed significantly. In some tests the payload maintained an almost constant velocity during the collapse, whereas in other tests the velocity increased during the collapse. These data showed that the extent of the collapse and the time to recover were somewhat random; the drag area during the collapse phase was different for every test.

These four flight tests, over a wide range of dynamic pressures, left no doubt that collapse was a serious design problem. The design specifications for this system were very stringent. The parachute system was required to decelerate the 2465-lb payload from an altitude of 150 ft at aircraft release velocities from 300 to 800 KCAS to a velocity of 65 ft/s (at sea level) or 70 ft/s (at 5000 ft mean sea level) at ground impact. These specifications could not be met with this 40-ft parachute if any appreciable drag was lost due to parachute collapse during the 3 s between parachute deployment and ground impact.

Deceleration of a 2465-lb payload from a velocity of 800 knots to a velocity of 70 ft/s at low altitude in 2 or 3 s involves the transfer of a large amount of kinetic energy from the payload to the air around it. The air is accelerated in the direction of the payload motion and has a tendency to overtake the parachute at the end of the deceleration process. If the initial kinetic energy of the payload is large and the deceleration is very rapid, the wake behind the parachute may overrun or recontact the parachute and cause it to collapse. This is shown schematically in Figures 5.14a, b, and c.

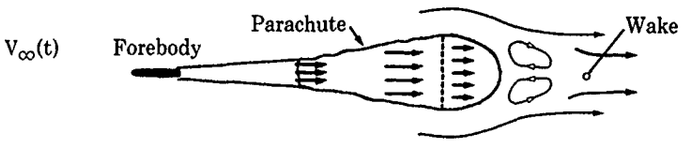
Sandia immediately initiated an extensive analytical and flight test program in an effort to understand the collapse phenomena and develop a new design whose performance was not compromised by postinflation wake recontact. Spahr and Wolf[5.77] verified analytically that the parachute wake could overrun the parachute. They did so by adding an approximate unsteady wake model to the parachute inflation code INFLAT. The wake was represented by creating "slugs" of air whose momentum corresponded to the momentum extracted from the payload by the parachute during a short time interval during inflation. Each slug moved along the flight path at a velocity dictated by its momentum. The location of the slugs was tracked by the computer program, which also tracked the decelerating parachute and payload. Their computed slug trajectories showed that the wake behind the 40-ft-diameter parachute could indeed catch up to the parachute and cause it to collapse. INFLAT predictions of velocity, canopy diameter, and deceleration versus time for the flight test shown in Figure 5.13 are compared with the flight test data in Figures 5.15a, b, and c, respectively.

Parametric sensitivity studies were then made with the modified INFLAT code to obtain more insight into this phenomenon. From their computer studies, Spahr and Wolf concluded that, because the 40-ft parachute inflates so rapidly, most of the forebody momentum is contained in a very short length of wake, causing the wake to overrun the canopy and the parachute to collapse. This led to the speculation that a larger parachute, which inflates more slowly, would spread the payload's momentum over a longer length of wake. This would allow more of the momentum of the wake to dissipate before the wake contacts the parachute, thereby decreasing the severity of the parachute-wake interaction. The INFLAT code calculations provided qualitative design information.

Ashurst[5.78] provided additional insight to this wake-interaction problem by modeling the fluid mechanics of a forward-facing rigid cup impulsively started with vortex shedding at the cup lip. Although his model was different from Spahr and Wolf's, he was also able to show that canopy collapse was caused by the wake behind the parachute catching up to the canopy from behind. Years later, the conformal mapping method developed by Sarpkaya[5.65] and the vortex methods developed by Strickland,[5.58] Sarpkaya,[5.59] and Sarpkaya and Lindsey[5.60] also reproduced the wake recontact phenomenon for two-dimensional shapes.

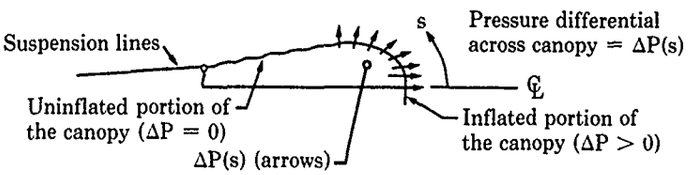
Free-flight tests of 26.5-ft-diameter solid-canopy parachutes and 20-ft-diameter ribbon parachutes were conducted at Sandia's Rocket Sled Track to assess this model of parachute collapse. The collapse phenomenon was reproduced in these tests, and the model of collapse was confirmed experimentally by attaching colored streamers to the parachute canopies and observing their motion as the wake approached the canopy from behind.

Wake diagram



- Large forebody/parachute velocity sweeps energetic wake away from the parachute
- No collapse of the parachute yet

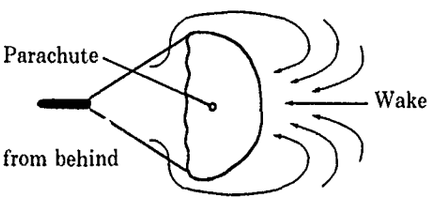
Pressure diagram



- Large differential pressures across inflated portion of canopy
- No differential pressures across uninflated portion of canopy

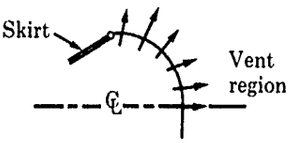
Figure 5.14a. Wake and pressure diagrams of parachute early in the process

Wake diagram



- Forebody and parachute have slowed down
- Energetic wake is catching up to the canopy from behind

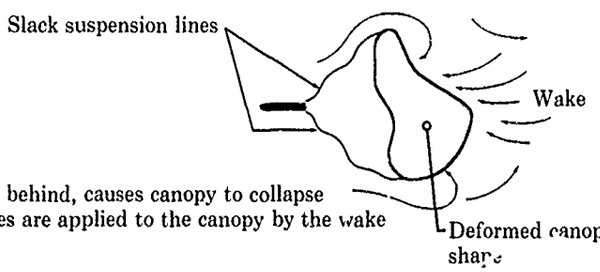
Pressure diagram



- Largest canopy pressure differentials are in the skirt regions at this time
- Canopy can experience overinflation and unloading

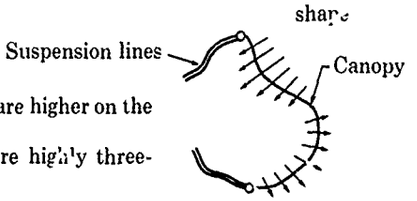
Figure 5.14b. Parachute inflation with full-open canopy

Wake diagram



- Wake strikes canopy from behind, causes canopy to collapse
- Both axial and radial forces are applied to the canopy by the wake

Pressure diagram



- On some portions of the canopy, pressures are higher on the outside than on the inside ($\Delta P < 0$)
- The parachute geometry and flow field are highly three-dimensional
- Loads on forebody are difficult to predict

Figure 5.14c. Parachute collapse

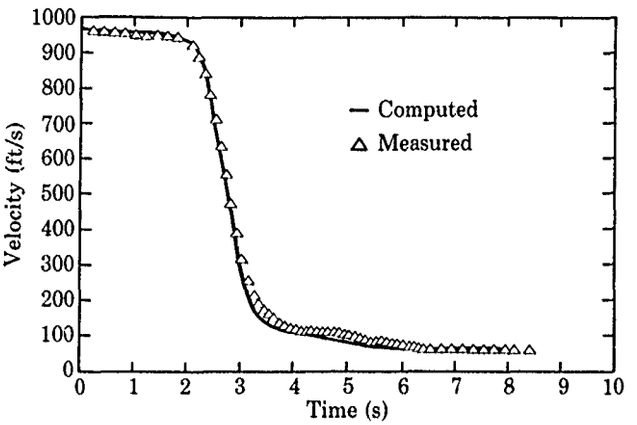


Figure 5.15a. Computed and measured velocity histories for 40-ft parachute

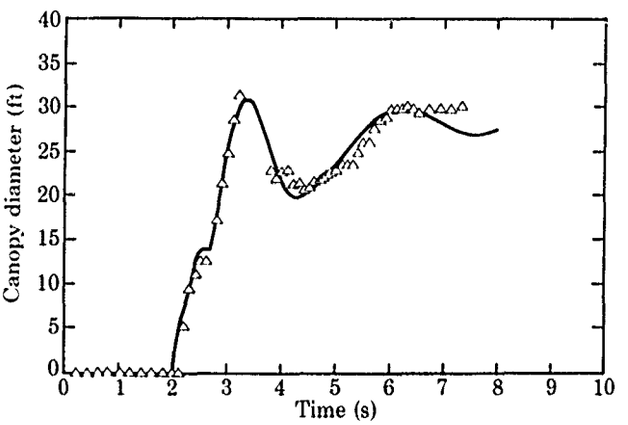


Figure 5.15b. Computed and measured parachute diameter histories for 40-ft parachute

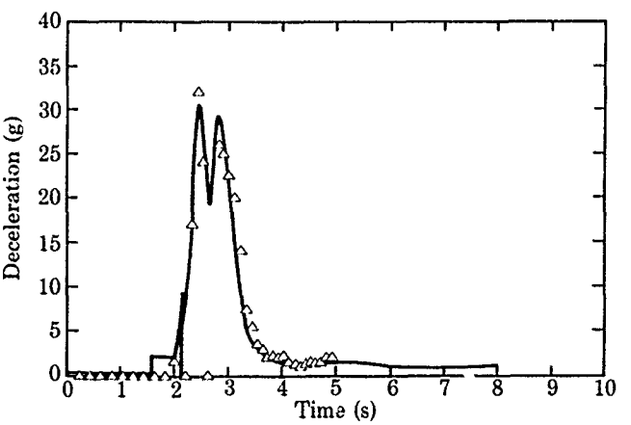


Figure 5.15c. Computed and measured deceleration histories for 40-ft parachute

Three flight tests—one sled test at maximum-design dynamic pressure and two aircraft drop tests at low dynamic pressure—were conducted to evaluate modifications to reduce the severity of collapse. It was postulated that the wake recontact of the canopy is aggravated by the sudden shedding of vorticity at the skirt as the canopy diameter exceeds the steady-state, full-open diameter at the end of the canopy inflation process. Therefore, the 40-ft parachute was fitted with a 77-ft-long permanent reefing line at the canopy skirt on these three tests to observe its effect on canopy collapse. In each test, the deformation of the canopy due to wake recontact was not as severe as in tests where no permanent reefing line was used. Similar results were obtained with sled track tests when the 26.5-ft solid canopies and 20-ft ribbon parachutes were flown with and without permanent reefing lines. However, these flight tests did not confirm that the shedding of vorticity at the canopy skirt was the principal cause of wake recontact and, subsequently, of parachute collapse. It is possible that permanent reefing alleviates parachute collapse because it decreases the drag area of the parachute (the momentum exchange from the payload to the wake would be spread over a longer wake) and allows the parachute to outrun its wake.

An attempt was made to correlate the magnitude of the 40-ft parachute collapse (admittedly a very subjective judgment) with canopy inflation time. It was postulated (Spahr and Wolf[6.77]) that parachutes that inflate rapidly may experience greater collapse than those that inflate slowly, because of the greater concentration of momentum in the wake of air behind the canopy. However, no definitive correlation of the magnitude of collapse with canopy inflation time was observed from flight tests of the 40-ft parachute. This lack of correlation may be caused by the wake of air missing the canopy (even when it has enough momentum to overtake the parachute), rather than by an incorrect hypothesis of the collapse mechanism. The energetic wake can miss the parachute because of curvature of the payload/parachute trajectory with respect to the wake, crosswinds that interact differently with the wake and the parachute, and the aircraft wake/downwash that may displace the wake relative to the canopy. These "miss" mechanisms were confirmed by films taken of TTR flight tests, sled tests, and subscale parachute inflation experiments at Sandia's Sol Se Mete cable site.

The extensive collapse studies led to the design of a 46.3-ft-diameter ribbon parachute, reefed for 0.85 s (after deployment is initiated) with a 23-ft-long line, and permanently reefed with an 89-ft-long line to control overinflation. Johnson and Peterson[3 6] describe the design of this 46.3-ft parachute, which meets the payload system design requirements and minimizes the collapse phenomenon. The design of this parachute is further discussed in Chapter 12.

Our experience with the 40-ft-diameter parachute is an indication that wake recontact may be a direct consequence of using strong, lightweight materials such as Kevlar in high-performance parachute design. With Kevlar, a parachute can be made large enough to cause rapid deceleration of the payload while being small enough to fit in its allotted volume in the payload. If this is true, then parachute designers will need analytical or empirical methods to help them know what design parameters to adjust in order to avoid collapse.

Strickland and Macha[5 79,5.80] conducted a series of drop tests of a 10-ft-diameter ringslot parachute from a helicopter where they systematically varied the payload weight and the Froude numbers. Their experimental data, which included velocity and parachute diameter time histories, provided considerable insight into the collapse phenomenon. The onset of the wake recontact occurs at a ratio of deployment velocity to terminal velocity of ~4 and becomes progressively more severe as the velocity ratio increases to ~10. From their experiments, Strickland and Macha developed a parameter that predicts the onset of collapse as a function of velocity ratio and mass ratio (defined as the payload mass divided by the mass of air contained in a cube of size D_e). They also present correlations on inflation times, time to canopy collapse, and opening load factors, which may be applied to other parachutes.

Oler[5 81] modeled the fluid and payload motion as a coupled transient phenomenon for predicting the transient deceleration of the parachute and the development of a trailing wake. His work is a refinement of the approach taken by Spahr and Wolf.[5 77] He correlated the parachute opening process using an empirical expression for the parachute's drag area as a function of time during inflation. Similarity velocity profiles are used to describe the wake velocity distributions. An integral momentum balance is applied to relate the parachute drag force to the rate of change of momentum in the fluid. His predictions of velocity decrease, and wake recontact with the canopy, etc., correlated well with the data of Strickland and Macha.

Sarpkaya[5.65] conducted experiments of towed circular arcs in a water channel where the models could be decelerated in the same way that a payload is decelerated by the drag of the parachute in full-scale flight. His results show wake recontact and provide the drag history and flow field during the wake development and recontact. Oler et al.[5.82] used a tow tank to investigate cambered plates that are impulsively started, then held at constant velocity, and then decelerated at a constant rate. Their experimental results confirm predictions by Strickland[5.58] and Sarpkaya[5.59] for 120° and 180° plates, but not for 240° plates. They indicate the range of porosity and decelerating conditions for which wake recontact can be expected to occur.

Strickland[5.83] and Fullerton, Strickland, and Sundberg[5.84] have developed approximate methods for calculating aircraft downwash on parachute performance. Payload/parachute system turnover and wake recontact may be strongly influenced by the wake of the delivery aircraft. This is especially true if it is a large, heavy aircraft, maneuvering at the time that the parachute is rapidly inflating close to the aircraft. Strickland[5.83] calculated that, for a 2 g pull-up, downwash velocities of ~35 ft/s occurred on the parachute system along with streamwise velocities of ~35 ft/s, which could contribute to the wake recontact problem. Fullerton, Strickland, and Sundberg[5.84] refined the vortex panel representation of the aircraft's wing, combined the vortex panel method with a two-body trajectory code, and showed good agreement between predicted downwash velocities and those measured in a NASA wind tunnel test of a B-1B.

One can envision requirements for payload deceleration for which wake recontact cannot be avoided. In such circumstances, the designer might consider a cluster of smaller parachutes rather than a single large parachute. The cluster system might reduce collapse effects by spreading the payload's momentum over a larger-diameter wake, and the smaller cluster canopies might better resist collapse and reinflate more quickly than a single large parachute.

5.4 Trajectory dynamics

Engineers have been solving the equations of motion for the parachute and payload under the influence of gravitational and aerodynamic forces for many years, albeit with different levels of approximation, degrees of freedom, and numbers of independent bodies included in their models. Purvis[1.21] has identified the various analytical techniques needed to predict system performance during all phases of parachute operation, from "free flight" of the payload (before parachute deployment), through inflation, to steady-state descent. The necessary techniques are listed in the left column of Table 5.4. The solid symbols indicate which techniques are required for the various stages. The importance of trajectory analysis is obvious, since it is the only technique required for every stage. Excellent discussions of trajectory dynamics are given by Purvis[1.21] (his Trajectory and Loads lecture), the Parachute Design Guide,[2.1] Ewing, Bixby, and Knacke,[1.7] and Cockrell.[1.6] These references give the equations of motion, axis system, and simplifying assumptions. Other important basic references are White and Wolf,[4.72] Wolf,[4.73] Tory and Ayres,[4.74] Neustadt et al.,[4.81] Sundberg.[5.4] Gamble,[5.85] Whitlock,[5.86] Doyle and Burbick,[5.87] and Cutchins, Purvis, and Bunton.[5.88]

Table 5.4. Stages of System Flight

Modeling Technique	Stages				
	Payload Free Flight	Decelerator Deployment	Inflation	System Deceleration and Turnover	System Descent
Trajectory dynamics	•	•	•	•	•
Elastic structure dynamics		•	•		
Decelerator steady-state aerodynamics		•	•	•	•
Decelerator unsteady aerodynamics			•	•	

Purvis[1.21] points out that trajectory analysis consists of the numerical or analytical solution of a set of time-dependent differential equations which, subject to specified initial conditions and parachute design parameters, describe the motion of a system. Trajectory analysis methods may generally be characterized by two parameters: the number of degrees of freedom of the equations of motion and the axis system (or systems) in which the equations are written. Purvis[1.21] shows the input parameters and the output variables of a 2-DOF, a 3-DOF, and a 6-DOF trajectory analysis. He states that one of the simplest and most efficient methods of writing and solving the 6-DOF flight dynamics equations (see Ref. 5.88) uses earth-fixed axes for the translational equations, body axes for the rotational equations, and a direction cosine matrix for converting variables between the two axis systems. He uses this approach for the development of both the 2-DOF and 3-DOF models.

The simplest trajectory model is called a *point mass system,* wherein all physical attributes of the body (or bodies), such as its mass, lift, and drag, are concentrated at a single point in space. The motion of a 2-DOF point mass system is constrained to the vertical plane, and because of the point mass assumption the system has no rotational inertia. The two degrees of freedom are horizontal and vertical translation. For symmetric parachutes flying at low angle of attack, the only forces acting on the point are gravity and the decelerator drag force. The drag force must always lie along the system velocity vector. This point mass model is usually used for preliminary design calculations if only general flight parameters (e.g., total range or time from release to ground impact) are desired.

The next level of approximation in trajectory analysis is the 3-DOF system, which adds rotational motion to the horizontal and vertical motion modeled in the 2-DOF equations. The system is still constrained to the vertical plane, but the forces acting on it are more complex. Since the payload now has a horizontal axis, the orientation of the velocity vector with respect to this axis produces both an axial force and a normal force, both of which are a function of the angle of attack. The 3-DOF analysis requires a more complex model of the decelerator-payload geometry, and the simulation results will then be "model-dependent."

Purvis defines four basic types of decelerator models that may be used with the 3-DOF trajectory equations. They are (1) massless, (2) rigid single-body, (3) rigid two-body, and (4) elastic. In the massless decelerator model, the decelerator remains aligned along the payload velocity vector. The decelerator produces only a drag force, which acts through the attachment point and thus generates a stabilizing moment.

The rigid single-body model assumes that the decelerator axis of symmetry remains aligned with the longitudinal axis of the payload. The decelerator produces a drag force, a lift force, and a moment. All forces and moments are assumed to act at the system's center of mass, which is not the same as the payload's center of gravity. This model requires detailed knowledge of the decelerator aerodynamics and further assumptions about the effective decelerator mass and rotational inertia. The output is deceleration, velocity, altitude, range, and pitch angle.

The rigid two-body model assumes that the decelerator and the payload system consist of a point mass connected to a rigid body by a massless rigid link that is pinned at the attachment point. This model contains the desired attributes of both the massless model and the rigid single-body model. It also has all of the drawbacks of the rigid single-body model and requires additional equations to represent two-body coupling.

In the elastic model, mass node equations of motion for the decelerator and elastic suspension lines are solved simultaneously with the payload's rigid body equations. This model is the most complicated, but the most physically realistic, of the four. Purvis discusses this in detail in his lecture, "Numerical Simulation of Decelerator Deployment."[1.21]

For many high-performance parachute applications (low-altitude delivery of a payload, for example), it is necessary to compute the pitch angle as well as the trajectory angle because the design requirements may specify a minimum payload impact angle or angle of attack. Hence, these 3-DOF codes are a requirement for many high-performance parachute design iterations preliminary to selecting a parachute system.

White and Wolf[4.72] studied the three-dimensional motion of a freely descending parachute with a 5-DOF analysis (the roll motion is neglected) to investigate parachute dynamic stability. Wolf[4.73] continued this work by studying the three-dimensional motion of a nonrigid parachute and payload system to investigate dynamic stability. He assumed that both the parachute and the payload have

5 degrees of freedom (roll neglected) and that they are coupled together with a riser. These studies are discussed in Section 4.4.2.

Purvis[1.21] refers to Whitlock[5.86] for the development of the 6-DOF equations of motion. He uses a modified Euler scheme, which is as accurate as a fourth-order Runge-Kutta method, to solve the equations of motion. The computer code output is deceleration, velocity, altitude, range, cross-range, heading angle, pitch angle, and roll angle.

When details of the flight trajectory or payload/parachute motion must be calculated, the parachute and payload may have to be modeled separately. Schatzle and Curry[3.14] make reference to unpublished work of Sundberg and Meyer who developed and used a sophisticated 12-DOF digital code to calculate the motion of a two-body (parachute and payload) system. Both the payload and the parachute were modeled with 6 degrees of freedom each and were elastically coupled together. This code (called SANAF) was developed jointly by the USAF and Sandia. Schatzle and Curry calculated the motion of a two-stage lifting parachute and payload followed by a conventional parachute decelerating the payload.

Schatzle and Curry[3.14] developed a 9-DOF analog/digital code to simulate the flight characteristics of a payload retarded by a lifting parachute and then by a second-stage conventional drogue parachute. Their simulations agreed well with calculations using a 12-DOF digital code and with flight test data (see Section 3.2.1.3).

Doherr and Schilling[5.89] developed a 9-DOF model for predicting the complex motion of both the payload and the parachute when the parachute is rotating. The 3-DOF parachute is connected to the 6-DOF payload by a joint. They show the data needed to describe the payload and parachute in their model. The list of required information is long, emphasizing again that the engineer must provide more details about the physical and aerodynamic characteristics of both payload and parachute when using trajectory models with many degrees of freedom. Doherr and Schilling's computer simulation includes animation of the payload/parachute motion and is an excellent example of what modern trajectory dynamics codes can (and should) provide the parachute designer.

Future trajectory codes will be designed to track multiple bodies connected by elastic lines. The advantage of using multiple bodies connected by elastic lines is that the equations describing the motion of each body are independent of all other bodies except the force (and moment) applied to the body by the connecting lines. Thus, two elastically connected 6-DOF bodies are treated as two 6-DOF bodies, rather than as a single 12-DOF system. This allows greater flexibility in the allowable configurations, since a special set of coupled differential equations is not required for each possible configuration. The model for the elasticity and damping between each mass of a multibody dynamic code must be chosen carefully to avoid physically unrealistic behavior such as excessive rebound when tension is first applied to textile structural elements.

Sandia has begun development of such a trajectory dynamics code; some of its characteristics are reported by Fullerton, Strickland, and Sundberg.[5.84] It will incorporate various submodels for parachute system trajectories as they are developed. The mathematical models of inflation physics that need to be developed and incorporated into the general trajectory code include apparent mass, aircraft downwash and wake, parachute wake, aerodynamic force and moment coefficients of canopies, inflation, cluster interaction, line extraction, line aerodynamic coefficient, material tension with strain rate and hysteresis, and other specialized models. This trajectory code will be structured so that new or improved models can be added to the code, and only those of interest for a particular simulation need be invoked.

Three types of bodies are incorporated into the code, and any combination of these three can be used for any trajectory analysis. The bodies are (1) a 3-DOF point mass body with drag as the only aerodynamic force, (2) a 3-DOF body with angular orientation determined by its relative position to another body, and (3) a 6-DOF body with six components of aerodynamic forces and moments. The generality of the code is intended to allow solutions to a variety of parachute flight scenarios. These include turnover of a payload from a low-altitude release with either a single parachute or a parachute cluster, extraction of cargo from an aircraft including modeling of the platform rotation at load transfer, and the ability to model parachute deployment, including line sail. The code has been used, even in this early stage of code development, to model a high-speed snatch of a riser and a parachute. Eventually, the capability of optimizing a trajectory as a function of various parachute design parameters will be included.

References

5.1 R. D. Moog, "Aerodynamic Line Bowing During Parachute Deployment," AIAA 75-1381, November 1975.

5.2 J. W. Purvis, "Prediction of Parachute Line Sail During Lines-First Deployment," *J Aircraft*, Vol. 20, No. 11, November 1983.

5.3 J. W. Purvis, "Improved Prediction of Parachute Line Sail During Lines-First Deployment," AIAA 84-0786, April 1984.

5.4 W. D. Sundberg, "Finite-Element Modeling of Parachute Deployment and Inflation," AIAA 75-1380, November 1975.

5.5 A. M. Kuethe and J. D. Schetzer, *Foundations of Aerodynamics*, John Wiley and Sons, New York, NY, 1959.

5.6 H. E. Widdows, *Parachute Deployment Control Assembly*, United States Patent 3,145,956, August 25, 1964.

5.7 E. K. Huckins III, "Snatch Force During Lines-First Parachute Deployments," *J Spacecraft*, Vol. 8, No. 3, March 1971.

5.8 H. G. Heinrich, "A Parachute Snatch Force Theory Incorporating Line Disengagement Impulses," AIAA 73-464, May 1973.

5.9 L. R. Poole and J. L. Whitesides, "Suspension-Line Wave Motion During the Lines-First Parachute Unfurling Process," *AIAA Journal*, Vol. 12, No. 1, January 1974.

5.10 D. F. McVey and D. F. Wolf, "Analysis of Deployment and Inflation of Large Ribbon Parachutes," *J Aircraft*, Vol. 11, No. 2, February 1974.

5.11 A. K. Banerjee, and L. R. Utreja, "Drogue Parachute Deployment Dynamics of the Space Shuttle Solid Rocket Booster," AIAA 75-1383, November 1975.

5.12 K. E. French, "A First-Order Theory for the Effects of Line Ties on Parachute Deployment," AIAA 79-0450, March 1979.

5.13 D. J. Cockrell, I. D. Huntley, and R. M. Ayres, "Aerodynamic and Inertial Forces on Model Parachute Canopies," AIAA 75-1371, November 1975.

5.14 T. Von Kármán, "Note on the Analysis of the Opening Shock of Parachutes at Various Altitudes," Army Air Corps Scientific Advisory Group, ATI 200 814, August 1945.

5.15 S. K. Ibrahim, "Potential Flowfield and Added Mass of the Idealized Hemispherical Parachute," *J Aircraft*, Vol. 4, No. 2, March-April 1967.

5.16 H. G. Heinrich, "Aerodynamic Deceleration – Chapter III: The Physical Process of Parachute Inflation," Parachute Course on Aerodynamic Deceleration, University of Minnesota Center for Continuation Study, July 6-16, 1965.

5.17 T. Sarpkaya, "Methods of Analysis for Flow Around Parachute Canopies," AIAA 91-0825, April 1991.

5.18 H. G. Heinrich, "A Linearised Theory of Parachute Opening Dynamics," *Aeronautical Journal*, December 1972.

5.19 P. R. Payne, "A New Look at Parachute Opening Dynamics," *Aeronautical Journal*, February 1973.

5.20 G. C. DeSantis, "An Analysis of Parachute System Parameters," AIAA 73-487, May 1973.

5.21 T. Yavuz and D. J. Cockrell, "Experimental Determination of Parachute Apparent Mass and Its Significance in Predicting Dynamic Stability," AIAA 81-1920, October 1981.

5.22 D. J. Cockrell, K.-F. Doherr, and S. J. Polpitiye, "Further Experimental Determination of Parachute Virtual Mass Coefficients," AIAA 84-0797, April 1984.

5.23 D. J. Cockrell, Y. I. Frucht, and R. J. Harwood, "A Revision of the Added Mass Concept as Applied to Parachute Motion," AIAA 89-0895, April 1989.

5.24 B. C. Cochran, B. R. White, and J. M. Macha, "Experimental Investigation of Added Mass During Parachute Deceleration—Preliminary Results," AIAA 91-0853, April 1991.

5.25 J. A. Eaton, "Added Mass and the Dynamic Stability of Parachutes," *J Aircraft*, Vol. 19, No. 5, May 1982.

5.26 H. G. Heinrich and D. P. Saari, "Parachute Opening Shock Calculations With Experimentally Established Input Functions," *J Aircraft*, Vol. 15, No. 2, February 1978.

5.27 D. F. Wolf, "A Coupling Apparent Mass for Parachute Inflation Equations," AIAA 89-0933, April 1989.

5.28 D. Wolf, "A Simplified Dynamic Model of Parachute Inflation," *J Aircraft,* Vol. 11, No. 1, January 1974.

5.29 D. E. Waye and D. W. Johnson, "The Effects of Unsteady Aerodynamics on Single and Clustered Parachute Systems," AIAA 89-0934, April 1989.

5.30 T. Sarpkaya and M. Isaacson, *Mechanics of Wave Forces on Offshore Structures,* Van Nostrand Reinhold, New York, 1981.

5.31 D. Cockrell, "Apparent Mass—Its History and Its Engineering Legacy for Parachute Aerodynamics," AIAA 91-0827, April 1991.

5.32 B. W. Roberts and K. R. Reddy, "A Discussion of Parachute Inflation Theories," AIAA 75-1351, November 1975.

5.33 J. W. Purvis, "Theoretical Analysis of Parachute Inflation Including Fluid Kinetics," *J Aircraft,* Vol. 19, No. 4, April 1982.

5.34 K. E. French, "Inflation of a Parachute," *AIAA Journal,* Vol. 1, No. 11, November 1963.

5.35 F. O'Hara, "Notes on the Opening Behaviour and the Opening Forces of Parachutes," *J Royal Aeronautical Society,* Vol. 53, November 1949.

5.36 W. L. Garrard, "Application of Inflation Theories to Preliminary Parachute Force and Stress Analysis," AIAA 91-0862, April 1991.

5.37 G. C. Greene, "Opening Distance of a Parachute," *J Spacecraft,* Vol. 7, No. 1, January 1970.

5.38 H. G. Heinrich, "Opening Time of Parachutes Under Infinite-Mass Conditions," *J Aircraft,* Vol. 6, No. 3, May-June 1969 (also AIAA 68-12, January 1968).

5.39 H. G. Heinrich, "Theory and Experiment on Parachute Opening Shock and Filling Time," *Proceedings of the Royal Aeronautical Society Symposium on Parachutes and Related Technology,* London, September 1971.

5.40 J. S. Lingard, "A Semi-Empirical Theory to Predict the Load-Time History of an Inflating Parachute," AIAA 84-0814, April 1984.

5.41 B. Wilcox, "The Calculation of Filling Time and Transient Loads for a Parachute Canopy During Deployment and Opening," Sandia Corporation, SC-4151(TR), February 1958.

5.42 L. R. Jamison, "A Method for Calculating Parachute Opening Forces for General Deployment Conditions," AIAA First Aerodynamic Deceleration Systems Conference, Houston, Texas, September 1966.

5.43 W. P. Ludtke, "A Technique for the Calculation of the Opening-Shock Forces for Several Types of Solid Cloth Parachutes," AIAA 73-477, May 1973.

5.44 W. P. Ludtke, "Notes on a Generic Parachute Opening Force Analysis," AIAA 86-2440, October 1986.

5.45 H. G. Heinrich, R. A. Noreen, and J. C. Hedtke, *Analysis of the Opening Dynamics of Solid Flat and Ringslot Parachutes With Supporting Wind Tunnel Experiments,* USAF AFFDL-TR-71-95, February 1972.

5.46 R. A. Toni, "Theory on the Dynamics of a Parachute System Undergoing Its Inflation Process," AIAA 70-1170, September 1970.

5.47 R. M. Nerem and F. A. Pake, "A Model and Calculation Procedure for Predicting Parachute Inflation," AIAA 73-453, May 1973.

5.48 E. L. Keck, "A Computer Simulation of Parachute Opening Dynamics," AIAA 75-1379, November 1975.

5.49 C. H. Eldred and M. M. Mikulas Jr., "Transient Aerodynamic Pressures During Unsteady Parachute Processes," AIAA Third Aerodynamic Deceleration Systems Conference, Dayton, Ohio, September 1970.

5.50 B. W. Roberts, "A Contribution to Parachute Inflation Dynamics," AIAA/DoD 2nd Aerodynamic Deceleration Systems Conference, El Centro, California, USAF FTC-TR-69-11, April 1969.

5.51 B. W. Roberts, "Aerodynamic Inflation of Shell Type, Parachute Structures," *J Aircraft,* Vol. 11, No. 7, July 1974. Also, *Proceedings of The Royal Aeronautical Society Symposium on Parachutes and Related Technologies,* London, September 1971.

5.52 K. R. Reddy, "Unsteady Vortex Flow Past an Inflating, Decelerating Wedge," AIAA 73-449, May 1973.

5.53 K. R. Reddy and B. W. Roberts, "Inflation of a Multi-Element Parachute Structure," AIAA 75-1353, November 1975.

5.54 P. C. Klimas, "Inflating Parachute Canopy Differential Pressures," *J Aircraft,* Vol. 16, No. 12, December 1979.

5.55 J. W. Purvis, "Numerical Prediction of Deployment, Initial Fill, and Inflation of Parachute Canopies," AIAA 84-0787, April 1984.

5.56 J. Meyer and J. W. Purvis, "Vortex Lattice Theory Applied to Parachute Canopy Configurations," AIAA 84-0795, April 1984.

5.57 H. H. McCoy and T. D. Werme, "Axisymmetric Vortex Lattice Method Applied to Parachute Shapes," AIAA 86-2456, October 1986.

5.58 J. H. Strickland, "A Vortex Panel Analysis of Circular-Arc Bluff-Bodies In Unsteady Flow," AIAA 89-0930, April 1989.

5.59 T. Sarpkaya, *Discrete Vortex Analysis of Unsteady Flow About Two-Dimensional Cambered Plates,* Sandia National Laboratories, SAND87-7160, October 1987.

5.60 T. Sarpkaya and P. J. Lindsey, "Unsteady Flow About Porous Cambered Shells," AIAA 90-0314, January 1990.

5.61 Y. I. Frucht and D. J. Cockrell, "A Discrete Free Vortex Method of Analysis for Inviscid Axisymmetric Flows Around Parachute Canopies," AIAA 91-0850, April 1991.

5.62 S. Shirayama and K. Kuwahara, "Computation of Flow Past a Parachute by a Three-Dimensional Vortex Method," AIAA 86-0350, January 1986.

5.63 J. H. Strickland, "On the Utilization of Vortex Methods for Parachute Aerodynamic Predictions," AIAA 86-2455, October 1986.

5.64 H. Higuchi and W.-C. Park, "Computations of the Flow Past Solid and Slotted Two-Dimensional Bluff Bodies With Vortex Tracing Method," AIAA 89-0929, April 1989.

5.65 T. Sarpkaya, "An Experimental Investigation of Decelerating Flow About 2-Dimensional Cambered Plates," Sandia National Laboratories, SAND87-7159, October 1987.

5.66 H. Higuchi, "Wake Behind a Circular Disk in Unsteady and Steady Incoming Streams," AIAA 91-0852, April 1991.

5.67 J. W. Oler, J. H. Lawrence, and T. D. Adamson, *Unsteady Aerodynamic Loads on Rigid Two-Dimensional Parachutes,* Sandia National Laboratories Contractor Report SAND88-7024, August 1990.

5.68 S. M. Belotserkovskii, M. I. Nisht, A. T. Ponomarev, and O. V. Reysv, *Computer-Aided Study of Parachutes and Ultralight Aircraft,* published by Izdatel'stvo "Mashinostroenie," 1987. In Russian.

5.69 E. C. Steeves, "Prediction of Decelerator Behavior Using Computational Fluid Dynamics," AIAA 86-2457, October 1986.

5.70 E. C. Steeves, "Analysis of Decelerators in Motion Using Computational Fluid Dynamics," AIAA 89-0931, April 1989.

5.71 K. Stein, "Computations of the Flow Characteristics of Aerodynamic Decelerators Using Computational Fluid Dynamics," AIAA 91-0866, April 1991.

5.72 D. W. Barnette, "Preliminary Numerical Simulations for Parachutes Using a Navier-Stokes Solver on a Zoned Grid," AIAA 91-0876, April 1991.

5.73 H. G. Heinrich and R. A. Noreen, "Analysis of Parachute Opening Dynamics With Supporting Wind-Tunnel Experiments," *J Aircraft,* Vol. 7, No. 4, July-August 1970.

5.74 H. G. Heinrich, *Pressure and Canopy Profile Data of 20° Conical Ribbon Parachutes During Inflation,* SAND77-7012, Sandia National Laboratories, July 1977.

5.75 P. C. Klimas, "Compressibility Effects on Parachute Transient Pressures," *J Aircraft,* Vol. 15, No. 10, October 1978.

5.76 J. M. Macha, "An Introduction to Testing Parachutes in Wind Tunnels," AIAA 91-0858, April 1991.

5.77 H. R. Spahr and D. F. Wolf, "Theoretical Analysis of Wake-Induced Parachute Collapse," AIAA 81-1922, October 1981.

5.78 W. T. Ashurst, "Large Eddy Simulation Via Vortex Dynamics," AIAA 83-1879, July 1983.

5.79 J. H. Strickland and J. M. Macha, *Wake Recontact: An Experimental Investigation Using a Ringslot Parachute,* SAND88-3058, Sandia National Laboratories, January 1989.

5.80 J. H. Strickland and J. M. Macha, "A Preliminary Characterization of Parachute Wake Recontact," AIAA 89-0897, April 1989. Also, *J Aircraft,* Vol. 27, No. 6, June 1990.

5.81 J. W. Oler, "Prediction of Parachute Collapse Due to Wake Recontact," AIAA 89-0901, April 1989.

5.82 J. W. Oler, J. H. Lawrence, T. D. Adamson, and K. A. Dunmire, "Aerodynamic Loads on Rigid Two-Dimensional Parachutes During Wake Recontact," AIAA 91-0863, April 1991.

5.83 J. H. Strickland, "An Approximate Method for Calculating Aircraft Downwash on Parachute Trajectories," AIAA 89-0899, April 1989.

5.84 T. J. Fullerton, J. H. Strickland, and W. D. Sundberg, "A Vortex Panel Method for Calculating Aircraft Downwash on Parachute Trajectories," AIAA 91-0875, April 1991.

5.85 J. D. Gamble, *A Mathematical Model for Calculating the Flight Dynamics of a General Parachute Payload System,* NASA TN D-4859, December 1968.

5.86 C. H. Whitlock, "Advances in Modeling Aerodynamic Decelerator Dynamics," *Astronautics and Aeronautics,* Vol. 11, No. 4, April 1973.

5.87 G. R. Doyle Jr. and J. W. Burbick, *Users Manual—Dynamics of Two Bodies Connected by an Elastic Tether, Six Degrees of Freedom Forebody and Five Degrees of Freedom Decelerator,* NASA CR-120261, April 1974.

5.88 M. A. Cutchins, J. W. Purvis, and R. W. Bunton, "Aeroservoelasticity in the Time Domain," *J Aircraft,* Vol. 20, No. 9, September 1983.

5.89 K.-F. Doherr and H. Schilling, "9DOF-Simulation of Rotating Parachute Systems," AIAA 91-0877, April 1991.

CHAPTER 6

STRUCTURAL ANALYSIS

6.1 Background

The Parachute Design Guide[2.1] discusses the need to calculate the parachute stresses during the design process. The stress distribution in canopies and suspension lines is required if the designer is to minimize the parachute weight and the packed volume. Packed volume is at a premium for high-performance parachute systems; many parachutes must be pressure-packed to densities of over 40 lb/ft^3 (roughly the density of oak) because of payload volume limitations.

The stresses in a canopy are caused by the aerodynamic loads acting on the various structural components of the fabric material. A stress analysis requires knowledge of the shape and fabrication details of the fabric's structure, the application of the aerodynamic loads, and the characteristics of the fabric material. The fabric's load-carrying elements have little stiffness and therefore can support only tension loads, not bending or compression loads. Each type of fabric has its own strength and elongation characteristics. As was discussed in Chapter 3, the shape and construction vary with the type of canopy, and the transient shape during opening changes with dynamic pressure and Mach number.

Maximum stresses for high-performance parachutes occur during the opening process, which is a period of rapidly changing shape and aerodynamic loading. This has been verified experimentally many times, with measurements of snatch and opening-shock loads along with observed structural failure of suspension lines and canopies. As noted above, the stresses in a parachute canopy depend on the inflated shape, which depends on the stress distribution. This interaction requires that the solutions of stress and shape be obtained simultaneously in some iterative fashion. As the parachute inflates, it deforms to a shape that results in dynamic equilibrium of forces and inertias in all members. For example, the summation of canopy aerodynamic forces and inertial loads is reacted by the suspension line forces. Steps in the structural analysis of a parachute are to determine the shape and stress distributions for specified states of inflation until the system has reached equilibrium conditions to ensure that the maximum stress has been calculated. Much effort has been expended in predicting and measuring the total suspension line forces for high-performance parachutes. These total loads are much easier to predict or to measure than the local stresses in the canopy during inflation.

6.2 Analytical methods and design applications

Thorough literature surveys of analytical methods dating back to the Royal Aircraft Establishment studies in 1919 (the earliest known work), along with descriptive discussions of each method, are presented by Mullins and Reynolds[6.1] and Garrard et al.[6.2] The reader is referred to these excellent papers for background material on analytical methods.

Knacke[2.1] provides some general guidelines for the structural design of a flat ribbon parachute, including the calculation of the stress in a horizontal ribbon as a function of the camber or the unsupported length (distance between verticals or radials). Jaeger, Culver, and Dellavedowa[6.3] developed a method for estimating the maximum horizontal ribbon and radial tape stresses in conical ribbon parachutes. The upper portion of the canopy was assumed to be a cone with zero meridional stress, and the lower was assumed to be an ellipsoid with zero hoop tension.

Matejka[6.4] used the Jaeger, Culver, and Dellavedowa method to analyze the stresses (and factors of safety) in the canopy and suspension lines of 12-, 16-, 20-, 24-, and 28-ft-diameter reefed, conical ribbon parachutes tested by Sandia in its parachute research drop test program (see Maydew and Blanchard[2.12]). Forty-nine drop tests were made at parachute deployment dynamic pressures of 280 to 1910 lb/ft^2 (deployment Mach numbers of 0.6 to 1.2). There was no parachute damage on 29 of the tests at deployment dynamic pressures up to 1360 lb/ft^2, but the parachutes suffered minor to major damage on the other 20 flight tests at the higher dynamic pressures. Matejka used the Jaeger, Culver, and Dellavedowa method to calculate the stress on the maximum-loaded horizontal ribbon (and its location on the canopy) at the opening shock for the 29 successful tests. The factor of safety of these 1000-lb and 1500-lb horizontal ribbons varied from 1.28 to 9.52 for these 29 tests. The combined strength of the suspension lines for these parachutes varied from 144,000 lb for the 12-ft-diameter canopy to 324,000 lb for the 24-ft-diameter canopy. The suspension line factor of safety varied from 2.9 to 21.9 for the 29 successful tests. These test data, along with the stress analysis, formed a data

base for the Sandia design of heavy-duty ribbon parachutes for stores in that early time period. Minimum safety margins resulting from that data set, which were adopted for future designs, were 1.5 for horizontal ribbons and 3.0 for suspension lines.

Heinrich and Jamison[6.5] developed a method to calculate the stress of a fully inflated guide surface parachute. The guide surface parachute is widely used (usually fabricated in small sizes) as a pilot/extraction parachute or for store/bomb stabilization. The maximum stresses are probably encountered at full inflation for these essentially infinite mass conditions, because of the short filling time and because the dynamic pressure does not decrease very much while the parachute is inflating.

Heinrich and Jamison[6.6] developed a general analytical method for calculating the stress of an inflating or a fully inflated parachute. It can be applied to any type of canopy fabricated of solid cloth, concentric rings, or ribbons. They assume that the canopy profile of the fully inflated parachute is either known or can be obtained from full-size or model experiments. They use the method of O'Hara[5.35] for the intermediate canopy shapes for calculating the stresses during inflation.

Asfour[6.7] proposed that the maximum stress on a canopy is related to the radial velocity, parallel to the plane of the skirt, when each concentric ring of the canopy reaches its maximum diameter. At this instant, the radial component of the air inflow must be decelerated. This deceleration results in a transient hoop stress imposed on the ring of cloth. Asfour developed an expression for evaluating this stress, designated as snap stress, relating it to diameter and filling time.

Roberts[5.50,6.8] developed a theoretical aeroelastic model for an inflating parachute and obtained a numerical solution for the shape and stress distribution of a flat circular parachute with uniform pressure distribution. Roberts observed the closely coupled, complex relationship between the stress analysis and the pressure distribution during opening.

A major contribution to the stress analysis of high-performance parachutes was made by a group at Northrop Corporation during the design of the Apollo parachute system. This numerical method, termed CANO, is discussed by Mullins et al.,[3.39] Mullins and Reynolds,[6.1] and Reynolds and Mullins.[6.9] They developed an analytical method for determining the unique shape and internal distribution that satisfies equilibrium and boundary conditions for a parachute under the influence of known riser and aerodynamic forces. They treated the parachute as a deformable membrane, using finite elements with nonlinear elastic properties to represent the structure. An iterative procedure, performed by a digital computer, was used to find the equilibrium shape. Reefed and nonreefed configurations can be analyzed, and the canopy may be fully or partially inflated. They showed that predicted canopy shapes and failure loads agreed with aerial drop test results. They used this numerical method to successfully design the 17-ft-diameter conical ribbon drogue parachute and the 83.5-ft-diameter ringsail main parachute for the Apollo Earth Landing System.

Reynolds and Mullins[6.9] extended the CANO model to include the effect of vertical ribbons in the solution of canopy shape and stress distribution. Their parametric study showed that (1) the vertical ribbons have no significant effect on the profile shape of the canopy or on the horizontal ribbon loads, but can have a significant effect on the radial member loads; (2) the number of gores have a significant effect on the circumferential and meridional loads in the canopy; and (3) the effect of canopy cone angle on circumferential and meridional loads can be significant.

Houmard[6.10] developed an analytical method of predicting the dynamic stresses during parachute inflation to design the 53-ft-diameter disk-gap-band parachute[3.45,3.46] for the Viking Mars lander. He used an energy approach that assumed that the work performed by the inflation gas is equal to the strain energy capacity of the parachute. His computer program uses pressure distributions, canopy profile shapes, and deployment loads as functions of time during inflation along with nonlinear load-elongation material characteristics. He obtained axisymmetrical cloth stress distributions for a finite number of points in time during parachute opening.

Garrard and Muramoto[1.20] provided instruction on "Use of CANO for Stress Analysis in Ribbon Parachutes" at the 1982 University of Minnesota Helmut G. Heinrich Short Course on Parachute Systems Technology in Minneapolis. CANO2 is a digital computer code, written in FORTRAN, that predicts the stress distribution for an axisymmetric parachute in a reefed, partially inflated or fully inflated configuration. The canopy is approximated as a collection of finite meridional and horizontal elements, smoothly connected to form a gore. Allowances are made for arbitrary gore shapes, material load-strain properties, axial loads, and differential pressure distributions. They improved the computational efficiency and the solution convergence by adding a Newton-Raphson procedure. They indicated that the predicted canopy stresses obtained from CANO2 approximate the stresses measured in wind tunnel tests. They thoroughly document this new version of CANO2 in their lecture notes.

At the 1985 University of Minnesota/Sandia National Laboratories Decelerator Systems Engineering Course in Albuquerque,[1.21] Garrard, Konicke, and Peterson provided instruction on "A Parachute Stress Analysis Code for Microcomputer Use." They discuss a computer code called CANOPC, which is a simplified version of CANO2 and was designed to be used on an IBM PC equipped with an 8087 Math Co-processor. CANOPC is written in FORTRAN. Features of CANO2 that were eliminated in CANOPC were provisions for optimization, weight calculation, the inclusion of verticals, and the direct simulation of reefing. They provide instructions for using CANOPC on the IBM PC to calculate canopy stresses.

Sandia has used the CANO stress analysis code for several designs of high-performance parachute systems. Wolf[6.11] and co-workers at Sandia conducted a preliminary design and analysis of the Space Shuttle Solid Rocket Booster recovery system for the NASA-Marshall Space Flight Center. The baseline specifications for this preliminary design study was a 100-ft/s water impact of the 154,000-lb solid-fuel booster with nose extraction of the drogue parachute at 19,000 ft altitude at a dynamic pressure of 200 lb/ft^2. A 54-ft-diameter conical ribbon parachute (with one reefed stage) and a cluster of three 104-ft-diameter conical ribbon parachutes (with two reefed stages) were chosen as a baseline design for aerodynamic loading and stress analysis calculations. The maximum specified parachute inflation loads were 228,000 lb for the drogue and 130,000 lb for each of the three main parachutes. The recommended design factors, which include the safety factor and the joint, loop, seam, abrasion, fatigue, etc., losses for the risers, lines, radials, ribbons, vent and skirt bands, and reefing lines are given in Table 6.1. These recommended design factors were based primarily on Sandia's experience in designing heavy-duty ribbon parachutes for weapon systems. Wolf used INFLAT code[5.28] time-dependent drag predictions along with flight and wind tunnel aerodynamic data as input to the CANO code. Typical stress calculations are shown in Figures 6.1 and 6.2, which illustrate the calculated failure indices for the fully inflated drogue and single main parachutes, respectively. The elements are numbered from the vent band to the skirt band. The failure index is defined as the calculated load divided by the rated strength of the ribbon. Thus the failure index defines the proximity of the material to the failure strength. This study by Wolf's parametric CANO analysis of aerodynamic loads and stresses provided preliminary guidance for the baseline design later adopted by NASA for the SRB recovery system.

Table 6.1. Suggested Set of Design Factors for the SRB Drogue and Main Parachutes

			Component					
Row	Factor		Risers	Lines	Radials	Ribbons	Vent or Skirt Bands	Reefed Lines
1	Safety	D	—	1.5†	1.5†	1.5†	3.0*	3.0*
		M	3.0*	1.5†	1.5†	1.5†	3.0*	3.0*
2	Joint, loop, seam	D	0.8	0.9	0.9	0.8	0.9	0.9
		M	—	0.95	0.95	1.0	1.0	1.0
3	Abrasion	D	—	0.95	0.95	0.95	1.0	1.0
		M	1.0	0.95	0.95	1.0	1.0	1.0
4	Fatigue	D	—	0.95	0.95	0.90	0.95	1.0
		M	0.95	0.95	0.95	0.90	0.95	1.0
5	Water‡	D	—	0.98	0.98	1.0	0.98	1.0
		M	0.98	0.98	0.98	1.0	0.98	1.0
6	Ultraviolet	D	—	0.95	0.95	0.95	0.95	1.0
		M	1.0	0.95	0.95	0.95	0.95	1.0
7	Combined material factor, rows 2 to 6	D	—	1.32	1.32	1.46	1.26	1.11
		M	1.34	1.32	1.32	1.46	1.26	1.11
8	Load variation: side deployment or cluster	D	—	1.0	1.0	1.0	1.0	1.0
		M	1.25	1.25	1.25	1.25	1.25	1.25
9	Design factor (1)×(7)×(8)	D	—	2.0	2.0	2.2	3.8	3.3
		M	5.0	2.5	2.5	2.7	4.7	4.2

* Failure results in system failure
† Standard-cargo and special weapon
‡ Keep wet
D = Drogue parachutes
M = Main parachutes

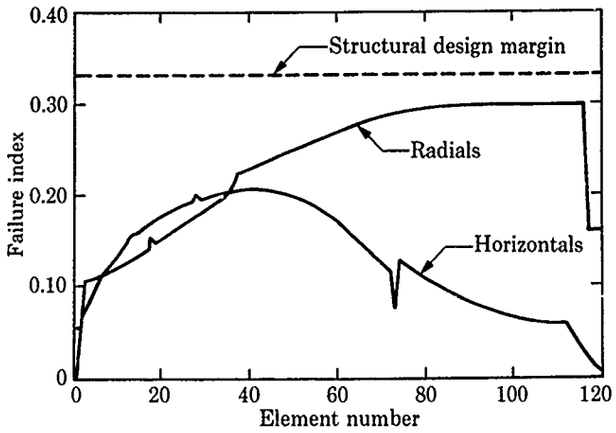


Figure 6.1. Failure indices for fully inflated SRB drogue parachute

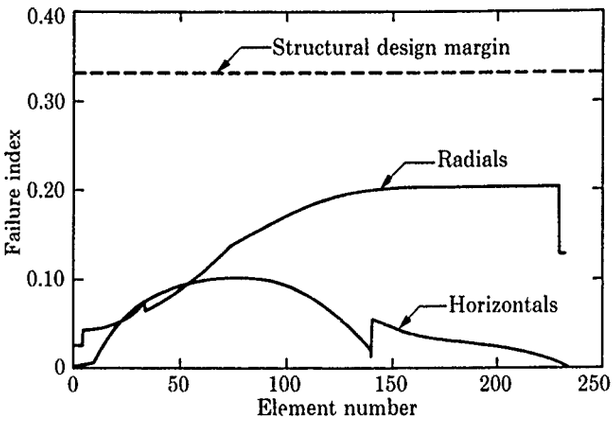


Figure 6.2. Failure indices for fully inflated SRB main parachute

Johnson and Peterson[3,6] designed a 46.3-ft-diameter conical ribbon parachute to retard a 2465-lb payload delivered at speeds up to 800 KCAS and at altitudes as low as 150 ft above ground level. Because the packed volume was limited to 5.7 ft^3 for this payload, it was necessary to use Kevlar as well as nylon in the parachute construction to provide the strength for the maximum-design opening-shock load of 165,000 lb. A stress analysis was conducted using CANO to optimize the ribbon and suspension line strengths in order to minimize weight and volume. This 60-gore, 20-degree conical parachute, which is reefed with a 23-ft reefing line, was analyzed for both the reefed and disreefed conditions. CANO was used in conjunction with experimental canopy pressure distributions for reefed and full-open canopy configurations. CANO models the continuous ribbons, radials, vent reinforcement, and skirt reinforcement as finite membrane elements and it predicts the inflated shape of the canopy for the given pressure distribution and axial load. Figure 6.3 shows the maximum structural load ratio (tensile load in the ribbon divided by the rated strength) for each ribbon and radial element for the 46.3-ft-diameter parachute for all pressure distributions and reefed/disreefed configurations. Thirty-five flight tests (aircraft drop, rocket-boosted, and sled-launched) verified the adequacy of the design, including the stress analysis. Incipient damage to the canopy and suspension lines was observed at flight conditions where CANO-predicted structural load ratios approached the structural design margin of 0.46.

Peterson et al.[1,2] designed a 5-ft-diameter, 20-degree conical Kevlar/nylon parachute to decelerate an 800-lb store from initial parachute deployment conditions of Mach 2.15 at 11,000 ft altitude (dynamic pressure of 4400 lb/ft^2). Calculations of structural margins for the parachute were made using the CANO code. The maximum parachute inflation load used for these calculations was 49,400 lb (65 g). CANO-predicted load ratios (material rated strength divided by predicted stress) were over 2.5 for all structural elements of the canopy. These load ratios were deemed necessary to survive ribbon flutter, which is not taken into account by CANO. The minimum load ratio was 1.9 for the Kevlar suspension lines. Nineteen flight tests verified the design of this supersonic parachute, including the stress analysis.

Sundberg[6,12] developed a new computer code, called CALA, to perform structural analysis of canopies. CALA refers to *CA*nopy *L*oads *A*nalysis. It is an extension of the CANO code work done by the Northrop Company and the University of Minnesota. The CALA code is considered an improvement over CANO because it has better convergence reliability, is more clearly written, and is easier to use. The equations were reformulated for the new solution method. CALA assumes a symmetric canopy, a steady-state condition, and no strength in the vertical direction. It computes the inflated shape, loads in horizontal members, radial members, vent lines and suspension lines, and total drag. Constructed geometry, material properties, dynamic pressure, and canopy pressure distribution are required as inputs. The CALA code includes the most important aerodynamic loading, which is the pressure differential across the horizontal members. Aerodynamic forces that are ignored are the forces on the suspension lines, vent lines, and the radial and vertical members in the gaps between the horizontal ribbons. The skin friction and flag drag of the horizontal members are also ignored. The CALA code shape prediction is compared in Figure 6.4 with shape data taken by Pepper and Reed[4,7] in the LTV Low-Speed Wind Tunnel of a 3-ft-diameter ribbon parachute; the agreement is good. The stress distributions in a 64-ft-diameter solid-canopy parachute, as calculated by the CANO and CALA codes, show good agreement in Figure 6.5. It should be noted that CANO requires a total drag force as input, whereas CALA calculates a total drag force from an input dynamic pressure.

At the 1987 University of Minnesota/Carl-Cranz-Gesellschaft Parachute Systems Technology Course in Wessling, West Germany,[1,22] Garrard discussed using the CANO and CALA codes for parachute design. He made several comparisons of CANO calculations with experimental data and concluded that, for the ribbon and solid parachutes tested, the calculated stresses tended to be larger than the measured stresses. The CANO code dates from the late 1960s, and there have been enormous developments in finite-element coding methods and digital computers since then. He indicated that the CALA code, although limited to much the same application as CANO, does have better convergence properties and is more easily understood.

The authors recommend that the CALA code be used for the structural analysis of high-performance parachutes at any stage of the parachute design. The predictions of CALA are limited, however, because accurate pressure distributions around the canopy are difficult to measure or calculate. Despite this limitation, CALA is and has been a very useful and reliable design tool for Sandia parachute systems.

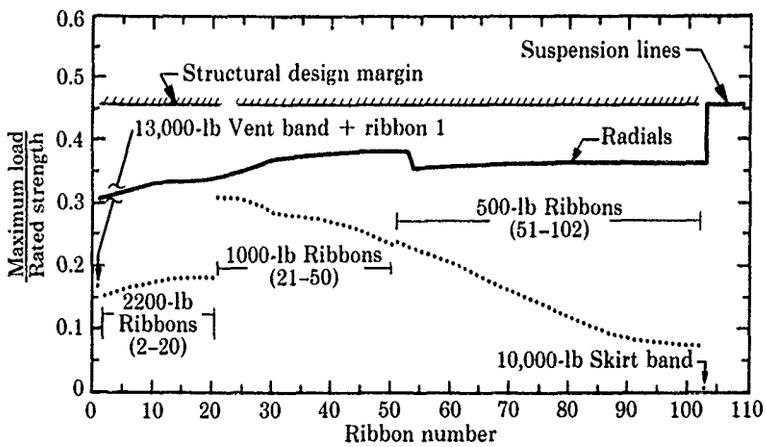


Figure 6.3. Maximum structural load ratios for 46.3-ft-diameter parachute

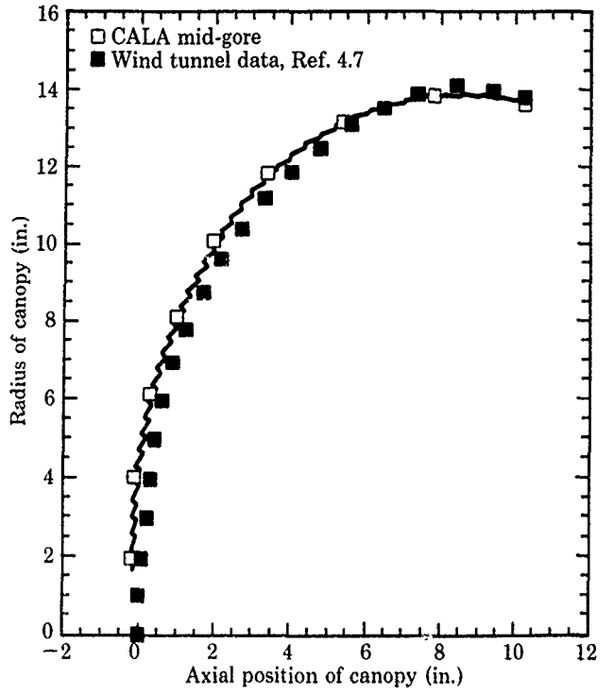


Figure 6.4. Comparison of shape predicted by CALA code with shape measured in wind tunnel test of 3-ft-diameter ribbon parachute

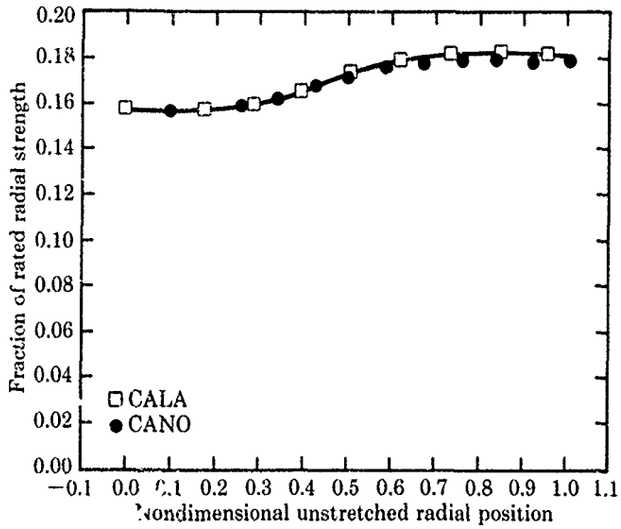


Figure 6.5. Comparison of radial loads predicted by the CALA and CANO codes for a 64-ft-diameter solid-canopy parachute at a dynamic pressure of 5.8 lb/ft^2

6.3 Stress measurement

Heinrich and Noreen[6.13] designed an Omega sensor to measure stresses in a 2-ft-diameter wind tunnel model parachute. The design of this high-sensitivity sensor is based on the theory that a curved beam experiences very high stresses and deformations when exposed to small bending moments. Such a beam is fabricated by cutting a slit in a short section of tubing made of an elastic material. A strain gauge is bonded to this beam to register its deformation, which is an indication of the stress acting on the free ends. To prevent the beam from influencing the gore curvature, the curved beam is fastened to the canopy cloth by means of flexible textile cloth. Heinrich and Noreen attached Omega sensors at stations 50%, 75%, and 90% of the distance around the canopy from vent to skirt on a 2-ft-diameter, solid flat circular parachute. Their parachute canopy stress measurements in low-speed wind tunnels agreed well with their theory; both their stress theory and wind tunnel data indicated that the stress levels increase from skirt to vent, primarily because of an increase in the bulge radius.

Heinrich and Saari[6.14] measured the circumferential stresses on 5-ft-diameter solid-canopy and ringslot parachutes in a low-speed wind tunnel during inflation under infinite mass conditions and at steady state. Five Omega sensors were placed along gore centerlines, and a force link measured stresses and the parachute force versus time. Radial stresses were measured on a 3-ft-diameter solid flat circular parachute at steady state. The vent-to-skirt stress distribution for the 14% porosity ringslot parachute is shown in Figure 6.6, where σ_m^* is the maximum stress divided by the nominal diameter times the dynamic pressure of the parachute and S* is twice the distance from the vent center divided by the parachute's nominal diameter. The plotted data from five wind tunnel test runs illustrate the repeatability of the experiment. The ringslot parachute data show that the stress is about equal at the vent and at the skirt during inflation, whereas the stress is higher at the skirt than at the vent under steady-state conditions.

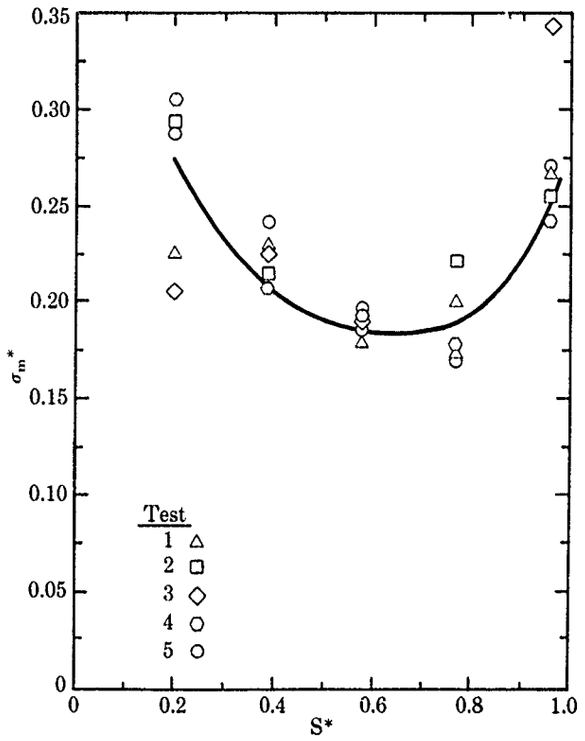


Figure 6.6. Maximum stress, σ_m^*, along gore centerline of ringslot parachute, dynamic pressure = 9.0 lb/ft^2

Braun and Doherr[6.15] investigated the properties of the Omega sensor for stress measurements by conducting tests with a 3.5-ft-diameter circular flat parachute deployed from 4.3-in.-diameter test vehicles that were launched horizontally from a cannon operating on compressed air. In 20 free-flight tests, they simultaneously measured the radial and circumferential stresses in adjacent

gores. For comparison, the tensile force at the confluence point was also sensed by means of a force transducer. The maximum radial stress was about four times the maximum circumferential stress.

Garrard and co-workers at the University of Minnesota have continued experimenting with Omega sensors to measure stress distribution in wind-tunnel-model parachute canopies. Konicke and Garrard[6.16] measured the circumferential stress in a 4.6-ft-diameter flat ribbon parachute of 20% porosity during inflation and at steady state. They concluded that the ratio of the maximum stress during inflation to the steady-state stress ranges from ~1.25 to 1.75, with the maximum value occurring near the skirt and the minimum occurring at ~30% of the distance from the apex to the skirt. This ratio of maximum stress to steady-state stress is much smaller in slotted parachutes than in solid parachutes.

Garrard and Muramoto[6.17] used the CANO code to calculate the stresses for the steady-state wind-tunnel-model parachute test conditions of Konicke and Garrard.[6.16] They compared measured stresses with the calculated stresses in Reference 6.17; this is believed to be the first comparison of calculated CANO stresses with wind tunnel experimental data.

Garrard, Konicke, and Wu[6.18] conducted low-speed wind tunnel tests of 18-in.-diameter models of a 25% porosity ribbon parachute. The parachute was instrumented with Omega sensors for stress measurements and pressure taps for pressure measurements. The canopy shape was measured photographically. They indicated that the stresses calculated using CANO tended to be higher than the measured stresses. The shapes predicted using CANO were not very close to the shapes measured photographically. However, if the vent boundary conditions of CANO are changed so that the calculated and measured shapes nearly match, then the calculated stress is much lower and closer to the measured stress. Garrard et al.[6.2] compared wind tunnel stress data for an 18-in.-diameter ribbon parachute with stress calculated using a modified version of CANO; this modified version gave a better representation of canopy shape and stress. Figure 6.7 shows a comparison of the measured stress distribution with calculated stress from the original CANO code and the modified version (CANO3) with two different vent boundary conditions. When the vent boundary condition was changed to give a good match of canopy shape, then the calculated stress was much closer to the measured stress (the lower, calculated stress curve in Figure 6.7). Garrard et al. show that CANO3 does not converge as rapidly as CANO, and that there are other limitations on CANO3 use. They also conclude that

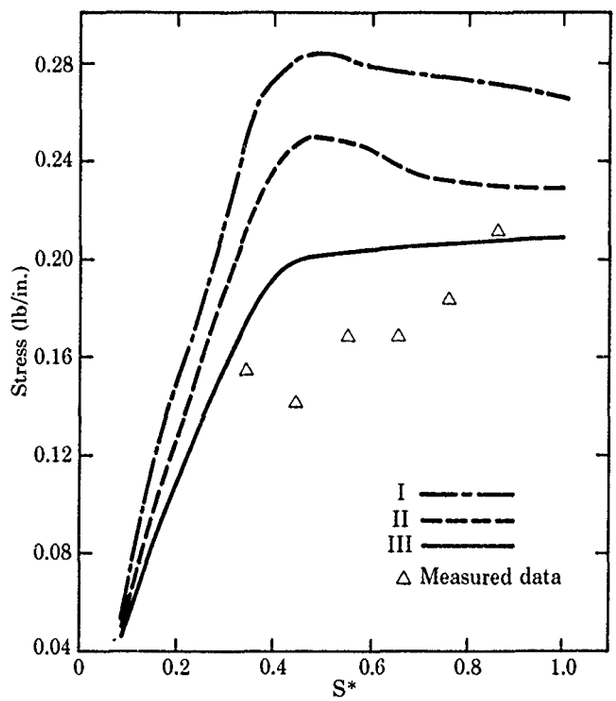


Figure 6.7. Calculated and measured stress vs. S* for 7.8 lb/ft^2 dynamic pressure: (I) CANO conventional vent slope; (II) CANO3 conventional vent slope; (III) CANO3 modified vent slope

perhaps a new structural design code should be developed that could benefit from the rapid strides that have been made in finite-element methods and computers in the last 20 years. The authors believe that the CALA code satisfies these criteria.

Niemi[6.19] provides a critical review of the state of the art for measurement of stress in parachute fabrics. He reviews the Omega sensor in detail and explains some of the problems associated with its use. Other types of stress- or strain-measuring transducers that have been used with parachutes, or that show potential, are also reviewed.

Methods of measuring stresses and pressures simultaneously in full-scale high-performance parachute systems during the canopy-filling process and in steady state in flight tests need to be developed to verify any stress-prediction code. Simultaneous pressure distributions and stress measurements are required because comparisons of calculated and measured stresses are appropriate only if the codes use measured pressure distributions as inputs. Further development of both pressure and stress measurement techniques is needed in order to make such measurements on inflating parachutes at realistic flight conditions.

References

6.1 W. M. Mullins and D. T. Reynolds, "Stress Analysis of Parachutes Using Finite Elements," *J Spacecraft*, Vol. 8, No. 10, October 1971.

6.2 W. L. Garrard, M. L. Konicke, K. S. Wu, and K. K. Muramoto, "Measured and Calculated Stress in a Ribbon Parachute Canopy," *J Aircraft*, Vol. 24, No. 2, February 1987.

6.3 J. A. Jaeger, I. H. Culver, and R. P. Dellavedowa, *A Study of the Load Distribution in a Conical Ribbon Type Parachute*, Report 8641, Lockheed Aircraft Corporation, Burbank, California, August 1952.

6.4 D. Q. Matejka, *The Structural Integrity of a Parachute During Opening Shock*, Sandia Corporation, SCTM 52-58(51), March 1958.

6.5 H. G. Heinrich and L. R. Jamison Jr., *Stress Analysis of a Fully Inflated Ribless Guide Surface Parachute*, USAF AFFDL-TR-65-111, September 1965.

6.6 H. G. Heinrich and L. R. Jamison Jr., "Parachute Stress Analysis During Inflation and at Steady State," *J Aircraft*, Vol. 3, No. 1, January-February 1966.

6.7 K. J. Asfour, "Analysis of Dynamic Stress in an Inflating Parachute," *J Aircraft*, Vol. 4, No. 5, September-October 1967.

6.8 B. W. Roberts, "The Shape and Stresses in an Arbitrarily Shaped Gore Parachute Under Arbitrary Pressure Distribution," AIAA 70-1197, September 1970.

6.9 D. T. Reynolds and W. M. Mullins, "Stress Analysis of Ribbon Parachutes," AIAA 75-1372, November 1975.

6.10 J. E. Houmard, "Stress Analysis of the Viking Parachute," AIAA 73-444, May 1973.

6.11 D. F. Wolf, *Space Shuttle Solid Rocket Booster (SRB) Recovery System, Sandia Laboratories Progress Report, March 1974 Through February 1975*, SAND75-0077, Sandia Laboratories, February 1975.

6.12 W. D. Sundberg, "A New Solution Method for Steady-State Canopy Structural Loads," AIAA 86-2489, October 1986.

6.13 H. G. Heinrich and R. A. Noreen, "Experimental Stress Analysis on Inflated Model Parachutes," AIAA 73-445, May 1973.

6.14 H. G. Heinrich and D. P. Saari, "Parachute Canopy Stress Measurements at Steady State and During Inflation," *J Aircraft*, Vol. 15, No. 8, August 1978.

6.15 G. Braun and K.-F. Doherr, "Experiments With Omega Sensors for Measuring Stress in the Flexible Material of Parachute Canopies," *J Aircraft*, Vol. 17, No. 5, May 1980.

6.16 T. A. Konicke and W. L. Garrard, "Stress Measurements in a Ribbon Parachute Canopy," *J Aircraft*, Vol. 19, No. 7, July 1982.

6.17 W. L. Garrard and K. K. Muramoto, *Calculated and Experimental Stress Distributions in a Ribbon Parachute Canopy*, Interim Technical Report from University of Minnesota for Sandia National Laboratories, Contract 16-9903, September 1982.

6.18 W. L. Garrard, M. L. Konicke, and K. S. Wu, "A Comparison of Measured and Calculated Stress in Solid and Ribbon Parachute Canopies," AIAA 86-2488, October 1986.

6.19 E. E. Niemi Jr., "A Critical Review of the State of the Art for Measurement of Stress in Parachute Fabrics," AIAA 89-0925, April 1989.

CHAPTER 7

WIND TUNNEL TESTING

7.1 Motivation

Throughout this AGARDograph, we have emphasized the need for experimental data to provide insight into the physical phenomena associated with parachute inflation and deceleration. Data are also required to calibrate inflation, performance, and structural prediction codes. Because of the approximations in the parachute design codes, data may be the only source of parachute design information. To meet these needs for parachute aerodynamic data, hundreds of parachute tests in wind tunnels have been conducted over the past 50 years. Much of these test data, along with the testing techniques and the instrumentation, have been published in the open literature.

The Parachute Design Guide[2.1] provides a good discussion of the virtues and drawbacks of testing parachutes in wind tunnels; they are as valid today as they were 27 years ago.

Test conditions can be better controlled in a wind tunnel than in flight tests. Accurate measurements of both parachute and fluid dynamic parameters may be made, and considerable data can be obtained within a relatively short time. Airflow, as well as parachute motion, can be observed in a wind tunnel. Comparative trends determined from wind tunnel testing can be applied to full-scale parachutes in free flight. Excellent parachute design information has been obtained by both scale-model and full-scale testing in wind tunnels. Results from wind tunnel tests have contributed significantly to the advancement of aerodynamic decelerator technology. Wind tunnel testing is a valuable parachute design tool when used in conjunction with analysis, computer simulation, and flight testing.

Wind tunnel testing of parachutes is not without its limitations, however. The size of the test section, coupled with the need to minimize measurement errors caused by the presence of the test section walls surrounding the parachute, result in the need to test parachutes that are usually smaller than the parachute used in the actual free-flight application. Available sizes and strengths of the textile materials limit the size and construction of subscale-model parachutes. Incorporating both geometric and structural scaling into the model parachute is usually not possible. The degrees of freedom for motion of the parachute/forebody combination are more constrained in the wind tunnel than in flight. As is the case for all other flight vehicles when tested in a wind tunnel, it is normally impossible to match the important aerodynamic scaling parameters, such as Mach number and Reynolds number, to their flight values. Perhaps the greatest limitation of wind tunnel testing for high-performance parachutes is that the velocity of the oncoming air does not decelerate rapidly as it does in flight, when the parachute drag slows the payload. Because of the limitation of constant airstream velocity, no existing wind tunnel is able to reproduce the nonsteady fluid dynamic phenomena that dominate the behavior of high-performance parachutes in the presence of a decelerating airflow approaching the canopy.

Listings of subsonic and transonic/supersonic/hypersonic wind tunnels used for wind tunnel testing of parachutes are given in Table 7.1 and Table 7.2, respectively. Most of these facilities were identified by Ewing, Bixby, and Knacke;[1.7] they furnish additional descriptive information about each tunnel's capabilities, including instrumentation. Additional details on these wind tunnels are given by Peñaranda and Freda[7.1] and in the AEDC *Test Facilities Handbook*.[7.2] During the past 30 years, Sandia has conducted 70 wind tunnel tests of high-performance parachutes; the wind tunnels used by Sandia are identified in Tables 7.1 and 7.2 with an asterisk.

The advantages, disadvantages, and limitations of wind tunnel testing of high-performance parachutes are reviewed in this chapter. Sections on measuring parachute drag, pressure distributions, stability, stress, and aerodynamic heating are included. A separate section on wind tunnel blockage for parachute testing is presented with recent wind tunnel data that provide design criteria for selecting the optimum size of the parachute model. Finally, a conceptual design for a parachute wind tunnel that simulates the nonsteady aerodynamics of rapidly decelerating parachute systems is discussed.

Table 7.1. Subsonic Wind Tunnels in the U.S.

Facility and Location	Type of Facility and Throat	Test Section Size (ft)	Mach Range	Reynolds Number (10^6/ft)	Total Temp. (°R)	Dynamic Pressure (lb/ft^2)
* AFFDL Vertical Wind Tunnel, Wright-Patterson AFB, OH	Annular return, continuous flow, open throat	12‡×12	0–0.14	0–0.91	Amb	0–26
NASA-Langley Spin Tunnel, Hampton, VA	Annular return, continuous flow, closed throat	25×20	0–0.08	0–0.62	Amb	0–10
* NASA-Ames 40×80-ft Subsonic Wind Tunnel, Moffett Field, CA	Closed circuit, single return, continuous flow, closed throat	40×80	0–0.3	0–0.21	Amb–600	0–262
NASA-Langley Full-Scale Tunnel, Hampton, VA	Closed circuit, double return, continuous flow, open throat	30×60×56	0–0.14	0–1.0	Amb	0–30
NASA-Langley V/STOL Transition Research Wind Tunnel, Hampton, VA	Closed circuit, single return, continuous flow, closed throat	14.5×21.75×50	0–0.32	0–0.55	Amb	0–135
NASA-Ames 7×10-ft Subsonic Wind Tunnel, Moffett Field, CA	Closed circuit, single return, continuous flow, closed throat	7×10×15	0–0.33	0–0.23	Amb	0–210
NASA-Langley High-Speed 7×10-ft Tunnel, Hampton, VA	Closed circuit, single return, continuous flow, closed throat	6.6×9.6×10	0.2–0.9	0.1–3.2	490–620	200–750
* United Technologies Large Subsonic Wind Tunnel, East Hartford, CT	Closed circuit, single return, continuous flow	18†/8†×16×40	0.26–0.90	0–4.5	500–590	0–709
* LTV Low-Speed Wind Tunnel, Grand Prairie, TX	Closed circuit, single return, continuous flow	7×10×16	0.03–0.30	0.26–2.25	500–600	2–135
* General Dynamics Corp. Subsonic Wind Tunnel, San Diego, CA	Closed circuit, single return, continuous flow	8×12×15	0.04–0.37	0.25–2.5	Amb	2–200
* Lockheed-Georgia Co. Low-Speed Wind Tunnel, Marietta, GA	Closed circuit, single return, continuous flow	30×26×63	0.13	0–1	Amb	0.5–25
	Closed throat, tandem test sections	16×23×43	0.26	0–2	Amb	2–100
* NASA-Lewis 9×15-ft V/STOL Tunnel, Cleveland, OH	Continuous flow	9×15×28	0–0.2	0–1.4	550	0–72

* Sandia conducted parachute tests in these wind tunnels
† octagonal
‡ diameter
Amb = ambient

Table 7.2. Transonic, Supersonic, and Hypersonic Wind Tunnels

Facility and Location	Type of Facility and Throat	Test Section Size (ft)	Mach Range	Reynolds Number (10^6/ft)	Total Temp. (°R)	Dynamic Pressure (lb/ft^2)
AEDC 16-ft Transonic Propulsion Wind Tunnel, Arnold AFS, TN	Closed circuit, single return, variable density, continuous flow	16×16×40	0.2–1.6	0.1–7.5	410–620	3.3–1300
* NASA-Langley 16-ft Transonic Tunnel, Hampton, VA	Closed circuit, single return, atmospheric, continuous flow	15.5†×22	0.2–1.3	1.2–3.7	510–640	57–905
NASA-Ames 14-ft Transonic Wind Tunnel, Moffett Field, CA	Closed circuit, single return, atmospheric, continuous flow	13.5×13.9 ×33.75	0.6–1.2	2.8–5.2	500–640	425–885
NASA-Ames 11-ft Transonic Wind Tunnel (Unitary), Moffett Field, CA	Closed circuit, single return, variable density, continuous flow	11×11×22	0.5–1.4	1.7–9.4	540–610	150–2000
* Naval Ship R&D Center Transonic Wind Tunnel, Bethesda, MD	Closed circuit, continuous flow, variable pressure	7×10×19	0.25–1.17	1–5	530–610	50–900
* Calspan Corp. Transonic Wind Tunnel, Buffalo, NY	Closed circuit, single return, variable density, continuous flow	8×8×18.75	0–1.35	0–12.5	520–620	0–2600
Aircraft Research Assn. Ltd. 9×8-ft Transonic Wind Tunnel, Bedford, England	Closed circuit, variable density, continuous flow	9×8	0–1.4	1.5–5.5	545–580	0–1090
AEDC 16-ft Supersonic Propulsion Wind Tunnel, Arnold AFS, TN	Closed circuit, single return, variable density, continuous flow	16×16×40	1.5–4.75	0.1–2.6	560–1110	30–570
* NASA-Lewis 10×10-ft Supersonic Wind Tunnel, Cleveland OH	Open and closed circuit, single or nonreturn, variable density, continuous flow	10×10×10	2.0–3.5	0.12–3.4	500–1150	20–700
* NASA-Ames 9×7-ft Supersonic Wind Tunnel, Moffett Field, CA	Closed circuit, single return, variable density, continuous flow	9×7×10	1.55–2.5	0.86–6.5	520–610	200–1450
* NASA-Lewis 8×6-ft Supersonic Wind Tunnel, Cleveland, OH	Closed cycle for aerodynamic testing	8×6×39	0.4–2.0	3.6–4.8	560–700	200–1240
NASA-Ames 8×7-ft Supersonic Tunnel (Unitary), Moffett Field, CA	Closed circuit, single return, variable density, continuous flow	8×7×16	2.4–3.5	0.5–5.0	520–610	200–1000

(continued)

Table 7.2. (continued)

Facility and Location	Type of Facility and Throat	Test Section Size (ft)	Mach Range	Reynolds Number (10^6/ft)	Total Temp. (°R)	Dynamic Pressure (lb/ft^2)
AEDC, VKF Supersonic Wind Tunnel A, Arnold AFS, TN	Closed circuit, variable density, continuous flow	3.33×3.33×7	1.5–6.0	0.3–9.2	530–750	49–1800
AEDC, VKF Hypersonic Wind Tunnel B, Arnold AFS, TN	Closed circuit, recycling, variable density, continuous flow	4.33‡	6 and 8	0.3–4.7	850–1350	43–590

* Sandia conducted parachute tests in these wind tunnels
† octagonal
‡ diameter

7.2 Types of tests

The parachute aerodynamic characteristics of drag, stability, inflated shape, and lift-to-drag ratio under steady-state conditions and constant oncoming velocity (called "infinite mass loading") can be studied with accurate results in wind tunnels. The deployment process (the nonsteady conditions), in which drag and shape grow rapidly, has also been studied in wind tunnels within the infinite mass loading approximation. Both steady-state and nonsteady parachute testing is discussed.

7.2.1 Drag

In 1948, Heinrich[2,7] measured the drag coefficients of sheet-metal models of guide surface parachutes in a subsonic wind tunnel. He concluded that the drag coefficient for the brake guide surface parachute is ~0.90 and that of the stabilization guide surface parachute is ~0.75. He suggested that fabric guide surface parachutes have a higher drag coefficient than sheet-metal models because their form varies and their surface is rougher. These were probably the first wind tunnel tests of a high-performance parachute configuration.

Pepper and Post[7,3] measured the drag of 12-, 18-, and 24-in.-diameter guide surface parachutes and 9-, 12-, 15-, and 18-in.-diameter ringslot parachutes in the LTV 7-ft by 10-ft Low-Speed Wind Tunnel. The parachute models were attached to a 4-in.-diameter forebody, which was supported on the wind tunnel centerline by a vertical strut attached to the balance turntable (for drag measurements) mounted on the floor of the test section. The drag coefficient data varied considerably with parachute model size, again illustrating the need for dimensionally stable model parachutes and careful structural and geometric scaling of full-scale parachutes down to wind-tunnel-model size.

Heinrich and Haak[4,1] measured the drag and normal force of 12.6-in.-diameter guide surface and 16.6-in.-diameter ribbon and ringslot metallic and textile parachute models in a 38-in. by 54-in. subsonic wind tunnel. The models were supported on a lower-plate turntable and the forebody was attached to the tunnel with guy wires. The normal-force sensing element was mounted near the apex of the parachute between the model and the strut-supported sting. The tangent-force pickup was mounted between the strut in the rear of the test section and the centerline sting. Both sensing elements incorporated standard strain gauge circuits mounted on elastic cantilever beams. The wind tunnel turntable was set to angle of attack and the force data were then recorded on an oscillograph. They measured normal force and drag at angles of attack up to 50 degrees.

Landon[7,4] conducted a comprehensive series of three tests in the Aircraft Research Association Ltd. 9-ft by 8-ft Transonic Wind Tunnel, at Mach numbers up to 1.38, of 1-ft-diameter models of flat, conical, and hemisflo ribbon parachutes. He systematically varied the suspension line length, cone angle, and porosity of these parachutes in these parametric tests. The model parachute was deployed, after the tunnel flow field was established, from an ogive-cylinder pod that was strut-supported from the tunnel floor. An axial-force strain gauge transducer was mounted in the pod. A recorder was connected in parallel with the tunnel's data-logging system to record the dynamic drag signals of the parachute through the strain-gauged tension link (to a frequency limit of 120 Hz). High-speed motion pictures (up to 2800 frames per second) were taken of each parachute release/deployment and inflation. Landon presents carpet plots of drag coefficient (as a function of porosity, line length, and Mach number), transient drag measurements, and high-speed film clips of the deployment and filling processes. This is a valuable set of wind tunnel data because of the systematic variation of the parachute parameters over the subsonic/transonic Mach number test range.

Bacchus, Vickers, and Foughner[4.6] and Moog, Bacchus, and Utreja[4.50] discuss the scale-model wind tunnel tests of the 54-ft-diameter drogue and the cluster of three 115-ft-diameter Space Shuttle Solid Rocket Booster (SRB) main parachutes. These tests were conducted in the NASA-Langley 16-ft Transonic Wind Tunnel at a Mach number of 0.13. In the Phase 1 test,[4.6] various drogue parachute deployment concepts and performance characteristics were studied. Based on the Phase 1 test, a baseline deployment method was selected for drogue parachutes. A parametric investigation of this deployment method to size the pilot parachute, break ties, etc., was performed in the Phase 2 test.[4.50] The Phase 2 test also included parametric steady-state drag measurements of full-open and reefed drogue and main parachutes (with and without the SRB forebody), main parachute cluster tests, and disreef tests.

The Phase 1 test was conducted using SRB forebody models and 1/8-scale (6.75-ft-diameter), 20-degree conical ribbon parachutes which represents a tunnel blockage of ~8% when the parachute is fully inflated. Four methods of deploying the drogue parachute were studied in the wind tunnel. Because steady-state drag data were needed over an SRB angle-of-attack range of 70 to 180 degrees, two forebody models were designed. One was a complete SRB model for testing at a booster angle of attack of 180 degrees (nozzle forward). The second represented the forward 40% of the complete SRB and was used for the angle-of-attack range of 70 to 130 degrees. All of the deployment tests were conducted with the partial SRB model, which was mounted to the floor of the 16-ft tunnel. Instrumentation for this Phase 1 test consisted of a single-component load cell (1400-lb-capacity) for measuring the steady-state drag of the drogue parachute and a 100-lb-capacity load cell for measuring the transient drag of the pilot parachute and the nose cap. Digital and oscillograph recordings of the load cell readout were obtained. Photographic coverage included high-speed cameras operating at 125 frames per second. Typical drag data for the drogue are shown in Figure 7.1, which illustrates the small effect of forebody interference due to SRB angle of attack on the drag. Parachutes with porosities of 16% and 24% were tested in this Phase 1 test.

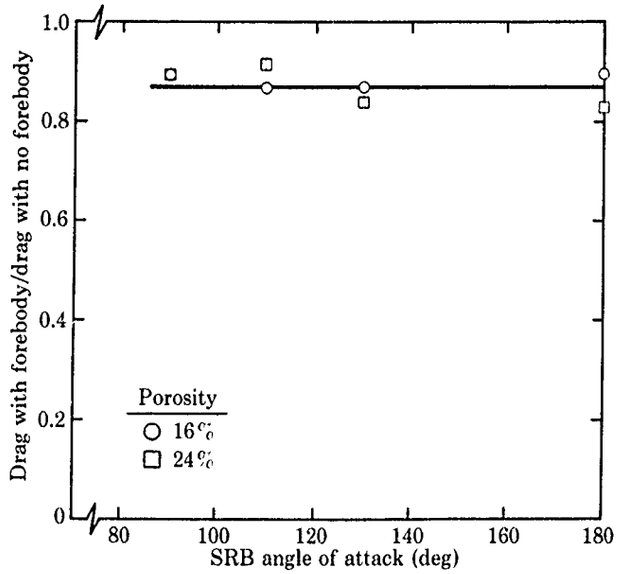


Figure 7.1 Forebody interference effect on SRB drogue parachute drag (taken from Ref. 4.6)

The Phase 2 experiments consisted of testing 6.75-ft-diameter drogue models of 16%, 20%, and 24% porosity conical ribbon parachutes with different suspension line lengths. In addition, main parachute tests were conducted of both a single model and a cluster of three 6.5% models (115-ft-diameter full-scale) of conical ribbon parachutes (with and without SRB forebody) of 16%, 20%, and 24% porosity and with different suspension line lengths. A 1000-load cell was used for the single parachute tests and a 4000-lb load cell was used for the cluster tests. The load cell output was recorded on an oscillograph that traced force-time history. A continuous analog signal of load cell reading and the dynamic pressure were recorded on magnetic tape, along with a time code. Figure 7.2 shows good agreement between wind tunnel and flight test drag coefficients as a function of

suspension line length for the drogue and single main parachutes. Other typical wind tunnel data on the reefed and full-open parachutes are shown in Figure 4.28.

Sandia conducted a series of wind tunnel tests to develop an extensive data base of drag of conical ribbon parachutes. McVey, Pepper, and Reed[44] conducted a parametric wind tunnel study of drag in conjunction with the wind tunnel pressure test reported by Pepper and Reed[47] and discussed in Section 7.2.2. Three-foot-diameter conical ribbon parachutes were tested at subsonic speeds to measure the effect of reefing line length, porosity, and suspension line length on the drag. The drag data were measured with a force balance located in the wind tunnel ogive-cylinder model forebody. Typical data illustrating the effects of porosity and reefing line length are shown in Figure 4.23.

Peterson and Johnson[432] measured the drag of a 15-in.-diameter conical ribbon parachute at several axial stations behind an ogive-cylinder forebody, with and without fins, in a subsonic wind tunnel. The parachute model was also tested without a forebody to measure the effect of suspension line length on drag. The forebody was wire-supported in the wind tunnel, and an axial-force strain gauge balance was located in the forebody to measure the drag. In addition to measuring drag, an 80-tube total head pressure rake was used to survey the forebody turbulent wake at several axial stations behind the model. The rake could be traversed both vertically and axially while the wind tunnel was operating. The 80 pressures were recorded using eight differential pressure transducers, which were scanned with a Scanivalve at a given vertical location in the model wake. These velocity distributions were determined at five axial locations aft of the forebody base. Typical data are presented in Figures 4.5, 4.15, and 4.16.

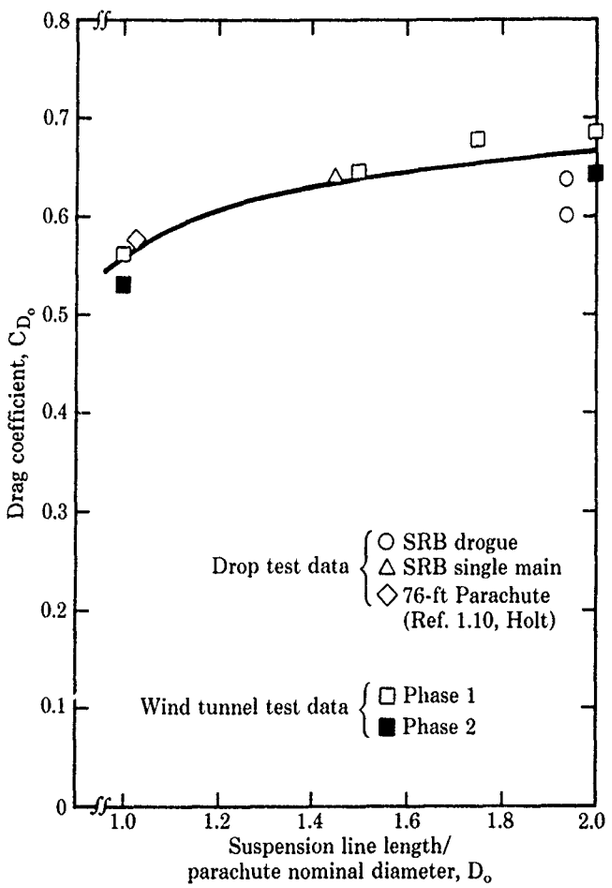


Figure 7.2 Comparison of full-open drag coefficient of SRB drogue and single main parachutes (taken from Ref. 4.50)

Baca[4.44,7 5] measured the effects of canopy number, riser length, and reefing on the drag performance of 16-in.-diameter clustered ribbon and solid parachutes in the LTV 7-ft by 10-ft subsonic wind tunnel. An axial load cell was placed in the 4.5-in.-diameter ogive-cylinder model that was wire-supported in the tunnel to measure the parachute drag. Typical data in Figures 4.29 and 4.25 illustrate the effects of riser length and number of canopies on the drag efficiency of unreefed and reefed ribbon parachutes, respectively.

Purvis[4 8] tested 5-ft-diameter parachutes with 8, 16, and 32 gores in a solid canopy and four 10% porosity flat ribbon canopies with 5, 10, 20, and 40 horizontal ribbons in the LTV 7-ft by 10-ft subsonic wind tunnel. He combined these data with other subsonic wind tunnel data of 3-ft-diameter and 6-ft-diameter parachutes in a format that illustrated the effects of inflated diameter, porosity, reefing line length, suspension line length, number of gores, and number of ribbons on parachute drag. Some of these effects are illustrated in Figures 4.2 through 4.4 for unreefed parachutes and Figure 4.24 for reefed parachutes.

Supersonic and hypersonic wind tunnel tests to measure parachute drag were conducted by Engstrom and Meyer,[7.6] Maynard,[4.2] Mayhue and Bobbitt,[4 18] Corce,[4.19] and Pepper, Buffington, and Peterson.[3.22] Engstrom and Meyer[7.6] tested 10- to 12-in.-diameter metal and fabric, flat and conical ribbon parachutes of varying porosities and suspension line lengths at supersonic speeds in the NASA-Langley 4-ft by 4-ft Unitary Plan Wind Tunnel. The fabric parachutes were tested at Mach numbers 1.9 to 2.1 and the rigid models were tested at Mach numbers 1.7 to 3.5. The fabric parachutes were deployed in the wind tunnel from a centerline sting support that housed a drag link. The stainless-steel parachute models were supported by a four-support yoke-type sting; drag measurements were not made with these models. High-speed schlieren photographs were taken of the flow field about the fabric and metal models.

Maynard[4.2] tested 6- to 15-in.-diameter fabric ribbon parachutes at Mach numbers of 1.9 to 3.0 and 8-in.-diameter metal ribbon parachutes at Mach numbers of 1.57 to 3.9 in the NASA-Langley 4-ft by 4-ft Unitary Wind Tunnel. The instrumentation and testing techniques were very similar to the tests of Engstrom and Meyer.[7 6]

Mayhue and Bobbitt[4 18] tested 5.4-ft-diameter disk-gap-band parachutes of 10.0%, 12.5%, and 15.0% porosity at Mach numbers 2.0 to 3.0 in the AEDC 16-ft Supersonic Propulsion Wind Tunnel. Tensiometer and load cell measurements, along with motion picture films, were taken for canopy angles of attack of up to 20 degrees. The parachute was deployed from the cylindrical base of a floor strut-supported forebody that housed the load cell. A tensiometer and swivel were located between the three-legged bridle and the suspension lines. Mayhue and Bobbitt found good agreement between these wind tunnel parachute drag data and full-scale parachute flight data.

Corce[4 19] tested 5- and 8-in.-diameter supersonic-X parachutes in the AEDC 50-in.-diameter Hypersonic Wind Tunnel B at Mach 8. The forebody consisted of a 6-in.-diameter, 20-degree cone supported by floor and ceiling-swept struts. Parachute forces and moments were measured with a six-component strain gauge balance mounted in the conical forebody. A wake survey rake, equipped with pitot pressure, cone static pressure, and total temperature probes, was used to determine local flow conditions downstream of the cone. The parachute motion was recorded with two high-speed 16mm motion picture cameras. The parachutes were fabricated of nylon, Kevlar, and BBB.

Pepper, Buffington, and Peterson[3.22] tested 15-in.-diameter hemisflo and 20-degree conical ribbon parachutes behind several forebodies in the NASA-Ames 9-ft by 7-ft Supersonic Wind Tunnel at Mach numbers 1.5 to 2.5. They measured the effects of Mach number, forebody shape and diameter, canopy porosity (10% and 20%), and inflated canopy diameter on the supersonic drag. The forebodies were strut-supported from the tunnel's side wall, and a strain gauge axial-force beam was placed in the forebody to measure drag. Ninety-three parachute models were fabricated for this wind tunnel test. The test parachute was placed in a small deployment bag and secured to the base of the forebody. The parachute was deployed after the tunnel was started. High-speed video and motion picture cameras and the tunnel data acquisition system were used to record parachute deployment, to observe parachute motion, and to document parachute structural integrity. Schlieren photographs were used to observe the flow field around the forebody and parachute. A color schlieren photograph of the parachute flow field at a wind tunnel test Mach number of 1.9 is shown in Figure 4.11 The motion pictures and schlieren photographs were needed to validate and interpret the drag data. Typical data from this test are shown in Figures 4.20 through 4.22.

Lingard, Barnard, and Kearney[4.24] conducted a comprehensive wind tunnel test series to investigate the inflation, drag, and stability of 20-degree conical ribbon, equiflo, hyperflo, supersonic-X, and ballute parachute models over the Mach number range of 0.5 to 4.35. The inflated diameter of all of the parachute models (which were fabricated of Kevlar) was ~4.3 in. The suspension

line length was about twice the parachute's constructed diameter. The tests were conducted in the supersonic wind tunnels 4 and 4b at the Institut Aerotechnique de St-Cyr, France. These blowdown wind tunnels have rectangular test sections 35.3 in. high by 33.5 in. wide. All five parachute types were tested at Mach numbers 0.5, 1.15, 1.5, and 2.0 in tunnel 4. The equiflo, hyperflo, and ballute parachute models were also tested at Mach numbers of 2.8, 3.4, 3.8, and 4.35 in tunnel 4b.

The 1.8-in.-diameter ogive-cylinder-boattail forebody was strut-supported from the tunnel floor and ceiling. A ring dynamometer with four active strain gauges was placed in the forebody to measure axial force. Output from the dynamometer was sent to a chart recorder and to a computer that sampled the signal at a rate of 500 Hz. The parachute was connected to the dynamometer by a swivel to obviate spin-up. The parachute canopy was packed in a sleeve in the forebody; the canopy was deployed by releasing the drag-producing forebody-base endplate after the wind tunnel was brought up to speed. Visual records of parachute deployment and filling were obtained by a high-speed video camera operating at 200 frames per second, and the schlieren images were recorded by a standard video camera operating at 25 frames per second. The drag coefficients were determined from the time-averaged "steady-state" drag force measured by the dynamometer. Typical drag data for the five parachutes tested in tunnel 4 are presented in Figure 7.3. Lingard, Barnard, and Kearney present an excellent discussion of the scaling effects associated with using their 1/30-scale parachute models. They conclude that the results give a sound basis for comparative assessment of the five canopies and that the data for all of the canopies, except for the ribbon parachute, are quantitatively valid. They also conclude that parachutes with a shaped gore defining their flying shape perform better in the supersonic regime than parachutes whose flying shape is determined largely by local pressure distribution.

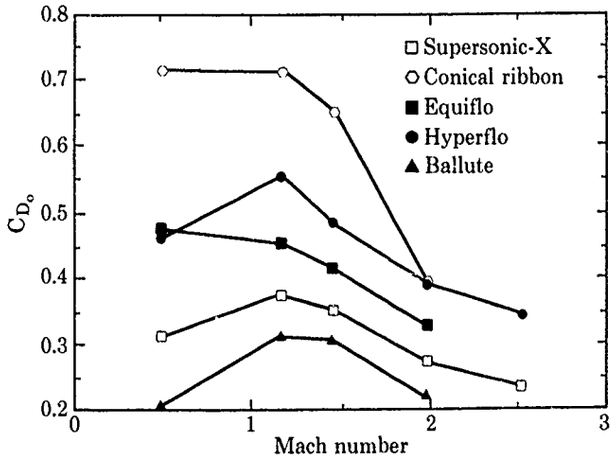


Figure 7.3 The effect of Mach number on the drag coefficient measured in a wind tunnel (taken from Ref. 4.24)

7.2.2 Pressure distribution

One of the first wind tunnel canopy pressure distribution tests of fully inflated, high-performance parachutes was conducted in 1959 by Sandia National Laboratories at the United Technologies Large Subsonic Wind Tunnel. To obtain data for stress analysis, static pressure measurements were made by Dickie[4.58] over the canopy of a 34-in.-diameter flat ribbon parachute of 25% geometric porosity in this 8-ft subsonic wind tunnel.

Niccum, Goar, and Lenius[4.62] tested steel models that simulated inflating hemisflo canopies (3.42-in. nominal diameter with porosities of 17% and 27%) and fully inflated, flat ribbon canopies (inflated mouth diameter of 1.94 in. with porosities of 15%, 20%, 25%, and 35%) at Mach numbers of 0.8, 1.2, and 3.0. These models were sting-mounted at the apex, and the sting housed the tubing for the pressure taps that were located internally and externally around the canopy. They also independently measured the mass flow through these model canopies. They took extensive shadowgraphs of the canopy flow field, both with and without model suspension lines.

The most comprehensive wind tunnel pressure distribution test of high-performance parachutes is that reported by Pepper and Reed.[4.7] They tested a model 3-ft-diameter conical ribbon parachute

of 10%, 15%, 20%, 25%, 30%, and 40% geometric porosities in two 7-ft by 10-ft subsonic wind tunnels at dynamic pressures of 35 to 600 lb/ft^2. Suspension line lengths of 1.0, 1.5, and 2.0 parachute constructed diameters and reefing line lengths of 19 in., 38 in., and 57 in. were tested. The first series of tests consisted of measuring the pressure distribution inside and outside the canopy at 46 orifice locations for infinite mass and canopy-inflated (either reefed or full-open) test conditions. The static pressure instrumentation consisted of two flexible, clear-plastic strip tubes (1/16 in. OD and 1/32 in. ID) glued and tied to each radial, alternating inside and outside the canopy and extending out aft of the vent. Notches were cut in the tubes at 23 radial stations on both inside and outside of the canopy. The flexible pressure tubing terminated in a Scanivalve; a pressure transducer scanned the 46 ports to record the pressure data.

Side view photographs were taken of each test configuration to determine canopy profile shape. Typical data from this test are given in Figures 4.36 through 4.38. The effects of porosity, suspension line length, and reefing line length on the canopy pressure distribution were carefully measured in this parametric test program. The second series of wind tunnel tests consisted of measuring the differential pressure distribution across the canopy during the inflation of a 25% porosity, 3-ft-diameter canopy after disreefing under infinite mass test conditions. Differential pressure is the pressure on the inside of the canopy minus the pressure on the outside of the canopy at the same canopy location. The suspension line length was 1.0 parachute constructed diameter and the reefing line length was 19 in. Seven Kulite differential pressure transducers were sewn to the inside of the canopy at seven radial stations distributed in a helical pattern from skirt to vent. Typical transient pressure data during canopy filling from a reefed condition are shown in Figure 7.4.

Klimas[5 75] extended the experiments of Pepper and Reed by testing 12% and 25% porosity, 3-ft-diameter conical ribbon parachute models in the Calspan Corporation's 8-ft Transonic Wind Tunnel at Mach numbers of 0.3, 0.6, 0.9, and 1.2 at a constant dynamic pressure of 225 lb/ft^2. The parachute models were attached to a 4-in.-diameter streamlined forebody that was cable-mounted on the wind tunnel centerline. The transient canopy differential pressure distribution was measured during inflation (after cutting the 9-in.-long reefing line) with six Kulite pressure transducers, which were recorded on magnetic tape. The transducers were sewn to the radials at equal intervals from near the vent to near the skirt, and they were evenly distributed circumferentially. Typical maximum pressure differential coefficient data are shown in Figure 7.5 as a function of Mach number for the two different porosities at a radial position 30% from the vent.

Roberts[4 55] measured the pressure distribution across 9-in.-diameter flat circular disks with one to eighteen concentric slots (porosities of 2% to 33%) in a 7-ft by 10-ft subsonic wind tunnel. He concluded that the Coanda or jet entrainment effects are dominant in the flow through and immediately behind low-porosity aerodynamic bodies such as disks or parachutes.

Henfling and Purvis[4 70] measured the pressure distribution across the surface of 1.8-in.-wide parachute ribbons at five chordwise points and several spanwise stations in a low-speed tunnel using flexible pressure tubing sewn to the ribbons. Variable reluctance differential pressure transducers were used to measure the five chordwise pressures for each test run at a given spanwise ribbon station. The transducer output was amplified and a Hewlett-Packard 1000 computer system was used for pressure data acquisition and reduction. Their data indicate that both the ribbon curvature and angle of attack have significant effects on the pressure-loading distribution.

The references cited provide additional insight on the techniques and instrumentation that may be used to make successful pressure measurements across a canopy. Minimizing the intrusion of the measurement instrumentation on the pressure field on the canopy is difficult because the fabric thickness is less than the thickness of the measuring device. Placing instrumentation away from the measurement location is recommended, but the displacement distance must be minimized in order to obtain valid transient pressure data. Each reference describes techniques having both strengths and weaknesses; no single approach serves all needs. Pressures measured on textile parachutes can be used to indicate trends and general levels expected on full-scale parachutes as long as the model parachutes do not stretch unrealistically during wind tunnel testing.

Pepper and Reed[4 7] and Klimas[5 75] are good sources of data on high-performance, conical ribbon parachutes for infinite mass conditions for both canopy filling from a reefed shape (nonsteady) and for canopy filled (either reefed or full-open). They investigated the effects of reefing line length, suspension line length, porosity, and Mach number on canopy pressure distribution. However, as noted in Section 4.3.2, the wind tunnel parachute models were so flexible that they significantly changed the effective porosity at these test dynamic pressures. Hence, these pressure data correlations should be used only to indicate trends.

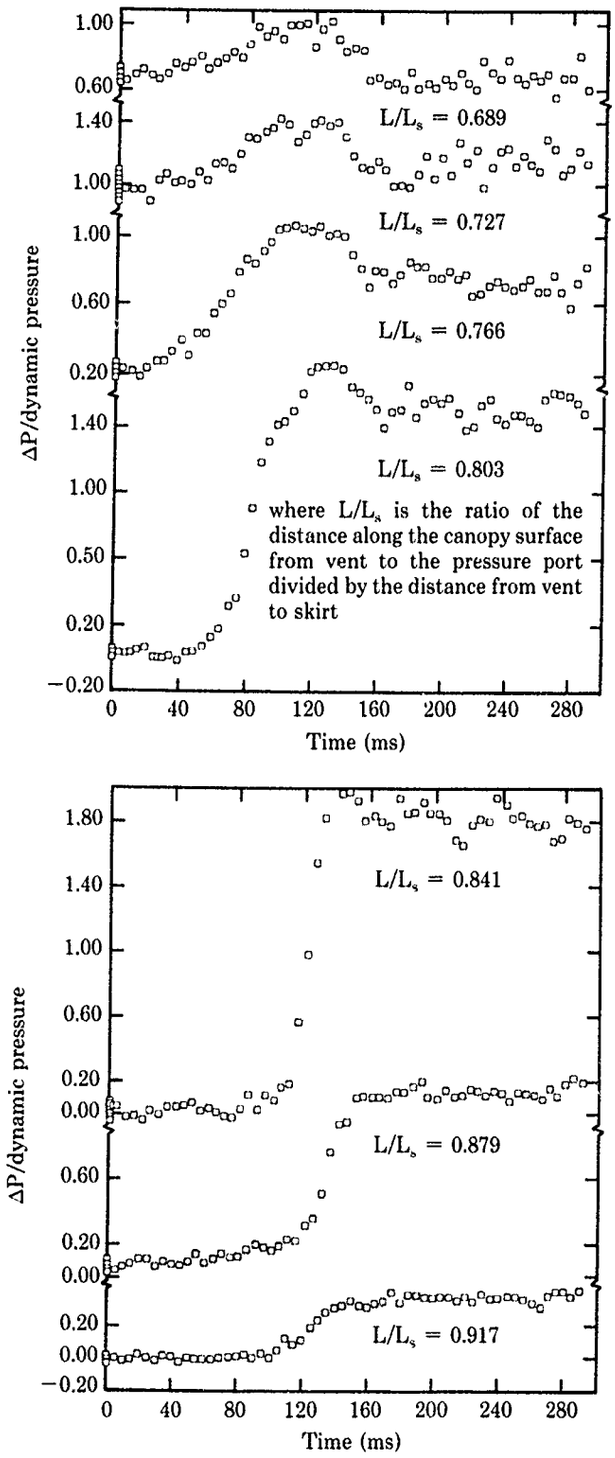


Figure 7.4 Transient pressure data for 3-ft-diameter ribbon parachute after disreefing from 19-in. reefing line length in LTV Low-Speed Wind Tunnel ($q=75$ lb/ft^2)

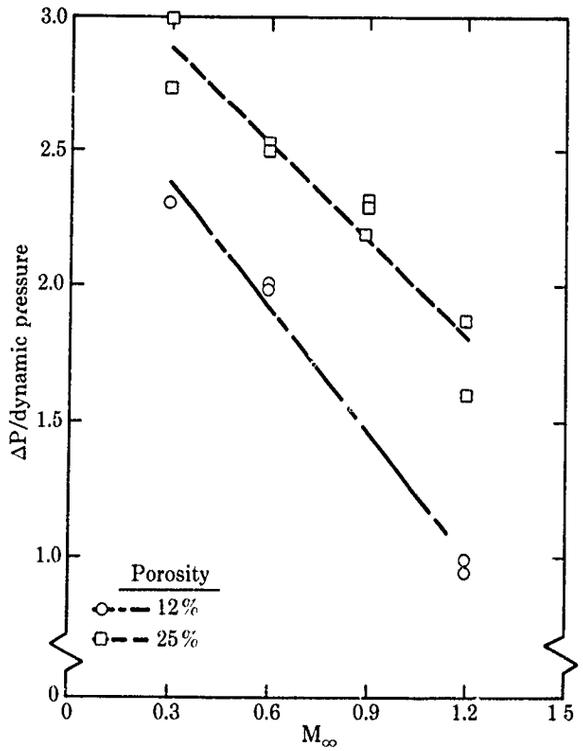


Figure 7.5 Transient differential pressure coefficients, $L/L_s = 0.30$

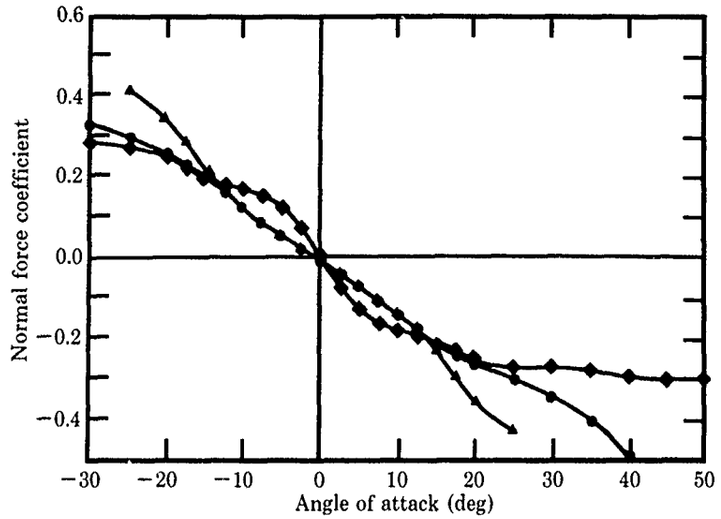
7.2.3 Stability

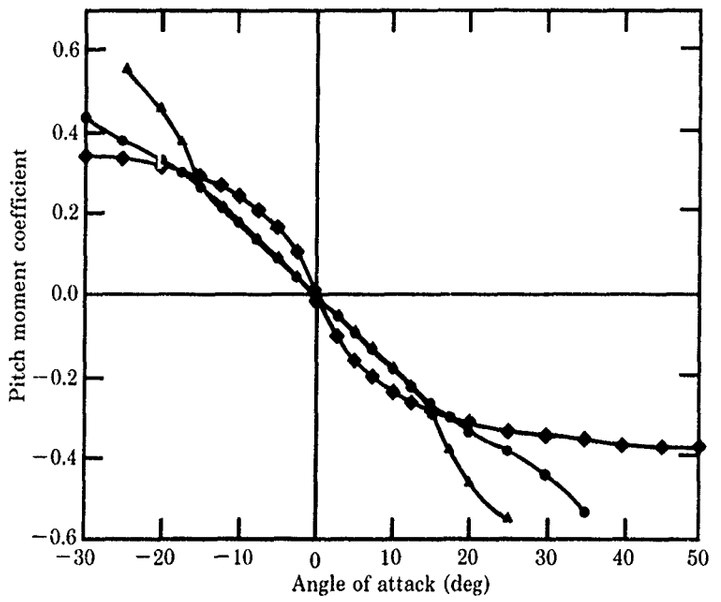
Heinrich[2.7] in 1947 conducted static stability tests of 1-ft-diameter guide surface parachute models in a low-speed subsonic wind tunnel. He measured the normal force, tangential force, and moment coefficient of both stabilization and brake-type guide surface parachutes. The amplitude of oscillation of the brake-type parachute varied from 2 to 5 degrees; the amplitude of oscillation of the stabilization parachute varied from 1.5 to 3 degrees, depending on the porosity.

Heinrich and Haak[4.1] measured the static stability of 12.6-in.-diameter guide surface and 16.6-in.-diameter ribbon and ringslot metallic and fabric parachute models in a low-speed wind tunnel. The test setup is described in Section 7.2.1. Typical normal force and pitching moment data for two fabric parachute models and one metallic guide surface model are presented in Figure 7.6.

Lingard, Barnard, and Kearney[4.24] measured the stability characteristics of 20-degree conical ribbon, equiflo, hyperflo, supersonic-X, and ballute parachutes at Mach numbers 0.5 to 4.35. The test setup is described in Section 7.2.1. Typical data on the amplitude of oscillation versus Mach number for the five parachutes are presented in Figure 7.7.

The paucity of wind tunnel data on parachute static stability shows the difficulty of measuring the pitching moment of a flexible canopy in a wind tunnel; hence, most parachute designers have relied on flight test data to verify their approximate estimates of parachute stability characteristics. In general, however, high-performance ribbon or guide surface parachutes are very stable, and the designer can rely on approximate estimates for the first design prior to the corroborating flight tests.





	Nominal porosity	Effective porosity
	(ft^3/ft^2 minimum)	
▲	120	0.042
●	30	0.010
■ Metallic	0	0.0

Figure 7.6. Characteristic coefficients vs. angle of attack for ribbed guide surface parachutes of various nominal porosities (taken from Ref. 4.1)

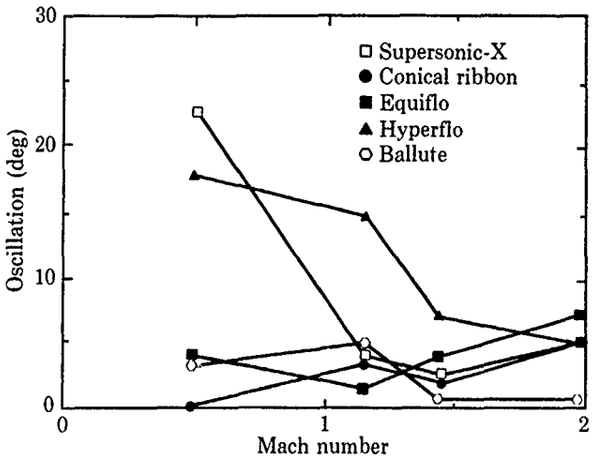


Figure 7.7 Effect of Mach number on parachute static stability (taken from Ref. 4.24)

7.2.4 Lifting parachute aerodynamic characteristics

Rychnovsky and Everett[3.15] conducted a series of tests of 3- and 4-ft-diameter lifting parachutes in the LTV 7-ft by 10-ft Low-Speed Wind Tunnel. The lifting ribbon parachute is described in Section 3.2.1.3 (see Figures 3.8 and 3.9b). The parachute model was attached to a single-component load cell that was supported in the test section by a streamlined horizontal strut. The load cell was free to rotate in the vertical plane so that it could align with and measure the axial force of the parachute. The parachute was photographed with a motion picture camera during the test, and the angle of attack was measured with a rotary potentiometer. The angle of attack and the axial load were measured during inflation and in steady state. The lift-to-drag ratio was obtained from the trim angle-of-attack condition. Collapse tests, in which the parachute was forced to rotate beyond its trim angle to its collapse angle, were also conducted. The most promising parachute model from these series of tests had a trim angle of 25 degrees, a collapse angle of 31 degrees, and an L/D of 0.47. They also discuss data from three-component force tests of 16-in.-diameter lifting parachute models tested in the University of Minnesota subsonic wind tunnel. They included six-component force data taken of 39-in.-diameter lifting parachute models in the LTV 7-ft by 10-ft subsonic wind tunnel. The special model support and strain gauge balance system is discussed later in Section 7.4. They also tested lifting parachute models in the Naval Ship Research and Development Center's 7-ft by 10-ft Transonic Wind Tunnel at dynamic pressures up to 400 lb/ft^2, where they measured trim angles of up to 31 degrees.

Bolton, Holt, and Peterson[3.19] discuss the results of wind tunnel tests of five 39-in.-diameter lifting parachute models in the LTV subsonic wind tunnel. Detailed measurements were made of canopy pressure distributions, suspension line forces, parachute stability, and damping characteristics. For the inflation tests, the model parachutes were attached to a model body suspended by cables in the center of the wind tunnel test section. The model parachute was reefed to a small diameter and allowed to stream behind the body as the wind tunnel was brought up to the desired test condition. An electrically fired explosive squib cut the reefing line to initiate inflation. Simultaneously with disreefing, a flash bulb was fired to mark the start of inflation in the high-speed motion pictures. Data were obtained from a body-mounted drag cell, which measured the total parachute drag force, and from 12 suspension line force gauges, which measured the line loads for pairs of suspension lines. The instrumentation and test setup are described in more detail in Section 7.4. Typical L/D data for the five lifting parachute configurations are presented in Figure 3.9a. The maximum trim angle measured was ~46 degrees and the maximum L/D was ~0.9.

Bolton, Holt, and Peterson[3.19] conducted full-scale wind tunnel tests of 13-ft-diameter lifting parachutes in the NASA-Ames 40-ft by 80-ft wind tunnel (see Figure 3.10). These tests were conducted to obtain comparative data on canopy lift, rolling moment, yaw damping, and inflation characteristics in a controlled environment. A full-scale payload (an ogive-cylinder with T fins) was mounted on the standard wind tunnel struts for this test. The forebody was 18 in. in diameter and 12 ft long. Potentiometers were used to measure the model pitch and yaw angles. Parachute axial force

and roll moment were measured by strain gauges located within the forebody. Croll et al.[3.18] provide further information on the forebody and the test setup. Measurements of parachute pitch, yaw, and roll relative to the forebody were made using small computer-controlled video cameras mounted on the model base. Croll et al.[7.7] provide additional information on the computerized video data system and present data plots of typical parachute performance. The dynamic behavior of the full-scale lifting parachute was also studied during inflation and during the return-to-trim position from a large initial yaw angle. High-speed film coverage, parachute loads, and forebody motion data were obtained for both inflation and yaw damping tests. More details of instrumentation and test setup are given in Section 7.4.

7.2.5 Aerodynamic heating

Schoeck, Hool, and Eckert[4.91] measured the bulk and local heat transfer on 2-in.-wide and 1/4-in.-thick test slats mounted in the test section (6 in. by 12.5 in.) of a subsonic-flow wind tunnel. The test slats were fabricated of aluminum strips attached to a Bakelite frame (for the overall upstream and downstream heat transfer measurements) and of Bakelite strips (for the local heat transfer measurements). They were spaced at different distances across the 12.5-in. test section width to vary the effective porosity of the simulated ribbon canopy. Iron-Constantan thermocouples were used to measure the transient temperatures. The transient heat transfer method was used to measure heat transfer coefficients on the test slat; this method consists of measuring the cooling rate of a body whose thermal conductivity can be considered infinite. The measurements covered the Reynolds number range from 0.03×10^5 to 0.6×10^5 and from 2.5×10^5 to 5×10^5, where the Reynolds number is based on ribbon/slat width and on the average velocity and properties in the slots between the ribbons. Their results are presented as Nusselt number versus Reynolds number and the data trends are consistent. The maximum local heat transfer coefficient, which exists at the upstream edge of the ribbon, was about twice the average value on the upstream side for the low Reynolds number tests and from four to five times the average value for the high Reynolds number tests.

Scott and Eckert[4.92] also conducted heat transfer studies on ribbons in the Heat Transfer Laboratory at the University of Minnesota. They used a pressurized wind tunnel to conduct tests on full-scale ribbons of flat circular parachutes with a geometric porosity of 20.5%. The wind tunnel test section was 6 in. by 8 in., and the average flow-approach velocity was 134 ft/s. Three stainless-steel test slats (instrumented with iron-Constantan thermocouples), each 2.1 in. high, 6 in. wide, and 0.312 in. thick, were mounted to resemble the array of ribbons in a ribbon parachute. The measurements were made at Reynolds numbers of one to ten million, where the Reynolds number is based on ribbon width and on the velocity and temperature of the flow in the slots between the ribbons. The pressure ratio applied to the ribbon was varied from 1.4 to 26.3. They used a transient energy balance to measure local and average heat transfer, which they compared with available analyses.

Corce[4.19] tested 5- and 8-in.-diameter nylon, Kevlar 29, and BBB material supersonic-X parachute models in a 50-in.-diameter, Mach 8 wind tunnel at AEDC to measure drag (see Section 7.2.1). The temperature limits of these materials (defined as 20% of the room temperature strength) are nylon, 860°R; Kevlar 29, 1210°R; and BBB, 1410°R. The tunnel is normally operated at a stagnation temperature of 1350°R to avoid liquefaction in the test section. The tunnel was operated at the stagnation temperature of 1350°R for tests of the BBB model only; the tunnel was operated at lower stagnation temperatures for the nylon and Kevlar parachute models so as to avoid thermal damage. Corce observed different drag coefficients as a function of stagnation temperature; he attributed the differences to the effect of temperature on the parachute material rather than to the fact that the wind tunnel was operating below the liquefaction limit of 860°R.

7.2.6 Stress measurements

Detailed discussions on techniques for making stress measurements are provided by Heinrich and Saari,[6.14] Konicke and Garrard,[6.16] and Garrard et al.[6.2] Heinrich and Saari measured the circumferential stress in a 5-ft-diameter ringslot canopy in a subsonic wind tunnel during parachute inflation under infinite mass conditions and in steady state. Konicke and Garrard measured the circumferential stress in a 4.64-ft-diameter, 20% porosity flat ribbon parachute in a subsonic wind tunnel. Garrard et al. measured the circumferential stress in an 18-in.-diameter, 25% porosity ribbon parachute in a subsonic wind tunnel. Omega gauges were used for stress measurements for all three wind tunnel tests. Additional testing details are presented in Section 6.3, and complete descriptions of the testing technique and instrumentation are given in the three references cited above.

7.2.7 Other parachute-related wind tunnel tests

Heinrich[7.8] measured the relationship between effective porosity and differential pressure of rigid steel and nylon ribbon grids of various geometric forms and geometric porosities in a subsonic mass

flow facility. The grid sample holder provides a total opening of 10 in^2; three to ten ribbons 1/4, 3/8, and 5/8 in. wide with geometric porosities of 0.125 to 0.50 were tested. He measured the effective porosities and the discharge coefficients.

Bacchus, Vickers, and Foughner[4,6] conducted tests of four different schemes to deploy a 1/8-scale model (6.75 ft in diameter) of the Space Shuttle Solid-Fuel Booster recovery system's drogue parachute in the NASA-Langley 16-ft Transonic Tunnel at a test Mach number of 0.17. The basic test objectives and experimental setup were described in Section 7.2.1. The deployment tests used the forward 40% of the SRB model mounted vertically on the tunnel floor; the angle of attack could be varied from 70 to 180 degrees. Two high-speed motion picture cameras were mounted on the tunnel's side wall. One camera viewed the SRB forebody for recording the nose cap ejections and drogue pack extractions. With the aid of timing marks, the film from this camera was also used to determine the velocities of the actual nose cap ejection. The second side wall camera was mounted farther downstream so as to view the canopy stripping action and canopy inflation. A third high-speed camera was mounted on the tunnel sting support system and viewed the complete sequence looking upstream. From analysis of the film, it was possible to evaluate each deployment based on the following criteria:

- Nose cap ejection velocity
- Nose cap clearance
- Nose cap behavior as a pilot drag device
- Drogue pack dynamics during drogue deployment
- Suspension line and canopy deployment characteristics

These testing techniques provided quantitative measurements of the dynamic performance of scaled models of the SRB drogue parachute deployment system in a controlled wind tunnel test environment. This in turn provided the SRB parachute system designers with valuable data for the selection of the optimum deployment system, because this dynamic performance is not amenable to calculation. This test is a good illustration of how a wind tunnel test can yield worthwhile quantitative information on the dynamic behavior of parachute systems during such transient processes as deployment, inflation, etc.

Heinrich and Madigan[7,9] developed a twin balance for measuring tangent, normal, and moment coefficients of each parachute in a twin cluster in a wind tunnel. The force sensing elements were bending beams with strain gauges. The two stings of the balance were joined at the front by a common pivot and supported at the rear by a circular arc. The pivot was connected to the upper and lower wind tunnel turntables by guy wires, and the arc was supported by posts to the turntables. The aerodynamic coefficients of the cluster can be calculated from the six component measurements of individual parachutes. A twin cluster of 12-in.-diameter solid cloth, flat circular parachutes was tested in a subsonic wind tunnel. The interference of each parachute upon the other was established and the aerodynamic coefficients of the cluster were determined. The interference effects were significant. New experimental techniques with the appropriate instrumentation should be developed to measure the aerodynamic coefficients of parachute clusters in a controlled wind tunnel test environment.

Wolf and Croll[7,10] conducted a series of tests of 3-ft-diameter conical ribbon parachutes in the LTV 7-ft by 10-ft subsonic wind tunnel to measure the drag and the force in parachute reefing lines during inflation to the reefed condition. The suspension line lengths tested were 1.0, 1.5, and 2.0 times the constructed diameter, and canopies with geometric porosities of 10%, 15%, 20%, and 25% were tested. The parachutes were attached to a cable-mounted forebody (3.25 in. in diameter and 30 in. long) suspended at the tunnel centerline. A 500-lb-capacity load cell, mounted to a gimbal, was attached to the aft end of the forebody to measure drag. The reefing line force was measured with a miniature tensiometer (a strain-gauged hollow tube, 0.6 in. long and 0.09 in. in diameter) bonded to the reefing line. All data were recorded simultaneously on analog magnetic tape for posttest analysis and on an oscillograph for monitoring purposes during the test. High-speed (400 frames per second) motion picture coverage was obtained with two orthogonal-view mounted cameras.

Prior to the test, a parachute model was rigged with an instrumented reefing line of lengths between 19 in. and 67 in. Next, a 9-in.-long reefing line with an electrically initiated line cutter was installed through the same reefing rings. After tunnel flow was established, a sequence timer was activated to start the high-speed motion picture cameras, trigger the event marker, and fire the reefing line cutter. The magnetic tape recorder and oscillograph were manually started before initiation of the sequence timer. Data were taken while the parachute inflated from its initial reefed condition (using a 9-in.-long line) to its next reefed (instrumented) condition. A photograph of the test setup is shown in Figure 7.8.

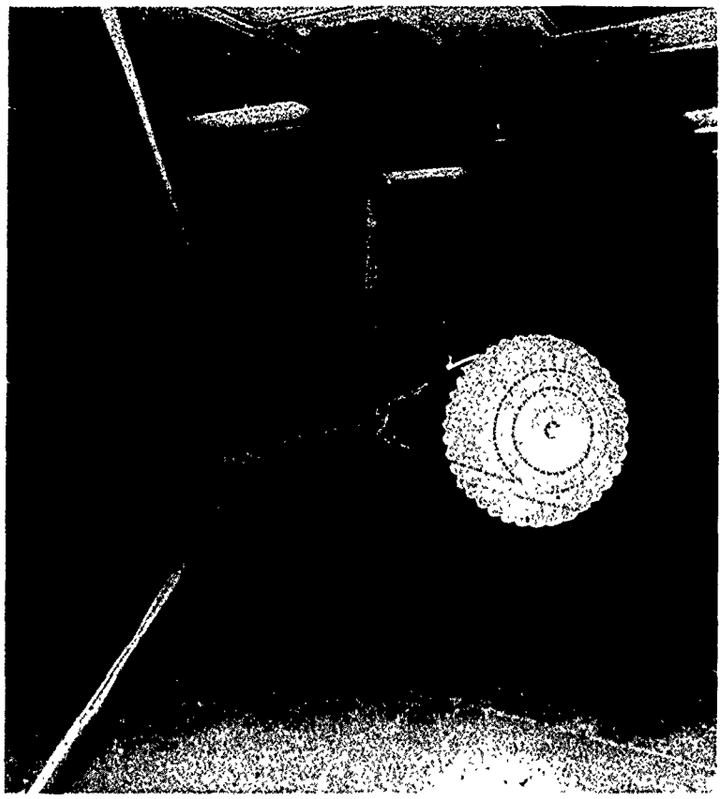


Figure 7.8. Reefing tests of 3-ft-diameter parachutes in LTV subsonic wind tunnel

Reduced data plots and tabular listings were obtained by digitizing (at 1000 samples per second) the analog magnetic tapes after the test using the Sandia Wind Tunnel Data Acquisition and Control System. Typical digital plots of drag and reefing line force during the disreefing event are shown in Figure 7.9. This parametric test series shows the effects of reefing line length (L_r), suspension line length (L_{SL}), and canopy porosity (λ_g) on the transient drag (F_a) and reefing line loads (T_r) while the canopy is filling to the reefed conditions. These data should be very useful for the preliminary design of a high-performance reefed ribbon parachute.

Higuchi[7.11] experimentally investigated the flow field past flat and curved grid models simulating segments of a ribbon parachute in low-speed wind tunnels. Flow visualizations (primarily oil flow) and surface pressure measurements were made to study the effects of the spacing ratio and the Reynolds number. A flow visualization study on the wake behind a ribbon parachute was conducted.

Higuchi[7 12] used a towing tank and a subsonic wind tunnel to study the wakes behind a solid disk, a slotted disk, a solid parachute model, and a ribbon parachute model. The structures of the unsteady wake patterns were measured and analyzed. In addition, the effect of rapid model deceleration on the wake was visualized. The wake vortices overtaking the decelerating disk model were documented.

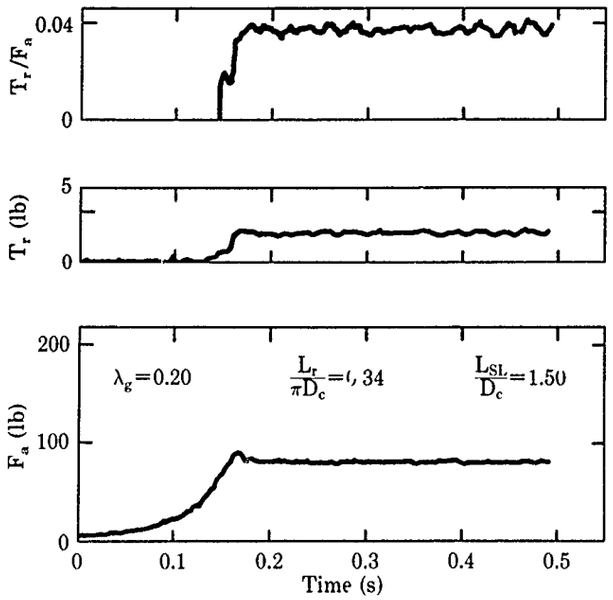


Figure 7.9. Sample digital data plot from LTV wind tunnel parachute reefing test

7.3 Wind tunnel blockage

The air flowing around a parachute in the sky is unconstrained—it goes where it pleases. The air flowing around a parachute being tested in a wind tunnel, however, is constrained by the walls of the test section. The presence of the walls alters the natural shape of the streamlines at that same distance from the parachute. In subsonic and transonic flows, the disturbance by the walls on those streamlines is communicated to the rest of the flow field, including regions directly upstream of the canopy and streamlines that flow into the canopy. In this manner, the "blockage" of the wind tunnel walls changes the airflow in which the parachute is flying. Since the parachute is a textile structure, these changes in airflow may cause changes in parachute shape. The data taken from wind tunnel tests where blockage is excessive are therefore incorrect because they were obtained from a distorted parachute shape flying at a different free-stream velocity than is usually measured in the tunnel. Cockrell[16] provides a good description of the effects of blockage caused by model parachute canopies.

Maskell[7,13] shows that the dominant effect of blockage constraint is a simple increase in the fluid's free-stream velocity, in part related to the volume distribution of the body itself, termed *solid blockage*, and in part related to the displacement effect of the wake, termed *wake blockage*. Cockrell notes that unless the blockage area ratio, which is defined as the ratio of the cross-sectional area of the body to the cross-sectional area of the fluid stream at the body location, is small (under 15%), the disturbance to the flow pattern around the body and its downstream wake, which is caused by blockage, is extreme. For bluff bodies such as parachute canopies, Cockrell recommends blockage areas of less than 5%. For blockage areas under 10%, Cockrell presents four methods for correcting the parachute drag coefficients for the wind tunnel blockage.

Baca[4,44] tested 15-in.-diameter solid and ribbon parachute models in clusters up to eight in the LTV 7-ft by 10-ft subsonic wind tunnel to determine the effects of canopy number, canopy type, riser length, and reefing on drag. Typical data are shown in Figure 4.29. Baca estimated the blockage and decrease in dynamic pressure by using the parachute's constructed diameter (assuming an imporous canopy normal to the flow) to calculate the blockage area of the model. He measured the dynamic pressure at 13 axial locations on the tunnel ceiling, with and without the full-open solid-canopy model installed. He then used the dynamic pressure measured at the axial station closest to the plane of the parachute skirt to calculate the blockage and the corrected drag coefficient. The increase in measured dynamic pressure and the blockage are compared to the estimates in Table 7.3. The measured blockage varied from 3.0% (one canopy) to 13.7% (eight canopies). In general, the measured dynamic pressure and the corresponding blockage were higher than the estimated values.

Macha and Buffington[7.14] measured the blockage of 6-ft-diameter, 20-degree conical ribbon parachutes of 7%, 15%, and 30% geometric porosities in six different wind tunnels (see Table 7.4). Note that the blockage ratios varied from 0.02 to 0.22 in the different wind tunnels. Single parachutes were tested in all six tunnels; clusters of two and three parachutes were tested in tunnels 1 through 3 only. The parachutes were attached to a single-component load cell mounted inside a 3.2-in.-diameter by 18-in.-long ogive-cylinder body that was positioned at the tunnel centerline using steel wires extending to the side walls of the tunnel. The base pressure was measured with twelve pressure orifices manifolded together, located on the outside centerline of each gore 12 in. from the apex. The orifices consisted of 0.035-in.-diameter holes drilled in 0.5-in.-diameter rigid plastic disks sewn to the outer surface of the canopy. The manifolded pressure tubing (one line) was attached to one of the suspension lines and this base pressure was measured with a pressure transducer. The inflated diameter of the parachutes was measured with high-speed motion picture cameras.

Table 7.3. Wind Tunnel Blockage and Dynamic Pressure Increase for Solid Parachutes

Number of Parachutes	Dynamic Pressure Increase at Ceiling (%)		Blockage	
	Estimated	Measured	Estimated	Measured
1	3.7	6.2	1.8	3.0
2	7.4	9.2	3.5	4.3
3	11.5	12.8	5.3	5.8
4	15.6	17.8	7.0	7.9
5	20.2	22.4	8.8	9.6
6	24.8	25.1	10.5	10.6
7	30.0	31.2	12.3	12.7
8	35.2	34.3	14.0	13.7

Table 7.4. Wind Tunnels Used in the Blockage Study

Wind Tunnel	Blockage Ratio
Lockheed 30×26 ft	0.019
NASA-Langley 14×22 ft	0.048
NASA-Lewis 9×15 ft	0.116
General Dynamics 8×12 ft	0.166
NASA-Ames 7×10 ft	0.217
LTV 7×10 ft	0.217

Macha and Buffington correlated their blockage data using the approximate correction method of Maskell,[7.13] which was developed for a variety of nonlifting two- and three-dimensional bluff bodies. Maskell gives the effective dynamic pressure (q) as

$$q/q_u = 1 + K_M \cdot \left[(C_D S)_u / C\right] \quad , \tag{7.1}$$

where C is the cross-sectional area of the wind tunnel, the subscript u indicates that the drag area ($C_D S$) data are uncorrected, and K_M is the bluff-body blockage factor for the model shape of interest. Since K_M is independent of the geometric blockage, the form is suitable for on-line correction during data reduction, even for parachutes where the inflated diameter may not be known a priori. Maskell indicates that the base pressure (near-wake pressure) is related to the bluff-body blockage factor by

$$K_M = -1/C_p \quad , \tag{7.2}$$

where C_p is the pressure coefficient. K_M can be evaluated for a particular parachute by directly fitting Eqs. 7.1 and 7.2 to drag or pressure measurements on models over a range of geometric blockage ratios.

Macha and Buffington summarize in Figure 7.10 the blockage data for single parachutes. The data are evaluated for three different porosities, from both drag and base pressure measurements, and from six different wind tunnels. The best fit of K_M for the three porosities is 1.85 for this ribbon parachute,

which compares with 2.8 for a nonporous disk and 3.4 for a sphere in subcritical flow. This correlation works very well for a wide range of blockage ratios and parachute porosities. They also present blockage data for two- and three-cluster systems; the derived K_M is 1.35 and 1.59, respectively.

In summary, it is recommended that engineers planning subsonic wind tunnel tests of high-performance ribbon parachutes use the blockage corrections of Macha and Buffington[7.14] to correct the measured drag for the flow-constraining influence of the wind tunnel walls. By measuring the base pressure of the parachute and using the correlation they propose, accurate opening-shock drag data can be obtained in subsonic wind tunnels for blockage ratios as high as 15%. This technique allows the use of larger parachutes in any wind tunnel, which alleviates fluid dynamic and structural scaling problems encountered when applying wind-tunnel-model data to full-scale flight. For determination of aerodynamic coefficients, the projected area of the inflated aerodynamic decelerator should generally not exceed 10% to 15% of the test section area.

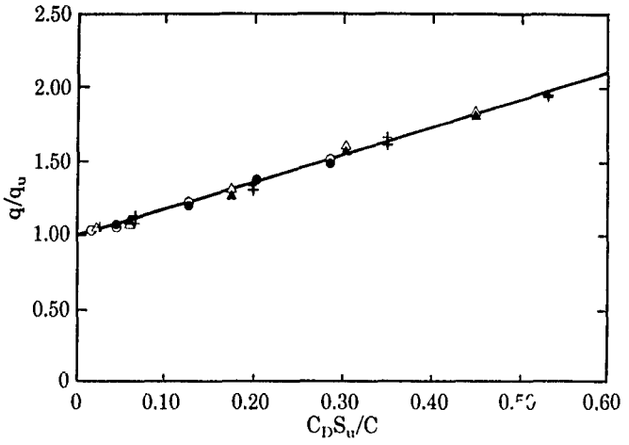


Figure 7.10. Effect of wall constraint on effective dynamic pressure for single parachutes

7.4 Special parachute instrumentation and testing methods

In general, there is a paucity of detailed information in the literature on special instrumentation or testing methods for parachute wind tunnel testing. Most authors emphasize the wind tunnel test results rather than the instrumentation or the testing method. Hence, the only references selected for this section were papers where these testing techniques were discussed in detail and the authors were familiar with the work. The reader is also referred to the other references in this chapter where some discussion of the testing technique is made.

Croll and Peterson,[3 17,7 15,7 16] Croll et al.,[7 7] and Croll et al.[7 17] describe in detail a computer-controlled video instrumentation technique for the wind tunnel testing of lifting parachutes. During testing of lifting parachutes, it was necessary to correlate the relative motion between the parachute and forebody to the loads exerted by the parachute on the forebody as a function of time during dynamic (deployment and filling) tests, disreefing, and for a full-open canopy. A computerized video instrumentation technique was developed to provide this correlation during a full-scale wind tunnel test of lifting parachute configurations. This instrumentation consisted of a small, rugged TV camera, mounted on the forebody base, which tracked the positions of two lights attached to the inside of the parachute canopy. The positions of the lights were digitized by an on-line minicomputer and converted to yaw, pitch, and roll angles relative to the forebody. These data were obtained 30 times per second and stored in disk memory along with instantaneous values of the axial force and rolling moment exerted by the parachute on the forebody. The motion-force correlations made it possible to determine the yaw damping of the lifting parachute and provided information on the specific sources

of rolling moments generated by the parachute. The lifting parachute is described in Chapter 3 and in Section 7.2.4 of this chapter. A photograph of a 13-ft-diameter lifting parachute being tested at the NASA-Ames 40-ft by 80-ft Subsonic Wind Tunnel is shown in Figure 3.10. The experimental wind tunnel setup is illustrated in Figure 7.11 and a block diagram of the instrumentation system is shown in Figure 7.12.

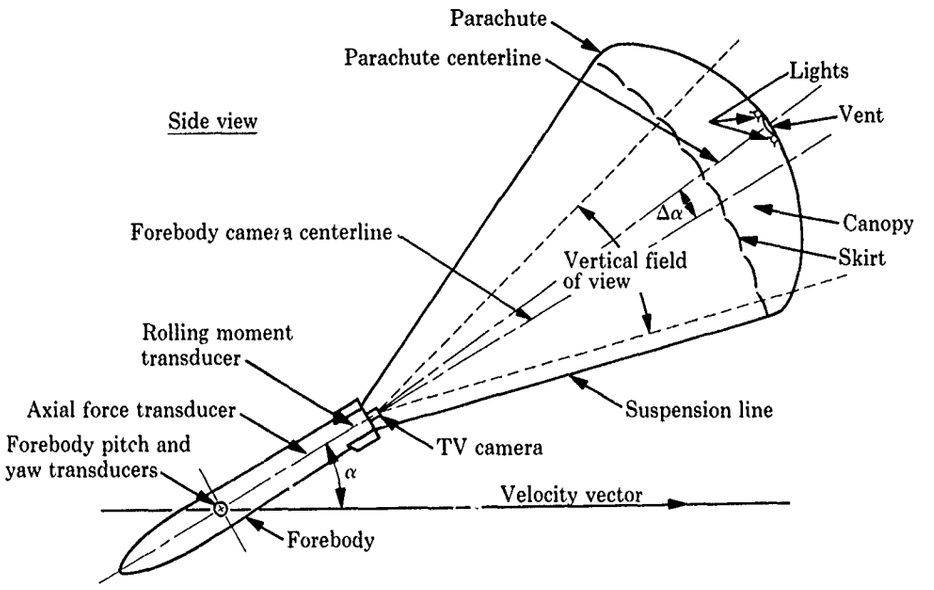


Figure 7.11. Experimental setup and instrumentation summary

Croll et al.[77] summarize most of the testing methods used at Sandia to obtain wind tunnel data for high-performance parachute designs. Figure 7.13 shows a sting support rig developed for testing 39-in.-diameter parachutes in the LTV 7-ft by 10-ft Low-Speed Wind Tunnel. It consists of a six-component (normal force, pitching moment, side force, yawing moment, rolling moment, and axial force) balance mounted aft of the canopy with a pipe projecting through the parachute vent to support a streamlined body to which the parachute suspension lines are attached. The parachute was installed on the sting unit at a roll angle of 90 degrees to provide a large sweep in pitch angle through the tunnel turntable and a smaller yaw sweep through the standard pitching-strut mechanism. This system yielded parachute forces and moments as functions of pitch and yaw angles, as well as parachute trim angle.

A sketch of a typical cable support rig is shown in Figure 7.14. Forebodies up to 36 in. long with diameters up to ~4.5 in. were supported by cables at zero angle of attack and used to measure drag when parachutes had to have freedom of movement. Drag links internally mounted on gimbals, small roll-drag balances, or a full six-component balance were used to obtain the required data. This type of rig was used extensively to measure steady-state roll, roll and/or drag, and six-component forces and moments, respectively. Disreefing and inflation tests were also done with cable rigs. Variations of this cable rig were developed for the LTV, Calspan, NSRDC, and NASA-Langley facilities.

A photograph of a strut support rig used for small-scale testing is shown in Figure 7.15. Most Sandia small-scale lifting parachute testing was done on this strut support rig because it was the most suitable rig for force, dynamic, and parachute position measurements. This rig, with a 4.5-in.-diameter and 36-in.-long forebody, was used in the LTV 7-ft by 10-ft tunnel. A six-component balance, specifically designed to measure parachute forces and moments, was incorporated into the base of the strut-mounted forebody model. A rod mounted on a transverse bearing, through the approximate full-scale center-of-gravity location, attached the model to the two faired struts while a rear-located push rod controlled angle of attack. This rig was mounted on the standard tunnel turntable to allow variable yaw angle.

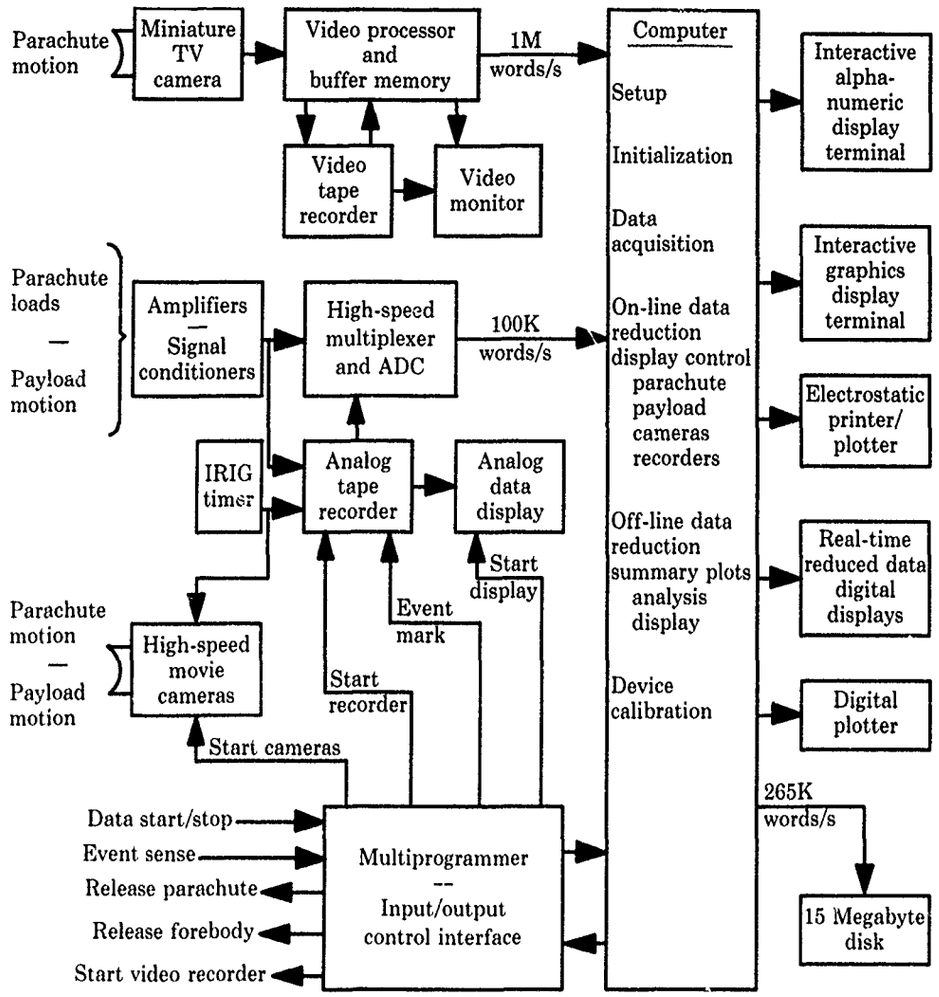


Figure 7.12. Block diagram of instrumentation system

Figure 7.16 shows a strut support rig used for full-scale testing. This full-scale support rig (shown with an 18-in.-diameter forebody model) was used in the NASA 40-ft by 80-ft tunnel with a 13-ft-diameter lifting parachute; the rig is similar in operating principle to the LTV strut-mounting system. A photograph of the inflated parachute in this tunnel is shown in Figure 3.10 and the test setup is described in Section 7.2.4. The forebody model was free to pitch from +30 degrees to −45 degrees and could yaw ±20 degrees. The forebody could also be locked at zero yaw angle for unstable parachutes or to limit the system's degrees of freedom. The parachute's axial force and rolling moment were measured by strain gauge load cells located within the forebody. The angular position of the forebody relative to the tunnel axis was measured by geared potentiometers placed at the pivot point of the forebody. The tunnel's standard external balance system was used to measure the six-component force and moment data for the entire configuration. Parachute-only data were obtained by subtracting out the forebody and strut support tares.

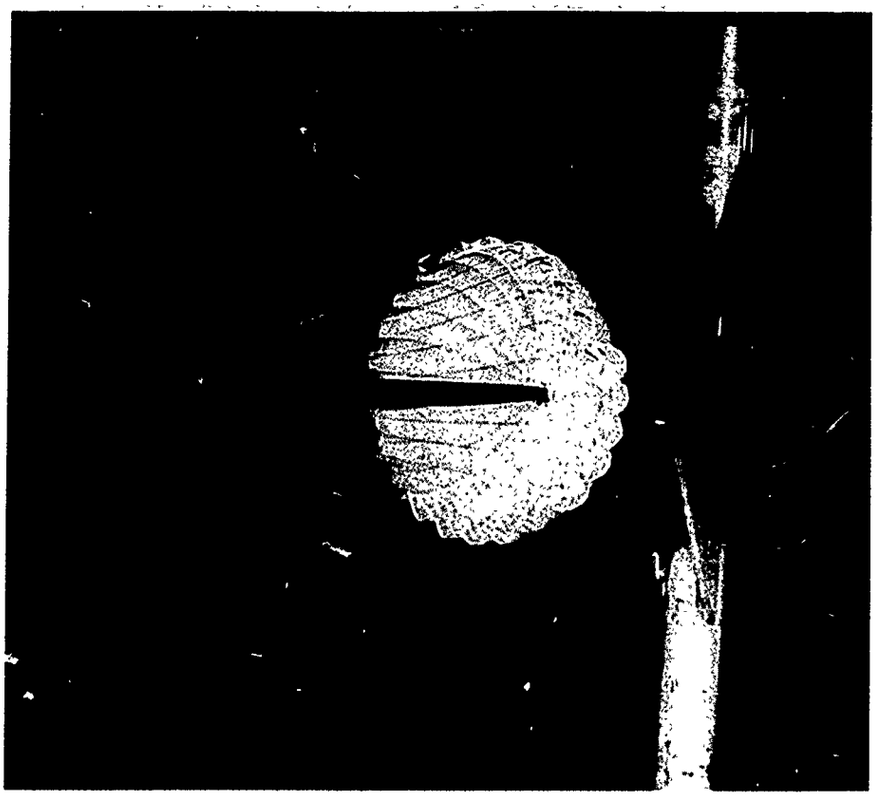


Figure 7.13. Sting support rig for testing parachutes in the LTV Low-Speed Wind Tunnel

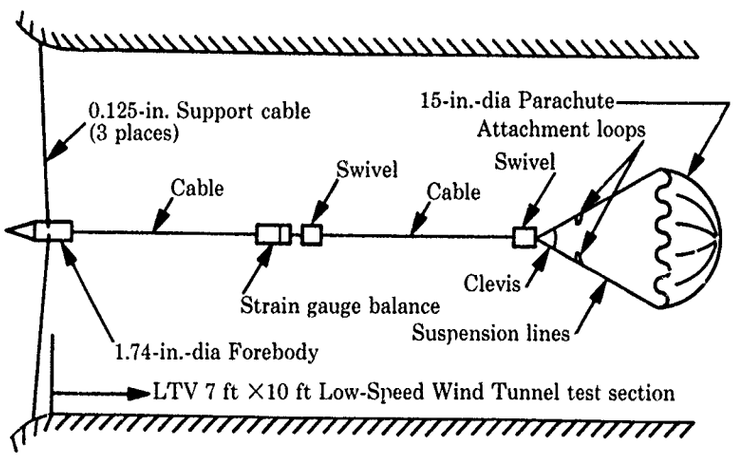


Figure 7.14. Cable rig for parachute drag

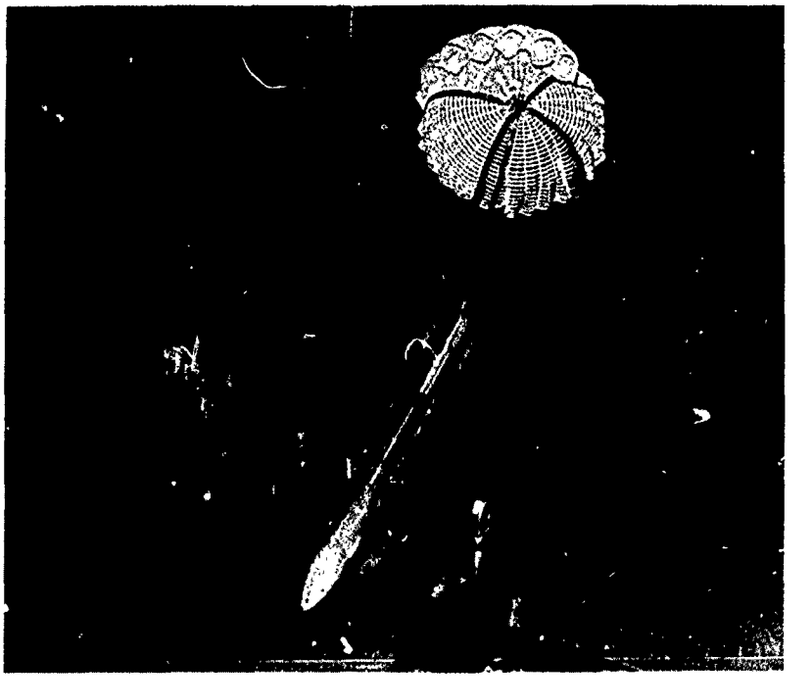


Figure 7.15. Strut support rig for testing parachutes in the LTV Low-Speed Wind Tunnel

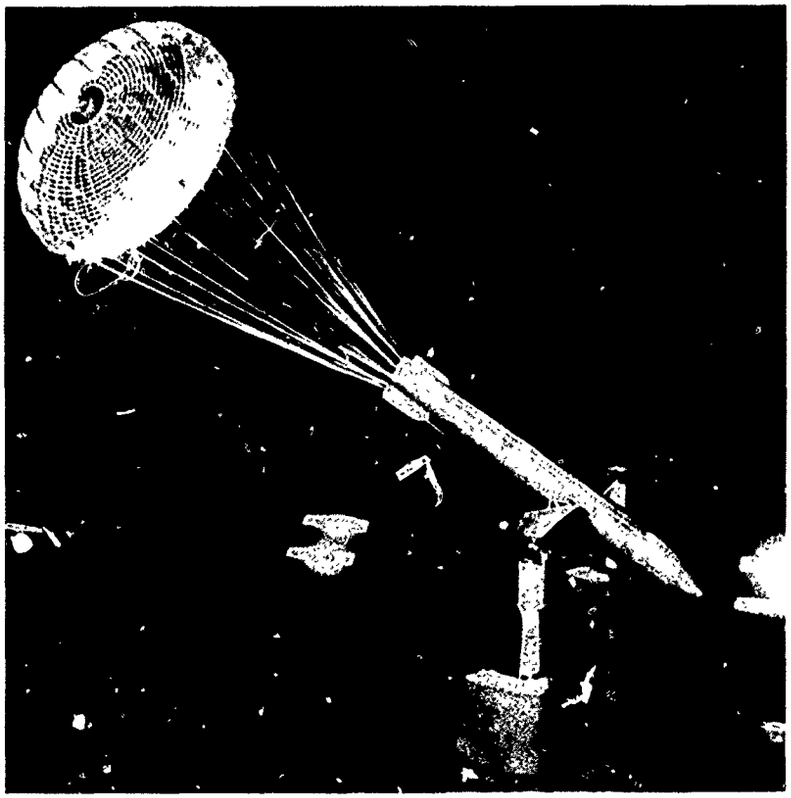


Figure 7.16. Strut support rig for testing full-scale parachutes in the NASA-Ames 40-ft by 80-ft Subsonic Wind Tunnel

7.5 Model parachute design and fabrication

In 1948, Knacke[2.4] identified the difficulties of testing FIST (flat ribbon) parachutes in a wind tunnel:

> Extreme care is a prerequisite for the evaluation of wind tunnel data obtained from model FIST parachutes. It is very difficult to build small parachute models, of diameters ranging from 1 to 2 feet, with adequate dynamic and geometric similarity. Both canopy shape and individual ribbon position are of prime importance. The individual ribbons of a FIST become distorted during inflation and stimulate uniform flow separation. Very small textile models of relatively stiff ribbons do not exhibit this characteristic in scale. The effect is entirely lost with sheet metal models. Furthermore, very small scale models require high porosity values. Experiments with textile models of diameters of 3 to 4 feet will result, however, in useful and transferable data.

Subsequent experience with wind tunnel testing of scale-model ribbon parachutes during the last 30 years verifies Knacke's observations. In order to obtain meaningful data from subscale parachutes in a wind tunnel and apply the data to full-scale flight parachutes, both aerodynamic and structural scaling laws must be observed. Since parachute growth rate during the initial phase of inflation is dominated by bending stiffness, particularly in the skirt region, the stiffness of the wind tunnel model in relation to the aerodynamic stresses in the parachute must be taken into account. The static fold height of a sample specimen is a convenient parameter that can be used to determine if the correct stiffness has been achieved.

Schmidt and Fu[7.18] applied the π-theorem of dimensional analysis to identify similarity parameters to describe the physical processes of parachute flight. They developed dimensionless parameters, which included fluid parameters such as velocity and parachute parameters such as size and modulus of cloth elasticity, for scaling down parachutes to simulate both the steady-state descent and the filling process for full-scale parachutes.

Bacchus, Vickers, and Foughner[4.6] applied the laws of dynamic similarity to establish scale factors for the Space Shuttle SRB nose cap, drogue parachute (6.75-ft-diameter wind tunnel model) and the flow conditions for tests in the NASA-Langley 16-ft Transonic Propulsion Wind Tunnel. They scaled the porosity of the conical ribbon drogue parachute to provide the same drag coefficient as the full-scale, 54-ft-diameter parachute. They also considered the stiffness index of the scale-model ribbon parachute.

Weber and Garrard[7.19] tested several ribbon parachutes (12- and 15-in.-diameter) of the same geometric porosity but different flexibility in the University of Minnesota's subsonic wind tunnel under steady-state conditions. They found that the number of gores was a dominant factor influencing inflated canopy shape. No correlation was found between model flexibility and measured aerodynamic performance.

Klimas, Widdows, and Croll[7.20] developed a modular asymmetric parachute for wind tunnel testing in order to conduct parametric studies by varying geometric porosities in the side and bottom gores of a 24-gore conical ribbon lifting parachute 40 in. in diameter. The top 7 gores were lined to develop lift. The test program in the LTV 7-ft by 10-ft wind tunnel called for 100 model parachutes to test all of the combinations of porosities. A modular construction method, consisting of gore panels that fit together with nylon zippers, was developed. The zippers were sufficiently strong, flexible, and narrow to approximate conventionally constructed radials. Each canopy comprised four "zip-in panels," two 7-gore (top and bottom) panels, and two 5-gore (side) panels. This type construction required ten 5-gore and nine 7-gore panels to make the 100 different canopies, and represented about a 20-fold saving in gore panels over conventional constructions. This modular model parachute fabrication technique has been used since 1981 at Sandia to conduct other wind tunnel tests; in recent years, it has been used especially for symmetrical ribbon parachutes.

Lingard, Barnard, and Kearney[4.24] fabricated 4.3-in.-diameter Kevlar conical ribbon, equiflo, hyperflo, supersonic-X, and ballute parachute models for wind tunnel tests at Mach 0.5 to 4.35. The design of each of these parachutes is discussed in their paper.

7.6 Conceptual design of a parachute wind tunnel for nonsteady testing

Maximum payload decelerations with high-performance parachutes are about 200 g, and peak design loads can exceed 500,000 lb. For many large parachutes, peak loads occur while the parachute is in the early stages of inflation, typically at an inflated diameter that is only 30% of the fully open diameter. The time from parachute deployment to full inflation is very short, and the oncoming airstream velocity decreases significantly while the parachute is inflating. The nonsteady fluid

dynamic effects, which account for the added mass of entrained air in the equation of motion for high-performance systems, can contribute loads as large as the quasi-steady drag (i.e., the drag calculated using the instantaneous parachute shape, size, and drag coefficient). Further, the parachute wake, generated near the deployment velocity, can overtake the decelerating canopy/payload and cause parachute collapse. A typical force-time history for a high-performance parachute is shown in Figure 7.17. Note that the total drag is ~50% higher than the quasi-steady drag, and the peak load occurs with the parachute only about 30% open. With performance and inflation characteristics like this, it is easy to conclude that the important phenomena associated with high-performance parachute inflation are dominated by nonsteady effects.

Parachute nonsteady aerodynamics

Total drag force = "steady" drag + "nonsteady" drag

$$D = [C_D(t)][S(t)][\tfrac{1}{2}\rho V^2(t)] + \frac{d}{dt}(m_f V)$$

where m_f is the added mass of entrained air

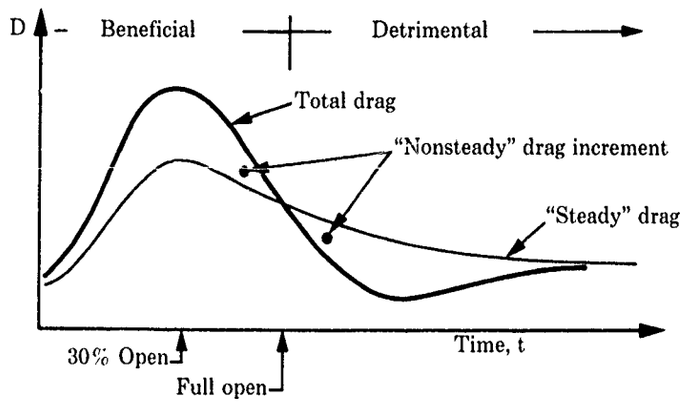


Figure 7.17. The effect of nonsteady aerodynamics on parachute drag

At the present time, no ground-based experimental facilities are available to simulate the nonsteady aerodynamic environment experienced by high-performance parachute systems under realistic deployment conditions. Flight testing does not permit all of the important data, such as canopy pressure or stress distributions, to be obtained because of experimental constraints. In addition, flight data are subject to uncertainties introduced by locally varying winds. Infinite mass testing, with the oncoming velocity constant instead of decreasing, is not able to simulate the important coupling between deceleration and inflation. Finally, computational codes that can accurately predict the dynamics of a compliant structure in nonsteady, three-dimensional flow do not exist, and it is doubtful that such codes can be developed without benchmarking data from a nonsteady wind tunnel. What is needed is a wind tunnel designed specifically to test parachutes, one in which the model under test is allowed to decelerate as it inflates. Sandia has commissioned a conceptual design study of such a facility with DSMA International, Missisauga, Ontario, Canada. The results of this joint Sandia/DSMA conceptual design are discussed by Aeschliman et al.[7.21] and are summarized in this section.

Macha[7.22] developed similarity parameters for testing model parachutes in a nonsteady wind tunnel. He derived the similarity parameters from the set of equations describing the inflation dynamics of the parachute canopy and the resulting deceleration of the parachute/payload system. The equation of motion for the system yields the relationships among the primary variables of mass, time, velocity, and linear dimension. Consideration of the radial momentum equation of the inflating canopy introduces additional similarity parameters involving material properties such as canopy mass and the tensile elasticity and bending stiffness of the fabric. From these primary Froude number and mass ratio scaling laws, Macha concludes that time in the model system, like velocity is proportional to the square root of the linear dimension. He also shows that deceleration is the same in both the model and prototype systems, and that model forces scale as the fluid density, the square of the linear dimension, and the square of the velocity.

As an example of the application of these scaling laws, consider a prototype system with a payload weight of 750 lb, a parachute constructed diameter of 24 ft, a deployment velocity of 650 ft/s, and a measured peak deceleration of 30 g. A constructed parachute diameter of 5 ft is chosen for the model system. Therefore, the scaled deployment velocity and payload weight are 297 ft/s and 6.8 lb, respectively. The peak deceleration of 30 g is the same for the model as for the prototype, but the parachute opening time for the model is about half the opening time of the prototype. At the high decelerations typical for high-performance parachutes, the gravitational force has a negligible influence on system dynamics during the inflation process. This generally allows relaxing the requirement for Froude number scaling, so that the velocity becomes a free parameter that is no longer tied to model scale. This offers several advantages for wind tunnel testing. If compressibility effects are considered important, the Mach numbers can be matched and a strict requirement for matching model acceleration can be relaxed.

A number of basic facility characteristics for a parachute wind tunnel were specified by Sandia. Macha's studies of scaling laws and parachute material properties dictated a minimum constructed diameter of 5 ft for the model parachute. A study of blockage effects of parachutes in steady-flow wind tunnels showed that, for models of this size, a minimum test section area of 200 ft^2, preferably in the shape of a circular or near-circular cross section, is required. Maximum airspeed of at least 450 ft/s was specified. Also specified was that transonic testing speeds be studied to determine whether they could be achieved at reasonable cost. The minimum model acceleration was specified as 30 g. The feasibility of a variable density facility was to be examined, and a choice between continuous and intermittent facilities was to be made. The tunnel would be capable of steady-state testing in addition to its primary mission of nonsteady flow testing; however, this steady-state testing capability should not be the cost driver.

DSMA studied three basic design types of facilities for nonsteady testing: fixed airspeed with model accelerating downstream, fixed model with decelerating airspeed, and a combination of these approaches. They developed a one-dimensional method of characteristics solution to the transient flow problem for a tunnel in which the airspeed is reduced. Test section lengths of 20 and 40 ft, with speed control by downstream choke, were inputs to the predictions. Results showed that, for high-performance parachute models, there are significant velocity transients in time and space in the 20-ft test section, but they become unacceptably large in the 40-ft test section. A 20-ft length is considered too short from the viewpoint of interaction with the choke flow field. Further, the decelerating airstream concept violates both kinematic and dynamic similarity with the actual flight environment. The pressure distribution over the model and the streamlines of the tunnel flow field are not identical to those in flight, because the deceleration is not uniform along the length of the test section (as required by a true Galilean transformation). Wind tunnel designs with decelerating test section velocity were discarded for these reasons.

Initially, the continuous wind tunnel was included as a study candidate since it would easily meet the secondary requirement of steady-state testing. However, this continuous wind tunnel option was quickly discarded because of the enormous power requirements and greatly increased shell costs, especially for the variable density option. Also, the short parachute inflation times (1 to 2 s) were ideally matched to an intermittent operation mode.

The design type selected is a wind tunnel to be operated in steady state, at constant dynamic pressure, while the parachute is deployed from rest and allowed to accelerate downstream through the tunnel. The tunnel airspeed would correspond to the scaled deployment velocity for the model parachute, and the velocity-time history would be given by the wind speed in the model's frame of reference. Two concepts were considered. The first was to allow the parachute to free-fly with a payload mass scaled from the full-scale payload mass. The parachute is essentially self-powered, and no control during the test is required or even possible. However, the requirement to specify payload mass, which for many simulations may be only a few pounds, imposes a severe design constraint on the free-flying instrumentation and data storage system. The second concept was to support the parachute from a model cart that moves downstream with the parachute. The motion of the cart must be controlled such that the cart exerts the same force on the parachute as would be exerted by the scaled payload mass if the parachute were free-flying. This approach has a great advantage in that any desired acceleration-time or force-time history can be generated, and the constraint on the size and mass of the instrumentation and data storage (or transmission) system is essentially eliminated. The model cart concept was chosen because of its inherent advantage, recognizing that the propulsion and control of the cart is a technically difficult design. Aeschliman et al.[7,21] discuss the control issues and instrumentation.

The design drivers relating to facility operation were that the parachute wind tunnel be as simple as possible to operate and maintain (minimal manpower requirements, operation costs, and turnaround time) and that the safety hazards to personnel be minimized. An initial specification of 30 minutes turnaround time (between test runs) was subsequently relaxed to 60 minutes, primarily to reduce compressor costs. However, it was estimated that since most model changeouts would require about an hour, the increased turnaround time would not greatly affect overall tunnel productivity.

Three drive systems were considered for the intermittent tunnel: indraft, injector, and blowdown. The technology for each is well established. The indraft and injector systems have the advantage of greater simplicity and lower installation and operating costs; the blowdown design offers the advantages of variable-density operation and the widest operating envelope. Based on a comparison of the relative cost and capabilities of these three options, an injector-driven design was tentatively selected. The test section diameter is 16 ft and the test section length is 100 ft, with an overall wind tunnel length of 408 ft. Six 28-in.-diameter injectors would be used to drive the tunnel (Figure 7.18). Injector air is supplied at a pressure of 300 lb/in^2 from 34,000 ft^3 of storage. An option that was identified in the study is the use of slotted walls and a coaxial plenum. This option, which could be incorporated at relatively little additional installed cost, provides the potential for transonic testing up to Mach 1.15.

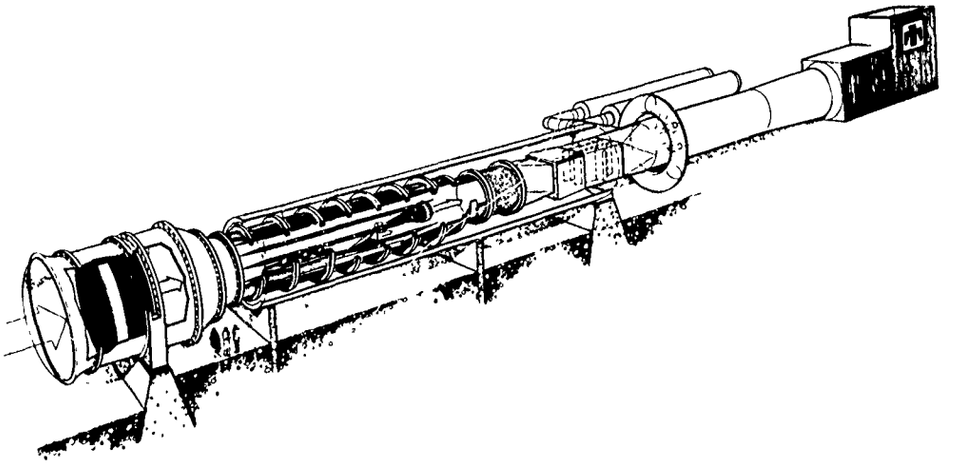


Figure 7.18. Perspective drawing of a transonic, injector-driven parachute wind tunnel

The transonic, injector-driven parachute wind tunnel design is shown in perspective in Figure 7.18. The model cart and drive are conveniently located in the outer 26-ft-diameter plenum, between adjacent slots. Various options for the cart propulsion were studied; an electomagnetic drive system, modeled after a newly developed launcher for carrier-based aircraft, appears to be the most promising. Flow control is provided by a downstream choke and is expected to provide adequate airspeed control over the Mach number range 0.1 to 1.15. Figure 7.19 shows the expected performance envelope (run time vs. Mach number) for both the subsonic and transonic versions of the parachute wind tunnel.

This concludes the chapter on wind tunnel testing. Parachute aerodynamicists have proved that valuable design data on high-performance parachutes can be obtained in steady-flow wind tunnels if the test is carefully planned with the right test setup (to simulate full-scale performance) and adequate instrumentation, including secondary instrumentation to help interpret and validate the primary instrumentation. However, a large nonsteady parachute wind tunnel is needed to test high-performance parachutes under simulated rapid payload deceleration and controlled test conditions.

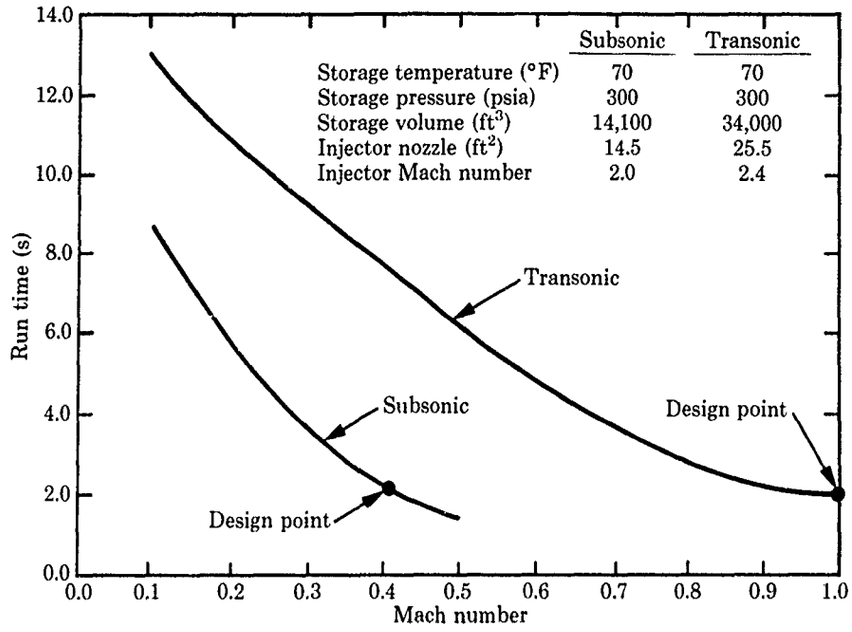


Figure 7.19. Injector wind tunnel performance envelope

References

7.1 F. E. Peñaranda and M. S. Freda, *Aeronautical Facilities Catalogue, Volume I—Wind Tunnels,* NASA RP-1132, January 1985.

7.2 *Test Facilities Handbook,* Twelfth Edition, Arnold Engineering Development Center, Arnold Air Force Station, Tennessee, March 1984.

7.3 W. B. Pepper and H. N. Post, "Wind-Tunnel Tests of Small Decelerator Stabilizers," *J Aircraft,* Vol. 8, No. 2, February 1971.

7.4 R. H. Landon, "Results to Complete the Programme on 1 Ft. Research Parachutes Deployed in the ARA Transonic Tunnel," Aircraft Research Association Limited, Model Test Note M39/2/4, December 1971.

7.5 B. K. Baca, *An Experimental Study of the Performance of Clustered Parachutes in a Low-Speed Wind Tunnel,* SAND85-0813, Sandia National Laboratories, December 1985.

7.6 B. A. Engstrom and R. A. Meyer, *Performance of Trailing Aerodynamic Decelerators at High Dynamic Pressures,* Part III: Wind Tunnel Testing of Rigid and Flexible Parachute Models, USAF WADC TR 58-284, 1959.

7.7 R. H. Croll, D. E. Berg, C. S. Johnson, and G. J. Smith, "Computerized Video Instrumentation Technique for Wind Tunnel Testing of Parachutes," AIAA 81-1929, October 1981.

7.8 H. G. Heinrich, "The Effective Porosity of Ribbon Grids," *Z. Flugwiss.* 14 (1966), Heft 11/12.

7.9 H. G. Heinrich and D. K. Madigan, "A Method of Measuring Aerodynamic Coefficients of a Twin Parachute Cluster," University of Minnesota under Sandia Corporation Contract 04-8811, Technical Report, April 1978.

7.10 D. F. Wolf and R. H. Croll, "Wind-Tunnel Measurements of Dynamic Reefing Line Force in Ribbon Parachutes," *J Aircraft,* Vol. 18, No. 1, January 1981.

7.11 H. Higuchi, "An Experimental Investigation of the Flow Field Behind Grid Models," AIAA 86-2460, October 1986.

7.12 H. Higuchi, "Flow Visualization Studies of Wake Behind Axisymmetric Bluff Bodies, Including Parachute Canopy Models," AIAA 89-0898, April 1989.

7.13 E. C. Maskell, *A Theory of the Blockage Effects on Bluff Bodies and Stalled Wings in a Closed Wind Tunnel,* ARC R&M 3120, Aeronautical Research Council, United Kingdom, November 1965.

7.14 J. M. Macha and R. J. Buffington, "Wall-Interference Corrections for Parachutes in a Closed Wind Tunnel," AIAA 89-0900, April 1989.

7.15 R. H. Croll and C. W. Peterson, "A Computer-Controlled Video Instrumentation Technique for Wind Tunnel Testing of Full-Scale Lifting Parachutes," AIAA 78-785, April 1978.

7.16 R. H. Croll and C. W. Peterson, "A Novel TV Instrumentation Technique," *Sandia Technology,* SAND78-1209, July 1978.

7.17 R. H. Croll, P. C. Klimas, R. E. Tate, and D. F. Wolf, "Instrumentation and Techniques for Parachute Wind Tunnel Testing," IEEE Publication 79 CH 1500-8 AES, September 1979.

7.18 U. Schmidt and K. H. Fu, *The Theory of Similitude and Theoretical Considerations Concerning Parachute Model Laws,* DFL-Bericht Nr. 0469, Braunschweig, West Germany, May 1968.

7.19 T. Weber and W. L. Garrard, "The Effects of Flexibility on the Steady-State Performance of Small Ribbon Parachute Models," AIAA 81-1923, October 1981.

7.20 P. C. Klimas, H. E. Widdows, and R. H. Croll, "Modular Asymmetric Parachute for Wind Tunnel Testing," *J Aircraft,* Vol. 20, No. 1, January 1983.

7.21 D. P. Aeschliman, J. M. Macha, D. D. McBride, G. M. Elfstrom, D. H. v. n Every, and R. Fedoruk, "Conceptual Design of a Parachute Wind Tunnel," 70th Semi-Annual Meeting of the Supersonic Tunnel Association, Preston, Lancashire, England, October 11-12, 1988.

7.22 J. M. Macha, "Similarity Parameters for Model Parachutes," Lecture Notes, Parachute Systems Technology Short Course, Framingham, Massachusetts, sponsored by Aerospace Engineering Department, University of Minnesota, June 11-15, 1990.

CHAPTER 8

PARACHUTE MATERIALS

8.1 Background

Knacke[8.1] summarizes the improvements in textile fibers from pre-World War II to 1989 (see Figure 8.1). Before World War II, silk was the primary material used for personnel and high-performance parachutes. Silk was replaced by nylon, which became available in the early 1940s. During the past 40 years, nylon fabrics have been used extensively as parachute materials.

Ewing, Bixby, and Knacke[1.7] and the Parachute Design Guide[2.1] provide excellent descriptions (with the significant references) of the materials used for fabricating all classes of parachute systems up through the mid-1970s. The Parachute Design Guide[2.1] gives good descriptions of manufactured fibers used for high-performance parachutes before 1963. These concise material descriptions are repeated below for the convenience of the reader.

Nylon is a polyamide in which less than 85% of the amide linkages are attached directly to two aromatic rings (nylon 6, nylon 6.6). The fiber is strong, durable, elastic, abrasion resistant, and only slightly absorbent. Oxidizing agents and mineral acids cause degradation of nylon depending upon time of exposure, temperature, and concentration. The fiber is essentially inert to alkalies and is generally not affected by organic solvents except some phenolic compounds and formic acid. In dry heat, nylon 6.6 resists degradation and discoloration up to 250°F. It sticks at 445°F and melts at 415°F. In flame, the fiber burns slowly with melting and is usually self-extinguishing when removed from the flame.

Aramid is a polyamide in which at least 85% of the amide linkages are attached directly to two aromatic rings (Nomex, Kevlar). The fiber is strong, dimensionally stable, resists heat, and is only slightly absorbent. Aramid fibers do not melt and are self-extinguishing when removed from flame. Nomex has elastic and energy absorption properties similar to nylon, but maintains its strength when exposed to elevated temperatures for long periods. It degrades rapidly above 550°F. Kevlar is a high modulus (low stretch) fiber which exhibits very good strength and stability, even at temperatures in excess of 500°F.

Fluorocarbon is polymerized from tetrafluoroethylene monomer (Teflon). The fiber is non-absorbent, resists high temperature and most chemicals. The fiber does not degrade below 400°F. It sublimes above 559°F, and vapors are toxic. It presents a very low coefficient of friction in contact with other materials.

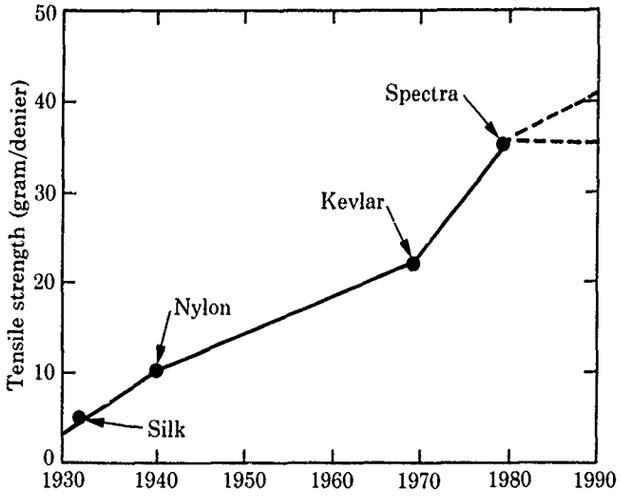


Figure 8.1. Growth in strength of fibers used for parachute fabrics (taken from Ref. 8.1)

Nylon will not be discussed in this report, except as it applies to degradation studies, since complete descriptions are given in References 1.7 and 2.1. This chapter will be limited to a discussion of the advances since the mid-1970s in materials that have been extensively used for high-performance parachutes. The development and application of Kevlar since the mid-1970s will be covered in detail, because the availability of Kevlar has had a major impact on the design of high-performance parachute systems. Nomex will not be covered since it has rarely been used for a high-performance parachute application. Teflon cloth is used extensively for lining deployment bags (the low coefficient of friction minimizes the burning of ribbons and lines during high-speed deployment). Teflon will be discussed in Chapter 9, Deployment Systems.

8.2 Kevlar development and application

Improvements in textile fibers used for parachute fabrics have contributed significantly to the design of lighter and smaller volume parachute packs. Reducing the required volume for parachute compartments is of major importance for most retardation systems. The development of Kevlar in the 1970s improved the available fiber strength, and the useful temperature range was increased from 200°F for nylon to 500°F for Kevlar. Table 8.1 illustrates the major differences in material characteristics between Kevlar and nylon; stainless steel is included as a reference. The drawbacks of Kevlar are its loss in strength due to moisture absorption or smog storage environment; it is not as resistant to abrasion, and it is slightly more difficult to manufacture compared to nylon. Another drawback of Kevlar is its higher cost, about a factor of 3 greater than nylon. Kevlar is an excellent material for primary load-carrying members such as suspension lines, and it reduces the parachute's weight and volume. These characteristics make it ideal for one-time use in ordnance high-performance parachutes.

Table 8.1. Comparison of Nylon and Kevlar Material Characteristics

Material	Elongation (%)	Specific Gravity	Ultimate Tensile Strength (lb/ft^2)	Relative Strength-to-Weight Ratio
Kevlar 29	4 to 5	1.44	400,000	2.70
Nylon 66	16 to 28	1.14	117,000	1.00
Stainless steel	1.1	8.00	185,000	0.22

In reporting work sponsored by the USAF Materials Laboratory, Coskren, Abbott, and Ross[8.2] describe the detailed study of the mechanical characteristics of Kevlar 29 and Kevlar 49 and the design of 80 ribbons, tapes, webbings, cords, sewing threads, and canopy and pack fabrics. In general, weights of the various Kevlar items were only about one-third those of their nylon counterparts. They compare the fiber and yarn properties of Kevlar 29 with other materials in Table 8.2.

Peters[8.3] conducted wind tunnel tests of Kevlar parachutes in the USAF Arnold Engineering Development Center's 16-ft Transonic Propulsion Wind Tunnel. He tested 6.4-ft-diameter, 20-degree conical ribbon parachutes, constructed of nylon, Kevlar 29, and nylon/Kevlar, at Mach numbers 0.6 to 1.2. Twenty-eight deployments were made from a strut-mounted cylindrical forebody (with a flared base) for comparative evaluations of parachute drag and performance. A 20,000-lb capacity, dual-element load cell was used to measure the transient drag, including the snatch load, during deployment and the steady-state drag. The load cell outputs were digitized and recorded on magnetic tape for on-line, steady-state data reduction, and were recorded by a high-speed (2500 samples per second) digital data recording system for off-line data reduction of parachute drag dynamics. Motion picture and television cameras were used to monitor the parachute deployment. Peters concluded that Kevlar parachutes exhibit a shorter damping time for opening-shock load dynamics than nylon parachutes. He observed that a savings of 57% in weight and 65% in volume could be realized by using Kevlar in place of nylon.

Abbott, Coskren, and Pinnell[8.4] developed Military Specifications for 71 Kevlar parachute materials (ribbons, tapes, etc.). Forty-five designs are listed in Table 8.3. These materials were designed to take advantage of Kevlar's high strength-to-weight ratio while giving due consideration to structural stability, joint efficiency, and cost.

Table 8.2. Comparison of Fiber and Yarn Properties (taken from Ref. 8.2)

	Nylon	Polyester	Nomex	Fiberglass	Kevlar 29
Specific gravity	1.14	1.38	1.38	2.50	1.44
Rupture strength:					
gpd	6 to 9	6 to 8	5	9 to 10	20 to 25
psi$\times 10^{-6}$	90 to 130	100 to 140	90	300	350 to 450
Rupture elongation (%)	15 to 25	12 to 20	15 to 20	3 to 5	4
50% room-temperature strength (°F)	350	400	500	650	550
Initial tensile modulus:					
gpd	40	100	140	350	550
psi$\times 10^{-6}$	0.6	1.8	2.5	11	10.5
Bending modulus:					
gpd	50	—	—	300	400
psi$\times 10^{-6}$	0.7	—	—	9	8
Torsional shear modulus:					
gpd	2.7	4.5	916	—	14.6
psi$\times 10^{-6}$	0.04	0.08	0.17	—	0.27
Rupture energy (ft-lb/lb):					
static	16,000	12,000	22,000	—	6,000
dynamic	12,000	11,000	12,000	—	11,000
Lateral critical velocity (ft/s)	2,020	1,550	1,450	900	1,870

gpd = grams per denier
psi = lb/in^2

Table 8.3. MIL-T-87130 Tape and Webbing (taken from Ref. 8.4)

Type	Class	Width (in.)	Strength (lb)
I	1	1/2	250
	2	1/2	550
	3	1/2	800
II	1	9/16	500
IV	1	3/4	500
	4	3/4	3,000
	5	3/4	4,500
VI	2	1	525
	3	1	750
	4	1	1,000
	5	1	1,500
	6	1	2,500
	7	1	3,000
	8	1	4,000
	9	1	6,000
	10	1	9,500
	11	1	12,500
VII	1	1-1/8	1,100
	2	1-1/8	2,750
	6	1-1/8	13,500
VIII	1	1-1/4	800
IX	1	1-1/2	500
	2	1-1/2	1,100
	5	1-1/2	3,000
X	1	1-3/4	1,000
	2	1-3/4	1,200
	3	1-3/4	2,500
	5	1-3/4	4,900
	6	1-3/4	4,500
	7	1-3/4	6,500
	8	1-3/4	8,000
	9	1-3/4	10,000
	11	1-3/4	15,000
	13	1-3/4	20,000
XI	3	2	400
	5	2	600
	7	2	800
	9	2	1,000
	11	2	1,500
	13	2	2,000
	14	2	2,500
	15	2	3,000
	16	2	4,000
	17	2	5,000
	19	2	8,000

Developed but not yet included in the specification: 1 in., 370 lb, 1-3/4 in., 3000 lb, 2 in., 6000 lb.

Goodwin, Abbott, and Pinnell[8.5] conducted tensile tests of Kevlar tapes, webbings, and ribbons. Testing procedures used for nylon materials were found to be unsatisfactory for testing the Kevlar materials; Kevlar's high strength and low elongation can result in premature breaks. Their extensive testing with a wide variety of Kevlar parachute component materials led to the adoption of new jaws and testing techniques designed to give breaks in the free length with nearly simultaneous failure of all warp yarns, high values of breaking strength, and low variability.

Pinnell[8.6] tested a reefed Kevlar 15.3-ft-diameter conical, continuous ribbon parachute, at Mach numbers from 0.21 to 0.98, with 18 drop tests from an F-4 aircraft, and with 13 rocket-powered sled tests. He recorded a maximum opening-shock load of 29,000 lb. He concluded that Kevlar parachutes can be used to produce aerodynamic performance similar to that obtained from nylon parachutes of the same design. The two-stage reefing system was effective in controlling parachute drag area and opening-shock forces.

Pepper[8.7,8.8] conducted 12 sled-launched flight tests comparing Kevlar and nylon parachutes to demonstrate the feasibility of using Kevlar for high-performance parachutes. Because a large flight-test data base of over 500 aircraft drop tests was already available for a 12.5-ft-diameter nylon, 15-degree conical ribbon parachute for comparison, this parachute design was selected. This 16-gore nylon parachute used 9000-lb suspension lines and 3000-, 2000-, and 1000-lb horizontal ribbons distributed from vent to skirt, respectively. The nylon parachute weighed 43 lb and the Kevlar parachute 20 lb. Because of the difference in parachute weights, the length of the Kevlar pack was only 50% that of the nylon pack.

A two-rocket-stage sled system was used to eject the test vehicle (weighing between 400 and 600 lb) into the air for parachute deployment velocities of 650 to 1500 ft/s and dynamic pressures of 440 to 2100 lb/ft^2. Parachute deployment was initiated by a pressure switch that sensed the pitot pressure of the test vehicle. The pressure switch fired two thrusters, which ejected the tail lid at about 40 ft/s, deploying the 18-in.-diameter guide surface pilot parachute that deployed the main parachute bag. An 11-channel onboard telemetry system was used to measure deceleration, pitot pressure, and events. A laser tracker was used to obtain camera coverage of the parachute deployment and inflation, as well as metric position data to obtain velocity versus time.

Pepper's tests provided valuable insight into the differences between the inflation and performance of Kevlar 29 and nylon parachutes under dynamic deceleration conditions. Of particular interest were the opening-shock loads, which were expected to be higher for Kevlar because of its lower elongation. Some of the flight test data are presented in Figures 8.2 (peak inflation loads) and 8.3 (parachute filling times). Pepper concluded that (1) Kevlar can be used successfully to replace nylon in the construction of heavy-duty ribbon parachutes, with a 50% saving in weight and volume; (2) no discernible difference in maximum deceleration, filling time, or drag area could be found in comparing Kevlar parachutes with nylon parachutes; and (3) the Kevlar parachute design had to be altered from the nylon design in order to account for Kevlar's low elongation (4% to 7%).

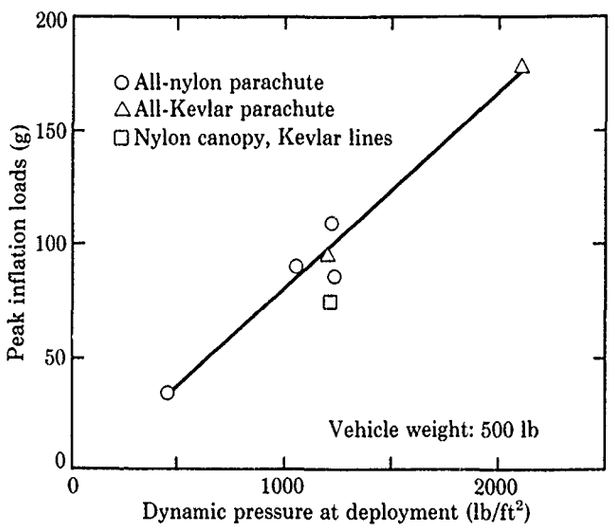


Figure 8.2. Peak inflation loads of a 12.5-ft-diameter parachute

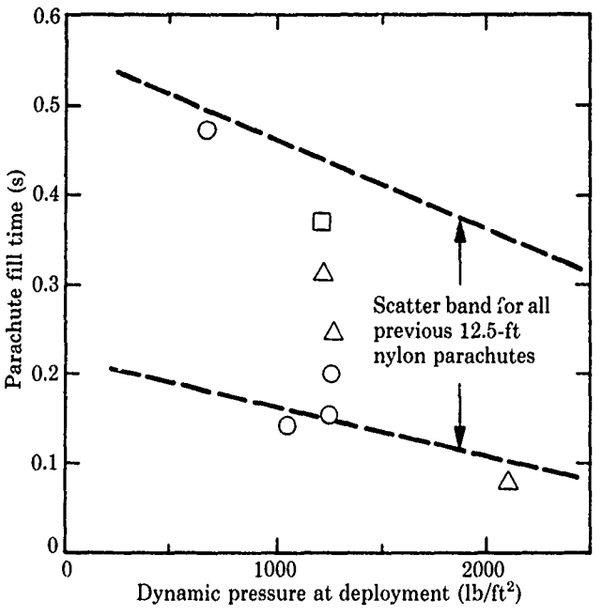


Figure 8.3. Filling time for a 12.5-ft-diameter parachute (symbols same as for Figure 8.2)

Ericksen,[8 9] Ericksen, Johnson, and Guess,[8.10] and Ericksen and Koch[8 11] discuss the development of Kevlar woven materials for application to high-performance parachutes at Sandia National Laboratories. Ericksen[8.9] found that the quasi-static tensile failure strength of the Kevlar 29 narrow fabrics increased as the strain rate increased, but the tensile strength of yarn did not vary appreciably with strain except when it had been subjected to a weaving operation. Ericksen, Johnson, and Guess[8.10] developed a 1-in.-wide Kevlar webbing (as well as 2-in.-wide, low-porosity, 550-lb reinforced selvage and low-porosity, 1000-lb nylon ribbons) for a 46-ft-diameter Kevlar/nylon parachute. The system weight and volume were critical parameters, which required that the material strength be closely matched to the design requirements. Ericksen and Koch[8 11] developed an alternating flat-to-tubular Kevlar tape (535 lb) to replace braided suspension lines and woven tape radials on the proposed new Crew Escape Module parachute system for the F-111 aircraft.

Peterson, Pepper, and Johnson,[1 20] Peterson et al.,[4 96] and Peterson and Johnson[1 22] discuss the application of Kevlar materials to high-performance parachute systems. These references give examples of parachutes that use Kevlar suspension lines, radials, ribbons, reefing lines, bridles, and skirt bands to show that they are much lighter and more resistant to aerodynamic heating than all-nylon parachutes. Table 8.4 gives seven examples of Sandia parachute systems that were retrofitted with Kevlar suspension lines; note that the resultant savings in parachute system weight varied from 16% to 33%. An example of a hybrid Kevlar/nylon parachute canopy is the 24-ft-diameter ribbon parachute[1 1] designed to retard a 760-lb store at deployment velocities as high as 800 knots at sea level. The 24-ft-diameter hybrid parachute has twice the drag area of the 17-ft-diameter all-nylon parachute it replaces, yet it weighs the same (84 lb) and is packed in the same volume (2.1 ft^2) as the 17-ft parachute. Kevlar suspension lines, radials, verticals, reefing line, and skirt reinforcement were used on this parachute in addition to some Kevlar horizontal ribbons (the 21 ribbons nearest the vent were nylon whereas the bottom 33 ribbons were Kevlar). The detailed design of this system, which has been mass-produced for a system application, will be discussed in Chapter 12. All-Kevlar canopies are usually necessary on parachutes that operate at supersonic speeds and elevated temperatures for extended periods of time. One example is a 19-in.-diameter ribbon parachute that was successfully designed to recover a 57-lb reentry vehicle nosetip (a Sandia project) at deployment dynamic pressures up to 9000 lb/ft^2. Specifications[8 12–8 16] were developed at Sandia for tape, webbing, cloth, thread, etc., for the Kevlar, nylon, and Teflon materials used in high-performance parachutes.

Pinnell[1 21] lectured on Kevlar textile technology at the July 1985 University of Minnesota/Sandia National Laboratories Decelerator Systems Engineering Course in Albuquerque, New Mexico. He provided detailed information on Kevlar yarns, textile properties, materials development, and tensile testing.

Table 8.4. Examples of Sandia Parachute Systems Retrofitted With Kevlar Suspension Lines

Description of Parachute System	Original Nylon Suspension Lines	Replacement Kevlar Suspension Lines	Potential Weight Reduction* (%)	Kevlar Radials	Comments on Advantages of Kevlar Lines
12.5-ft ribbon Navy Trainer Unit	9000-lb webbing	6000-lb webbing	27	Yes	Kevlar lines allowed flotation bags to be added to canopy without increasing parachute weight
15-ft ribbon ARIES 1st stage	1500-lb braided	2000-lb braided	21	No	Kevlar lines allowed canopy diameter to be increased from 12.6 to 15 ft without increasing parachute pack volume
13-ft ribbon lifting parachute	9000-lb webbing	13,500-lb webbing	25	Yes	Kevlar parachute weighed less but provided higher performance than original nylon configuration
36-ft ringsail recovery parachute	2250-lb webbing	2000-lb braided	20	No	Both retrofitted and new ringsails with Kevlar lines were tested successfully
4-ft guide surface, shell recovery parachute	550-lb braided	1500-lb braided	16	Yes	Kevlar lines are much more resistant to abrasion, but weigh no more than the nylon lines they replaced
12.5-ft ribbon SLAP-TV parachute	9000-lb webbing	9000-lb webbing	33	Yes	Sandia's first attempt in using Kevlar lines with a nylon canopy
8-ft ribbon recovery parachute	1500-lb tubular	1500-lb braided	16	Yes	Kevlar lines were required to pack parachute in limited volume
6.44-ft ribbon LBRV†	1500-lb webbing	2000-lb braided	26	No	Same as above
8-ft ribbon Sadarm recovery parachute	1500-lb webbing	3500-lb braided	100% increase in line strength for 16% weight increase	No	Twice the line strength of original parachute

* The potential weight savings refer to the reduction in weight that would occur if the nylon lines were replaced by Kevlar lines of the same strength and no other changes were made to the parachute.

† LBRV = large ballistic reentry vehicle.

Beare[8 17] developed a new, lightweight (1.1 oz/yd^2) parachute fabric based on a 55-denier Kevlar aramid fiber. This fabric has three times the strength of nylon at the same weight and thickness, and is nonmelting. Its primary application in parachutes is on nonmelting cockpit ejection parachutes for the Navy and Air Force to help reduce death and injuries if the canopy flies through the fireball.

In reviewing new materials available for aerodynamic applications, Ravnitzky[8 18] noted that Kevlar 29 is generally specified for decelerator textiles because it offers a combination of high tenacity, acceptable modulus, and denier availability. He indicated that Kevlar analogs were being produced in Germany (Twaron) and in Russia; the Soviets have used para-aramid materials for the suspension lines and reinforcement tapes on main and reserve parachutes used for the Soyuz-TM spacecraft recovery.

In summary, it has been demonstrated in several design applications and many flight tests of these different systems that Kevlar can be used successfully for high-performance parachutes. Critical

applications where Kevlar is required are for some supersonic systems (where high temperatures result from aerodynamic heating) and for systems in which parachute pack weight and volume must be kept to a minimum.

8.3 New materials

Ravnitzky[8.18] reviewed many new materials suitable for aerodynamic applications (Table 8.5). Of particular note is Spectra, discussed by Knacke,[8.1] a high-modulus polyethylene that is part of the family of polyolefin fibers, which includes polyethylene and polypropylene.

Benefield[8.19] reports that Spectra is an ultra-high-molecular-weight, extended-chain polyethylene fiber manufactured by a unique process that produces longer, highly oriented polymer chains. Spectra possesses the low density and chemical inertness of polyethylene, and has ten times the strength of steel. It is now being made available for parachute applications. It is resistant to ultraviolet rays and most chemicals. Its principal drawbacks are its cost and its maximum temperature limitation of only 150°F.

Johnson[8.20] discusses expanded polytetrafluoroethylene (PTFE) fibers. PTFE is the generic name for DuPont's Teflon fluorocarbon polymer. Expanded PTFE fibers are a new class of high-strength, high-modulus fibers for fabric designers. They combine the known qualities of chemical resistance and low coefficient of friction with the unique characteristics of high abrasion resistance, high strength, and low elongation to generate tough, durable, stand-alone fabric constructions.

At the U.S. Army Natick RD&E Center in Natick, Massachusetts, Lombardi and Kaplan[8.21] engineered the gene for spider silk into a bacteria that produces a fiber with 5 to 10 times the tensile strength of steel. The fiber can be stretched about 18% without breaking. The bacteria in turn produces a spider silk protein. Lombardi reports that his method of producing spider silk involves sophisticated biotechnology, but that existing fiber-spinning technology could be used.

Table 8.5. Materials Reviewed for Parachute Applications (taken from Ref. 8.18)

polyamides
polyesters
para-aramids
liquid-crystal polyesters
meta-aramids
silica/ceramics/aluminas
polyolefins
polyacetals
sulfurs
fluoropolymers
fluorocarbon polymers
polyimides
polybenzimidazole
liquid-crystal polymer fibers
polyetheretherketone
silicon carbide
carbon/boron
reinforced films
knits/nonwovens/papers
metal/alloy textiles

8.4 Material degradation

The intent of this section is to provide the designer of high-performance parachutes with information on the degradation of nylon and Kevlar fabrics due to flight testing, aging, environment (including high humidity), sewing, and packing. Schulman and Johnstone[1.10] measured the tensile properties of nylon, Dacron, Nomex, polybenzimidazole, fiberglass, and Chromel R at ambient and elevated temperatures in air and in a vacuum. Boone[8.22] measured the fatigue and strain characteristics of Kevlar yarn and cord under constant stress. Tests were performed on materials of Kevlar, nylon, linen, rayon, and cotton, with emphasis on Kevlar. Polyamide and cellulose cords, yarns, and webbings were loaded statically at various percentages of nominal breaking strengths using an Instron

tester. The effects of cumulative loadings at several percentage loads were investigated. Kevlar, although very high in tenacity and low in elongation, behaves as do other polymers under constant load—there is no tensile or elongation point corresponding to the yield point or elastic limit in metals. There is, rather, a constant yielding that, at a given load, decreases logarithmically with time and undergoes one or more changes in slope before failure.

Ericksen and Orear[8.23] investigated the effects of moisture on the strength of Kevlar 29 ribbon parachute fabrics using Instron machines. Individual yarn samples and various fabrics were soaked in water for periods of 15 to 60 minutes. Yarn strength did not change; however, the fabric strength was reduced from 3% to 13%, depending on the weave construction. Additional experiments eliminated as possible mechanisms such factors as the weaving process, yarn swelling, and increased abrasion in the presence of moisture. Other tests demonstrated that increased interyarn friction occurs when moisture is present. These test results suggest that the moisture-enhanced friction restrains highly loaded filaments from adjusting their position and relieving stress concentrations.

Ericksen[8.24] investigated the effects of folding on the strength of Kevlar 29 and nylon parachute materials. Instrumentation of a packed Kevlar parachute showed a maximum pressure of 30 lb/in^2 on the folds. After 1 year storage, the maximum pressure decreased to <10 lb/in^2. Samples from the packed parachute showed no loss in strength after 1 year in packed storage or after an additional 2.5 years in a loosely packed condition. Results from laboratory tests of folded nylon and Kevlar with 13-lb/in^2 pressure on the folds showed no change in strength relative to unfolded control samples for time up to 3.5 years.

Mead et al.[8.25,8.26] conducted accelerated aging tests of nylon 66 and Kevlar 29 yarns in humid air, smog, and ozone to establish aging trends in these environments. Tensile strength of nylon yarn aged in a humid environment (50% relative humidity at room temperature) for 6 months was reduced from 40% at 110°C to 85% at 150°C. Kevlar yarns in the same environment lost from 10% (at 130°C) to 32% (at 170°C) of their strength. Nylon exposed to smog for 6 months lost ~63% of its tensile strength, compared to a 7% loss in ozone. Loss of Kevlar strength was ~27% in smog and insignificant in ozone. Figure 8.4 illustrates the effect of smog on the failure load of nylon and Kevlar.

Ericksen, Pepper, and Whinery[8.27] discuss the effects of sewing, packing, storage environment, and parachute deployment on the strength of materials used in the fabrication of a nylon/Kevlar 24-ft-diameter ribbon parachute.[11] Ribbon parachute materials, listed in Table 8.6, were tested during development and production of the 24-ft parachute and after 2.5 years of exposure at ambient conditions at four storage sites. Materials were stored in containers that were vented to the atmosphere but not exposed to rainfall or sunlight at locations representing arctic, tropic, desert, and industrial environments. Instron tensile tests of as-woven samples of nylon and Kevlar showed no appreciable change in strength after storage for 32 months in these four environments.

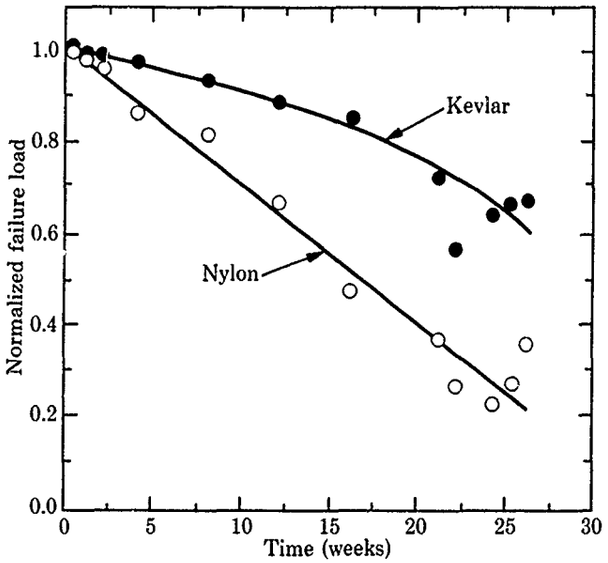


Figure 8.4. Effect of smog on strength of unknotted yarn

The tensile strength of the 1000-lb Kevlar ribbons from 18 production lots of 24-ft-diameter parachutes was also measured. The average breaking strength of the production-lot ribbons increased slightly; the overall average breaking strength was about 1300 lb. Sewing (the sewn samples were segments of radials or verticals sewn to the 1000-lb Kevlar) caused a reduction in strength of 11% to 23%; a splice reduces the strength by ~31%. Production-lot ribbons were tested to simulate the conditions of a folded wet parachute subjected to freezing conditions and then deployed; the reduction in strength was about the same as the loss due to sewing.

Table 8.6. Fabrics Tested for Heavy-Duty Ribbon Parachutes

Width (in.)	Strength (lb)
Kevlar narrow fabrics	
2	1,000
2	2,000
0.5	550
1	4,000
1.125	13,500
1.75	15,000
Nylon narrow fabrics	
2	3,000
0.625	2,200
1	9,000
1.75	10,000

Note: These fabrics are described in MIL-T-5608, MIL-W-83144, and MIL-T-87130.

The 24-ft parachute is pressure-packed to a density of 43 lb/ft^2 using a hydraulic press and an electric motor lacing puller. The first parachutes were packed in a relatively low-humidity environment. The strength of several Kevlar ribbons and webbings is listed in the first column of Table 8.7. When these parachutes were packed in a high-humidity environment, much higher hydraulic pressures were required to achieve the design pack volume. It was determined that the higher packing pressures necessitated by the moisture in the parachute materials caused tearing of the 1000-lb ribbons during packing and subsequent flight tests. A temperature-cycling test (the pack temperature was held at 45°C for extended periods of time, with shorter excursions to 65°C and −52°C during the 1-year exposure) showed that the 1000-lb ribbons failed at only 673 lb. Another 24-ft-diameter parachute was exposed to water for an unknown length of time; the pack weight increased from 90 lb to 97 lb, and the tensile strength of the 1000-lb ribbon decreased to 607 lb (see Table 8.7).

Table 8.7. Strength of Fabrics From Packed Parachutes

	Average Strength (lb)			
Fabric Type	Packed under low humidity	Packed under low humidity, then thermal-cycled	Packed under low humidity, then immersed in seawater	Average of all tests after deployment below 1200 lb/ft^2 dynamic pressure
1000-lb Kevlar ribbon	978	673	607	918
Yarn from 1000-lb ribbon	3.92	3.94	—	—
2000-lb Kevlar ribbon	2,050	1,750	1,904	1,968
3000-lb Kevlar ribbon	3,383	3,100	3,333	2,895
13,500-lb Kevlar ribbon	--	13,025	13,145	14,090
Radial (Kevlar)	13,900	12,700	13,630	14,250
Mini-radial (Kevlar)	1,457	1,237	920	1,379
Skirt band (Kevlar)	13,067	12,850	—	—

Pepper[11] tested the 24-ft-diameter parachute 110 times, at dynamic pressures up to 2650 lb/ft^2. In all cases, the materials withstood the applied loads, and parachute performance and design requirements were met. The average strength of the Kevlar ribbons and webbing for the recovered parachutes tested after the flight tests at dynamic pressures below 1200 lb/ft^2 is listed in the last column of Table 8.7. Test results from the development of this parachute showed that relatively large reductions in strength occur when the ribbons are sewn together, when the parachutes are packed in a high-humidity environment, and when packed parachutes absorb large amounts of moisture or undergo thermal cycling.

Ericksen[8.28] measured the loss in tensile strength of Kevlar narrow fabrics due to moisture combined with folding and compression of the fabric. Fabric samples were exposed to 96% relative humidity, or they were soaked in water before compression or before moisture was introduced while they were compressed. The Kevlar fabrics exhibited a 10% to 30% loss in tensile strength after wet compression compared to the samples compressed dry. Similar tests on nylon did not show this effect.

Auerbach et al.[8.29] studied the effect of ribbon surface treatments on tensile strength. Routine quality-assurance evaluations of nylon ribbons used on test-deployed parachutes revealed strength degradation where blue-ink stencils were used on the ribbons for markings. Hence, an accelerated aging study of the effects of ink and sizing chemicals (used for coating fabrics in parachute fabrication) on tensile strength was conducted. Nylon ribbons and Kevlar webbings were treated with these materials and stored under ambient temperature conditions and at 60°C for periods of up to 8 months. Small increases in strength were observed under ambient conditions whereas small decreases were observed at elevated temperatures. However, none of these laboratory results correlated with those obtained from postmortem tests of test-deployed parachutes.

Auerbach[8.30] studied the kinetics for the degradation of nylon 66 and Kevlar 29 yarns at elevated temperatures and over a broad range of humidities. He developed a rate relationship that models the degradation and permits computation of rate constants.

Tadios[8.31] summarized the aging effects on 25-year-old nylon ribbon parachutes (16.5- and 48-ft-diameter) and 64-ft-diameter solid-canopy parachutes. Five 64-ft-diameter parachutes were disassembled and samples from each parachute were randomly selected for testing with Instron or Scott tensile testers. The structural evaluations included breaking strength, tearing strength, air permeability, and melting point. The test results were compared with the Mil-Specs (Table 8.8a) since the strength data from the original production lots were not available. In general, the material properties of the 64-ft solid-canopy parachute were within specifications after 25 years.

Tadios also tested three 16.5-ft-diameter ribbon parachutes and compared the results with the Mil-Specs (Table 8.8a). On the average, the canopy ribbons failed to meet the required minimum breaking strength, but the remainder of the parachute parts met their respective specifications. Six 48-ft-diameter ribbon parachutes were disassembled and the ribbon and webbing samples were tested (Table 8.8b). The maximum loss in strength of the horizontal ribbons was 13.3%, whereas the maximum loss in strength of the suspension lines was 7.8% compared to the Mil-Specs. Two 16.5-ft ribbon extraction parachutes were disassembled and the ribbon and webbing samples were tested (Table 8.8b). The maximum loss in strength of the horizontal ribbons was 16.6% and the average loss

Table 8.8a. Material Specifications for 64-ft and 16.5-ft Parachutes

Part	Mil-Specs	Strength (lb)
64-ft-diameter solid-canopy parachutes		
Gores: sections 1 to 4	MIL-C-8021	200
Gores: sections 5 to 9	MIL-C-7350	90
Risers	MIL-W-4088, T-18	6,000
Suspension lines	MIL-W-5625, 1/2 in.	1,000
Skirt band	MIL-W-5625, 1 in.	4,000
16.5-ft-diameter ribbon parachutes		
Canopy: section 1	MIL-T-5608, T-5, Cl-E	3,000
Canopy: sections 2, 3	MIL-T-5608, T-2, Cl-E	1,000
Suspension lines	MIL-W-4088, T-18	6,000
Vertical tapes	MIL-T-5-38, T-5	500
Skirt band	MIL-W-27657, T-19,	10,000
	with 1-ply tape	1,000

in strength of the suspension lines was 11%, compared to the Mil-Specs. One may question, however, the validity of comparing the results of the ribbon tests with the Mil-Specs since the strengths specified in the Mil-Specs are for virgin, as-woven materials whereas the ribbons tested consisted of sewn sections. Ericksen, Pepper, and Whinery[8.27] observed that the addition of sewn material causes a decrease in ribbon strength of 11% to 23%.

Table 8.[illegible]. Material Specifications for 48-ft and 16.5-ft Parachutes

Part	Mil-Specs	Strength (lb)
	48-ft-diameter ribbon parachutes	
Suspension lines	MIL-W-27657, T-2	4,000
Vertical tapes	MIL-T-5038, T-5, 9/16 in.	500 (2-ply)
Radial ribbons	MIL-T-5608, T-2, Cl-E	1,000 (2-ply)
	with 1-ply webbing	4,000
Reefing line	MIL-W-4088, T-20	9,000
	16.5-ft-diameter ribbon parachutes	
Suspension lines	MIL-W-27567, T-3	3,000
Vertical tapes	MIL-T-5068, T-5, 9/16 in.	500 (2-ply)
Radial ribbons	MIL-T-5608, T-2, Cl-E	1,000 (2-ply)
	with 1-ply webbing	3,000

References

8.1 T. W. Knacke, "Parachutes, Yesterday, Today and Tomorrow," AIAA 89-0880, April 1989.

8.2 R. J. Coskren, N. J. Abbott, and J. H. Ross, "Kevlar 29 and 49 in Parachute Fabrics," AIAA 75-1360, November 1975.

8.3 W. L. Peters, *Comparison of Parachute Performance at Transonic Mach Numbers for Conical Ribbon Parachutes Constructed of Nylon and Kevlar-29 Materials*, USAF AEDC-TR-76-21, February 1976.

8.4 N. J. Abbott, R. J. Coskren, and W. R. Pinnell, "The Development of Military Specifications for Kevlar Parachute Component Materials," AIAA 79-0473, March 1979.

8.5 S. L. Goodwin, N. J. Abbott, and W. R. Pinnell, "Tensile Testing of Kevlar Tapes, Webbings and Ribbons," AIAA 79-0424, March 1979.

8.6 W. R. Pinnell, "Design Criteria for and Development of Kevlar Ribbon Parachutes," AIAA 79-0430, March 1979.

8.7 W. B. Pepper, "Kevlar—A New Fiber for Parachutes," *Sandia Technology*, Vol. 5, No. 2, SAND79-1070, September 1979.

8.8 W. B. Pepper Jr., "Evaluation of Kevlar-29 vs Nylon for 3.81 m (12.5 ft) Diam Ribbon Parachutes," *J Aircraft*, Vol. 17, No. 3, March 1980.

8.9 R. H. Ericksen, "The Influence of Strain Rate on the Quasi-Static Tensile Strength of Kevlar 29 Narrow Fabrics," AIAA 81-1943, October 1981.

8.10 R. H. Ericksen, D. W. Johnson, and T. R. Guess, "Development of New Ribbons and Webbings for High-Performance Parachutes," AIAA 84-0811, April 1984.

8.11 R. H. Ericksen and R. Koch, "Development of an Alternating Flat to Tubular Kevlar Parachute Tape," AIAA 89-0910, April 1989.

8.12 Sandia National Laboratories Specification SS323241, "Tape and Webbing, Textile, Kevlar-Aramid, Intermediate Modulus," June 1978.

8.13 Sandia National Laboratories Specification SS323243, "Thread, Textile, Kevlar-Aramid, Intermediate Modulus," June 1978.

8.14 Sandia National Laboratories Specification SS323244, "Polytetrafluoroethylene (Teflon) Cloth," November 1978.

8.15 Sandia National Laboratories Specification SS323279 "Cloth, Textile, Kevlar-Aramid, Intermediate Modulus," December 1980.

8.16 Sandia National Laboratories Specification SS333416, "Ribbon, Tape, and Webbing, Textile, Nylon," May 1979.

8.17 S. D. Beare, "New Lightweight Parachute Fabrics of Kevlar Aramid Fiber," AIAA 89-0911, April 1989.

8.18 M. J. Ravnitzky, "Innovative Parachute Materials," AIAA 89-0909, April 1989.

8.19 K. Benefield, "Spectra® High-Performance Fibers for the Fabrication of Lightweight Parachute Systems," AIAA 89-0912, April 1989.

8.20 M. E. Johnson, "Expanded PTFE (Polytetrafluoroethylene) Fibers: Extending the Limits of Textile Technology in Aerodynamic Decelerator Systems," AIAA 89-0913, April 1989.

8.21 S. J. Lombardi and D. L. Kaplan, "Isolation, Cloning, and Physiochemical Characterization of Spider Silk From the Golden Orb-Weaver, *Nephila clavipes*," 199th American Chemical Society Meeting, Boston, Massachusetts, April 1990.

8.22 J. D. Boone, "Fatigue and Strain Characteristics of 'Kevlar' Yarn and Cord Under Constant Stress," AIAA 75-1363, November 1975.

8.23 R. H. Ericksen and L. Orear, "Wet Strength of Kevlar 29 Ribbon Parachute Fabrics," *J Aircraft*, Vol. 17, No. 4, April 1980.

8.24 R. H. Ericksen, "Effect of Folding on the Strength of Kevlar 29 and Nylon Parachute Materials," *Fiber Science and Technology*, Vol. 15, 1981.

8.25 J. W. Mead, K. E. Mead, I. Auerbach, and R. H. Ericksen, "Accelerated Aging of Nylon 66 and Kevlar 29 in Elevated Temperature, Elevated Humidity, Smog, and Ozone," *Ind Eng Chem Prod Res Dev*, Vol. 21, No. 2, 1982.

8.26 J. W. Mead, K. E. Mead, I. Auerbach, and R. H. Ericksen, *Aging of Nylon 66 and Kevlar 29 in Stress Environments*, SAND82-0768, Sandia National Laboratories, September 1982.

8.27 R. H. Ericksen, W. B. Pepper, and L. D. Whinery, "Preliminary Results of the Effects of Sewing, Packing, and Parachute Deployment on Material Strength," AIAA 84-0813, April 1984.

8.28 R. H. Ericksen, "The Strength of Kevlar Narrow Fabrics as Influenced by Folding and Compression in the Presence of Moisture," AIAA 86-2476, October 1986.

8.29 I. Auerbach, L. D. Whinery, D. W. Johnson, K. E. Mead, and D. D. Sheldon, "Effects of Parachute-Ribbon Surface Treatments on Tensile Strength," AIAA 86-2480, October 1986.

8.30 I. Auerbach, "Kinetics for the Degradation of Nylon and Kevlar Parachute Materials," AIAA 86-2478, October 1986.

8.31 E. L. Tadios, "A Summary of Aging Effects on 25-Year-Old Nylon Parachutes," AIAA 89-0918, April 1989.

CHAPTER 9

DEPLOYMENT SYSTEMS

9.1 Purpose and operation of deployment systems

Chapter 5 dealt with the complex nonsteady aerodynamic environment of high-performance parachute inflation. It is important to realize that none of that environment will exist unless the parachute is deployed in an orderly sequence, with proper control of the aerodynamic and inertial loads that govern the deployment process. Parachutes can be designed to withstand very high inflation loads, but only if they are "healthy" after they are removed from the payload and positioned properly for the load-bearing structure to accept the inflation forces that follow. Design of the deployment system (which includes the design of the deployment method and the deployment bag, bag-lacing cut knives, suspension line ties, canopy ties, and other cut or break ties) is just as important in the successful design of a high-performance parachute as the accurate prediction of aerodynamic or structural loading of the canopy during inflation. However, there is little documentation on the design of deployment systems in the literature.

Many critical events must take place during parachute deployment. Table 5.1 lists the deployment sequence for a 24-ft-diameter parachute deployed from the base of a 760-lb test vehicle at a dynamic pressure of ~2600 lb/ft^2. A gas-generator-powered telescopic tube, installed along the centerline of the parachute pack, deployed the parachute at a velocity of ~160 ft/s relative to the test vehicle. The deployment times for this system vary from 0.15 s to 0.40 s, depending on the deployment dynamic pressures. *Deployment time* is defined as the time from deployment initiation until the lines and canopy are stretched out as the bag separates from the canopy (i.e., just before the canopy starts to fill). To ensure orderly deployment of the suspension lines and canopy without damage to the parachute, it is essential that each deployment event occur in the right sequence and in a repeatable fashion. When these events do not occur properly and in the correct sequence, the parachute fails to perform its intended function.

A visual description of an orderly deployment of a high-performance, 46.3-ft-diameter ribbon parachute from a 2465-lb store is shown in Figure 5.2. First the suspension lines and then the canopy are stretched out in the sky after being pulled out of the deployment bag by the deployment system (pilot parachutes, in this case). The sequence of events that occur during the satisfactory deployment of this parachute system is given in Table 5.2. Again, note that all deployment events take place over a very short time span.

A properly designed deployment system will

- provide reliable and repeatable parachute operation
- provide repeatable time intervals for each stage of the parachute's opening process, from the parachute's deployment signal until the canopy is fully inflated
- minimize the magnitude of the snatch load (i.e., ensure that it is much less than the opening-shock load)
- minimize the occurrence of anomalies such as canopy inversions and canopy fish-hooking
- avoid interference of any part of the parachute system with the payload or the carrier aircraft, missile, rocket, shell, etc.
- provide repeatable parachute snatch and opening-shock loads, and
- minimize the opportunity for canopy or suspension line damage during opening due to nonuniform canopy loading, friction burning, premature exit of suspension lines or canopy from the bag, twisted suspension lines, etc.

The purpose of this chapter is to present sufficient design information to allow the designer to select reliable and repeatable deployment systems for high-performance parachute systems.

9.2 Deplcyment methods

9.2.1 Background

The Parachute Design Guide,[2.1] Ewing, Bixby, and Knacke,[1.7] and Knacke,[1.20] among others, discuss different methods of initiating deployment. In his lectures in the Helmut G. Heinrich Short Course on Parachute Systems Technology at the University of Minnesota (and in a similar course in

Albuquerque in 1985), Knacke[1.20] offers some very practical design advice on parachute deployment systems. He gives examples of deployment concepts, including the advantages and disadvantages, of (1) uncontrolled deployment, (2) semicontrolled pilot parachute deployment, (3) static line deployment, (4) controlled deployment (lines-first), (5) canopy-first deployment, (6) mortar deployment, and (7) rocket extraction. He also lists methods of deployment initiation, including (1) cover extraction, (2) pilot parachute, (3) pilot parachute cover, (4) drogue gun, (5) mortar, and (6) rocket extraction. A schematic of a "controlled" deployment is illustrated in Figure 9.1.

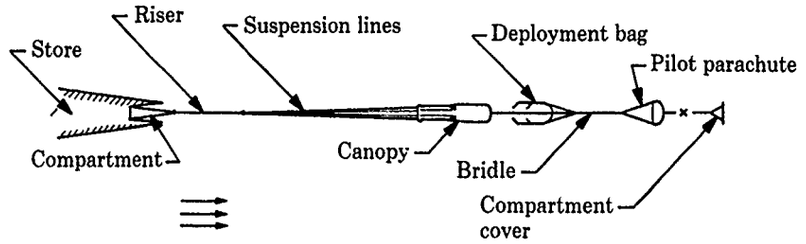


Figure 9.1. Controlled deployment

Huckins[9.1] conducted a study to develop techniques for selecting and analyzing parachute deployment systems. Deployment systems based on forced ejection, extraction using a drogue parachute, and extraction using a rocket motor were considered. General equations approximating the linear dynamics of deployment before inflation were derived. The problems associated with each type of deployment technique were identified and compared.

Poole and Huckins[9.2] mathematically modeled the elasticity in parachute suspension lines during the deployment process. The massless-spring approximation was evaluated. Equations that govern the elastic response of the suspension lines were combined with those governing the motion of the vehicle and the deployment bag. This set of governing equations was integrated numerically and the results were compared with flight test data. Agreement was satisfactory except during periods of rapid fluctuations in line tension.

Four methods of deploying parachute systems are discussed below, with examples from extensively tested flight systems. It should be noted, however, that many times a designer will use combinations of these methods to achieve reliable deployment of high-performance parachutes.

9.2.2 Pilot and drogue parachutes

A large main parachute can be deployed by attaching its deployment bag to a smaller parachute (called a pilot parachute) and using the drag of the pilot parachute to remove the main bag from the payload and strip the main parachute out of the bag. Since the force used to deploy the main parachute is related to the drag of the pilot parachute, snatch loads and bag strip velocities are a function of the deployment dynamic pressure and pilot parachute size. Using a pilot parachute has proved to be successful when the range of payload velocity at the time of deployment does not vary by more than a factor of 3 or 4. A drogue parachute decelerates and/or stabilizes a store prior to main parachute deployment.

Pepper[3.3,3.4] used a heavy-duty, 18-in.-diameter guide surface pilot parachute (coated with silicone rubber) to deploy the bag containing a temporarily reefed, 20-ft-diameter heavy-duty ribbon parachute from the base of the test vehicle. This deployment system was successfully used at supersonic deployment conditions up to Mach 2.43 and dynamic pressures of 5700 lb/ft^2. The pilot parachute itself was deployed by using a gas-generater drogue gun to eject a 1-lb mass attached to the pilot parachute.

Johnson[3.50] developed an overwater recovery system for 150-lb sounding rocket payloads that have achieved apogee altitudes of 10^6 ft. The recovery system was designed to position the payload's center of gravity at 45% to 55% of the body length at reentry. This ensured that the payload assumes a high-drag configuration (flat spin) during and after reentry. While in the flat spin, the payload decelerates to subsonic velocities. The first-stage parachute is deployed at an altitude of 15,000 ft by a baroswitch closure that fires a pressure cartridge and ejects the rear cover of the payload. A sketch of the rear cover and ejection mechanism is shown in Figure 9.2. A 3-ft-diameter ribless guide surface parachute is used to stabilize and decelerate the payload so that the main recovery system can be deployed

without damage. After 10 s, cutters are initiated to sever the load bridle and to release the 3-ft pilot parachute that then deploys the main recovery system (6-ft-diameter guide surface parachute) from a deployment bag. Thirteen rocket payload recovery systems (see Johnson[3.51] and Fowler, Maydew, and Barton[3.52]) have evolved from this concept to recover weights of up to 1000 lb. Over 300 rocket payloads have been recovered (to date) by nine U.S. and NATO organizations from launches of 23 different rocket systems from 15 locations worldwide. Approximately 100 of the recovered rocket payloads were flown on NASA-Wallops Island rocket systems; Sandia furnished the recovery systems for these payloads.

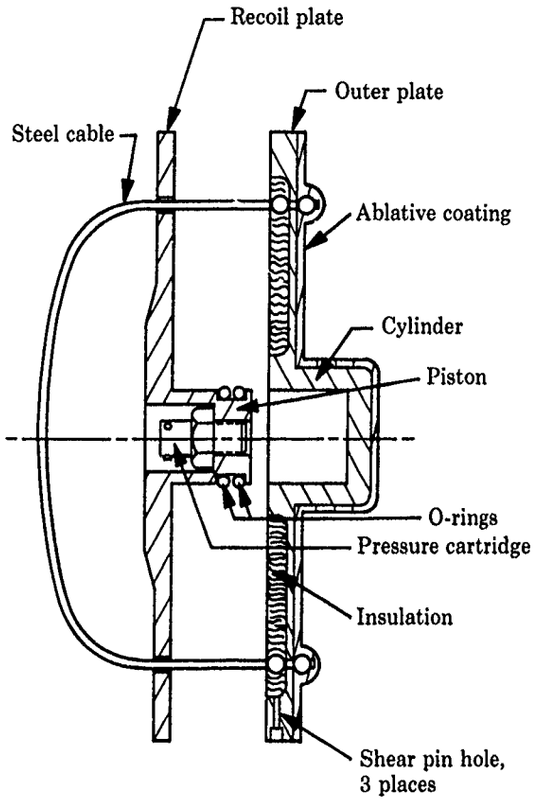


Figure 9.2. Rear cover of rocket payload recovery system

Knacke[1.10] discusses the method of deploying the parachute system for the 10,000-lb Apollo Command Module landing system. The recovery sequence starts with ejection of the apex cover at an altitude of 25,000 ft. A 7.2-ft-diameter ringslot parachute is used to help further remove the apex cover and to prevent recontact between the cover and the command module. The two 16.5-ft-diameter ribbon drogue parachutes (one is a back-up) are then mortar-ejected; they stabilize and decelerate the command module. At 10,000 ft altitude, the drogue parachutes are disconnected by ordnance cutters, and three 7.2-ft-diameter ringslot pilot parachutes are deployed by a mortar. Each pilot parachute individually extracts one of the three 85.5-ft-diameter ringsail main parachutes.

Maydew and Johnson[3.1] used a 3-ft-diameter ribless guide surface parachute to deploy a 22.2-ft-diameter reefed ribbon main parachute from the base of an 18-in.-diameter, 2100-lb store. The heavy-duty nylon main parachute weighed 135 lb and was deployed at low altitudes at Mach numbers from 0.57 to 1.70 and at deployment dynamic pressures up to 2720 lb/ft^2. This parachute system is described in more detail in Section 3.2.1.2. Closure of a timer 0.6 s after store release from the aircraft initiated the explosive separation of the tail can from the test vehicle, which in turn deployed the pilot parachute that was packed on the base of the main parachute pack. Closure of a pitot probe pressure switch initiated the explosive separation of the tail can for the rocket-boosted tests.

Pepper[9.3] developed a two-stage parachute system for the overwater recovery of a reentry vehicle nose cone. The 102-lb vehicle reentered at an altitude of 300,000 ft at a velocity of 18,700 ft/s. Recovery was initiated at 28,000 ft altitude by ejecting the aft 62 lb of the vehicle mass with a telescoping tube powered with a hot-gas generator. After ~8 s, the tail cover was pressure-ejected (with an explosive cartridge) out of the vehicle base; the tail cover deployed the pilot parachute bag by means of a bridle (see Figure 9.3). The 19-in.-diameter ribbon pilot parachute stabilized and decelerated the 40-lb payload for 1.9 s and then deployed the lightweight 3-ft-diameter ribless guide surface parachute. A special bridle/lug arrangement was designed so that the pilot parachute could be released by firing a single ordnance line cutter. Detailed descriptions of the deployment method, parachute specifications, packing methods, and deployment bags are given by Pepper. This program resulted in the first recovery of a high-beta reentry vehicle at sea, off Wallops Island, Virginia. The recovered carbon nosetip was analyzed, and wind tunnel models of the ablated nosetip were tested in wind tunnels by many research organizations to study the effects of ablation on boundary layer transition.



Figure 9.3. Nosetip Recovery Vehicle parachute system

Pepper[9.4] developed an 8-ft-diameter nylon/Kevlar ribbon parachute to recover a 266-lb payload (which consisted of three spent Zuni rocket motors in a spin-up ca...ster) at deployment dynamic pressures of 500 to 1690 lb/ft^2. He developed an 18-in.-diameter Kevlar (to resist heating damage during rocket burn) guide surface parachute to extract the main parachute bag from the canister. The 8-ft main parachute weighed 6.3 lb and was packed in a two-leaf, 5-in.-diameter by 24-in.-long bag. The pilot parachute was deployed by the explosive ejection (aft) of the parachute container lid.

Johnson and Peterson[3.6] developed a 46.3-ft-diameter nylon/Kevlar parachute to decelerate a 2465-lb vehicle from transonic speeds (deployment dynamic pressures of 300 to 2130 lb/ft^2) to ground impact velocities of ~70 ft/s from aircraft delivery at low altitudes. Initially in the program, a 5-ft-diameter nylon/Kevlar conical ribbon parachute (packed on the base of the main parachute bag) was used to deploy the 46.3-ft-diameter parachute. A tractor rocket deployment system was also considered, but the pilot parachute system was chosen as the baseline design because of cost considerations. The principal disadvantage of pilot parachutes is that the rate of deployment and the deployment loads on the main parachute are proportional to the dynamic pressure acting on the pilot parachute. A pilot parachute that works well at a dynamic pressure of 300 lb/ft^2 may generate excessive opening-shock loads at a dynamic pressure of 2130 lb/ft^2. Conversely, a pilot parachute that works well at high speeds may take too long to deploy the main parachute at the lowest aircraft delivery speeds.

The 5-ft-diameter pilot parachute is deployed by the explosively ejected vehicle base plate. It was successfully used for 32 flight tests, with no damage in deploying the 46.3-ft parachute. On two subsequent supersonic flight tests, the pilot parachute collapsed shortly after initial inflation, causing severe suspension line sail and canopy damage to both main parachutes (see Figure 5.3). The line sail, which is discussed in Section 5.2.1, was caused in part by the high payload angle of attack at the time

of parachute deployment. The high payload angle of attack was caused by the interaction of the aircraft flow field with the payload at supersonic speeds. With the payload flying at a high angle of attack and at supersonic speeds, the wake behind the store is turbulent and contains large lateral-velocity components and pressure gradients. The 5-ft pilot parachute was not able to remain inflated in such a violent wake flow field. The shock waves generated by the F-111 aircraft caused the pilot parachute to collapse after the initial inflation. Once the pilot parachute collapsed, it could not provide enough drag to avoid the severe suspension line sail shown in Figure 5.3. Computer simulations (described in Section 5.2.1) indicated that a pilot parachute with an effective drag area of $\sim$17 ft^2 would avoid serious suspension line sail problems during store releases from the F-111 aircraft.

A cluster of three small ribbon parachutes was proposed as a replacement for the single 5-ft-diameter pilot parachute. Although clusters of parachutes have been used as main recovery parachutes for years (e.g., the Space Shuttle SRB recovery system), the authors could find no references in the literature that describe the use of a cluster of parachutes to deploy a main parachute. Each pilot parachute canopy was 3.8 ft in diameter and was tied to each of the other canopies at the skirt by a 9-in.-long nylon tether. Figure 9.4 compares the cluster parachute configuration to the single 5-ft pilot parachute and shows where the pilot parachutes are located with respect to the payload wake. The cluster configuration was selected because it has approximately 80 percent more canopy area than the single 5-ft pilot parachute and because the individual canopies of the cluster can extend farther out of the payload wake into the less turbulent airstream, where the dynamic pressure is higher. It was postulated that a cluster parachute might reinflate more rapidly (if collapse occurs) than the 5-ft parachute, because the cluster parachute can move out of the payload wake into less turbulent air. As shown in Figure 9.4, the 5-ft parachute must reinflate while the skirt is totally immersed in the turbulent payload wake.

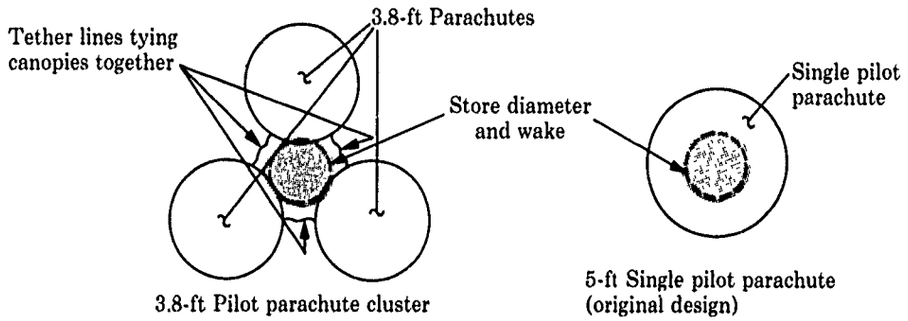


Figure 9.4. Relationship between the store wake and pilot parachutes for the cluster of 3.8-ft pilot parachutes and the original 5-ft single store pilot parachute

Each 3.8-ft-diameter cluster parachute has twelve gores containing three skirt-to-vent nylon mini-radials and eight 1500-lb, 2-in.-wide nylon ribbons spaced 0.56 in. apart. A continuous ribbon construction is used with 4000-lb nylon vent reinforcement and 4000-lb Kevlar skirt reinforcement. The 80-in.-long suspension lines use the same figure-eight construction seen on the main parachute. They are arranged in three groups for each parachute; the line groups are attached to a plate at the aft end of the main parachute deployment bag. The suspension line material is 1-in.-wide, 4000-lb Kevlar, and the radial backing is 1-in.-wide, 2400-lb Kevlar. The design load for each cluster parachute is 21,800 lb. The three pilot parachutes (Figure 9.5) are packed in an envelope deployment bag that is pulled out of the payload by a bridle attached to the payload tail plate. The tail plate is ejected explosively to initiate the deployment process.

Two flight tests were conducted at Sandia's Tonopah Test Range to measure the drag force generated by the pilot parachute cluster in the wake of the payload. In each test, the cluster was towed for 3.5 s while drag measurements were made before the cluster was released and allowed to deploy the main parachute for vehicle recovery. Using this technique, drag data were obtained for Mach numbers between 0.5 and 1.5. A peak deceleration force of 29,000 lb (12 g) was measured at Mach 1.5. Although this drag force is higher than the 5-ft pilot parachute drag, the drag of the cluster flying in the wake of the payload is between 40% and 60% lower than the drag of the cluster flying in undisturbed air. This result confirms that the payload wake was a major cause of the poor performance of the 5-ft pilot parachute.

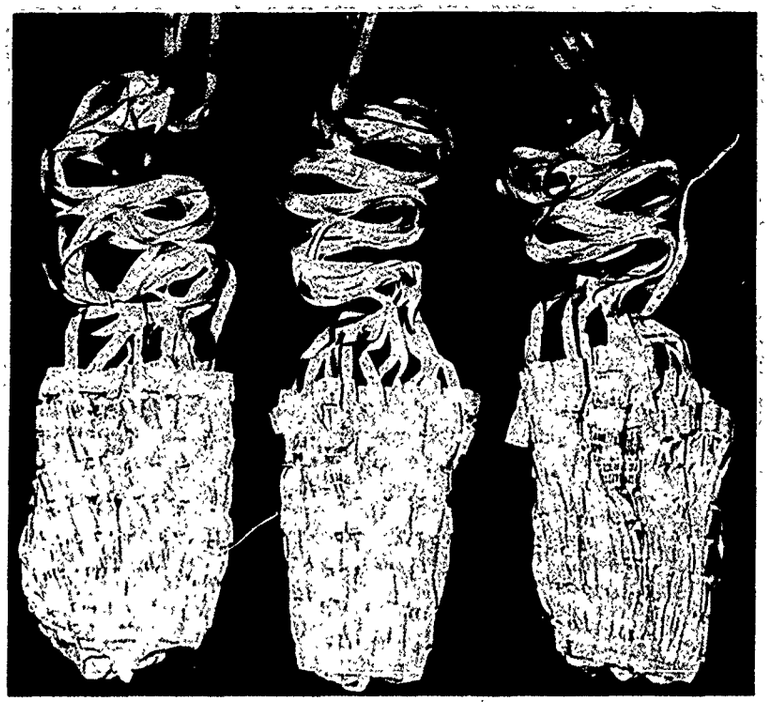


Figure 9.5. Cluster of three 3.8-ft-diameter pilot parachutes

This pilot parachute cluster was used for the rest of the par e system development program. Thirty-five flight tests (aircraft drop, rocket-boosted, and roc boosted sled on track) were conducted by Johnson and Peterson,[3 6] and the performance of the cluster pilot parachute system always surpassed that of the 5-ft pilot parachute. The cluster system eliminated line sail problems at all velocities, except at 800 KCAS, when released from an aircraft. At this highest velocity, the pilot parachute cluster experienced a reduction in drag caused by the shock waves emanating from the aircraft and the wake generated by the payload flying at angles of attack approaching 25 degrees. The pilot parachutes would not stay fully inflated in this severe environment. In the absence of the aircraft shock waves and payload angle-of-attack effects, however, the cluster provided high drag and no line sail, as was observed in seven sled and rocket tests at velocities between 800 and 860 KCAS. Bag strip velocities were high (400 to 450 ft/s for 660 KCAS deployments), but were unavoidable in order to obtain orderly deployments at the 300 KCAS release conditions. The performance of the main parachute was not compromised by these high bag strip velocities, however. No damage to the pilot parachutes occurred on any of these tests. A detailed stress analysis was performed on the pilot parachutes during the design using the CANO code (see Reynolds and Mullins[6.9]) in conjunction with canopy pressure distributions measured in wind tunnels.

Pepper[9 5] developed a 6.4-ft-diameter Kevlar/nylon parachute to recover a 130-lb reentry vehicle nose cone (launched by a Minuteman missile from Vandenberg AFB, California) at sea near Kwajalein Atoll in the South Pacific. Mass jettison from the payload, which occurred at 14,500 ft altitude on reentry, was used to decelerate the reentry vehicle to subsonic speeds. Parachute deployment was then initiated at ~2100 ft altitude. Approximately 8.6 s after mass jettison, the lid is fired off the parachute can by a gas generator; the lid extracts the reaction plate by means of six steel aircraft cables. The 16-in.-diameter pilot parachute bag is attached to the reaction plate by a four-leg bridle. The pilot parachute is extracted from its bag by the reaction plate and deploys at five payload base diameters behind the nose cone. The pilot parachute then pulls out the main bag, and the 6.4-ft-diameter parachute is deployed (with a swivel to prevent parachute roll-up) at five payload base diameters behind the cone. Five rocket-sled development tests of this parachute system were conducted before the successful reentry flight test was achieved in the South Pacific.

Buckley[9.6] developed a two-stage (33-in.-diameter Kevlar ribbon first stage and 9.5-ft-diameter nylon solid canopy second stage) parachute system to recover the guidance and telemetry sections (80 lb) of a 5-in.-diameter ground-to-air missile. Deployment conditions were at altitudes of 1000 ft to 40,000 ft and at missile velocities up to Mach 1.5. The deployment sequence is initiated by a g-switch that senses rocket-motor burn; a preset timer then fires an explosive bolt, which releases the Marmon clamp that secures the rocket motor to the recovery section. At the same time, an explosive gas charge between the motor and the parachute is fired to aid in safe rocket-motor separation. A 9-s-delay line cutter is activated at line stretch of the first-stage drogue parachute, which releases the lines connecting the drogue parachute to the payload. The drogue then acts as a pilot parachute, extracting the main parachute at a deployment velocity of ~250 ft/s.

Johnson[3.37] proposed a new parachute recovery system for the 3130-lb F-111 Crew Escape Module (CEM) to achieve a rate of descent requirement of 25 ft/s at 5000 ft altitude. His system consisted of a cluster of three 49-ft-diameter ringslot/solid-canopy parachutes, a Kevlar deployment bag, and an explosively fired drogue gun to deploy the pilot parachute. A parachute catapult ejected the main parachute at a velocity of 45 ft/s. Military Specifications define the angle-of-attack range of the CEM to be from −30 degrees to +120 degrees. In general, the parachute deployments will have a large crosswind component and may include deployment of the parachute system into the wind. In all conditions, it is mandatory that the pilot parachute be deployed and inflate very rapidly in order to control the deployment of the parachute system and to minimize the line sail. Line sail occurs when the air loads on the suspension lines cause premature breaking of the line ties and deployment of the lines. This can result in rotation of the deployment bag and damage to the suspension lines and parachute canopies when they are dragged over the edge of the deployment bag.

The F-111 parachute design specifications require that the parachute system be capable of deployment at dynamic pressures varying between 10 and 300 lb/ft^2. This wide range of dynamic pressures complicates the design of the pilot parachute, because a pilot parachute large enough for use at a low dynamic pressure provides too much drag at high dynamic pressures and, conversely, a pilot parachute sized for high dynamic pressure is too small for use at the low dynamic pressure. A dual parachute system (Figure 9.6) is the baseline pilot parachute design. A 5-ft-diameter guide surface parachute is placed inside a 10-ft-diameter circular flat parachute. The attachment of the 10-ft parachute to the pilot parachute riser is designed to be released at a drag-force level of 2000 lb. This is accomplished by failure of the stitch pattern, which holds the two loops to the pilot parachute riser (see Figure 9.6). If the dynamic pressure is high enough (~ 40 lb/ft^2) to cause the 10-ft parachute to break away, the 5-ft parachute is left inflated, ready to deploy the main parachutes. The pilot parachutes are deployed by the drogue gun that is fired when the catapult has moved the packed parachute recovery system approximately 8 to 10 in. A 2-lb mass is ejected from the drogue gun at 200 ft/s and deploys the pilot parachutes canopy-first from a deployment bag located on the aluminum endplate of the main parachute deployment bag. In summary, Johnson concludes that it has been difficult to deploy parachute systems crosswind without excessive line sail, but that the dual pilot parachute system should aid in minimizing the line sail problem.

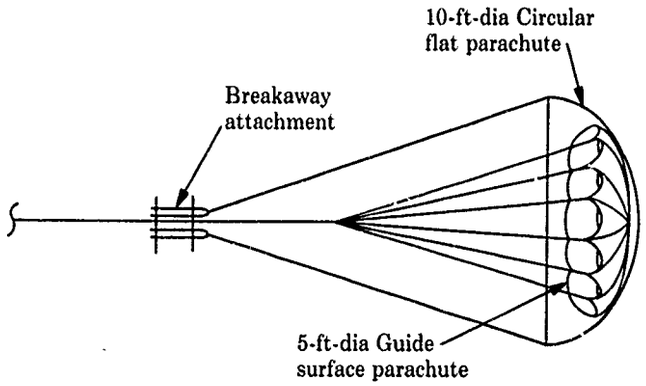


Figure 9.6. Dual pilot parachute system for CEM recovery parachute

9.2.3 Mortars and drogue guns

A mortar is a reliable means for imparting enough velocitv to the parachute bag to ensure its deployment. The packed parachute (in its deployment bag) is packaged in a mortar tube between a sabot and the aft cover. The sabot acts as a piston to propel the bag out of the tube. The sabot and its seal shield the parachute from the hot gases generated by the propellant burning in the breech. The propellant gases are contained between the base plate and the rapidly accelerating sabot.

Mortars are used when the performance of pilot parachutes is questionable; examples of this are for tumbling payloads, for thrusting the main parachute through the payload's base recirculation region, and for deployments in some extraterrestrial atmospheres. A disadvantage of using mortars may be their heavier weight, compared to pilot parachutes, and their high reaction loads. Sometimes a mortar is used to deploy a pilot parachute.

A drogue gun fires a drogue slug with a pilot parachute through the wake of a payload into uniform airflow. The advantage is fast, reliable, and uniform parachute deployment from blunt and/or oscillating forebodies.

Murrow and McFall[9.7] conducted rocket and balloon tests of disk-gap-band, ringslot, and cross parachutes with diameters of 30 to 65 ft, at a nominal deployment Mach number of 1.6 at altitudes of 122,000 to 159,000 ft, to gain experience in supersonic parachute deployments at dynamic pressures of ~10 lb/ft^2. The parachutes were deployed unreefed from a 12-in.-diameter mortar at velocities greater than 100 ft/s. After the deployment bag's mouth tie was cut, the unrestrained parachute suspension lines were pulled from the bag as it moved away from the payload. Then the bag was stripped from the canopy, exposing the canopy to the airstream. The mortar-type deployments were consistent and reliable. Th· only deployment problem encountered was the damage caused by the deployment bag's overtaking and penetrating the parachute shortly after bag stripping.

Moog et al.[3.46] and Gillis[3.44] discuss the Viking decelerator system. This system consists of a single-stage, mortar-deployed, 53-ft-diameter disk-gap-band parachute. Full-scale flight tests were conducted using a simulated Viking vehicle at Mach numbers 0.47 to 2.18 at dynamic pressures of 6.9 to 14.6 lb/ft^2. A single-stage mortar was used to eject the packed parachute from the rear of the spacecraft. The mortar, which has a volume of 2.2 ft^3, is designed to eject a mass of ~102 lb at velocities near 112 ft/s. Ejected components include the parachute assembly, deployment bag, cover, and sabot. Moog et al. concluded that parachute ejection (from mortar fire through line stretch, bag stripping, and initial inflation) was free from significant anomalies.

Whalley[9.8] discusses the development of the USAF B-1 Crew Module parachute recovery system. The parachute recovery system must be capable of operating at speeds from Mach 0 to 2.3 at altitudes from 0 to 70,000 ft. The recovery system consists of a mortar-deployed 14.2-ft-diameter conical ribbon parachute, for initial stabilization and deceleration, and a cluster of three 69.8-ft-diameter ringsail main parachutes to provide a terminal descent rate of 29 ft/s for the 8700-lb crew module. Main parachute deployment is by means of two (redundant systems for increased reliability) mortar-deployed 8.4-ft-diameter ringslot (pilot) parachutes. The drogue mortar assembly, which is ~30 in. long and 16 in. in diameter, is designed to eject a weight of 83 lb to a velocity of 83 ft/s; the pilot mortar assembly, which is ~13 in. long and 6 in. in diameter, is designed to eject a weight of 7.5 lb to a velocity of 99 ft/s.

Pleasants[9 9] discusses the flight qualification of mortar-actuated parachute deployment systems. He outlines an adequate and cost-effective approach for a flight qualification program for a typical mortar-actuated parachute system including tolerances, test conditions, test equipment, and instrumentation. Mortar functional tests allow evaluation of cartridge to environmental exposure, operational assessment of flight-type hardware, validation of minimum ejection velocity, and maximum reaction load and assessment of bridle deployment.

Rodier, Thuss, and Terhune[9 10] summarize the design of the parachute system for the Galileo/Jupiter entry probe launched from the Space Shuttle in 1989. The probe enters the hydrogen/helium atmosphere of Jupiter at an approximate speed of 107,000 mph. Once in Jupiter's atmosphere, the probe aerodynamically decelerates from entry velocity to approximately Mach 1, with deceleration loads up to 400 earth-gravity g forces. An onboard g-switch initiates the deployment sequence. At approximately Mach 1, a mortar-fired, 3.74-ft-diameter ribbon pilot parachute is deployed. After 1.25 s, three explosive nuts are fired, allowing the pilot parachute to remove the probe aft cover and deploy the 12.48-ft-diameter conical ribbon main parachute. Approximately 3 s later, the main parachute is used to separate the forward shell of the deceleration module from the descent module.

The descent module, which is supported by the main parachute, then descends through the Jovian atmosphere for ~30 min to gather data. Rodier, Thuss, and Terhune present sketches of the deployment sequences and the mortar and pilot parachute assemblies.

Moog, Sheppard, and Kross[4,12] discuss the results of Space Shuttle Solid Rocket Booster (SRB) deceleration subsystem B-52 drop tests. The SRB decelerator system consists of an 11.5-ft-diameter ribbon pilot parachute, a 54-ft-diameter ribbon drogue parachute, and a cluster of three 115-ft-diameter ribbon main parachutes to decelerate the 170,000-lb SRB to an impact velocity of 85 ft/s. Parachute deployment is initiated after SRB reentry at an altitude of 15,300 ft at Mach 0.5. A special drop-test vehicle, designed to test this parachute system, included a different method of separating the SRB nose cap (i.e., the use of a drogue gun rather than the thrusters used for the space flight). After B-52 separation, a drogue gun, located on the end of the nose cap, fires a 1-lb slug at a relative velocity of 210 ft/s. This slug deploys the 2-ft-diameter vane parachute from the bag mounted on the nose cap cover. Three explosive bolts are then fired to allow the nose cap cover to separate, causing the nose cap extraction parachute (reefed 10.5-ft-diameter ribbon) to deploy. After a suitable time period, three explosive bolts located at the nose cap base are fired, allowing the nose cap to separate. A bridle attached to the nose cap then deploys the 11.5-ft-diameter pilot parachute. This drogue gun method worked well for these parachute development and demonstration flight tests.

9.2.4 Thrusted base plate

A thrusted base plate is frequently used to provide a positive method of parachute deployment. The base plate is attached to the payload; its thrust may be either aerodynamic or pyrotechnic. The parachute bag is usually attached with a bridle or tether line to the base plate. When the base plate is thrusted away from the payload, it deploys the main parachute. Very strong pyrotechnic forces are required to deploy main parachutes using this method.

Banerjee and Coppey[9,11] developed an analytical method for predicting the ejection velocity at which the SRB nose cap would separate from the Space Shuttle SRB in a reasonable time, with some contact permitted on the exposed parachute pack. The SRB nose cap, which is 75 in. high and 67 in. in diameter, forms the top part of the SRB nose cone; it weighs ~300 lb. Banerjee and Utreja[5,11] show photographs of the SRB nose cap with the drogue parachute, bag, and bridle; they analyze the dynamics of the drogue parachute. The SRB parachute system and deployment flight conditions are discussed in this section and by Moog, Sheppard, and Kross.[4,12] The SRB nose cap is ejected at a velocity of ~80 ft/s by means of three pyrotechnic thrusters. After separation, the nose cap pulls out (by means of a tether line) the 10.5-ft-diameter pilot parachute, which in turn pulls out the 54-ft-diameter drogue parachute that subsequently deploys the cluster of three 115-ft-diameter main parachutes. This nose cap thruster method of initiating parachute deployment has been used successfully on many reentry-from-space flight tests for SRB recovery.

A parachute deployment system (consisting of an attachment plate, a telescopic deployment tube assembly, a deployment plate, an explosive gas generator, and a linear-shaped charge-staging cutter) was developed for the lifting parachute system described in Chapter 3 (see Rychnovsky[3,9]). The packed parachute system, which is ~17 in. in diameter, is shown in Figure 9.7. The attachment plate is inside of and fixed to the payload afterbody, and supports by cantilever the deployment tube assembly and the two parachute systems (13-ft-diameter modified conical ribbon first stage and 38-ft-diameter ringsail second stage) packed on the tube assembly. The suspension lines of both parachute systems were attached to the attachment plate to transmit the parachute drag loads to the payload. The deployment plate forms the base of the parachute assembly, which contains the 13-ft parachute packed in a deployment bag followed by an end cap and then the 38-ft parachute packed in a deployment bag. Both parachutes are packed around the centered deployment tube assembly.

The explosive gas generator seals the forward end of the tube assembly and, when fired, generates the proper gas pressure to propel the inner tube of the telescopic assembly (and the deployment plate) to the rear and out the base of the payload, thereby deploying the 13-ft parachute lines-first. The resulting velocity at suspension line stretch of the 13-ft parachute is ~80 ft/s. A plug on the inner tube, which seals within the aft end of the outer tube, contains the hot gases and particles from the gas generator. The shaped charge-staging cutter severs the Kevlar suspension lines of the 13-ft parachute from the attachment plate ~5 s after aircraft release of the payload. The 13-ft parachute then extracts the 38-ft parachute deployment bag from the payload and the parachute is deployed lines-first.

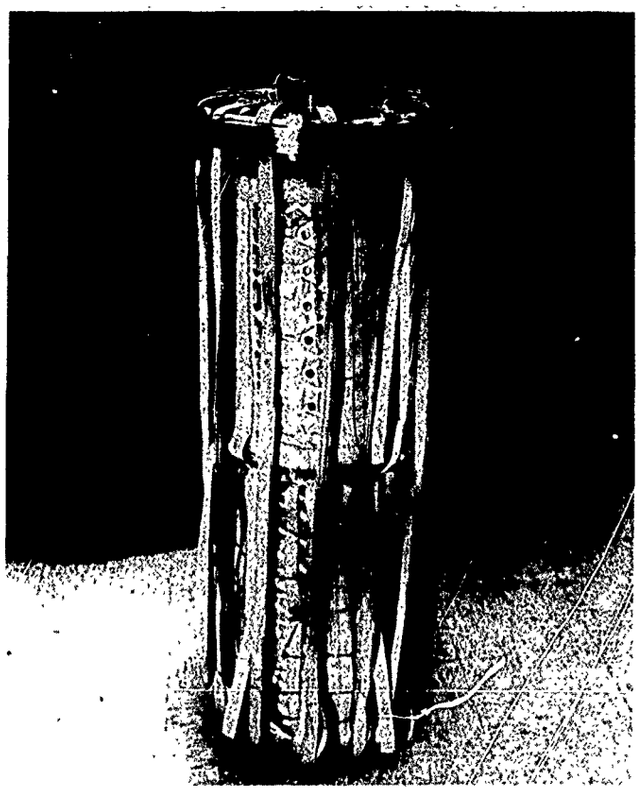


Figure 9.7. Lifting parachute pack

Pepper[1.1,4 13] developed a 24-ft-diameter Kevlar/nylon ribbon parachute for decelerating a 760-lb test vehicle for parachute deployment conditions of up to Mach 1.5 (dynamic pressures from 300 to 2800 lb/ft^2). Seventy flight tests were conducted to develop this parachute system; a peak deceleration of 240 g was measured. A sketch of the parachute test vehicle and the parachute pack is shown in Figure 9.8. The 24-ft parachute is packed around a set of telescoping aluminum tubes. A 12-point suspension line load ring, a deployment plate, and an assembly of cutters (to stop the outer tube) are the remaining parts of this assembly. The parachute is deployed by firing the gas generator (which produces pressures of 9500 to 13,000 lb/in^2) into the volume enclosed by the telescoping tubes. The parachute reaches line stretch in ~0.165 s; the parachute is deployed at a velocity relative to the vehicle of ~165 ft/s. The aft 11 in. of the tail can is separated by the shearing of six aluminum pins during deployment by action of the pusher plate. This tail can and the parachute bag, which deploy with the parachute, are attached to the apex of the canopy with four 9000-lb nylon straps to prevent them from colliding with the canopy as it inflates and the system decelerates. The outer tube, about which the parachute is packed, remains attached to the inner tube. The momentum of the outer tube is absorbed by a system of cutters that displace metal as the tube is brought to a stop, thereby preventing damage to the parachute. This deployment system of a thrusted telescoping tube has provided repeatable and reliable parachute deployments for the 70 development flight tests and for the many subsequent system flight tests.

Webb and Palm[9.12] developed a two-stage parachute system to recover a 500-lb surveillance drone. This consisted of a 5.6-ft-diameter first stage and a 31-ft-diameter second stage; both were ribbon parachutes made of nylon and Kevlar and were packed under pressure. The aft parachute compartment door was jettisoned to initiate parachute deployment (i.e., the door extracts the drogue deployment bag). The drogue parachute acts for 6 s, and then the second-stage main parachute is deployed.

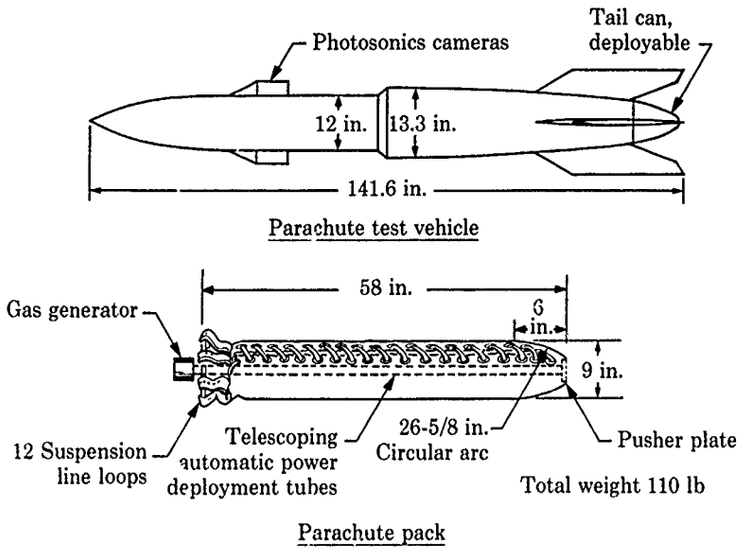


Figure 9.8. Parachute test vehicle and pack

Behr[9,13] developed a parachute system for the Army's High-Speed Airdrop Container (HISAC). The 825-lb HISAC will be aircraft-delivered from altitudes as low as 200 ft above ground level and speeds as high as Mach 0.95. The parachute system consists of an aerodynamically thrusted tail plate, the drogue parachute and bag, and the main parachutes and bag. The initially reefed (for 0.8 s) 8.5-ft-diameter nylon ribbon drogue parachute operates for 1.5 s and decelerates the vehicle from a maximum dynamic pressure of 1330 lb/ft^2 down to a safe dynamic pressure of ~200 lb/ft^2, where the cluster of three T-10 (35-ft-diameter flat extended skirt) parachutes can be deployed. An air scoop (25 in^2 of frontal area) is attached to the periphery of the tail plate and oriented to the top of the vehicle. An arming wire is pulled (after release of the vehicle from the aircraft) to release the air scoop, allowing rotation into the free-stream. The air scoop air-loading causes the tail plate to rotate about its base; two additional drag flaps, located on the bottom of the tail plate, are deployed after the tail plate has rotated ~15 degrees. This combined drag rotates the tail plate out of its latch mechanism at the bottom of the vehicle. The tail plate then quickly accelerates downstream, and pulls the drogue bag and parachute out of the vehicle. The drogue operates for 1.5 s and then separates from the vehicle after deploying the main parachute cluster.

9.2.5 Tractor rockets

Tractor rocket deployment systems have been considered as alternates for two high-performance parachute systems at Sandia. A tractor rocket system was studied by Johnson and Peterson[3,6] to deploy the 46.3-ft-diameter ribbon parachute used to decelerate a 2465-lb payload released from aircraft flying at transonic speeds and low altitudes. This tractor rocket system was studied as a back-up deployment system for the cluster of three 3.8-ft-diameter ribbon parachutes adopted as the baseline design. The parachute deployment dynamic pressures for this payload range from 300 to 2130 lb/ft^2. The principal disadvantage of pilot parachutes is that the rate of deployment and the deployment loads on the main parachute are proportional to the dynamic pressure acting on the pilot parachute. A pilot parachute that works well at high speeds may take too long to deploy the main parachute at the low aircraft release speeds. A tractor rocket system is illustrated in Figure 9.9. The tractor motor burned for approximately 0.4 s, with an average thrust of ~2000 lb. The main parachute is deployed by firing the rocket motor and allowing the rocket thrust to pull the main parachute deployment bag out of the payload's aft assembly. The principal advantage of this system is that the deployment forces are determined by the rockets' thrust rather than by the dynamic pressure of the deployment. Its principal disadvantages are higher cost, greater complexity, and greater weight compared to a pilot parachute deployment system.

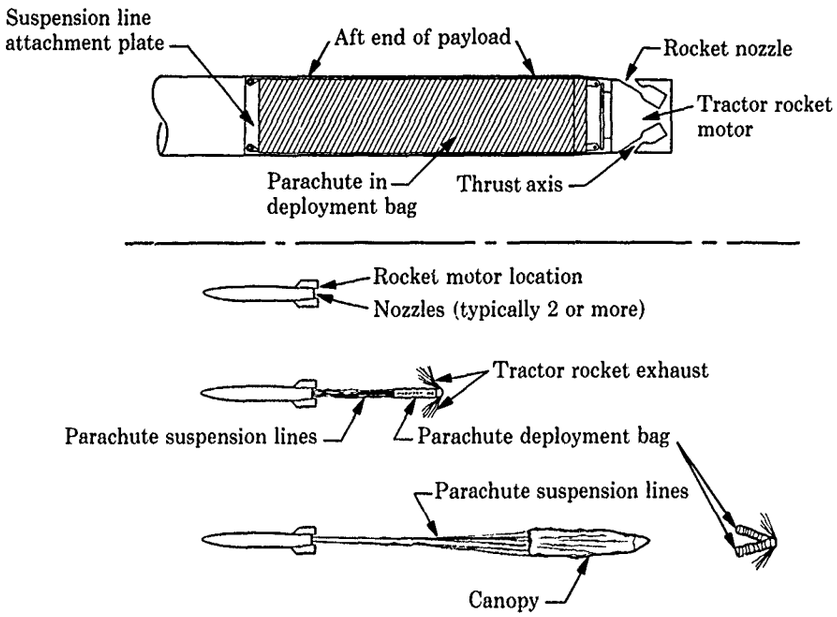


Figure 9.9. Tractor rocket parachute deployment system

Feasibility of the tractor rocket system was investigated using a 22.2-ft-diameter ribbon parachute rather than the baseline 46.3-ft-diameter main parachute. Static firings were made to determine the thermal effects of the rocket exhaust plume on typical parachute and deployment bag materials. No thermal damage to the materials was observed in these tests. Two static deployment tests were conducted to demonstrate that the tractor rocket could deploy a parachute system in an orderly manner. A 22.2-ft-diameter nylon ribbon parachute and a 24-ft-diameter nylon/Kevlar parachute were used in these tests; no damage to the parachute materials was observed. Three flight tests of the tractor rocket deployment system were conducted at Sandia's TTR ballistic range using the 22.2-ft parachute and a 2200-lb test vehicle released from an A-7C aircraft. Figure 9.10 is a photograph of the tractor rocket deploying the parachute during one of these tests. The horizontal displacement and velocity of the tractor rocket relative to the payload are presented in Figure 9.11 for each test. Deployment control was excellent, deployment loads were low, and there was no damage to either the deployment bag or the parachute. A final test was conducted at Sandia's sled track to evaluate the tractor rocket deployment of the 22.2-ft parachute when the payload was flying at an angle of attack. The deployment was successful, with negligible suspension line sail. Johnson and Peterson demonstrated that the tractor rocket system provided more orderly and reliable parachute deployments than the cluster pilot parachute system for this wide range of deployment dynamic pressures. However, cost considerations prompted the selection of the pilot parachute system for the baseline design.

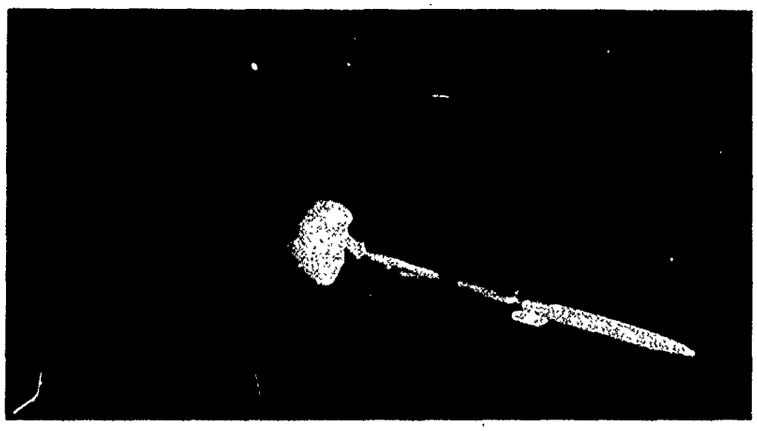


Figure 9.10. Tractor rocket deployment of a 22.2-ft parachute

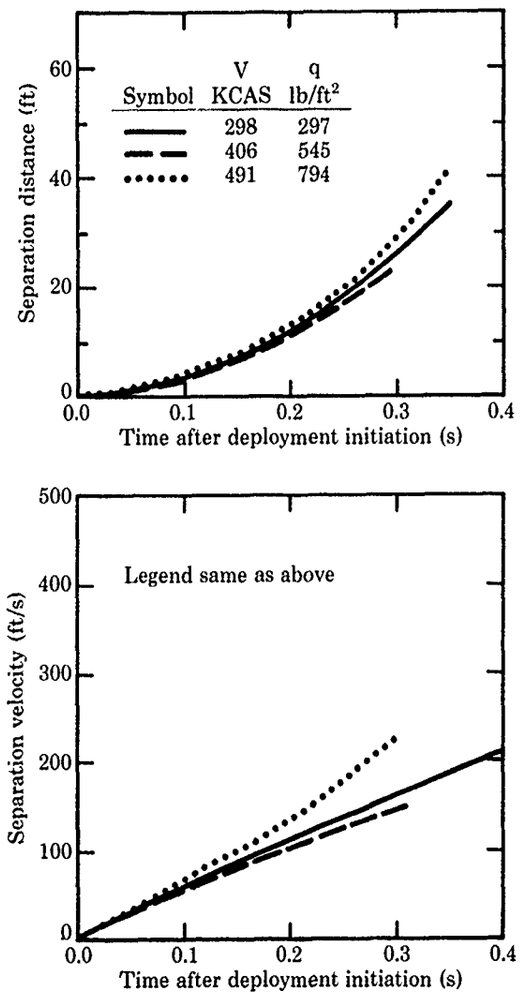


Figure 9.11. Performance results of tractor rocket flight test
(V and q are deployment velocity and dynamic pressure, respectively)

Peterson et al.[1,2] developed a 5-ft-diameter ribbon parachute to recover an 800-lb payload flying at both subsonic and supersonic speeds; deployment dynamic pressures ranged from 440 to 4400 lb/ft^2. They developed two methods of parachute deployment: separable high-drag wedge fins and a tractor rocket system. The separable 25-degree wedge fins, used in six flight tests, performed so successfully that this technique replaced the tractor rocket as the baseline design for the deployment system, even though the tractor rocket system performed flawlessly; again, the lower cost of the wedge fin system was the primary consideration for this selection. Figure 9.12 is a sketch of the tractor rocket system used for this application. The flight parachutes were packed in a two-leaf Kevlar deployment bag. The finished pack measured 4.5 in. in diameter, was ~35 in. long, and weighed ~10 lb. The base diameter of the tractor rocket measured 4.5 in. and was 9 in. long. The exhaust from eight nozzles, canted 25 degrees from the axial centerline, was directed forward from near the motor base. The tractor rocket was required to provide a differential velocity of 150 ft/s at canopy stretch (7.5 ft behind the payload). The motor delivered a total impulse of 100 lb-s in 0.1 s. Parachute deployment was initiated by firing the tractor rocket. Thirty milliseconds after igniting the tractor rocket, a shaped charge was used to sever the aft section of the payload. The axial component of thrust from the tractor rocket pulled the aft payload section away from the main payload, deploying the parachute in the process. The results from the two flight tests, shown in Figure 9.13, demonstrate that the differential velocity requirement of 150 ft/s was met. The tractor rocket was used successfully in ten flight tests at deployment dynamic pressures between 1660 and 4470 lb/ft^2; the sequence times from initiation of deployment to canopy stretch ranged from 0.08 s to 0.13 s.

In summary, the tractor rocket deployment technique should be considered in the design of high-performance parachute systems whenever complete control of the deployment process and consistent deployment times are required for a wide range of deployment speeds. However, the tractor rocket system is more costly, more complex, and heavier than other deployment systems.

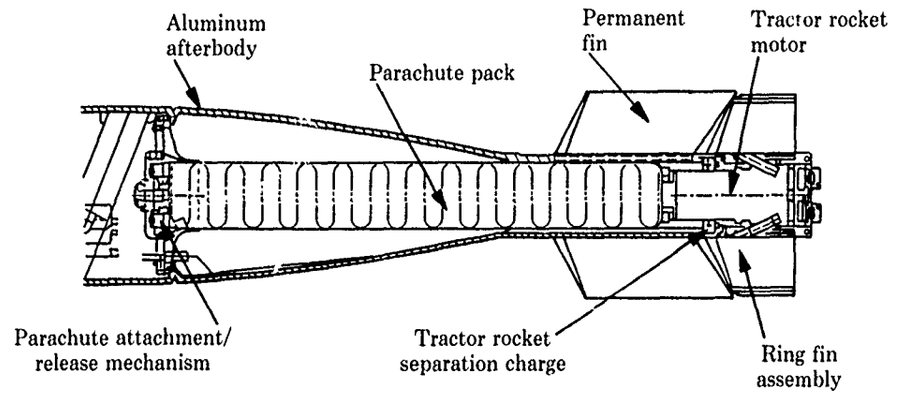


Figure 9.12. Payload with tractor rocket motor parachute deployment system

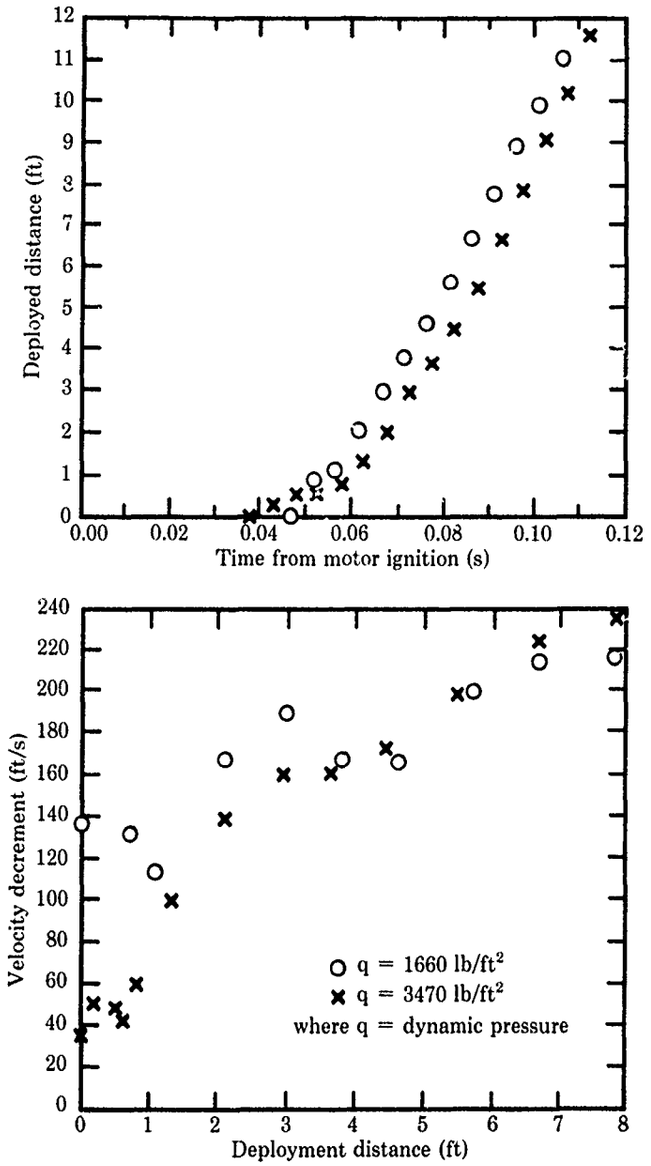


Figure 9.13. Flight test performance results of tractor rocket deployment

9.3 Deployment bags

9.3.1 Background

The Parachute Design Guide[2 1] and Ewing, Bixby, and Knacke[1,7] provide very descriptive discussions of deployment bag designs. Widdows[5 6] received a patent for his pioneering work in the '50s on the design of deployment bags for high-performance parachute systems. The primary advantages of deployment bags are (1) the drag area of the deployed parachute mass is minimized, which reduces the snatch load; (2) the canopy is more correctly placed relative to the payload at the start of the opening process, which reduces parachute malfunctions; and (3) friction damage to the canopy or suspension lines from ribbon or line rubbing is reduced because of the protection afforded by the bag and associated line ties, canopy ties, closure flaps, etc. One disadvantage is the possibility of friction burns to the canopy or suspension line (from the bag liner) during the high-speed removal of the parachute from the bag.

A deployment bag provides controlled, incremental, and orderly deployment of the suspension lines and the canopy as the bag separates from the payload. Some of its essential design features are separate sections for the canopy and the suspension lines plus closure flaps locked with breakable ties or other means of ensuring that the flap opens at line stretch. Both canopy and suspension line ties are used for high-performance parachutes to ensure orderly deployment. Deployment bag closure flaps are often secured closed with webbing loops that must be strong enough to stay locked during handling, installation in the payload, and deployment, and yet open readily at the proper time near the end of the deployment sequence. In some designs, where the inner flaps separate the line and canopy sections, the last two bights of the suspension line bundle are inserted through the loops to lock the canopy section of the bag. At very high speeds, the bights inserted in the loops will burn and melt; hence, an alternative satisfactory method is to close each section of the deployment bag with a retainer that is tied closed and is severed with cut knives. Similarly, suspension line stows are passed through the locking loops in the closure flaps at the end of the deployment bag in order to close the suspension line section and ensure orderly deployment.

The deployment bag design for extraction by pilot parachute or by prior-stage drogue parachute (see Figure 9.14) must incorporate a strong bridle harness with longitudinal webbing along the bag's exterior. This harness must be capable of transferring the extraction loads along the length of the pack. The bag's end closure, the canopy and suspension line ties, the closure flap between bag sections, and the bag's wall friction all work together to prevent premature dumping of the parachute from the bag until it has been released by increasing the bridle tension, which actuates the unlocking device (e.g., a lacing cutter). This ensures orderly payout of the suspension lines and canopy during the stretch-out process, and the deployment bag prevents premature initiation of canopy inflation. Complete stretch-out of both the lines and canopy is enhanced by use of a bridle attached to the apex of the canopy and the bag, attached either permanently or with a breakaway line (vent break cord) strong enough to give the parachute an adequate drag force. The permanently attached bridle must be long enough to permit the bag to strip completely from the canopy and strong enough to withstand the pilot parachute drag loads and inertial loads. The breakaway bridle attachment is often used when

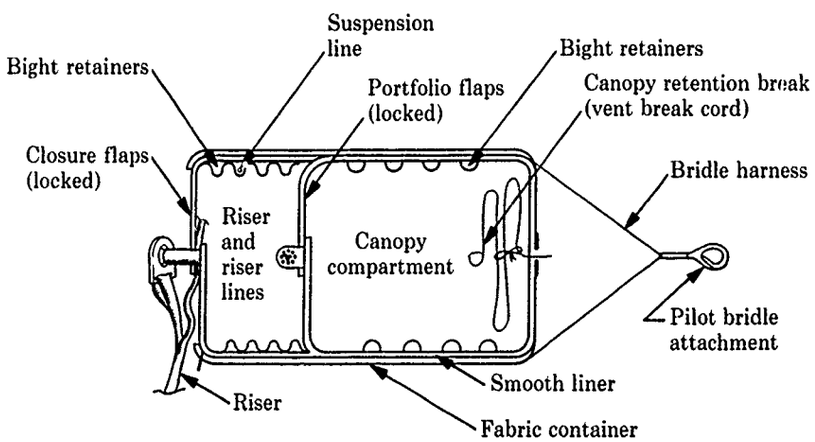


Figure 9.14. Schematic arrangement of bridle-extraction bag pack

the deployment comes as a result of a prior-stage drogue parachute; it is also used when permanent attachment of the deployment bag and pilot parachute to the main parachute could have an adverse effect on the inflation or operation of the main canopy.

9.3.2 Theory

We were able to locate a few papers in the literature that model the effects of bag strip and line ties on parachute deployment. Purvis discusses the effect of line ties in his computer simulation of line sail in References 5.2 and 5.3. Toni[1,10] developed a theory for the dynamics of bag strip for a parachute deployment by a pilot parachute. Heinrich[5.8] developed a parachute snatch force theory that incorporated the riser and suspension line disengagement impulses. He showed that the disengagement impulses strongly affect the magnitude of the snatch force, which in turn affects the design of the deployment bag. French[5.12] developed a first-order theory for calculating the parachute/forebody separation velocity and deployment time; he included the effects of ties on the deployment of a pilot-parachute-extracted main parachute. Ties temporarily restrain a fold or folds of a parachute until deployment. Ties extend the time required for deployment, and reduce the relative velocity between the parachute and its attached forebody prior to line stretch.

9.3.3 Bag design

As was mentioned in Chapter 2, Sandia started its Low-Level Delivery (LLD) program in 1954 to investigate the feasibility of releasing payloads at transonic speeds from aircraft flying at low altitudes (100 to 300 ft). This was a cooperative program with the Parachute Branch at the USAF Wright Air Development Center in Dayton, Ohio; the parachutes were fabricated and packed in an experimental parachute shop at the USAF Air Materiel Command, Norton AFB, San Bernardino, California. Maydew[9.14] proposed that Sandia develop a parachute laboratory to design, fabricate, and pack high-performance parachutes for the LLD and other programs. Sandia's Parachute Laboratory was placed in operation in 1958. Harold E. Widdows, who for several years had worked on the LLD program in the experimental parachute shop at Norton AFB, directed the technical work in the Parachute Laboratory from 1958 until his retirement in 1989. Under his leadership, major contributions to the technology of high-performance parachutes were made in the areas of parachute design, layout, fabrication, packing (especially pressure packs), and deployment bag design, including layout and fabrication. One of his many technical contributions was in the design and fabrication of heavy-duty deployment bags. These unique bag designs have been the key to Sandia's successful development of high-performance parachutes for over 30 years. He was issued a patent (Widdows[5.6]) for "Parachute Deployment Control Assembly" on August 25, 1964; the concepts patented were a summary of his deployment bag design and development work since 1954. These concepts have been successfully used to date by Sandia for the design of high-performance parachute systems.

Pepper and Cronin[9.15] conducted four rocket-boosted sled tests to investigate the use of line ties in controlling the snatch load while deploying a 110-lb simulated parachute pack (lines-first deployment) at 800 ft/s using two 10,000-lb-strength, 50-ft-long nylon lines. The pack was deployed from a cone-cylinder forebody permanently attached to the rocket sled. Cameras manufactured by Photosonics, Inc. (operating at 400 frames per second) and a 15,000-lb-capacity load cell were mounted on the cone cylinder to photograph the deployment and to measure the dynamic loads (including the final snatch load), respectively. The deceleration load data from the load cell was telemetered to a receiving station near the sled track. A 1.5-ft-diameter guide surface pilot parachute, deployed by a small drogue gun, was used to ensure drag separation of the simulated pack from the sled at deployment. Line ties in six strengths (from 200 to 1500 lb) were located at 5- to 15-ft intervals along the 50-ft lines; the 1500-lb line was used to tie the 30- to 50-ft-long portion of the suspension line. The tests showed that the line ties were very effective in controlling the shock load at line stretch; the maximum load measured was 10,000 lb.

Pepper[1.1,4.13] developed a 24-ft-diameter Kevlar/nylon ribbon parachute to decelerate a 760-lb payload after deployment at low supersonic speeds at low altitude. A photograph of the 9.1-in.-diameter and 51-in.-long pack is shown in Figure 9.15. Pressure packing with a hydraulic press, along with an electric motor bag-lacing puller, was used to achieve the high pack density of 43 lb/ft^3. The parachute and bag weighed ~90 lb. Note that this two-leaf bag is fabricated of Kevlar and nylon, and 1500-lb nylon webbing is used to lace the bag together. The time sequence for deploying this 24-ft parachute is given in Table 5.1; note that the time required to deploy this parachute (with 28-ft-long suspension lines) is only 0.15 to 0.40 s. The breaking strengths of the line ties and canopy ties are given in Table 5.1. The line retainer consists of two 1500-lb tubular nylon webbings. The suspension line ties consist of two 200-lb nylon tapes located at 15 stations in the bag. The canopy retainer (which separates the suspension lines from the canopy) is a 1500-lb tubular nylon webbing. The canopy is tied to the bag at three stations with two 200-lb nylon tapes each.

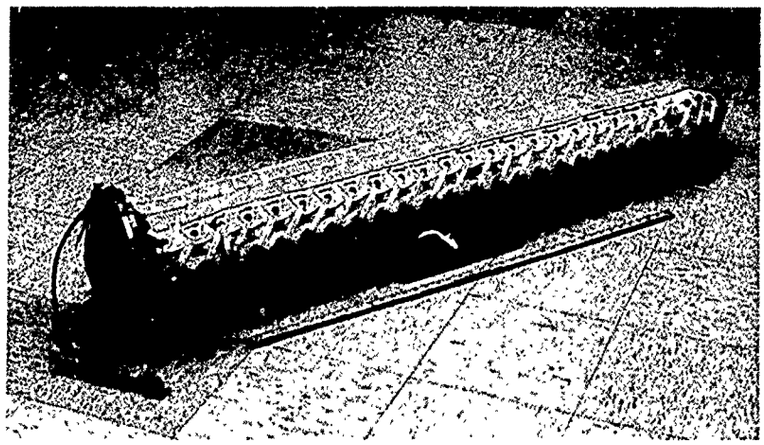


Figure 9.15. Photograph of a 9.1-in.-diameter, 51-in.-long pack

The bag is constructed of 7.25-oz nylon duck cloth and is lined with Teflon cloth to minimize friction burning of the canopy and lines due to the high exit velocities (~165 ft/s) of the parachute from the bag. Woven nylon webbing, 1.72 in. wide and of 1200-lb strength, is used for longitudinal reinforcement on the outer edge of the bag and for radial reinforcement at three stations on the aft end (pointed) of the bag. Woven nylon webbing, 1.72 in. wide and of 4000-lb strength, is used for radial reinforcement at both extreme ends of the bag. Poly(vinyl butyral)-coated Kevlar webbing, 1.75 in. wide and of 20,000-lb strength, is sewn longitudinally on the outer edge of the bag (two per panel) to transmit the dynamic loads from the thrusting tail plate. Poly(vinyl butyral)-coated Kevlar webbing, 1 in. wide and of 4000-lb strength, is sewn to the outer edge of the bag to support the lacing grommets; one continuous Kevlar webbing is used in a zig-zag fashion, back and forth radially and longitudinally, across the panel to support the 20 grommets on each side of the panel. This same 4000-lb Kevlar webbing is used for the canopy tie loops on the inside of the panel at the aft end of the bag. Poly(vinyl butyral)-coated Kevlar webbing, 1 in. wide and of 6000-lb strength, is used for the line tie loops on the inside and on the front end of the bag.

Johnson and Peterson[36] developed a Kevlar-nylon 46.3-ft-diameter conical ribbon parachute to retard a 2465-lb payload delivered at speeds up to 800 KCAS and at altitudes as low as 150 ft above ground level. A photograph of the 46.3-ft parachute stretched out on a packing table is shown in Figure 9.16. A photograph of the packed parachute (16.5 in. in diameter and 46 in. long) is shown in Figure 9.17. The sequence of events during deployment of this parachute from its four-leaf deployment bag is given in Table 5.2. Note that the bag stripping time varies from 0.4 s to 0.7 s. The breaking strength of the line ties, canopy ties, bag lacing, and vent break cord is also given in Table 5.2. The bag lacing is made of 2000-lb braided Kevlar, which is severed with cut knives. The canopy retainer is a 6000-lb nylon webbing, which is also severed with cut knives. There are twelve 90-lb nylon line ties (three longitudinal stations on four panels) and a total of eighty 500-lb nylon line ties (twenty stations on four panels). There are sixteen 200-lb nylon canopy ties (four stations on four bag panels). A 1000-lb nylon tape is used for the vent break cord.

The cluster of three 3.8-ft-diameter ribbon pilot parachutes is packed into an envelope-type deployment bag (see Figure 9.18) that is attached to the main pack aft of the aluminum end cap (see Figures 9.17 and 9.19). Because the pilot parachute cluster is deployed by an 18-in.-diameter plate that is explosively ejected into the airstream at the payload base, the pilot parachutes can be subjected to very high forces during high-speed deployments. To prevent premature deployment under these conditions, the bag contains provisions for a vent break cord, closure flaps for the canopy compartment that must be cut open, and several line ties. The pilot parachute deployment bag, which is constructed entirely of Kevlar materials, is attached to the tail plate with six 3500-lb Kevlar lines. The suspension lines for the pilot parachute system are attached to the end cap that forms the aft closure of the deployment bag for the 46.3-ft-diameter parachute.

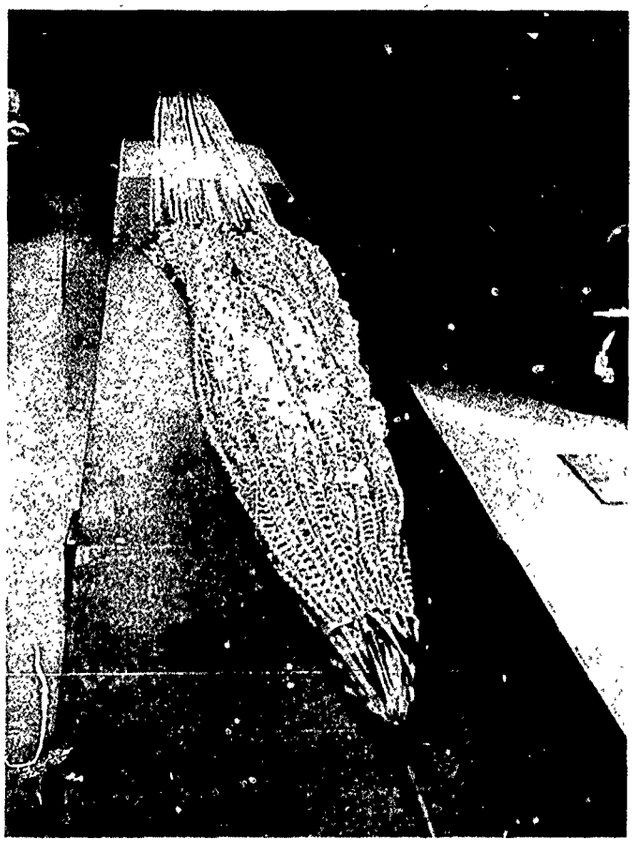


Figure 9.16. A 46.3-ft-diameter parachute stretched out on a packing table

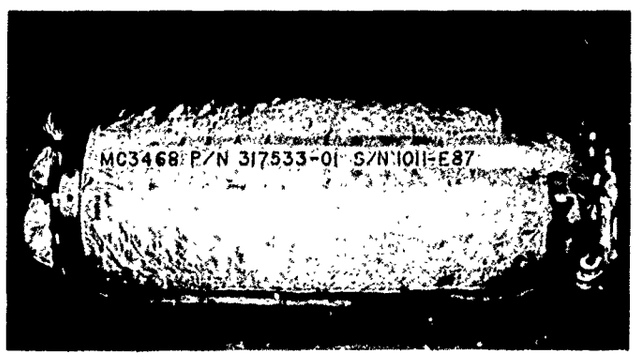


Figure 9.17. Packed parachute

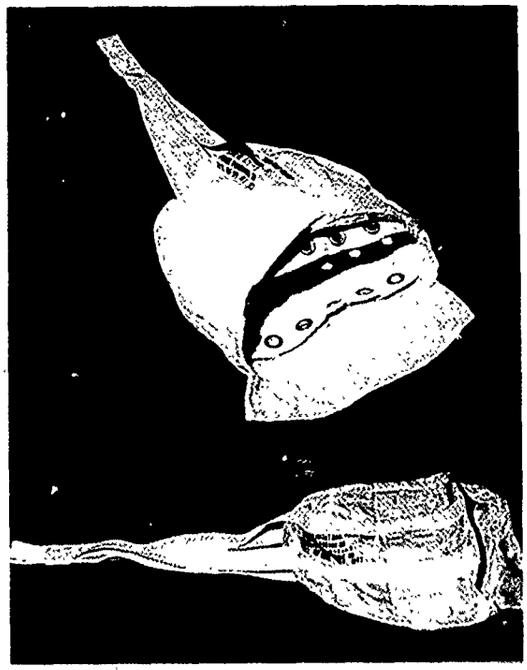


Figure 9.18. Pilot parachute deployment bag

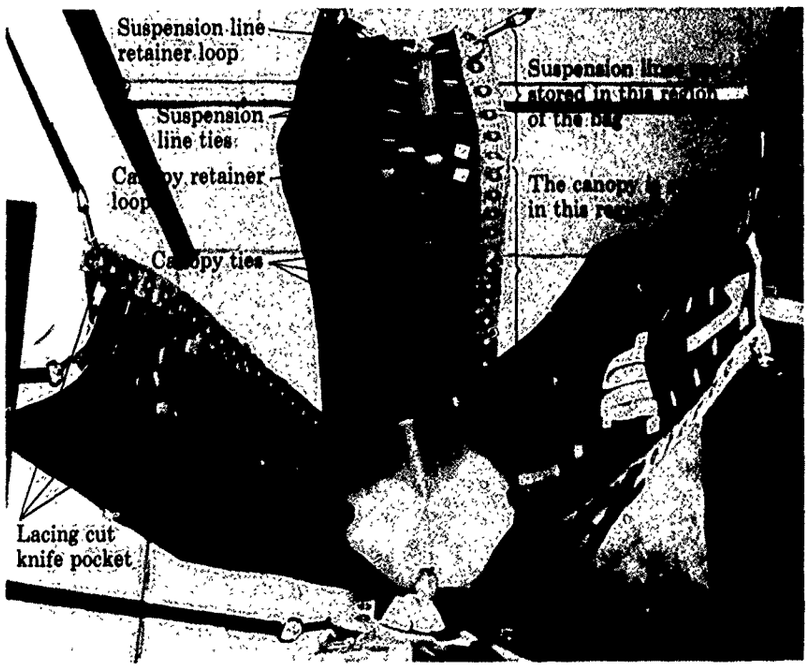


Figure 9.19. Main parachute deployment bag

The deployment bag for the main parachute (Figure 9.19) consists of four identical panels mechanically attached to an aluminum end cap. The pilot parachute loads are transferred from the end cap to longitudinal webbings on each bag panel. The panels are constructed from Kevlar materials for strength, with a Teflon lining to prevent friction burning of the parachute during high-speed deployments. Loops are placed on the inside of the bag panels for canopy ties, the canopy retainer, line ties, and the line compartment retainer. The vent break cord in the main parachute is attached to an eyebolt on the end cap. The line and canopy ties provide orderly deployment of both the suspension lines and the canopy, and are designed to break during deployment. The canopy and line retainers prevent premature failure of the canopy ties and line ties when the pilot parachute system is exerting high accelerations to the main parachute system. Both of the retainers are cut out during the normal deployment sequence. The four deployment bag panels are provided with reinforced grommet strips used to lace the bag panels together. The lacing reduces the diameter of the assembly during the packing operation; the system is pressure-packed with a hydraulic press.

The bag is constructed of 3-oz/yd Kevlar cloth and lined with Teflon cloth. The canopy tie loops, line tie loops, canopy retainer loops, and line retainer loops (on the inside of each panel) are made of 1-in.-wide, 6000-lb Kevlar webbing. Two 1.75-in.-wide, 20,000-lb Kevlar webbings are sewn longitudinally to the outside of each panel to transfer the pilot parachute cluster loads to the main parachute bag. The 18 lacing grommets along each side of the four panels are attached radially to the outside of the panels with 1.75-in.-wide, 4000-lb Kevlar webbings. The front of each bag panel (near the endplate) is radially reinforced with 1.75-in.-wide, 10,000-lb Kevlar webbing. Similarly, the aft section of each bag panel is radially reinforced with 1.75-in.-wide, 4000-lb Kevlar webbing. A 1-in.-wide, 10,000-lb Kevlar webbing along the centerline of each panel longitudinally reinforces each panel.

In summary, both of these heavy-duty deployment bags (for the 24- and 46.3-ft-diameter parachutes) have been successfully used in dozens of flight tests, spanning a wide range of deployment dynamic pressures at deployment speeds up to low supersonic. The information presented in this chapter on deployment methods and deployment bags should provide the designer of a high-performance parachute system with sufficient data for a preliminary design. More detailed information is available, of course, from each of the references cited. The authors wish to emphasize again that the design of the deployment system is just as important as the design of the parachute, if repeatable, reliable operation of high-performance parachutes is to be achieved.

References

9.1 E. K. Huckins III, "Techniques for Selection and Analysis of Parachute Deployment Systems," NASA TN D-5619, January 1970.

9.2 L. R. Poole and E. K. Huckins III, "Evaluation of Massless-Spring Modeling of Suspension-Line Elasticity During the Parachute Unfurling Process," NASA TN D-6671, February 1972.

9.3 W. B. Pepper, *Development of a Parachute Recovery System for a Reentry Nose Cone (NRV)*, SAND75-0564, Sandia Laboratories, September 1977.

9.4 W. B. Pepper, "Development of an 8-ft-dia Ribbon Parachute for Recovery of a Test Device at Transonic Speeds," AIAA 84-0793, April 1984.

9.5 W. B. Pepper, "Comparison of Theoretical and Experimental Performance of a 6.44-ft-dia Parachute," *J Spacecraft and Rockets*, Vol. 22, No. 6, November-December 1985.

9.6 J. A. Buckley, "Missile Recovery System for High-Speed, Small-Caliber Missiles," AIAA 86-2462, October 1986.

9.7 H. N. Murrow and J. C. McFall Jr., "Some Test Results From the NASA Planetary Entry Parachute Program," *J Spacecraft and Rockets*, Vol. 6, No. 5, May 1969.

9.8 I. A. Whalley, "Development of the B-1 Crew Module Parachute Recovery System," AIAA 73-467, May 1973.

9.9 J. E. Pleasants, "Flight Qualification of Mortar-Actuated Parachute Deployment Systems," AIAA 75-1403, November 1975.

9.10 R. W. Rodier, R. C. Thuss, and J. E. Terhune, "Parachute Design for the Galileo Jupiter Entry Probe," AIAA 81-1951, October 1981.

9.11 A. K. Banerjee and J. M. Coppey, "Post-Ejection Impacts of the Space Shuttle Solid Rocket Booster Nose Cap," *J Spacecraft*, Vol. 12, No. 10, October 1975.

9.12 D. Webb and L. Palm, "Development of a Nylon-Kevlar Recovery System for the CL-289 (AN/USD 502) Surveillance Drone," AIAA 81-1952, October 1981.

9.13 V. L. Behr, "The Development and Testing of the HISAC Parachute Recovery System," AIAA 89-0921, April 1989.

9.14 R. C. Maydew, *Sandia Corporation Parachute Research Facilities Proposal*, SCTM 151-56-51, Sandia Corporation, July 1956.

9.15 W. B. Pepper and D. C. Cronin, "Experimental Research on Parachute Deployment Load Control by Use of Line Ties," *J Aircraft*, Vol. 6, No. 1, January-February 1969.

CHAPTER 10

ANCILLARY DEVICES, PARACHUTE FABRICATION, AND PACKING

10.1 Ancillary devices

10.1.1 Reefing line cutters

Parachute reefing may be required for parachute systems that are deployed at high dynamic pressures to control the opening-shock loads and to provide successive parachute drag areas. This will maximize performance of the parachute system while minimizing the parachute's weight and packed volume. Reefing is discussed in Section 4.2.7, and Knacke[1.8] provides a thorough discussion of reefing methods and techniques for calculating reefed parachute drag areas. This section describes the hardware used to cut the reefing line at the precise time during the inflation process such that the purpose of parachute reefing is accomplished.

The Parachute Design Guide[2.1] and Ewing, Bixby, and Knacke[1.7] discuss reefing line cutters and illustrate their operation with sketches and photographs. Barlog[10.1] provides an excellent description of the components used to reef a parachute. They consist of the reefing line, reefing rings, the reefing line cutter, and the cutter pocket or some other means for mounting the cutter to the parachute system. The reefing line cutter is generally a pyrochemical device with mechanical or electrical actuation. Mechanical actuators are activated by pulling an actuator to fire the cutter directly or to begin the timer mechanism. Energy to operate the cutter is normally obtained by attaching a line to the actuator and the other end to the suspension line. When the portion of the suspension line with the actuator line is deployed, the actuator is pulled from the reefing line cutter. Actuation of the initiation mechanism results in work energy being imparted to the pyrochemical cartridge of the cutter. The cartridge contains a propellant material that generates a high-pressure gas within the confines of the assembly. The gas pressure forces the cutter blade to pass through the cutter aperture, cutting the reefing line and allowing the canopy to inflate to the next reefed diameter or to its full-open diameter.

Pyrotechnic reefing line cutters have a high energy level and a favorable weight-to-volume ratio. Barlog[10.1] provides detailed design information and sketches of the initiation mechanisms, the cartridges, and the cutter assemblies for the Mercury-Gemini, Apollo, and Space Shuttle SRB parachute recovery systems.

The Parachute Design Guide[2.1] offers suggestions on the detailed design of reefing line cutters. Ewing, Bixby, and Knacke[1.7] report that reefing line cutters are available in a variety of sizes and delay times. Line cutters are usually fabricated of anodized aluminum or stainless steel, with the pyrotechnic elements hermetically sealed. Steel bodies are recommended if dense pressure packing of the parachute is anticipated. Pyrotechnic time delays of up to 30 s and a tolerance of $\pm 10\%$ at standard temperatures are typical, but the accuracy may vary by as much as $\pm 25\%$ over a wide temperature range. Figure 10.1 is a photograph of reefing line cutters in use at Sandia and elsewhere in 1968.

The Parachute Design Guide[2.1] describes the USAF MC-1 reefing line cutter. It had been standardized for operation in systems using heavy-duty nylon reefing lines with a tensile strength of up to 14,000 lb. A Type T-2 explosive actuator and a time delay powder train are used to actuate and govern the cutting sequence. The reefing line is cut with a knife propelled by the powder charge, and the device is actuated by the removal of an arming wire. This device can be reused simply by changing the time delay powder train; however, the barrel of the cutter should be cleaned of all residue before it is reused, to ensure free travel of the knife. Time delays are available for intervals of 0.75, 1, 2, 4, 6, 8, and 10 s.

The MC-1 cutter was used extensively by Sandia and the U.S. Air Force before 1968 for disreefing high-performance ribbon parachutes. However, repeated use in dense packs (sometimes to the density of oak) resulted in such deformation and damage to the cutter that it would not operate. The smaller and lighter weight Ordnance Associates cutter was also used, but the thin-walled tube would deform during pressure packing, which degraded the reliability. Hence, the Half-Moon cutter (on the right in the photograph in Figure 10.1) was developed and patented by Gallagher[10.2] to better withstand the pressure packing loads. It was also easier to attach the lighter weight Half-Moon cutter securely to the canopy to ensure that it would stay attached during the snatch-loading of the parachute system. The

Half-Moon cutter was extensively tested with time delays of 0.5 s, the application to cut the 9000-lb reefing line in the 22.2-ft-diameter parachute described by Maydew and Johnson.[3.1]

Pepper, Bradley, and Jacoby[10.3] developed a reefing line cutter incorporating an RC circuit electronic time delay. This reefing line cutter (Figure 10.2) consists of the housing, anvil, cutter blade, shear screw, Atlas mechanical actuator, actuator adapter, spacer washer, thermal battery, squib, and electronic time delay. The housing design is similar to the Half-Moon cutter designed by Gallagher. The cutter was designed for time delays of up to 10 s (the time delay can be changed by changing the resistance of the RC circuit). The cutter was designed to improve upon the $\pm 20\%$ accuracy of the time delay of the pyrotechnic cutter. The ground environmental tests and the flight tests indicated that the electronic timer was accurate to $\pm 2.5\%$ of the 0.45-s time delay over a temperature range of $-65°F$ to $+160°F$. In addition, its reliability was >0.99 and estimated storage life was >10 years.

Craig[3.21] developed a pyrotechnic-actuated reefing line cutter which, in response to an electrical firing signal, severs a nylon or Kevlar reefing line. A programmable time-delayed firing signal was provided by means of an interconnecting cable, which is attached to one of the suspension lines of

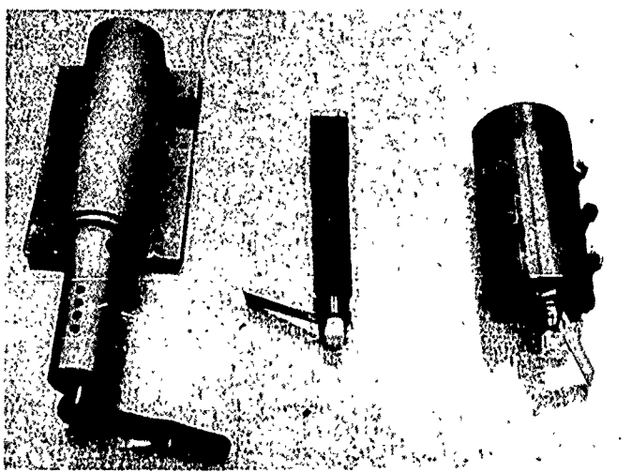


Figure 10.1. Reefing line cutters: MC-1, Ordnance Associates, and Sandia Half-Moon

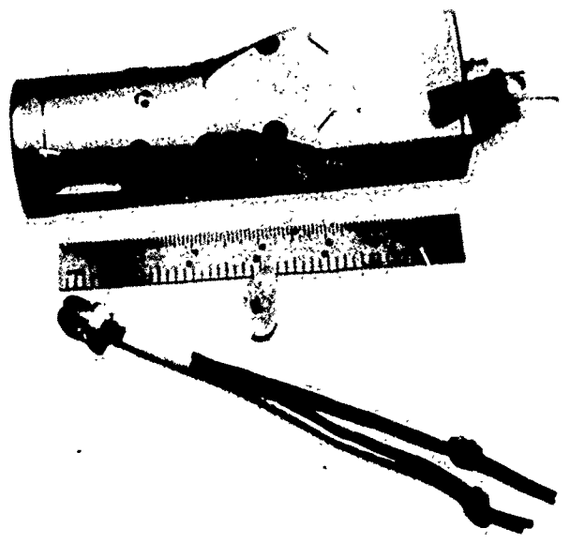


Figure 10.2. Electronic time delay reefing line cutter

the parachute and terminates in a molded plastic connector attached to the cutter assembly (Figures 10.3a and 10.3b). The cutter is roughly 4 in. wide and 8 in. long. Development test data show that the cutter is more than adequately designed to cut 12,000-lb nylon webbing or 13,500-lb Kevlar webbing over a temperature range of −60°C to +90°C. This cutter has been used for many development and system flight tests for the 24-ft-diameter parachute described by Pepper[1.1] and has proved to be very reliable. However, this electrically initiated cutter is much more expensive than a pyrotechnic time delay cutter.

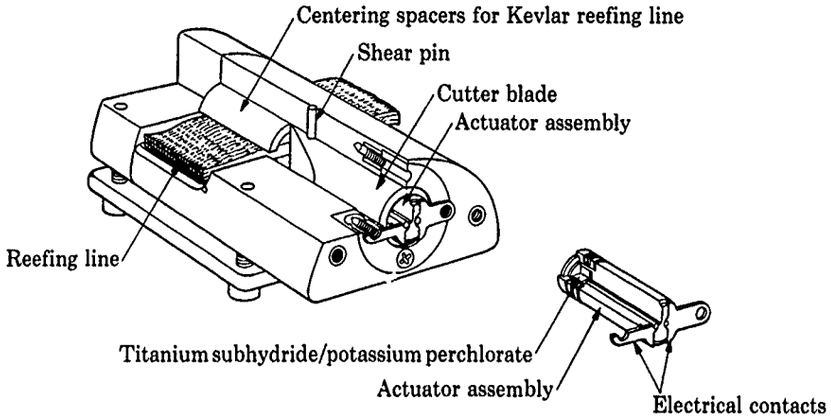


Figure 10.3a. Reefing line cutter

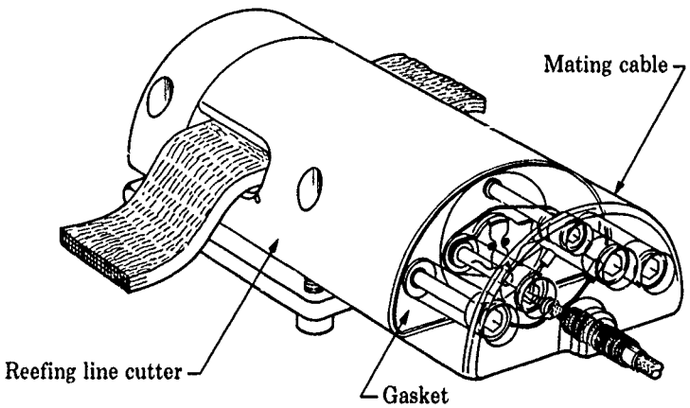


Figure 10.3b. Reefing line cutter and cable assembly

Craig[10.4] developed a pyrotechnic propellant-actuated reefing line cutter to sever a 13,500-lb Kevlar parachute reefing line. Disreefing occurs at 0.85 s after deployment initiation. Timing is provided by an electronic timer module that is an integral part of the cutter. Other design features (Figure 10.4) include a hermetically sealed actuator that is threaded and O-ring-sealed into the body; a stainless-steel solid cylindrical cutter blade with an attached elastomer obturator (which provides a reliable dynamic gas seal throughout the blade stroke); and semicircular Teflon inserts that center and shroud the reefing line webbing during the blade stroke. The average function time for the cutter varies <4% over temperature extremes of −55°C and +80°C. The cutter described by Craig[3.21] was used as the starting point for the design of this cutter. The same type of explosive was used to propel the same type of knife through the 13,500-lb Kevlar reefing line.

Later during the development of this cutter, the method of cutting the reefing line was changed from an explosively driven knife to a knife actuated by a pyrotechnic propellant. During the development, an attempt was made to control the manufacturing costs by using aluminum for the housing (rather than steel) and reducing the required machining to a minimum. This resulted in a weight of only 1.97 lb for the aluminum cutter.

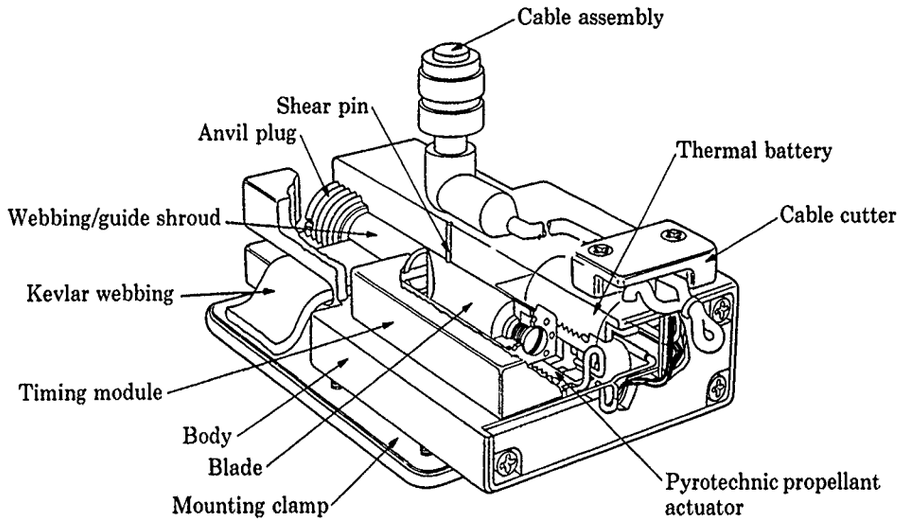


Figure 10.4. Reefing line cutter

Failure of the suspension lines that carried the reefing line cutters occurred on some flight tests. Changing the method of attaching the cutter to the suspension line/skirt band joint minimized those failures. A photograph of the reefing line cutter installation is shown in Figure 10.5. This cutter was used in the development and system tests of the 46.3-ft-diameter parachute described by Johnson and Peterson.[3,6] Extensive ground and flight tests have proved the reliability and repeatability of this cutter, even for pack densities of 40 lb/ft^3. As might be expected, this cutter is much more expensive than a pyrotechnic time delay cutter.

At Sandia, Massis has developed a pyrotechnic time delay cutter with lower temperature sensitivity than was observed in previous pyrotechnic timers. This design is currently being used on systems at Sandia because it has the desirable features of low weight, high reliability and repeatability, and low cost (compared to the electronic timing cutters). A sketch of this state-of-the-art cutter is shown in Figure 10.6. A considerable number of ground and flight tests have been successfully conducted with this cutter.



Figure 10.5. Reefing line threaded through cutter and reefing rings

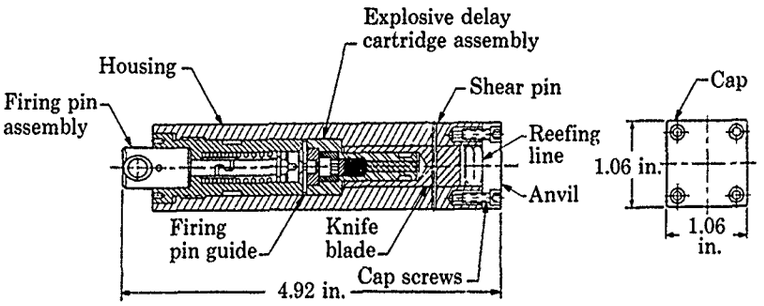


Figure 10.6. Pyrotechnic time delay reefing line cutter

10.1.2 Cut knives

The Parachute Design Guide[2.1] and Ewing, Bixby, and Knacke[1.7] discuss the use of cut knives in the packing of multiple-canopy decelerator systems to release ties and holding tapes and webbings at the appropriate point in the deployment process so as to provide controlled sequential deployment. Tables 5.1 and 5.2 describe how cut knives are used to cut bag lacing, suspension line retainer webbing, and canopy retainer webbing in the deployment bag to ensure orderly deployment of high-performance parachute systems. This is also discussed in the context of deployment bag design in Section 9.3.

A photograph of a typical cut knife installation is shown in Figure 10.7. These cut knives cut the bag lacing for the three 3.8-ft-diameter pilot parachutes used to deploy the 46.3-ft-diameter parachute described by Johnson and Peterson.[3.6] Note that the cut knives are attached to the suspension lines and are activated to cut as the suspension lines become taut during the lines-first deployment. Cut knives are used in a similar fashion to cut the bag lacing, suspension line retainer, and canopy retainer for the 46.3-ft-diameter parachute (see Table 5.2). This very reliable cut knife technique (which requires quality control in the packing procedure) has been used for many years on many different systems at Sandia to help ensure orderly deployment of high-performance parachute systems.



Figure 10.7. Cut knives installed and laced for three 3.8-ft-diameter pilot parachutes in bag

10.1.3 Flotation bags and location aids

Overwater recovery of rocket and other payloads requires the careful design of a flotation bag (integrated with the parachute design) and the associated location aids. The Parachute Design Guide[2.1] and Ewing, Bixby, and Knacke[1.7] provide general guidelines on the design of flotation bags and the associated equipment. The flotation bags discussed in this section, however, will be those developed by Sandia since 1963 for the overwater recovery of rocket payloads. They have been used to recover dozens of payloads, weighing up to 1000 lb, from rocket apogees of up to two million feet. Design information on these systems is given by Holt[1.24] and Johnson.[3.50,3.51,10.5,10.6]

Holt[1,24] discusses the design, development, and testing of a ram-air-inflated flotation device originally conceived at Sandia. A common means of providing auxiliary flotation is to use inflatable fabric structures using construction techniques for fabricating life rafts and marker buoys. These structures are usually inflated by compressed carbon dioxide or nitrogen. For small payloads, however, the gas bottle and valve were found to constitute a large part of the total recovery system weight and volume. Holt proposed to use the ram-air passing through the parachute vent to inflate the flotation bag in order to save recovery system weight and volume. The cylindrical bag would fill with air and then the weight of the payload would hold the open end under water, thereby trapping the air in the bag.

The initial design is shown in Figure 10.8. The flotation bag is attached by nylon webbings (which run the length of the bag) to the vent of the guide surface parachute. All seams were made with a self-curing rubber cement. An elastic skirt was added at the base of the bag to help keep the bag inflated when the load on the parachute was relieved. Also added was a nylon funnel to direct the airflow from the parachute vent into the flotation bag. Two bags of different length-to-diameter ratios were tested; both had a volume of ~3 ft^3. Aircraft drop tests and rocket flight tests demonstrated the feasibility of this ram-air bag concept when used in conjunction with the CO_2-inflated flotation bag. Holt reported a 20% saving in weight and volume in the recovery of 150-lb payloads with this ram-air system.

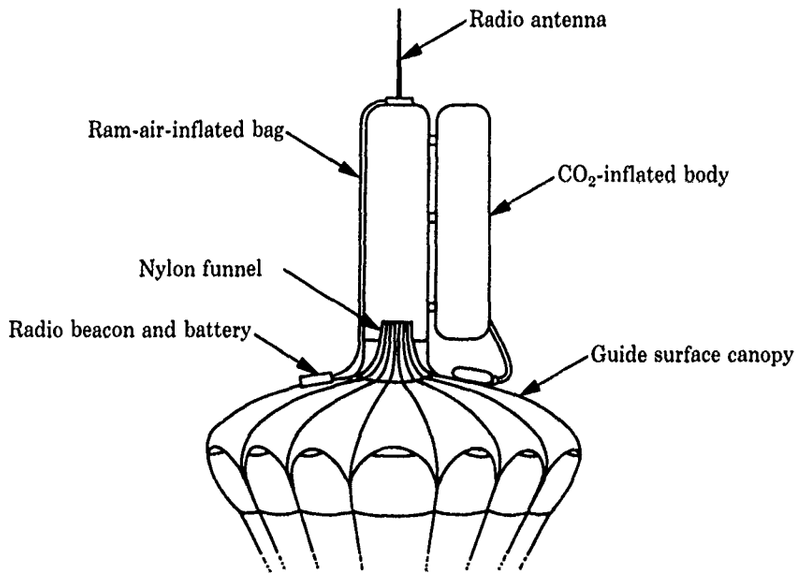


Figure 10.8. Operational recovery system

Johnson[3.50,3.51,10 6] subsequently describes the early evolution of overwater recovery systems for high-altitude sounding rockets at Sandia. The original requirement for a recovery system was that it retrieve (from the sea) 9-in.-diameter payloads weighing 150 lb in air (90 lb in water) after descent from a rocket apogee of 1×10^6 ft. The payloads were required to float for at least 24 hours in a heavy sea, and have location equipment included as part of the recovery system.

The recovery system developed to satisfy these requirements is shown in Figure 10.9. The payload is separated from the rocket booster at high altitude and forced to enter a flat spin (by passive control of the center of gravity), which produces high drag. After deceleration of the payload in the flat spin, the recovery sequence is initiated by a baroswitch closure, which fires a pressure cartridge and ejects the rear cover of the payload. The baroswitch is normally set to operate at 15,000 ft altitude, but it has been set to operate as low as 5000 ft altitude. A 3-ft-diameter ribless guide surface parachute was initially used to stabilize the payload and provide enough deceleration so that the main recovery system could be deployed without damage. Upon deployment of the 3-ft parachute by the ejected cover, two 10-s time delay bridle cutters are initiated. After the 10-s delay, either cutter will cut the load bridle and release the 3-ft parachute, which then deploys the main recovery system from a deployment bag. The main recovery parachute is a 6-ft-diameter ribless guide surface parachute.

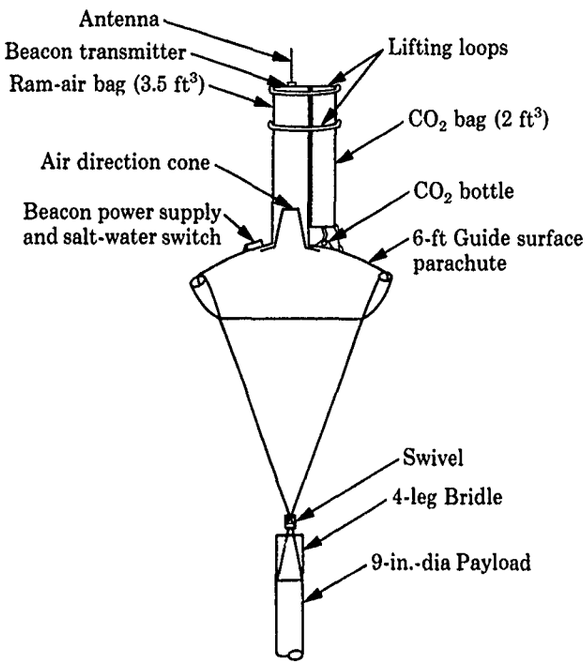


Figure 10.9. The 9-in.-diameter payload recovery system

The flotation bags, air direction cone, and pockets for the CO_2 bottle and locator beacon were attached as shown in Figure 10.9. The complete recovery system weighed 14 lb, occupied 700 in^3 of payload volume, and fitted into the 9-in.-diameter payload. Johnson[10.6] discusses the development program to reduce the weight and volume of the locator beacon (transmitter and power supplies) and the CO_2 bottles and valves. At Sandia's test ranges on Kauai, Hawaii, and on Johnston Atoll, nine successful rocket flights demonstrated the feasibility of this recovery system.

Johnson[3.51] used the same concept to develop an overwater recovery system for 12- to 13-in.-diameter payloads weighing up to 275 lb (170 lb in water) with a redundant flotation capability. This system used an 8-ft-diameter guide surface parachute, a 3.5-ft^3 CO_2 bag, and a 7-ft^3 ram-air bag. The recovery system weighed 17 lb and occupied 1140 in^3 of payload volume.

Recovery of payloads weighing up to 275 lb in air and up to 170 lb in water soon became mandatory. With the advent of larger-diameter payloads and the sealing of large sections of the payload, there arose the possibility that some payloads would float. The recovery system was required to provide a dual flotation capability for payloads that would not float. Water tank tests of the recovery systems with the cylindrical flotation bags showed that the bags would lie flat in the water. Since the locator beacon transmitter and antenna were mounted on the end of the bag, the antenna would be horizontal, resulting in a poor antenna pattern for an aircraft search. Also, any sea action would cause the antenna to be under the water at least part of the time. Therefore, development was started on a spherical flotation bag (Figure 10.10), which would provide a more satisfactory mounting position for the locator beacon transmitter and antenna.

The ram-air bag is sewn to the vent of the 8-ft-diameter parachute, and the CO_2 bag is tied to the top inside of the ram-air bag. Water-tank tests showed that the ram-air bag and beacon antenna remained nearly vertical as a result of the weight of the wet parachute, the CO_2 bottle, and the beacon power supply. Tests conducted in the open ocean with a floating payload showed similar results, and even if the flotation bag assembly is completely inverted it will right itself with the antenna within 30 degrees of vertical. In tests conducted with nonfloating payloads, the spherical ram-air bag retained nearly 100% of its air volume after water impact, compared to about 80% for the cylindrical bags. This recovery system weighs 14 lb and occupies 700 in^3 of payload volume. It replaced the two cylindrical ram-air bag systems described earlier for all of the rocket payload recoveries at Sandia. Figure 10.11 is a photograph of a recovered payload being towed back to land, and Figure 10.12 is a photograph of a typical payload after recovery.

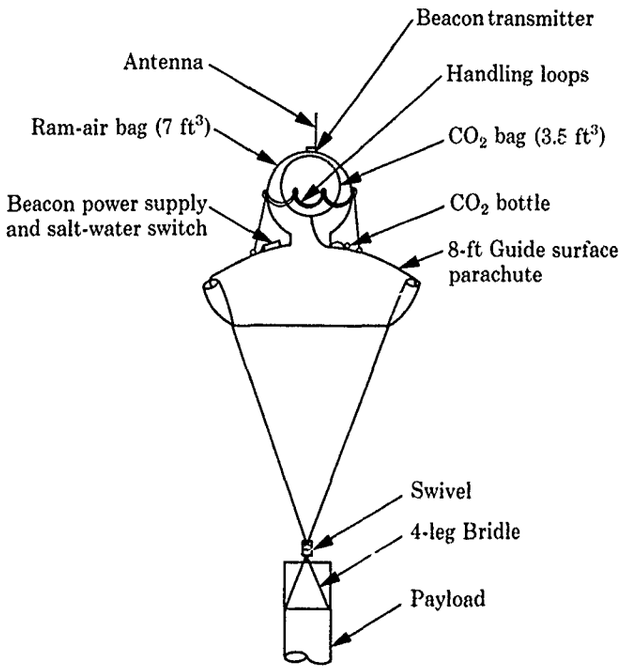


Figure 10.10. Universal recovery system

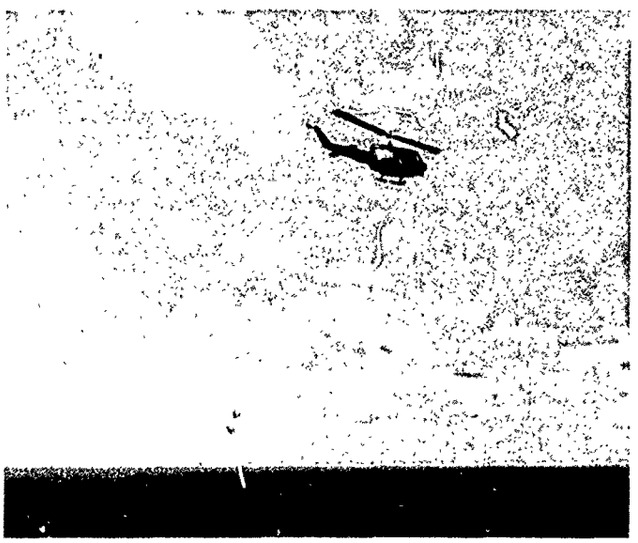


Figure 10.11. Recovered payload being towed back to land

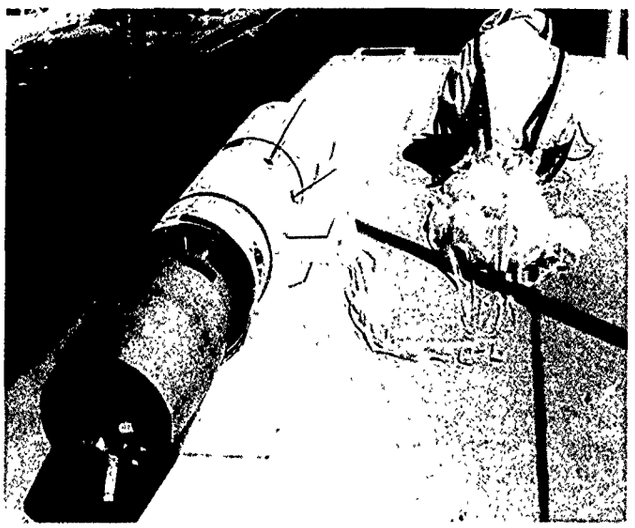


Figure 10.12. Typical payload after sea recovery

Johnson[3.51] discusses the development of systems to recover rocket payloads weighing 50 to 1000 lb. Table 10.1 summarizes the six different recovery systems used for overwater rocket flights. The recovery system weights do not include any part of the payload structure or the heat shield/deployment device because these weights vary from payload to payload; however, they do include the location aids such as strobe light and RF transmitter. The recovery system weight is plotted as a function of payload weight in Figure 10.13 for these six systems. The latest recovery systems retain the concept of flotation bag redundancy but do not use the CO_2 bag. A one-way valve is inserted in the mouth of the ram-air-inflated flotation bag to prevent the air from escaping (Figure 10.14). The material above the anti-inversion straps is unsupported and constructed to lie flat. When the pressure inside the bag exceeds the pressure outside (no inward flow), the valve collapses to its flat condition and seals the inlet to the bag. In addition to the valve, a divider is included that separates the flotation bag into two compartments. This retains the redundant flotation capability. Generally, the flotation equipment is sized so that half of the bag will float the payload with a buoyancy margin of 1.5. Elimination of the CO_2 bottle and plumbing greatly increased the packing efficiency of the recovery systems and reduced the weight.

Table 10.1. Recovery System Parameters

System Config.	Date, First Flight Test	Max. Payload Weight (lb)	Min. Buoyant Force Req'd (lb)	Max. Impact Vel. (ft/s)	First-Stage Chute Dia. (ft)	Second-Stage Chute Dia. (ft)	Flotation Bag Volume		Packed System	
							Ram-Air (ft^3)	CO_2 (ft^3)	Volume (in^3)	Weight (lb)
Mods 1, 2, 2.1	7/67	275	150	80	3.5*	8*	7	3.5	900	16
Mod 3	6/69	500	225	70	4*	12*	14	7	1420	27
Mod 4	10/71	375	170	60	4*	12*	7	3.5	1190	23
Mod 5	8/70	125	75	70	2*	6*	3.5	—	470	8
Mod 6	11/71	200	125	75	3*	7*	5.8	—	500	9.5
Mod 7	10/72	1000	750	50	8†	24†	35	—	2400	40

Note: The terrain for all systems is water.
* Ribless guide surface
† Conical ribbon
‡ Personnel guide surface

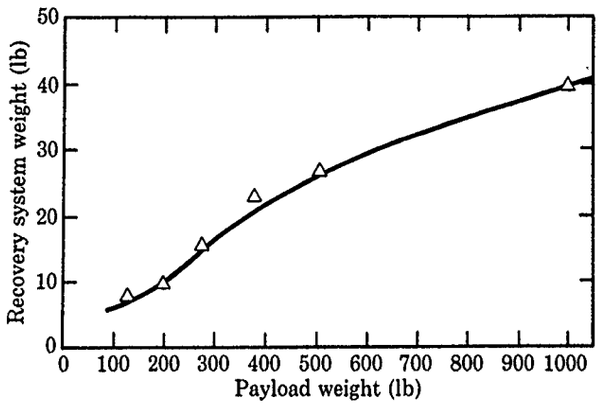


Figure 10.13. Recovery system weight vs. payload weight for Sandia's overwater recovery systems

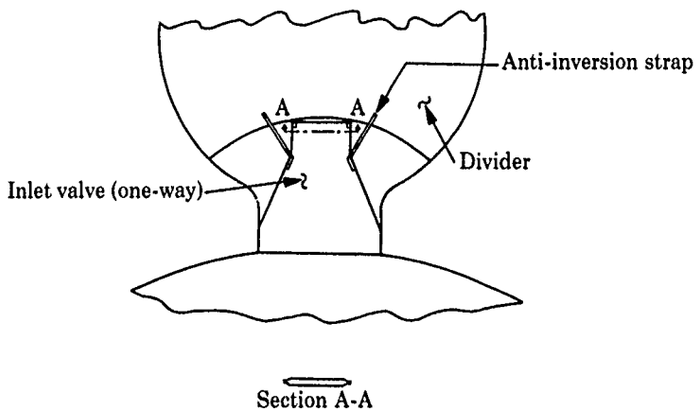


Figure 10.14. Inlet valve of a ram-air-inflated flotation bag

The recovery aids are shown in Figure 10.15. The RF transmitter is designed to operate from a power source of 3 to 10 V. The transmitter is modulated to have an easily identified audio signal. Normally, the transmitter is mounted on top of the flotation bag, which also has a four-wire-ground plane. The antenna is constructed from three sections of steel measuring tape, which is easy to stow when the recovery system is packed. Experience shows the output power of the transmitter to be completely adequate. Most difficulties in airborne electronic searches generally arise as a result of marginal receiving and direction-finding equipment. The strobe light used a xenon flash tube, which is flashed 90 times per minute with 20 joules released per flash. The output of this tube has been adequate for night searches but marginal for use during daylight hours.

The battery module will operate either the transmitter or the strobe light. It contains four AA-size alkaline cells nominally rated at 1.5 V per cell and a magnetically controlled reed switch that actuates the location aids. When the recovery system is deployed, a small magnet is pulled from the battery module and the reed switch is allowed to close. The 6.25-V battery module will operate the transmitter for several days at gradually decreasing power output. Tests have shown that the battery voltage is still greater than 5 V after 24 hours of operation. The battery module will operate the strobe light in excess of 30 hours.

In summary, these versatile recovery systems have been used to recover many types of rocket payloads since 1963. Their overall reliability is greatly influenced by the reliability of the electrical-mechanical deployment components. Expensive onboard cameras, instruments, attitude control systems, and telemetry equipment have been recovered with these systems in dozens of rocket flights.



Figure 10.15. Location aids and battery module

10.2 Fabrication and packing

10.2.1 Parachute drawings and fabrication

The Parachute Design Guide[2.1] and Ewing, Bixby, and Knacke[1.7] discuss fabrication procedures of textile parachutes. Ewing, Bixby, and Knacke provide an excellent discussion of general fabrication methods, including sections on layout, marking, cutting, machine stitching, strengths of joints and seams, types of stitches, stitches per inch, thread tension, and seam or stitching type. They also discuss construction details such as cloth structural elements, seams and hems, stitch patterns, line connections, skirt attachments, line splicing, and riser attachments. Finally, they review factory equipment, including patterns, cutting knives, line marking fixtures, sewing machines, and inspection tables.

Other selected references are "Sewing Machines, Industrial . . . ,"[10.7] "Stitches, Seams and Stitching,"[10.8] Ronquillo,[10.9,10.10] Rychnovsky,[3.20] Johnson,[3.5] Tubis,[10.11] and Waye.[3.7] Sewing machines suitable for the production of parachutes are governed by the requirements of Reference 10.7. In some cases, standard industrial sewing machines may be modified to better perform a specific sewing operation. The use of multiple-needle (2, 3, or 4) sewing machines is common practice for such operations as main seams, radial and vertical tapes, as well as for skirt and vent bands. Reference 10.8, "Stitches, Seams and Stitchings" (1965 and 1977), is the Federal Standard used in parachute fabrication.

Unlike mechanical drawings, which are controlled by conventions established over many years, there are no comprehensive rules or standardized practices for textile drawings. To fill this need, Ronquillo[10.9] developed procedures for the formation and interpretation of textile drawings for the manufacture of parachute systems. He combined the conventions used for mechanical drawings with the special textile drawing requirements to develop a method for making comprehensible parachute drawings. He developed drawing conventions, illustrated views or sections on separate sheets, provided examples of textile drawings, and provided a complete glossary of parachute terms. Ronquillo[10.10] reported on the continuation of this work and discussed the parachute drawing standards currently in use at Sandia. His method adopts some of the basic, standardized, and conventional drawing practices used in making mechanical drawings and introduces new drafting techniques unique to parachute drawings. These drawing techniques are being used by others in the parachute industry. The Naval Surface Weapons Center is preparing standards for parachute and textile drawings in the U.S. using Ronquillo's work and inputs from other government parachute users and private industry.

Rychnovsky[3.20] developed stringent fabrication and quality assurance procedures to ensure the symmetrical manufacture of lifting parachutes. Wind tunnel and flight tests had shown that the forces generated by high-dynamic-pressure deployment of a lifting parachute create unacceptably high roll moments unless the parachute is very symmetrical. The symmetry of the 13-ft-diameter lifting ribbon parachute (see Chapter 3) is controlled by the accuracy of the position and the alignment of the

horizontal, vertical, and radial ribbons. This parachute has 744 intersections of the horizontals and radials and over 1000 intersections of the horizontals and verticals. Rychnovsky developed a pattern for fabrication that accurately marks all parts of the canopy before assembly. Using accurate marking templates, the horizontals, radials, and verticals are marked on both sides of all intersections, under tension. The system he developed is based on computer-generated marking patterns for each part of a typical gore. The most difficult part of the parachute to fabricate was the intersection of the verticals, radials, and horizontals. Positioning and aligning the materials in this area was difficult, as was the sewing without distortion, because of the bulk material involved.

Johnson[3.5] invented the "mini-radial," with tapes for stabilizing the horizontal ribbons that terminate at a horizontal ribbon away from the radial (see Figure 3.2). Johnson developed procedures for accurately marking and fabricating parachutes with mini-radials. Because the mini-radials are perpendicular to the horizontal ribbons, the computations and the markings are simplified. Fabrication was greatly simplified because mini-radials reduced the three-ribbon intersecting joint to a two-ribbon intersection (horizontals and radials), which is much easier to fabricate. Johnson's all-radial construction for continuous ribbon parachutes represents a major breakthrough in the design and fabrication of high-performance canopies. This construction was described in detail in Chapter 3. A fixture is useful in assembling the parachute. The horizontals were placed across the fixture and the full radials and mini-radials along the fixture for attachment in their proper relationship to each other.

Tubis[10.11] investigated alternate textile joining methods to replace sewn joints in parachute fabrication. He contacted over fifty adhesives companies and selected seven solvent-based adhesives and four hot-melt adhesives for his study. Testing of peel strength, shear strength, and seam flexibility of the adhesives on MIL-C-7020 Type-II nylon cloth revealed that the N-OO hot-melt adhesive (supplied by General Fabric Fusing, Inc., of Cincinnati, Ohio) was the most promising candidate. The seam efficiencies were >100% and the peel strength was >17.5 lb/in. Ten N-OO hot-melt adhesive seams were placed in each of eight 26-ft-diameter conical parachute canopies and tested on a whirl tower at deployment speeds of 175, 225, and 275 knots. These tests showed that the N-OO hot-melt adhesive was as good as the sewn joints, and possibly better.

Waye[3.7] developed an interactive computer code to aid in the design of conical ribbon parachutes. The program was written to include single conical and polyconical parachutes. The code determines the pattern length, vent diameter, radial length, ribbon top and bottom lengths, and geometric local and average porosity for the designer with inputs of constructed diameter, ribbon widths, ribbon spacings, radial width, and number of gores. The gores are designed with one mini-radial in the center with an option for the addition of two outer mini-radials. The code output provides all of the dimensions necessary for the construction of the parachute. The program will aid the designer in developing and comparing parachute parametric configurations quickly and easily. Waye provides a sample design (with code inputs and outputs) for a 5.2-ft-diameter, 20-degree conical ribbon parachute.

10.2.2 Packing

The Parachute Design Guide[2.1] and Ewing, Bixby, and Knacke[1.7] briefly describe parachute packing. Ewing, Bixby, and Knacke discuss inspection (light) tables, packing tables, parachute tensioning devices, canvas stowage bins (on wheels), packing tools, and packing presses. Packing tables, used to extend and fold parachutes for final packing into deployment bags, must be adequately wide, long, and smooth. The working surface is finished smoothly and is free of any defects that could cause snagging or could pull the threads of fine fabrics. Physical characteristics of the table will vary with usage requirements. Typical packing tables stand about 30 to 36 in. high. Table minimum width and length depend on the type parachute being packed, the length being at least equal to the stretched length of the pleated canopy portion, suspension lines, and risers. A typical packing table for rigging personnel parachutes is 3 ft wide and 40 to 45 ft long. A table as wide as 6 ft and well over 100 ft long is used for packing large cargo or aerospace vehicle recovery parachutes.

Figure 9.16 shows a 46.3-ft-diameter nylon/Kevlar ribbon parachute stretched out on packing tables in the Sandia Parachute Laboratory. These tables are 3 ft high, 4 ft and 6 ft wide, and 10 ft long; ten are used end-to-end to provide a 100-ft overall length for packing large parachutes. The canopy is laid out on the 6-ft-wide tables and the suspension lines on the 4-ft-wide tables. Figure 10.16 is a photograph of part of the Sandia Parachute Laboratory illustrating the flotation bag fabrication (near table) and layout for packing a nylon/Kevlar ribbon parachute (far table), as well as portable sewing machines and other equipment. A prime requirement in a parachute laboratory is excellent artificial lighting. The lighting level in the Sandia Parachute Laboratory is approximately 75 footcandles. Photographs of hydraulic presses used for pressure packing are shown in Figure 10.17.



Figure 10.16. Sandia Parachute Laboratory

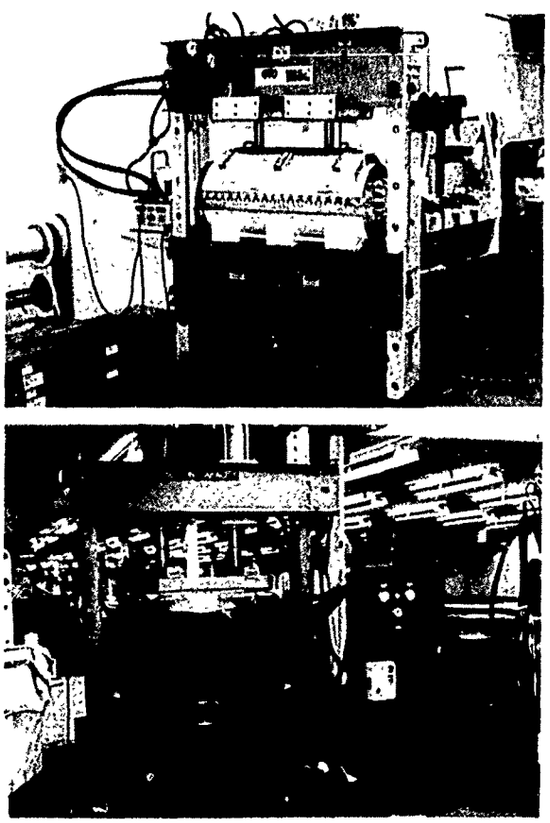


Figure 10.17. Hydraulic presses used for pressure packing

A USAF Technical Manual[10.12] provides complete and detailed instructions for the packing of the F-111 Crew Module parachute recovery system, which consists of a 70-ft-diameter ringsail nylon main parachute and a 6-ft-diameter vane nylon pilot parachute. The parachute pack weighs 116 lb and the packing density is 48.4 lb/ft^2. The packed dimensions are 13.8 in. thick, 15.1 in. wide, and 33.0 in. long. The parachute/bag pressure packing requires twelve separate installations of the bag in the hydraulic press, with pressures of up to 2000 lb/in^2 being applied.

Sandia engineers have developed complete instructions for packing a prototype cluster of three 49-ft-diameter parachutes in the F-111 Crew Escape Module (see Johnson[3.37]). Although this parachute system is not used on the F-111, its packing procedures are discussed here as an example of the steps included in the packing process. The recovery parachute assembly consists of a 5-ft-diameter guide surface pilot parachute coupled to a 10-ft-diameter flat conical pilot parachute, a 5-ft-diameter vent control parachute, and three 49-ft-diameter main parachutes. The main and vent control parachutes are packed in the main parachute deployment bag, and the dual pilot parachutes are packed in the pilot parachute bag. A main riser is attached to the main parachute cluster bridle, which is packed within the main parachute deployment bag.

The packing procedures listed below for this prototype cluster are an indication of the many critical steps that need to be taken in the packing of a high-performance parachute system. Obviously, not every step in the list is needed for all parachute systems. However, the omission of any step or the failure to follow each procedure carefully can lead to the destruction of the parachute, even when the parachute has adequate structural design strength. The packing procedures must be rigorously followed in the order specified so as to obtain high reliability during parachute deployment.

- Requirements
- Packing facilities and equipment
- Materials
- Packing team
- Recovery parachute assembly components and hardware
- Forms and records
- Packing notes
- Assembling deployment bag
- Preparation for packing, left main parachute
- Straightening suspension lines
- Stacking of canopy gores, left parachute
- Installing reefing lines
- Preparation for packing, right main parachute
- Preparation for packing, top main parachute
- Installation of deployment line
- Installation of sequence line
- Installation of reefing line cutters
- Installation of line ties
- Temporary skirt ties, parachute skirt
- Installation of vent control parachute
- Packing parachutes into deployment bag
- Load bridle attachment
- Stowing the suspension lines
- Stowing the load bridle
- Lacing the deployment bag

These procedures are carefully developed by the parachute laboratory technician and the parachute design engineer based on trial-and-error experience in packing prototypes for evaluation by flight test during the parachute development process. It is very important to carefully specify every packing detail, including extensive use of photographs (color is recommended for nylon/Kevlar parachutes) to illustrate examples, for use by production packers who may lack experience in packing prototype parachutes. In addition, Sandia routinely trains production packers in their production parachute packing facility, and certifies that the production team can pack parachutes of the quality required for high reliability during deployment. This training and certification is required before parachutes are packed for production usage.

Widdows[10.13] provides packing and installation instructions for Sandia's rocket payload recovery system. This report presents the complete procedural packing techniques, a listing of packing facilities and equipment needed, records to be maintained, and inspection requirements. There are 105 separate instructions, illustrated with 51 photographs, in the packing procedures for the 8-ft-diameter ribbon first-stage parachute and the 24-ft-diameter second-stage parachute with ram-air bag. The parachute assembly installation requires 25 separate instructions, illustrated with eight photographs.

Johnson and Peterson[3.6] describe a 46.3-ft-diameter conical ribbon parachute used for the high-speed, low-altitude delivery of a 2465-lb payload. Figure 9.16 shows this parachute laid out on the packing table. The four-leaf deployment bag is shown in Figure 9.19, with callouts showing canopy ties, line ties, etc. Figure 10.18 illustrates the reefing line cutter installation and Figure 10.5 shows the reefing line threaded through the reefing rings and the cutter. Figure 10.19 illustrates the skirt ties and how the gores are placed into four groups, and Figure 10.20 shows the bag laces being tightened in the lacing machine. In Figure 10.21, the packed parachute is being shaped in the hydraulic press, and in Figure 10.22 it is being gauged for diameter. A photograph of the final packed parachute system is shown in Figure 9.17.

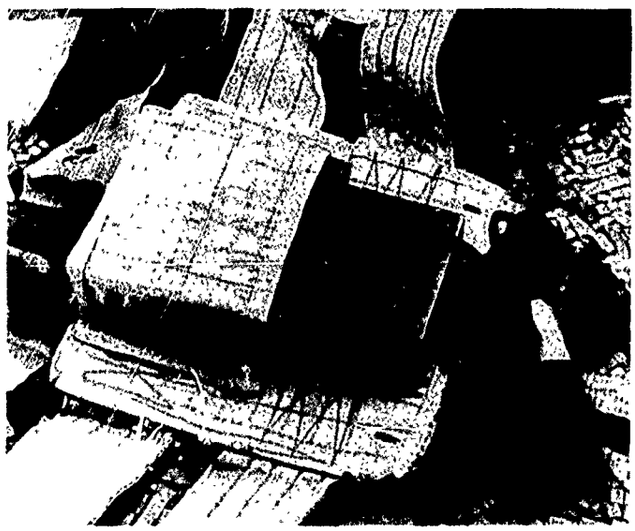


Figure 10.18. Reefing line cutter installation

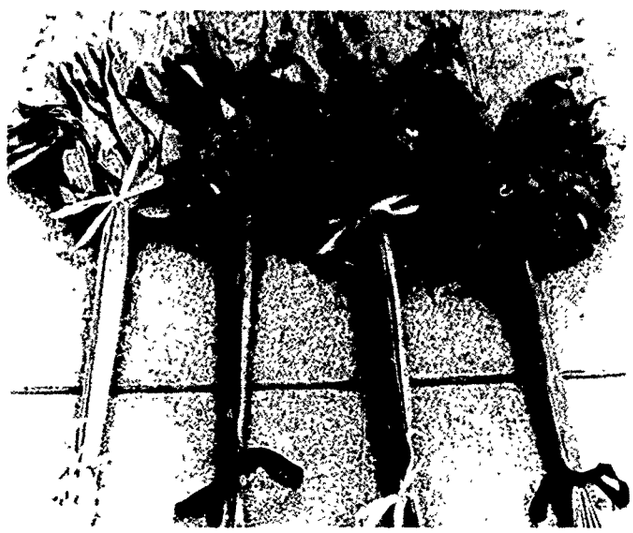


Figure 10.19. Skirt/line bundle ties

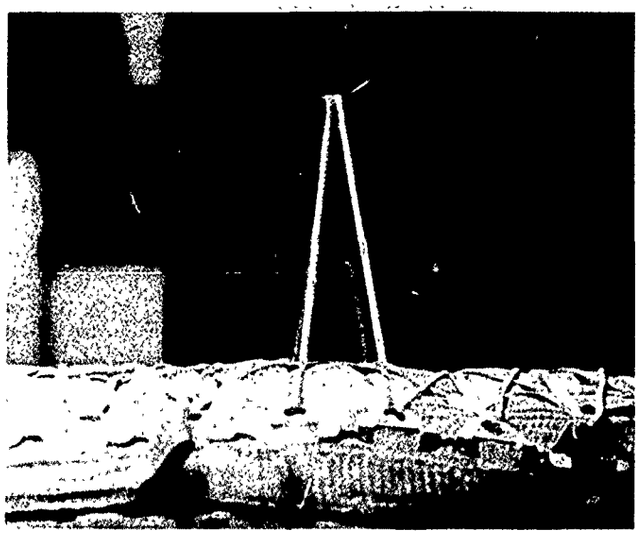


Figure 10.20. Lacing is tightened in lacing machine

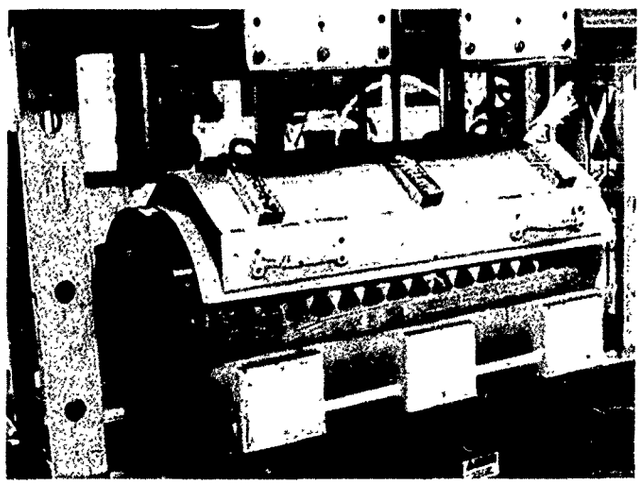


Figure 10.21. Parachute in shaping fixture on press



Figure 10.22. Size gauging of packed 46.3-ft-diameter parachute

10.2.3 Reliability

The Parachute Design Guide[2.1] and Ewing, Bixby, and Knacke[1.7] discuss parachute component and system reliability. Because of the value of the payload, most high-performance parachute systems must meet stringent reliability requirements. It is necessary to quantify parachute system reliability requirements; the statement that "high" or "very high" reliability is required is not sufficient. It is necessary to have some firm basis to trade off the reliability requirements for a parachute system against such penalties as weight, volume, cost, development time, etc. A reliability level can then be determined that can be practically attained. *Ultra-reliability* (>0.999) requirements include such applications as most personnel parachutes, space-vehicle-recovery decelerator systems, and similar critical applications where costs are very high or where assurance of mission success is very high. The *very high reliability* requirements are for cargo delivery, missile and drone recovery, weapons delivery, etc. These very high reliability requirements result from a trade-off of cost, development time, personnel training, or other factors involved in the compromises required in the usual military parachute system development programs.

The three major causes of unreliability in high-performance parachute operations are poor design, materials failure, and human error in parachute fabrication, packing, and use. Poor design is usually not a major failure factor in actual flight-test use of operational parachutes, because design errors are usually eliminated during development. Materials failures may be divided into failures of the fabric and static-hardware portions of the parachute and failures of the active-function mechanical devices necessary for parachute system operation. To understand the failures of the fabric portions of the parachute, it is necessary to compare the strength of the material in each section of the parachute against the local stress during the critical opening/loading condition. The probability of failure will depend on the probability of the specific section of the canopy or suspension lines encountering high stress during parachute operation. Everything possible should be done in the parachute design, construction, and operation to minimize the possibility of selecting a low-strength piece of material (e.g., a priori testing of mill-run samples) and to minimize the possibility of high loading by limiting the deployment dynamic pressure.

Failures of mechanical devices are a more straightforward problem. The cause of failure of static hardware, whose functions are primarily passive, may be attributed to the distribution of stresses placed on the components. However, there is another group of mechanical devices that must perform active functions during the deployment or operation of the parachute system. This group consists of reefing line cutters, interstage disconnects, deployment-initiation devices, etc. These active mechanical devices must function in an environment that may include low temperatures, shock, vibration, acceleration, and other factors. Assessment of reliability requires testing adequate numbers of such devices under conditions closely simulating the use environment to determine the probability of failure.

The third cause of parachute failure—human error—is more difficult to assess. Human error in the parachute design process is part of the design problem rather than the parachute-use reliability problem. Human errors in parachute construction are probably the primary causes of failure in the operation of most types of high-performance parachutes. The human error in the manufacturing process is difficult to evaluate in reliability studies. Reliability is primarily a function of quality control by the manufacturer, and this is a function of proper training of personnel and thorough inspection of the parachute system at the various stages of fabrication.

Jailer, Freilich, and Norden[10.14] have found human error in packing to be one of the major failure-producing factors. Sandia's experience with high-performance parachutes verifies this conclusion. Two portions of the packing process should be analyzed with the intent of reducing errors; they are (1) the canopy layout, folding, tying, and stowing in the deployment bag and (2) the installation of hardware and auxiliary devices required for parachute operation. Jailer, Freilich, and Norden reported that the majority of human-error failures in packing were not in the canopy portion of the operation but, rather, in the auxiliary device installation. Observation of the packing process for large and complex parachute systems showed that during layout, examination, folding, and canopy stowage the inspection process can follow each individual packing operation because the parts are large and easily visible to the inspector. However, the hardware devices (such as reefing line cutters) are small and are not as visible to the inspector; hence, more errors occur. Therefore, it is essential that very specific packing orders be provided (with example photographs) to the parachute packers and that the packers be trained and certified before they are allowed to do production packing.

Jailer, Freilich, and Norden[10.14] present a complete methodology for parachute reliability assessment. They discuss many of the necessary auxiliary data, including values for human-error rates observed in parachute packings, the reliability of mechanical devices commonly used in parachute systems, and mathematical tables to facilitate computations. Reliability is inversely related to the expected rate of failure; it can be measured by subtracting the expected probability of failure from unity. In any given parachute use, the reliability of each portion of the parachute system is determined at a virtually instantaneous time, rather than over a period of time. For example, the maximum load on the suspension lines, and thus the maximum probability of a line breaking, comes either in the opening shock or in the snatch force. Consequently, from a reliability viewpoint, a parachute is a "one-shot" system. The probability distribution of parachute failure can only take on a finite number of values; it is called a *discrete distribution*. The probability distribution best describing such a system is the *binomial distribution*; it expresses mathematically the probability, f(x), that failure will occur exactly x times in N independent trials of the system, where p is the expected probability of failure:

$$f(x) = \frac{N!}{x!\,(N-x)!}\, p^x (1-p)^{N-x} \quad . \tag{10.1}$$

The use of this binomial distribution to calculate parachute system reliability is discussed in detail by Jailer, Freilich, and Norden[10.14] and Ewing, Bixby, and Knacke.[1.7] An example calculation of the reliability of a reefing line cutter is given by Bradley.[10.15] He defines the reliability, R, as the probability that the electronic reefing line cutter will cut the reefing line within ±5% of the preset time delay after the lanyard has been pulled. The reliability equation is

$$R = 1 - Q \quad , \tag{10.2}$$

where Q is the sum of the factors A through E given in Table 10.2. The solution to this equation, using the values given in Table 10.2 (which are considered conservative), gives a reliability of 0.99. The considered failure events and the assumptions are listed in Table 10.2. Pepper, Bradley, and Jacoby,[10.3] in continuing with the development of this reefing line cutter, performed a considerable number of environmental tests. They concluded that the reliability of the production units for this cutter would be >0.999.

Table 10.2. Failure Events

Event Symbol	Event Description	Estimated Probability of Failure
A	Failure of the firing pin to strike and transmit to the thermal battery primer the energy required to fire the primer, given that sufficient force is transmitted to the lanyard by the parachute system	0.002
B	Failure of the thermal battery to deliver an output sufficient to operate the electronics, given that event A has not occurred	0.003
C	Failure of the electronics to deliver an appropriate fire signal to the cartridge after the preset time delay, given proper thermal battery operation	0.004
D	Failure of the electrically fired cartridge to deliver sufficient energy to the cutter, given that a correct signal is received from the electronics	0.0005
E	Failure of the cutter to shear the wire and sever the reefing line, given that the cutter receives an appropriate amount of energy from the cartridge	0.0003
Q	Failure of the electronic reefing line cutter to sever the reefing line	0.01

Assumptions:

In the reliability analysis, the following assumptions are made:

1. The failure events are statistically independent or mutually exclusive.
2. The reefing line cutter will be correctly installed in the parachute.
3. The "safety pin" is removed at the proper time.
4. The parts from which the assemblies are made will be of quality and reliability suitable for weapons applications.

Sandia parachute design engineers have insisted for many years that the only method to prove the reliability of a high-performance parachute system for ordnance deceleration was to conduct flight tests over the range of deployment dynamic pressures. There are no ground test facilities (unsteady flow wind tunnel, rocket exhaust, whirl tower, sled track, etc.) where the nonsteady flow associated with high-performance parachute deployment and inflation could be duplicated. The number of flight tests required (with no parachute system failures) to prove a desired reliability for two confidence levels is presented in Table 10.3. Sandia has used this flight testing technique (aircraft drop, rocket boost, and rocket-sled ejection) for many years to verify the reliability of its parachute systems.

Table 10.3. Number of Flight Tests With No Failures Required to Verify Reliability of Parachute System

	Flight Tests With No Failures	
Reliability	50% Confidence Level	90% Confidence Level
0.90	7	15
0.95	14	44
0.99	69	235
0.995	145	470
0.999	720	2340

References

10.1 S. J. Barlog, "Practical Aspects of Reefing Cutter Design," AIAA 79-0418, March 1979.

10.2 J. P. Gallagher, *Line Cutter*, United States Patent 3,335,493, August 15, 1967.

10.3 W. B. Pepper, G. H. Bradley Jr., and W. C. Jacoby, *Development of an Electronic Time Delay Reefing Line Cutter for Parachutes*, Sandia Laboratories, SLA-73-0989, December 1973.

10.4 J. R. Craig, *Development of the MC3462A Pyrotechnic-Propellant-Actuated Reefing Line Cutter*, Sandia National Laboratories, SAND81-2482, June 1982.

10.5 D. W. Johnson, *A Recovery System for the Sandia Hawk Series of Sounding Rockets*, Sandia Laboratory, SC-RR-65-470, November 1965.

10.6 D. W. Johnson, "Evolution of the Recovery System for High Altitude Sounding Rockets," AIAA 68-959, September 1968.

10.7 Federal Specification 00-S-256E (3), "Sewing Machines, Industrial (General Specification)," January 1970.

10.8 Federal Standard No. 751A, "Stitches, Seams and Stitchings," January 1965; also Amendment 1, June 1977.

10.9 K. L. Ronquillo, *Procedures for the Formation and Interpretation of Textile Drawings*, Sandia Laboratories, SAND78-2430, July 1979.

10.10 K. L. Ronquillo, "Parachute Drawing Standards Currently in Use at Sandia National Laboratories," AIAA 89-0927, April 1989.

10.11 R. I. Tubis, "Alternate Textile Joining Methods for Parachute Canopy Seams," AIAA 84-0812, April 1984.

10.12 *Technical Manual Inspection, Repair, Overhaul and Packing Instructions—Recovery Parachute Assembly*, Part No. C-801-G, USAF T.O. 14D3-2-1, June 1971.

10.13 H. E. Widdows, *Packing and Installation Instructions for Sandia Laboratories/NASA/DFVLR Rocket Payload Parachute Recovery System (P/N T19328-000)*, Sandia Laboratories, SLA-73-0997, April 1974.

10.14 R. W. Jailer, G. Freilich, and M. L. Norden, *Analysis of Heavy-Duty Parachute Reliability*, USAF WADD Technical Report 60-200, June 1960.

10.15 G. H. Bradley Jr., *Preliminary Development Report on the Electronic Reefing Line Cutter*, Sandia Laboratories, SC-DR-70-865, April 1971.

CHAPTER 11

FULL-SCALE TESTING

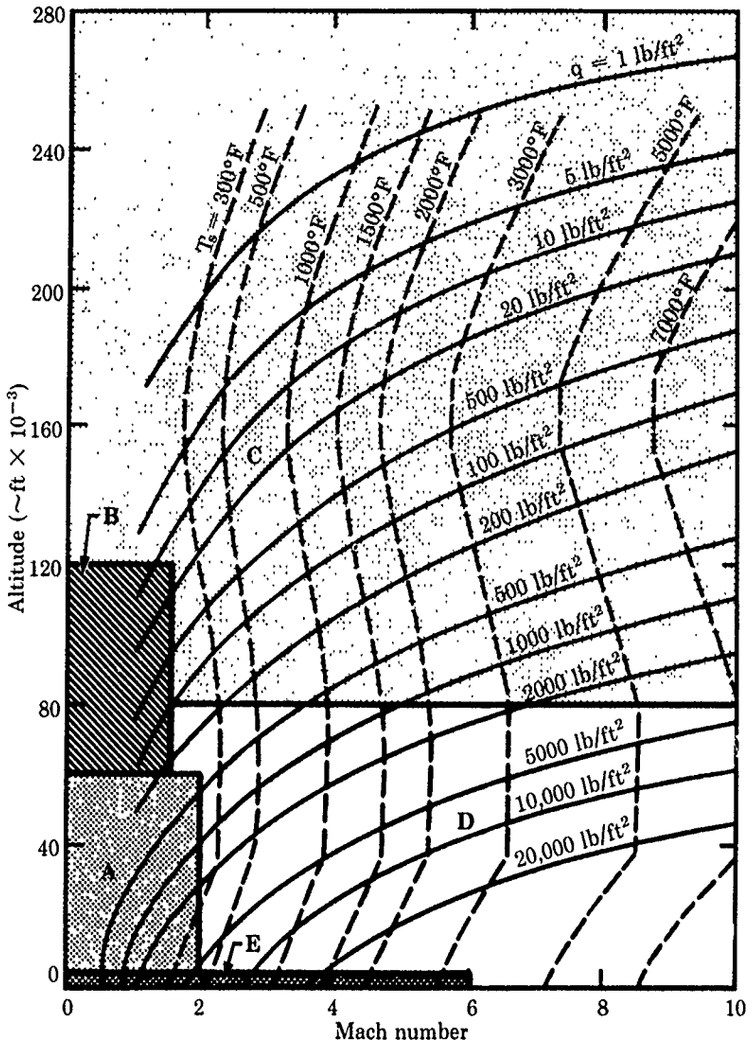
11.1 Background

Johnson[11.1] discusses the role of full-scale testing in the design of parachutes. Historically, it has been difficult to separate full-scale testing from the design of high-performance parachute systems because advancements in parachute system design and development have come about by trial and error. Usually, calculations are made to determine the basic parameters for the parachutes to be used in a system. The detailed design (including selection of materials, sewing, etc.) of the parachutes, deployment bags, risers, and other parts of the system must be done by someone with many years of parachute design experience. The parachute system is then fabricated, packed, and flight-tested. Since full-scale flight testing has been such an integral part of the parachute design cycle, the test equipment and facilities (test range, sled track, etc.) must be available to the design engineer.

Full-scale tests fall in one of two general categories: functional or performance-based. Functional tests are those conducted to demonstrate whether a system or component of the system will operate as predicted when tested under known conditions. These tests provide a "yes or no" answer and are generally conducted without instrumentation in the test vehicle. Performance tests are those conducted to obtain and evaluate specific performance characteristics of a system or component over a wide range of test conditions. These characteristics can then be compared with those of similar systems tested over the same range of test conditions. Until the very complicated equations for the nonsteady flow about an inflating parachute can be solved numerically, full-scale performance tests will also be required to measure some of the coefficients used in empirical design methods and to validate the final design of the parachute system.

The Parachute Design Guide[2.1] and Ewing, Bixby, and Knacke[1.7] discuss the advantages and disadvantages of full-scale testing methods, such as aircraft or balloon drop, rocket boost, aircraft or rocket sled tow, and rocket sled test vehicle ejection. A chart of altitude versus Mach number for various free-flight methods (from Ref. 1.7) is given in Figure 11.1. Most high-performance parachutes are tested by methods A (aircraft launch, gravity drop), D (aircraft or ground launch, boosted vehicle), or E (ground vehicle launch and other methods). A principal advantage of free-flight test methods is the absence of physical restraint on the motion of the decelerator-load system. Free-flight test methods provide a finite mass test capability and allow for dynamic simulation of vehicle effects on the decelerator after deployment. The full range of test conditions can be duplicated by this method, and it is possible to demonstrate the actual performance of the complete system functions. Observation and measurements of system stability, flight trajectory, rate of descent, drift tendencies, and other phenomena are also attainable during tests. A disadvantage of free-flight testing methods, when compared with captive methods, is that it is difficult to control and measure test conditions and to observe precise motion of test items. Of course, the high costs and extreme complexity of the test equipment, especially for high-speed and high-altitude testing, are sometimes unavoidable. Gravity drop tests are those in which an unpowered test vehicle, with its packed parachute and attached test item, is launched from a stationary or moving aerial platform to free-fall under the influence of gravity. Boosted vehicle tests are those in which the test vehicle, with its packed parachute and attached test item, is launched from the ground or from an aerial platform and boosted by rocket motors to desired speeds and altitudes prior to deployment.

The following sections discuss full-scale testing at instrumented ballistic ranges, at sled tracks, and at other facilities. Also discussed is the design of instrumented parachute test vehicles.



T_s - - - - - - = $T\,[1 + (0.2 \times 0.9M^2)] - 460°$

q ——— = $0.7\,PM^2$

T_s and q based on U.S. Standard Atmosphere 1962

Free-flight test methods

A = Aircraft launch, gravity drop
B = Balloon launch, gravity drop
C = Balloon launch, boosted vehicle
D = Aircraft or ground launch, boosted vehicle
E = Ground vehicle launch and other methods

Figure 11.1. Free-flight full-scale testing methods (taken from Ref. 1.7). M is Mach number, P is atmospheric pressure, q is dynamic pressure, T_s is stagnation temperature, and T is atmospheric temperature.

11.2 Instrumented ballistic ranges

Table 11.1 lists the instrumented ballistic ranges in the United States suitable for the full-scale testing of parachutes. Also listed are the types of tests and the test support services (neither is all-inclusive). More detailed information is presented in *Technical Manual—Tonopah Test Range Capabilities,*[11.2] *Major Test Facilities of the Naval Weapons Center,*[11.3] *AFFTC User's Handbook,*[11.4] *Test Capabilities—Yuma Proving Ground,*[11.5] *White Sands Missile Range Users' Handbook,*[11.6] *ADTC Technical Facilities,*[11.7] and *Major Range and Test Facility Base—Summary of Capabilities.*[11.8] Reference 11.8 provides the most up-to-date description of the DoD instrumented ballistic ranges in the United States. The other major instrumented ballistic range is at the Tonopah Test Range (TTR),[11.2] which is operated by Sandia National Laboratories for the U.S. Department of Energy. Both References 11.2 and 11.8 provide points of contact to obtain more information about the DOE and the DoD instrumented ranges, respectively. The importance of these ranges to the parachute technical community cannot be understated. Even with much-improved numerical parachute design tools, the ability to conduct full-scale tests of parachutes is essential to the parachute designer. Sustaining a viable capability in parachute testing should be the common goal of all parachute users and designers.

Table 11.1. Instrumented U.S. Ranges

Range	Types of tests	Test support services
Air Force Flight Test Center Edwards AFB Lancaster, CA Control agency: USAF Range size: 5 × 14 mi	A/C drops A/C tow A/C flight	Telemetry, cinetheodolites, telescopic tracking cameras, ground-to-air motion picture cameras, video recording and playback, rawinsonde, data reduction, photo processing laboratory, space positioning on test range, IRIG timing system
White Sands Missile Range White Sands Missile Range, NM Control agency: U.S. Army Range size: 40 × 100 mi	A/C drops A/C tow Balloon launch Ground launch	Telemetry, cinetheodolites, telescopic tracking cameras, ground-to-air motion picture cameras, video recording and playback, rawinsonde, radar tracking, documentary photography (16mm), IRIG timing system
Eglin Gulf Test Range Eglin Air Force Base, FL Control agency: USAF Range size: 200 × 500 mi over water	A/C drops A/C tow Ground launch	Telemetry, cinetheodolites, telescopic tracking, rawinsonde, data reduction, ground-to-air motion picture cameras, photo processing laboratory, IRIG timing system
Naval Weapons Center China Lake, CA Control agency: USN Range size: 30 × 40 mi	Sled tow Sled launch A/C launch	Telemetry, cinetheodolites, telescopic tracking cameras, ground-to-air motion picture cameras, video recording and playback, radar tracking, data reduction, photo laboratory, space positioning on track range, IRIG timing system
Tonopah Test Range Tonopah, NV Control agency: SNL/DOE Range size: 26 × 24 mi	Ballistics A/C drops A/C tow Ground launch	Telemetry, cinetheodolites with G-band radar ranging, telescopic tracking cameras (35 and 70mm), video recording and playback, rawinsonde, radar tracking, documentary photography (16, 35, and 70mm), IRIG timing system, data reduction, laser tracking
Yuma Proving Ground Yuma, AZ Control agency: U.S. Army	A/C drops Personnel	Telemetry, cinetheodolites, telescopic tracking cameras, video recording and playback, laser tracking

11.2.1 Aircraft drops

The most common method for free-flight testing of high-performance parachutes uses cargo, bomber, and fighter aircraft or helicopter as the launch platform for a gravity drop-test vehicle (see Figure 11.1). With fighter-type aircraft, the test vehicle is usually suspended from a pylon mount under the wing or is centered under the fuselage. The drop is initiated by the pilot's remote activation

of the bomb release at the required test conditions of aircraft speed, altitude, and direction at the test range. At some ranges the range flight controller will indicate to the pilot when to release the store, based on real-time radar tracking data; this method improves the probability that the store will impact a specific ground target and/or that optimum cinetheodolite and documentary film coverage is obtained. The range flight controller directs the pilot to the right altitude, aircraft speed, and azimuth. Stores are also mounted on pylons on bomber aircraft and helicopters for free-flight drop-testing of parachutes. Bombers can usually carry a larger store in their bomb bay than can be carried externally on pylons.

Ewing, Bixby, and Knacke[1.7] (p. 201) present a table of achievable launch conditions for parachute testing. Holt[4.45] discusses the results of thirty B-52 drop tests of 20,000- to 45,000-lb vehicles at TTR to test a 76-ft-diameter ribbon parachute. The main parachute was deployed immediately after aircraft release using a 5-ft-diameter guide surface pilot parachute and an 18-ft-diameter ribbon drogue parachute. The release altitudes varied from about 25,000 to 45,000 ft and the release velocities from 550 to 780 ft/s. Moog, Sheppard, and Kross[4.12] discuss the testing of the Space Shuttle Solid Rocket Booster parachute system in which a 48,000-lb test vehicle was decelerated after its release from a B-52 aircraft. A 50,000-lb test vehicle is the approximate upper weight limit for aircraft drop tests.

Maydew and Johnson[3.1] discuss the results of 29 low-altitude tests (conducted at TTR) of a 22.2-ft-diameter parachute deployed from a 2100-lb store released from A-4 or F-4 aircraft at Mach numbers 0.57 to 1.22. Pepper[1.1] conducted 31 drop tests at TTR, using A-7, F-4, and F-111 aircraft, to test a 24-ft-diameter ribbon parachute decelerating a 760-lb store. The maximum test conditions were Mach 1.32 at 5400 ft altitude and Mach 1.72 at 60,500 ft altitude. The minimum test condition was Mach 0.51 at 1170 ft altitude. These two series of flight tests may represent the current upper limit of aircraft speed for parachute testing using gravity-drop techniques.

Figure 11.2 shows a 2465-lb test vehicle (see Johnson and Peterson[3.6]), separating from a B-1 aircraft, with the 46.3-ft-diameter parachute partially inflated. Figure 11.3 shows the same test vehicle with the fully inflated parachute impacting the snow-covered concrete target at TTR.

Parachute designers and test engineers should always be aware of the hazards of parachute testing with aircraft drops. The test vehicle must safely separate from the aircraft so that the aircraft and the crew are not endangered. Military organizations usually require an analysis of the aircraft-store separation and, if this is approved, a series of separation tests at increasing Mach numbers or dynamic pressures to demonstrate safe separation at the required test conditions. The analysis may consist of numerical modeling and computer solution of the approximate flow field (and trajectory) about the separating store and/or wind tunnel tests of scale-model store/aircraft separation. For best results, contemporary wind tunnel tests conducted for release and separation consist of a sting-supported (fixed in the airstream) aircraft model with an instrumented (5- or 6-component strain gauge balance) sting-supported store model. The store model translates in the X-Y plane in the wind tunnel in a trajectory based on real-time aerodynamic measurements (with feedback to the store trajectory apparatus) from the store's strain gauge output. The 4-ft Transonic Wind Tunnel at AEDC (see Ref. 7.2) has provided this captive trajectory store-separation testing capability for many years. In a survey of Sandia's work in store separation, Spahr[11.9] discusses the use of numerical codes, the use of wind tunnel testing, the use of analogy in store separation, and the steps required to provide information on store separation to the military services before the first flight test of a new store. He reminds the reader that poor store-separation design can result in the loss of the aircraft—a case in point was an F-14A in 1973. Schindel[11.10] in 1975 published a complete survey of store-separation studies conducted in NATO countries (AGARDograph No. 202).

Another area of concern is the premature deployment of the parachute before the store is safely clear of the aircraft. The aircraft could be damaged and the crew endangered if a deployment device such as a thruster, tractor rocket, endplate, or pilot parachute (or the main parachute) impacted the aircraft. The safe separation time varies as a function of release velocity, altitude, store location on the aircraft (wing pylon vs. bomb bay, for example), and type of aircraft. Hence, careful analytical studies, corroborated with full-scale flight tests, are made at Sandia to determine the optimum safe separation times for each aircraft for the high-performance, low-altitude parachute systems described by Maydew and Johnson,[3.1] Pepper,[1.1] and Johnson and Peterson.[3.6] Spahr[11.9] discusses the unique hazards posed to delivery aircraft from parachute system components or from parachutes deployed immediately after the store is released from the aircraft.

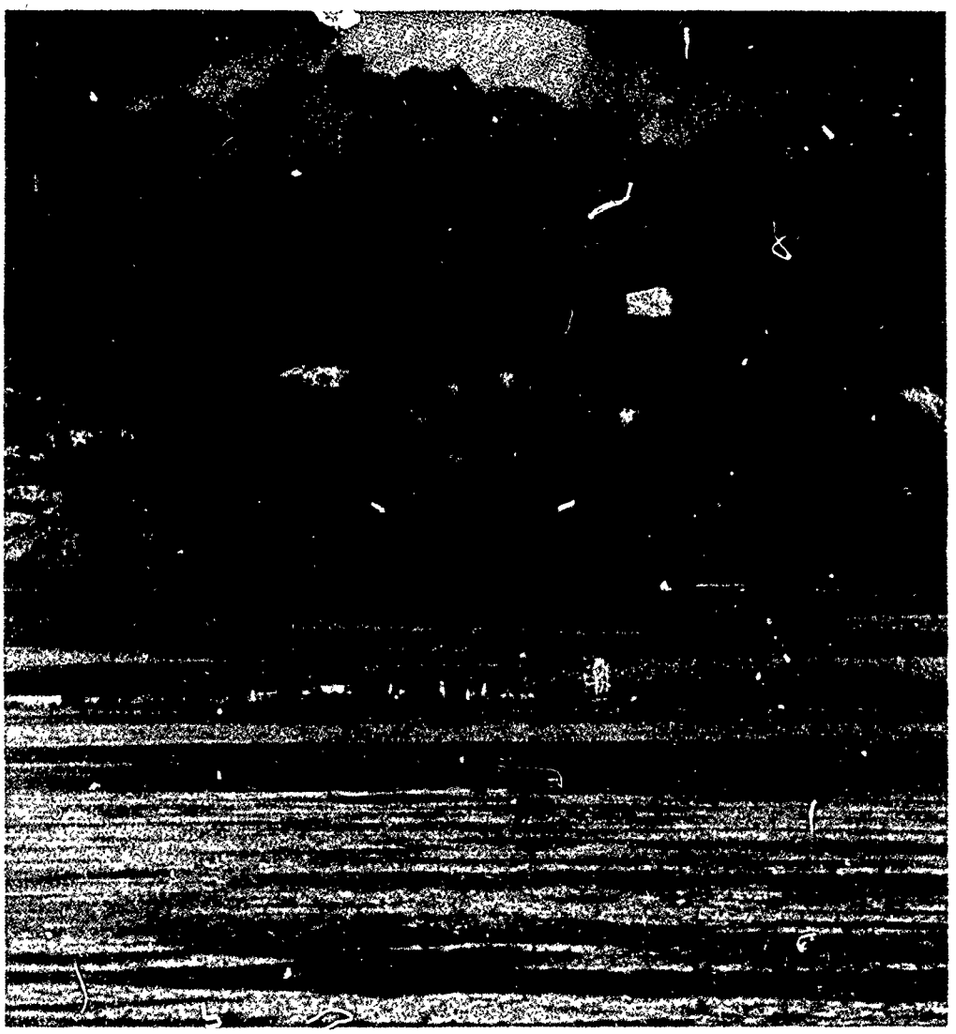


Figure 11.2. A 46.3-ft-diameter parachute inflating after release of store from B-1



Figure 11.3. Impact on concrete target (at TTR) of store with 46.3-ft-diameter parachute

11.2.2 Rocket boosting

An important area of the Figure 11.1 test map is covered by aircraft-launched or ground-launched rocket-boosted vehicles. Of these two test methods, the aircraft-launched vehicle is used less frequently, because qualifying a test vehicle of this type for safe carriage and launch from an aircraft is a costly and time-consuming program in itself. Hence, only ground-launched rocket-boosted parachute test vehicle systems will be discussed here. Ground-launched vehicles are commonly used to test decelerators at higher Mach numbers or dynamic pressures not obtainable with current aircraft. In many cases, the designer may want to qualify the decelerator at higher dynamic pressures than the aircraft can fly to prove the structural capability (a margin of safety) of the parachute system. Generally, the test vehicle is boosted from the ground by a single solid-propellant motor. The need for higher test speeds, higher altitudes, or heavier payloads may require the use of multistage rocket boosters, but this increases the complexity and reduces the reliability of the system. In some cases, an aircraft-launched rocket-boosted vehicle may be more feasible than a ground-launched multistage rocket-boosted system.

Kane and Barth[11.11] designed a supersonic test vehicle (weighing 1130 lb) that was boosted with an M-5 Jato (Nike) to test 20-ft-diameter ribbon parachutes at deployment dynamic pressures of 2000 to 3000 lb/ft^2. The maximum deployment dynamic pressure that could be obtained for testing before that time was ~2000 lb/ft^2; this was accomplished by releasing a 7500-lb test vehicle from an aircraft at 45,000 ft altitude and deploying the parachute at about Mach 1.3 at low altitude. This new supersonic test vehicle was used for many parachute programs, and this was the beginning of many rocket-boosted tests of high-performance parachutes at Sandia's Tonopah Test Range. The results of the first four tests of supersonic parachute deployment using this test vehicle are described by Kane.[2.13,2.14] The reefed 20-ft-diameter parachute was successfully tested at deployment Mach numbers of 1.45 to 1.57 at dynamic pressures of 1950 to 2840 lb/ft^2. Kane recorded maximum snatch and opening-shock deceleration loads of 44 and 119 g, respectively, from onboard accelerometer data transmitted to a telemetry ground station.

Engstrom[11.12] developed a Cree test vehicle (with three stages of Nike M-5E1 boosters) to test small (~2- to 4-ft-diameter) hemispherically shaped ribbon parachutes at Mach numbers up to 3, altitudes up to 70,000 ft, and dynamic pressures up to 1720 lb/ft^2. Pepper[3.3,3.4] used the Sandia supersonic test vehicle (with the addition of a second Nike booster stage) to boost an 1100-lb store to test 20-ft-diameter reefed ribbon parachutes at Mach numbers up to 2.43 and dynamic pressures up to 5700 lb/ft^2. Pepper and Maydew[2.15] discuss tests of a 12.5-ft-diameter ribbon parachute at dynamic pressures up to 4200 lb/ft^2 and Mach numbers up to 1.94; this 500-lb test vehicle was boosted with a Genie motor. Maydew and Johnson[3.1] report on tests of a 22.2-ft-diameter reefed ribbon parachute at dynamic pressures up to 2720 lb/ft^2 (Mach 1.70); this 2100-lb store was boosted with an Honest John motor. Pepper[1.1] conducted tests of a 24-ft-diameter ribbon parachute at dynamic pressures up to 2700 lb/ft^2 (Mach 1.58); this 760-lb store was boosted with a Nike motor. Johnson and Peterson[3.6] used an Honest John motor to boost their 2465-lb test vehicle up to dynamic pressures of 2400 lb/ft^2 (Mach 1.5) to test a reefed 46.3-ft-diameter ribbon parachute.

Rollstin[11.13] describes the development of an Honest John boosted vehicle to test 5-ft-diameter ribbon parachutes with an 800-lb payload at dynamic pressures of 1800 to 4400 lb/ft^2 (with overtests to 5000 lb/ft^2), corresponding to Mach numbers of 1.3 to 2.3. A photograph of this vehicle on a rocket launcher at TTR is shown in Figure 11.4. The quadrant elevation launch angle of about 18 degrees allowed parachute deployment at altitudes of 10,000 to 12,000 ft. The dynamic pressure and Mach number at booster burnout were 10,000 lb/ft^2 and 3.1, respectively. Figure 11.5 shows a profile view of a trajectory that provides a nominal parachute deployment dynamic pressure of 3500 lb/ft^2. The pressure output of a pitot tube, which is mounted on the nose of the test vehicle, is used to obtain the desired deployment dynamic pressure. The pitot tube is connected to a previously set pressure switch that provides an electrical signal to explosively separate the afterbody from the test vehicle at the desired dynamic pressure, thereby deploying the parachute. Typical system error in obtaining the desired dynamic pressure was <2%.

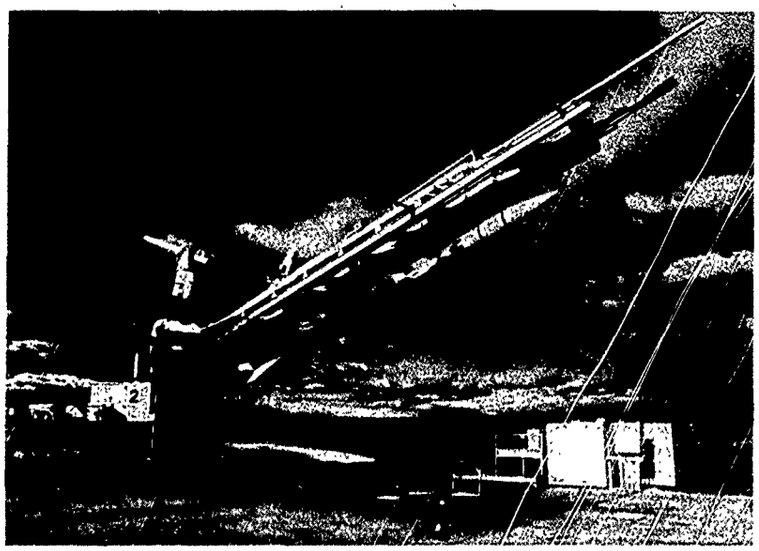


Figure 11.4. Honest John boosted test vehicle on launcher at TTR

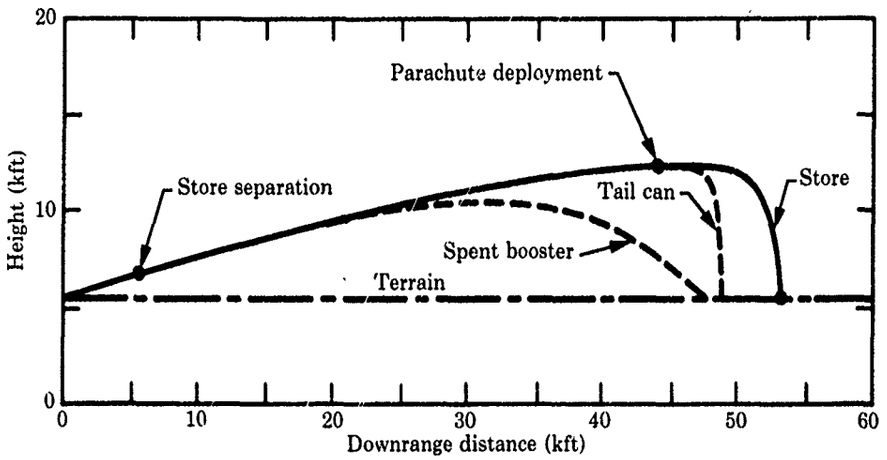


Figure 11.5. Trajectory profile of parachute test vehicle boosted to supersonic speeds

11.2.3 Ballistic range instrumentation

Range instrumentation is addressed in References 1.7, 2.1, and 11.2 to 11.8. The Sandia-operated DOE Tonopah Test Range (Ref. 11.2) is discussed in detail since the authors are more familiar with the capabilities of this range, and the capabilities of the other ranges are similar. Figure 11.6 is a functional block diagram of a typical TTR test operation for an aircraft-delivered store with approach and release directed by a ground-based test controller. Figure 11.7 shows the location of the camera, radar, and telemetry stations on the 525 square mile TTR. The tracking and data acquisition systems (including optical trackers, radars, and telemetry) at TTR provide both versatility and high accuracy to obtain the best field test results. Much of the equipment was custom designed and built by Sandia personnel; the balance of the equipment (built to TTR specifications) was purchased from manufacturers.

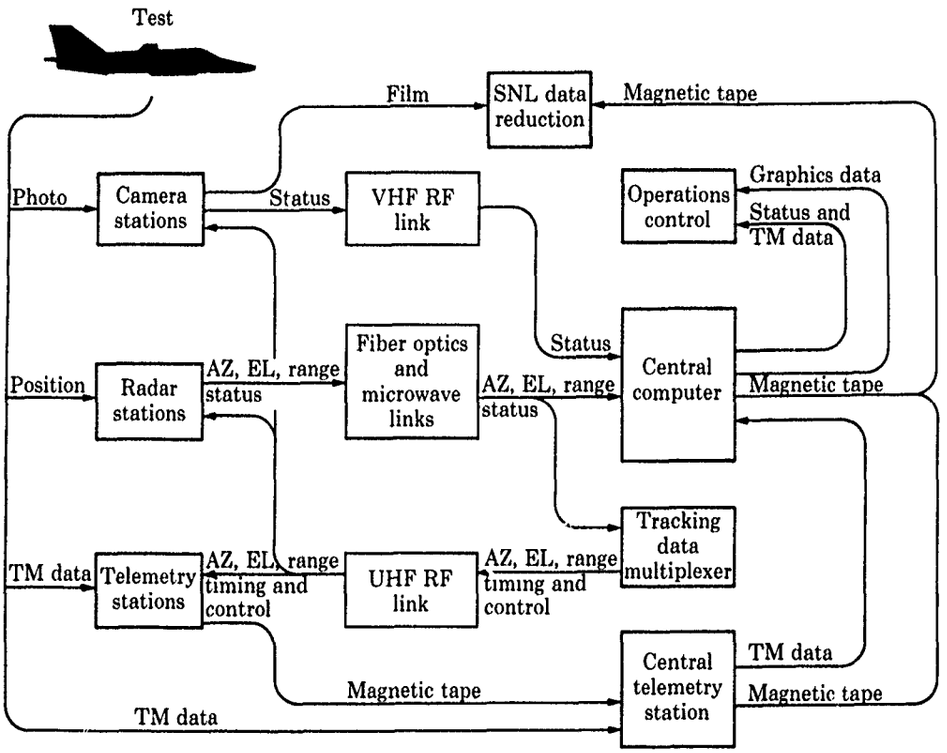


Figure 11.6. Functional block diagram of a typical TTR operation for an aircraft-delivered store, where AZ = azimuth, EL = elevation, TM = telemetry

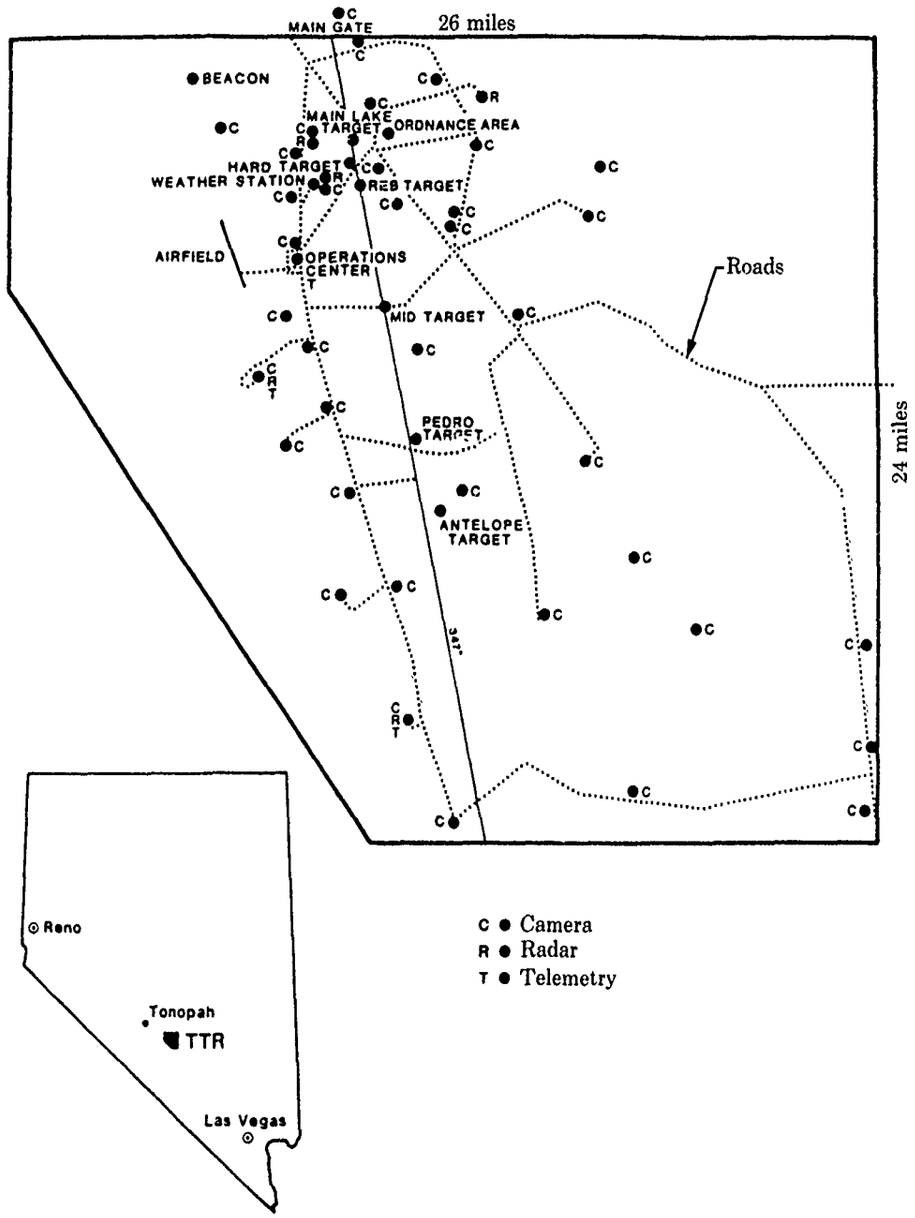


Figure 11.7. Location of targets, instrumentation, Operations Center, and roads at Tonopah Test Range

11.2.3.1 Radars

TTR is equipped with five tracking radars: two G-band (5400 to 5900 MHz) and three I-band (8900 to 9600 MHz). Table 11.2 gives the specifications and performance data for all five radar systems. The five units are strategically located to cover all range targets and aircraft or ballistic vehicle entry paths. The three I-band radars are mobile and can be easily moved to fill any gap in coverage that might occur because of a special test. Radar R18 is the primary unit for tracking rawinsondes.

Closed-circuit television cameras mounted on the pedestals are boresighted with the antennas to provide real-time television coverage of the radar targets. The video is used by radar operators for angle tracking when ground clutter or test conditions require it. Digital annotations are superimposed on TV signals that provide time of day, azimuth, elevation, and range data. The video is transmitted by fiber optics or microwave to the Central Computer for observation both during and after the test.

Digital data are transmitted from each radar to the Control Center and the Central Computer facility. These digital signals provide real-time trajectory data to drive plotting boards and graphics displays. All radar data are recorded in the Central Computer for posttest analysis of space position and trajectory. Tracking data from all operational radars are multiplexed and transmitted by RF link to all other tracking stations on the range. A microcomputer at each receiving station receives the data and computes azimuth and elevation-pointing angles and range data for target acquisition and camera focusing. The radars are routinely used for aircraft store drops, rocket launches, and artillery round firings.

11.2.3.2 Optical trackers

Optical trackers provide two categories of test data: test documentation and target vehicle space position data. Currently in use are 4 fixed-location trackers and 17 mobile trackers. All stations are equipped with landline or RF links for communications and for receiving timing and target acquisition information. Trackers can be deployed at any of the locations shown in Figure 11.7.

The six ME-16 and three SM-mount tracking telescopes constitute the principal equipment used to obtain sequential photographic engineering records. The mobile units are positioned on surveyed sites as required for a test operation. The ME-16 (16-in.-diameter primary mirror) is built around a Newtonian telescope with a prime focal length of 117.5 in. The telescope is installed in a high-accuracy mount that permits simultaneous azimuth and elevation tracking. These greater focal-length lenses have temperature correction features and are kept in focus with radar digital range data, which ensures high-resolution target images at all distances of 1000 yards or more.

Most of the telescopes use 35mm Photosonic 4E pin-registered cameras, which run at rates of 6 to 360 frames per second. Maximum tracking velocity for the ME-16's is about 20 degrees per second. The SM-mounts are small, highly mobile trackers. The newest type in use is the ABA Lightweight Optical Tracking System (LOTS), which can track at velocities up to 57 degrees per second. Two mounts carry 12-in. Newtonian telescopes with 60-in. focal lengths. The LOTS SM-mount uses a Photosonic 4E camera.

A variety of high-speed and special-purpose cameras are available at the Range. Rotating-prism cameras (16mm and 35mm) with frame rates from 100 to 10,000 frames per second, with a range of lenses, are used. Other available cameras are streak (35 to 250 ft/s), 35mm Mitchell and Photosonic, and 70mm Photosonic.

Eight Model EOTS (Sandia-modified) and one EOTS-C/F Contraves cinetheodolites are used at TTR to obtain metric photographic data. These mobile tracking instruments (they can be positioned at many locations, see Figure 11.7) are mounted on Parabam trailers and are protected by astrodomes. These Contraves have been modified to permit target acquisition with radar assistance through use of the Range Tracking Vector Translation System. They use a 60-in. and a 120-in. focal-length lens system and have frame rates of 5, 10, 20, or 30 frames per second. Three cinetheodolites are equipped with a G-band radar ranging system, which, along with the azimuth and elevation data, provides a one-station space position solution for any incoming test vehicle equipped with a 5400- to 5900-MHz radar transponder. Cameras on these mounts are synchronized to expose like frames simultaneously. Recorded on each picture frame are target image, plus IRIG time, and elevation and azimuth angle annotations. Data reduction of these films provides position versus time (primary source), velocity (primary source), acceleration (primary source for some tests), and altitude data. The space position data, obtained from an optimized cinetheodolite solution and translated to the TTR rectilinear coordinate system, is accurate to within ± 1 ft.

Table 11.2. Specifications and Performance Data for Radar Systems

Radar Type	M-33 Modified Conical Scan	DIR Monopulse
Transmitter		
PRF	700	156, 312, 625
Pulse width	0.25 μs	1.0, 0.25 μs
Multiple pulse	No	Yes
Peak power output	250 kW	250 kW
Final stage	Coaxial magnetron I-band (8.4–9.6 GHz)	Coaxial magnetron I-band (8.4–9.6 GHz)
Pedestal		
Prime mover	Electric motor	Electric motor
Maximum velocity	700 mil/s azimuth 500 mil/s elevation	700 mil/s azimuth 500 mil/s elevation
Antenna		
Type	Lens	Cassegrain parabolic
Size	6 ft	8 ft
Gain	37 dB	43 dB
Polarization	Vertical	Vertical
Receiver (solid-state)		
Type	One-channel	Three-channel
Mode	Skin	Skin/beacon
Range tracking		
Type	Digital	Digital
Mode	Skin	Skin/beacon
Maximum tracking:		
Rate	10,000 yd/s	10,000 yd/s
Data granularity	1 yd	1 yd
Angle tracking		
Tracking precision for 20-dB s/n target	±0.5 mil rms	±0.15 mil rms
Digital data system		
Angle encoders	16-bit synchron/digital	16-bit synchron/digital
Data output	16-bit angles 20-bit range	16-bit angles 20-bit range
Data rate	100 frames/s	100 frames/s
Closed-circuit television		
Lens (focal length)	40 in.	20/60 in, 7-70 in. zoom
Annotation	Time of day, azimuth, elevation, range	Time of day, azimuth, elevation, range

MPS-25 Monopulse	MPS-36 Monopulse	R18 Conical Scan
160, 320, 640 1.0, 0.5, 0.25 μs Yes 1.0 MW Coaxial magnetron G-band (5.4–5.95 GHz)	160, 320, 640 1.0, 0.5, 0.25 μs Yes 1.0 MW Crossed-field amplifier (coherent) G-band (5.4–5.95 GHz)	500 1.0, 0.25 μs No 200 kW Coaxial magnetron I-band (9.1–9.6 GHz)
Hydraulic 800 mil/s azimuth 500 mil/s elevation	PM torquer 800 mil/s azimuth 500 mil/s azimuth	Dual dc motors 266 mil/s azimuth and elevation
Parabolic 12 ft 44 dB Vertical	Parabolic 12 ft 43 dB Vertical, horizontal, right or left circular	Parabolic 8 ft 43 dB Vertical
Three-channel Skin/beacon	Two-channel Skin/beacon	One-channel Skin/beacon
Digital Skin/beacon	Digital Skin/beacon	Digital Skin/beacon (single-pulse)
20,000 yd/s 1 yd	20,000 yd/s 1 yd	2500 m/s 2 m
±0.1 mil rms	±0.2 mil rms	±0.5 mil rms
18-bit optical 18-bit angles 24-bit range 100 frames/s	20-bit optical 20-bit angles 24-bit range 100 frames/s	16-bit synchron/digital 16-bit angles 18-bit range 100 frames/s
40/120 in. Time of day, azimuth, elevation, range	40/120 in. Time of day, azimuth, elevation, range	7–70 in., 200 m Time of day, azimuth, elevation, range, altitude

Rollstin[11.13] discusses the errors in radar tracking and optical tracking during periods of rapid accelerations (rocket boosting) and decelerations (parachute opening). Figure 11.8a compares the vehicle velocity during boost from optical track with the velocity derived from onboard accelerometers. Figure 11.8b compares the vehicle dynamic pressure during parachute deployment from optical track with the dynamic pressure derived from onboard accelerometers.

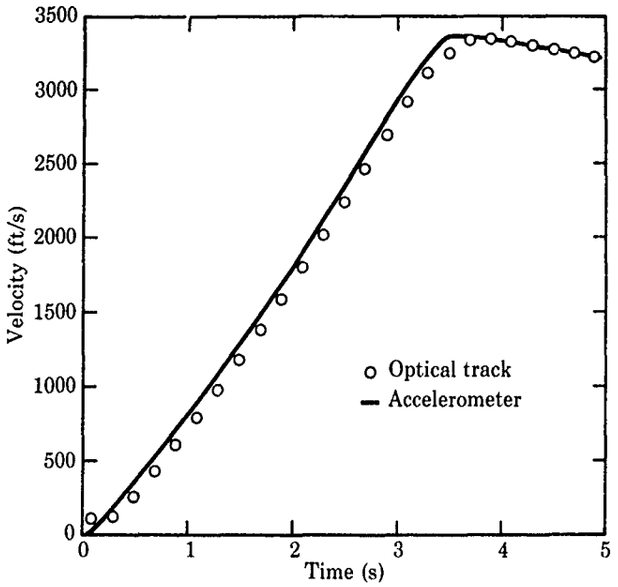


Figure 11.8a. Velocities of parachute test vehicle inferred from optical track and accelerometer data during boost

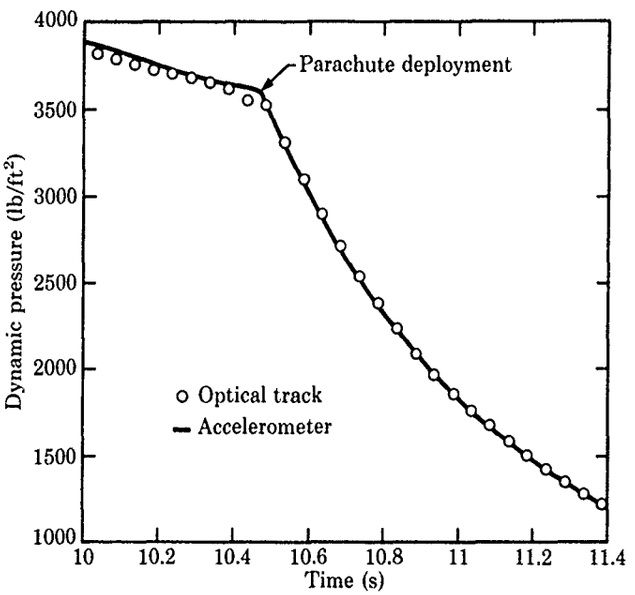


Figure 11.8b. Dynamic pressure of parachute test vehicle inferred from optical track and accelerometer data during the parachute deployment

11.2.3.3 Telemetry

Two fixed and two mobile ground stations provide complete range coverage of RF signals in the 1435- to 1535-MHz and 2200- to 2300-MHz telemetry bands. The Master Ground Station, located in the Operations Center, is the controlling element for telemetry functions; it provides reception, recording, real-time display, and posttest playback of telemetry data. The other ground stations serve as backups for receiving and recording data. The mobile stations are located where they can ensure coverage of critical areas of the test vehicle trajectory. At least two ground stations are operated during any test.

Analog tape recorders record either Pre-D receiver outputs or the receiver video outputs, depending on the modulation format or the customer's requirements. IRIG-B timing and a station multiplex containing reference frequencies and receiver automatic gain control signals are also recorded, along with a voice channel with the UHF air-to-ground radio network and a VHF ground-to-ground range operations network. Any of the other range voice networks can be recorded on the telemetry tape when required.

The data needed to make real-time go-no-go decisions are displayed in several ways, including analog meters, oscillographs or strip charts, oscilloscopes, spectrum analyzers, computer printouts, and CRT displays. The Central Computer accepts pulse-code modulated data in real-time and posttest modes, and produces listings and/or plots in engineering units. Most playback and quick-look data processing requirements can be fulfilled within 24 hours after a test. Detailed descriptions of each station's equipment and capabilities are given in Table 4.3 of Reference 11.2.

11.3 Sled track testing

Sled track facilities are used for parachutes deployed from (and held captive to) a rocket sled and for those deployed from a sled-ejected test vehicle. Both testing methods are expensive—the latter, in Sandia's experience, is more expensive than aircraft drops or rocket boosting. The Parachute Design Guide[2 1] lists some of the advantages and disadvantages of the captive rocket sled method. Major disadvantages are asymmetry of the flow field due to ground interference, testing limited to small parachute sizes, and the lack of vehicle/parachute deceleration simulation (infinite mass testing). Correct deceleration-simulation testing is very important for high-performance parachute design validation. Sled ejection avoids these major captive-sled disadvantages, but testing costs are higher because of the design and fabrication of the ejector. Aircraft flow-field effects on parachute performance are not simulated during sled ejection tests. This is not a problem except for large parachutes deployed near heavy aircraft, when aircraft downwash may cause parachute canopy collapse.

Ewing, Bixby, and Knacke[1,7] report that track facilities can be used to simulate flight trajectories under accurately programmed, closely controlled, and rigorously monitored conditions. In effect, the track can be used as a giant wind tunnel, making possible many experiments not possible in conventional facilities. Ewing, Bixby, and Knacke and Pirrello, Hardin, and Heckart[11 14] describe the major tracks in the United States. Brief descriptions of the tracks are given in the following sections, including examples of captive-sled and sled-ejector testing.

11.3.1 Holloman High-Speed Test Track

This track facility is operated by the USAF Armament Division, 6585th Test Group, at Holloman AFB, New Mexico. This aerospace ground test facility has capabilities for dynamic testing of crew escape systems; aerodynamic decelerators; rain, dust, and particle erosion; guidance and aeropropulsion systems; impact testing; hypersonic and transonic aerodynamic testing at high Reynolds number; dispenser system testing; explosive blast-testing; and for launch into free flight. This track is the longest (50,788 ft), most precisely aligned, and most highly instrumented of its kind. The master rail is aligned 0.005 in. with respect to a reference (fiducial) line established with better than first-order accuracy over its nearly 10-mile length. A precision-space time system provides a velocity reference better than 0.01 ft/s. Test speeds of up to 8200 ft/s have been demonstrated. Depending on payload size, accelerations greater than 200 g have been demonstrated; sled weights range from 100 to 30,000 lb. Sleds travel on a set of heavy-duty crane rails spaced 7 ft apart on a foundation designed to resist vertical (down) loads of 70,000 lb per slipper on any two slippers. Water is used to decelerate and stop the test sled at the conclusion of a run. Telemetry equipment and extensive photographic capabilities are available for complete instrumentation of a sled test.

11.3.2 Naval Weapons Center's supersonic test tracks

Reference 11.3 gives a detailed description of this track testing facility. It consists of three separate tracks—the Supersonic Naval Ordnance Research Track (SNORT), the Transonic Test Track, and the Terminal and Exterior Ballistics Test Track—each with specific capabilities. Complete telemetry and photographic coverage, as well as sled velocity measurements, is provided for all three tracks.

The SNORT track is used for captive-flight, aeroballistics, fuze, guidance system, aircraft damage, terminal ballistics, crosswind firing, projectile recovery, and aircraft and capsule escape system and rain erosion tests. The facility is a 21,550-ft-long, two-rail, 56.5-in.-gauge, precisely aligned, heavy-duty track located near the southwest corner of the China Lake complex. Either monorail or dual-rail test vehicles can be used; the track will withstand dual-rail vertical loads of up to 136,000 lb. Speeds up to 600 ft/s can be attained. The sled is decelerated the last two miles with a water trough located between the rails.

The Transonic Test Track is used for captive-flight and aerodynamic testing of parachute deployment, missile components, and aircraft damage in addition to target profile recognition fuze tests. The track is 14,560 ft long, two-rail, and 56.5-in. gauge. Test vehicles can be accelerated up to speeds of 2000 ft/s, and sleds weighing up to 6600 lb have been tested. Deceleration is by means of a probe that drags through loose sand spread between the rails over the last portion of the track.

The Terminal and Exterior Ballistics Test Track is used for impacting a stationary target at the end of the track and for launching a weapon from the sled at the end of the track into flight with trajectories several hundred feet high over a broad deep valley. The facility is 3000 ft long, two-rail, precisely aligned, and heavy-duty with a 33-7/8-in. gauge. Monorail or dual-rail test vehicles can be used. Sleds weighing up to 10,000 lb can be accommodated, and speeds up to 4500 ft/s are attainable. Portable equipment is used to control and instrument tests.

11.3.3 Sandia Rocket Sled Track

Located at Kirtland AFB in Albuquerque, New Mexico, the Rocket Sled Track is operated for the Department of Energy by Sandia National Laboratories. The track is 10,000 ft long with a 22-in.-gauge dual rail. This narrow gauge provides dual-rail stability while minimizing sled mass and frontal area; this reduces significantly the propulsion requirements at higher velocities. The maximum test velocity, using a monorail sled, is ~6600 ft/s. The sled is normally stopped at the track end by a water brake; sleds can be recovered after achieving speeds of up to 4000 ft/s. Of the approximately 250 sled tests conducted annually in the United States, about 50 of them take place at the Sandia track.

Laser-controlled tracking offers excellent centered high-speed motion picture coverage of the test item and provides accurate space position and velocity and acceleration data within a few minutes after the test. An argon-ion laser beam is optically routed to a double-gimbal-mounted mirror on the roof of the tracker trailer. The mirror directs the laser beam to the test devices to be tracked. A reflective material on the test devices returns laser energy to the double-gimbal-mounted mirror for optical transmission to an image dissector within the tracker. The reflected beam is analyzed to determine the direction of test vehicle motion. A closed-loop servo system repositions the mirror to keep the laser beam on the test devices. Shaft encoders read out the mirror azimuth and elevation coordinates, and a beam-modulating technique determines slant ranges to the test devices. These three coordinates, read at 1000 samples per second, provide test vehicle position-time data recorded digitally in a minicomputer. The laser tracker measures the trajectory of the sleds and ejected payloads—it locks onto the unit even though it may be only 4 ft long and 3 in. in diameter, and traveling at 6000 ft/s. These trackers have slew rates of 3 radians/s, and the trajectory position-time data is accurate to ±2 ft. Tracking data is available immediately after the test is conducted.

Computers in the laser trackers provide real-time trajectory data for test control and for directing slaved equipment. For example, parachutes can be deployed on command, through an RF link from the tracker to the test vehicle, when the test vehicle is at the desired velocity. However, onboard timers are the most common means of activating parachute deployment during sled tests since sled velocity is predictable to within 2%. Test vehicle accelerations are measured by transducers and telemetered to ground stations. Extensive photometric coverage of parachute tests is obtained from independent tracking cameras—cameras in the laser tracker using the same optical path as the laser beam and cameras on mounts slaved to the laser tracker. Both S- and L-band telemetry are available.

In addition to tow testing, vehicles weighing up to 2500 lb may be ejected upward from the sled to altitudes of 250 ft in order to obtain free-flight parachute performance data. The first ejector sled was built in 1962—a pneumatically driven piston tosses the test item into the air while the sled is moving. Tests have been conducted of parachute-retarded stores that fly for a mile and still hit a 40-ft^2 target. At shorter distances and without a parachute, the miss distance to a target is only an inch or two. A high degree of test precision can be achieved with this ejection technique since sled velocity, ejection position, and ejection altitude can be closely controlled. Thus, payloads can be accurately placed into target arenas. This technique also permits testing temperature-preconditioned payloads from −160°F to +65°F. Temperature shrouds are removed from the payload just before the launch.

Parachute tests are also conducted captive to rocket sleds. The most common is the cross-flow deployment test. Parachutes are deployed at oblique angles to the airstream to investigate inflation under cross-flow conditions. An example is the Space Shuttle SRB decelerator subsystem that was tested at the Sandia track. The Space Shuttle SRB assumes a near-horizontal attitude upon reentry; the predicted attitude is between 10 degrees nose down and 50 degrees nose up. The parachutes are mounted in the nose cone of the booster and are deployed forward from the booster; thus, the pilot and drogue parachutes are deployed in a severe cross-flow condition. The drogue parachute orients the booster with the flow before deployment of the main parachute. To test to these cross-flow deployment conditions, SRB nose cones with decelerator systems were mounted on a rocket sled for tests at the 10-degree nose-down and 50-degree nose-up conditions. The sleds were then launched to the test velocity, where the nose cones were jettisoned by thrusters, which deployed the pilot parachute, which in turn deployed the drogue parachute.

In addition to parachute and other aerodynamic testing, the sled track is used extensively for impact fuzing and other impact tests (aircraft, nuclear reactor, nuclear waste container, etc.). Radiography (x rays) is used to look through fireballs or inside a ballistic case to view crush-up as it happens. Sandia makes extensive use of reverse ballistic testing, accelerating rocket sled targets into payloads positioned at the end of the track. This technique permits the recovery of high-frequency data directly over hard-wire. Magnetic disks, located in a bunker adjacent to the sled track, record numerous channels of 2-MHz FM data during impacts. Digital data recording of 5 MHz is available. Impacts are photographed at 100K frames per second using rotating-mirror framing cameras.

11.3.4 Captive-sled parachute testing

Using rocket sleds at the Holloman High-Speed Test Track, Babish[3.30] conducted 20 tests of 5-ft-diameter nylon and Kevlar hemisflo ribbon parachutes at dynamic pressures up to 6000 lb/ft^2 (Mach 2.2). This comprehensive test program demonstrated the usefulness of the captive-sled technique for systematically testing small parachutes in a carefully controlled test environment and with accurate instrumentation. Three tests were made at Mach 1.2 using the Tomahawk sled to check out parachute deployment system techniques. Fourteen tests were conducted with the Arrowhead sled (see sketch in Figure 11.9) at Mach numbers 1.5, 1.8 and 2.2 (dynamic pressures of 2500, 3500, and 6000 lb/ft^2) to obtain comparative parachute performance and structural integrity data.

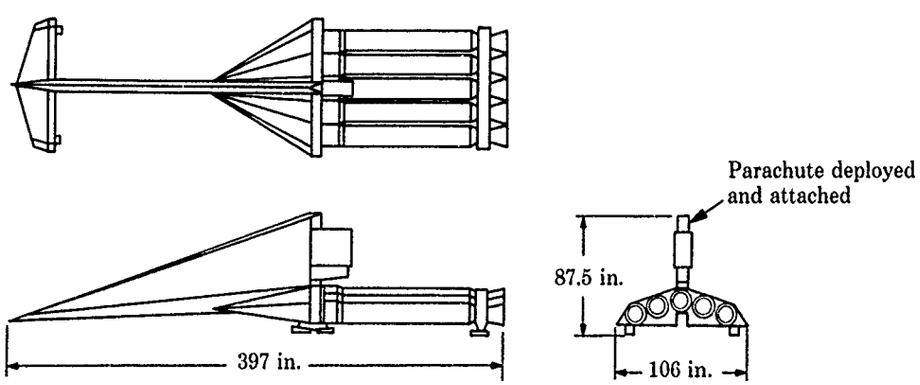


Figure 11.9. Sketch of the Arrowhead sled (taken from Ref. 3.30)

The Arrowhead sled operates either as a single-stage vehicle (with five Nike boosters) or, with a noncaptive pusher sled (also with five Nike boosters), as a two-stage test vehicle. The single-stage vehicle accelerates the initial sled weight of 11,700 lb to Mach 1.89 at motor burnout (burnout weight is 7900 lb); the total thrust is 245,000 lb. The two-stage vehicle, with the pusher sled, accelerates the Arrowhead sled to Mach 2.55 at motor burnout. Parachute deployment was initiated shortly after motor burnout, when the sled knives intercepted the screen box. Electrical current from the screen box fired the drogue gun squibs in the parachute deployment mechanism located at the top and at the base of the sled. The resulting gas pressure sheared the drogue gun mortar pin and propelled the deployment cone downstream from the sled. A schematic of a typical deployment sequence is shown in Figure 11.10. Excellent sled and parachute performance data (including photographic coverage) were obtained. Babish also discusses the aerodynamic design of the Arrowhead sled, including the wind tunnel testing.

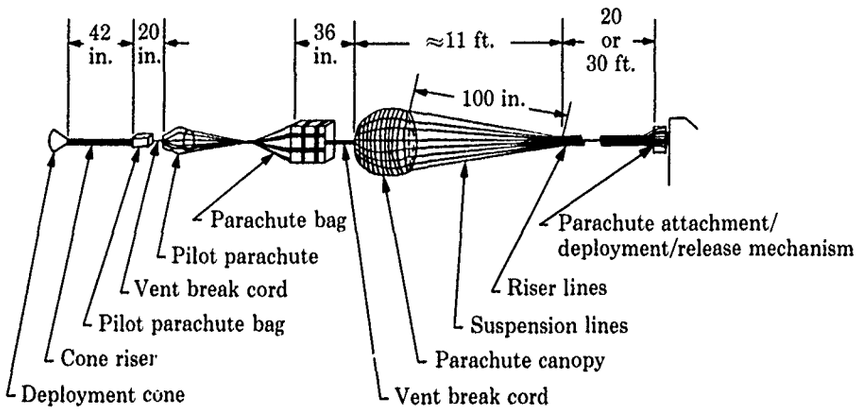


Figure 11.10. Sketch of a typical deployment sequence of Babish's supersonic captive-sled tests at Holloman AFB of 5-ft-diameter ribbon parachute (taken from Ref. 3.30)

11.3.5 Sled-ejector parachute testing at the Sandia Rocket Sled Track

Johnson and Peterson[3.6] discuss the results of eight sled-ejector (free-flight) tests at Mach 0.51 to 1.33 of their 46.3-ft-diameter ribbon parachute with the 2465-lb store. A photograph of the ejector sled at the start of rocket burn on the Sandia Rocket Sled Track is shown in Figure 11.11. The ejector system on the sled tosses the store 200 to 300 ft vertically before parachute deployment. The pneumatically operated ejector used a 10-in.-diameter piston with a 6-ft stroke to toss a 2400-lb test vehicle 300 ft vertically. These sled tests measured the effects of humidity and temperature on parachute performance. For example, the parachutes were soaked at temperatures of +160°F or −65°F for 36 hours before the tests. These types of environmental tests could not be conducted with aircraft drops or rocket boosting because of the long resoak time required to fly the aircraft to TTR or to install the parachute in the rocket test vehicle. Hence, the sled-ejector system is a very useful full-scale testing technique to qualify the parachute for the extreme temperature and humidity conditions required in the design specifications.

Pepper[1.1] conducted 28 sled-ejector tests of a 760-lb store to develop a 24-ft-diameter nylon/Kevlar parachute and to test the store characteristics during impact on a concrete target. Figure 11.12 shows this store/parachute system impacting the concrete target. These tests were conducted at parachute deployment velocities of ~610 to 1500 ft/s. The store was ejected about 120 ft vertically after booster burnout, then the parachute was deployed with a gas-generator-powered telescoping tube. A photograph of the ejector sled is shown by Pepper[1.1] in his Figure 4. These parachute packs were also conditioned to temperatures of −65°F and +160°F for long periods before the sled tests in order to measure the effect of temperature extremes on parachute performance.

Pepper[2.11,9.3,9.5] utilized the sled ejector to develop small (19-in.-diameter to 6.4-ft-diameter) guide surface or ribbon parachutes to recover (at sea) reentry vehicle nose cones weighing 40 to 130 lb. In Reference 9.3, he describes the results of 12 sled tests in which he qualified the 19-in.-diameter ribbon nylon parachute (with a 40-lb payload) at deployment dynamic pressures up to 2400 lb/ft^2. In Reference 2.11, Pepper describes the results of ten sled-ejector tests and five captive-sled tests in which he qualified the 19-in.-diameter ribbon Kevlar parachute (with a 57-lb payload) at deployment

dynamic pressures up to 9000 lb/ft^2. Lastly, in Reference 9.5, he discusses the results of five sled-ejector tests in which he qualified a 6.4-ft-diameter Kevlar/nylon ribbon parachute (with a 130-lb payload) at deployment dynamic pressures up to 770 lb/ft^2. It should be noted that these were all very tight packs, because volume for a recovery system is at a premium in a reentry vehicle nose cone. In addition, the recovery systems for the 40-lb and 57-lb payloads also included flotation bags. All three of these recovery systems worked on the ICBM reentry vehicle flights; hence, good use was made of this parachute sled testing capability for design purposes.

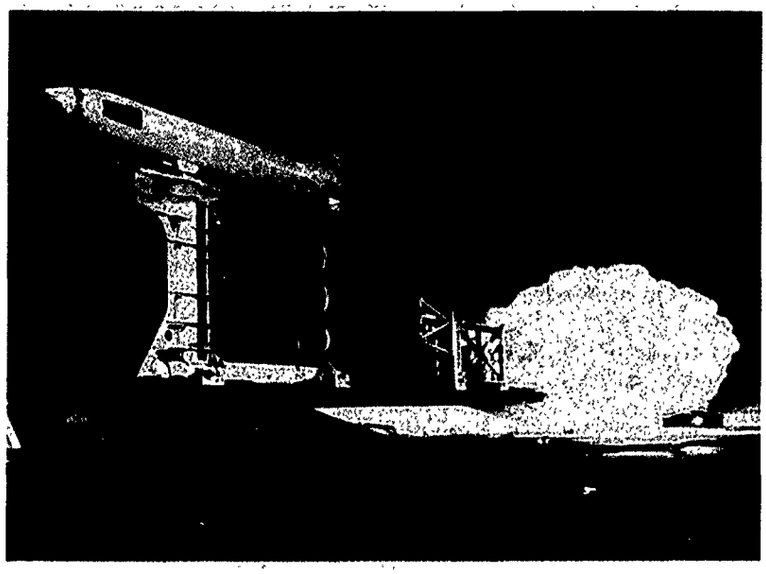


Figure 11.11. A 2200-lb store on an ejector sled on the Sandia track

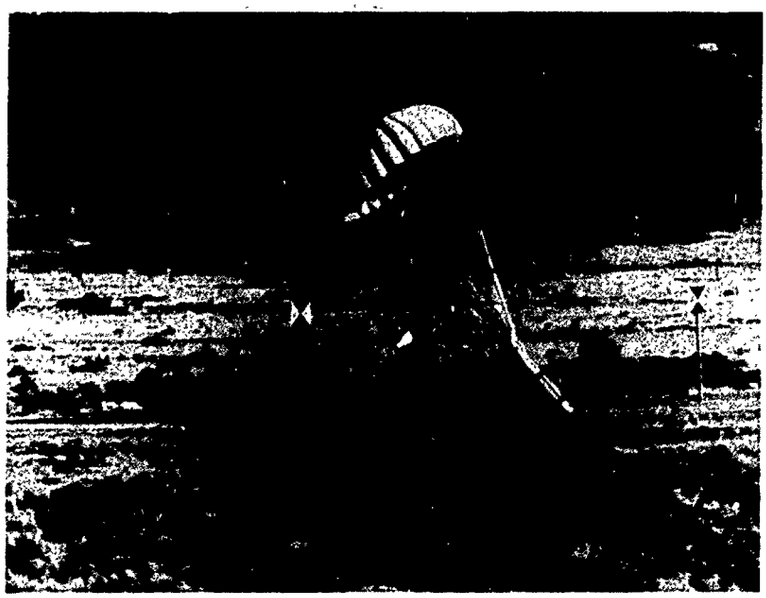


Figure 11.12. Hard-target impact of store with 24-ft-diameter parachute after Sandia sled track test

11.4 Other full-scale test methods

Balloon-launched parachute tests are discussed in the Parachute Design Guide,[2.1] by Ewing, Bixby, and Knacke,[1.7] and by Johnson.[11.1] However, this method of testing has not been used extensively for high-performance parachute testing. The Parachute Design Guide, [2 1] Johnson,[11 1] and Paulsen[11.15] discuss testing at the Parachute Whirl Tower Test Facility in El Centro, California. The Whirl Tower, which has been used for the development of high-performance parachutes, is 120 ft high; a 60-ft arm extends out from near the top of the tower to which is attached a 116-ft-long cable with the test gondola. The horizontal arm is rotated about the tower (with cable attached) at a maximum speed of 40.5 rpm. Parachutes can be deployed from the gondola at speeds up to ~430 knots. Parachutes as large as 35 ft in diameter have been tested; the test vehicles weigh from 250 lb (maximum-velocity tests) to 5000 lb (low-velocity tests). The test conditions are repeatable, and good photographic coverage is possible since the trajectory of the test item can be controlled. The Whirl Tower is no longer an active test facility.

Lin[11 16] discusses the use of a 140-mm gun to launch (at a 45-degree elevation angle) a 66-lb, 3-ft-long vehicle to test 32-ft^2 drag-area nylon and Fonlon ribbon parachutes at deployment Mach numbers of 1.76 to 2.34. Pop-out fins are deployed after barrel exit to stabilize the vehicle until the parachute is deployed. The aft 9-lb vehicle section is explosively separated (at a preset time) from the 51-lb nose section and deploys the test parachute for recovering the nose section. A second parachute is used to recover the aft section. Fifteen successful tests were conducted using this gun launch technique.

Downs and Bartlett[11 17] describe a new Royal Aeronautical Establishment compressed-air parachute test vehicle launcher. The 600-lb/in^2, 15.7-in.-diameter gas gun is capable of launching 308-lb test vehicles at muzzle velocities up to 525 ft/s or to altitudes >3000 ft. Twenty-one firings at elevation angles of 45 to 80 degrees have demonstrated the capability of this launcher for parachute testing. The instrumented range is equipped with radar, cinetheodolites, high-speed cameras, and video. The parachute test vehicles will be equipped with solid-state data recorders for measuring outputs of the accelerometer, load cell, and pressure transducer. After recovery from the range, the recorder is downloaded to a portable PC-compatible recorder.

Sandia has developed an aerial cable facility used for parachute and ordnance testing. It consists of two parallel cables (100 ft apart) that span a mountain canyon 4800 ft wide. The height above the ground at midspan is 600 ft. The cables are referred to as the "Pull-Down Cable" and the "Trolley Cable"; both are used for parachute testing. The trolley cable was originally developed for free-fall testing of conventional ordnance, which might detonate on impact. Later, a rocket pull-down capability was added to these facilities; this consists of a rocket test sled captive to a track to tow test devices (using wire rope towing lines) from the overhead test platforms to ground test arenas. Payloads weighing up to 2500 lb can be accelerated to velocities of 800 ft/s using this rocket pull-down technique. Typical targets impacted are concrete runways, earth, water, steel, trees, rice paddies, military vehicles, and tanks. Several camera stations provide high-speed photometric data. Both the free-fall and rocket pull-down techniques have been used to test parachutes. Free-fall tests can be turned around quickly, thereby providing an inexpensive method for full-scale (but low-velocity-deployment) testing. Anemometers can be placed at selected elevations along the drop path to define the wind fields. A net may be used in the drop-test impact zone for soft recovery of test vehicles. Parachutes may either be predeployed or deployed during the cable test, depending on the test objectives. A laser tracker data van provides telephoto 16mm color motion pictures and X,Y,Z displacement and velocity data of test units during flight. Since the facility is in a remote mountain/canyon area, tests involving large amounts of explosives can be conducted safely.

11.5 Test vehicles

The Parachute Design Guide,[2 1] Ewing, Bixby, and Knacke,[1 7] and Johnson[11.1] discuss the design and use of parachute test vehicles. Special-purpose test vehicles have been designed for gun-launched, sled ejector, whirl tower, balloon drop, aircraft drop, aircraft rocket boost, ground rocket boost, and other flight tests. There are literally dozens of descriptions in the open literature for the design of parachute test vehicles. This section on test vehicles will be limited to a few representative vehicles used for aircraft drop and ground rocket-boosted testing of high-performance parachutes.

The initial testing of a new decelerator system with a special test vehicle should not preclude testing the parachute with a vehicle that reproduces the aerodynamic configuration of the actual store, because the performance of the parachute can be significantly influenced by the flow field about the actual store and the stability of the actual store. In some programs, the decelerator system may be one

of several subsystems making up the total system. The components of the decelerator system must be tested separately before being integrated into the total system. The parachute system designer should employ the most realistic testing and test vehicles available to qualify the parachute system before integration is accomplished.

11.5.1 Examples of test vehicle designs

A photograph of a parachute test vehicle on an F-7U aircraft is shown in Figure 11.13. This 24-in.-diameter, 223-in.-long test vehicle was used extensively by Sandia in the late fifties and early sixties to test 16- to 40-ft-diameter heavy-duty ribbon parachutes at low altitudes at Mach numbers 0.6 to 1.0 (see Maydew and Blanchard[2.12]). The vehicle weight could be varied from ~1750 lb to 2600 lb; two aft-mounted, aft-facing 16mm Fairchild cameras (film speeds of 80 or 200 frames per second) were used to photograph the parachute deployment and opening. This film coverage of the parachute opening was so valuable to the Sandia parachute designers (especially when deployment anomalies or canopy failures occurred) that vehicle onboard cameras became "standard instrumentation" for all parachute test vehicles, when the design permitted. The 4-ft-long spike facilitated vehicle recovery and the test vehicles were used many times.

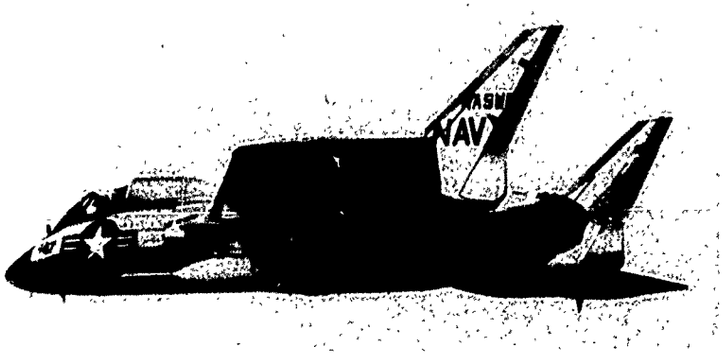
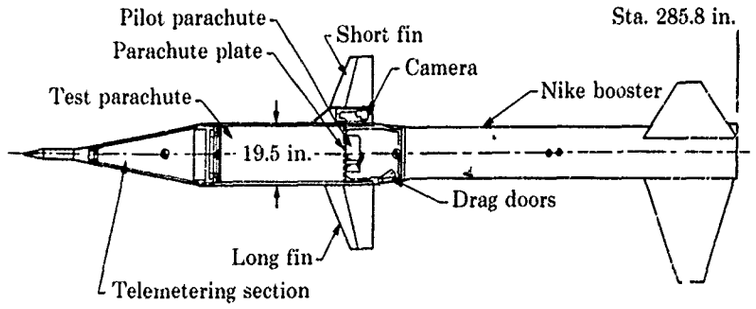


Figure 11.13. Sandia parachute test vehicle carried on F-7U aircraft

Downing and Engstrom[11.18] summarize parachute test vehicles and testing methods. They focus on the design of rocket-boosted sled test vehicles and ground-launched, rocket-boosted parachute test vehicles. Kane and Barth[11.11] describe the design of Sandia's supersonic parachute test vehicle, which was used by Pepper[3.3,3.4] and others to test 20-ft-diameter heavy-duty ribbon parachutes at dynamic pressures up to 5700 lb/ft^2. A sketch of this test vehicle is shown in Figure 11.14. Two different fin spans were used with this supersonic parachute test vehicle.



	Weight
Launch	2420 lb
Booster with fins	1280 lb
Second stage	1130 lb

Figure 11.14. Supersonic parachute test vehicle

Samuels and Fournier[11.19] conducted extensive wind tunnel tests at angles of attack from −4 degrees to +20 degrees to determine the static longitudinal aerodynamic force and moment characteristics of a decelerator test vehicle at Mach 0.6 to 2.86. The 1/4-scale model consisted of a spherically blunted nose cone and a cylinder followed by a flare; three cone-cylinder pods were equally spaced around the flare.

Moog, Sheppard, and Kross[4.12] describe the 48,000-lb drop-test vehicle used with a B-52 aircraft to test the 54-ft-diameter drogue parachute and the cluster of 115-ft-diameter main parachutes for the Space Shuttle Solid Rocket Booster recovery system. Because the SRB weight is 170,000 lb, it was not possible to develop significant loads in more than one reefing stage of the drogue or main parachute using the 48,000-lb test vehicle. The weight mismatch between the SRB and the test vehicle required careful planning in the test program to demonstrate the capability of the drogue and the mains from these drop-test vehicle test data. Moog, Sheppard, and Kross include a good description of the drop-test vehicle.

Rollstin[11.13] describes the rocket-boosted 800-lb parachute test vehicle used for testing 5-ft-diameter ribbon parachutes at dynamic pressures up to 5000 lb/ft^2. This 13-in.-diameter, 10.5-ft-long test vehicle is shown on the launcher at TTR in Figure 11.4. Figure 11.15 shows the vehicle in supersonic flight—as evidenced by the attached shock waves—during booster burn.

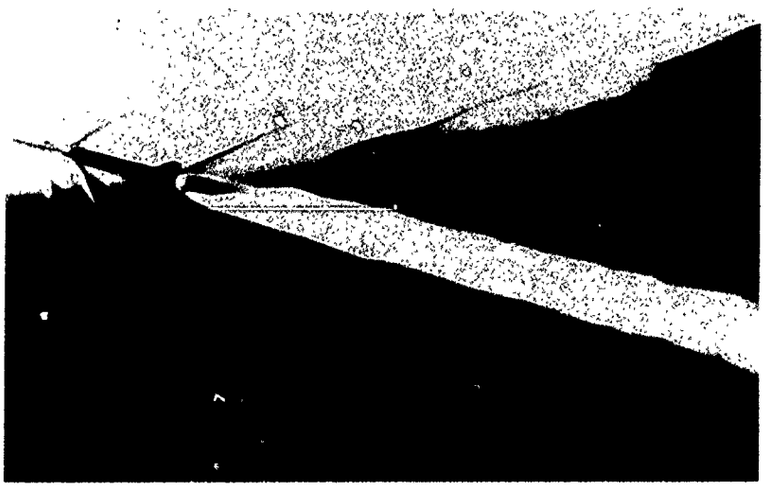


Figure 11.15. Honest John boosted store

Hanlon and Poole[11.20] discuss the development of 2600-lb and 3400-lb test vehicles designed to perform aircraft drop tests on two-stage parachute systems to recover sounding rocket payloads at White Sands Proving Grounds, New Mexico, at terminal velocities of 25 and 30 ft/s. The second-stage parachute is 104 ft in diameter. The authors conducted 10 aircraft drop tests at Edwards Air Force Base, California, to flight-qualify these parachute systems.

Johnson[3.37] developed a cluster of three 49-ft-diameter parachutes to decelerate the 3130-lb F-111 Crew Escape Module (CEM) to an earth impact velocity of 25 ft/s. The parachute test vehicle was designed and used in the sixties, during the development of the original F-111 parachute system, and can only be dropped from the NASA B-52 operated by the Dryden Research Facility at Edwards AFB. The test vehicle, shown in a sketch in Johnson's paper, has a parachute bay with a catapult system that replicates the storage bay and catapult in the CEM. The vehicle is aerodynamically unstable, and a 4-ft-diameter guide surface parachute is attached to the aft end to keep the vehicle stable until the test parachute is deployed.

11.5.2 Onboard instrumentation

Johnson[11.1] summarizes test vehicle instrumentation systems. Instruments mounted on or within the test vehicle are typically used to measure forces, accelerations, angular motion, pressures, and sequencing of events such as booster separation or parachute deployment. The data most useful to the parachute designer are the drag forces produced by the decelerator. These data give the designer an

indication of the accuracy of the calculations used to predict parachute performance and the structural margins in the parachute. The drag force may be measured directly by a load cell or tensiometer, or it may be calculated from the measured accelerations. Some mechanical methods for measuring drag have been used in the past, but these were not very accurate or reliable and are not currently in use.

The data from the instruments on the test vehicle are generally transmitted to a ground receiving station by a telemetry link. In FM telemetry systems, the physical quantity to be measured is converted to an equivalent electrical signal. This signal is used to modulate the frequency of a subcarrier oscillator. These outputs are then mixed and used to modulate the frequency of the transmitter. Telemetry systems are now being used that transmit the data as a digital signal. These digital systems normally have greater accuracy than the FM type.

Another method of retrieving the data from the test vehicle is to store the data onboard the vehicle during the test by the use of a tape recorder or one of the new solid-state memory devices. After the test, the data can be read from the recovered vehicle and reduced to engineering data. Use of the recorder or memory device eliminates the need for a telemetry receiving station, but it is assumed that the test decelerator will not fail to such an extent as to cause the loss of the test vehicle and the data storage device.

As mentioned earlier, some of the most valuable data for the parachute designer are obtained from photographic coverage of the parachute deployment and inflation. Placing cameras onboard the test vehicle is usually the best way of obtaining detailed pictures of the parachute inflation for correlation with other data. Several types of cameras are available that will withstand the environment and provide satisfactory data.

Maydew and Johnson[3.1] conducted 20 aircraft drop and 9 rocket-boosted flight tests to develop a 22.2-ft-diameter ribbon parachute. Two 16mm cameras (mounted between the store fins) operating at 200 and 1000 frames per second were used to photograph the deployment and opening of the parachute for the rocket tests. An FM/FM analog telemetry system was used to record the accelerations, time sequences, and pitot pressures. Maydew and Johnson used two different methods for combining the onboard accelerometer data with the metric theodolite data in order to calculate the parachute drag area versus time during the rapid store deceleration while the parachute was filling at the transonic deployment conditions. They concluded that the accuracy of dynamic pressure (velocity) during periods of high deceleration (20 to 70 g) from the theodolite data was sufficient.

Pepper[1.1] conducted 31 aircraft drop and 11 rocket-boosted flight tests to develop a 24-ft-diameter ribbon parachute. Two 16mm cameras (Photosonic, Inc.) operating at 200 and 500 frames per second, mounted between the store fins, were used to photograph the parachute deployment and opening for the rocket tests. An 11-channel telemetry system measured accelerations/decelerations, ram-air pressure, and monitor functions.

Rollstin[11.13] and Peterson et al.[1.2] conducted 19 rocket-boosted flight tests to develop a 5-ft-diameter ribbon parachute. Two 16mm cameras (Photosonic, Inc.) operating at 200 and 1000 frames per second were installed and shrouded in the boattail section (see Figure 11.4) to view the parachute during deployment and opening. A typical photograph of the parachute taken with the onboard camera is shown in Figure 11.16. A telemetry system was used to measure accelerations/decelerations, pitot pressure, and monitor functions. Rollstin[11 13] did an error analysis of the onboard accelerometer data combined with radar and the cinetheodolite metric data. Instrumentation, telemetering, and/or data processing anomalies may cause vehicle deceleration measurement errors—5 to 10 percent of the measured values is not considered unusual. He developed a data reduction procedure to correct the onboard acceleration measurements and to correct the flight environment tracking data. Some of these corrected data are shown in Figures 11.8a and 11.8b. The axial accelerometers used for the store instrumentation are of the piezoelectric type and have a range of 100 g. Typical deceleration levels during the time of accelerometer-to-optical-track data match were from -5 g to -2 g. The extreme sensitivity error coefficient was 4.8% for the eleven flight tests analyzed. The average sensitivity error was 1.4%.

Behr[11 21] developed a strain gauge load sensor to measure individual parachute loads in a clustered parachute system. The load sensor consists of a clevis, a spool, and an instrumented clevis pin. This small load sensor can be inserted in the main nylon or Kevlar load bridle to measure transient and steady-state loads of individual parachutes. For flight tests, data can be acquired and telemetered to a ground station, or an onboard data acquisition and storage system can be used.

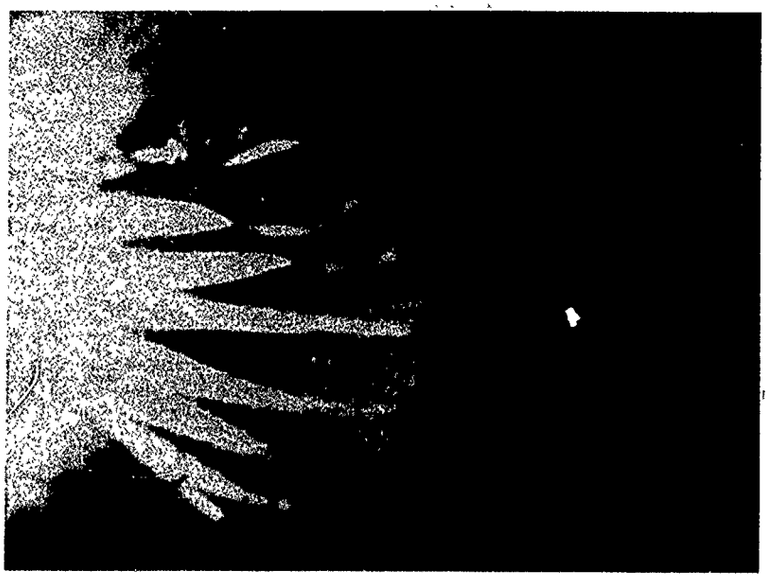


Figure 11.16. Inflation of a 5-ft-diameter Kevlar parachute at supersonic speeds, photographed with an onboard camera

Ryerson and Hauser[11 22] developed a small onboard data acquisition system that has been used for more than 50 flight tests at Sandia. This Stored Data Acquisition System (SDACS) is microprocessor-controlled. The system takes data from up to eight analog gauge inputs and converts these analog signals to digital data. The digital data are then stored in a memory for readout after the test. The maximum sampling rate per channel is 1600 samples per second for this solid-state device; memory size is 32,768 eight-bit samples. The typical battery life is one week. The microprocessor controller allows the system's operation to be changed without changing any hardware. The SDACS is simple, flexible, and inexpensive.

References

11.1 D. W. Johnson, "Test Procedures, Sensors and Facilities," University of Minnesota/Carl-Crantz-Gesellschaft Systems Technology Course, Wessling, West Germany, June 1987.

11.2 *Technical Manual—Tonopah Test Range Capabilities,* SAND81-1871, Sandia National Laboratories, June 1985.

11.3 *Major Test Facilities of the Naval Weapons Center,* NWC Technical Publication 5564, China Lake, California, April 1974.

11.4 *AFFTC Users' Handbook,* Air Force Flight Test Center, Edwards Air Force Base, California, June 1973.

11.5 *Test Capabilities—Yuma Proving Ground,* Department of the Army, Yuma, Arizona, June 1970.

11.6 *White Sands Missile Range Users' Handbook,* Vols. 1 and 2, U.S. Army, White Sands Missile Range, New Mexico, October 1980.

11.7 *ADTC Technical Facilities,* Vol. I - Range Instrumentation Systems and Technical Support Facilities (June 1972) and Vol. II - Land Test Areas (August 1971), Armament Development and Test Center, Eglin Air Force Base, Florida.

11.8 *Major Range and Test Facility Base—Summary of Capabilities,* Department of Defense, Under Secretary of Defense for Research and Engineering, DoD 3200.11-D, June 1983.

11.9 H. R. Spahr, "Store Separation of Nuclear Weapons," Society of Automotive Engineers, Inc., SAE Paper 871796, October 1987.

11.10 L. H. Schindel, "Store Separation," Advisory Group for Aerospace Research and Development, AGARDograph No. 202, June 1975.

11.11 M. T. Kane and B. L. Barth, *Final Design of Sandia's Supersonic Test Vehicle,* Sandia Corporation, SC-4449(RR), September 1960.

11.12 B. A. Engstrom, *Performance of Trailing Aerodynamic Decelerators at High Dynamic Pressures, Phases V and VI,* USAF WADC TR 58-284, February 1962.

11.13 L. R. Rollstin, "A Rocket System for Development Testing of a Retardation Parachute for a Supersonic Store," AIAA 86-2558, October 1986.

11.14 C. J. Pirrello, M. V. Hardin and M. V. Heckart, *An Inventory of Aeronautical Ground Research Facilities, Vol. III - Structural and Environmental Facilities,* NASA CR-1876, November 1971.

11.15 L. Paulsen, "Whirltower Test Facility," AIAA 89-0941, April 1989.

11.16 X. Lin, "The Gun-Launched Test for a Supersonic Parachute," AIAA 86-2474, October 1986.

11.17 P. R. Downs and R. P. Bartlett, "A Ground-Based Air-Operated Launcher for Parachute Testing," AIAA 89-0939-CP, April 1989.

11.18 J. R. Downing and B. A. Engstrom, "Parachute Test Vehicles and Methods," Sonderdruck aus dem Jahrbuch 1959 der WGL.

11.19 R. D. Samuels and R. H. Fournier, *Static Longitudinal Aerodynamic Characteristics of a Proposed Decelerator Test Vehicle,* NASA TN D-3862, February 1967.

11.20 P. D. Hanlon and C. J. Poole, "Flight Qualification Testing of a 2600 lb and a 3400 lb Capacity, Sounding Rocket Payload Recovery System," presented at the AIAA 10th Aerodynamic Decelerator Systems Technology Conference, April 1989.

11.21 V. L. Behr, "Measurements of Individual Parachute Loads in a Clustered Parachute System," AIAA 89-0923, April 1989.

11.22 D. E. Ryerson and G. C. Hauser, "Small Parachute Flight Data Acquisition System," AIAA 89-0924, April 1989.

CHAPTER 12

PARACHUTE DESIGN EXAMPLES

12.1 Background

Previous chapters of this AGARDograph have described the large number of options in parachute type and rigging parameters available to the parachute designer. Facing the designer are an equally large number of design, performance, and logistic requirements that somehow must be accommodated in the final parachute design. Typical design requirements for high-performance parachute systems include, but are not limited to, the parachute/payload shape, weight, and inertial characteristics; the time, fall distance, or range allotted for deceleration to a prescribed velocity; the allowable maximum or minimum decelerations to be generated by the parachute and imposed on the payload; and the maximum unit cost of the parachute in production. In combination, some of these requirements can be in conflict, requiring that trade-offs be proposed and evaluated during the design process. The design process itself contains many options, such as knowing which analysis tools to use, when to use them, where the applicable test data reside, and when to "declare ignorance" and generate new technical insight, analysis tools, or data.

The purpose of this chapter is to provide examples of how designers have struggled with this plethora of options and choices en route to designing a successful parachute system. Obviously, no two design problems are alike, but previous examples may be useful in giving the designer a better feel for how to use the technology base described throughout this AGARDograph. After discussing the issue of how design requirements affect parachute system cost, examples of the processes used for parachute design, taken from the literature, will be discussed in detail.

12.2 Cost trade-offs in parachute system design

A primary design consideration should be the cradle-to-grave costs of a parachute system. These costs are influenced by such factors as total quantities produced, desired service life, maintenance costs (including inspection and refurbishment), high-dynamic-pressure deployment performance requirements, reliability requirements, allowable weight and volume, deceleration performance requirements, deployment method, carrier aircraft or other aerospace carrier, cost of parachute system relative to the payload, fabrication and packing costs of the deployment bag and canopy, and test and storage environments.

The total quantities to be produced can influence the ratio of money and time spent on design versus fabrication. For instance, if the intent were to produce 100,000 or even 10,000 units, it would be cost-effective to spend money and time initially in designing for ease of fabrication and packing (with appropriate jigs and fixtures, for example) in order to minimize the unit production costs. Conversely, if only a few prototypes were fabricated for feasibility full-scale flight tests, the unit production costs could be much higher (the parachute prototypes could be handcrafted, for instance) so as to minimize the overall program costs.

The length of the intended service life can influence the cost of a parachute design. In designing a parachute for a 20-year service life, one must pay careful attention to the selection of materials and how their strength degradation and other properties would be affected by time and type of storage. Degradation of materials is discussed in Section 8.4. Usually, a parachute designed for a 20-year service life will cost more per production unit than one designed for a 1-year service life. Some parachute systems have a limited service life due to materials degradation in the parachute or degradation of chemical components, such as the explosive train of the pyrotechnic reefing line cutters. If the payload system is designed for a 20-year service life, then it may be necessary to disassemble the payload, remove the parachute system, inspect it, rework it, and reassemble it in the payload. This may require shipping the payload back to its refurbishment base. The costs of shipping, disassembly, refurbishment, reassembly, etc., should all be considered in the original design of the parachute system.

Deployment of high-performance parachutes for high-dynamic-pressure deployment can greatly influence the cost of the deployment system, the deployment bag, and the canopy. The asymmetric airflow around an aircraft flying at transonic or supersonic speeds can cause excessive store motion, which may induce line sail during deployment of the parachute. Line sail is also caused by insufficient pilot parachute drag, which is in part due to nonuniform inflation of the pilot parachute in this asymmetric/nonsteady flow field. The design of deployment bags (Section 9.3) with the right

combination of line ties, canopy ties, etc., needed to perform properly in this adversarial environment can increase the bag fabrication costs and, in particular, the packing procedures and the resulting packing costs. For example, a Teflon liner may be a necessary design feature of the deployment bag to prevent burning of the canopy and suspension lines during high-speed deployments when bag strip velocities may reach several hundred feet per second. The use of Kevlar instead of nylon can increase significantly the cost of the parachute, but that may be the only way to meet the deceleration requirements with limited parachute system weight and volume. Kevlar drives up the cost, but sometimes it is necessary to use Kevlar in order to meet the overall system requirements. In addition, the structural safety factors used in the design and the allowable weight and volume of the parachute pack may drive the design and increase its cost.

Reliability requirements may also increase the cost of a parachute system. Section 10.2.3 addresses the reliability issue. Table 10.3 shows that 145 successful flight tests are required to demonstrate a parachute system reliability of 0.995 with a 50% confidence level. Decreasing the required reliability to 0.95 greatly reduces the number of flight tests (only 14 required) and the expense. This reduced expense is especially true if high-performance fighter or bomber aircraft are used for the flight tests. Another trade-off in the cost of a parachute system design is the safety factor of ribbons and suspension lines versus reliability. The factor of safety, of course, depends on the accuracy in predicting the transient pressure distribution around the canopy during inflation (Chapter 5) and the corresponding stresses from the CALA or CANO codes (Chapter 6). Figure 6.3 illustrates the typical design margins used by Sandia for high-performance parachutes; the ratio of maximum load to rated strength of a textile member is 0.46 or below.

Another cost trade-off to consider is the cost of the parachute system relative to the payload. This is particularly true of man-rated systems, but it applies to inanimate payloads as well. A good example is the NASA Space Shuttle SRB recovery system. Tallentire[12.1] reports that successful recovery of the two solid rocket boosters, for subsequent refurbishment, results in a net saving of about $39M per mission, compared to the cost of expendable boosters. Since the unit cost of the SRB parachute recovery system is about $250,000, the cost leverage or advantage of recovering the SRB is very high. Hence, it was cost-effective to commit considerable monies up-front for the analytical design, wind tunnel testing, subscale flight testing, jigs and fixtures for fabrication and packing, and stringent quality control measures to obtain the most reliable recovery system possible. An intangible advantage of SRB recovery (which might be cost-effective) is the posttest inspection of the recovered booster case in order to study the effects of motor burn, vibration, aeroheating, dynamic loading, etc., on the booster case. Successive posttest inspections might reveal unsuspected design flaws that could be corrected before the SRB is tested again.

Johnson[3 51] developed inexpensive 8-ft-diameter parachute systems to recover 12-in.-diameter, 275-lb rocket payloads at sea for scientific experiments for Los Alamos National Laboratory and Lawrence Livermore National Laboratory. The total recovery costs for each payload, which included the leasing cost of the recovery ship or helicopter, was about $3000. Some of these payloads, which cost up to $250,000 each, were recovered several times (as many as eight) for refurbishment and reuse; this is another example of cost leverage and points to the importance of having a reliable recovery system. In addition, some of the scientific data were recorded onboard (x-ray detectors, for example) and not telemetered; therefore, payload recovery was very essential.

12.3 Design of a staged parachute system for low-altitude payload delivery

Behr[9.13] designed and tested a parachute system for the High-Speed Airdrop Container (HISAC) to be used by the U.S. Army to replace its current standard high-speed aerial delivery container, the CTU-2/A. The HISAC parachute system requirements (see Cyrus and Thibault[12.2]) were that it decelerate an 825-lb payload delivered from an aircraft at 300 ft above ground level (200 ft was desired) at velocities as low as 300 knots indicated airspeed (KIAS) and as high as Mach 0.95 (~630 KIAS at sea level). The container was required to impact the ground at less than 40 ft/s and strike within 20 degrees of vertical. Container longitudinal decelerations could not exceed 30 g. The weight limitation of the parachute system was ~80 lb; there were no rigid specifications on the allowable parachute volume. The primary aircraft carriers used would be the F-16 A/B/C/D and the F-111 D/E/F.

The preliminary parachute system design was done by Nellums.[12.3] Selection of the type of canopy for a particular application depends on such factors as cost, deployment dynamic pressure, store mass, allowable recovery system weight and volume, drag coefficient, required system stability, parachute size, and deceleration performance specifications. The general application of these high-performance parachutes, as well as the range of drag coefficients and the average angle of oscillation, is given in Table 3.1. Nellums considered three types of systems: a single main parachute, a cluster of three main parachutes, and a lifting parachute. All have advantages and disadvantages. The advantage of a single

main parachute is its simplicity; its disadvantage is the large moment of inertia about the pitch axis and, hence, poor rotation or turnover characteristics. The advantages of a cluster of main parachutes are improved reliability and a lower moment of inertia about the pitch axis—hence, improved turnover characteristics. The disadvantages are the added complexities of rigging and their higher costs. The advantage of a lifting parachute is its ability to trade velocity for altitude, thus yielding the lowest possible release altitude. Its disadvantage is the added complexity and weight of a vehicle roll-control system to maintain the orientation of the lifting parachute, thereby making the entire system the most costly of the three types considered. The desire to minimize the unit costs of the HISAC eliminated from consideration the lifting parachute. A preliminary study suggested that a clustered main system would best meet the HISAC design requirements.

Nellums[12 3] used the INFLAT code developed by Wolf[6.28] and McVey and Wolf[6.10] for the preliminary design. Nellums presents calculations for a 4.6-ft-diameter ribbon drogue parachute, which acts for 0.55 s and then deploys a cluster of three 21-ft-diameter ribbon parachutes (each with two reefing stages: a 6-ft-long reefing line that acts for 0.63 s followed by a 12.5-ft-long reefing line that acts for 0.32 s). His computer calculations assumed an aircraft release velocity of 1116 ft/s at an altitude of 300 ft with a vertical velocity of 16 ft/s. He plots deceleration, trajectory angle, velocity, angle-of-attack, and range versus altitude for this calculation. The results showed that, at 175 ft below the aircraft, the HISAC store velocity was 40 ft/s, the trajectory angle about 80 degrees, and the angle of attack about 10 degrees. These INFLAT calculations, however, were used only as general guidelines for the HISAC parachute system design because the approximations of the INFLAT model, especially when applied to a cluster of parachutes, limit the expected accuracy of the predicted peak inflation loads and angle of attack during turnover. However, these INFLAT calculations for the HISAC system showed that the weight of the parachute system would exceed the maximum 80-lb weight limitation of the design. This unacceptable weight and the desire to minimize costs led to a review of existing parachute systems in search of an on-the-shelf main parachute that would be feasible for HISAC application.

At this stage in the design process it was decided that flight testing, using a full-scale HISAC test vehicle and an A-7 aircraft, would be required to prove out these very stringent design requirements of impact velocity and impact angle for a very low altitude release. Thus, three parachute systems were flight-tested and their test results compared with the design requirements. Three parachute systems were proposed as alternatives to Nellums' original design. All three systems employed a reefed and staged ribbon drogue parachute that, in turn, deployed the main parachute(s). The main parachutes were either (1) a cluster of two reefed, 22-ft-diameter ringslot cargo extraction parachutes; (2) a single reefed, 35-ft-diameter high-strength T-10 personnel parachute; or (3) a cluster of three standard 35-ft-diameter T-10 personnel parachutes. The results of the flight tests showed that the store impact velocities for the two ringslot parachutes exceeded the 40-ft/s requirement. The store impact velocity for the single high-strength T-10 main parachute met the requirement of 40 ft/s. However, the vertical fall distance of the HISAC store to a 70-degree impact angle slightly exceeded the 300-ft requirement. Thus, the performance of the high-strength T-10 system was very marginal. The cluster of standard 35-ft-diameter T-10 parachutes produced results well within the specified requirements. Moreover, the main parachutes were not reefed, which minimized the complexity of the system. Based on these flight test results, the decision was made to use the cluster of three T-10 parachutes as the baseline design.

The parachute system consisted of the tail plate, the drogue parachute and bag, the staging system, the main parachutes and bag, and various bridles. The tail plate initiates the deployment by pulling the drogue parachute and bag out of the vehicle. This base plate is discussed in Section 9.2.4. The drogue parachute, which was designed specifically for the HISAC program, was required to decelerate the vehicle from a maximum dynamic pressure of 1330 lb/ft^2 down to a safe deployment dynamic pressure for the T-10 main parachutes of ~200 lb/ft^2. An 8.5-ft-diameter, 20-degree conical nylon ribbon parachute was designed to meet these requirements. The parachute is constructed of nineteen 2-in.-wide ribbons, with 0.625-in. gaps between ribbons, yielding an overall porosity of 19%. It contains 16 gores and is made with 1-in.-wide, 4000-lb suspension lines. The parachute is initially reefed with a 112-in. reefing line yielding a reefed diameter of ~3 ft; this results in a drag area of ~14 ft^2. The reefed parachute, if deployed at the maximum dynamic pressure, would produce a maximum drag (opening-shock force) of ~18,600 lb or a peak deceleration of ~22 g, well within the 30 g design limit. Two pencil reefing line cutters installed at the skirt of the parachute are actuated mechanically upon parachute line stretch. A pyrotechnic delay (0.8 s) allows the drogue parachute to operate initially in the reefed state. After the delay, the reefing line is severed and the parachute is allowed to inflate. Details of the drogue parachute, the staging system, and the main parachute system are given by Behr.[9.13]

12.4 Design of a 24-ft-diameter Kevlar/nylon ribbon parachute

This parachute was intended as a replacement for a 17-ft-diameter conical ribbon nylon parachute. The design goal was to double the drag area of the 17-ft parachute. However, the new parachute system could not exceed the packed weight and volume of the 17-ft-diameter nylon parachute. The parachute designer was provided with the following design requirements:

1. The store weighs 760 lb, is 142 in. long, and has a maximum diameter of 13.3 in. Space available in the aft end of the store for the parachute is a cylinder 9.1 in. in diameter and 51 in. long with an additional conical extension tapering to 5 in. in diameter in a 5-in. length. The telescoping-tube deployment system, which is concentric to this cylindrical envelope, is 2.4 in. in diameter and 56 in. long. Net space available for the parachute bag is 2.1 ft^3, and the allowable parachute weight is 90 lb.
2. The store is released at aircraft velocities of 330 to 800 KCAS, at altitudes as low as 50 ft above flat terrain or as low as 100 ft above irregular terrain from sea level to 10,000 ft altitude. To avoid damage to the aircraft, the parachute is deployed 0.3, 0.6, or 1.5 s after release, depending on the type of carrier aircraft. The objective of the parachute design is to minimize impact velocities. The maximum ejection velocity (vertically downward) is 16 ft/s.
3. The maximum angular oscillation of the parachute must be <5 degrees.
4. The time to line stretch after parachute deployment must be <0.2 s.
5. The requirement for trajectory repeatability is that the standard deviation of the variation in parachute opening time and drag on the range dispersion should not exceed 75 ft.
6. The design peak load on the store should not exceed 120,000 lb with the parachute at a 10-degree angle of attack.
7. The parachute must function properly after being completely soaked at temperatures ranging from $-65°F$ to $+220°F$.
8. The parachute will be protected from free moisture, jet fuels, lubricants, and hydraulic fluid but not from their fumes, or from humidity or ozone.
9. The parachute system's storage/service life must be 25 years.

12.4.1 The deployment system

A telescoping tube, mounted along the centerline of the parachute pack and powered by a gas generator (Figure 12.1), is used to eject the parachute pack aft from the vehicle at a relative velocity of about 165 ft/s. The gas generator can be fired at 0.30, 0.60, and 1.5 s after aircraft release. This deployment system is described in Section 9.2.4. The tail can and deployment bag are permanently attached to the vent region of the parachute by four 9000-lb nylon straps to prevent them from colliding with the canopy as it inflates and the system rapidly decelerates. The high strength and number of these straps is indicative of the extreme difficulty of controlling deployment hardware and bag at high bag strip velocities.

12.4.2 Main parachute and deployment bag design

In order to double the 17-ft parachute's drag area without increasing the weight, it was necessary to use Kevlar 29 in this parachute. This synthetic material, produced by DuPont, has a fiber tensile strength $>400{,}000$ lb/ft^2, compared to 100,000 lb/ft^2 for nylon. Kevlar is described in Section 8.2. Higher opening-shock loads were anticipated from the use of Kevlar in this parachute because of its low ultimate elongation ($\sim 5\%$ for Kevlar vs. 25% for nylon). Pepper[87,88] conducted exploratory free-flight deployment tests of a 12.5-ft-diameter Kevlar conical ribbon parachute and demonstrated that parachute weight and volume could be reduced by 50% by using Kevlar in place of nylon. He designed a 24-ft-diameter hybrid (Kevlar and nylon) parachute to decelerate this 760-lb store.

This 20-degree conical ribbon parachute has 24 gores and suspension lines. The gore construction is shown in Figure 12.2. The parachute is made of fifty-four 2-in.-wide continuous horizontal ribbons and seven vertical ribbons per gore. The vertical ribbons are made of double 1/2-in.-wide, 550-lb Kevlar tape. The top 21 horizontal ribbons (ribbon 1 is the vent band) are made of 2-in.-wide, 3000-lb reinforced-selvage nylon. Nylon was used because the differential circumference between the upper and lower edges of each continuous ribbon could cause stress concentration and failure of the low-elongation Kevlar. Smaller-width 1-in. Kevlar ribbons could have been used, as was done by Pepper,[8.7,8.8] but the savings in both weight and volume would have been small because of the short length of the top ribbons. Nylon was a more conservative and forgiving approach—recall that this was one of the earliest uses of Kevlar in a high-performance parachute system. Ribbons 22 through 31 were made of 2-in.-wide, 2000-lb Kevlar. To add gradual fullness, ribbon 22 was made 4 percent longer than normal; this fullness was graduated linearly to zero at ribbon 29. The fullness was added to prevent stress concentration in ribbon 21 (3000-lb nylon) and ribbon 22 (2000-lb Kevlar). Ribbons 32 through 54 (skirt band) were 2-in.-wide, 1000-lb Kevlar. The vent band was made of 1-3/4-in.-wide, 10,000-lb nylon and the skirt band was made of 1-3/4-in.-wide, 15,000-lb Kevlar. The suspension lines were made of 1-3/8-in.-wide, 13,500-lb Kevlar. The lines were constructed over the canopy with the figure-eight construction (one splice for four suspension lines); the lines were 28 ft long from suspension line lug loop to skirt band.

A major contribution to the stress analysis of high-performance parachutes was made by a group at Northrop Corporation (Mullins et al.[3.39]) in the early 1970s during the design of the Apollo parachute system. This code, termed CANO, has been modified by several groups (see Section 6.2), and has been used extensively by Sandia and other organizations for about the last 15 years for the stress analysis design of high-performance parachutes. However, the CANO structural analysis code was made operational on Sandia computers *after* this 24-ft hybrid parachute was designed by Pepper in late 1975. Pepper drew on his long parachute design experience to select the graduation of ribbon strength (from 3000 to 1000 lb) from vent to skirt. CANO code calculations in 1977 validated his selection of ribbon strengths, and by this time flight tests had also validated his design.

The fabric portion of the parachute and bag, which weighed 90 lb, was packed to a high density of 43 lb/ft^3 in a pack volume of 2.1 ft^3. A photograph of the parachute pack is shown in Figure 9.15. The deployment bag design and construction are discussed in Section 9.3.3. The time sequence for deploying this 24-ft-diameter parachute is given in Table 5.1, along with the breaking strength of the line and canopy ties. These design features came from the knowledge base of Pepper and the experienced technicians in Sandia's Parachute Laboratory.

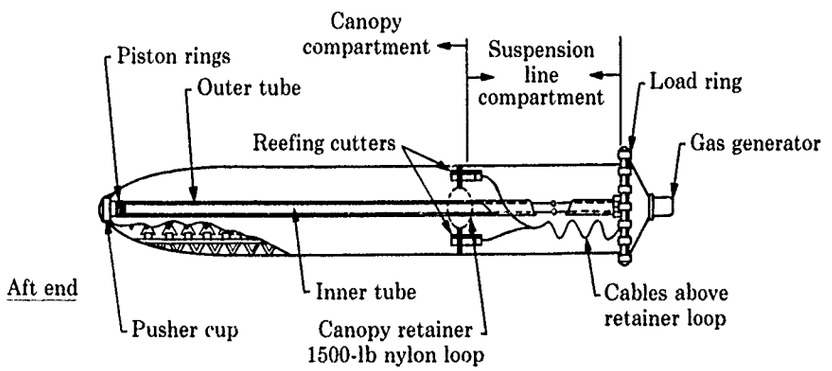


Figure 12.1. Sketch of 24-ft-diameter parachute pack and deployment system

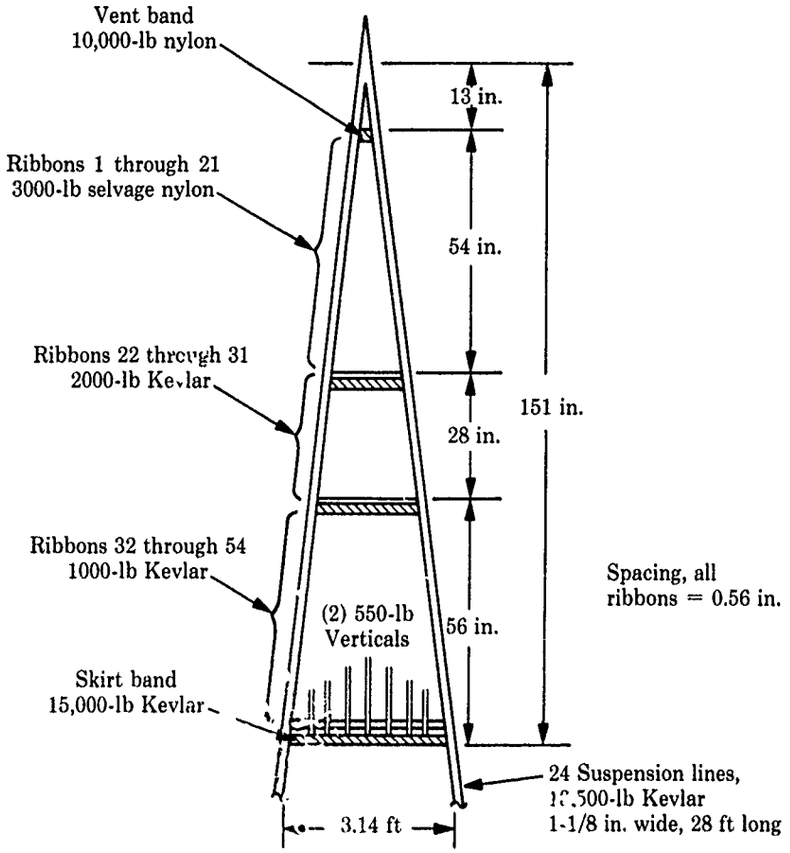


Figure 12.2. Gore design for 24-ft-diameter ribbon parachute

12.4.3 Flight test verification

Pepper[1.1] used the Sandia Rocket Sled Track (see Section 11.3.3) for the initial free-flight testing of this 24-ft-diameter Kevlar/nylon parachute at deployment speeds of 610 to 1500 ft/s. A photograph of the store impacting a concrete target at the sled track is shown in Figure 11.12. Better photographic coverage could be obtained from the sled track tests because of its more carefully controlled test conditions.

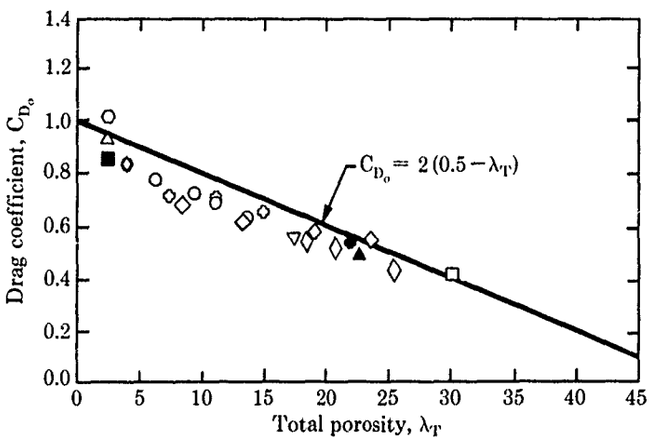
Knacke[1.8] developed a useful correlation of drag coefficient versus porosity for a number of parachute types. This correlation is presented in Figure 12.3. However, Pepper used flight tests to investigate the differences in parachute performance caused by the effects of geometric porosity. Canopy porosities of 26.5%, 20%, and 18% were investigated in the initial flight tests by varying the number of horizontal ribbons (50, 54, and 56, respectively) in the 24-ft canopy. Very little was known in 1976 about the effects of porosity on the filling time and opening shock of a Kevlar/nylon hybrid canopy. Sled test results suggested that the filling time was too long with the 50-ribbon design, and that the peak loads were too high with the low-porosity, 56-ribbon design. Hence, the 54-ribbon (20% porosity) canopy was selected as the baseline design early in the development program.

Seventy flight tests[1.1] (28 sled tests, 31 aircraft drop tests, and 11 rocket-boosted overtests) were conducted to verify the parachute design. These low-altitude tests were conducted at parachute deployment speeds of 580 to 1800 ft/s and at dynamic pressures of 330 to 2800 lb/ft^2. Figure 12.4 is a photograph of the parachute and the attached deployment bag after a sled test. The repeatability of the deployment time (from gas generator fire to suspension line stretch) as a function of dynamic

pressure at gas generator fire is shown in Figure 12.5. The mean time of ~0.23 s is relatively constant as a function of dynamic pressure, as would be expected for a positive pack-ejection-type deployment system. The canopy filling time from suspension line stretch to full-open as a function of dynamic pressure at gas generator fire is shown in Figure 5.12b. The filling times vary from ~0.2 s to ~0.9 s, with the mean ~0.35 s to 0.4 s. Equation 5.33 (from Knacke[1.8]) predicts a decrease in filling time from ~0.6 s to ~0.2 s as the deployment velocity increases from 600 to 1800 ft/s. However, the scatter of the filling time data precludes any definitive statement about the decrease of filling time with an increase in dynamic pressure. Similarly, the filling time data in Figures 5.12a, c, and d do not definitely prove that filling time decreases with increasing dynamic pressure. Perhaps the canopy's effective porosity increases with deployment dynamic pressure (due to cambering of the horizontal ribbons, which increases the porosity and the mass outflow) such that the canopy filling time is essentially constant.

The maximum deceleration drag loads on the store during parachute opening for rocket-boosted, sled, and aircraft drop tests are plotted in Figure 12.6 as a function of the dynamic pressure at gas generator fire. These measured deceleration loads compare fairly well with Knacke's[1.8] empirical method (Eq. 5.31), where the opening-shock factor is given in Figure 5.11 as a function of store weight divided by $C_D S$. Figure 12.7 compares the measured velocity decrease of the store with altitude decrease (fall distance) with trajectory calculations for both point mass and two-body 6-DOF calculations for a typical aircraft drop test. Measured wind data from towers and radar-tracked balloons (see Section 11.2.3) were used to back out the no-wind measured trajectory shown in Figure 12.7. The no-wind data agree fairly well with the two-body 6-DOF trajectory calculations. A photograph of the parachute full-open (taken with an onboard Photosonic camera—see Section 11.5.2) during a rocket-boosted test is shown in Figure 12.8.

The 70 development flight tests verified the adequacy of the parachute design, and the system was placed into production. Many subsequent flight tests verified that the design meets the design requirements.



Parachute configurations

- ○ Solid circular (11.9 ft dia)
- ● 10-deg Conical (100 ft dia)
- ○ Ringsail (88 ft dia)
- ◇ Flat ribbon (8.7 ft dia)
- ▽ 30-deg Conical ribbon (4.5 ft dia)
- ◊ 20-deg Conical ribbon (8.4 ft dia)
- ▲ Flat ribbon (10.5 ft dia)
- □ 30-deg Conical ribbon (6.9 ft dia)
- ◇ Ringslot (11.9 ft dia)
- △ 30-deg Conical ribbon (11.9 ft dia)
- ■ 1/4 Sphere (11.9 ft dia)
- ◇ 14.3% Full extended skirt (67.3 ft dia)
- ◆ 25-deg Conical ribbon (16.5 ft dia, Apollo ELS)

Figure 12.3. Effect of canopy porosity on drag coefficient for various parachutes (taken from Ref. 1.8)

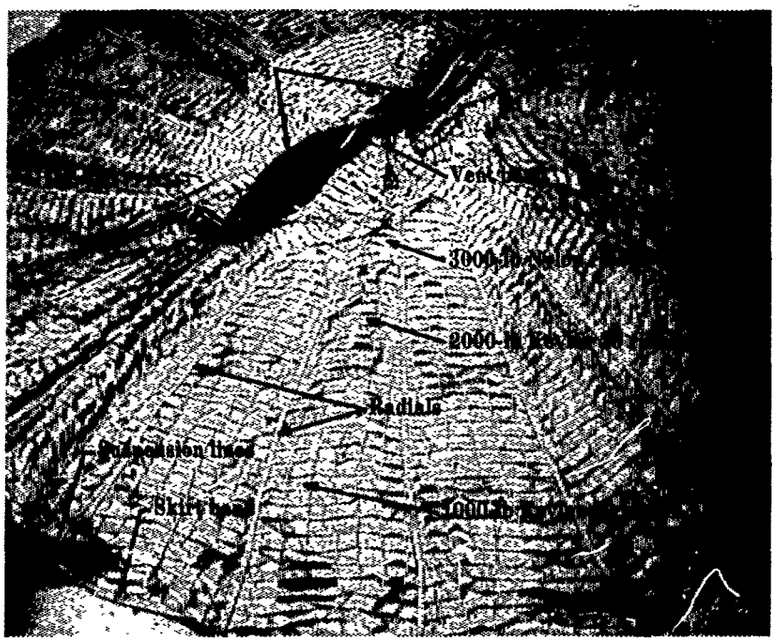


Figure 12.4. Recovered 24-ft-diameter parachute, after sled test

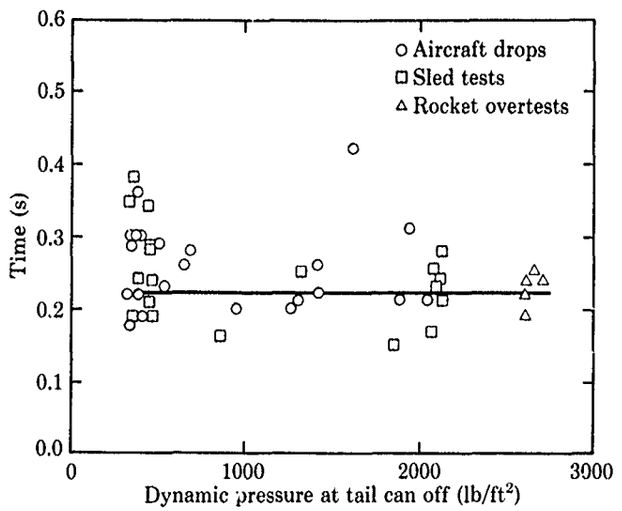


Figure 12.5. Effect of dynamic pressure on deployment time (from tail can off to line stretch)

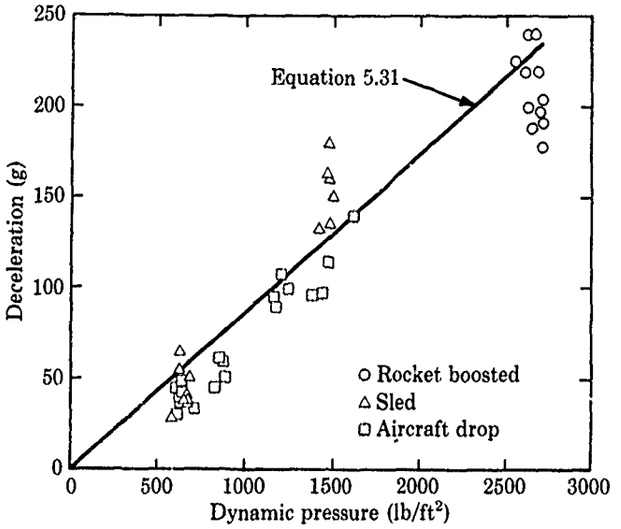


Figure 12.6. Opening-shock deceleration loads of 24-ft-diameter ribbon parachute

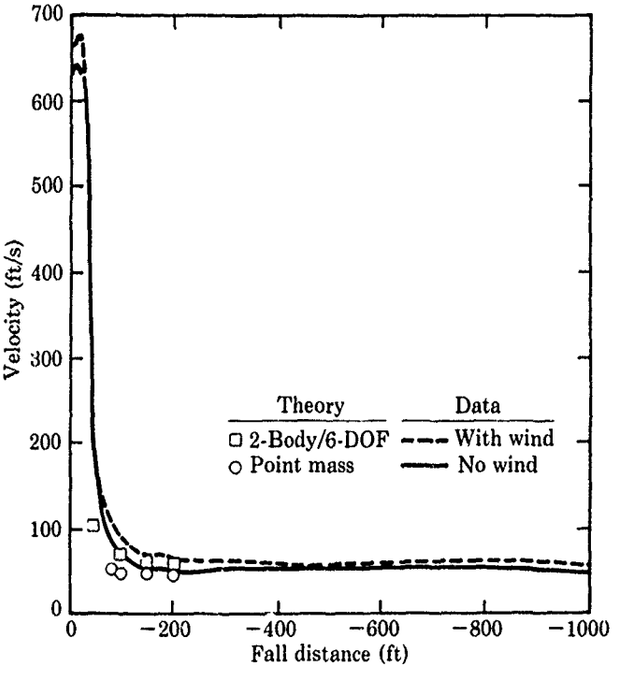


Figure 12.7. Variation of velocity with fall distance for full-open, 24-ft-diameter parachute



Figure 12.8. Photograph of a parachute taken by an onboard camera during rocket-boosted overtest

12.5 Design of a high-performance 46.3-ft-diameter Kevlar/nylon parachute

The parachute designer was furnished with these design requirements:

1. The store is 144 in. long, 18 in. in diameter, and weighs 2465 lb; it must be compatible with B-52, FB-111, and B-1 aircraft. Allowable volume in the aft section of the store for the parachute is a 16.8-in.-diameter, 45-in.-long (5.7 ft^3) cylinder.
2. The release conditions depend upon the delivery aircraft. Delivery velocity ranged from 300 KCAS to 800 KCAS (relaxed from 800 to 660 KCAS late in the development program) and release altitude could be as low as 150 ft above ground level. Parachute deployment delay times ranged from 0.4 s to 0.8 s.
3. Ground impact altitudes may vary from sea level to 10,000 ft, and the target types may vary from hard flat to hard irregular.
4. The specified impact velocity is 65 ft/s or less at mean sea level (MSL) and 70 ft/s at 5000 ft MSL.
5. The parachute system service life must be 20 years with no retrofits or repacks.
6. The maximum allowable axial deceleration load on the store during parachute inflation must not exceed 100 g.

12.5.1 The deployment system

The 46.3-ft-diameter nylon/Kelvar ribbon main parachute is deployed by a cluster of three 3.8-ft-diameter ribbon pilot parachutes deployed by an explosively ejected vehicle base plate. These pilot parachutes are packed in a bag attached to the base of the main parachute bag (see photograph of main parachute pack in Figure 9.17 and pilot parachute bag in Figure 9.18). Initially in the development program, a 5-ft-diameter ribbon pilot parachute was used, as discussed in Section 9.2.2. However, on a supersonic delivery flight test, the 5-ft-diameter parachute collapsed shortly after initial inflation, causing severe line sail (as shown in Figure 5.3) and main canopy damage. A line sail code developed by Purvis[5.2,5.3] was used to redesign the pilot parachute system, also described in Section 9.2.2. The line sail numerical simulation is compared with the flight test data in Figure 5.3. The design of the 3.8-ft-diameter conical ribbon parachute is described in Section 9.2.2.

The INFLAT parachute inflation code[5.10,5.28] was used to help predict the performance and deceleration load of the pilot parachute cluster. INFLAT approximates the parachute canopy as two mass nodes connected elastically to each other and to the payload. Tension forces in all elastic members, fluid inertia forces, aerodynamic forces (obtained empirically from scale-model subsonic wind tunnel tests), and gravitational forces are summed at each node to determine total inflation loads, inflation rates, and system trajectory parameters during inflation. The limitations of the INFLAT code for design use are outlined in Section 5.3.2.3.

A detailed stress analysis of the pilot parachute was performed using the CANO computer model (Ref. 3.39) in conjunction with experimental canopy pressure distributions. CANO models the continuous ribbons, radials, vent reinforcement, and skirt reinforcement as finite membrane elements. The maximum inflation loads calculated with INFLAT were used with CANO to calculate the quasi-steady loads (not flutter loads) in each ribbon and radial element. CANO also predicts the inflated shape of the canopy for the given pressure distribution and axial load.

Wind tunnel tests were used to measure the drag cluster efficiency factor for unreefed ribbon parachutes (Figure 4.29) as a function of number of parachutes in the cluster and the riser length. Figure 4.25 plots the drag cluster efficiency factor for reefed ribbon parachutes, as determined from subsonic wind tunnel tests. These data helped the designer size the pilot parachutes used in this system.

The pilot parachute cluster minimizes the losses in parachute drag due to the payload wake effects, especially shortly after release, when the payload is flying at supersonic speeds in the flow field surrounding the delivery aircraft and at a large angle of attack at the time of parachute deployment. Methods for estimating the drag loss due to forebody effects are discussed in Section 4.2.6. Figure 9.4 compares cross sections of payload wake with those of the inflated 5-ft-diameter single pilot parachute and the cluster. The payload wake usually flows directly into a single canopy, but it can flow between the canopies of a cluster. Even if the wake causes one of the parachutes to collapse, the other parachutes in the cluster can continue to deploy the main parachute. For these same reasons, a cluster of parachutes may be preferable to a single parachute for use in the severe aircraft-induced flow field, where parachute deployment usually takes place. The parachutes in the cluster are tied to each other

at the skirt by 9-in.-long nylon tether lines to prevent the parachutes from flying at an excessive angle of attack.

A series of photographs illustrating an orderly deployment of the 46.3-ft- diameter parachute using the cluster is shown in Figure 5.2. Johnson and Peterson[3.6] report that the cluster of three 3.8-ft-diameter pilot parachutes eliminated line sail problems at all aircraft release velocities except at 800 KCAS. At this highest velocity, the pilot parachute cluster experienced a reduction in drag caused by the shock waves emanating from the aircraft and the wake generated by the payload flying at angles of attack approaching 25 degrees; the pilot parachutes would not stay fully inflated in this severe environment. In the absence of the aircraft shock waves and payload angle-of-attack effects, however, the cluster provided high drag and no line sail (as has been observed in seven sled and rocket tests at deployment velocities between 800 and 860 KCAS). Bag strip velocities were high (400 to 450 ft/s for deployment velocities of 660 KCAS), but were necessary to obtain orderly deployments at the low 300 KCAS release condition. These high bag strip velocities occasionally caused the two suspension lines carrying the reefing line cutters to fail. However, these two failed suspension lines do not create a parachute reliability problem or cause an appreciable loss in parachute performance. No damage to the pilot parachutes occurred on any of the tests.

12.5.2 Design and flight testing of first prototype (40-ft-dia) main parachute

The INFLAT[5 10,5.28] parachute inflation code was used to help predict the performance of the main parachute. The original design was a 40-ft-diameter conical ribbon parachute with 60 gores and continuous ribbon and all-radial construction (see Johnson[3.5] and Figure 3.2). The CANO[3.39] structural analysis code, in conjunction with wind-tunnel-measured canopy pressure distributions, was used to determine the canopy stresses and materials.

The 40-ft parachute had to be reefed to control inflation loads at the maximum deployment speeds. Table 4.1 presents the effect of reefing ratios on the drag and the static stability of several high-performance parachutes as determined from subsonic wind tunnel tests. A correlation by Purvis[4.8] of drag coefficient versus diameter ratio (inflated diameter/constructed diameter) for subsonic speeds for solid and ribbon canopies is presented in Figure 4.2. This is a useful correlation for preliminary designs of reefed parachutes. The inflated diameter depends, of course, on reefing ratio, geometric porosity, and the number of gores. The effect of reefing ratio on the drag area ratio (reefed drag/full-open drag) of conical ribbon parachutes, as determined from wind tunnel and flight test data, shown in Figure 4.27 is an excellent correlation for design purposes. This correlation was formulated as part of the aerodynamic design of the 54-ft-diameter drogue parachute for the SRB recovery system. Knacke[1 8] developed plots of reefing ratio versus drag area ratio for five parachutes, including ribbon, ringslot, and ringsail; these plots are shown in Figure 12.9.

The reefing line selected for the 40-ft parachute was 21 ft long (increased to 23 ft after the first two flight tests). It was cut 0.9 s after parachute deployment. The reefing line length and the disreefing time were selected to produce predicted reefed and disreefed decelerations of 85 g (187,000 lb) at this release condition. The reefed drag area was about 20% of the full-open, terminal descent drag area of 673 ft^2.

Thirteen flight tests (three ejector-sled, two rocket-boosted, and eight aircraft drop tests) were conducted with this 40-ft-diameter parachute. The fourth flight test, PDU-4, was conducted at TTR; the A-7C aircraft released the store at 514 KCAS at 2051 ft above the terrain. The main parachute developed a peak deceleration of 32 g, as predicted, and inflated from canopy stretch to full-open diameter in 0.98 s. No damage to the parachute was observed. Shortly after reaching its full-open diameter, however, the canopy of the main parachute experienced a major collapse (Figure 5.13). Opposite sides of the canopy skirt almost touched, and there was risk that the suspension lines or cut knife lanyards could become entangled. The main parachute recovered from the collapse and eventually reinflated. This wake-induced collapse is discussed in more detail in Section 5.3.3.

A thorough review of the PDU-4 flight test films suggested that the parachute collapse phenomenon is caused by the mass of air behind the parachute canopy. As the 40-ft parachute decelerates the store, it takes the momentum from the store and transfers it to the wake of air behind the canopy. The parachute decelerates the store so rapidly that the energetic wake catches up to the parachute and recontacts it from behind. When this happens, there is a higher pressure acting on the outside of the canopy than inside the canopy, causing the canopy to collapse. A series of flight tests of 26.5-ft-diameter solid-canopy parachutes and 20-ft-diameter ribbon parachutes were conducted at the Sandia Rocket Sled Track to assess this model of collapse. The collapse phenomenon was reproduced in these tests, and the model of collapse was confirmed experimentally by attaching colored streamers to parachute canopies and observing their motion as the wake approached the canopy from behind.

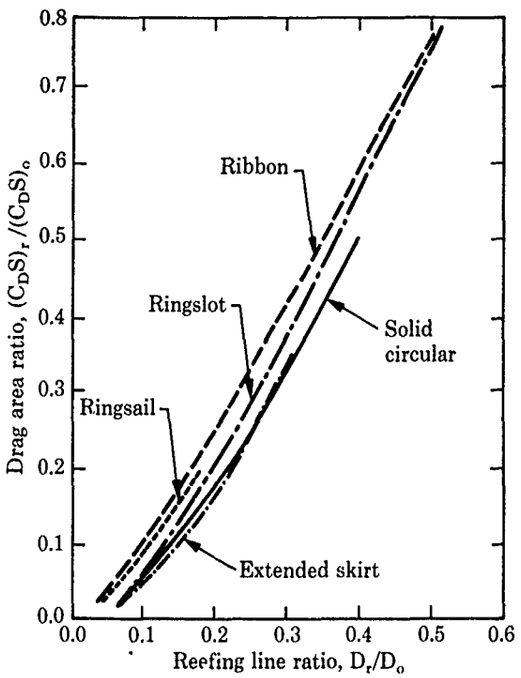


Figure 12.9. Reefing ratio vs. reefing line ratio for various parachutes (taken from Ref. 1.8)

In addition to conducting flight tests to provide insight into the collapse phenomenon, a few flight tests were proposed to evaluate modifications to the 40-ft parachute that could possibly reduce the severity of collapse. It was postulated that wake recontact of the canopy is aggravated by the sudden shedding of vorticity at the skirt as the canopy diameter exceeds the steady-state, full-open diameter at the end of the canopy inflation process. If this is true, then the use of a permanent reefing line to prevent the 40-ft parachute from overinflating could reduce the severity of parachute collapse. The 40-ft parachute was fitted with a 77-ft-long permanent reefing line at the canopy skirt for three flight tests (conducted at deployment dynamic pressures of 295 to 1885 lb/ft^2) to observe the effect of the permanent reefing line on collapse. In each test, the deformation of the canopy due to wake recontact was not as severe as in tests where no permanent reefing line was used. Similar results were obtained at the Sandia Rocket Sled Track when 26.5 ft solid canopies and 20-ft ribbon parachutes were tested with and without permanent reefing lines. However, these tests did not confirm that shedding of vorticity at the canopy skirt was the principal cause of wake recontact and subsequent parachute collapse. It is possible that permanent reefing alleviates parachute collapse because it decreases the drag area of the parachute and allows the parachute to outrun its wake. Although it was apparent that the 40-ft main parachute had to be redesigned to minimize canopy collapse, more flight tests of the baseline 40-ft parachute configuration were conducted to obtain a data base on parachute collapse, inflation characteristics, and the structural integrity over the full range of deployment dynamic pressures.

Of particular interest were the flight tests at Tonopah Test Range to assess the structural integrity of the main parachute and to evaluate the accuracy of the CANO canopy stress prediction code. Two rocket-boosted flights (using Honest John boosters) were conducted to obtain higher deployment dynamic pressures than could be achieved using A-7 delivery aircraft. The deployment dynamic pressure of one rocket-boosted test was 2403 lb/ft^2; this represents a 13% overtest with respect to maximum design dynamic pressure. The 40-ft main parachute developed a peak deceleration load during the reefed stage of 216,000 lb, the highest load for a Sandia-developed parachute system. No parachute damage caused by inflation loads was observed on this flight, which is in agreement with CANO predictions. Parachute deployment damage (which may occur when the canopy skirt exits the deployment bag) was negligible. Damage to the 500-lb horizontal ribbons near the skirt was observed; this was believed to be from the tearing caused by the fluttering of the skirt ribbons before the ribbons

are aerodynamically loaded (before full inflation). The maximum loads, which occurred during the reefed stage, are plotted in Figure 12.10 as a function of dynamic pressure for these 13 flight tests. Knacke's empirical method of predicting peak loads (Eq. 5.31) is included for comparison. The predicted loads slightly underestimate the measured loads. The measured disreefed deceleration loads were between 8 and 18 g. The measured inflation times, from canopy stretch to full-open, are plotted in Figure 12.11. The reefing line length (21 or 23 ft) and the reefing line cutter fire delay time (0.5 s) causes the reefing line to be cut before it is loaded when the parachute system is deployed at dynamic pressures below ~650 lb/ft^2. At dynamic pressures above 650 lb/ft^2, canopy fill times are increased because the canopy is filled in the reefed condition before the reefing line is cut. Figure 12.11 shows that the filling time decreases slowly with dynamic pressure and that the mean filling time is ~1 s.

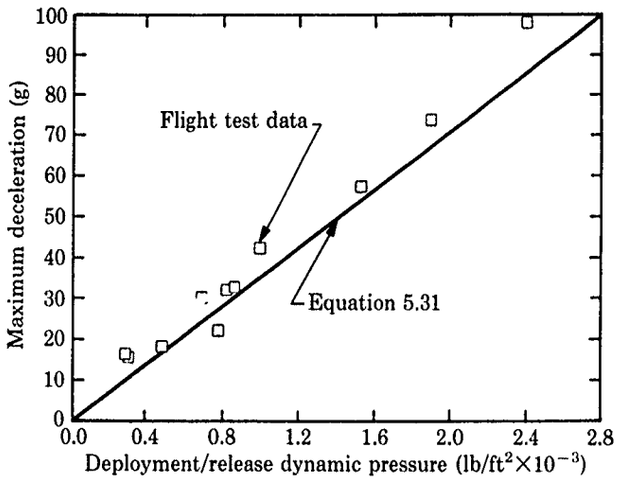


Figure 12.10. Maximum deceleration loads for the 40-ft-diameter main parachute

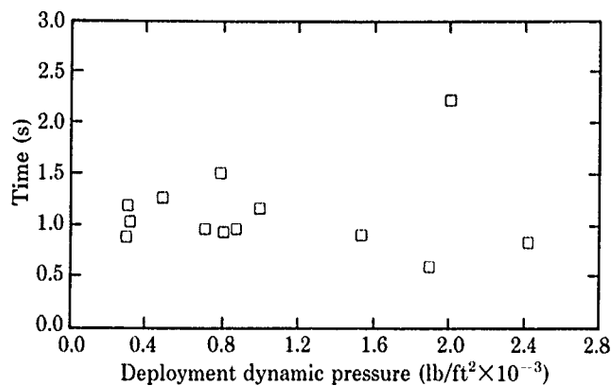


Figure 12.11. Time from canopy stretch to full-open for the 40-ft-diameter main parachute

12.5.3 Design and flight testing of second prototype (46.3-ft-dia) main parachute

Parachute inflation code predictions and flight test results of the 40-ft-diameter main parachute were carefully reviewed before a new main parachute design could be defined that would minimize collapse to meet the impact velocity requirements. The approximate INFLAT predictions suggested that the way to minimize collapse was to reduce the diameter of the canopy. However, a smaller canopy would not meet impact velocity requirements at minimum release altitude, so it was decided to design the new canopy as large as possible within the parachute pack weight and volume constraints. With a larger parachute, it might be possible to achieve the required impact velocity before canopy collapse. Furthermore, the larger diameter would provide the latitude to consider a variety of canopy modifications for reducing the severity of the collapse. The 46.3-ft diameter of this main parachute was achieved by adding 15 horizontal ribbons to the skirt of the 88-ribbon, 40-ft parachute. By adding ribbons at the skirt, the same patterns could be used for the original 88 ribbons; this reduced the time required to fabricate a new prototype. A permanent reefing line was used on the 46.3-ft main parachute because subscale tests showed that it reduced the severity of canopy collapse. The 89-ft permanent reefing line reduced the drag area of the 46.3-ft parachute to ~90% of its full-open drag area.

A detailed stress analysis of the main parachute was conducted using the CANO code; these results can be found in Figure 6.3, which shows the maximum structural load ratio (defined as the tensile load in the ribbon divided by the rated strength of the ribbon) for each ribbon and radial element of the 46.3-ft main parachute for all pressure distributions and reefed/disreefed configurations. The distribution of 2200-lb, 1000-lb, and 550-lb ribbons (from canopy vent to skirt) was established using these CANO results to minimize ribbon weight while requiring a structural load ratio of <0.46 for each ribbon and suspension line. The figure shows that the 550-lb ribbons are very lightly loaded. However, lighter ribbons were not substituted in this region because they must also survive flutter during deployment and inflation of the parachute.

The 46.3-ft-diameter, 20-degree conical ribbon main parachute contains 60 gores and 103 ribbons. Ribbons 1 through 20 are made of 2-in.-wide, 2200-lb nylon; ribbons 21 through 50 are made of 2-in.-wide, 1000-lb nylon; and ribbons 51 through 103 are made of 2-in.-wide, 550-lb nylon. All of the horizontal ribbon materials have reinforced selvages to maximize the tearing strength. The strength of the ribbons and their locations in the canopy were determined using the analytical techniques already described. The 1000-lb and 550-lb nylon ribbon weaves, described in Reference 8.10, were developed specifically for this parachute. The 44-ft-long suspension lines, made of 6000-lb Kevlar, employ the same figure-eight configuration as the pilot parachute suspension lines. Radial backing is made of 2400-lb Kevlar, vent reinforcement is 10,000-lb nylon, and skirt reinforcement is 10,000-lb Kevlar. Three mini-radials are used in each gore; the centerline mini-radial extends from skirt to vent and the outboard mini-radials extend from the skirt to ribbon 41. The parachute has a calculated geometric porosity of 21%, assuming minimal cambering of the horizontal ribbons. The 46.3-ft main parachute is reefed using a 23-ft-long, 13,500-lb Kevlar reefing line to control the inflation loads for high-speed deployments.

The reefing line cutter includes an electrically actuated thermal battery, a 0.9-s electronic timer, and a propellant-actuated cut knife to cut the reefing line. This reefing line cutter, described in Reference 10.4, is discussed briefly in Section 10.1.1. A sketch of the cutter is shown in Figure 10.4 and a photograph of the cutter installation in the parachute is shown in Figure 10.5. The thermal battery is actuated 0.1 s before the deployment of the pilot parachute is initiated. The reefing line is effective only at high parachute deployment velocities (above 650 KCAS) because of the short (0.9 s) time delay. The reefing line is cut before the canopy fully inflates to the reefed stage for parachute deployments at velocities less than 650 KCAS. As mentioned previously, an 89-ft-long permanent reefing line is used to control overinflation. The reefed drag area is about 20% of the full-open, terminal descent drag area of 866 ft^2.

The design of the main parachute deployment bag is discussed in Section 9.3.3. Figure 9.16 shows the 46.3-ft-diameter parachute stretched out on a packing table. Figure 9.19 shows the four-leaf deployment bag, with callouts for the line ties, canopy ties, etc. A photograph of the packed parachute is shown in Figure 9.17.

Flight tests were conducted with and without the 89-ft permanent reefing line to determine its effect on collapse. As predicted by the INFLAT code and subscale flight tests, the permanent reefing line reduced the amount of collapse, allowing the parachute to provide the necessary deceleration at a time when the unreefed parachute is recovering from collapse and providing little drag. In general, the collapse observed with the 46.3-ft parachute, permanently reefed, was significantly less severe than the collapse of the unreefed 40-ft main parachute.

Flight tests revealed that the inflation time was longer than predicted and not repeatable. This was thought to be related to high local porosity in the canopy. Measurements of the horizontal nylon selvage ribbons showed the porosity of the 1000-lb ribbons (21 through 50) to be 10%, whereas the porosity of the 550-lb and 200-lb ribbons was only 2%. A computer code, POROUS, was developed to calculate the local porosity distribution across the main canopy using the actual porosity of the 1000-lb ribbons. Figure 12.12 compares the calculated local porosity distribution along the canopy for the two ribbon porosities. Note that the local porosity is zero to a canopy radius of about 20 in. That is because these canopies were fitted with a solid-fabric 36-in. vent cap attached to the radials inside the parachute to decrease the porosity and thereby increase the inflation rate.

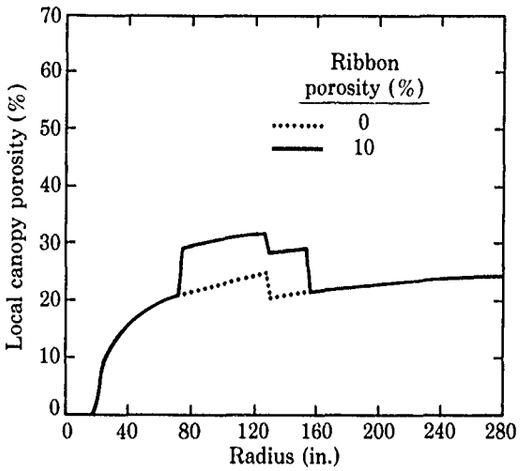


Figure 12.12. Predicted local porosity distributions for the main parachute for different 1000-lb ribbon porosities

With a local porosity greater than 30% where the 1000-lb ribbons are located, it is not surprising that the 46.3-ft parachute would occasionally experience slow inflations. Flight tests were conducted with and without vent caps and with porous 1000-lb horizontal ribbons. The 1000-lb ribbons were coated with RTV flexible silastic to reduce the porosity from 10% to 2% for test PDU-26. The parachute inflation times for four flight tests are shown in Figure 12.13. The data clearly show that there is no appreciable effect of the vent cap on the inflation time, whereas reducing the porosity of the 1000-lb ribbons reduced the inflation time of the parachute dramatically, from ~3.2 s to 1.8 s. New 1000-lb selvage ribbons were developed. Bally Ribbon Mills produced six new weaves, and comparative measurements of porosity and sewing characteristics were made at Sandia to evaluate those weaves. The weave selected had a porosity of 3%. This new 1000-lb ribbon was used for the final prototype 46.3-ft-diameter parachute. A sketch of three gores is shown in Figure 12.14.

The INFLAT code[5.10,5.28] was used to predict the maximum deceleration design load for this parachute at a deployment speed of 800 KCAS at an altitude of 5500 ft above sea level. These inflation load predictions are shown in Figure 12.15. Parametric INFLAT calculations suggested that collapse would not be a serious problem with this 46.3-ft parachute; the computations showed that, in some cases, the wake would overrun the parachute but the effects of canopy distortion on drag would not be significant.

Thirty-five flight tests of this parachute were conducted during the development program using test aircraft (A-7, B-52, and F-111), upward ejection from rocket sled, and ground-launched rockets. These tests were tabulated by Johnson and Peterson.[3.6] The measured (from optical data) inflation times are plotted in Figure 12.16. The mean inflation time is ~1.6 to 1.8 s and, within the large scatter

of the data, is invariant with dynamic pressure. These opening times are nearly twice those of the 40-ft parachute (Figure 12.11), which experienced severe canopy collapse. The longer opening times of the 46.3-ft main parachute minimize the collapse problem because the transfer of the momentum of the store to the wake is spread over a longer time period and over a larger-diameter air mass. The wake behind the 46.3-ft parachute is less energetic than the wake behind the 40-ft parachute; hence, there is less tendency for the parachute to collapse. The peak measured deceleration loads for these flight tests are compared with empirical predictions in Figure 12.17. The predicted loads are much higher than the measured loads over deployment dynamic pressures ranging from ~1200 to 2200 lb/ft^2. The exact cause of these low measured loads is unknown, although it is probably due to the local distribution of porosity (and the ribbon cambering during opening, which increases the effective porosity) along the canopy, which may increase the filling time and thereby decrease the magnitude of the opening-shock loads. These parachutes were constructed to tight dimensional tolerances, so the variations in canopy porosity due to variations in ribbon spacing should be small.

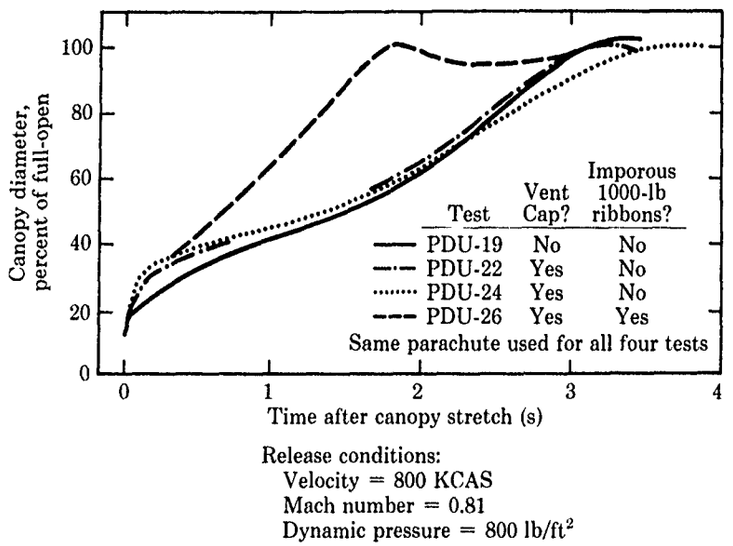


Figure 12.13. Effect of 1000-lb ribbon porosity and vent cap on inflation time of 46.3-ft-diameter main parachute

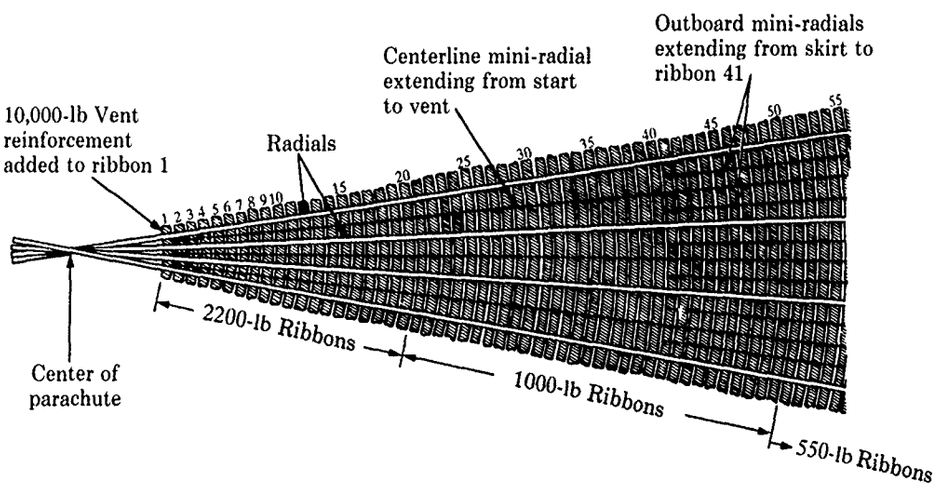


Figure 12.14. Gore design of 46.3-ft-diameter main parachute

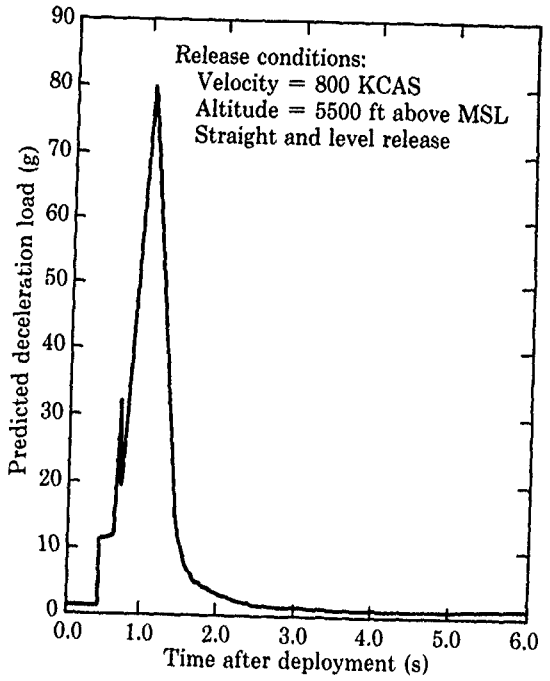


Figure 12.15. INFLAT inflation load predictions for the 46.3-ft-diameter main parachute

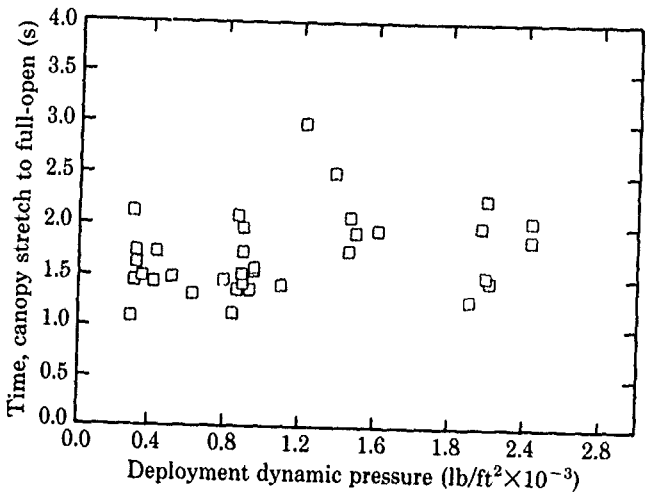


Figure 12.16. Measured inflation times for 46.3-ft-diameter main parachute

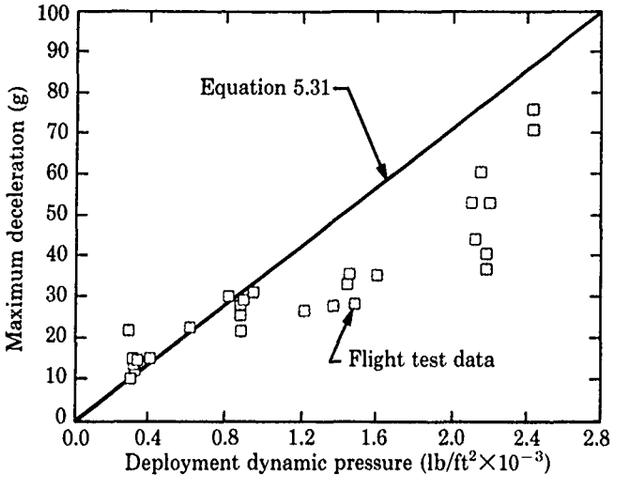
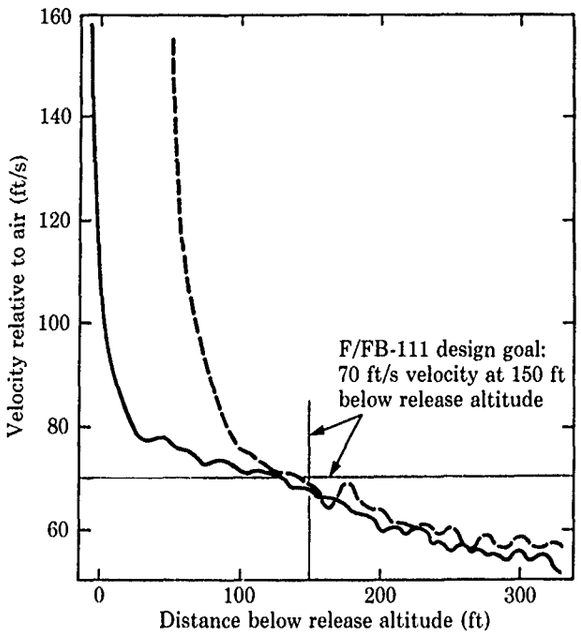


Figure 12.17. Peak inflation loads for 46.3-ft-diameter main parachute

Flight tests were conducted with F-111 aircraft at TTR at or near 800 KCAS release velocity at low altitudes in order to verify that the 46.3-ft parachute system met the requirements specified in Section 12.5. Figure 12.18 plots flight test data for two of those tests. The data show that the store is decelerated to an impact velocity of 70 ft/s at ~150 ft below the release altitude, as required by the system design specifications.

Figure 12.19 shows the effects, from many flight tests, of aircraft vertical velocity at release on store velocity after vertical fall distances (after release) of 150 and 200 ft. For aircraft vertical velocities less than −30 ft/s (30 ft/s downward), the total velocity of the store may be well above the desired 70 ft/s after 150 ft of fall, even when the parachute's performance is nominal. Conversely, the velocity of the store after 150 ft of fall is often 60 ft/s or less if the aircraft vertical velocity at time of release is 30 ft/s upward, even if the parachute experiences some wake recontact. The effects of aircraft vertical release velocity must be taken into account to properly assess the performance of a high-performance parachute.

After reviewing the flight test data from the main parachute configurations, it is possible to draw conclusions about the role of unsteady aerodynamics on the performance of a single large parachute used for the low-altitude delivery of a store. The data show that the parachute is inefficient during the rapid deceleration phase of parachute inflation as the store approaches terminal descent velocity. The loss in performance is caused by wake recontact (Section 5.3.3) and added mass effects (Section 5.3.1). The drag area of the parachute in terminal descent is ~866 ft^2 (which results in a terminal velocity of 55 ft/s at 5000 ft altitude), but the added mass effects and wake recontact reduce the instantaneous drag area significantly below the steady-state drag area while the store is decelerating. Figures 12.20 through 12.22 illustrate the effects of the transient aerodynamics on the parachute. PDU-45 was a rocket-boosted test at TTR in which the parachute was deployed at a dynamic pressure of 2182 lb/ft^2 (Mach 1.43) at an altitude of 9286 ft above MSL. Figure 12.20 plots store deceleration versus time, and Figure 12.21 shows the dynamic pressure decay from the time of deployment. Figure 12.22 shows the time variation of the effective drag area of the main parachute; it is determined by dividing the instantaneous deceleration by the instantaneous dynamic pressure. The maximum effective drag area during the inflation of the parachute is ~475 ft^2 at 1.55 s after canopy stretch. At this time, the parachute has reached its full-open diameter for the first time. This is shown in Figure 12.23, which is a plot of the diameters of the skirt and canopy versus time. Even though the canopy is at its maximum diameter at 1.55 s, the effective drag area is only 60% of the steady-state drag area. During the next second of flight, the effective drag area decreases rapidly to only ~200 ft^2. Figure 12.23 shows that this sudden decrease in effective drag area cannot be attributed to a change in canopy drag area; the loss is caused by the unsteady flow field around the canopy. After this time, the transient aerodynamic effects are diminished, and the effective drag area increases until the steady-state drag area of ~866 ft^2 is reached.



Release Conditions:

Legend	Test No.	Velocity (KCAS)	Trajectory Angle (deg.)	Delay Time (release to deployment) (s)
———	STU-83	779	+1.4 (climb)	0.86
- - -	STU-84	817	−0.9 (dive)	0.44

Figure 12.18. Velocity vs. fall distance from F-111 releases

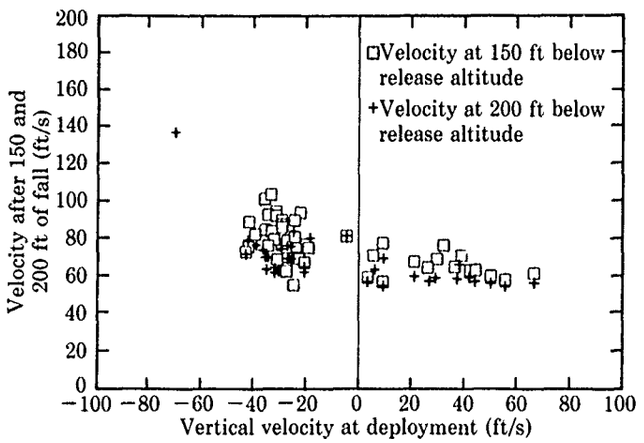


Figure 12.19. Effect of vertical velocity at release on the store velocity at fall distances of 150 ft and 200 ft

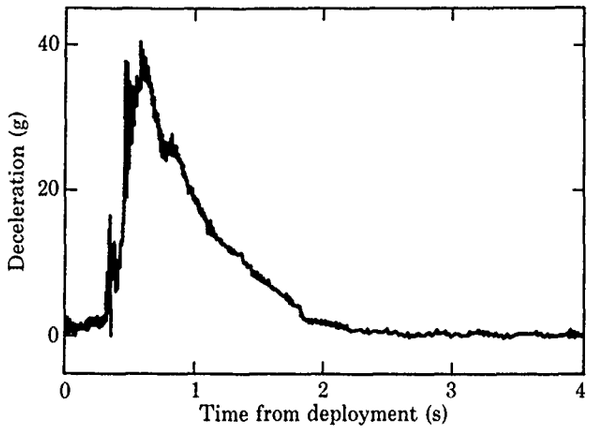


Figure 12.20. Axial deceleration history for PDU-45 store

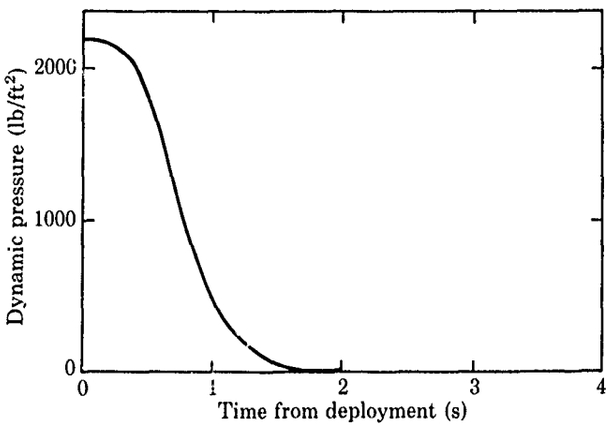


Figure 12.21. History of PDU-45 store dynamic pressure

To summarize the nonsteady aerodynamics, the flight data show that the drag coefficient (based on constructed area) for the parachute is ~0.30 during the period when the transient aerodynamics dominate and ~0.50 in terminal descent. As a result, the effective drag area during this nonsteady aerodynamics period is only ~60% of the terminal drag area of the parachute. Analytical estimates of the effects of added mass and wake recontact on this system support the conclusion that we have probably approached the limit in the performance that can be obtained from a single large parachute for the low-altitude delivery of a store.

Finally, Figure 12.24 shows a collage of photos of the 46.3-ft-diameter parachute decelerating the store after its low-altitude release from the B-1. Flight tests of the store/parachute system have demonstrated that the parachute meets all of the system requirements, despite the nonsteady aerodynamics effects described earlier.

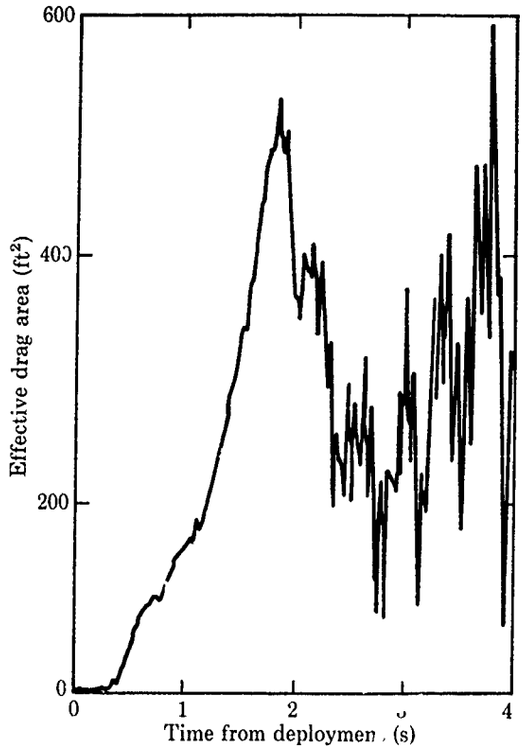


Figure 12.22. History of parachute effective drag area for PDU-45 test

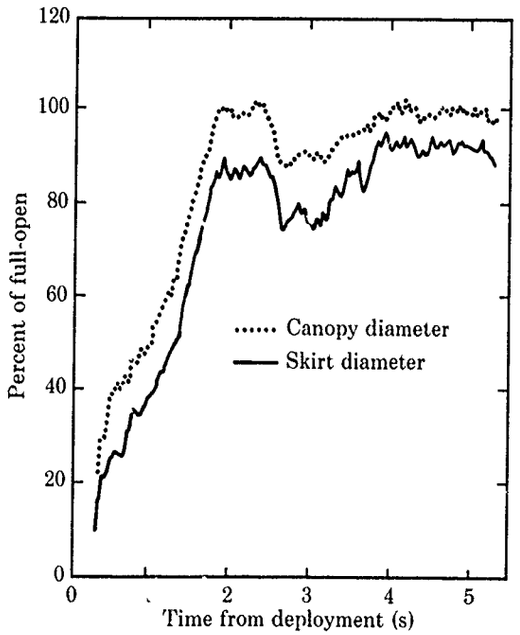


Figure 12.23. History of PDU-45 parachute canopy and skirt diameters

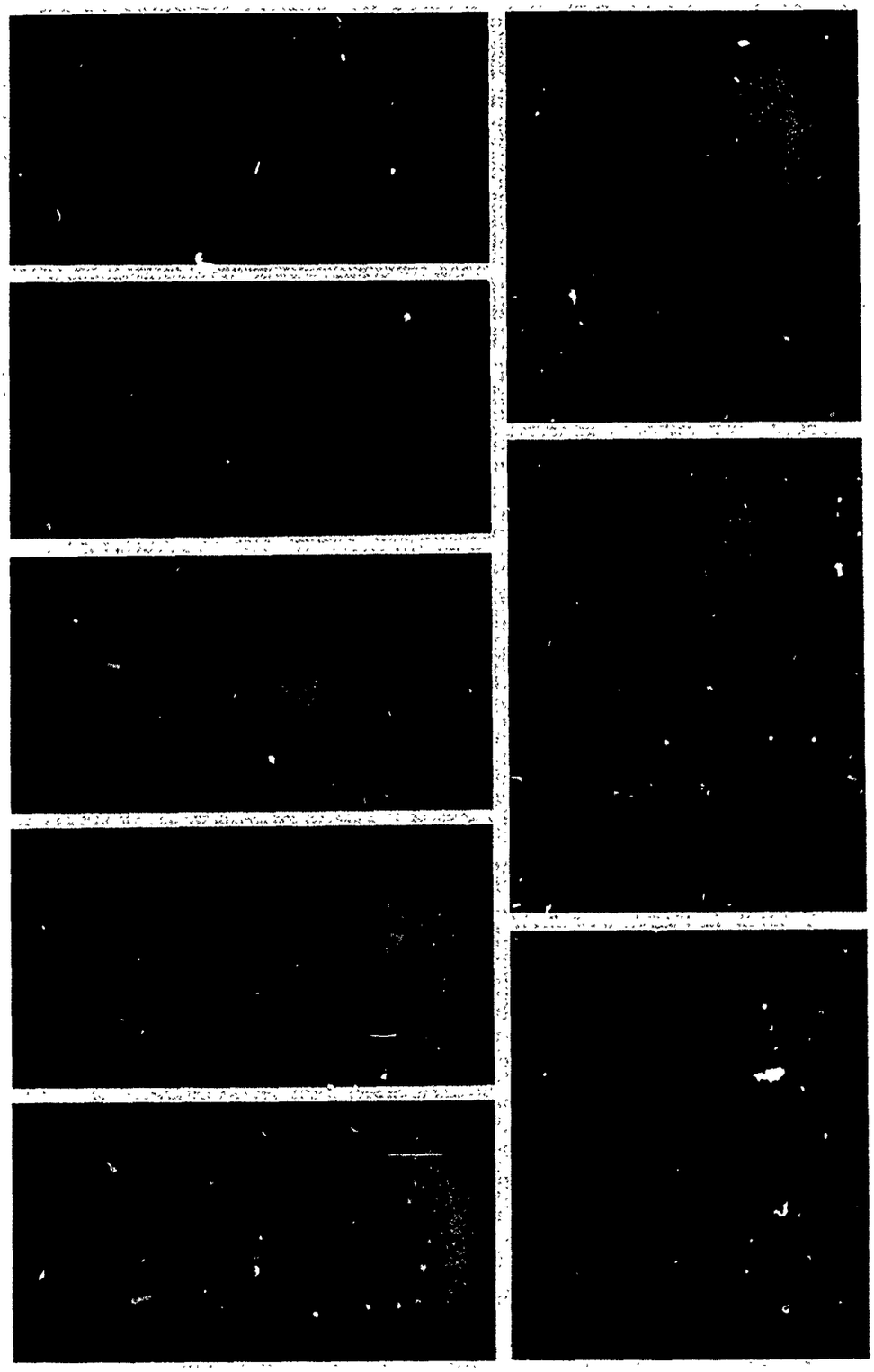


Figure 12.24. A 46.3-ft-diameter parachute shown decelerating the store after release from the B-1

12.6 Design notes on other high-performance parachute systems

This section provides the reader with a brief description of the design of three other parachute systems. The chapters or sections in this AGARDograph where each design is discussed and selected references that describe each design in greater detail are listed.

12.6.1 Design of a 5-ft-diameter Mach 2 parachute for missile payload deceleration

This parachute design was required to decele' 'e an 800-lb, 13-in.-diameter, 10.8-ft-long store to a terminal velocity of ~300 ft/s. The store is separated from a surface-launched missile, and the parachute is deployed at a maximum velocity of ~2300 ft/s. This corresponds to a dynamic pressure of 4400 lb/ft^2 and a Mach number of 2.15 at a deployment altitude of 11,000 ft MSL. The minimum parachute deployment velocity was 686 ft/s, which corresponds to a dynamic pressure of 440 lb/ft^2. No critical weight limitation was imposed on the parachute system, and the space available in the store afterbody for a parachute pack was a 4.5-in.-diameter cylinder about 40 in. long.

Peterson et al.[1.2] and Peterson[4.20] describe in detail the design and the wind tunnel testing and flight testing of these 3.7- to 5.3-ft-diameter ribbon parachutes. Supersonic wind tunnel tests of these parachutes are discussed by Pepper, Buffington, and Peterson.[3.22] The rocket system used to flight-test these parachutes is discussed by Rollstin.[11.13]

Forebody wake effects in supersonic flow are discussed in Section 4.2.6.2. Drag coefficients from subsonic to supersonic Mach numbers are given in Figures 4.8 and 4.9. Figure 4.11 presents a schlieren photograph of a hemisflo parachute in supersonic flow in the NASA-Ames 9-ft by 7-ft Supersonic Wind Tunnel. Figures 4.20 through 4.22 show supersonic wind tunnel drag data of ribbon parachutes measured in this wind tunnel (Ref. 3.22). The rocket booster testing of these parachutes at supersonic speeds is described in Section 11.2.2 (Ref. 11.13). Velocity and dynamic pressure flight test data, during store deceleration, are plotted in Figures 11.8a and 11.8b, respectively. A photograph of the store and rocket booster in flight is shown in Figure 11.15, and the inflated parachute, photographed with a camera onboard the store, is shown in Figure 11.16.

Peterson et al.[1.2] demonstrated the adequacy of the parachute design with 19 subsonic and supersonic flight tests. They concluded that the suspension line length, canopy configuration, and forebody wake have a major effect on supersonic/transonic parachute performance and stability.

12.6.2 Design of Space Shuttle SRB parachute recovery system

Godfrey[12.4] reported in 1973 that the NASA-Marshall Space Center was conducting extensive studies to establish the most cost-effective recovery system for the Space Shuttle Solid Rocket Boosters (SRBs). He suggested that empty-casing solid rocket boosters could be recovered by using state-of-the-art recovery systems at an estimated cost savings of 30% over the use of expendable solid rockets. His initial calculations showed that 146-ft-long, 160,000-lb empty boosters would separate from the Space Shuttle at an altitude of ~132,000 ft and a velocity of ~4500 ft/s, coast to an apogee of ~200,000 ft, and splash down in the ocean at ~120 nautical mile range. The SRBs' reentry into the atmosphere could be stabilized by aerodynamics and mass characteristics at a high angle of attack. This "broadside" reentry would use SRB body drag to dissipate energy and to mitigate the severe reentry conditions for parachute deployment. Godfrey concluded that the fundamental design drivers were the initial conditions for recovery subsystem initiation and the terminal or impact velocity of the SRB.

Wolf[6.11] reported on preliminary design and analysis studies of the SRB recovery system, which were conducted by Sandia for NASA in 1974-1975. The recovery system baseline specified by NASA in March 1974 consisted of a single drogue parachute and a three-parachute main system. The 54-ft-diameter drogue was extracted from the front of the broadside SRB by the ejected nose cap. A single reefed stage for the drogue parachute was used to rotate the SRB to a tail-first attitude, and the full-open drogue provided the proper main parachute deployment conditions. A cluster of three 104-ft-diameter main parachutes was then deployed by the drogue. Two reefed stages were used to minimize the main parachute inflation loads, and the full-open cluster provided the desired water-entry speed of 100 ft/s. The main conclusions from the Sandia studies were: (1) the choice of conical ribbon drogue and main parachutes was best for a state-of-the-art development program; (2) desired safety design margins, as confirmed by a stress analysis, existed in both the drogue and main parachutes; (3) the drogue parachute should be deployed by a 15- to 20-ft-diameter pilot parachute rather than by the ejected nose cap; (4) *a flight test design verification program for the parachute system was an absolute requirement;* and (5) a B-52 carrier aircraft should be used for the test program in conjunction with a 50,000-lb parachute test vehicle. Computer simulations of parachute inflations of all the stages showed that the opening loads of the parachutes could be simulated with

this test vehicle. NASA subsequently adopted the pilot parachute concept to deploy the drogue parachute and decided to conduct a comprehensive flight test program using the B-52 as the carrier aircraft.

In 1975, Bacchus, Vickers, and Foughner[4.6] conducted an extensive wind tunnel investigation of 1/8-scale models of the proposed SRB recovery parachutes (54-ft-diameter drogue and 104-ft-diameter mains) and four drogue parachute deployment techniques. Their interference-free steady-state wind tunnel drag data showed excellent agreement with Sandia's full-scale flight test drag data for 23- and 76-ft- diameter, 20-degree conical ribbon parachutes. The optimum wind-tunnel deployment technique tested was the SRB nose cap deployment of a pilot parachute that in turn deployed the drogue parachute. This deployment scheme was subsequently adopted by NASA as its baseline design.

Six papers on the SRB recovery system design were presented at the 1979 AIAA 6th Aerodynamic Deceleration Systems Conference.[1.14] By this time, NASA had decided to increase the main parachute diameter to 115 ft. The baseline performance schematic of the Space Shuttle, the SRBs, and the SRB recovery is shown in Figure 12.25. Runkle and Drobnik[12.5] describe in detail the 50,000-lb parachute test vehicle (PTV), which was designed to take parachute opening-shock loads of up to 300,000 lb and be compatible with B-52 pylon carriage with satisfactory release and separation. Spahr[11.9] calculated the release and separation characteristics of this PTV from the B-52 pylon using a computer code that modeled the PTV/B-52 flow field and the resulting initial flight path of the PTV. Kross and Webb[12.6] conducted tests at Sandia's Rocket Sled Track to evaluate the SRB nose cap/11.5-ft-diameter pilot parachute system for deploying the 54-ft-diameter drogue parachute. Two sled tests of the full-scale hardware demonstrated that the nose cap separation, followed by the pilot parachute, was a satisfactory method of deploying the 54-ft-diameter drogue parachute.

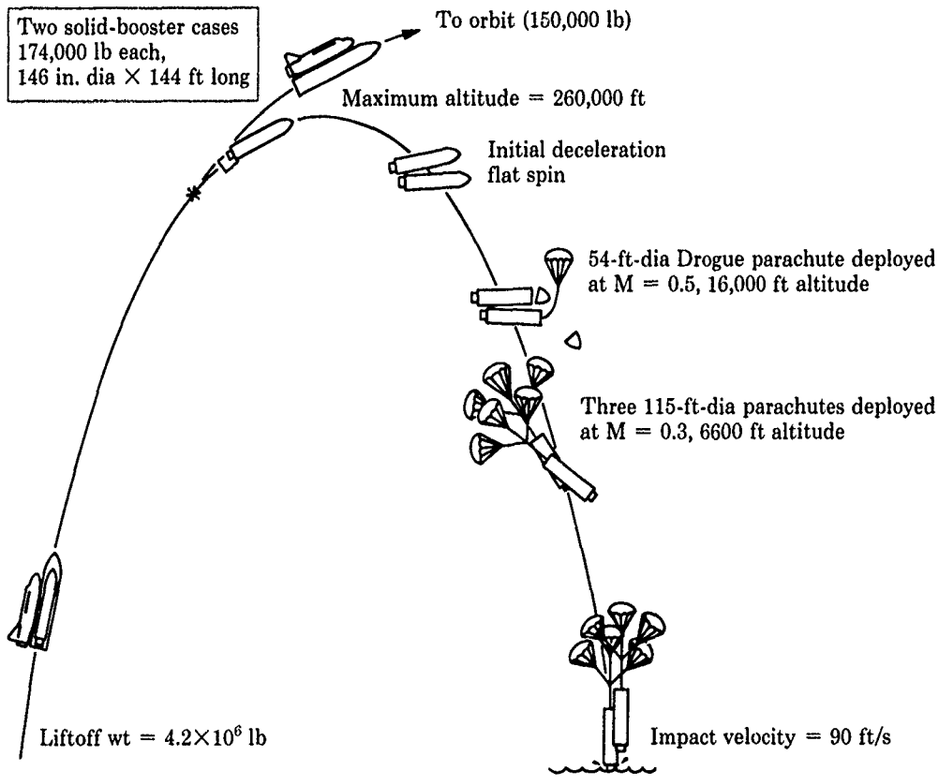


Figure 12.25. Performance schematic of NASA Space Shuttle recovery system

Rodier[12.7] discusses the design of the two-stage skirt reefing system for the 54-ft-diameter 20-degree conical ribbon drogue parachute. This drogue parachute has 60 gores, a porosity of 16%, and weighs 1150 lb. The parachute design aerodynamic load limit is 270,000 lb. The 15,000-lb-strength nylon suspension lines are 105 ft long. The canopy horizontals, starting at the apex, consist of forty-six 2000-lb, forty 1500-lb, and thirty-three 1000-lb nylon ribbons. The two stages of reefing are 60% and 80% of full-open drag area, with redundant reefing line cutters in each stage. The reefing lines are three plies of 12,000-lb nylon.

Runkle and Woodis[1.3] conducted an overtest of the drogue parachute at a planned deployment dynamic pressure of 284 lb/ft^2 (or 1.3 times the 218-lb/ft^2 maximum dynamic pressure expected during SRB recovery) to evaluate the structural integrity of the parachute. The predicted peak drogue aerodynamic load was 301,000 ± 43,000 lb, compared to the maximum predicted operating aerodynamic load of 225,000 lb during SRB recovery. The actual dynamic pressure at drogue parachute deployment (a 48,000-lb PTV was dropped from the B-52 to test the drogue parachute) was 331 lb/ft^2. The drogue "exploded" at an aerodynamic load of about 548,000 lb. The excellent onboard camera footage showed a classic failure of a high-performance canopy when loaded far beyond its intended design limits. The instrumentation showed a good correlation of aerodynamic load and parachute area during opening. Posttest analysis revealed that the reefing system had been damaged by the snatch load, and both reefing lines had failed. As a result of this test, the reefing lines were changed from two plies to three plies of 12,000-lb nylon, and other modifications were made to the reefing system. A great deal of valuable design information was obtained from the analysis of this parachute test failure.

Moog, Sheppard, and Kross[4.12] discuss the results of six aircraft drop tests of the SRB decelerator subsystem, which consists of a 11.5-ft-diameter pilot parachute, a 54-ft-diameter drogue parachute, and a cluster of three 115-ft-diameter main parachutes. The 115-ft-diameter main parachute has a canopy of 16% porosity and is constructed of 20-degree conical ribbons with 96 gores. The radial members of the all-nylon canopy are made of two plies of 3000-lb webbing, the horizontal ribbons consist of either 460-lb or 1000-lb tapes, and the reefing lines are made of two plies of 9000-lb webbing. Each of the 96 suspension lines is made of 6000-lb nylon webbing. Each main parachute weighs 1600 lb. The design-limit load for the main parachute is 174,000 lb. The suspension lines, dispersion bridles, and risers are 62 ft, 70 ft, and 40 ft long, respectively. Moog, Sheppard, and Kross concluded from these aircraft drop test results (functional demonstrations of the subsystems, drag verification, and structural overload testing) that the subsystem was ready for qualification testing on the Space Shuttle development flights. Moog, Bacchus, and Utreja[4.50] compared wind tunnel test data with the drop test results to predict the performance of the SRB flight parachutes. The parameters assessed included full-open terminal drag coefficients, reefed drag area, opening characteristics, clustering effects, and forebody interference.

Woodis[12.8] discussed the recovery of the SRBs from the first Space Shuttle flight of April 12, 1981. Tallentire[12.1] discusses the design and development of the SRB recovery system; the flight test program; the design techniques, major equipment, facilities, and procedures; post-mission inspection, repair, repacking, and verification; and the performance of the subsystem on the first six shuttle flights. Figure 12.26 is a photograph of the SRB with the three main parachutes. Water impact damage to the SRB skirt led to a decision to increase the diameter of the main parachute from 115 ft to 136 ft, with the same porosity of 16% and the same 20-degree conical design. The new parachute has 160 gores (and suspension lines) versus 96 gores for the smaller main parachute. The weight of the new design increased 496 lb per parachute, to a total parachute system weight of approximately 2100 lb.

The SRB decelerator system offered many design challenges because of the large payload weight and the reentry environment. The designers decided early in the program to stick with state-of-the-art, proven parachute concepts; for example, the new material Kevlar was not extensively used. Kevlar is used for the parachute reefing lines and in the pilot parachute. This conservative approach led to a very successful decelerator design for the SRB.



Figure 12.26. Photograph of an SRB with three 115-ft-diameter parachutes (courtesy of NASA)

12.6.3 Design of parachute recovery systems for artillery shells

The first documentation of Sandia work to develop a parachute system to recover a spinning artillery shell fired from a cannon was presented by Pepper and Fellerhoff[3.53] in 1969. Sandia has conducted over 300 flight tests to date to recover 155-mm and 8-in. shells. Several generations of shell recovery systems were developed in a successful effort to increase recovery system reliability. This recovery capability allows the designer to conduct in-flight component structural tests, in-flight component functional tests, and posttest analysis of the shell's components after they have been subjected to the severe gun-launch environment. It also allows the use of a complex and expensive telemetry system to measure flight environments and to monitor components during flight; the system is then recovered, refurbished, and reused.

Waye, Peterson and Botner[1.4] discuss the design and performance of these 155-mm and 8-in. shell recovery systems. The very severe launch and parachute deployment environments are presented in Table 12.1. A schematic of a typical flight path is shown in Figure 12.27. Both shells are tested at the Tonopah Test Range (special gun emplacements have been constructed) by firing the shells at a near-vertical elevation angle. The shells reach an apogee of 40,000 to 70,000 ft, depending on the propellent charge and vehicle weight. After reaching apogee, the rapidly spinning shells fall in a base-first orientation, which places the nose-mounted recovery system at the trailing end of the projectile. Trajectory calculations are made to predict the setting for the onboard electronic timer (see Figure 12.28) to deploy the parachute at a dynamic pressure of 10 to 15 lb/ft^2. The deployment signal from the timer fires a detonator and initiates a pyrotechnic train that sets off an aluminum linear shape charge, which severs the ogive from the swivel base. The explosive forces and aerodynamic forces remove the ogive; the exposed canopy is subsequently deployed by centrifugal and aerodynamic forces. The parachute inflates, the swivels are engaged, and the shell decelerates to terminal velocity; impact velocities are between 100 and 120 ft/s. The axial ground impact deceleration on the projectiles is estimated to average ~110 g, with deceleration spikes about two to three times greater. These low impact decelerations are in sharp contrast to the high (12,000 to 20,000 g) axial accelerations experienced by the shell and components at launch.

Both recovery systems consist of a package that forms the nose of the projectile. A thin-walled ogive contains the parachute. The suspension lines of the parachute are attached to a small parachute swivel, which in turn is attached to a steel aircraft cable (see Figures 12.29a and 12.29b). The other end of the cable is attached to the main swivel in the swivel plate, which is attached to the projectile. The swivel plate is also attached to the ogive, and the parachute, suspension lines, and cable are packaged in the hollow cavity formed by the ogive and the top of the swivel plate. The swivel plate contains an explosive charge, which cuts the ogive free to deploy the parachute, and a timer that initiates the explosive charge.

The 155-mm and 8-in. shells weigh 100 lb and 200 lb, respectively, and their recovery systems weigh 11 lb and 15 lb, respectively. Guide surface parachutes were selected for the artillery shell recovery systems because of their highly reliable inflation characteristics and high drag coefficient of 0.8. The parachutes (4-ft-diameter for the 155-mm shell and 8-ft-diameter for the 8-in. shell) are made of 1.6 oz/yd^2 nylon and contain twelve 1500-lb tensile-strength Kevlar suspension lines. The parachutes are packed into the shell ogives, with a Teflon liner to prevent friction burns during gun launch and deployment.

Table 12.1. Maximum Artillery Shell Environment at Gun Launch and Parachute Deployment

	155-mm	8-in.
Gun Launch		
Axial acceleration (g)	20,000	12,000
Radial acceleration (rad/s^2)	400,000	200,000
Muzzle velocity (ft/s)	3,000	2,200
Spin rate (rpm)	18,000	12,000
Deployment		
Dynamic pressure (lb/ft^2)	15	15
Spin rate (rpm)	15,000	10,000

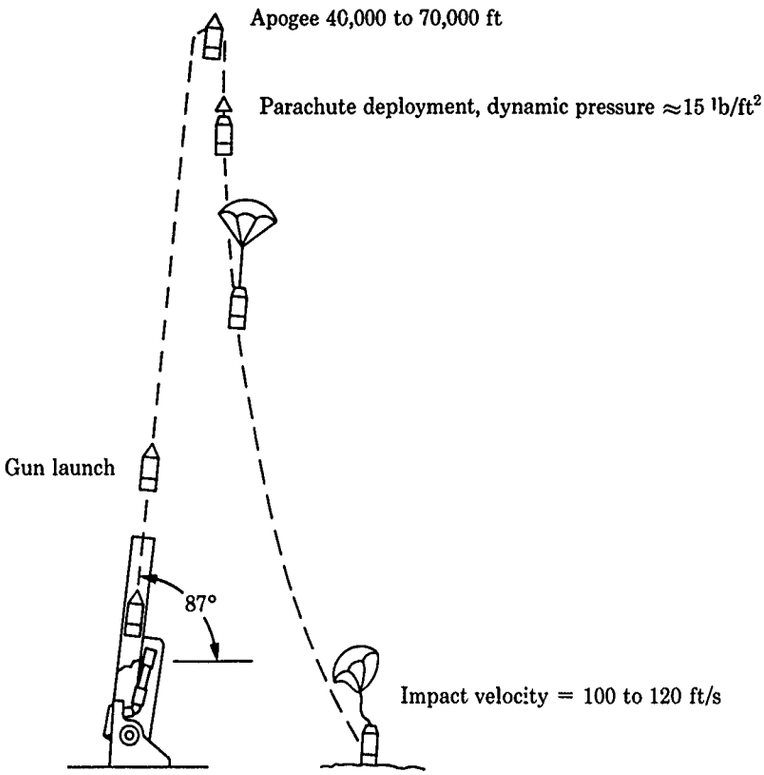


Figure 12.27. Flight path of a retarded artillery shell

The double-swivel system was necessary for a successful recovery system because of a nutation phenomenon that occurs during descent. Benedetti[12.9] modeled the translational and rotational motions of a spinning projectile descending on a parachute. He showed, through numerical solutions as well as closed-form analytical solutions, that the Magnus moment causes the large nutational motion of the projectile. When the center of pressure for the Magnus force is aft of the projectile center of mass, the Magnus moment causes a large, unstable nutational motion that turns the spinning projectile upside-down while it is descending on the parachute (Figure 12.30). During descent, the shell shifts from a base-down orientation to a nose-down orientation due to this nutation. During nutation, the main swivel effectively decouples the shell rotation from the cable, and the parachute swivel allows the cable and shell to rotate around the parachute. If either swivel is damaged, the parachute suspension lines will become twisted and the parachute will stream. The cable assembly consists of two left-hand-lay, 3/16-in.-diameter steel aircraft cables with a breaking strength of 4200 lb each. These cables are attached to the parachute suspension lines, which are behind the aft end of the projectile during the nutation process. A steel wear block is swaged to the cables near the lower end. This block is positioned so that when the shell shifts it rubs on the edge of the swivel plate and the cut edge of the ogive. As the wear block rubs on these edges, it removes spin energy from the shell. The shell then becomes unstable in the nose-down orientation and rotates back to the base-down orientation prior to ground impact.

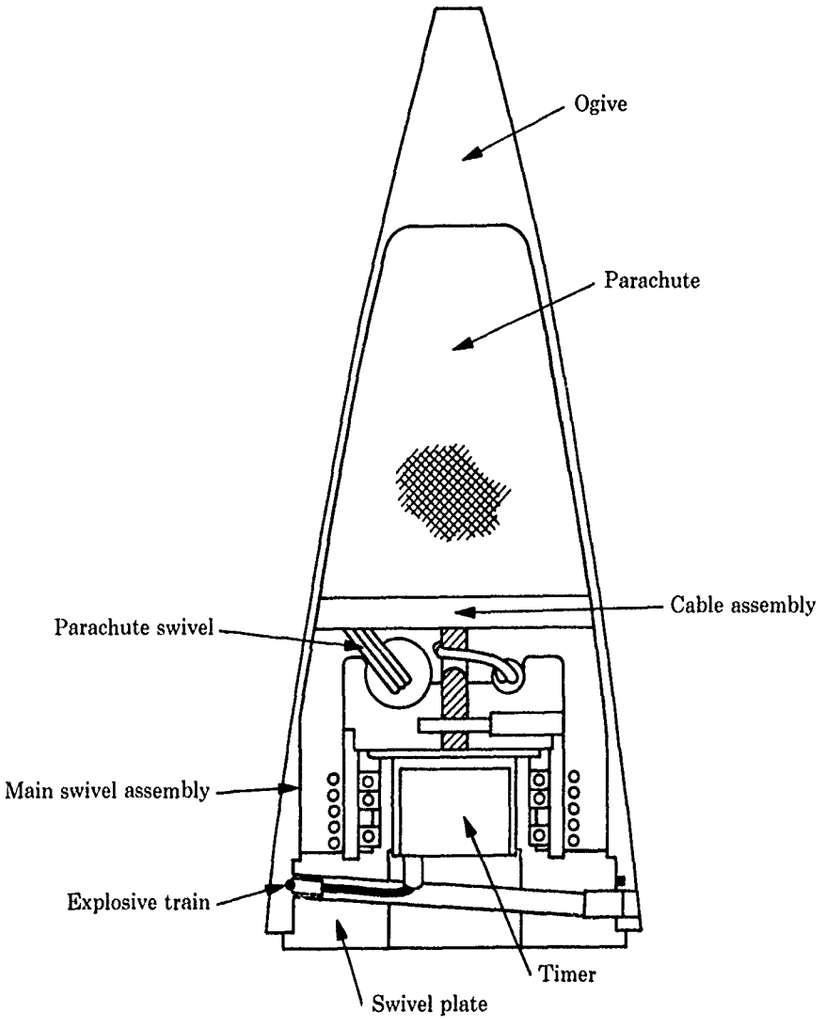


Figure 12.28. Schematic of the 155-mm recovery system

Waye, Peterson, and Botner[14] discuss some of the design modifications that were made to increase the reliability of these recovery systems. The redesigned systems have proved to be more than 95 percent successful for the recovery of 8-in.-diameter artillery shells and more than 85 percent successful for the recovery of 155-mm-diameter artillery shells. Based on the very severe launch environment and parachute deployment conditions and the extensive set of full-scale test data, these recovery success rates are respectable.

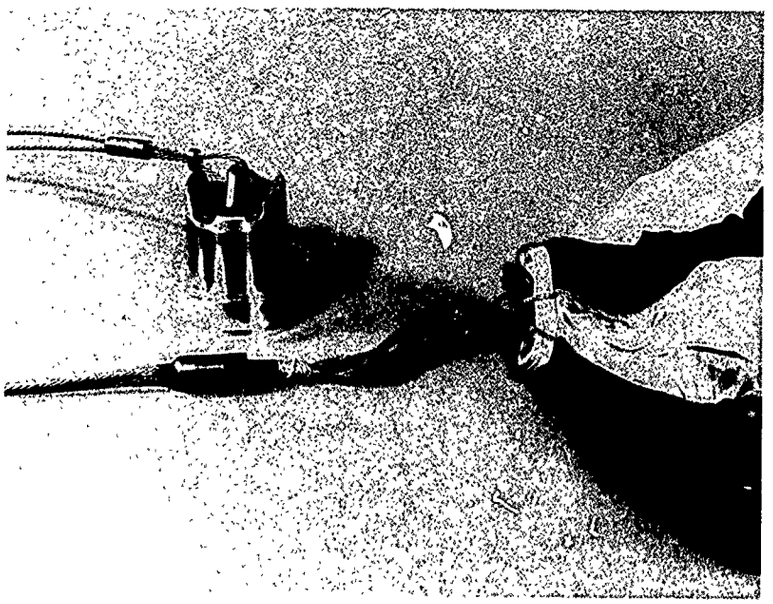


Figure 12.29a. The 155-mm recovery system

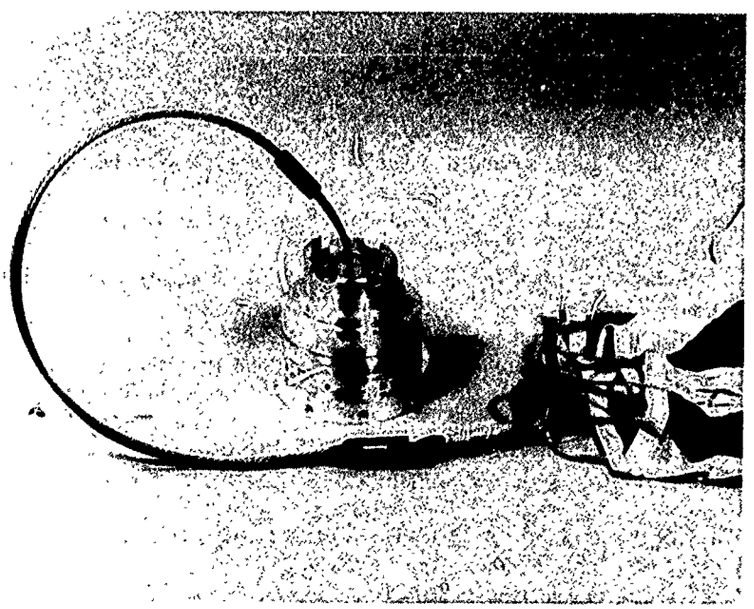


Figure 12.29b. The 8-in. recovery system

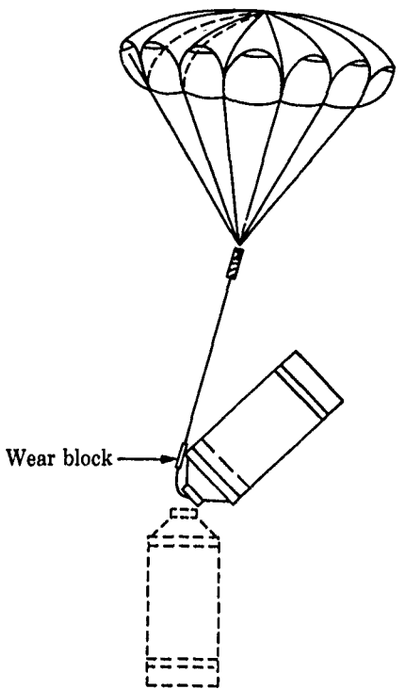


Figure 12.30. Projectile nutation

References

12.1 F. I. Tallentire, "The Space Shuttle Solid Rocket Booster Recovery System," *Journal of the British Interplanetary Society,* Vol. 37, pp. 55-64, 1984.

12.2 J. Cyrus and G. Thibault, "Development of the High-Speed Air Drop Container (HISAC), a Status Report," AIAA 89-0884, April 1989.

12.3 R. O. Nellums, *Conceptual Design of a High-Speed Airdrop Container (HISAC) System,* SAND84-0902, Sandia National Laboratories, 1984.

12.4 R. E. Godfrey, "Space Shuttle Booster Recovery Planning," AIAA 73-441, May 1973.

12.5 R. E. Runkle and R. F. Drobnik, "Space Shuttle Solid Rocket Booster Decelerator Subsystem—Air Drop Test Vehicle/B-52 Design," AIAA 79-0466, March 1979.

12.6 D. A. Kross and R. W. Webb, "Space Shuttle Solid Rocket Booster Decelerator Subsystem Rocket Sled Test Program," AIAA 79-0437, March 1979.

12.7 R. W. Rodier, "Reefing the Space Shuttle SRB-DSS Drogue Parachute," AIAA 79-0434, March 1979.

12.8 R. Woodis, "Space Shuttle Solid Rocket Booster (SRB) Decelerator Subsystem," AIAA 81-1911, October 1981.

12.9 G. A. Benedetti, *Flight Dynamics of a Spinning Projectile Descending on a Parachute,* SAND89-8419, Sandia National Laboratories, February 1989.

CHAPTER 13

SUMMARY AND CONCLUSIONS

Several factors have forced parachute technology to advance very rapidly during the past two decades. The expansion of the flight envelopes of modern aircraft, missiles, rockets, reentry vehicles, and spacecraft has required increased parachute performance. In addition, payloads have become much more expensive, making parachute recovery more a requirement than an option. These factors have prompted a phenomenological approach for developing parachute technology. The goal of this approach is to understand enough about the time-dependent aerodynamics and structural dynamics of the inflating parachute to allow constructing approximate models of the inflation process that, in turn, could be used as parachute design tools. New design tools have been developed for modern high-performance parachutes and additional design data have been obtained. The purpose of this AGARDograph is to identify the "state of the science" in parachute design and to summarize modern parachute design and testing procedures, taken from over 400 references, that might be useful to parachute designers.

Methods for predicting the aerodynamics of inflating parachutes continue to be the most needed tool for assisting the parachute designer. The extraordinary complexity of parachute aerodynamics, however, has made development of numerical parachute inflation tools a slow process, which today is still far from completion. High-performance parachutes often generate rapid decelerations and attendant nonsteady aerodynamic phenomena. As an initial approach to these nonsteady aerodynamic phenomena, scientists have proposed steady-state aerodynamic approximations that provide some physical insight into parachute inflation and are useful for preliminary design. Semiempirical, analytical, and inviscid methods are coupled with data from wind tunnel and flight tests to form the basis for parachute design today. These resources are adequate for predicting parachute drag once the inflation process is complete. They show that the parachute designer must account for forebody wake effects, consider the decreases in parachute drag due to Mach number, and allow for the interaction of parachutes in a cluster of multiple canopies. However, the analytical methods are still unable to predict quantitative pressure distributions for parachute canopies in a constant-velocity airstream. Experimental data are limited by our lack of knowledge about how to scale data to large flight systems, but the data are useful in identifying the important physical processes of parachute operation. Without extensive data on parachute drag, canopy pressure distributions, and the surrounding flow field, development of numerical design and performance prediction tools will not be possible.

Computational methods that replicate the *nonsteady* aerodynamics of an inflating parachute are even rarer than steady aerodynamic models. Simple algebraic expressions based on data from a limited data base of parachute types and flight conditions at the time of inflation are all that are available to parachute designers at the present time. The development of computational parachute inflation models has progressed to the point where their *potential* value has been proved, but such tools are not yet ready for general use by the parachute community. The lack of parachute inflation predictive models is the most serious deficiency within the parachute technical community today, and the greatest handicap to parachute engineers. Efforts to develop and validate semiempirical, numerical inflation models based on the equations for the momentum of the parachute should receive top priority within the parachute community.

Concurrently with the development of semiempirical, numerical, nonsteady parachute aerodynamic models, the authors believe that research to obtain full Navier-Stokes solutions of the flow around and through an inflating parachute should be emphasized. With the continuing advancements in mainframe computer capabilities (more storage and faster computations), Navier-Stokes calculations of parachute inflation will undoubtedly become the parachute engineering design tools for future high-performance parachute designs. Development of Navier-Stokes methods for predicting parachute inflation will also require high-fidelity experimental data, which at present are still unavailable. Controlled measurements of parachute flow field, canopy pressure distributions, and drag during inflation and deceleration are very much needed for the validation of parachute aerodynamics codes.

Methods for determining the strength of materials used in parachutes are more advanced than methods for determining inflation aerodynamics and drag performance. Approximate methods such as CALA work well for circular symmetric parachutes, and they serve as appropriate design tools for use by the general parachute community. Advancements made in the structural model in CALA could include a finite element representation of *all* elements of the canopy, rather than just ribbons and

radials. Such an approach would also accommodate canopy types that do not have circular symmetry. At the present time, the greatest limitation in using the CALA code is not knowing what pressure distribution to provide as input to the stress calculations. Since the weakest link in the accuracy of stress calculations is attributed to inadequate representation of the nonsteady aerodynamics of parachute inflation and deceleration, higher priority should be given to the development of aerodynamic models than to stress models.

In view of the inadequacies of available parachute design codes, both ground test assets (such as wind tunnels) and flight test ranges are absolutely essential to the parachute designer. Advancements in instrumentation and data acquisition systems have allowed us to learn more about parachute inflation from ground and flight tests than was believed possible two decades ago. Simulation of the nonsteady aerodynamics of an inflating, decelerating parachute in a *controlled* environment is a necessity for the parachute community, but no such capability exists anywhere in the world today. Even in steady flows, improved instrumentation and test techniques are needed to measure the flow field around parachutes so that aerodynamic numerical codes can be validated.

Flight test facilities should be treated as national assets, with a strategic management plan that does not change with every dip in the budget. They are precious resources that must be shared, sustained, and kept as affordable as possible because numerical design codes will never replace the need for flight testing. Because of their high cost of operation, flight test ranges are always prime candidates for closure in lean budgetary years. For the same reason, once they are closed, they will probably never be reopened. It is crucial that they be managed as strategic national assets so that they will be available over the long haul.

The parachute community has relied on non-parachute requirements to drive the development of strong, lightweight textile materials; whenever new materials were developed, the parachute community focused its research on learning how to utilize those new materials in parachute design. This approach has been successful and is an appropriate strategy for the future, given the relatively small quantity needed for advanced parachute textiles compared to the large quantities of advanced textiles needed in other disciplines and markets. The parachute community should develop an accessible data base of material specifications and arrange for a "caretaker" to ensure that changes made to these specifications are documented and made known to all users of parachute materials.

Parachute deployment and packing are the least analytical, most experiential aspects of parachute technology. Some success has been achieved in modeling the important features of parachute deployment in a computer code. However, the secrets of parachute deployment bag design and packing reside only in the minds of experienced technicians and designers. To ensure that this knowledge base is not lost, new technicians and engineers should work with experienced people.

The complexity of the parachute inflation problem, the magnitude of the research that must be done, and the small size of the parachute community all suggest that future parachute technology development will not be completed successfully unless it is given higher priority and is pursued as a national/international collaborative effort of scientists and engineers. No single laboratory has either the resources or the talent mix to solve all of the critical parachute technology problems by itself. Obtaining high priority for this work is itself a formidable problem because the parachute community has done little to convince its own management and sponsors that parachute design is a technical issue rather than an art form. The parachute community has every incentive to try new approaches for developing parachute technology: the success of future high-performance parachute systems depends on whether the community will push to treat parachute design as a technology, whether they will work together or separately to develop that technology, and whether they can earn endorsement by parachute users that developing parachute technology now is the only way to avoid the expensive, time-consuming problems that are likely to surface in future system development programs.

AUTHOR INDEX

Abbott, N. J. 170-172
Adamson, T. D. 112, 121
Aebischer, A. C. 38
Aeschliman, D. P. 163-165
Alexander, W. C. 26, 37, 50-51, 81
Anderson, J. E. 81
Arenson, D. L. 5, 35, 45, 51
Arnold, W. V. 50-51, 81
Asfour, K. J. 130
Ashurst, W. T. 117
Auerbach, I. 176, 178
Ayres, R. M. 78, 100-101, 121

Babish, C. A. 26, 50, 54, 61, 239-240
Baca, B. K. 65, 67, 145, 155
Bacchus, D. L. 45, 67-68, 143-144, 153, 162, 273-274
Ballinger, J. G. 72
Banerjee, A. K. 98, 189
Barlog, S. J. 203
Barnard, S. 54, 145-146, 149, 151, 162
Barnette, D. W. 113
Barth, B. L. 229, 243
Bartlett, R. P. 242
Barton, W. R. 35, 183
Baxter, A. C. 78
Beare, S. D. 174
Behr, V. L. 191, 245, 250-251
Belotserkovskii, S. M. 112
Bendura, R. J. 31, 130, 188
Benedetti, G. A. 277
Benefield, K. 175
Berg, D. E. 152, 157-158
Berndt, R. J. 114
Birkebak, R. 81
Bixby, H. W. 3, 5, 11-39, 45, 50, 56, 60, 64, 67, 76-77, 81, 88, 96-100, 106, 121, 139, 169-170, 181, 196, 203, 207, 213-214, 219-220, 223-224, 226, 231, 237, 242
Blanchard, T. 6, 129, 243
Block, L. C. 81
Bloetscher, F. 26, 50-51, 81
Bobbitt, P. J. 50, 145
Bolton, W. R. 20-23, 151
Boone, J. D. 175
Botner, W. T. 2, 35, 276, 278
Bottorff, M. R. 31, 130, 253, 259-260
Bradley, G. H. 204, 220-221
Braun, G. 135
Braun, J. F. 67, 77
Brown, W. D. 69
Buckley, J. A. 187
Buckner, J. K. 26
Buffington, R. J. 26-27, 50, 54, 62, 80, 145, 156-157, 272
Buhler, W. C. 66
Bunton, R. W. 121-122
Burbick, J. W. 121
Burns, F. T. 57

Chang, P. K. 61
Cochran, B. C. 101
Cockrell, D. J. 2-3, 5, 44, 69, 76, 78-79, 100-101, 105-106, 112, 121, 155
Coppey, J. M. 189
Corce, J. D. 51, 81, 145, 152
Coskren, R. J. 170-171
Craig, J. R. 23, 204-205
Croll, R. H. 20, 22, 152-153, 157-158, 162
Cronin, D. C. 197
Culver, I. H. 129
Curry, W. H. 20, 23, 123
Cutchins, M. A. 121-122
Cyrus, J. 250

Dale, J. N. 74, 76
Deitering, J. S. 26, 50-51
Dellavedowa, R. P. 129
DeSantis, G. C. 101
Deweese, J. H. 114
Dickie, G. D. 74, 146
Doherr, K.-F. 36, 78-79, 101, 123, 135
Downing, J. R. 5, 35, 45, 51, 243
Downs, P. R. 242
Doyle, G. R. 121
Drobnik, R. F. 273
Dunmire, K. A. 121

Eaton, J. A. 78, 101
Eckert, E. R. G. 81, 152
Eckstrom, C. V. 31, 50-51
Eckstrom, D. J. 56-59
Eldred, C. H. 111
Elfstrom, G. M. 163-165
Engstrom, B. A. 6, 26, 35, 45, 51, 145, 229, 243
Ericksen, R. E. 78-80, 121
Ericksen, R. H. 173, 176, 178-179
Etherton, B. D. 57
Everett, R. N. 20-21, 151
Ewing, E. G. 3, 5, 11-39, 45, 50, 56, 60, 64, 67, 76-77, 81, 88, 96-100, 106, 121, 139, 169-170, 181, 196, 203, 207, 213-214, 219-220, 223-224, 226, 231, 237, 242

Fedoruk, R. 163-165
Fellerhoff, R. D. 35, 276
Ferrier, A. R. 34
Foughner, J. T. 26, 45, 50, 143, 153, 162, 273
Fournier, R. H. 244
Fowler, G. A. 35, 183
Freda, M. S. 139
Freeston, W. D. 81
Freilich, G. 220

French, K. E. 98, 107, 197
Frucht, Y. I. 101, 105, 112
Fu, K. H. 162
Fullerton, T. J. 121, 123

Galigher, L. L. 26, 50
Gallagher, J. P. 203
Gamble, J. D. 121
Gardella, J. W. 81
Garrard, W. L. 71-72, 76, 107, 110, 129-131, 133, 136, 152, 162
Gillis, C. L. 31, 81, 183
Goar, K. J. 74, 76, 146
Godfrey, R. E. 272
Goldstein, S. 56
Goodwin, S. L. 172
Greene, G. C. 107
Gross, R. S. 35, 51
Guess, T. R. 173
Guiteras, J. J. 78-80, 121

Haak, E. L. 45, 50-51, 56, 74, 78, 142, 149-150
Hall, A. A. 56
Hanlon, P. D. 244
Hardin, M. V. 237
Hartnett, J. P. 81
Harwood, R. J. 78, 101, 105
Hauser, G. C. 246
Heckart, M. V. 237
Hedtke, J. C. 109
Heinrich, H. G. 5 31, 34, 45, 50-51, 54, 56-59, 67, 72, 74-76, 78, 97, 100-102, 107, 109, 113-114, 130, 135, 142, 149-150, 152-153, 197
Heins, W. 78
Henfling, J. F. 76, 147
Henke, D. W. 60-61
Higgins, M. W. 28
Higuchi, H. 112, 154
Hilliard, E. F. 26, 50-51
Hislop, G. S. 56
Holbrook, J. W. 74-75, 76, 113
Holt, I. T. 1, 20-22, 26-27, 49-50, 54, 62, 66-67, 80-81, 97, 107, 114-115, 133, 144, 151, 173, 194-195, 207-208, 226, 245, 272
Homan, M. L. 26, 50-51
Hool, J. N. 81, 152
Houmard, J. E. 130
Huckins, E. K. 97, 182
Huntley, D. J. 100-101
Huntley, I. D. 100-101

Ibrahim, S. K. 69-71, 100-101
Isaacson, M. 105

Jacoby, W. C. 204, 220
Jaeger, J. A. 129
Jailer, R. W. 220
Jamison, L. R. 109, 130
Johnson, C. S. 152, 157-158
Johnson, D. W. 2, 17-20, 29, 35, 47-48, 56-57, 64, 66-67, 81, 88-90, 95, 97, 103-105, 107, 115, 120, 132, 144, 173, 178, 182-187, 191-193, 198-199, 204, 206-209, 211-214, 216-217, 223, 226, 229, 237, 240, 242, 244-245, 250, 260, 264-266
Johnson, M. E. 175
Johnstone, D. S. 175
Jones, R. S. 81

Kane, M. T. 6, 50, 229, 243
Kaplan, D. L. 175
Kearney, P. 54, 145-146, 149, 151, 162
Keck, E. L. 109
Klimas, P. C. 20, 22, 70, 101, 111, 114, 147, 152, 157, 162
Knacke, T. W. 3, 5, 11-39, 45, 50-52, 56, 60, 64, 67-68, 76-77, 81, 88, 96-100, 102, 104, 106-110, 121, 129, 139, 162, 169-170, 175, 181-183, 196, 203, 207, 213-214, 219-220, 223-224, 226, 231, 237, 242, 254-255, 257, 260-262, 267
Koch, R. 173
Konicke, M. L. 129, 131, 136
Konicke, T. A. 136, 152
Krall, K. M. 81
Kross, D. A. 47, 67, 189, 226, 244, 273, 274
Kuethe, A. M. 95
Kuwahara, K. 112

Landon, R. H. 142
Larrivee, J. A. 78-80, 121
Lau, R. A. 31, 61, 130, 188
Lawrence, J. H. 112, 121
Lemke, R. 31
Lenius, W. W. 74, 76, 146
Lester, W. G. S. 78
Lin, X. 242
Lindh, K. G. 31, 130, 253, 259-260
Lindsey, P. J. 112, 117
Lingard, J. S. 54, 107, 145-146, 149, 151, 162
Lombardi, S. J. 175
Ludtke, W. P. 109
Ludwig, R. 78

Macha, J. M. 101, 114, 120, 156-157, 163-165
Madigan, D. K. 153
Maskell, E. C. 155-156
Matejka, D. Q. 129
Maydew, R. C. 6, 17-19, 35, 44, 48, 66-67, 97, 107, 115, 129, 183, 197, 204, 226, 229, 243, 245
Mayhue, R. J. 50, 145
Maynard, J. D. 45, 145
McBride, D. D. 163-165
McClow, J. H. 5, 35, 45, 51
McCoy, H. H. 112
McFall, J. C. 188
McGirr, P. A. 38
McShera, J. T. 61

McVey, D. F. 45, 65, 97-98, 109-110, 144, 251, 259-260, 264
Mead, J. W. 176
Mead, K. E. 176, 178
Melzig, H. D. 74, 113-114
Meyer, J. 112
Meyer, R. A. 145
Meyer, S. D. 20
Mikulas, M. M. 111
Moog, R. D. 31, 47, 67-68 89, 93, 95, 130, 143-144, 188-189, 226, 244, 274
Morris, F. B. 28
Mullins, W. M. 31, 129-130, 186, 253, 259-260
Muramoto, K. K. 71-72, 76, 129-130, 136, 152
Murrow, H. N. 188

Nellums, R. O. 250-251
Nerem, R. M. 60-61, 81, 109
Neustadt, M. 78-80, 121
Niccum, R. J. 74, 76, 146
Niemi, E. E. 137
Nisht, M. I. 112
Norden, M. L. 220
Noreen, R. A. 61, 67, 74, 76, 109, 113, 135
Norman, L. C. 57

O'Hara, F. 107, 130
Oler, J. W. 112, 120-121
Olevitch, A. 81
Orear, L. 176
Ottensoser, J. 74, 113-114

Pake, F. A. 109
Palm, L. 190
Park, W.-C. 112
Parker, J. A. 81
Paulsen, L. 242
Payne, P. R. 101
Pederson, P. E. 6, 50
Peñaranda, F. E. 139
Pepper, W. B. 1, 6, 19, 26-27, 31, 35-36, 44-48, 50, 54, 62, 65-67, 74, 76, 80-81, 87, 97, 107, 114-115, 133, 142, 144-147, 172-173, 176, 178-179, 182, 184, 186, 190, 197-198, 204-205, 220, 226, 229, 240-241, 243, 245, 252-254, 272, 276
Peters, W. L. 170
Peterson, C. W. 1-3, 19-22, 26-27, 29, 35, 47, 49-51, 54, 56-57, 62, 64, 67, 80-81, 88-90, 95, 97, 103-104, 107, 115, 120, 131-133, 144-145, 151, 157, 173, 184-186, 191-195, 198-199, 206-207, 217, 226, 229. 237, 240, 245, 260, 264-266, 272, 276, 278
Pinnell, W. R. 170-173
Piper, J. L. 76
Pirrello, C. J. 237
Pleasants, J. E. 188
Polpitiye, S. J. 101
Ponomarev, A. T. 112
Poole, C. J. 244
Poole, L. R. 97, 182
Post, H. N. 142
Preisser, J. S. 31. 51
Purvis, J. W. 28, 45-46, 65, 76, 89, 91-92, 95, 106, 111-112, 121-123, 145, 147, 197, 259, 260

Rao, P. P. 61
Ravnitzky, M. J. 174-175
Reddy, K. R. 106, 111
Reed, J. F. 45, 65, 74, 76, 114, 133, 144, 146-147
Reynolds, D. T. 31, 129-130, 186, 253, 259-260
Reysv, O. V. 112
Riabokin, T. 56-59
Riffle, A. B. 26, 35, 51, 64, 66-67, 78
Roberts, B. W. 71, 106, 111, 130, 147
Rodier, R. W. 188-189, 274
Rollstin, L. R. 1, 26-27, 49-50, 54, 62, 80, 107, 115, 133, 194-195, 229-230, 236-237, 244-245, 272
Ronquillo, K. L. 213
Rosenlof, K D. 45, 66
Rosenthal, A. J. 81
Ross, J. H. 170-171
Ruiz-Urbieta, M. 81
Runkle, R. E. 2, 50, 273-274
Rust, L. W. 61, 78
Ryan, P. E. 72
Rychnovsky, R. E. 20-21, 23, 151, 189, 213-214
Ryerson, D. E. 246

Saari, D. P. 74, 79, 102, 109, 114, 135, 152
Saliaris. C. 78
Samuels, R. D. 244
Sarpkaya, T. 101, 105, 112, 117, 121
Schatzle, P. R. 20, 23, 123
Schetzer, J. D. 95
Schilling, H. 123
Schindel, L. H. 226
Schlichting, H. 56
Schmidt, P. K. 74, 113
Schmidt, U. 162
Schmitt, J. C. 67
Schoeck, P. A. 81, 152
Schoppee, M. M. 81
Schulman, S. 175
Scott, C. J. 81, 152
Sheldon, D. D. 178
Shen, C. Q. 78
Sheppard, J. D. 47, 67, 189, 226, 244, 274
Shirayama, S. 112
Siemers, P. M. 31, 130
Slayman, R. G. 31, 130
Smith, G. J. 152, 157-158
Spahr, H. R. 78, 117, 120, 226, 273
Speelman, R. J. 28
Steeves, E. C. 113
Stein, K. 113
Steinberg, J. M. 81
Steinberg, S. 31, 130

Strickland, J. H. 112, 117, 120-121, 123
Sundberg, W. D. 91, 93-94, 98, 109, 121, 123, 133
Swain, L. M. 56
Synofzik, R. 36

Tadios, E. L. 178
Tallentire, F. I. 250, 274
Tate, R. E. 20, 22, 152, 157
Temin, S. C. 81
Terhune, J. E. 188-189
Thibault, G. 250
Thuss, R. C. 188-189
Timmons, J. D. 31, 130, 188
Toni, R. A. 97, 109, 197
Tory, C. 78, 121
Tubis, R. I. 213-214

Uotila, J. I. 45, 75-76
Utreja, L. R. 45, 66-68, 98, 143-144, 189, 274

van Every, D. H. 163-165
Vaughn, J. B. 74, 76
Vickers, J. R. 45, 143, 153, 162, 273
Von Kármán, T. 100

Wailes, W. K. 66
Walcott, W. B. 67, 77
Waye, D. E. 1-2, 20, 26-27, 35, 49-50, 54, 62, 80, 105, 107, 115, 133, 194-195, 213-214, 245, 272, 276, 278
Webb, D. 190
Webb, R. W. 273
Weber, T. 162
Weinberg, S. A. 38
Werme, T. D. 112
Whalley, I. A. 188
Whinery, L. D. 176, 178-179
White, B. R. 101
White, F. M. 78, 121-122
Whitesides, J. L. 97
Whitlock, C. H. 121, 123
Widdows, H. E. 95, 97, 162, 196-197, 217
Wilcox, B. 109
Wolf, D. F. 20, 22, 78, 97-98, 102-103, 106, 109-110, 117, 120-122, 131, 152-153, 157, 251, 259-260, 264, 272
Woodis, R. 2, 50, 274
Wu, K. S. 76, 129, 136, 152

Yavuz, T. 101

SUBJECT INDEX

Aerodynamic decelerator conferences, listing 3
Aerodynamic forces
  Added mass 99-105
  Deployment forces 88-98
  Drag 15, 44-52, 56-68, 99-106, 110, 113-121, 142-148, 155-159, 163, 172, 182, 185-187, 244-245, 254-255, 257, 259-262, 264-267, 270
  General parachute aerodynamics 43, 44
  Normal force 45, 92, 158
Aerodynamic heating 81, 152
Aircraft
  Crew module, F-111 29, 31, 95, 187, 244
  Crew module, XS-2 5
  Landing approach parachutes 102
Altitude measurement 224-226, 233-236, 238-239
Analog/digital computer simulation 22, 123
Angle of attack 45, 76, 79, 92, 122, 143, 150-151
Apollo capsule 31, 68, 130, 183
Artillery shells, recovery systems (see testing, artillery shell)
Axial force (see aerodynamic forces, drag)

Ballistic ranges (see testing, ballistic ranges)
Ballute 15, 37, 51, 55, 145
Base pressure 58
Break cords/ties 88, 181, 198-201, 216-217

CALA 75, 133
CANO 75, 130-136, 259
Canopy
  All-radial 19, 265
  Apex 12
  Biconical 12
  Collapse (see collapse)
  Fabrication 162, 213-214, 219
  Filling time (see inflation, inflation time)
  Geometry 12-39, 254, 265
  Gore 12, 65, 130, 254, 265
  Horizontal ribbons 13, 17, 27, 130-131, 251, 253-254, 256, 263-265, 274
  Layout 12-39, 162, 213-214, 254, 265
  Mini-radials 13, 19-20, 265
  Porosity 15-17, 21, 44-50, 62-65, 70-81, 98, 101, 113-114, 143-146, 150, 254-255, 264-265
  Pressure distribution (see pressure, canopy, distribution)
Canopy (continued)
  Radial ribbons 12, 13, 17, 19-20, 27-29, 131-133, 177-179, 185, 214, 256, 263
  Shape 15, 52-54, 74-75, 147, 241, 258, 271, 275
  Skirt band 12-13, 18, 20, 38, 133, 178-179, 253-254, 256, 263
  Stress distribution 129-137, 253, 259, 261
  Ties 87-88, 90, 196-201
  Vent 12-38, 54-55, 70-72, 98, 131-133, 148, 158, 216, 253-254, 256, 263-265
  Vertical ribbons 14, 16-19, 27-28, 30, 214, 253-254
Cluster parachutes
  Drag coefficient 65-68
  Stability 77-78
  Wind tunnel blockage 155-156
Collapse 43, 116-121, 260-270
Coordinate system 122-123
Cut knives (see deployment, cut knives)

Deceleration measurement 19, 24, 87, 97, 104, 114-115, 119, 132-133, 185, 236, 244-246, 251, 255, 257, 260-262, 265-267, 269, 274
Decelerator characteristics 11-39
Deployment
  Bags 11, 87-91, 96-98, 181-187, 196-201, 214-218, 253, 259
  Cut knives 87-88, 90, 207
  Methods 181-195
  Mortars and drogue guns 182, 188-189
  Pilot parachutes (see pilot parachutes)
  Thrusted base plate 189-191, 251-253
  Tractor rocket 182, 191-195
  Sequencing 87-88, 90-99
  Systems 181-201
Design safety factors 129-133
Diameter
  Constructed 14
  Nominal 14
  Projected 14
Drag (see aerodynamic forces, drag)
Dynamic pressure measurement 236, 245
Dynamic stability 76, 78-80, 105

Environmental simulation 175-179
Extraction parachutes (see pilot parachutes)

Fabrication methods (see canopy, fabrication)
Fabrics 169-179
Facilities (see testing)
Filling distance (see inflation, filling distance)
Filling time (see inflation, inflation time)
FIST 5, 8, 28
Flotation devices 207-212
Forebody wake interference (see listings under wakes)

Gore shape (see canopy, gore)

Heat-resistant drogue structure 6, 81
High-temperature-resistant materials 81, 169, 175

Infinite mass condition 98, 102, 142, 147
Inflation
  Filling distance 107
  Inflation time 98, 105-110, 114-115, 173, 181, 262, 265-266, 270
  Opening forces 1-2, 19, 24, 87, 98-106, 109-115, 129-133, 172, 184-185, 203, 229, 251-252, 254-255, 257, 259-262, 265-267, 269, 272-274
  Snatch load (see snatch load)
Instrumentation
  Ballistic range 225, 231-237
  Test vehicle 244-246
  Wind tunnel (see wind tunnel, instrumentation)

Joints and seams
  Strength loss 176-179
  Testing 176-179

Kevlar 1-2, 9, 20, 23, 48, 81, 90, 120, 133, 169-178, 184-187, 197-201, 214, 246, 252-254, 256, 259, 263, 274, 276

Lift/drag 21
Lifting decelerator (see parachutes, type, lifting conical ribbon)
Location devices 208-213
Low level (altitude) delivery 6, 20, 24-26, 115-117, 132, 197-198, 217, 226-230, 240-241

Materials
  Degradation of strength 175-179
  Strength 170-171, 176-179
  Testing 170-179
Mercury capsule 31
Missile and rocket payload recovery 2, 35, 67-68, 81, 130-132, 174, 182-184, 186-190, 207-213
Moment of inertia 122
Moment
  Pitching 22-24, 76-79, 149-152, 157-159
  Rolling 22-24, 151-152, 157-159
  Yawing 22-24, 151-152, 157-159
Navier-Stokes equations 112-113
Nominal parachute area 14
Nominal parachute diameter. 14
Normal force (see aerodynamic forces, normal force)

Omega sensor, stress 7, 135-137
Opening forces (see inflation, opening forces)
Opening time (see inflation, inflation time)
Oscillation (see stability)

Packing procedures 185, 190-191, 196-201, 214-219
Parachutes, type
  Ballute (see ballute)
  Disk-gap-band 15, 31-32, 50, 81, 130, 145, 188
  Equiflo 145-146, 149
  Guide surface, ribbed 5-6, 15, 31-34, 51, 72-73, 130, 142, 149-150
  Guide surface, ribless 15, 34-35, 182-184, 208, 210-211, 240-241
  Hemisflo 6, 15, 26-27, 50-51, 62, 64, 80, 115, 142, 145
  Hyperflo 6, 51, 54-55, 81, 145-146, 149
  Lifting conical ribbon 8, 15, 20-26, 123, 151-152, 157-161
  Parasonic 60
  Pilot parachutes (see pilot parachutes)
  Ribbon, conical 6, 15-20, 45-51, 54, 57, 62-68, 80-81, 87-89, 97, 103, 107, 113-115, 129-134, 142-151, 153, 155-157, 162, 170, 172-179, 183-194, 197-201, 211, 217, 226-229, 240, 244-246
  Ribbon, flat circular 5, 14-16, 45, 64, 72-74, 129, 136, 142, 152
  Ringsail 15, 30-31, 64, 66, 68, 130, 183, 188
  Ringslot 5, 15, 28, 50, 64, 67, 74, 102, 135, 142, 146, 149, 183, 188
  Ringslot/solid canopy 29, 187
  Rotafoil 5, 15, 35-36, 51
  Rotating flexible decelerator 35-36, 38
  Supersonic guide surface 54-55
  Supersonic-X 51, 54-55, 81, 145-146, 149, 152
  Vortex-ring 15, 35, 37, 51
Pilot parachutes 15, 35, 88-96, 114, 143, 172, 181-187, 196-201, 208, 216, 259-260, 274
Pocket bands 13, 18
Porosity (see canopy porosity)
Pressure packing 215-218

Pressure, canopy
  Analytical methods 69-71, 111-113, 130
  Coefficient 71, 73
  Distribution 69-76, 146-149
  Measurement 70-76, 113-114, 130, 136, 146-148

Quality assurance (see reliability)

Rate of descent measurement 233-236
Reefing
  Canopy skirt 18, 63-68, 114-115
  Drag, reefed 63-68, 114-115, 145, 153
  Line cutters 18, 63-64, 85, 203-207, 217, 221
  Permanent 81, 120
  Pressure distribution 147
  Ratio 64, 107
  Rings 18, 63
  Static stability 64, 77-78
Reentry vehicle recovery 184, 186, 240
Reliability 219-221
Roll-control system 22
Rolling moment (see moment, rolling)

Scaling laws 162-164
Sewing/seams 175-179, 213-214
Simulated deployment testing 143, 181-195
Sled ejector testing (see testing, sled ejector)
Sled captive/tow testing (see testing, captive sled)
Sled tracks 223, 237-239
Snatch load 19, 96-98, 181
Solid Rocket Booster, Space Shuttle, recovery system 2, 45, 47, 66-68, 98, 103, 131, 143, 153, 162, 189
Sounding rocket payload recovery (see missile and rocket payload recovery)
Spacecraft recovery 130, 188
Squidding 63, 80-81
Stability 15, 63, 76, 121-123, 149
  Dynamic 76, 78-80, 122
  Static 76-78, 149-152, 157-161
Stabilization parachutes 5, 15, 31-35
Standard atmosphere 224
Steady aerodynamic forces 43-81
Stitching (see sewing/seams)
Strength, joints and seams 175-179
Strength, material degradation 175-179
Stress measurements 135-138
Suspension lines 12, 18, 88-98, 129-133, 173-174, 178-179, 181-182, 185-192, 196-201, 203, 206-207, 216, 240
System reliability 219-221

Testing
  Aircraft drop test 5-6, 19, 24-26, 45, 48, 66, 78, 90, 104, 115-117, 132, 172, 183-186, 191-192, 223-228, 243, 249-274
  Artillery shell 2, 276-280
  Ballistic ranges 6, 25-26, 116, 223-225, 231-237
  Captive sled 5-6, 50-51, 223, 239-240
  Ejector sled 81, 108, 115-117, 172, 186, 197, 223, 240-241
  Rocket-boosted 6, 19, 27, 48-49, 66, 80-81, 103, 115, 132, 182-184, 207-212, 223-225, 229-230, 244, 254-258, 261, 264, 272
  Whirl tower 242
  Wind tunnel 5-6, 45, 49-53, 57-63, 70-81, 113-114, 134-136, 139-166, 226
Textiles (see materials)
Torpedoes 5, 31, 34

Velocity measurement 225-226, 233-241, 244-245
Viking decelerator 31, 188

Wakes
  Forebody, hypersonic 61
  Forebody, subsonic 56-59, 78
  Forebody, transonic and supersonic 59-63, 80-81, 89-90, 143-146
  Parachute (see canopy collapse)
Wind tunnel
  Instrumentation 22, 135-138, 142-161
  Listing 139-142

REPORT DOCUMENTATION PAGE

1. Recipient's Reference	2. Originator's Reference	3. Further Reference	4. Security Classification of Document
	AGARD-AG-319	ISBN 92-835-0649-9	UNCLASSIFIED

5. Originator Advisory Group for Aerospace Research and Development
North Atlantic Treaty Organization
7 rue Ancelle, 92200 Neuilly sur Seine, France

6. Title DESIGN AND TESTING OF HIGH-PERFORMANCE PARACHUTES

7. Presented at

8. Author(s)/Editor(s) R.C. Maydew and C.W. Peterson
Editor, K.J. Orlik-Rückemann

9. Date November 1991

10. Author's/Editor's Address See flyleaf.

11. Pages 306

12. Distribution Statement This document is distributed in accordance with AGARD policies and regulations, which are outlined on the back covers of all AGARD publications.

13. Keywords/Descriptors

Parachutes	Wind tunnel tests
Parachute fabrics	Flight tests
Design	Numerical analysis
Aerodynamics	Structural analysis

14. Abstract

This AGARDograph provides general state-of-the-art procedures for the design and testing of high-performance parachutes. This includes the use of aerodynamic and structural analysis and application of numerical codes to predict parachute inflation, deceleration forces, payload and parachute trajectories, and canopy/suspension line stresses. Design problems such as parachute collapse, parachute line sail, parachute stability, and body-wake interaction are discussed. The use of nylon, Nomex, Kevlar, Teflon, and other materials is covered. Techniques for the design and fabrication of prototype parachutes and deployment bags are presented, and parachute packing methods are discussed. A section is included on testing of model parachutes in wind tunnels. Full-scale testing, using a sled track or aircraft drop or rocket boost to deploy the parachute at the desired Mach number and altitude, and descriptions of onboard and ground-based instrumentation are outlined. Example parachute designs are given for differing system requirements of payload weight, deployment Mach number and dynamic pressure, parachute weight/volume, etc.

Design and testing information from 418 publications was synthesized for inclusion in this AGARDograph. These publications include eleven AIAA Aerodynamic Decelerator Conferences (1966–1991), four parachute technology workshops (1982–1990), the 1963 and 1978 USAF Parachute Design Guides and other open-literature parachute papers.

This AGARDograph has been produced at the request of the Fluid Dynamics Panel of AGARD.

AGARDograph 319 Advisory Group for Aerospace Research and Development, NATO DESIGN AND TESTING OF HIGH-PERFORMANCE PARACHUTES by R.C. Maydew and C.W. Peterson Published November 1991 306 pages This AGARDograph provides general state-of-the-art procedures for the design and testing of high-performance parachutes. This includes the use of aerodynamic and structural analysis and application of numerical codes to predict parachute inflation, deceleration forces, payload and parachute trajectories, and canopy/suspension line stresses. Design problems such as parachute collapse, P.T.O.	AGARD-AG-319 Parachutes Parachute fabrics Design Aerodynamics Wind tunnel tests Flight tests Numerical analysis Structural analysis	AGARDograph 319 Advisory Group for Aerospace Research and Development, NATO DESIGN AND TESTING OF HIGH-PERFORMANCE PARACHUTES by R.C. Maydew and C.W. Peterson Published November 1991 306 pages This AGARDograph provides general state-of-the-art procedures for the design and testing of high-performance parachutes. This includes the use of aerodynamic and structural analysis and application of numerical codes to predict parachute inflation, deceleration forces, payload and parachute trajectories, and canopy/suspension line stresses. Design problems such as parachute collapse, P.T.O.	AGARD-AG-319 Parachutes Parachute fabrics Design Aerodynamics Wind tunnel tests Flight tests Numerical analysis Structural analysis
AGARDograph 319 Advisory Group for Aerospace Research and Development, NATO DESIGN AND TESTING OF HIGH-PERFORMANCE PARACHUTES by R.C. Maydew and C.W. Peterson Published November 1991 306 pages This AGARDograph provides general state-of-the-art procedures for the design and testing of high-performance parachutes. This includes the use of aerodynamic and structural analysis and application of numerical codes to predict parachute inflation, deceleration forces, payload and parachute trajectories, and canopy/suspension line stresses. Design problems such as parachute collapse, P.T.O	AGARD-AG-319 Parachutes Parachute fabrics Design Aerodynamics Wind tunnel tests Flight tests Numerical analysis Structural analysis	AGARDograph 319 Advisory Group for Aerospace Research and Development, NATO DESIGN AND TESTING OF HIGH-PERFORMANCE PARACHUTES by R.C. Maydew and C.W. Peterson Published November 1991 306 pages This AGARDograph provides general state-of-the-art procedures for the design and testing of high-performance parachutes. This includes the use of aerodynamic and structural analysis and application of numerical codes to predict parachute inflation, deceleration forces, payload and parachute trajectories, and canopy/suspension line stresses. Design problems such as parachute collapse, P.T.O.	AGARD-AG-319 Parachutes Parachute fabrics Design Aerodynamics Wind tunnel tests Flight tests Numerical analysis Structural analysis

parachute line sail, parachute stability, and body-wake interaction are discussed. The use of nylon, Nomex, Kevlar, Teflon, and other materials is covered. Techniques for the design and fabrication of prototype parachutes and deployment bags are presented, and parachute packing methods are discussed. A section is included on testing of model parachutes in wind tunnels. Full-scale testing, using a sled track or aircraft drop or rocket boost to deploy the parachute at the desired Mach number and altitude, and descriptions of onboard and ground-based instrumentation are outlined. Example parachute designs are given for differing system requirements of payload weight, deployment Mach number and dynamic pressure, parachute weight/volume, etc.

Design and testing information from 418 publications was synthesized for inclusion in this AGARDograph. These publications include eleven AIAA Aerodynamic Decelerator Conferences (1966—1991), four parachute technology workshops (1982—1990), the 1963 and 1978 USAF Parachute Design Guides and other open-literature parachute papers.

This AGARDograph has been produced at the request of the Fluid Dynamics Panel of AGARD.

ISBN 92-835-0649-9

parachute line sail, parachute stability, and body-wake interaction are discussed. The use of nylon, Nomex, Kevlar, Teflon, and other materials is covered. Techniques for the design and fabrication of prototype parachutes and deployment bags are presented, and parachute packing methods are discussed. A section is included on testing of model parachutes in wind tunnels. Full-scale testing, using a sled track or aircraft drop or rocket boost to deploy the parachute at the desired Mach number and altitude, and descriptions of onboard and ground-based instrumentation are outlined. Example parachute designs are given for differing system requirements of payload weight, deployment Mach number and dynamic pressure, parachute weight/volume, etc.

Design and testing information from 418 publications was synthesized for inclusion in this AGARDograph. These publications include eleven AIAA Aerodynamic Decelerator Conferences (1966—1991), four parachute technology workshops (1982—1990), the 1963 and 1978 USAF Parachute Design Guides and other open-literature parachute papers.

This AGARDograph has been produced at the request of the Fluid Dynamics Panel of AGARD.

ISBN 92-835-0649-9

parachute line sail, parachute stability, and body-wake interaction are discussed. The use of nylon, Nomex, Kevlar, Teflon, and other materials is covered. Techniques for the design and fabrication of prototype parachutes and deployment bags are presented, and parachute packing methods are discussed. A section is included on testing of model parachutes in wind tunnels. Full-scale testing, using a sled track or aircraft drop or rocket boost to deploy the parachute at the desired Mach number and altitude, and descriptions of onboard and ground-based instrumentation are outlined. Example parachute designs are given for differing system requirements of payload weight, deployment Mach number and dynamic pressure, parachute weight/volume, etc.

Design and testing information from 418 publications was synthesized for inclusion in this AGARDograph. These publications include eleven AIAA Aerodynamic Decelerator Conferences (1966—1991), four parachute technology workshops (1982—1990), the 1963 and 1978 USAF Parachute Design Guides and other open-literature parachute papers.

This AGARDograph has been produced at the request of the Fluid Dynamics Panel of AGARD.

ISBN 92-835-0649-9

AGARD

NATO OTAN

7 RUE ANCELLE · 92200 NEUILLY-SUR-SEINE

FRANCE

Téléphone (1)47.38.57.00 · Télex 610 176

Télécopie (1)47.38.57.99

DIFFUSION DES PUBLICATIONS AGARD NON CLASSIFIEES

L'AGARD ne détient pas de stocks de ses publications, dans un but de distribution générale à l'adresse ci-dessus. La diffusion initiale des publications de l'AGARD est effectuée auprès des pays membres de cette organisation par l'intermédiaire des Centres Nationaux de Distribution suivants. A l'exception des Etats-Unis, ces centres disposent parfois d'exemplaires additionnels; dans les cas contraire, on peut se procurer ces exemplaires sous forme de microfiches ou de microcopies auprès des Agences de Vente dont la liste suite.

CENTRES DE DIFFUSION NATIONAUX

ALLEMAGNE
Fachinformationszentrum,
Karlsruhe
D-7514 Eggenstein-Leopoldshafen 2

BELGIQUE
Coordonnateur AGARD-VSL
Etat-Major de la Force Aérienne
Quartier Reine Elisabeth
Rue d'Evere, 1140 Bruxelles

CANADA
Directeur du Service des Renseignements Scientifiques
Ministère de la Défense Nationale
Ottawa, Ontario K1A 0K2

DANEMARK
Danish Defence Research Board
Ved Idraetsparken 4
2100 Copenhagen Ø

ESPAGNE
INTA (AGARD Publications)
Pintor Rosales 34
28008 Madrid

ETATS-UNIS
National Aeronautics and Space Administration
Langley Research Center
M/S 180
Hampton, Virginia 23665

FRANCE
O.N.E.R.A. (Direction)
29, Avenue de la Division Leclerc
92320, Châtillon sous Bagneux

GRECE
Hellenic Air Force
Air War College
Scientific and Technical Library
Dekelia Air Force Base
Dekelia, Athens TGA 1010

ISLANDE
Director of Aviation
c/o Flugrad
Reykjavik

ITALIE
Aeronautica Militare
Ufficio del Delegato Nazionale all'AGARD
Aeroporto Pratica di Mare
00040 Pomezia (Roma)

LUXEMBOURG
Voir Belgique

NORVEGE
Norwegian Defence Research Establishment
Attn: Biblioteket
P.O. Box 25
N-2007 Kjeller

PAYS-BAS
Netherlands Delegation to AGARD
National Aerospace Laboratory NLR
Kluyverweg 1
2629 HS Delft

PORTUGAL
Portuguese National Coordinator to AGARD
Gabinete de Estudos e Programas
CLAFA
Base de Alfragide
Alfragide
2700 Amadora

ROYAUME UNI
Defence Research Information Centre
Kentigern House
65 Brown Street
Glasgow G2 8EX

TURQUIE
Milli Savunma Başkanlığı (MSB)
ARGE Daire Başkanlığı (ARGE)
Ankara

LE CENTRE NATIONAL DE DISTRIBUTION DES ETATS-UNIS (NASA) NE DETIENT PAS DE STOCKS DES PUBLICATIONS AGARD ET LES DEMANDES D'EXEMPLAIRES DOIVENT ETRE ADRESSEES DIRECTEMENT AU SERVICE NATIONAL TECHNIQUE DE L'INFORMATION (NTIS) DONT L'ADRESSE SUIT.

AGENCES DE VENTE

National Technical Information Service
(NTIS)
5285 Port Royal Road
Springfield, Virginia 22161
Etats-Unis

ESA/Information Retrieval Service
European Space Agency
10, rue Mario Nikis
75015 Paris
France

The British Library
Document Supply Division
Boston Spa, Wetherby
West Yorkshire LS23 7BQ
Royaume Uni

Les demandes de microfiches ou de photocopies de documents AGARD (y compris les demandes faites auprès des CDV) doivent comporter la dénomination AGARD, ainsi que le numéro de série de l'AGARD (par exemple AGARD-AG-315). Des informations analogues, telles que le titre et la date de publication sont souhaitables. Veuiller noter qu'il y a lieu de spécifier AGARD-R-nnn et AGARD-AR-nnn lors de la commande de rapports AGARD et des rapports consultatifs AGARD respectivement. Des références bibliographiques complètes ainsi que des résumés des publications AGARD figurent dans les journaux suivants:

Scientifique and Technical Aerospace Reports (STAR)
publié par la NASA Scientific and Technical
Information Division
NASA Headquarters (NTT)
Washington D.C. 20546
Etats-Unis

Government Reports Announcements and Index (GRA&I)
publié par le National Technical Information Service
Springfield
Virginia 22161
Etats-Unis

(accessible également en mode interactif dans la base de données bibliographiques en ligne du NTIS, et sur CD-ROM)

Imprimé par Specialised Printing Services Limited
40 Chigwell Lane, Loughton, Essex IG10 3TZ

AGARD
NATO OTAN
7 RUE ANCELLE · 92200 NEUILLY-SUR-SEINE
FRANCE
Téléphone (1)47.38.57.00 · Telex 610 176
Telefax (1)47.38.57.99

DISTRIBUTION OF UNCLASSIFIED AGARD PUBLICATIONS

AGARD does NOT hold stocks of AGARD publications at the above address for general distribution. Initial distribution of AGARD publications is made to AGARD Member Nations through the following National Distribution Centres. Further copies are sometimes available from these Centres (except in the United States), but if not may be purchased in Microfiche or Photocopy form from the Sales Agencies listed below.

NATIONAL DISTRIBUTION CENTRES

BELGIUM
Coordonnateur AGARD — VSL
Etat-Major de la Force Aérienne
Quartier Reine Elisabeth
Rue d'Evere, 1140 Bruxelles

CANADA
Director Scientific Information Services
Dept of National Defence
Ottawa, Ontario K1A 0K2

DENMARK
Danish Defence Research Board
Ved Idraetsparken 4
2100 Copenhagen Ø

FRANCE
O.N.E.R.A. (Direction)
29 Avenue de la Division Leclerc
92320 Châtillon

GERMANY
Fachinformationszentrum
Karlsruhe
D-7514 Eggenstein-Leopoldshafen 2

GREECE
Hellenic Air Force
Air War College
Scientific and Technical Library
Dekelia Air Force Base
Dekelia, Athens TGA 1010

ICELAND
Director of Aviation
c/o Flugrad
Reykjavik

ITALY
Aeronautica Militare
Ufficio del Delegato Nazionale all'AGARD
Aeroporto Pratica di Mare
00040 Pomezia (Roma)

LUXEMBOURG
See Belgium

NETHERLANDS
Netherlands Delegation to AGARD
National Aerospace Laboratory, NLR
Kluyverweg 1
2629 HS Delft

NORWAY
Norwegian Defence Research Establishment
Attn: Biblioteket
P.O. Box 25
N-2007 Kjeller

PORTUGAL
Portuguese National Coordinator to AGARD
Gabinete de Estudos e Programas
CLAFA
Base de Alfragide
Alfragide
2700 Amadora

SPAIN
INTA (AGARD Publications)
Pintor Rosales 34
28008 Madrid

TURKEY
Millî Savunma Başkanlığı (MSB)
ARGE Daire Başkanlığı (ARGE)
Ankara

UNITED KINGDOM
Defence Research Information Centre
Kentigern House
65 Brown Street
Glasgow G2 8EX

UNITED STATES
National Aeronautics and Space Administration (NASA)
Langley Research Center
M/S 180
Hampton, Virginia 23665

THE UNITED STATES NATIONAL DISTRIBUTION CENTRE (NASA) DOES NOT HOLD STOCKS OF AGARD PUBLICATIONS, AND APPLICATIONS FOR COPIES SHOULD BE MADE DIRECT TO THE NATIONAL TECHNICAL INFORMATION SERVICE (NTIS) AT THE ADDRESS BELOW.

SALES AGENCIES

National Technical
Information Service (NTIS)
5285 Port Royal Road
Springfield, Virginia 22161
United States

ESA/Information Retrieval Service
European Space Agency
10, rue Mario Nikis
75015 Paris
France

The British Library
Document Supply Centre
Boston Spa, Wetherby
West Yorkshire LS23 7BQ
United Kingdom

Requests for microfiches or photocopies of AGARD documents (including requests to NTIS) should include the word 'AGARD' and the AGARD serial number (for example AGARD-AG-315). Collateral information such as title and publication date is desirable. Note that AGARD Reports and Advisory Reports should be specified as AGARD-R-nnn and AGARD-AR-nnn, respectively. Full bibliographical references and abstracts of AGARD publications are given in the following journals:

Scientific and Technical Aerospace Reports (STAR)
published by NASA Scientific and Technical
Information Division
NASA Headquarters (NTT)
Washington D.C. 20546
United States

Government Reports Announcements and Index (GRA&I)
published by the National Technical Information Service
Springfield
Virginia 22161
United States
(also available online in the NTIS Bibliographic Database or on CD-ROM)

Printed by Specialised Printing Services Limited
40 Chigwell Lane, Loughton, Essex IG10 3TZ

ISBN 92-835-0649-9